

ADVANCES in COMPUTATIONAL Fluid Dynamics

GUEST EDITORS: MAHESH T. DHOTRE, NANDKISHOR KRISHNARAO NERE, SREEDRIYA VEDANTAM,
AND MANDAR TABIB





Advances in Computational Fluid Dynamics

International Journal of Chemical Engineering

Advances in Computational Fluid Dynamics

Guest Editors: Mahesh T. Dhotre,
Nandkishor Krishnarao Nere, Sreepriya Vedantam,
and Mandar Tabib



Copyright © 2013 Hindawi Publishing Corporation. All rights reserved.

This is a special issue published in “International Journal of Chemical Engineering.” All articles are open access articles distributed under the Creative Commons Attribution License, which permits unrestricted use, distribution, and reproduction in any medium, provided the original work is properly cited.

Editorial Board

Muthanna Al-Dahhan, USA
Miguel J. Bagajewicz, USA
Alfons Baiker, Switzerland
Jerzy Bałdyga, Poland
Mostafa Barigou, UK
Gino Baron, Belgium
Hans-Jörg Bart, Germany
Raghunath V. Chaudhari, USA
Jean-Pierre Corriou, France
Donald L. Feke, USA
James J. Feng, Canada
Rafiqul Gani, Denmark
Jinlong Gong, China
Thomas R. Hanley, USA
Michael Harris, USA

Kus Hidajat, Singapore
Vladimir Hlavacek, USA
Xijun Hu, Hong Kong
M. G. Ierapetritou, USA
Dilhan M. Kalyon, USA
Kyung Aih Kang, USA
Iftekhar A. Karimi, Singapore
B. D. Kulkarni, India
Deepak Kunzru, India
Janez Levec, Slovenia
Jose C. Merchuk, Israel
Badie I. Morsi, USA
S. Murad, USA
Dmitry Murzin, Finland
Ahmet N. Palazoglu, USA

Fernando T. Pinho, Portugal
Peter N. Pintauro, USA
Doraiswami Ramkrishna, USA
Alírio Rodrigues, Portugal
Jose Alberto Romagnoli, USA
Adrian Schumpe, Germany
Moshe Sheintuch, Israel
Katsumi Tochigi, Japan
Evangelos Tsotsas, Germany
Toshinori Tsuru, Japan
Tapio Westerlund, Finland
Jaime Wisniak, Israel
King Lun Yeung, Hong Kong
Zhibing Zhang, UK

Contents

Advances in Computational Fluid Dynamics, Mahesh T. Dhotre, Nandkishor Krishnarao Nere, Sreepriya Vedantam, and Mandar Tabib
Volume 2013, Article ID 917373, 2 pages

Large Eddy Simulation for Dispersed Bubbly Flows: A Review, M. T. Dhotre, N. G. Deen, B. Niceno, Z. Khan, and J. B. Joshi
Volume 2013, Article ID 343276, 22 pages

Bubble Dynamics of a Single Condensing Vapor Bubble from Vertically Heated Wall in Subcooled Pool Boiling System: Experimental Measurements and CFD Simulations, Arijit A. Ganguli, Aniruddha B. Pandit, and Jyeshtharaj B. Joshi
Volume 2012, Article ID 712986, 11 pages

CFD Simulation of Annular Centrifugal Extractors, S. Vedantam, K. E. Wardle, T. V. Tamhane, V. V. Ranade, and J. B. Joshi
Volume 2012, Article ID 759397, 31 pages

CFD Modeling of Solid Suspension in a Stirred Tank: Effect of Drag Models and Turbulent Dispersion on Cloud Height, Shitanshu Gohel, Shitalkumar Joshi, Mohammed Azhar, Marc Horner, and Gustavo Padron
Volume 2012, Article ID 956975, 9 pages

A *Priori* Direct Numerical Simulation Modelling of the Curvature Term of the Flame Surface Density Transport Equation for Nonunity Lewis Number Flames in the Context of Large Eddy Simulations, Mohit Katragadda and Nilanjan Chakraborty
Volume 2012, Article ID 103727, 14 pages

Analysis of Hydrodynamics of Fluid Flow on Corrugated Sheets of Packing, Kumar Subramanian and Gnter Wozny
Volume 2012, Article ID 838965, 13 pages

Mixing Study in an Unbaffled Stirred Precipitator Using LES Modelling, Murielle Bertrand, Delphine Parmentier, Olivier Lebaigue, Edouard Plasari, and Frédéric Ducros
Volume 2012, Article ID 450491, 11 pages

Chemical Kinetic Study of Nitrogen Oxides Formation Trends in Biodiesel Combustion, Junfeng Yang, Valeri I. Golovitchev, Pau Redón Lurbe, and J. Javier López Sánchez
Volume 2012, Article ID 898742, 22 pages

Computational Fluid Dynamics of Two-Opposed-Jet Microextractor, Pritam V. Hule, B. N. Murthy, and Channamallikarjun S. Mathpati
Volume 2012, Article ID 264184, 11 pages

Numerical Studies on Heat Release Rate in Room Fire on Liquid Fuel under Different Ventilation Factors, N. Cai and W. K. Chow
Volume 2012, Article ID 910869, 13 pages

Effects of Gravity and Inlet Location on a Two-Phase Countercurrent Imbibition in Porous Media, M. F. El-Amin, Amgad Salama, and Shuyu Sun
Volume 2012, Article ID 210128, 7 pages



Numerical Simulation of LVAD Inflow Cannulas with Different Tip, Guang-Mao Liu, Hai-Bo Chen, Fu-Liang Luo, Yan Zhang, Han-Song Sun, Jian-Ye Zhou, and Sheng-Shou Hu
Volume 2012, Article ID 596960, 8 pages

Optimization of Wind Turbine Airfoil Using Nondominated Sorting Genetic Algorithm and Pareto Optimal Front, Ziaul Huque, Ghizlane Zemmouri, Donald Harby, and Raghava Kommalapati
Volume 2012, Article ID 193021, 9 pages

CFD Simulation of Transonic Flow in High-Voltage Circuit Breaker, Xiangyang Ye and Mahesh Dhotre
Volume 2012, Article ID 609486, 9 pages

The Flow Pattern in Single and Multiple Submerged Channels with Gas Evolution at the Electrodes, A. Alexiadis, M. P. Dudukovic, P. Ramachandran, A. Cornell, J. Wanngård, and A. Bokkers
Volume 2012, Article ID 392613, 9 pages

CFD Modeling of Gas-Liquid Bubbly Flow in Horizontal Pipes: Influence of Bubble Coalescence and Breakup, K. Ekambara, R. Sean Sanders, K. Nandakumar, and J. H. Masliyah
Volume 2012, Article ID 620463, 20 pages

Editorial

Advances in Computational Fluid Dynamics

Mahesh T. Dhotre,¹ Nandkishor Krishnarao Nere,² Sreepriya Vedantam,³ and Mandar Tabib⁴

¹ABB Switzerland Ltd., Fabrikstrasse 13a, 5400 Baden, Switzerland

²Aditya Birla Science and Technology Company Ltd., Plot No. 1 & 1-A/1, MIDC Talaja, Panvel, Maharashtra 410208, India

³CEPD Division, National Chemical Laboratory (NCL), Pashan Road, Pune 411008, India

⁴Flow Technology Group, SINTEF Materials and Chemistry, Grønbygge, Gløshaugen, Trondheim, Norway

Correspondence should be addressed to Mahesh T. Dhotre; mahesh.dhotre@ch.abb.com

Received 19 December 2012; Accepted 19 December 2012

Copyright © 2013 Mahesh T. Dhotre et al. This is an open access article distributed under the Creative Commons Attribution License, which permits unrestricted use, distribution, and reproduction in any medium, provided the original work is properly cited.

1. Introduction

Over the past few decades, Computational Fluid Dynamics (CFD) has emerged as a powerful tool for the design and optimization of new products and processes. It is widely used in a variety of applications and industries such as chemical, petroleum, aerospace, automotive, power generation, polymer processing, medical research, construction, meteorology, and so forth. Some of the key offerings include the design reliability and reduction in the time and cost of the product development.

A significant research is being carried out in a quest to model the physics accurately and to develop robust and efficient numerics (solution algorithms and accurate discretization methods). The interaction between the CFD and disciplines like solid mechanics and optimization algorithm is also evolving. However, focus of the research still remains on the most challenging topics in fluid mechanics, namely, the turbulence and the multiphase flow that also form the common theme of papers presented in this special issue.

1.1. Turbulence. Direct Numerical Simulation approach requires no modeling. However, it remains a research tool with today's available computer power and useful for gaining insight into turbulence physics, calibrating the models, and scaling laws. For practical engineering applications, a great deal of efforts are devoted to the development of turbulence models (e.g., approaches based on Reynolds Averaged Navier Stokes (RANS) equations). The strengths and weaknesses of these models are now well known and alternatives approaches

such as Large Eddy Simulation (LES) and hybrid RANS/LES turbulence models are being explored.

At this stage, the development in high-performance computing has huge impact on the computational progress. The RANS approach is being used for more complex problems involving unsteadiness, coupled physics, and complex geometry. LES has become feasible for the simplified industrial systems and even being attempted for more realistic geometries. However, bottleneck is better models for small scale turbulence and associated computational cost for integrating CFD with the design cycle in the industry.

1.2. Multiphase Flow. Multiphase flow combined with the turbulence pose formidable challenge for simulation even for the dilute dispersed phase. Many approaches are being considered mainly through, variation in reference frame representations (Eulerian or Lagrangian); phase coupling (intrapphase and/or interphase coupling); and particle/flow details (e.g., resolution around single bubble or bulk description of many bubbles). These approaches come with huge variations in computational time and predictive capability.

The challenge is also to incorporate important flow details such as (a) the impact of deformation rate on bubble/particle breakup and coalescence, (b) the phenomenon like turbulent modulation (dispersed phase particle can either augment or attenuate the turbulence in the continuous phase), (c) turbulent dispersion (the eddies in the continuous phase can cause dispersed particles to be transported from regions of higher concentration to regions of lower concentration).

The multiphase research is being driven by all these aforementioned challenges and progress is under way. The significant contributions are required to arrive to a stage where it can be used with a higher degree of confidence.

2. Summary

The special issue covers a broad spectrum of CFD applications and developments. There are sixteen papers presented; two reviews discuss the state-of-the-art CFD modeling and its applications for the dispersed bubbly flows and annular flow in centrifugal extractors. Three papers focus on important multiphase flows topics: the bubble dynamics in the boiling phenomena, bubble coalescence and breakup in gas liquid bubbly flows and effect of drag models and turbulent dispersion in solid suspension. CFD and design related applications have been explored in papers for two-opposed-jet microextractor, high voltage circuit breaker and corrugated sheets of packing in a gas liquid contactors. Optimization algorithm and CFD coupling is investigated in one paper for the design of wind turbine airfoil. CFD analysis is presented in two papers for predicting the heat release rate in fire application and tip structure design of LVAD inflow cannula in medical application. One paper examines the influence of gravity on countercurrent imbibition of two-phase flow in porous media. LES approach is explored in two papers for applications in combustion and mixing in stirred precipitator. In another two separate papers, simulations are presented investigating chemical kinetics of nitrogen oxides formation and flow pattern in submerged channels at electrodes.

We hope that the issue will be interesting for scientists from both the industry and academia as well as for practicing engineers involved in CFD simulations. The earnest desire of this issue is also to provide insights into some of the open questions by throwing light on the requirements for further research.

*Mahesh T. Dhotre
Nandkishor Nere
Sreepriya Vedantam
Mandar Tabib*

Review Article

Large Eddy Simulation for Dispersed Bubbly Flows: A Review

M. T. Dhotre,¹ N. G. Deen,² B. Niceno,³ Z. Khan,⁴ and J. B. Joshi^{4,5}

¹ ABB Switzerland Ltd., 5400 Baden, Switzerland

² Multiphase Reactors Group, Department of Chemical Engineering and Chemistry, Eindhoven University of Technology, The Netherlands

³ Laboratory for Thermal-Hydraulics, Nuclear Energy and Safety Department, Paul Scherrer Institute, Switzerland

⁴ Institute of Chemical Technology, Matunga, Mumbai 400 019, India

⁵ Homi Bhabha National Institute, Anushakti Nagar, Mumbai 400 094, India

Correspondence should be addressed to M. T. Dhotre; maheshdhotre@gmail.com

Received 14 June 2012; Revised 31 October 2012; Accepted 18 November 2012

Academic Editor: Nandkishor Nere

Copyright © 2013 M. T. Dhotre et al. This is an open access article distributed under the Creative Commons Attribution License, which permits unrestricted use, distribution, and reproduction in any medium, provided the original work is properly cited.

Large eddy simulations (LES) of dispersed gas-liquid flows for the prediction of flow patterns and its applications have been reviewed. The published literature in the last ten years has been analysed on a coherent basis, and the present status has been brought out for the LES Euler-Euler and Euler-Lagrange approaches. Finally, recommendations for the use of LES in dispersed gas liquid flows have been made.

1. Introduction

Gas-liquid flows are often encountered in the chemical process industry, but also numerous examples can be found in petroleum, pharmaceutical, agricultural, biochemical, food, electronic, and power-generation industries. The modelling of gas-liquid flows and their dynamics has become increasingly important in these areas, in order to predict flow behaviour with greater accuracy and reliability. There are two main flow regimes in gas-liquid flows: separated (e.g., annular flow in vertical pipes, stratified flow in horizontal pipes) and dispersed flow (e.g., droplets or bubbles in liquid). In this work, we consider only dispersed bubbly flows.

Dispersed Bubbly Flow. The description of bubbly flows involves modelling of a deformable (gas-liquid) interface separating the phases; discontinuities of properties across the phase interface; the exchange between the phase; and turbulence modelling. Most of the dispersed flow models are based on the concept of a domain in the static (Eulerian) reference frame for description of the continuous phase, with addition of a reference frame for the description of the dispersed phase. The dispersed phase may be described in the same static reference frame as the continuous, leading to the Eulerian-Eulerian (E-E) approach or in a dynamic (Lagrangian)

reference frame, leading to the Eulerian-Lagrangian (E-L) approach.

In the E-L approach, the continuous liquid phase is modelled using an Eulerian approach and the dispersed gas phase is treated in a Lagrangian way; that is, the individual bubbles in the system are tracked by solving Newton's second law, while accounting for the forces acting on the bubbles. An advantage here is the possibility to model each individual bubble, also incorporating bubble coalescence and breakup directly. Since each bubble path can be calculated accurately within the control volume, no numerical diffusion is introduced into the dispersed phase computation. However, a disadvantage is, the larger the system gets the more equations need to be solved, that is, one for every bubble.

The E-E approach describes both phases as two continuous fluids, each occupying the entire domain, and interpenetrating each other. The conservation equations are solved for each phase together with interphase exchange terms. The E-E approach can suffer from numerical diffusion. However, with the aid of higher order discretization schemes, the numerical diffusion can be reduced sufficiently and can offer the same order of accuracy as with E-L approach (Sokolichin et al. [1]). The advantage here is that the computational demands are far lower compared to the E-L approach, particularly for

systems with higher dispersed void fractions. We review these approaches here with respect to the turbulence descriptions.

Turbulence Modelling. The major difficulty in modelling multiphase turbulence is the wide range of length and time scales on which turbulent mixing occurs. The largest eddies are typically comparable in size to the characteristic length of the mean flow. The smallest scales are responsible for the dissipation of turbulence kinetic energy. The Direct Numerical Simulation (DNS) approach, with no modelling, resolves all the scales present in turbulence. However, it is not feasible for practical engineering problems involving high Reynolds number flows. The Reynolds-Averaged Navier–Stokes (RANS) approach is more feasible; it models the time-averaged velocity field either by using turbulent viscosity or by modelling the Reynolds stresses directly.

The large eddy simulation (LES) falls between DNS and RANS in terms of the fraction of the resolved scales. In LES, large eddies are resolved directly, that is, on a numerical grid, while small, unresolved eddies are modelled. The principle behind LES is justified by the fact that the larger eddies, because of their size and strength, carry most of the flow energy (typically 90%) while being responsible for most of the transport, and therefore they should be simulated precisely (i.e., resolved). On the other hand, the small eddies have relatively little influence on the mean flow and thus can be approximated (i.e., modelled). This approach to turbulence modelling also allows a significant decrease in the computational cost over direct simulation and captures more dynamics than a simple RANS model.

In RANS models often the assumption of isotropic turbulence is made for the core of the flow, which is not valid in dispersed bubbly flows; that is, the velocity fluctuations in the gravity direction are typically twice those in the other directions. This assumption is not made in LES for large structures of the flow, giving LES an advantage over RANS for the core regions of the flow. However, the situation is different close to the walls, where LES' assumption of isotropic turbulence is heavily violated, due to the absence of large eddies close to the walls.

2. LES for Dispersed Bubbly Flows

In dispersed bubbly flows, the large-scale turbulent structures interact with bubbles and are responsible for the macroscopic bubble motion, whereas small-scale turbulent structures only affect small-scale bubble oscillations. Since, large scales (carrying most of the energy) are explicitly captured in LES and the less energetic small scales are modelled using a subgrid-scale (SGS) model, LES can reasonably reproduce the statistics of the bubble-induced velocity fluctuations in the liquid.

There are three important considerations for modelling of dispersed bubbly flows.

- (1) Separation of length scales of the interface, that is, micro-, meso-, and macroscales. The separation of these scales forms the basis for “filtering” the Navier–Stokes equations and applying proper model

equations for multiphase situation. Important for dispersed flow is to identify the scales at which the governing equations are to be applied; microscales, that is, scales which are small enough to describe individual bubble shapes; mesoscales, which are comparable to bubble sizes; and macroscales, which entail enough bubbles for statistical representation.

- (2) The grid-scale equations. Depending on the ratio of the length scales introduced above, with the grid resolution we can afford, on a given computer hardware, a proper form of the governing equations must be chosen. For instance, if the mesh size is in the micro-scale order, one can use single-fluid, interface tracking techniques to solve the problem. If, on the other hand, the grid size is large enough for statistical description of bubbles, the E-E approach can be used. Should the grid size be comparable to the meso-scales, we are in a limiting area for both approaches, and special care must be taken in order to solve equations which describe the underlying physics consistently.
- (3) The physical models. Depending on the selected grid-scale equations, physical models of various complexities must be employed. The options here are numerous, whether they concern turbulence modelling or interphase modelling, but these models are generally simpler in case more of the microscales are resolved.

In the following sections, we describe each of these three elements to model turbulent dispersed bubbly flow.

2.1. Filtering Operation. The aim of filtering the Navier-Stokes equations is to separate the resolved scales from the SGS (nonresolved). The interface between the phases, and the level of detail required in its resolution/modelling, defines the filter in a multiphase flow.

When LES is applied at a micro-scale, filtering of turbulent fluctuations needs to be combined with interface tracking methods. These methods have been developed and used in both dispersed flow and free surface flow by Bois et al. [2], Toutant et al. [3, 4], Magdeleine et al. [5], Lakehal [6], and Lakehal et al. [7]. These methods require that all phenomena having an influence on space and time position of the interface are also simulated. For the amount of details required and the large size of practical problems of interest, these types of models should merely be seen as a support for the modelling and validation of more macroscopic approaches and cannot address a real industrial-scale problem (Bestion [8]).

When LES is applied at a macro-scale, the interface resolution is not considered. However, in practical simulations, these would require too coarse grids, leading to poor resolution of turbulence quantities. Much more often we are in the meso-scale region, in which the mesh size is comparable to bubble sizes. This pushes the main assumptions of the E-E approach to its limit of validity, and the grid is not fine enough for full interface tracking. In other words, the mesh requirement for E-E multiphase modelling conflicts with the requirements by LES approaches [9].

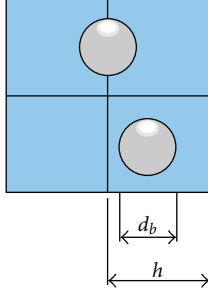


FIGURE 1: Milelli condition (from Niceno et al. [10]).

The issue of the requirement of the mesh size was first addressed by Milelli et al. [11] who carried out a systematic analysis and performed a parametric study with different mesh sizes and bubble diameters. They showed that for case of a shear layer laden with bubbles it was possible to provide an optimum filter width $1.2 < \Delta/d_b < 1.5$, where Δ is the filter width and d_b is the bubble diameter (shown in Figure 1). This means that the grid space should be at least 50% larger than the bubble diameter. The constraint imposed on the ratio Δ/d_b implies that the interaction of bubbles with the smallest resolved scales is captured without additional approximation.

2.2. Grid-Scale Equations. The principle of the LES formulation is to decompose the instantaneous flow field into large-scale and small-scale components via a filtering operation. If $\bar{\phi}_f$ denotes the filtered or grid-scale component of the variable ϕ_f that represents the large-scale motion then

$$\phi_f = \underbrace{\bar{\phi}_f}_{\text{resolved}} + \underbrace{\phi'_f}_{\text{subgrid}}, \quad (1)$$

where ϕ is the variable of interest, subscript f refers either to the liquid or the gas phase. In the remainder of this paper, we omit the bars of all resolved variables for the sake of simplicity. The following filtered equations are obtained:

$$\frac{\partial}{\partial t} (\alpha_f \rho_f \mathbf{u}_f) + \Delta \cdot (\alpha_f \rho_f \mathbf{u}_f) = 0, \quad (2)$$

$$\begin{aligned} \frac{\partial}{\partial t} (\alpha_f \rho_f \mathbf{u}_f) + \Delta \cdot (\alpha_f \rho_f \mathbf{u}_f \mathbf{u}_f) \\ = -\nabla \cdot (\alpha_f \boldsymbol{\tau}_f) - \alpha_f \nabla p + \alpha_f \rho_f \mathbf{g} + \mathbf{M}_f. \end{aligned} \quad (3)$$

The right hand side terms of (3) are, respectively, the stress, the pressure gradient, gravity, and the momentum exchange between the phases due to interface forces.

The SGS stress tensor which reflects the effect of the unresolved scales on the resolved scales is modelled as

$$\boldsymbol{\tau}_f = -\mu_{\text{eff},f} \left(\nabla \mathbf{u}_f + (\nabla \mathbf{u}_f)^T - \frac{2}{3} I (\nabla \cdot \mathbf{u}_f) \right), \quad (4)$$

where $\mu_{\text{eff},f}$ is the effective viscosity.

In the E-E approach, separate equations are required for each phase (see (3), $f = l, g$), together with interphase exchange terms (for details, Drew [12]). In most of the

investigations, turbulence is taken into consideration for the continuous phase by SGS models. The dispersed gas phase is modelled as laminar, but influence of the turbulence in the continuous phase is considered by a bubble-induced turbulence (BIT) model.

In the E-L approach, there are two coupled parts: a part dealing with the liquid phase motion and a part describing the bubbles motion. The dynamics of the liquid are described in a similar way as in the E-E approach, whereas the bubble motion is modelled through the second law of Newton.

Since, the governing equations for the liquid and gas phase are expressed in the Eulerian and Lagrangian reference frames, respectively; a mapping technique is used to exchange interphase coupling quantities. Depending upon the volume fraction of the dispersed phase, one-way (e.g., $\alpha_g < 10^{-6}$) or two-way coupling between gas phase to liquid phase ($10^{-6} < \alpha_g < 10^{-3}$) prevails. In both cases, bubble-bubble interactions (i.e., collisions) can be neglected, but the effect of the bubbles on the turbulence structure in the continuous phase has to be considered for higher volume fraction and does not play any role in lower volume fraction of gas phase Elgobashi [13]. The work reviewed here considers the two-way coupling which consists of the following.

2.2.1. Forward Coupling (Liquid to Bubble). In the forward coupling, calculated liquid velocities, velocity gradients, and pressure gradients on an Eulerian grid are interpolated to discrete bubble locations for solving the Lagrangian bubble equation motion.

2.2.2. Backward or Reversed Coupling (Bubble to Liquid). The forces available at each bubble's centroid need to be mapped back to the Eulerian grid nodes in order to evaluate the reaction force F . The two-way interaction (forward and backward) is accomplished with a mapping method, for example, PSI-cell method [14], modified PSI-wall-method [15], or mapping functions discussed by Deen et al. [16].

2.3. Interfacial Forces. The motion of a single bubble with constant mass can be written according to Newton's second law:

$$m_b \frac{d\mathbf{v}}{dt} = \sum \mathbf{F}. \quad (5)$$

The bubble dynamics are described by incorporating all relevant forces acting on a bubble rising in a liquid. It is assumed that the total force, $\sum \mathbf{F}$, is composed of separate and uncoupled contributions originating from pressure, gravity, drag, lift, virtual mass, wall lubrication and wall deformation turbulent dispersion:

$$\sum \mathbf{F} = \mathbf{F}_P + \mathbf{F}_G + \mathbf{F}_D + \mathbf{F}_L + \mathbf{F}_{VM} + \mathbf{F}_{TD} + \mathbf{F}_{WL} + \mathbf{F}_{WD}. \quad (6)$$

For each force the analytical expression or a semiempirical model is used, based on bubble behaviour observed in experiment or in DNS.

To summarize, the influence/contribution of these forces are as follows.

- (1) The modeling of the lift force for capturing bubble plume meandering and bubble dispersion is important. However there is an uncertainty regarding appropriate value or correlation representing lift coefficient. There is also recommendation that bubble size-dependent lift coefficient should be chosen [17].
- (2) The value of the lift coefficient can be different than the one used in RANS approach. It is because of different handling of factors responsible for bubble dispersion, that is, the interaction between the bubbles and influence of turbulent eddies in the liquid phase. In RANS approach, they are considered by means of the lift and turbulent dispersion force, with uncertainty of exact contribution of the individual forces. Most of the investigators use a constant value of the lift coefficient ($C_L = 0.5$), while the value of the turbulent dispersion coefficient is varied (0.1 to 1.0) to get good agreement with the experimental data. However, in LES, bubble dispersion caused by liquid phase turbulent eddies is implicitly calculated, and a more realistic contribution of the lift force can be used. The coefficient for the effective lift force thus may vary between the two approaches [18].
- (3) The virtual mass force is proportional to the relative acceleration between the phases and is negligible once a pseudosteady state is reached. It has little influence on the simulation results for bubble plumes [19], Milelli [20]. It is mainly because of the acceleration and deceleration effects are restricted to small end regions of the column. A constant coefficient is used in almost all investigations.
- (4) In LES, through filtering, velocities are decomposed into a resolved and a SGS part. The resolved part of the turbulent dispersion is implicitly computed. However, in case of a bubble size smaller than the filter size, turbulent transport can be present at SGS level and should be considered [9]. This can be done using a one-equation model, wherein it can be modelled by replacing the total kinetic energy by SGS contribution (k_{SGS}). By the same argument, other forces also need modelling at SGS level.

The values or expressions for the coefficient of drag, lift and virtual mass force used by different investigators are given in Tables 1 and 3.

2.4. SGS Models. It is well known that in turbulent flow energy generally cascades from large to small scales. The primary task of the SGS model therefore is to ensure that the energy drain in the LES is same as obtained with the cascade fully resolved as one would have in a DNS. The cascading, however, is an average process. Locally and instantaneously the transfer of energy can be much larger or much smaller than the average and can also occur in the opposite direction (“backscatter”).

2.4.1. Smagorinsky [21] Model. The simplest, well-known, and mostly used Smagorinsky [21] model is based on the

Boussinesq hypothesis. It requires the definition of time and length scales and a model constant. Smagorinsky used the following expression to calculate the turbulent viscosity, that is, the SGS viscosity:

$$\mu_{\text{eff},l} = \mu_{\text{lam},l} + \rho_l (C_S \Delta)^2 \sqrt{S^2}, \quad (7)$$

where $\mu_{\text{lam},l}$ is the (laminar) dynamic viscosity, C_S is the Smagorinsky constant, S is the characteristic strain tensor of filtered velocity, and Δ is the filter width, usually taken as the cubic root of the cell volume.

In the single-phase flow literature, the value of the constant used is in the range from $C_S = 0.065$ (Moin and Kim [22]) to $C_S = 0.25$ (Jones and Wille [23]). The value of C_S used in gas-liquid flows varies from that of single phase flow and is in the range of 0.08 to 0.12 [11, 20, 24, 25]. The lower range of C_S value, compared to single phase, could be attributed to the interphase coupling term, which acts as a form of SGS model and can make contribution to the turbulent kinetic energy dissipation. The sensitivity analysis carried out for C_S value shows that larger C_S values can produce excessive damping effect to the liquid velocity field and eventually leads to a steady-state solution [26, 27].

The main reason for the frequent use of the Smagorinsky model is its simplicity. Its drawbacks are that the constant C_S has to be calibrated and its optimal value may vary with the type of flow or the discretization scheme. Moreover, the model is purely dissipative and hence does not account either for the small-scale effect on the large scales adequately (by neglecting the “backscatter” of turbulent energy), while it acts purely as a drain for the turbulent kinetic energy.

The dynamic model, originally proposed by Germano et al. [28], eliminates some of these disadvantages by calculating the Smagorinsky constant as a function of space and time from the smallest scales of the resolved motion.

2.4.2. Dynamic SGS Model. The dynamic SGS model assumes SGS turbulent energy to be in local equilibrium (i.e., production = dissipation). The eddy viscosity is estimated from (7) but with a C_S as a local, time-dependent variable.

The basic idea is to apply a second test filter to the equations. The new filter width, twice the size of the grid filter, produces a resolved flow field. The difference between the two resolved fields is the contribution of the small scales whose size is in between the grid filter and the test filter. The information related to these scales is used to compute the model constant. The advantage here is that no empirical constant is needed and that the procedure allows the negative turbulent viscosity implying energy transfer from smaller to larger scales (energy back-scatter). This effect, in principle, allows both an enhancement and attenuation of the turbulent intensity introduced by the bubbles.

The model has a few drawbacks; wide fluctuations in dynamically computed constants can cause stability issues, along with additional computational expense.

2.4.3. One-Equation Model. In spite of the fact that dynamic SGS model calculates model constant C_S , thus making a constant-free model, it lacks the information on the amount

TABLE 1: Comparison of LES simulations.

No.	Author	Column D ($\times W$) \times H (m)	Sparger design	Bubble diameter	Range of V_G , m/s	Number of grid cells	Filter	SGS Model	BIT closure models ⁺	Drag C_D	Lift C_L	Virtual mass C_{VM}
(1)	Deen et al.* [19]	$0.15 \times 0.15 \times 0.45$	Perforated plate	4 mm	4.9×10^{-3}	$15 \times 15 \times 45$ $32 \times 32 \times 90$	$\Delta = 5-10$ mm	Smagorinsky, $C_S = 0.1$	(1)	(4)	0.5	0.5
(2)	Bove et al. [29]	$0.15 \times 0.15 \times 0.45$	Perforated plate	4 mm	4.9×10^{-3}	$15 \times 15 \times 45$ $9 \times 6 \times 30$	$\Delta = 10-17$ mm	Smagorinsky, $C_S = 0.05-0.2$	—	(2,4)	0.5	0.5
(3)	Zhang et al. [26]	$0.15 \times 0.15 \times 0.45-0.90$	Perforated plate	4 mm	4.9×10^{-3}	$15 \times 15 \times 45$ $15 \times 15 \times 90$	—	Smagorinsky, $C_S = 0.08-0.20$	(1, 2, 3)	(2) [#]	#	#
(4)	Tabib et al. [17]	0.15×1.0	Perforated plate	5 mm	20.0×10^{-3}	150000	$\Delta = 3$ mm	Smagorinsky, $C_S = 0.1$	(1)	(1)	#	#
(5)	Dhotre et al. [20]	$0.15 \times 0.15 \times 0.45$	Perforated plate	4 mm	4.9×10^{-5}	$15 \times 15 \times 50$ $15 \times 15 \times 100$	$d_B < \Delta$	Smagorinsky, $C_S = 0.12$ Germano	(1)	(1)	0.5	0.5
(6)	Ničeno et al. [9]	$0.15 \times 0.15 \times 0.45$	Perforated plate	4 mm	4.9×10^{-3}	$15 \times 15 \times 45$ $30 \times 30 \times 90$	Δ is equal to the grid spacing $\Delta/d_b = 1.5$	Smagorinsky, $C_S = 0.12$ OEM	(1, 2)	(1, 5)	0.5	0.5
(7)	Dhotre et al. [18]	2.0×3.4	Perforated plate	2.6 mm	4.9×10^{-3}	—	2.8 mm $< \Delta <$ 4.0 mm	Smagorinsky, $C_S = 0.12$	(1)	(5)	0.5	0.5
(8)	Niceno et al. [10]	$0.15 \times 0.15 \times 1.0$	Perforated plate	4 mm	4.9×10^{-3}	$30 \times 30 \times 100$	$\Delta = 5$ mm	OEM Germano	(1, 2)	(4, 5)	0.5	0.5
(9)	Tabib and Schwarz [30]	0.15×1.0	Perforated plate	3-5 mm	20.0×10^{-3}	—	—	OEM	(2)	Max [(1),(6)]	-0.05	—
(10)	van den Hengel et al. [31]	0.15×1.0	Perforated plate	3 mm	4.9×10^{-3}	$15 \times 15 \times 45$	$\Delta = 10$ mm	Smagorinsky	(1)	(3)	0.5	0.5
(11)	Hu and Celik [32]	$0.15 \times 0.08 \times 1.0$	Pipe sparger	1.6 mm	0.660×10^{-3}	$96 \times 50 \times 8$ $120 \times 80 \times 10$	PSI-ball method 2 mm	Smagorinsky, $C_S = 0.032$	(4)	(3)	0.5	0.5
(12)	Lain [27]	0.14×1.0	Porous membrane	2.6 mm	0.272×10^{-3}	$30 \times 30 \times 50$ $45 \times 45 \times 10$	$\Delta/d_b = 1.8$	Smagorinsky, $C_S = 0.1$	(4)	#	#	0.5
(13)	Darmana et al. [33]	$0.2 \times 0.03 \times 1.0$	Multipoint gas injection	4 mm	7.0×10^{-3}	$80 \times 12 \times 400$	$\Delta = 2.5$ mm	Vreman, $C_S = 0.1$	—	(3)	#	0.5
(14)	Sungkorn et al. [34]	$0.15 \times 0.15 \times 0.45$	Perforated plate	4 mm	4.9×10^{-3}	$30 \times 30 \times 90$	Δ is equal to the grid spacing $\Delta/d_b = 1.25$	Smagorinsky, $C_S = 0.10-0.12$	(6)	(3)	#	0.5
(15)	Bai et al. [35], Bai et al. [36]	$0.15 \times 0.15 \times 0.45$	Perforated plate	5 mm	5.0×10^{-3} 10.0×10^{-3} 15.0×10^{-3} 25.0×10^{-3}	$15 \times 15 \times 45$ $20 \times 20 \times 60$ $30 \times 30 \times 90$	—	Vreman Smagorinsky, $C_S = 0.1$	—	(3)	0.5	0.5

[#]The authors have studied the effect of this force over a range.

⁺Numbers indicated are referred to Table 2.

⁺⁺Numbers indicated are referred to Table 3.

TABLE 2: Bubble-induced turbulence models.

No.	Author	μ_{BIT}	$S_{k,\text{BIT}}$	$S_{\epsilon,\text{BIT}}$	Assumptions
(1)	Sato and Sekoguchi [37]	$\mu_{\text{BIT}} = \rho_L \alpha_G C_{\mu,\text{BIT}} d_B \mathbf{U}_G - \mathbf{U}_L $	0	0	
(2)	Pfleger and Becker [38]	0	$\alpha_L C_k \mathbf{M}_K \mathbf{U}_G - \mathbf{U}_L $	$\frac{\alpha_L}{k_L} C_\epsilon S_{k,\text{BIT}}$	
(3)	Troshko and Hassan [39]	0	$ \mathbf{M}_{D,L} \mathbf{U}_G - \mathbf{U}_L $	$0.45 \frac{3C_D \mathbf{U}_G - \mathbf{U}_L }{2C_{VM} d_B} S_{k,\text{BIT}}$	
(4)	Crowe et al. [14]				PSI cell/ball approximation
(5)	Sommerfeld [40]				Stochastic interparticle collision model
(6)	Sommerfeld et al. [41]				Langevin equation model

of SGS turbulent kinetic energy, a datum which may prove useful in modelling some aspects of dispersed flows (e.g., SGS bubble-induced turbulence).

The essence of the one-equation model is to solve additional transport equation for SGS turbulent kinetic energy:

$$\frac{\partial k_{\text{SGS}}}{\partial t} = \nabla [(\mu + \mu_{\text{SGS}}) \nabla k_{\text{SGS}}] + P_{k_{\text{SGS}}} - C_\epsilon \frac{k_{\text{SGS}}^{3/2}}{\Delta}. \quad (8)$$

Here, $P_{k_{\text{SGS}}}$ is production of SGS turbulent kinetic energy and is defined as

$$P_{k_{\text{SGS}}} = \mu_{\text{SGS}} |S_{ij}|, \quad (9)$$

and SGS viscosity is obtained from

$$\mu_{\text{SGS}} = C_k \Delta k_{\text{SGS}}^{1/2}. \quad (10)$$

The availability of the SGS turbulent kinetic energy allows for modelling of SGS interphase sorces such as bubble-induced turbulence and turbulent dispersion at SGS. The application of one-equation SGS model for bubbly flows is illustrated in more detail in sections below.

2.5. Effect of Bubble-Induced Turbulence (BIT). In the E-E approach, the turbulent stress in the liquid phase is considered to have two contributions, one due to the inherent, that is, shear-induced turbulence that is assumed to be independent of the relative motion of bubbles and liquid and the other due to the additional bubble-induced turbulence (Sato and Sekoguchi [37]). For BIT there are two modelling approaches. The first approach is proposed by Sato and Sekoguchi [37] and Sato et al. [42]:

$$\mu_{\text{BI},l} = \rho_f C_{\mu,\text{BI}} \alpha_g d_b |\mathbf{u}_g - \mathbf{u}_l|, \quad (11)$$

with $C_{\mu,\text{BI}}$ as a model constant which is equal to 0.6 and d_b as the bubble diameter. Milelli et al. [11, 24] found that the modelling of the bubble-induced turbulence did not improve the results. They tried two different formulations: the Tran model and the Sato model and found that they have negligible effect. This was attributed to fact that the bubble-induced viscosity (and turbulence) is not crucial, the turbulence being mainly driven by the liquid shear, and a low void fraction

($\approx 2\%$ leading to $\mu_{\text{BI},l} \approx 10^{-2}$ kg/(ms)) did not significantly modify the situation. It was thought that in a case in which the bubbles actually drive the turbulence (via buoyancy and/or added mass forces), the situation would be different. However, in subsequent studies, similar observations were made in bubble plumes simulated by Deen et al. [19], Dhotre et al. [20], Ničeno et al. [9].

The second approach for the modelling of BIT allows for the advective and diffusive transport of turbulent kinetic energy. This model incorporates the influence of the gas bubbles in the turbulence by means of additional source terms in the k_{SGS} equation and is taken to be proportional to the product of the drag force and the slip velocity between the two phases. This approach was used in work of Niceno et al. [10] through the use of a one-equation model. They found significant influence of the additional source terms as used by Pfleger et al. [43], as shown in Figure 2.

Figure 2 shows the comparison of the liquid kinetic energy obtained for the case of a bubble plume rising in a square column. It can be seen that the simulation without BIT underpredicts the turbulent kinetic energy. The use of the Sato model reproduced the double-peaked profile for kinetic energy. The Pfleger model also reproduced the experimental data very well. Figure 2(b) shows the ratio of the modelled SGS energy to the resolved energy. With no BIT, this ratio has the lowest value, whereas the Sato model yields more SGS energy, while the Pfleger model gives a ratio that is roughly twice as high, which is particularly pronounced in the middle of the column. Table 2 gives a summary of BIT models proposed by various investigators.

3. Numerical Details

Crucial parameters for obtaining reliable LES results are the time step selection, the total time for gathering good statistics of the averaged variables, and discretization schemes for the variables. The time step choice is determined by the criterion that the maximum Courant-Fredrichs-Levy (CFL) number must be less than one ($N_{\text{CFL}} = \Delta t u_{\text{max}} / \Delta x_{\text{min}} < 1$).

For flow variables, central difference should be used for discretization of advection terms and avoid using diffusive upwind schemes. However, for scalars variables, high-order schemes (MUSCL, QUICK, or Second-Order) may be

TABLE 3: Drag force models.

No.	Author	Equation
(1)	Ishii and Zuber [44]	$C_D = \frac{24}{Re}(1 + 0.1Re^{0.75})$
(2)	Tomiyama [45]	$C_D = \frac{(8/3) Eo (1 - E^2)}{E^{2/3} Eo + 16 (1 - E^2) E^{4/3}} F(E)^{-2}$ $E = \frac{1}{1 + 0.163 Eo^{0.757}} \text{ (Wellek et al. [46])}$ $F(E) = \frac{\sin^{-1} \sqrt{1 - E^2} - E \sqrt{1 - E^2}}{(1 - E^2)}$
(3)	Tomiyama [47] (pure system)	$C_D = \max \left[\min \left[\frac{16}{Re} (1 + 0.15 Re^{0.687}), \frac{48}{Re} \right], \frac{8}{3} \frac{Eo}{Eo + 4} \right]$
(4)	Ishii and Zuber [44] (distorted regime)	$C_D = \frac{2}{3} Eo^{1/2}$ $Eo = g \Delta \rho d_G^2 / \sigma$
(5)	Clift et al. [48]	$C_D = \frac{24}{Re} (1 + 0.15 Re_p^{0.687}), Re_p \leq 800$ $0.44 \quad Re_p > 800$
(6)	Tomiyama [47] (contaminated system)	$C_D = \max \left[\min \left[\frac{24}{Re} (1 + 0.15 Re^{0.687}), \frac{48}{Re} \right], \frac{8}{3} \frac{Eo}{Eo + 4} \right]$

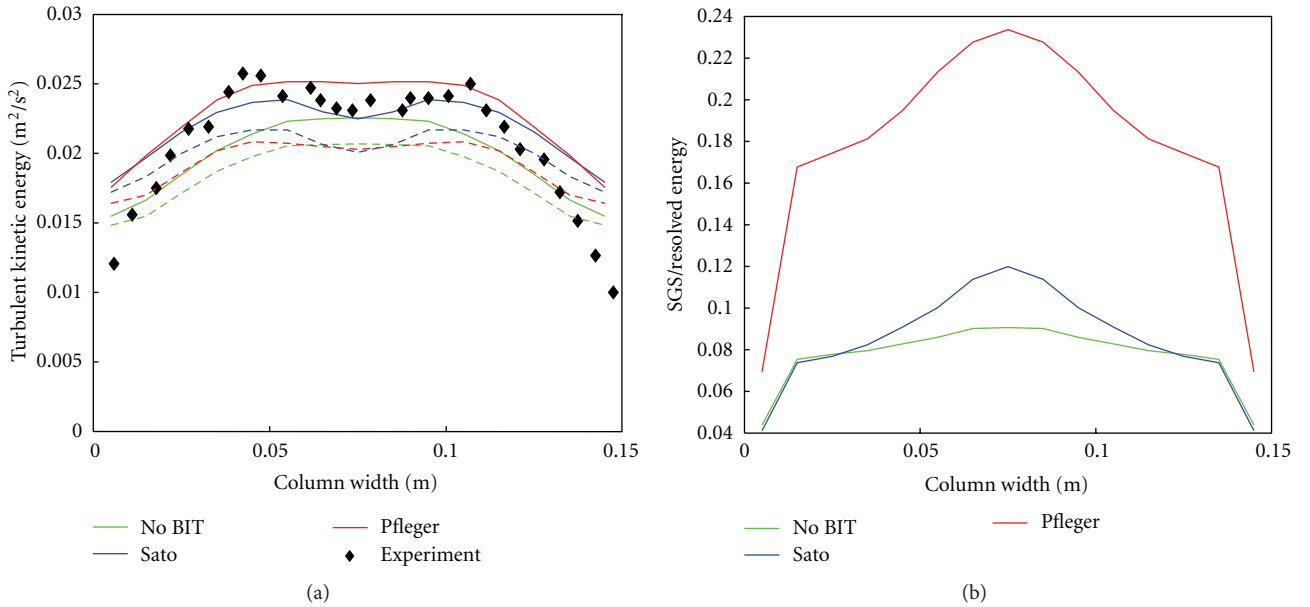


FIGURE 2: (a) Resolved (dashed) and total (continuous) liquid kinetic energy and (b) ratio of the modelled and resolved parts of the turbulent kinetic for various BIT models. (from Niceno et al. [9]).

tolerable to avoid nonphysical solutions (e.g., negative volume fractions). An alternative to high-order schemes are the bounded central differences. The risk with use of all but central scheme is their diffusivity. Their influence on LES may exceed the modelled SGS transport.

It is necessary to follow the initial phase of the simulation, wherein the turbulent structures develop starting from initial condition and to reach a statistically steady state. The duration of this phase depends on the flow characteristics.

The simulation must be run for a total time long enough to allow all turbulent instabilities that develop during this phase to be convected across the region of interest. However, the convecting velocities of the turbulent structures and the regions of interest are not always known a priori. This is why it is recommended to run the simulation a multitude (typically 5 times) of the slowest integral time scales, which often is the flow through time defined as the ratio of the system height over the bulk (superficial) velocity.

4. LES Prediction of the Flow Pattern for Dispersed Bubbly Flows

Here, we review different LES studies that were performed using the E-E and E-L approaches for simulating flow patterns in gas-liquid bubbly flows. Table 1 gives a summary of key numerical parameters (filter size, number of grids, SGS model, bubble diameter, coefficient for interfacial forces) and experimental details (geometrical dimension, sparger design, range of superficial gas velocity) used by investigators.

4.1. Euler-Eulerian (E-E) Approach

4.1.1. *Milelli et al. [11, 24, 49]*. Milelli et al. reported for the first time two-phase LES with E-E approach. They first investigated statistically 2D flow configuration and then free bubble plume.

They addressed important concerns related to the two-phase LES simulation. For instance, they found that the optimum ratio of the cutoff filter width (i.e., the grid) to the bubble diameter (d_b/Δ) should be around 1.5. That means mesh size should be at least 50% larger than the bubble diameter (Figure 1) so that (a) bubble size determines the largest scale modelled (b) and its interaction with the smallest calculated scale above the cut-off is captured. This is also supported by the scale-similarity principle of Bardina et al. [50].

Milelli [49] investigated LES for a free bubble plume and compared their predictions with the experiment of Anagbo and Brimacombe [51]. Here, they found that the mean quantities were not strongly affected by the different SGS models. Moreover they found little impact of the dispersed phase on the liquid turbulence, from the turbulent energy spectrum taken in the bubbly flow region which revealed a power-law distribution oscillating between $-5/3$ and $-8/3$ in the inertial subrange. The results conform to previous studies, which attributed the more dissipative spectrum to the presence of the dispersed phase. Hence, they found no influence of modifying the SGS model to account for bubble-induced dissipation.

Further, they observed in simulation that the lift coefficient value plays a major role in capturing the plume spreading and the used lift coefficient may differ for an LES compared to the one that is justified in an RANS approach. The plausible explanation here is from different handling of two factors responsible for bubble dispersion, that is, interaction between the bubbles and influence of turbulent eddies in the liquid phase.

4.1.2. *Deen et al. [19]*. Deen et al. [19] reported LES for gas-liquid flow in a square cross-sectional bubble column for the first time. They investigated the performance of RANS and LES approaches, influence of the interphase forces, and bubble-induced turbulence.

They found that RANS approach ($k-\epsilon$ model) overestimated the turbulent viscosity and could only predict low frequency unsteady flow. On other hand, LES as shown in Figure 3 reproduced high frequency experimental data and

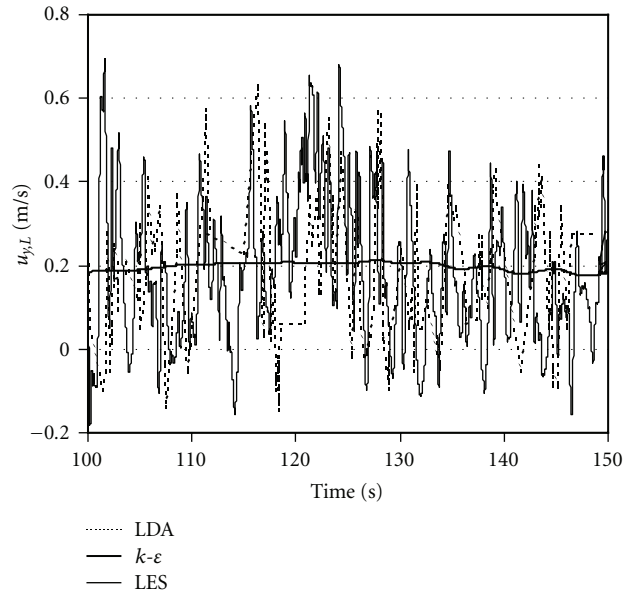


FIGURE 3: Time history of the axial liquid velocity at the centreline of the column, at a height of 0.25 m (from Deen et al. [19]).

predicted the strong transient bubble plume movements as in an experiment.

Furthermore, they also identified that the lift force is responsible for transient spreading of the bubble plume and in absence of it, only with drag force, the bubble plume showed no transverse spreading.

They considered the effective viscosity of the liquid phase with three contributions: the molecular, shear-induced turbulent (modelled using Smagorinsky model), and bubble-induced turbulent viscosities [37]. Like in the work of Milelli, they confirmed the marginal effect of the BIT on the predictions. The effect of virtual mass force on the simulated results was also found to be negligible.

4.1.3. *Bove et al. [29]*. Bove et al. [29] reported LES with E-E approach for the same square cross-sectional bubble column as used by Deen et al. [19]. They studied the influence of numerical modelling of the advection terms and the inlet conditions on LES performance. The upwind first-order and higher-order Flux Corrected Transport (FCT) schemes for both the phase fraction equations and the momentum equations were employed. The simulations using a second-order FCT scheme showed relatively good agreement with the measurement data of Deen et al. [19]. The authors showed that the proper discretization of the momentum and volume fraction equations is essential for correct prediction of the flow field.

Further, the LES results were found to be very sensitive to inlet boundary conditions (Figure 4). Three different inlet configurations simulated showed that the inlet modelling influences the predicted fluid flow velocity (as in Figure 4(a)) and an important fluid flow parameter, the turbulent viscosity (Figure 4(b)). In this work, the sparger (a perforated plate) was not modelled due to the difficulty in adapting the mesh grid to the geometry. They also suggested that near wall

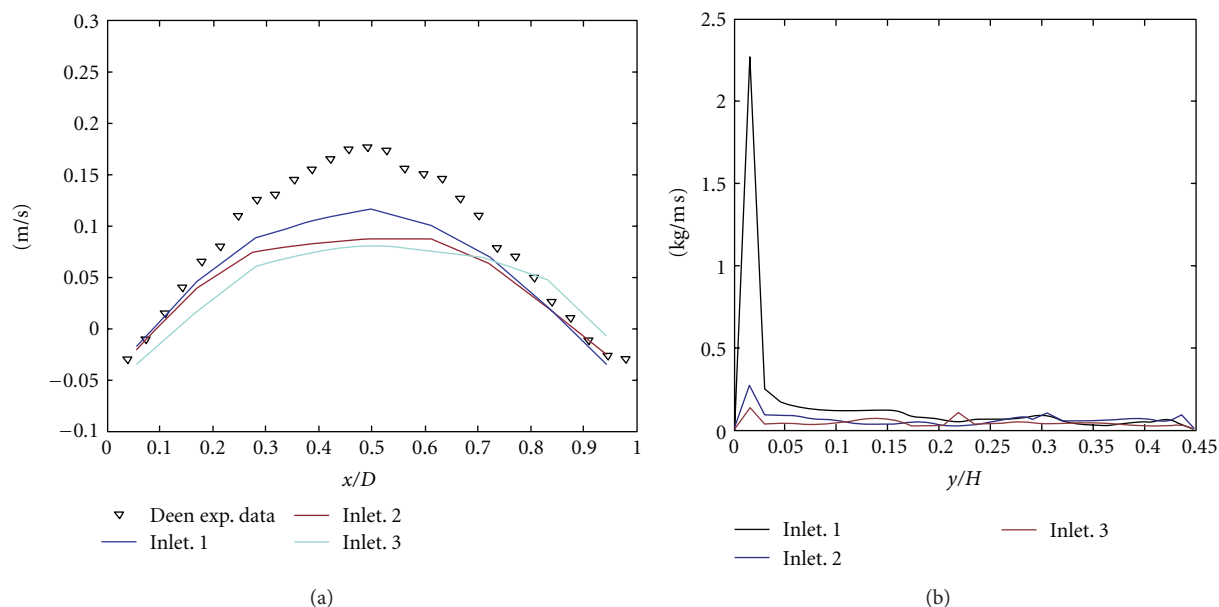


FIGURE 4: Comparison of (a) averaged axial liquid velocity profile at $y/H = 0.56$, (b) instantaneous viscosity profile along the height of the column (120 s) for three inlet conditions (from Bove et al. [29]).

region description in the SGS models is important, and the lack of the near wall modelling can lead to erroneous prediction of frictional stresses at the wall.

They used drag model for the contaminated water which gave a better prediction of the slip velocity; however, the velocity profile was underestimated for both gas and liquid phase. Reason for the underprediction was not clear, whether it was due to drag model or an improper value of the lift coefficient used or an error in the near wall modelling. Need for further work in this direction was suggested.

4.1.4. Zhang et al. [26]. Zhang et al. [26] reported LES in a square cross-sectional bubble column. They investigated the Smagorinsky model constant and carried out a sensitivity analysis. It was found that higher C_S values led to higher effective viscosity which dampens the bubble plume dynamics leading to a steep mean velocity profile (as shown in Figure 5). They obtained a good agreement with the measurements with C_S in range of 0.08–0.10. They also confirmed that the lift force plays a critical role for capturing the dynamic behaviour of the bubble plume.

They extended the work of Deen et al. [19] and predicted the dynamic behaviour in the square bubble column using a $k-\epsilon$ turbulence model extended with BIT.

4.1.5. Tabib et al. [17]. Tabib et al. [17] reported LES using E-E approach in a cylindrical column for a wide range of superficial gas velocity. In accordance with the earlier work, they confirmed the importance of a suitable lift coefficient and drag law. Moreover, they studied the influence of different spargers (perforated plate, sintered plate, and single hole) and turbulence models ($k-\epsilon$, RSM, and LES) using the experimental data of Bhole et al. [52]. The main findings from the study were that the RSM performs better than the $k-\epsilon$ model; the LES was successful in predicting the averaged

flow behaviour and was able to simulate the instantaneous vortical-spiral flow regime in the case of a sieve plate column, as well as the bubble plume dynamics in case of single-hole sparger. Finally, they concluded that LES can be effectively used for the study of the flow structures and instantaneous flow profiles.

4.1.6. Dhotre et al. [20]. Dhotre et al. [20] reported LES with an E-E approach for a gas-liquid flow in a square cross-sectional bubble column. They studied the influence of SGS models: Smagorinsky and Dynamic models of Germano et al. [28]. It was found that both the Smagorinsky model ($C_S = 0.12$) and the Germano model predictions compared well with the measurements.

They further investigated the value of C_S obtained from the Germano model. Reason for similar performance of both models was clear from the probability density function of C_S (from Germano model) over the entire column. As shown in Figure 6, the value of C_S has the highest probability in the range of 0.12–0.13. Like Zhang et al. [26], the authors confirmed that with a proper BIT model, RANS also performed well for mean quantities of flow variables. Figure 7 shows the comparison of the predicted instantaneous vector flow field for axial liquid velocity from all the three models (Smagorinsky, Germano and RANS).

It was further concluded that the Germano model can give correct C_S estimates for the configuration under consideration and, in general, can be used for other systems where C_S is not known as “a priori” from previous analysis.

4.1.7. Niceno et al. [10]. Niceno et al. [10] investigated LES with E-E approach for a gas-liquid flow in a square cross-sectional bubble column. They demonstrated the applicability of a one-equation model for the SGS kinetic energy (k_{SGS}).

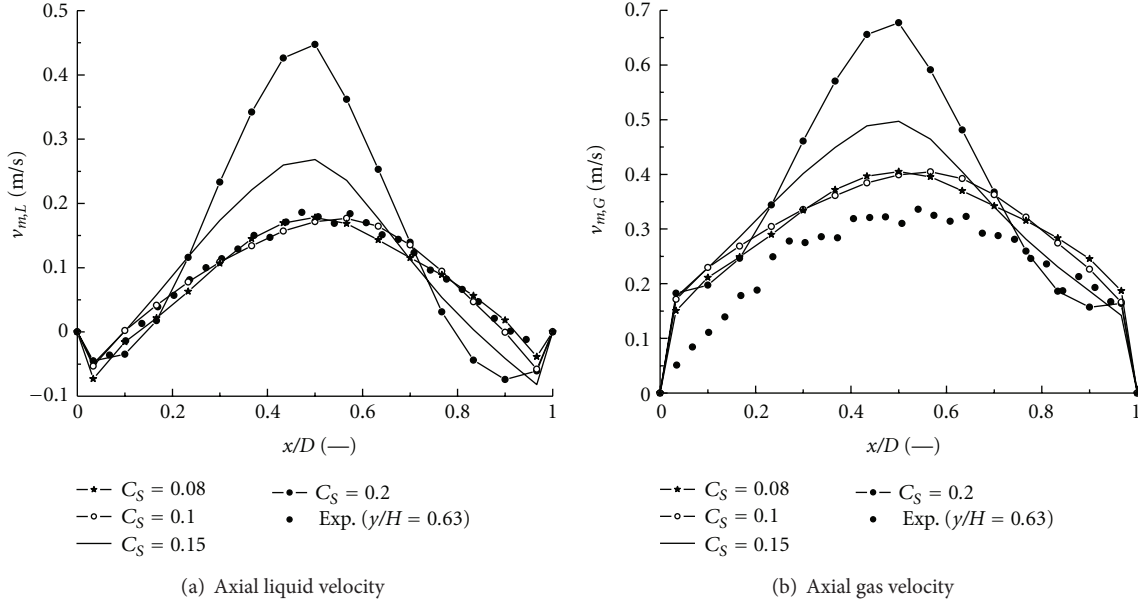


FIGURE 5: Comparison of the prediction and measurement of mean velocity of the both phases; the predicted profiles were obtained with different C_S values used in the SGS model (Zhang et al. [26]).

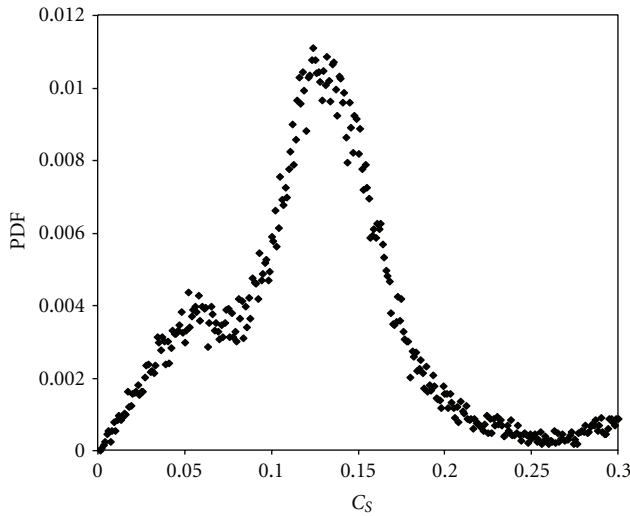


FIGURE 6: Probability density function for computed constant C_S in Germano model over entire column (from Dhotre et al. [9]).

The predictions showed that the one-equation SGS model gives superior results to the Germano model with the additional benefit of having information on the modelled SGS kinetic energy:

$$\mu_{\text{eff},l} = \mu_{\text{lam},l} + \rho_l C_k \Delta \sqrt{k_{\text{SGS}}}, \quad (12)$$

with $C_k = 0.07$ a model constant. They studied the influence of two approaches for bubble-induced turbulence: approach of an algebraic model (Sato et al. 1975) and extra source terms (as used in Pflger et al. 1999) in the transport equation for SGS kinetic energy approach. It was found that the latter approach improved the quantitative prediction of the turbulent kinetic

energy (as shown in Figure 2(a)). The modelled SGS kinetic energy for the Pflger model found to be much higher than for the Sato model (Figure 2(b)), indicating the Pflger model needs a more appropriate constant for LES.

They suggested that the modelled SGS information can be used to access the SGS interfacial forces, in particular the turbulent dispersion force. In their work, the effect of SGS turbulent dispersion force could not be determined as the bubble size was almost equivalent to the mesh size.

4.1.8. Dhotre et al. [18]. Dhotre et al. [18] extended LES with E-E approach for a gas-liquid flow in a large-scale bubble plume. The predictions at three elevations were compared with the measurement data of Simiano [55] and an RANS prediction. The LES approach was shown superior in capturing the transient behaviour of the plume (Figure 8) and predicts second-order statistics of the liquid phase accurately.

They emphasized the crucial role of the lift force in the prediction of the lateral behaviour of the bubble plumes. In the RANS approach the turbulent dispersion force is required to reproduce the bubble dispersion; however, in LES, bubble dispersion is implicitly calculated by resolving the large-scale turbulent motion responsible for bubble dispersion. The dependence of the bubble dispersion with the value of lift coefficient was also observed in Milelli et al. [11, 24], Deen et al. [19], Lain and Sommerfeld [56], Van den Hengel et al. [31], Tabib et al. (2008), and Dhotre et al. [20]).

Dhotre et al. [18] found good agreement with the measurement data at higher elevation, while discrepancies were observed at lower elevation, near the injector. The reason for the discrepancies was attributed to the absence of modelling bubble coalescence and breakup. This was also found in the

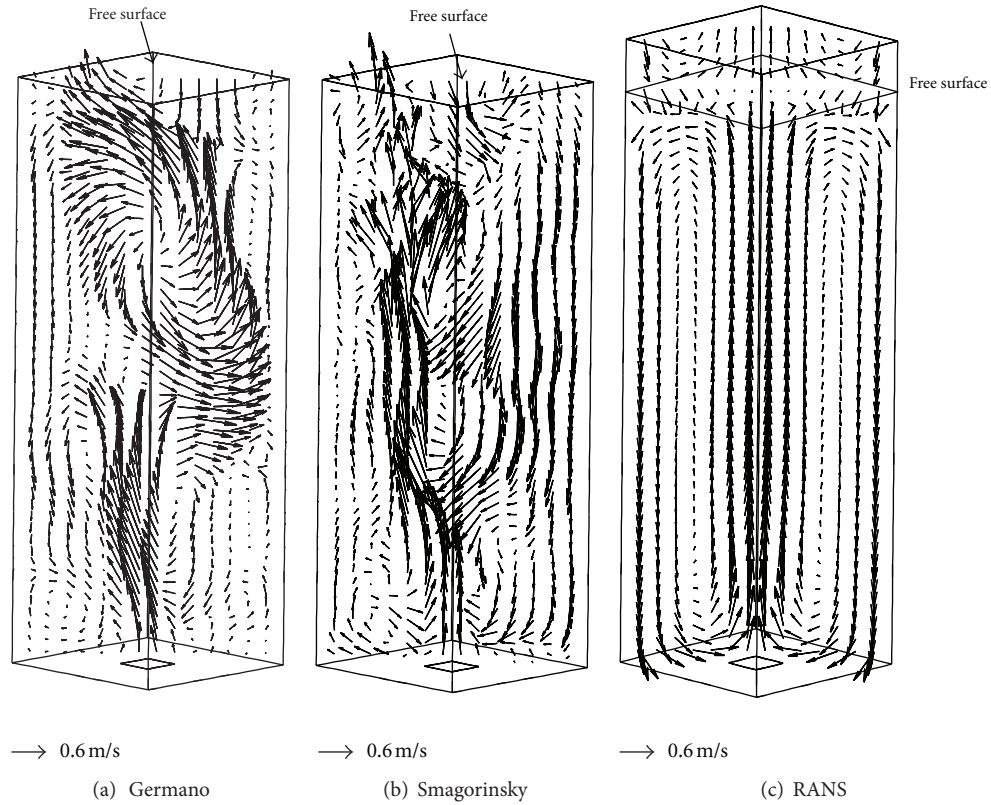


FIGURE 7: Predicted instantaneous vector flow field for axial liquid velocity after 150 s, for all three models (from Dhotre et al. [20]).

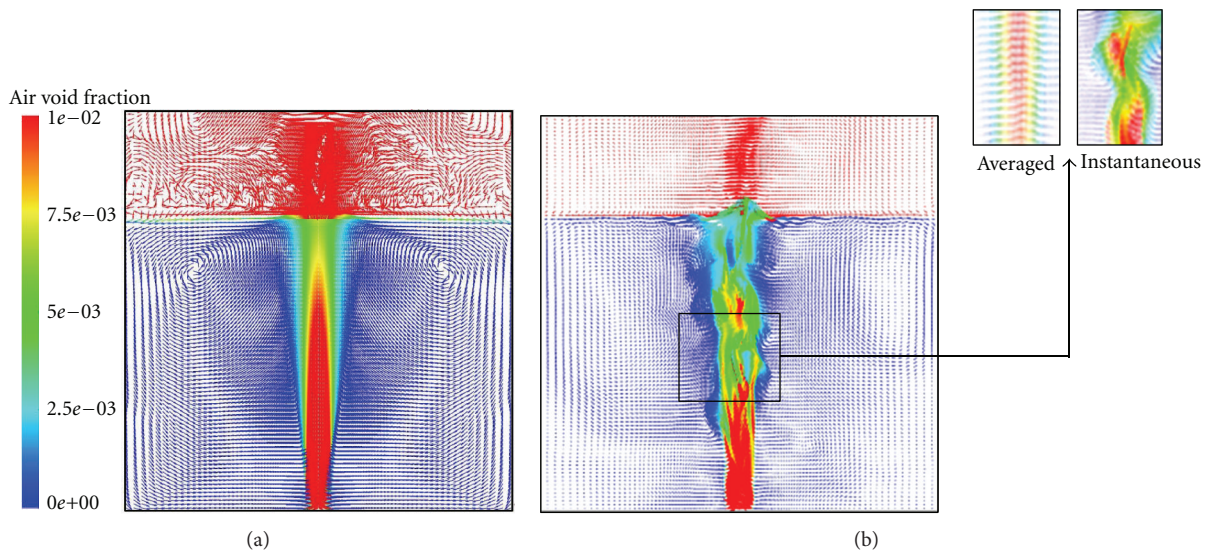


FIGURE 8: Comparison of $k-\epsilon$ model and EELES predictions; vector plot of axial velocity coloured with the void fraction in the midplane. (a) $k-\epsilon$ model (b) EELES (from Dhotre et al. [18]).

work of Van den Hengel et al. [31], wherein the authors showed that most of the coalescence occurs in the lower part of the column and recommended to consider bubble size distribution and coalescence and breakup models for reproducing the bubble behaviour near the sparger.

4.1.9. Niceno et al. [10]. Niceno et al. [10] reported LES with E-E approach for a gas-liquid flow in a square cross-sectional bubble column. They compared two different codes (CFX-4 and Neptune) and two subgrid-scale models (as in Figure 9). The prediction from the Smagorinsky model in the

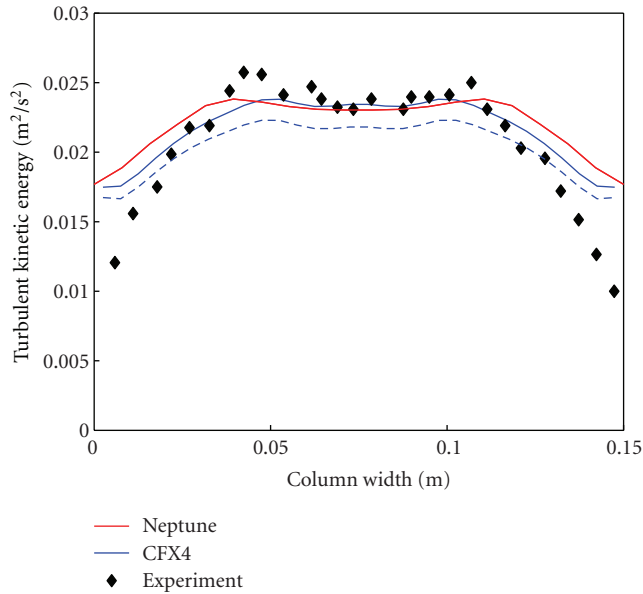


FIGURE 9: Comparison of liquid turbulent kinetic energy obtained with CFX-4 using one-equation model and Neptune CFD with Smagorinsky model and experimental data. The blue dashed line is the resolved, the blue continuous line is the total (resolved plus SGS) kinetic energy (from Niceno et al. [10]).

Neptune CFD code and the one-equation model of CFX-4 was compared with the measurement data of Deen et al. [19]. Agreement between the predictions from the two SGS models was found to be good, and it was concluded that the influence of the SGS model was small. This is in contradiction with earlier work of Van den Hengel et al. [31], where they showed significant contribution of the SGS model (Figure 10), which is discussed in more detail in section (4.2). It remains to be seen if this was due to the fine mesh used by the authors ($\Delta/d_b = 1.2$). Niceno et al. [10] argued that with the known flow pattern in a bubble column, that is, a dominant bubble plume meandering between the confining walls, the biggest eddy having most energy is of the size of the domain cross section. Thus, the grid used in their work was a compromise between sufficiently fine to capture the most energetic eddies, and sufficiently coarse to stay close to the Milelli criterion [11, 24]. Furthermore, they pointed out the limitations of LES with E-L or E-E approach without resolving interface; they indicated that the most influential interfacial forces (drag and lift) are modelled for the large-scale field and their effect from the small scale remains a question. On the other hand, they recommend large-scale simulation, as in the works of Lakehal et al. [25], which explicitly resolves the large-scale part of the interfacial forces and models the part at the SGS level, where the effects are smaller and hence less influential on the accuracy of the results.

4.1.10. *Tabib and Schwarz [30]*. Tabib and Schwarz [30] extended the work of Niceno et al. [9] and attempted to quantify the effect of SGS turbulent dispersion force for different particle systems, where the particle sizes would be smaller than the filter size. They used LES with E-E approach.

They used the formulation of Lopez de Bertodano [57] to approximate the turbulent diffusion of the bubbles by the SGS liquid eddies for a gas-liquid bubble column system [17]. The bubble size was in range of 3–5 mm. The mesh used in simulations was coarser than the bubble diameter. They found a high contribution from the SGS turbulent dispersion force, when compared with the magnitude of the other interfacial forces (like drag force, lift force, resolved turbulent dispersion force, and force due to momentum advection and pressure). Finally, Tabib and Schwarz concluded that for LES with E-E approach, when the mesh size is bigger than bubble size, the SGS turbulent dispersion force should be used, and a one-equation SGS-TKE model overcomes a conceptual drawback of E-E LES model.

4.2. Euler-Lagrangian (E-L) Approach

4.2.1. *Van den Hengel et al. [31]*. Van den Hengel et al. [31] reported LES with E-L approach for a gas-liquid flow in a square cross-sectional bubble column. The liquid phase was computed using LES, and a Lagrangian approach was used for the dispersed phase. They used a discrete bubble model (DBM) originally developed by Delnoij et al. [58, 59] and extended it to incorporate models describing bubble breakup and coalescence. The mean and fluctuating velocities predicted in the simulations showed a good agreement with the experimental data of Deen et al. [19].

Authors studied the influence of the SGS model on the predictions and found that without SGS model, the average liquid velocity and liquid velocity fluctuations are much lower compared to the case with a SGS model. This was due to the lower effective viscosity in this case, which led to less dampening of the bubble plume dynamics and subsequently to flatter mean liquid velocity profiles (as shown in Figure 10).

In this work also, the authors confirmed the important role of the lift coefficient in capturing the plume dynamics. They considered two lift coefficients ($C_L = 0.5$ and 0.3) and found that a smaller value of the lift coefficient led to higher average velocity and velocity fluctuations and less spreading of the plume, which resulted in overprediction of the average velocity in the centre of the column.

4.2.2. *Hu and Celik [32]*. Hu and Celik [32] studied LES with an E-L approach for the gas-liquid flow in a flat bubble column. The liquid phase was computed using LES, and a Lagrangian approach was used for the dispersed phase. The authors developed a mapping technique called particle-source-in-ball (PSI-ball) for coupling the Eulerian and Lagrangian reference frames. The concept is a generalization of the conventional particle-source-in-cell (PSI-cell) method as well as a template-function-based treatment [14].

They reported second-order statistics of the pseudo-turbulent fluctuations and demonstrated that a single-phase LES along with a point-volume treatment of the dispersed phase could serve as a viable closure model.

Hu and Celik reported that the predicted mean quantities (such as mean liquid velocity field) were in good agreement with the experimental data of Sokolichin and Eigenberger [54], as shown in Figure 11, and further gave an accurate

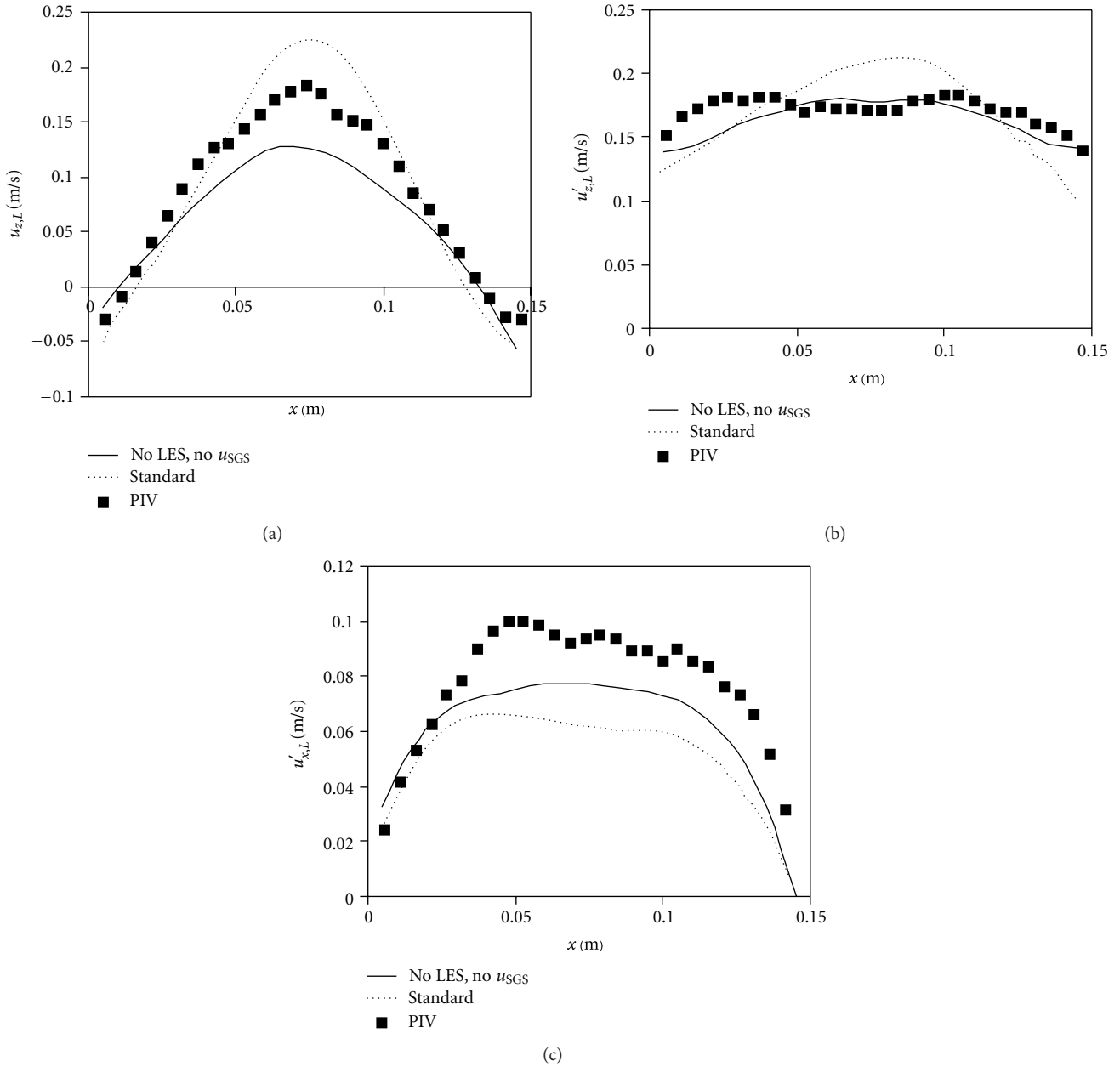


FIGURE 10: Comparison of the simulated and experimental liquid velocity and velocity fluctuations for cases with and without SGS model at a height of 0.255 m and a depth of 0.075 m. Effect of the SGS model (from Van den Hengel et al. [31]).

prediction of the instantaneous flow features, including liquid velocity fluctuations and unsteady bubble dispersion pattern. Hu and Celik also studied the influence of the Smagorinsky constant and found that the constant for multiphase systems falls in a relatively smaller range than for single-phase flows. Higher values of the C_S showed an excessive damping effect to the liquid field, which led to a steady-state solution. This observation is in accordance with other investigators [26, 31]. Furthermore, authors proposed to use C_S as a modeling parameter rather than a physical constant, as the interphase coupling terms used as well as the high frequency turbulent fluctuations contribute to the turbulent kinetic energy dissipation.

4.2.3. *Lain [27]*. Lain [27] reported an LES with E-L approach for a gas-liquid flow in a cylindrical bubble column. He used LES for the liquid phase, and a Lagrangian approach for the dispersed gas phase. The interaction terms between liquid and gas phases was calculated using the particle-source-in-cell (PSI-cell) approximation of Crowe et al. [14]. The bubbles were considered as a local source of momentum, and source term was added.

A simple model for the subgrid liquid fluctuating velocity to account for the BIT considered in this work was found to have no influence on the predictions. As in previous works, authors confirmed a strong dependency of the bubble dispersion in the column on the value of transverse lift

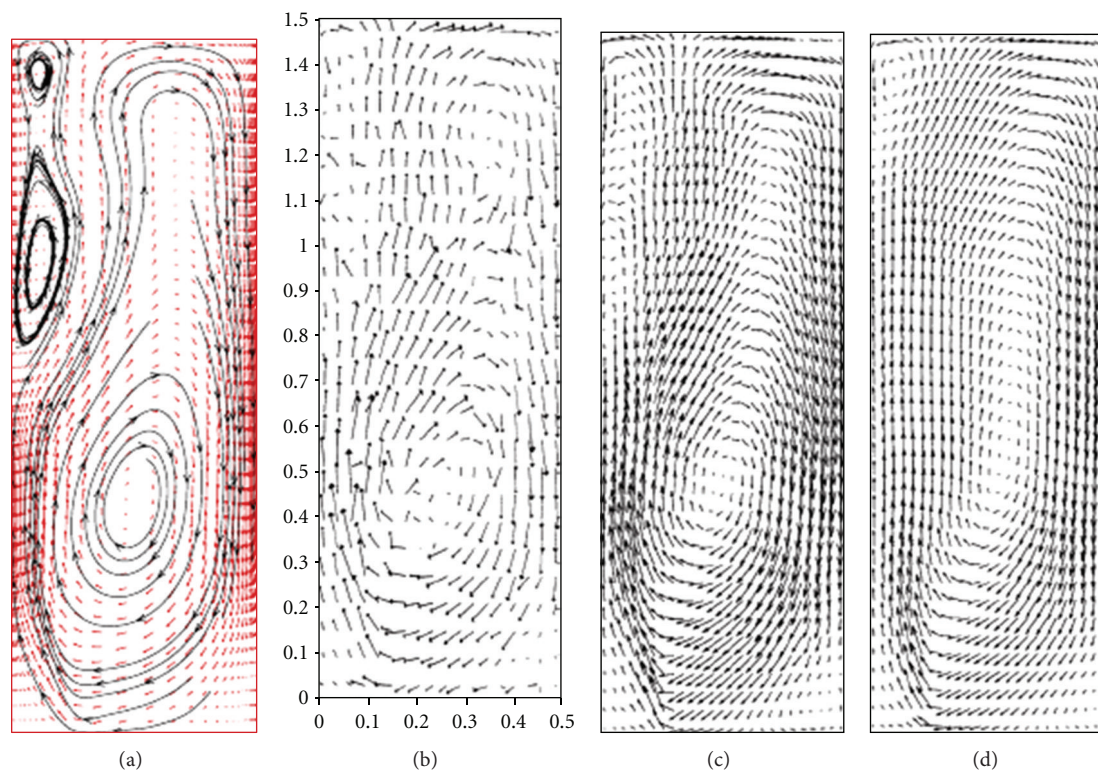


FIGURE 11: Long-time averaged liquid velocity field on middepth plane: (a) E-L approach, (b) LDA measurement of Becker et al. [53], (c) LDA measurement of Sokolichin and Eigenberger [54], and (d) 3D E-E simulations of Sokolichin and Eigenberger [54] (from Hu and Celik [32]).

force coefficient used. He concluded that the lift coefficient depends on the bubble-liquid relative velocity and was the main mechanism responsible for the spreading of bubbles across the column crosssection. He further compared the simulation results with particle image velocimetry (PIV) measurements (Border and Sommerfeld [60]) and $k-\epsilon$ calculations.

4.2.4. Darmana et al. [33]. Darmana et al. [33] used the LES with E-L approach for simulating the gas-liquid flow in a flat bubble column and validated the model with experimental data of Hartevelde et al. [61]. They investigated seven sparger designs and their influence on the flow structure. It was found that the model captures the influence of different gas sparging very well (e.g., Figure 12 shows one such case simulated). However, in all cases simulated, authors found systematic overprediction of dispersed phase distribution (25%), which was attributed to an inaccuracy of the drag force and the turbulence model at high gas void fractions.

4.2.5. Sungkorn et al. [34]. Sungkorn et al. [34] reported LES with the E-L approach for a gas-liquid flow in a square cross-sectional bubble column. They modelled the continuous liquid phase using a lattice-Boltzmann (LB) scheme, and a Lagrangian approach was used for the dispersed phase. For the bubble phase, the Langevin equation model [41] was used for estimating the effect of turbulence. The bubble collisions were described by a stochastic interparticle collision model

based on the kinetic theory developed by Sommerfeld [40]. The predictions showed a very good agreement with the experimental data for the mean and fluctuating velocity components. Figure 13 shows the snapshots of predicted the bubble dispersion patterns.

It was also found that their collision model leads to two benefits: the computing time is dramatically reduced compared to the direct collision method and secondly it also provides an excellent computational efficiency on parallel platforms. Sungkorn et al. [34] claim that the methodology can be applied to a wide range of problems. The investigations are valid for lower global void fraction, and further work is required to consider it for higher void fraction systems.

5. Application of LES

5.1. Preamble. The investigations discussed in earlier sections dealt with the use of LES for predicting the flow patterns. In the published literature, the knowledge of flow pattern has been employed for the estimation of equipment performance such as mixing (Joshi and Sharma [62], Joshi [63], Ranade and Joshi [64], Ranade et al. [65], and Kumaresan and Joshi [66]), heat transfer (Joshi et al. [67], Dhotre and Joshi [68]), Sparger design (Dhotre et al. [69], Kulkarni et al. [70]), gas induction (Joshi and Sharma [71], Murthy et al. [72]), and solid suspension (Raghava Rao et al. [73], Rewatkar et al. [74], and Murthy et al. [75]). Joshi and Ranade [76] have discussed the perspective of computational fluid dynamics

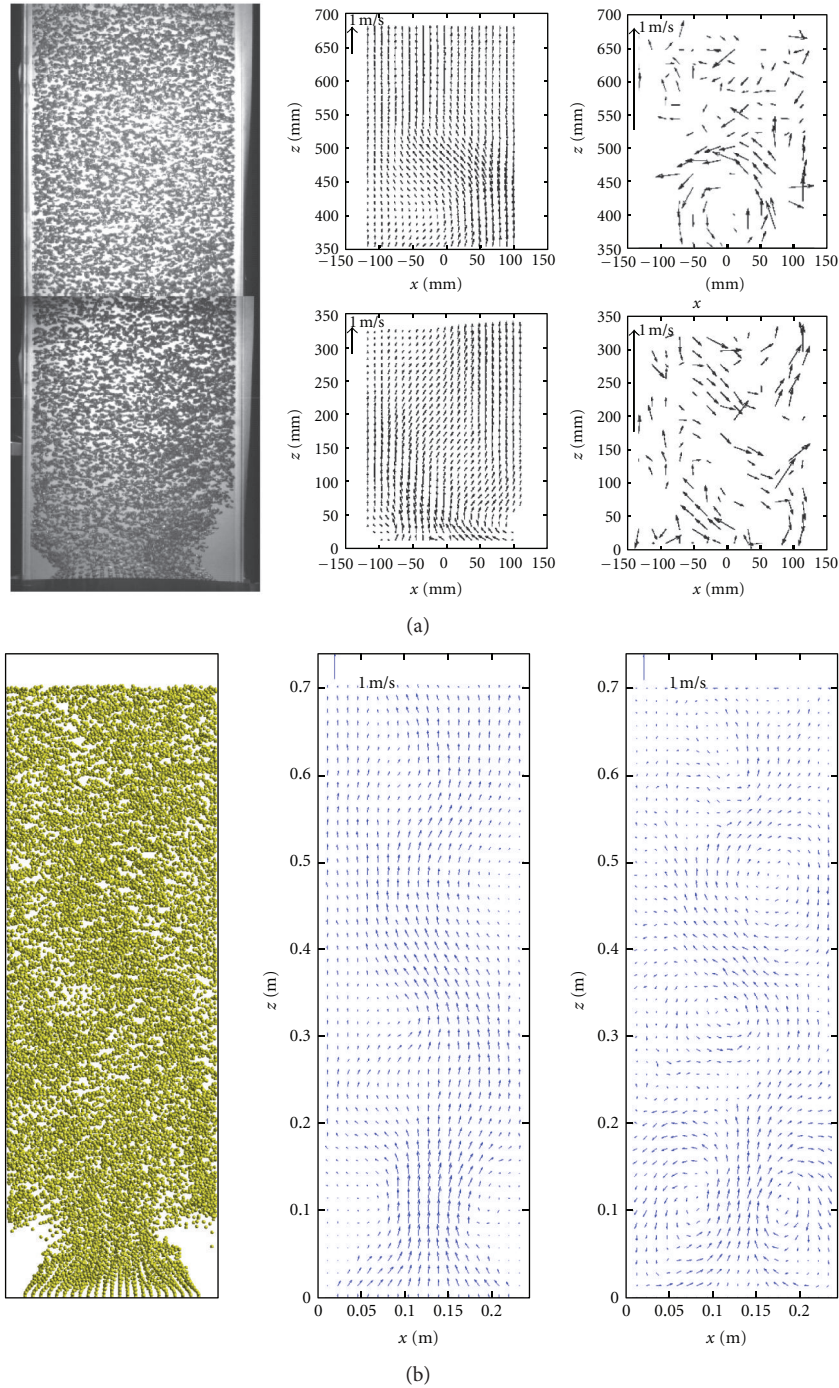


FIGURE 12: Instantaneous flow structure comparison between experiment (a) and simulation (b). From left to right: bubble positions, bubble velocity, and liquid velocity (from Darmana et al. [33]).

(CFD) in designing process equipment with their views on expectations, current status, and path forward. The LES simulations provide substantially improved understanding of the flow pattern. Therefore, in this section, the application of LES for design objectives like mixing, heat transfer, and chemical reactions by some investigators will be reviewed. The LES simulations have also been used in the identification of turbulent structures, their dynamics, and the role of

structure dynamics in the estimation of design parameters. The LES simulations have also been used in the estimations of terms in $k-\epsilon$ and RSM models such as generation, dissipation and transport of turbulent kinetic energy (k), the turbulent energy dissipation rate (ϵ), and Reynolds stresses. These estimations have improved the understanding of RANS ($k-\epsilon$ and RSM) models. These two applications of LES are also described briefly.

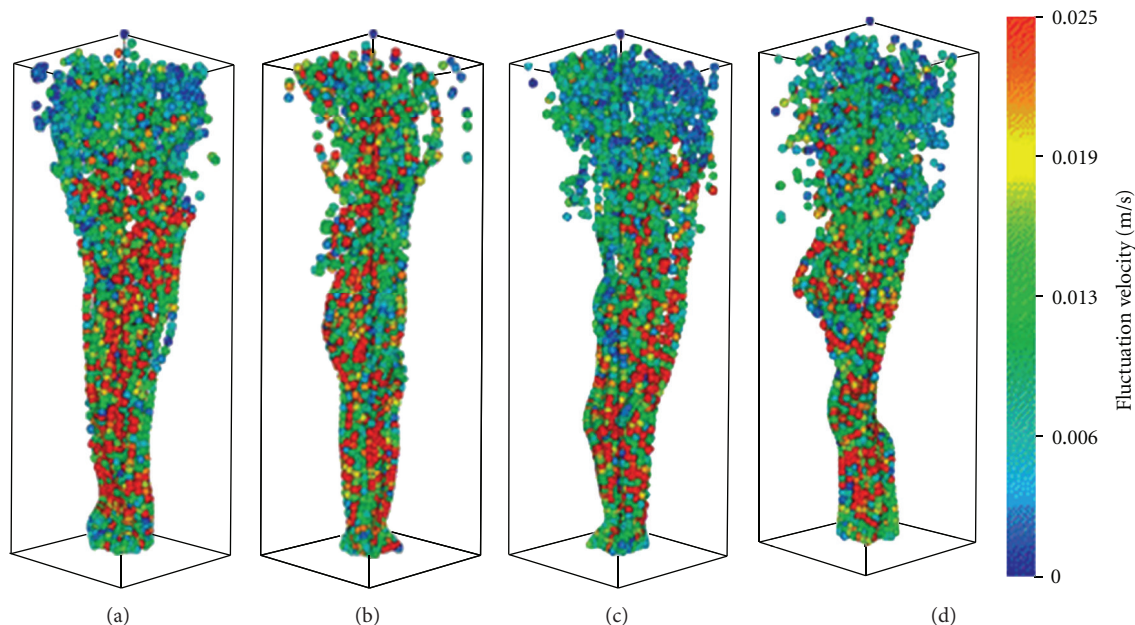


FIGURE 13: Snapshots of the bubble dispersion pattern after 20, 50, 100, and 150 s. The bubbles are coloured by the local magnitude of the liquid fluctuations (from Sungkorn et al. [34]).

5.2. Mass Transfer and Chemical Reaction

5.2.1. Darmana et al. [77, 78]. Darmana et al. [77, 78] used LES with E-L approach to simulate flow, mass transfer, and chemical reaction in flat bubble column. They considered mass transfer, rate in liquid-phase momentum equation and reaction interfacial forces in the bubble motion equation.

Also, the presence of various chemical species was accounted through a transport equation for each species. Darmana et al. estimated the mass transfer rate from the information of the individual bubbles directly. They used the model to simulate the reversible two-step reactions found in the chemisorption process of CO_2 in an aqueous NaOH solution in a lab-scale pseudo-2D bubble column reactor (e.g., Figure 14). They found good agreement between simulation and measurement for the case without mass transfer. In absence of an accurate mass transfer closure, the authors found that the overall mass transfer rate was lower compared to the measurement. However, the influence of the mass transfer on the flow agreed well with experimental data.

5.2.2. Zhang et al. [79]. Zhang et al. [79] followed a procedure similar to that used by Darmana et al. [78], although in this case an E-E approach was used to simulate flow, mass transfer, and chemical reactions in square cross-sectional bubble column [19]. Zhang et al. studied physical and chemical absorption of CO_2 bubbles in water and in an aqueous sodium hydroxide (NaOH) solution. They used a bubble number density equation for coupling of flow, mass transfer, and chemical reaction. The authors demonstrated the influence of the mass transfer and chemical reaction on the hydrodynamics, bubble size distribution, and gas holdup.

5.3. Mixing and Dispersion

5.3.1. Bai et al. [36]. Bai et al. [36] used LES with E-L approach to investigate the effect of the gas sparger and gas phase mixing in a square cross-sectional bubble column. The liquid phase was computed using LES, and a Lagrangian approach was used for the dispersed phase. They used the DBM and investigated the effect of two SGS models: Smagorinsky [21] and Vreman [80]. They compared the vertical liquid velocity and turbulent kinetic energy of the liquid phase at three different heights with PIV data and found that the model proposed by Vreman performed better than Smagorinsky model.

They further investigated the effect of the gas sparger properties (sparged area and its location) on the hydrodynamics in a bubble column and characterized the macromixing of the gas phase in the column in terms of an axial dispersion coefficient. They compared the predicted liquid phase dispersion coefficient with the literature correlations as shown in Figure 15. The range of superficial gas velocity investigated in work is low compared to what is common in industrial application. For large-scale reactors at high superficial velocities, Bai et al. recommended to extend the discrete bubble modelling with bubble coalescence and breakup.

5.4. Estimation of the Turbulent Dispersion Force. In the RANS approach, the drag and lift forces depend on the actual relative velocity between the phases, but the ensemble equations of motion for the liquid only provide information regarding the mean flow field. The random influence of the turbulent eddies is considered by modelling a turbulent dispersion force. By analogy with molecular movement, the

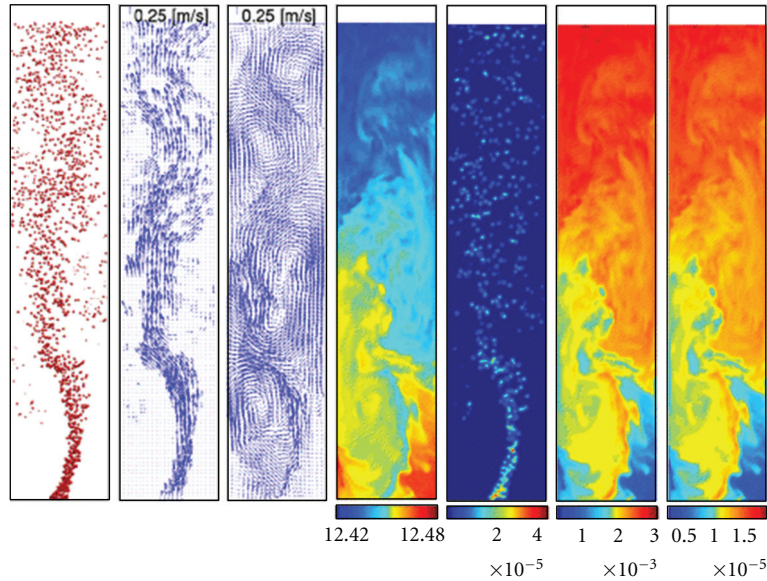


FIGURE 14: Instantaneous solution 10 s after the CO₂ gas is introduced. From left to right: bubble positions, gas velocity, liquid velocity, pH, respectively, and concentration of dissolved CO₂, HCO₃⁻, and CO₃²⁻ (kmol m⁻³) (from Darmana et al. [77]).

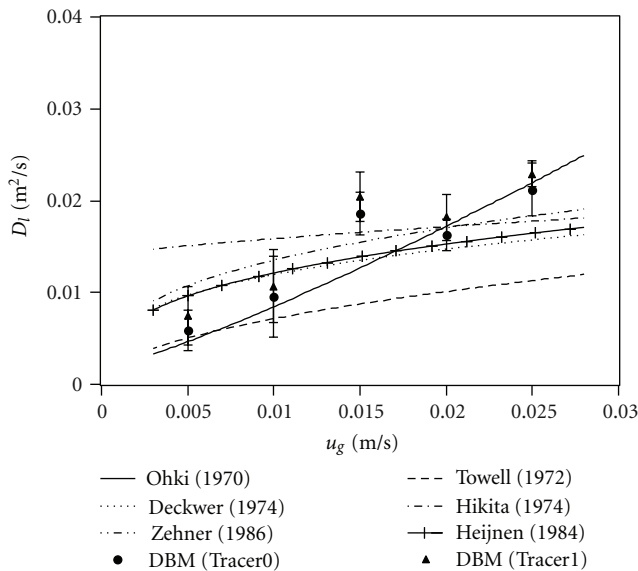


FIGURE 15: Comparison of the simulated liquid phase dispersion coefficient with the literature correlations (from Bai et al. [36]).

force is set proportional to the local bubble concentration gradient (or void fraction), with a diffusion coefficient derived from the turbulent kinetic energy. The value of the turbulent dispersion coefficient is chosen to get an agreement with the measurement data and is not known a priori.

In LES, the resolved part of the turbulent dispersion is implicitly computed, and hence one can use information from LES for calculating the magnitude of this force. The methodology depends on scales at which LES is to be applied. For instance, at the mesoscale, in the E-L approach, bubbles dispersed by drag and lift through turbulent eddies can be computed. At micro-scale LES, one might need to consider

bubble coalescence and breakup phenomena along with a reasonable number of bubbles. It can be computationally expensive, but in view of increasing available computer power, this should become feasible soon.

5.5. Dynamics of Turbulent Structures and the Estimation of Design Parameters. The turbulent flows contain flow structures with a wide range of length and time scales which control the transport processes. The length scales of these structures can range from column dimensions (highest) to Kolmogorov scales (lowest). However, not all the scales of turbulence contribute equally to different transport rates and mixing. If only mixing is the important design criterion, then the knowledge about the mean flow pattern (large-scale structures) would generally suffice the purpose (Ekambara and Joshi [81]). However, for the prediction of the gas holdup, bubble size distribution, true mass transfer coefficient, and heat transfer coefficient, the knowledge about all the scales is important [82, 83]. Hence, it is imperative to identify the scales and dynamics of turbulent flow structures and their relationship with the rates of different transport process. The present empirical design practices do not consider these basic mechanisms and conceals the detailed local information about the relationship between the turbulence and the equipment performance.

The subject of quantification of local turbulent flow structures and reliable estimation of transport properties has been reviewed by Joshi et al. [84] and [82, 83]. The velocity and pressure data from LES were analyzed using the mathematical techniques such as multiresolution analysis [85], wavelet transforms (discrete and continuous), proper orthogonal decomposition (POD), and hybrid POD-wavelet techniques (Tabib and Joshi [86], Tabib et al. [87], Sathe et al. [88], and Mathpati et al. [89]). These techniques give the size, shape penetration depth, and energy content of all the

flow structure in the system. This flow structure information can also be used for the construction of energy spectrum and for examining the scaling laws for turbulence in bubble columns. Such understanding of turbulence is expected to provide better insights into the transport phenomena. One such attempt has been reported by Deshpande et al. [90, 91].

5.6. Comparison of Turbulence Models. CFD provides detailed flow information within single- and multiphase reactors. Most popular and computationally inexpensive models such as k - ε model and Reynolds stress model (RSM) are widely used to predict the mean flow pattern. These models can give reliable estimation about the liquid phase mixing. However, they do not accurately predict the turbulence parameters such as turbulent kinetic energy and the dissipation rate due to inbuilt modelling assumptions as well as complexity of flow [11, 24]. These models are time averaged, and hence the information related to different turbulent structures is lost.

It is known that a large number of simplifying assumptions are made while deriving the k - ε and RSM models. Therefore, it is important to understand the gravity of these assumptions on the quantitative values of transport rates of k and ε due to convection, diffusion, and turbulent dispersion. It is also important to know the quantitative estimation of production and dissipation rates of k and ε . Therefore, it is important to estimate these five terms using k - ε , RSM, and LES models. From the LES simulations, the time series of velocity and pressure can be stored. These are subsequently used for the detailed comparison of k - ε , RSM, and LES models in terms of the rates of transport (convection, molecular and turbulent diffusion) and the rates of production, and the dissipation of k and ε for the case of dispersed bubbly flows [92].

6. Summary and Suggestions for Future Work

- (1) E-E and E-L LES are promising approaches for predicting unsteady, buoyancy-driven flow inducing large-scale coherent structures for gas-liquid dispersed flow. Care should be taken to clearly identify the scales (micro, macro, or meso) at which LES should be applied, in order to decide the level of interface resolution and modelling required. The approach of LES at mesoscales (i.e., without explicitly tracking interface) using E-E and E-L description has been reviewed for gas-liquid dispersed flow.
- (2) Pioneering work of Milelli et al. [11, 24] has initiated the LES approach for gas-liquid dispersed flows. The main contribution comes from insights in the cutoff filter requirement and SGS modelling.
- (3) The simulation and the experimental measurement of Deen et al. [19] in a square cross-sectional bubble column have triggered a systematic development of the two-phase LES for both E-E and E-L approaches.
- (4) The concept behind the LES is very simple but characterized by a large number of choices (regarding numerical and physical modelling) that all have significant influence on the results. However, it offers great potential in terms of determination of statistical quantities and instantaneous information about flow structures. This information can be extremely useful for the prediction of other physical processes behaviour (e.g., transport of scalar (temperature, concentration), chemical reactions).
- (5) From LES simulation with E-E/E-L approaches that were reviewed in this work, it is recommended that:
 - (a) The grid or filter size selection based on filter size to bubble diameter ratio Δ/d_b of 1.2 gives reasonable results.
 - (b) The Smagorinsky constant, C_s , is a modelling parameter rather than a physical constant. Although the constant value of the parameter gives satisfactory results, for unknown configuration, it should be estimated with Germano dynamic procedure (using the overall distribution of the constant through probability density).
 - (c) The lift force is the main mechanism for the dispersion, and the lift coefficient should be estimated though sensitivity of interfacial forces on values of slip velocity and gas holdup. The lift coefficient in LES can be different from that in RANS.
 - (d) The central difference scheme should be used for the discretization of advection terms for flow variables and high-order schemes (MUSCL, QUICK, or Second-Order) can be used for scalar variables.
 - (e) The minimum time for gathering statistics should be at least one flow through time (as defined as ratio of the system height over the bulk (superficial) velocity).
- (6) In advent of computer hardware, the E-L approach appears very promising for the near future. Further work in mapping functions for two-way coupling can expedite the development of this approach that can be used as a means of both predicting the properties of specific turbulent flows and providing flow details that can be used like data to test and refine other turbulence-closure models.
- (7) The approach for BIT with extra production terms into the SGS-turbulent kinetic energy equation (following the procedure described by Pfleger and Becker [38]) has shown to be more effective than the approach involving a bubble-induced viscosity [37]. It can be that the enhanced eddy viscosity in LES does not represented as realistic physical model, as the SGS turbulent kinetic energy. Nonetheless, it is an interesting issue, and more work in investigating the BIT should be undertaken.

- (8) Treatment of the interphase forces needs more attention.
- The drag and nondrag forces (lift, virtual mass force) can be modelled using resolved field approaches. The modelling of these forces for the SGS and their effect on the overall simulation results need to be evaluated.
 - One finds strong dependency of the bubble dispersion on the value of transverse lift force coefficient. The transverse lift, which depends on the bubble-liquid relative velocity, seems to be the main mechanism responsible for the spreading of the bubbles. It will help if one can estimate the separate contributions of each of these forces.
 - The virtual mass force has little influence on simulation results. So far, a constant coefficient has been used in all the investigations; however, dependence on void fraction has been shown in experiments. It would be good to have a correct description in order to improve results near the inlet where bubble acceleration effects are important.
- (9) The strong coupling between subgrid-scale (SGS) modelling and the truncation error of the numerical discretization can be exploited by developing discretization methods where the truncation error itself functions as an implicit SGS model. Such attempt can be useful and go in the direction of finding a universal SGS model.
- (10) In order to use LES for reliable predictions at minimum computational costs, understanding of the influence of discretization methods, boundary conditions, wall models, and numerical parameters (e.g., convergence criterion, time steps, etc.) is essential. The contribution focusing on these aspects should be undertaken for both E-E/E-L approaches.
- (11) Substantial development has been achieved in LES in the last decade for understanding bubbly gas-liquid dispersed flow. However, it is mainly restricted to low superficial gas velocities and gas fractions. Future work should focus on industrially relevant large-scale reactors at high superficial gas velocity. The modelling of bubble coalescence and breakup might be necessary, along with further clarity in filtering operations.
- (12) Joshi and coworkers have used LES for the identification of flow structures and their dynamics. They have proposed a procedure to use this information for the estimation of design parameters. Substantial additional work is needed for finding 3D information on the structure characteristics such as size, shape, velocity, and energy distributions

Nomenclature

C_D :	Drag force coefficient
C_L :	Lift force coefficient
C_{VM} :	Virtual mass coefficient
C_{TD} :	Turbulent dispersion coefficient
$C_{\epsilon 1}$:	Model parameter in turbulent dissipation energy equation (=1.44)
$C_{\epsilon 2}$:	Model parameter in turbulent dissipation energy equation (=1.92)
C_S :	Smagorinsky model constant
$C_{\mu, BI}$:	Model constant (Sato and Seguchi [37] model), (=0.6)
d_b :	Mean bubble diameter
D :	Diameter of the column (m)
F_P :	Force originating due to pressure (N/m ³)
F_G :	Gravitational force per unit volume of dispersion (N/m ³)
F_L :	Lift force per unit volume of dispersion (N/m ³)
F_{VM} :	Virtual mass force per unit volume of dispersion (N/m ³)
F_{TD} :	Turbulent dispersion force per unit volume of dispersion (N/m ³)
F_{WL} :	Wall lubrication force per unit volume of dispersion (N/m ³)
F_{WD} :	Wall deformation force per unit volume of dispersion (N/m ³)
H :	Height of column (m)
K :	Turbulent kinetic energy per unit mass (m ² /s ²)
K_{SGS} :	Subgrid-scale turbulent kinetic energy (m ² /s ³)
S :	Characteristic of strain tensor of filtered velocity
\mathbf{u} :	Instantaneous axial velocity (m/s)
W :	Width of column (m).

Greek Symbols

Δ :	Filter width
Δt :	Simulation time step
ϕ_f :	Grid-scale component of scalar
ϕ_f :	Resolved component of scalar
ϕ_f :	Filtered component of scalar
ϵ :	Turbulent energy dissipation rate per unit mass (m ² /s ³)
α :	Fractional phase holdup
α_g :	Fractional gas phase holdup
ρ :	Density (kg/m ³)
ρ_l :	Density of liquid (kg/m ³)
$\mu_{eff, f}$:	Effective viscosity of phase f (Pa s)
$\mu_{eff, l}$:	Effective viscosity of liquid phase f (Pa s)
$\mu_{am, l}$:	Molecular viscosity of liquid phase f (Pa s)
$\mu_{BI, l}$:	Bubble-induced viscosity (Pa s).

Subscripts

F:	Phase, g = gas phase, l = liquid phase
BI:	Bubble-induced.

Abbreviations

BIT: Bubble-induced turbulence
 E: Eulerian
 L: Lagrangian
 SGS: Subgrid-scale.

Acknowledgment

N. G. Deen would like to thank the European Research Council for its financial support, under its Starting Investigator Grant scheme, contract number 259521 (cutting bubbles).

References

- [1] A. Sokolichin, G. Eigenberger, A. Lapin, and A. Lübbert, "Dynamic numerical simulation of gas-liquid two-phase flows: Euler/Euler versus Euler/Lagrange," *Chemical Engineering Science*, vol. 52, no. 4, pp. 611–626, 1997.
- [2] G. Bois, D. Jamet, and O. Lebaigue, "Towards large eddy simulation of two-phase flow with phase-change: direct numerical simulation of a pseudo-turbulent two-phase condensing flow," in *Proceedings of the 7th International Conference on Multiphase Flow (ICMF '10)*, Tampa, Fla, USA, May-June 2010.
- [3] A. Toutant, M. Chandesris, D. Jamet, and O. Lebaigue, "Jump conditions for filtered quantities at an under-resolved discontinuous interface—part 1: theoretical development," *International Journal of Multiphase Flow*, vol. 35, no. 12, pp. 1100–1118, 2009.
- [4] A. Toutant, M. Chandesris, D. Jamet, and O. Lebaigue, "Jump conditions for filtered quantities at an under-resolved discontinuous interface—part 2: a priori tests," *International Journal of Multiphase Flow*, vol. 35, no. 12, pp. 1119–1129, 2009.
- [5] S. Magdeleine, B. Mathieu, O. Lebaigue, and C. Morel, "DNS up-scaling applied to volumetric interfacial area transport equation," in *Proceedings of the 7th International Conference on Multiphase Flow (ICMF '10)*, p. 12, Tampa, Fla, USA, May-June 2010.
- [6] D. Lakehal, "LEIS for the prediction of turbulent multi-fluid flows applied to thermal hydraulics applications," in *Proceedings of the XFD4NRS*, Grenoble, France, September 2008.
- [7] D. Lakehal, M. Fulgosi, S. Banerjee, and G. Yadigaroglu, "Turbulence and heat exchange in condensing vapor-liquid flow," *Physics of Fluids*, vol. 20, no. 6, Article ID 065101, 2008.
- [8] D. Bestion, "Applicability of two-phase CFD to nuclear reactor thermalhydraulics and elaboration of best practice guidelines," *Nuclear Engineering and Design*, vol. 253, pp. 311–321, 2012.
- [9] B. Ničeno, M. T. Dhotre, and N. G. Deen, "One-equation subgrid scale (SGS) modelling for Euler-Euler large eddy simulation (EELES) of dispersed bubbly flow," *Chemical Engineering Science*, vol. 63, no. 15, pp. 3923–3931, 2008.
- [10] B. Niceno, M. Boucker, and B. L. Smith, "Euler-Euler large eddy simulation of a square cross-sectional bubble column using the Neptune CFD code," *Science and Technology of Nuclear Installations*, vol. 2009, Article ID 410272, 2009.
- [11] M. Milelli, B. L. Smith, and D. Lakehal, "Large-eddy simulation of turbulent shear flows laden with bubbles," in *Direct and Large-Eddy Simulation IV*, B. J. Geurts, R. Friedrich, and O. Metais, Eds., pp. 461–470, Kluwer Academic Publishers, Amsterdam, The Netherlands, 2001.
- [12] D. A. Drew, "Averaged field equations for two-phase media," *Studies in Applied Mathematics*, vol. 50, no. 2, pp. 133–165, 1971.
- [13] S. Elgobashi, "Particle-laden turbulent flows: direct simulation and closure models," *Applied Scientific Research*, vol. 48, no. 3–4, pp. 301–314, 1991.
- [14] C. T. Crowe, M. P. Sharma, and D. E. Stock, "The particle-source-in cell (PSI-CELL) model for gas-droplet flows," *Journal of Fluids Engineering*, vol. 99, no. 2, pp. 325–332, 1977.
- [15] G. Hu, *Towards large eddy simulation of dispersed gas-liquid two-phase turbulent flows [Ph.D. thesis]*, Mechanical and Aerospace Engineering Department, West Virginia University, Morgantown, WV, USA, 2005.
- [16] N. G. Deen, M. V. S. Annaland, and J. A. M. Kuipers, "Multi-scale modeling of dispersed gas-liquid two-phase flow," *Chemical Engineering Science*, vol. 59, pp. 1853–1861, 2004.
- [17] M. V. Tabib, S. A. Roy, and J. B. Joshi, "CFD simulation of bubble column—an analysis of interphase forces and turbulence models," *Chemical Engineering Journal*, vol. 139, no. 3, pp. 589–614, 2008.
- [18] M. T. Dhotre, B. Niceno, B. L. Smith, and M. Simiano, "Large-eddy simulation (LES) of the large scale bubble plume," *Chemical Engineering Science*, vol. 64, no. 11, pp. 2692–2704, 2009.
- [19] N. G. Deen, T. Solberg, and B. H. Hjertager, "Large eddy simulation of the gas-liquid flow in a square cross-sectioned bubble column," *Chemical Engineering Science*, vol. 56, no. 21–22, pp. 6341–6349, 2001.
- [20] M. T. Dhotre, B. Niceno, and B. L. Smith, "Large eddy simulation of a bubble column using dynamic sub-grid scale model," *Chemical Engineering Journal*, vol. 136, no. 2–3, pp. 337–348, 2008.
- [21] J. Smagorinsky, "General circulation experiments with the primitive equations," *Monthly Weather Review*, vol. 91, pp. 99–165, 1963.
- [22] P. Moin and J. Kim, "Numerical investigations of turbulent channel flow," *Journal of Fluid Mechanics*, vol. 118, pp. 341–377, 1982.
- [23] W. Jones and M. Wille, "Large eddy simulation of a jet in a cross flow," in *Proceedings of the 10th Symposium on Turbulent Shear Flows*, pp. 41–46, The Pennsylvania State University, 1995.
- [24] M. Milelli, B. L. Smith, and D. Lakehal, "Large-eddy simulation of turbulent shear flows laden with bubbles," in *Direct and Large-Eddy Simulation IV*, B. J. Geurts, R. Friedrich, and O. Metais, Eds., pp. 461–470, Kluwer Academic Publishers, Amsterdam, The Netherlands, 2001.
- [25] D. Lakehal, B. L. Smith, and M. Milelli, "Large-eddy simulation of bubbly turbulent shear flows," *Journal of Turbulence*, vol. 3, pp. 1–20, 2002.
- [26] D. Zhang, N. G. Deen, and J. A. M. Kuipers, "Numerical simulation of the dynamic flow behavior in a bubble column: a study of closures for turbulence and interface forces," *Chemical Engineering Science*, vol. 61, no. 23, pp. 7593–7608, 2006.
- [27] D. Lain, "Dynamic three-dimensional simulation of gas liquid flow in a cylindrical bubble column Latin American," *Applied Research*, vol. 39, pp. 317–329, 2009.
- [28] M. Germano, U. Piomelli, P. Moin, and W. H. Cabot, "A dynamic subgrid-scale eddy viscosity model," *Physics of Fluids A*, vol. 3, no. 7, pp. 1760–1765, 1991.
- [29] S. Bove, T. Solberg, and B. H. Hjertager, "Numerical aspects of bubble column simulations," *International Journal of Chemical Reactor Engineering*, vol. 2, no. A1, pp. 1–22, 2004.

- [30] M. V. Tabib and P. Schwarz, "Quantifying sub-grid scale (SGS) turbulent dispersion force and its effect using one-equation SGS large eddy simulation (LES) model in a gas-liquid and a liquid-liquid system," *Chemical Engineering Science*, vol. 66, no. 14, pp. 3071–3086, 2011.
- [31] E. I. V. van den Hengel, N. G. Deen, and J. A. M. Kuipers, "Application of coalescence and breakup models in a discrete bubble model for bubble columns," *Industrial and Engineering Chemistry Research*, vol. 44, no. 14, pp. 5233–5245, 2005.
- [32] G. Hu and I. Celik, "Eulerian-Lagrangian based large-eddy simulation of a partially aerated flat bubble column," *Chemical Engineering Science*, vol. 63, no. 1, pp. 253–271, 2008.
- [33] D. Darmana, N. G. Deen, J. A. M. Kuipers, W. K. Harteveld, and R. F. Mudde, "Numerical study of homogeneous bubbly flow: influence of the inlet conditions to the hydrodynamic behavior," *International Journal of Multiphase Flow*, vol. 35, no. 12, pp. 1077–1099, 2009.
- [34] R. Sungkorn, J. J. Derksen, and J. G. Khinast, "Modeling of turbulent gas-liquid bubbly flows using stochastic Lagrangian model and lattice-Boltzmann scheme," *Chemical Engineering Science*, vol. 66, no. 12, pp. 2745–2757, 2011.
- [35] W. Bai, N. G. Deen, and J. A. M. Kuipers, "Numerical analysis of the effect of gas sparging on bubble column hydrodynamics," *Industrial and Engineering Chemistry Research*, vol. 50, no. 8, pp. 4320–4328, 2011.
- [36] W. Bai, N. G. Deen, and J. A. M. Kuipers, "Numerical investigation of gas holdup and phase mixing in bubble column reactors," *Industrial & Engineering Chemistry Research*, vol. 51, no. 4, pp. 1949–1961, 2012.
- [37] Y. Sato and K. Sekoguchi, "Liquid velocity distribution in two-phase bubble flow," *International Journal of Multiphase Flow*, vol. 2, no. 1, pp. 79–95, 1975.
- [38] D. Pflieger and S. Becker, "Modelling and simulation of the dynamic flow behaviour in a bubble column," *Chemical Engineering Science*, vol. 56, no. 4, pp. 1737–1747, 2001.
- [39] A. A. Troshko and Y. A. Hassan, "A two-equation turbulence model of turbulent bubbly flows," *International Journal of Multiphase Flow*, vol. 27, no. 11, pp. 1965–2000, 2001.
- [40] M. Sommerfeld, "Validation of a stochastic Lagrangian modelling approach for inter-particle collisions in homogeneous isotropic turbulence," *International Journal of Multiphase Flow*, vol. 27, no. 10, pp. 1829–1858, 2001.
- [41] M. Sommerfeld, G. Kohnen, and M. Rueger, "Some open questions and inconsistencies of Lagrangian particle dispersion models," in *Proceedings of the 9th Symposium on Turbulent Shear Flows*, Kyoto, Japan, 1993, paper no. 15-1.
- [42] Y. Sato, M. Sadatomi, and K. Sekoguchi, "Momentum and heat transfer in two-phase bubble flow-I. Theory," *International Journal of Multiphase Flow*, vol. 7, no. 2, pp. 167–177, 1981.
- [43] D. Pflieger, S. Gomes, N. Gilbert, and H. G. Wagner, "Hydrodynamic simulations of laboratory scale bubble columns fundamental studies of the Eulerian-Eulerian modeling approach," *Chemical Engineering Science*, vol. 54, no. 21, pp. 5091–5099, 1999.
- [44] M. Ishii and N. Zuber, "Drag coefficient and relative velocity in bubbly, droplet or particulate flows," *AIChE Journal*, vol. 25, no. 5, pp. 843–855, 1979.
- [45] A. Tomiyama, "Drag lift and virtual mass forces acting on a single bubble," in *Proceedings of the 3rd International Symposium on Two-Phase Flow Modeling and Experimentation*, Pisa, Italy, September 2004.
- [46] R. M. Wellek, A. K. Agrawal, and A. H. P. Skelland, "Shape of liquid drops moving in liquid media," *AIChE Journal*, vol. 12, no. 5, pp. 854–862, 1966.
- [47] A. Tomiyama, "Struggle with computational bubble dynamics," in *Proceedings of the 3rd International Conference on Multi-Phase Flow (ICMF '98)*, Lyon, France, June 1998.
- [48] R. Clift, J. R. Grace, and M. E. Weber, *Bubbles, Drops and Particles*, Academic Press, New York, NY, USA, 1978.
- [49] M. Milelli, *A numerical analysis of confined turbulent bubble plume [Diss. EH. no. 14799]*, Swiss Federal Institute of Technology, Zurich, Switzerland, 2002.
- [50] J. Bardina, J. H. Ferziger, and W. C. Reynolds, "Improved subgrid models for large eddy simulation," AIAA paper 80-1358, 1980.
- [51] P. E. Anagbo and J. K. Brimacombe, "Plume characteristics and liquid circulation in gas injection through a porous plug," *Metallurgical Transactions B*, vol. 21, no. 4, pp. 637–648, 1990.
- [52] M. R. Bhole, S. Roy, and J. B. Joshi, "Laser doppler anemometer measurements in bubble column: effect of sparger," *Industrial and Engineering Chemistry Research*, vol. 45, no. 26, pp. 9201–9207, 2006.
- [53] S. Becker, A. Sokolichin, and G. Eigenberger, "Gas-liquid flow in bubble columns and loop reactors—part II: comparison of detailed experiments and flow simulations," *Chemical Engineering Science*, vol. 49, no. 24, part 2, pp. 5747–5762, 1994.
- [54] A. Sokolichin and G. Eigenberger, "Applicability of the standard k- ϵ turbulence model to the dynamic simulation of bubble columns—part I: detailed numerical simulations," *Chemical Engineering Science*, vol. 54, no. 13-14, pp. 2273–2284, 1999.
- [55] M. Simiano, *Experimental investigation of large-scale three dimensional bubble plume dynamics [Dissertation no. 16220]*, Swiss Federal Institute of Technology, Zurich, Switzerland, 2005.
- [56] S. Lain and M. Sommerfeld, "LES of gas-liquid flow in a cylindrical laboratory bubble column," in *Proceedings of the 5th International Conference on Multiphase Flow (ICMF '04)*, Yokohama, Japan, 2004, paper no. 337.
- [57] M. Lopez de Bertodano, *Turbulent bubbly two-phase flow in a triangular duct [Ph.D. thesis]*, Rensselaer Polytechnic Institute, Troy, NY, USA, 1992.
- [58] E. Delnoij, F. A. Lammers, J. A. M. Kuipers, and W. P. M. van Swaaij, "Dynamic simulation of dispersed gas-liquid two-phase flow using a discrete bubble model," *Chemical Engineering Science*, vol. 52, no. 9, pp. 1429–1458, 1997.
- [59] E. Delnoij, J. A. M. Kuipers, and W. P. M. Van Swaaij, "A three-dimensional CFD model for gas-liquid bubble columns," *Chemical Engineering Science*, vol. 54, no. 13-14, pp. 2217–2226, 1999.
- [60] D. Bröder and M. Sommerfeld, "An advanced LIF-PLV system for analysing the hydrodynamics in a laboratory bubble column at higher void fractions," *Experiments in Fluids*, vol. 33, no. 6, pp. 826–837, 2002.
- [61] W. K. Harteveld, J. E. Julia, R. F. Mudde, and H. E. A. van den Akker, "Large scale vortical structures in bubble columns for gas fractions in the range of 5–25%," in *Proceedings of the 16th International Congress of Chemical and Process Engineering (CHISA '04)*, Prague, Czech Republic, 2004.
- [62] J. B. Joshi and M. M. Sharma, "A circulation cell model for bubble columns," *Transactions of the Institution of Chemical Engineers*, vol. 57, no. 4, pp. 244–251, 1979.

- [63] J. B. Joshi, "Axial mixing in multiphase contactors—a unified correlation," *Transactions of the Institution of Chemical Engineers*, vol. 58, no. 3, pp. 155–165, 1980.
- [64] V. V. Ranade and J. B. Joshi, "Flow generated by pitched blade turbines. 1. Measurements using laser Doppler anemometer," *Chemical Engineering Communications*, vol. 81, pp. 197–224, 1989.
- [65] V. V. Ranade, J. R. Bourne, and J. B. Joshi, "Fluid mechanics and blending in agitated tanks," *Chemical Engineering Science*, vol. 46, no. 8, pp. 1883–1893, 1991.
- [66] T. Kumaresan and J. B. Joshi, "Effect of impeller design on the flow pattern and mixing in stirred tanks," *Chemical Engineering Journal*, vol. 115, no. 3, pp. 173–193, 2006.
- [67] J. B. Joshi, M. M. Sharma, Y. T. Shah, C. P. P. Singh, M. Ally, and G. E. Klinzing, "Heat transfer in multiphase contactors," *Chemical Engineering Communications*, vol. 6, no. 4–5, pp. 257–271, 1980.
- [68] M. T. Dhotre and J. B. Joshi, "Two-dimensional CFD model for the prediction of flow pattern, pressure drop and heat transfer coefficient in bubble column reactors," *Chemical Engineering Research and Design*, vol. 82, no. 6, pp. 689–707, 2004.
- [69] M. T. Dhotre, K. Ekambara, and J. B. Joshi, "CFD simulation of sparger design and height to diameter ratio on gas hold-up profiles in bubble column reactors," *Experimental Thermal and Fluid Science*, vol. 28, no. 5, pp. 407–421, 2004.
- [70] A. V. Kulkarni, S. V. Badgandi, and J. B. Joshi, "Design of ring and spider type spargers for bubble column reactor: experimental measurements and CFD simulation of flow and weeping," *Chemical Engineering Research and Design*, vol. 87, no. 12, pp. 1612–1630, 2009.
- [71] J. B. Joshi and M. M. Sharma, "Mass transfer and hydrodynamic characteristics of gas inducing type of agitated contactors," *Canadian Journal of Chemical Engineering*, vol. 55, no. 6, pp. 683–695, 1977.
- [72] B. N. Murthy, N. A. Deshmukh, A. W. Patwardhan, and J. B. Joshi, "Hollow self-inducing impellers: flow visualization and CFD simulation," *Chemical Engineering Science*, vol. 62, no. 14, pp. 3839–3848, 2007.
- [73] K. S. M. S. Raghava Rao, V. B. Rewatkar, and J. B. Joshi, "Critical impeller speed for solid suspension in mechanically agitated contactors," *AIChE Journal*, vol. 34, no. 8, pp. 1332–1340, 1988.
- [74] V. B. Rewatkar, K. S. M. S. Raghava Rao, and J. B. Joshi, "Critical impeller speed for solid suspension in mechanically agitated three-phase reactors. 1. Experimental part," *Industrial and Engineering Chemistry Research*, vol. 30, no. 8, pp. 1770–1784, 1991.
- [75] B. N. Murthy, R. S. Ghadge, and J. B. Joshi, "CFD simulations of gas-liquid-solid stirred reactor: prediction of critical impeller speed for solid suspension," *Chemical Engineering Science*, vol. 62, no. 24, pp. 7184–7195, 2007.
- [76] J. B. Joshi and V. V. Ranade, "Computational fluid dynamics for designing process equipment: expectations, current status, and path forward," *Industrial and Engineering Chemistry Research*, vol. 42, no. 6, pp. 1115–1128, 2003.
- [77] D. Darmana, N. G. Deen, and J. A. M. Kuipers, "Detailed modeling of hydrodynamics, mass transfer and chemical reactions in a bubble column using a discrete bubble model," *Chemical Engineering Science*, vol. 60, no. 12, pp. 3383–3404, 2005.
- [78] D. Darmana, R. L. B. Henket, N. G. Deen, and J. A. M. Kuipers, "Detailed modelling of hydrodynamics, mass transfer and chemical reactions in a bubble column using a discrete bubble model: chemisorption of CO₂ into NaOH solution, numerical and experimental study," *Chemical Engineering Science*, vol. 62, no. 9, pp. 2556–2575, 2007.
- [79] D. Zhang, N. G. Deen, and J. A. M. Kuipers, "Euler-euler modeling of flow, mass transfer, and chemical reaction in a bubble column," *Industrial and Engineering Chemistry Research*, vol. 48, no. 1, pp. 47–57, 2009.
- [80] A. W. Vreman, "An eddy-viscosity sub-grid-scale model for turbulent shear flow: algebraic theory and applications," *Physics of Fluids*, vol. 16, no. 10, pp. 3670–3681, 2004.
- [81] K. Ekambara and J. B. Joshi, "Axial mixing in laminar pipe flows," *Chemical Engineering Science*, vol. 59, no. 18, pp. 3929–3944, 2004.
- [82] C. S. Mathpati, S. S. Deshpande, and J. B. Joshi, "Computational and experimental fluid dynamics of jet loop reactor," *AIChE Journal*, vol. 55, no. 10, pp. 2526–2544, 2009.
- [83] C. S. Mathpati, M. V. Tabib, S. S. Deshpande, and J. B. Joshi, "Dynamics of flow structures and transport phenomena. 2. Relationship with design objectives and design optimization," *Industrial and Engineering Chemistry Research*, vol. 48, no. 17, pp. 8285–8311, 2009.
- [84] J. B. Joshi, V. S. Vitankar, A. A. Kulkarni, M. T. Dhotre, and K. Ekambara, "Coherent flow structures in bubble column reactors," *Chemical Engineering Science*, vol. 57, no. 16, pp. 3157–3183, 2002.
- [85] S. S. Deshpande, J. B. Joshi, V. R. Kumar, and B. D. Kulkarni, "Identification and characterization of flow structures in chemical process equipment using multiresolution techniques," *Chemical Engineering Science*, vol. 63, no. 21, pp. 5330–5346, 2008.
- [86] M. V. Tabib and J. B. Joshi, "Analysis of dominant flow structures and their flow dynamics in chemical process equipment using snapshot proper orthogonal decomposition technique," *Chemical Engineering Science*, vol. 63, no. 14, pp. 3695–3715, 2008.
- [87] M. V. Tabib, M. J. Sathe, S. S. Deshpande, and J. B. Joshi, "A hybridized snapshot proper orthogonal decomposition-discrete wavelet transform technique for the analysis of flow structures and their time evolution," *Chemical Engineering Science*, vol. 64, no. 21, pp. 4319–4340, 2009.
- [88] M. J. Sathe, I. H. Thaker, T. E. Strand, and J. B. Joshi, "Advanced PIV/LIF and shadowgraphy system to visualize flow structure in two-phase bubbly flows," *Chemical Engineering Science*, vol. 65, no. 8, pp. 2431–2442, 2010.
- [89] C. S. Mathpati, M. J. Sathe, and J. B. Joshi, "Reply to 'comments on dynamics of flow structures and transport phenomena—part I: experimental and numerical techniques for identification and energy content of flow structures,'" *Industrial and Engineering Chemistry Research*, vol. 49, no. 9, pp. 4471–4473, 2010.
- [90] S. S. Deshpande, C. S. Mathpati, S. S. Gulawani, J. B. Joshi, and V. Ravi kumar, "Effect of flow structures on heat transfer in single and multiphase jet reactors," *Industrial and Engineering Chemistry Research*, vol. 48, no. 21, pp. 9428–9440, 2009.
- [91] S. S. Deshpande, M. V. Tabib, J. B. Joshi, V. Ravi Kumar, and B. D. Kulkarni, "Analysis of flow structures and energy spectra in chemical process equipment," *Journal of Turbulence*, vol. 11, article N5, pp. 1–39, 2010.
- [92] Z. Khan, C. S. Mathpati, and J. B. Joshi, "Comparison of turbulence models and dynamics of turbulence structures in bubble column reactors: effects of sparger design and superficial gas velocity," *Chemical Engineering Science*. In press.

Research Article

Bubble Dynamics of a Single Condensing Vapor Bubble from Vertically Heated Wall in Subcooled Pool Boiling System: Experimental Measurements and CFD Simulations

Arijit A. Ganguli, Aniruddha B. Pandit, and Jyeshtharaj B. Joshi

Institute of Chemical Technology, Matunga, Mumbai 400 019, India

Correspondence should be addressed to Jyeshtharaj B. Joshi, jb.joshi@ictmumbai.edu.in

Received 29 October 2011; Revised 22 February 2012; Accepted 26 March 2012

Academic Editor: Mahesh T. Dhotre

Copyright © 2012 Arijit A. Ganguli et al. This is an open access article distributed under the Creative Commons Attribution License, which permits unrestricted use, distribution, and reproduction in any medium, provided the original work is properly cited.

Bubble dynamics of a single condensing vapor bubble in a subcooled pool boiling system with a centrally heated cylindrical tank has been studied in the Rayleigh number range $7.9 \times 10^{12} < Ra < 1.88 \times 10^{13}$. The heat source in the system is steam condensing inside a vertical tube. The tube was placed in the center of the tank (300 mm i.d., 300 mm height) which is well filled with water. Experimental investigation has been carried out with High Speed Camera while Computational Fluid Dynamics (CFD) investigation has been performed using Volume of Fluid (VOF) method. The heat source has been modeled using simple heat balance. The rise behavior of condensing bubbles (change in size during rise and path tracking) was studied and the CFD model was validated both quantitatively and qualitatively.

1. Introduction

Pool boiling is a complex nonlinear dynamic process. The microscopic aspects of boiling process, for example, embryo nucleation and surface roughness determine its nature largely. The microscopic effects eventually exhibit in a macroscopic behavior. Further, boiling is a highly stochastic process and the precise prediction of the location and time of the generation, collapse, coalescence is difficult with the present status of knowledge. The condensation of bubbles in subcooled boiling systems is extremely important for studying the hydrodynamics during subcooled pool boiling. The simple reason for this is that condensation changes the shape and size of the bubbles. When a bubble is formed at the interstitial site in the case of nucleate boiling the bubble grows to a certain diameter and then departs from the interstitial site. As the bubble departs from the nucleation site, it tends to slide along the hot surface and detaches from the surface. The bubble then does not necessarily follow a straight path but moves near or away from the wall. In addition to experimental investigations,

Computational Fluid Dynamics (CFD) is useful to obtain better understanding of bubble dynamics.

Experimental investigations on dynamics of single vapor bubbles condensing in a subcooled boiling liquid have been carried out by Voloshko and Vurgaft [1] and an analytical model was developed. The authors found the relation between the dynamics of vapor bubble during condensation and intensity of heat exchange at vapor bubble interface. Bubble dynamics of vapor bubbles in subcooled liquids have been investigated (both experimentally and numerically) by researchers [2–9]. Numerical investigations using volume of fluid (VOF) method have been recently carried out by Ganguli [2]. Further, Jeon et al. [3] developed a CFD model for condensation of the bubble and sensitivity tests for different bulk temperatures and liquid velocities have been performed. Various parameters of the bubble, like bubble velocity, interfacial area, bubble diameter, and bubble volume obtained from CFD simulations were compared.

The unavailability of data on the bubble dynamics in pool boiling systems is the main motivation of the current work. Further, the hydrodynamics of bubbles in subcooled

boiling systems have been studied by bubbles being formed on a horizontal plate. The dynamics of bubbles on vertical tube are; however, different from the one on a horizontal plate. The flow generated due to heating of a vertical tube is different than the one on horizontal plate. Another important aspect is the Rayleigh numbers considered in this work. It may be noted that this range of Rayleigh numbers has not been investigated for subcooled pool boiling. The current work is an effort to develop a CFD model and validate the results with experiments.

2. Experimental Setup and Measurements

2.1. Experimental Set-Up. The experimental setup is similar to the one used by Ganguli et al. [10]. For producing a single bubble care has been taken for the bubble formation. The entire pipe has been buffed and an interstitial site has been made at the center of the pipe (Area = 3 mm²) for bubble formation as shown in Figure 1. The bubble size was dependent on the heat flux and for understanding the bubble sizes trial runs were performed and reproducibility of bubble sizes were noted.

2.2. Photographic Measurement. A digital video camera (Photron Fastcam 10KC, Resolution 512 × 480 pixels) together with halogen lamp (located at the opposite side of the camera) was used for taking pictures of the condensate films. All signals except video images were processed using the data acquisition system, consisting of A/D converter and a PC. The video images were analyzed by means of MATLAB software. All the instruments were calibrated before testing.

3. Computational Model

In this study, the VOF method [11] was used to simulate the bubble rise behavior in liquids having nonuniform velocity gradients. As the local pressure fluctuations were negligible compared to atmospheric pressure, the gas phase compressibility was neglected. Considering extremely low values of compressibility of water it was also considered as an incompressible fluid.

3.1. Assumptions. The following assumptions were made for the study.

- (1) Vapor (steam) and liquid (water) phases were considered as incompressible fluids.
- (2) No internal mass source are assumed. Hence the source terms for liquid and vapor have been considered to be equal.
- (3) Bubble generation and behavior is a stochastic phenomenon. Yet the bubble generation at the same interstitial site has been tracked for the single bubble analysis, and the effect of other bubbles on the single bubble has been neglected.
- (4) The bubble on the tube surface slides on the surface vertically upward for some distance and lifts off.

- (5) The shear due to the thermal boundary layer as soon as it is developed is assumed to be constant for the lifecycle of the bubble since very little change in velocity gradients occurs in 500 ms which is the maximum time period for any bubble to travel the vertical distance under consideration.

3.2. Volume of Fluid (VOF) Method. A two-phase model has been formulated in the Euler-Euler framework using VOF approach. The VOF model is a surface-tracking technique applied to a fixed Eulerian mesh. It is designed for two or more immiscible fluids where the position of the interface between the fluids is of interest. In the VOF model, the fluids share a single set of momentum equations and the volume fraction of each of the fluids in each computational cell is tracked throughout the domain. The field for all variables and properties is shared by the phases and represent volume-averaged values, as long as the volume fraction of each of the phases is known at each location. In each control volume the volume fractions of all the phases sum up to unity. Thus the variables and properties in any given cell are either purely representative of one of the phase, or representative of a mixture of the phases depending upon the volume fraction values. In other words, if the q th fluid volume fraction in the cell is denoted as ϵ_q , then the following three conditions are possible:

$\epsilon_q = 0$ the cell is empty (of the q th fluid),

$\epsilon_q = 1$ the cell is full (of the q th fluid),

$0 < \epsilon_q < 1$ the cell contains the interface between the q th fluid and one or more other fluids.

Based on the local value of ϵ_q the appropriate properties and variables are assigned to each control volume within the domain. Further, interphase mass transfer has been tracked by using the phase change model incorporated through a User Defined Function (UDF). For turbulence closure, realizable K - ϵ turbulence model has been incorporated. The governing equations for the entire region of the liquid and vapor are given later (5), (8), (9), (21) and (23). The explanation is given as follows.

The term on the right-hand side of (8) describes the mass transfer source term. This term can be calculated by using the mass transfer model (see the details in Section 3.3 below) and decides the extent of phase change (condensation). In the present system, we consider condensed water as the secondary phase and saturated steam as the primary phase. In the VOF modeling approach, the volume fraction equation is solved for the secondary phase. The primary phase volume fraction is computed based on the following constraint:

$$\sum_{q=1}^2 \epsilon_q = 1. \quad (1)$$

The terms on the right-hand side of (5) describe the forces acting on the fluid element in the control volume.

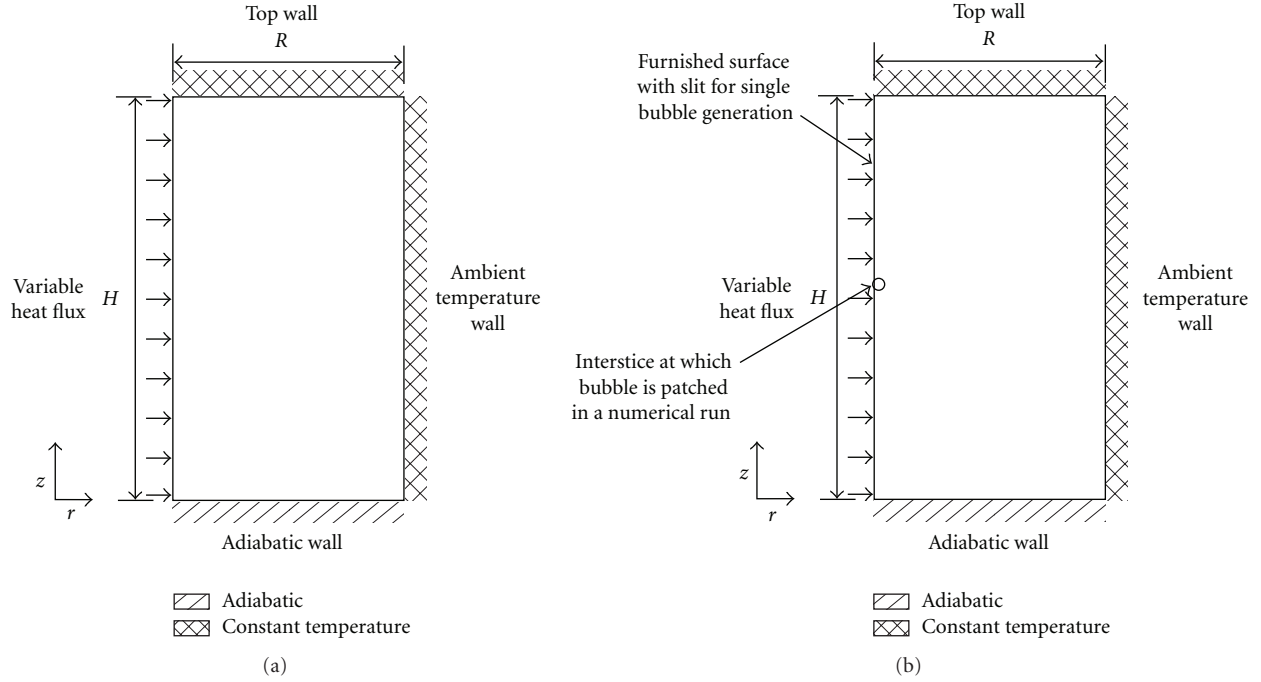


FIGURE 1: (a) Schematic of a dimensionless rectangular enclosure with leftside wall heated. (b) Schematic of a vertical rectangular enclosure with leftside wall heated and a bubble patched at the interstice.

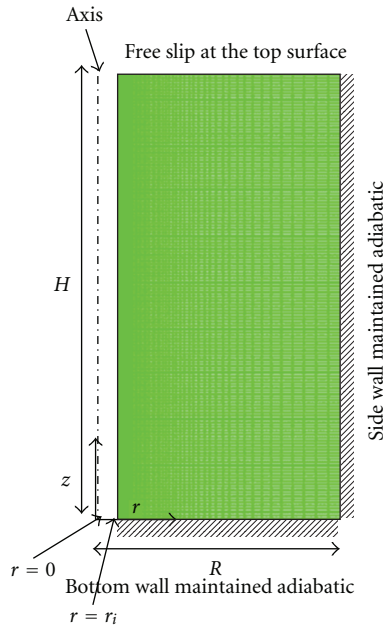


FIGURE 2: Sample grid of two dimensional (2D) cylindrical tank with left-hand wall heated.

These are the overall pressure gradient, the stresses, the gravitational force, and the body force due to surface tension effect. The momentum equation (5) is dependent on the

volume fraction of all the phases through the properties density ρ and viscosity μ :

$$\rho = \sum \epsilon_q \rho_q, \quad (2)$$

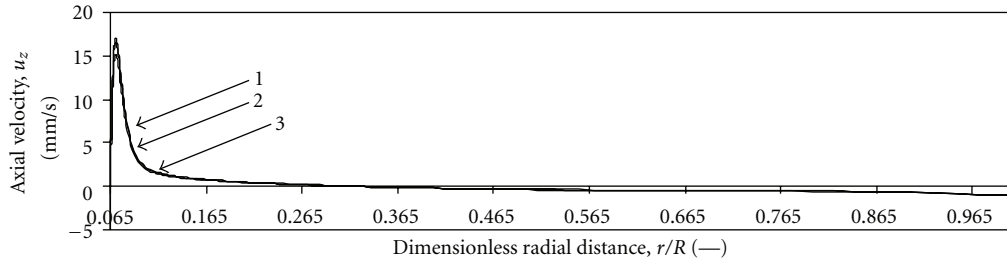
$$\mu = \sum \epsilon_q \mu_q. \quad (3)$$

The effective thermal conductivity k_{eff} in the energy equation (9) and effective viscosity μ_{eff} in the momentum equation (8) is shared by both phases. S_E is the source term in the energy equation that includes all the volumetric heat sources [W/m^3]. In the present application, this term represents a sink that accounts for the latent heat of condensation during the phase change. Energy E is mass averaged as shown below:

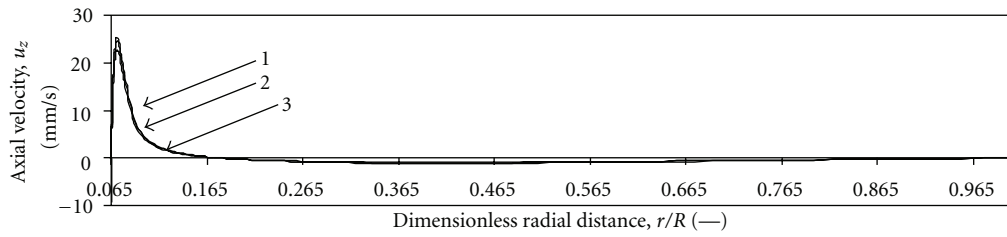
$$E = \frac{\sum_{q=1}^2 \epsilon_q \rho_q E_q}{\sum_{q=1}^2 \epsilon_q \rho_q}. \quad (4)$$

Further, the properties appearing in the transport equations are determined by the presence of the component phase in each control volume. In the present vapor-liquid system the volume fraction of the liquid is being tracked, the density and viscosity in each cell are given by (2) and (3).

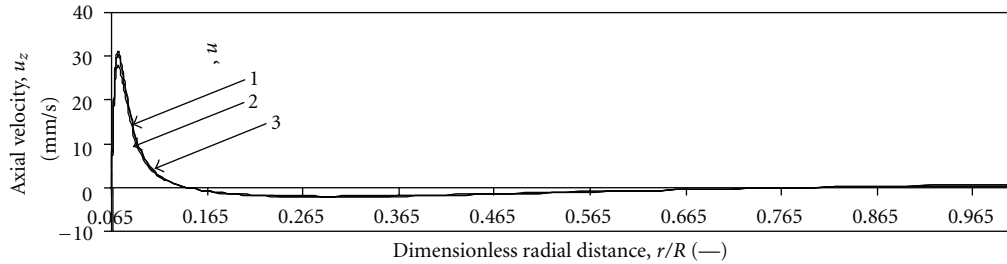
A single set of Navier-Stokes equation for an incompressible Newtonian flow was solved.



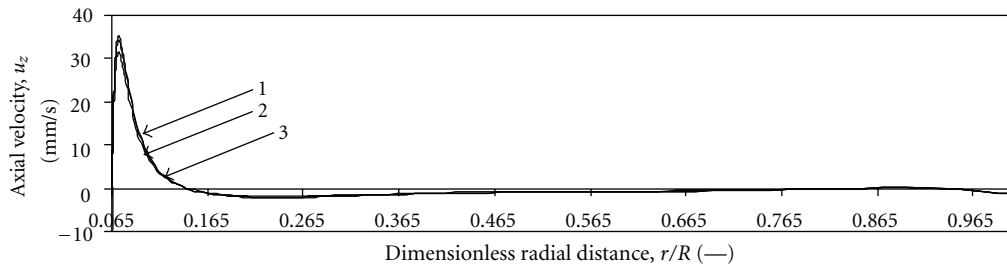
(a)



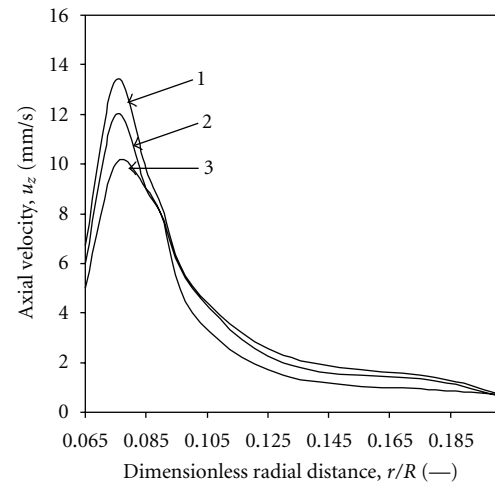
(b)



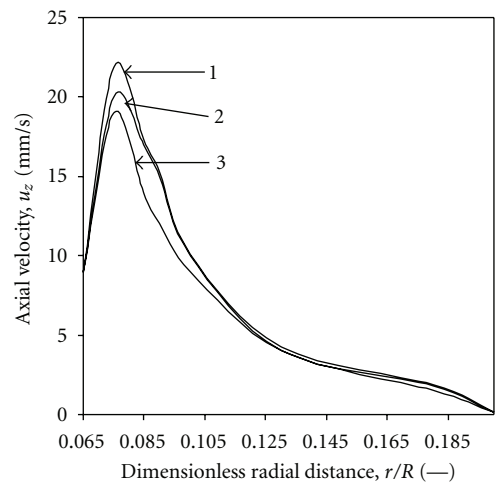
(c)



(d)



(e)



(f)

FIGURE 3: Continued.

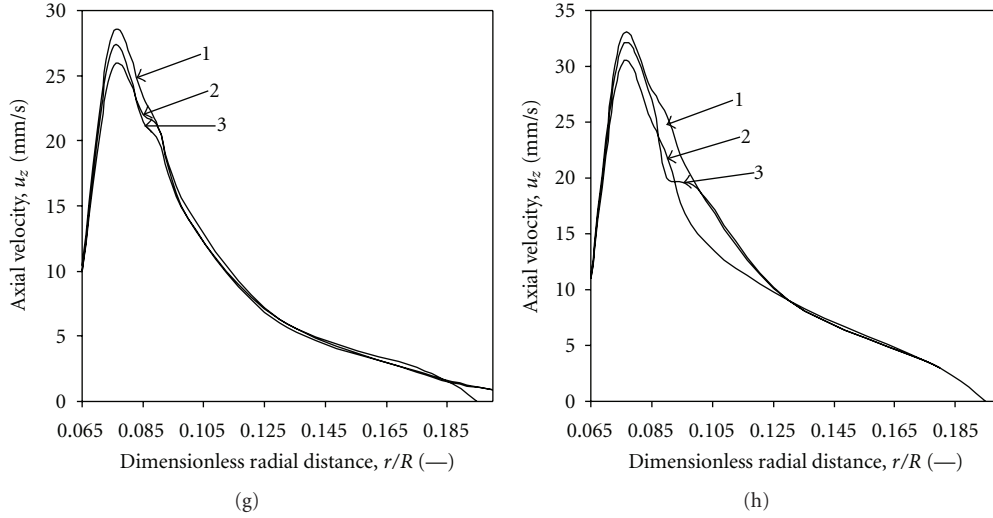


FIGURE 3: Variation of axial velocity with dimensionless radial distance for various grid sizes. (a) $z/H = 0.1$, (b) $z/H = 0.33$, (c) $z/H = 0.5$, and (d) $z/H = 0.8$. (e) Zoomed view of Figure 3(a), (f) Zoomed view of Figure 3(b), (g) Zoomed view of Figure 3(c), (h) Zoomed view of Figure 3(d). (1) 80×150 , (2) 100×175 , and (3) 100×200 .

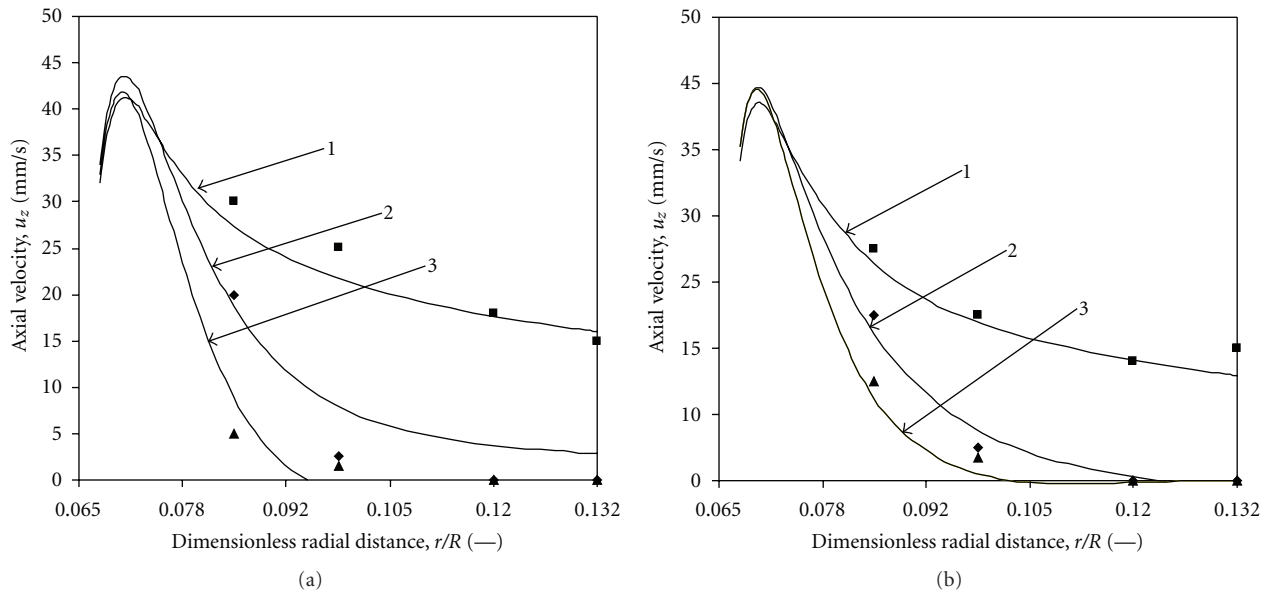


FIGURE 4: Axial velocity v/s , dimensionless radial distance. (a) $Ra = 8 \times 10^{12}$ (b) $Ra = 1.8 \times 10^{13}$.

Momentum equation is given below:

$$\begin{aligned} & \frac{\partial(\rho \in_q \langle u_k \rangle)}{\partial t} + \nabla \cdot (\rho \in_q \langle u_k \rangle \langle u_k \rangle) \\ & = -\in_q \nabla \langle p \rangle + \nabla \cdot \bar{\tau}_k \\ & \quad + \rho \in_q g + \vec{F}_q, \end{aligned} \quad (5)$$

$$\begin{aligned} \bar{\tau}_k & = \in_q \mu_{eff} (\nabla \langle u_k \rangle + (\nabla \langle u_k \rangle)^T) \\ & \quad + \in_q \left(\lambda_q - \frac{2}{3} \mu_{eff} \right) \nabla \cdot \langle u_k \rangle I. \end{aligned}$$

The CSF model of Brackbill et al. [12] was used to compute the surface tension force as a source term in the momentum equation for the cells containing the interface. The expression for \vec{F}_q is given by:

$$\vec{F} = \sigma \frac{\rho \kappa n}{1/2(\rho_l + \rho_v)}, \quad (6)$$

where σ is the coefficient of surface tension, \hat{n} is the surface normal which is proportional to the gradient of volume fraction, κ is the local surface curvature calculated as follows [12]:

$$\kappa = -(\nabla \hat{n}) = \frac{1}{|n|} \left[\frac{n}{|n|} \nabla |n| - (\nabla \cdot n) \right]. \quad (7)$$

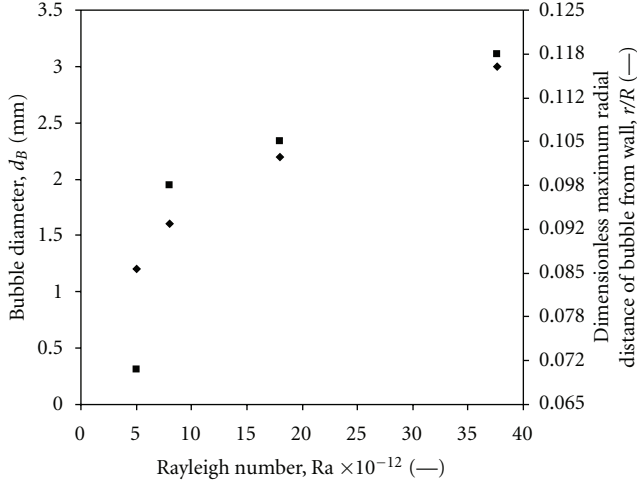


FIGURE 5: Variation of bubble diameter and maximum radial distance of bubble from the wall with Rayleigh number. radial distance from the wall bubble diameter.

The geometric reconstruction scheme [5] based on piecewise linear approach [4] was used for the reconstruction of the interface. In the VOF approach, the reconstructed interface is advected by solving an advection equation for the volume fraction of the dispersed phase. The equation for volume fraction is given as:

$$\frac{\partial(\rho \epsilon_q)}{\partial t} + \nabla \cdot (\rho \epsilon_q \langle u_k \rangle) = S_{\epsilon_q}. \quad (8)$$

Energy equation is given by:

$$\frac{\partial(\rho \epsilon_q H)}{\partial t} + \nabla \cdot (\rho \epsilon_q H \langle u_k \rangle) = \nabla \cdot \langle k_{eff} \nabla T \rangle - \epsilon_q \nabla \langle p \rangle + S_E. \quad (9)$$

The liquid phase volume fraction is computed from the following equation:

$$\epsilon_l + \epsilon_v = 1. \quad (10)$$

3.3. Computation of Interface Mass Transfer and Turbulence Modeling. A model for phase change in the present study has been used to simulate the condensation phenomena, which describes the interphase heat transfer of intrinsic flows and considers the heat transfer processes on each side of the phase interface. Therefore, the mass exchange source terms in mass equations and latent heat transfer term in energy equation have been incorporated in the modeled equation through UDF. At the liquid-vapor interface, the temperature should be equal to the saturation temperature.

Heat content on vapor side across the interface is given by:

$$q''_v = -\epsilon_v k_v \nabla T, \quad (11)$$

where q''_v vapor heat flux across the interface, ϵ_v is volume fraction of vapor, k_v is thermal conductivity of vapor, ∇T is

the temperature gradient at the liquid-vapor interface, and $\epsilon_v = \sum \epsilon_{v,j}$ where “j” represents the volume fraction of vapor at each cell of the vapor-liquid interface.

Similarly, the Heat Flux on the Liquid Side across the Interface is Given by:

$$q''_l = \epsilon_l k_l \nabla T, \quad (12)$$

where q''_l liquid heat flux across the interface, ϵ_l is volume fraction of liquid, k_l is thermal conductivity of liquid. The heat liberated during condensation (q_{cond}) in terms of latent heat is given by:

$$q_{cond} = \dot{m} \lambda_{cond}, \quad (13)$$

where \dot{m} represents the total mass transfer from vapor to liquid. Equation (13) can also be written as

$$\dot{m} = \frac{q_{cond}}{\lambda_{cond}}. \quad (14)$$

The total mass transfer rate is the sum of each cell's mass transfer rate in the interface region. Let \dot{m}'_j represent each cells mass transfer rate proportional to vapor volume fraction in the j th cell in the interface region and V_j is the volume of each cell. consisting of the vapor-liquid interface will have a spatial variation of the volume fraction ϵ at the region consisting of the vapor liquid interface, the mass transfer rate for two phase mixture is represented as follows [3]:

$$\dot{m} = \left(\frac{q_{cond}}{\lambda_{cond}} \right) \cdot \sum_j \epsilon_{q,j} V_j, \quad (15)$$

where $\epsilon_{q,j}$ is the volume fraction of the j th cell.

The heat liberated due to condensation can also be expressed as:

$$q_{cond} = q''_v - q''_l. \quad (16)$$

From (11)–(16) we have

$$\dot{m} = \frac{(-\epsilon_v k_v - \epsilon_l k_l) \nabla T \cdot \sum_j \epsilon_{q,j} V_j}{\lambda_{cond}}. \quad (17)$$

Thus, the mass source in the vapor phase is represented by:

$$S_{\epsilon_v} = - \frac{(\epsilon_v k_v + \epsilon_l k_l) \nabla T \cdot \sum_j \epsilon_{q,j} V_j}{\lambda_{cond}}. \quad (18)$$

Since there is no internal mass source, mass source for the liquid phase becomes

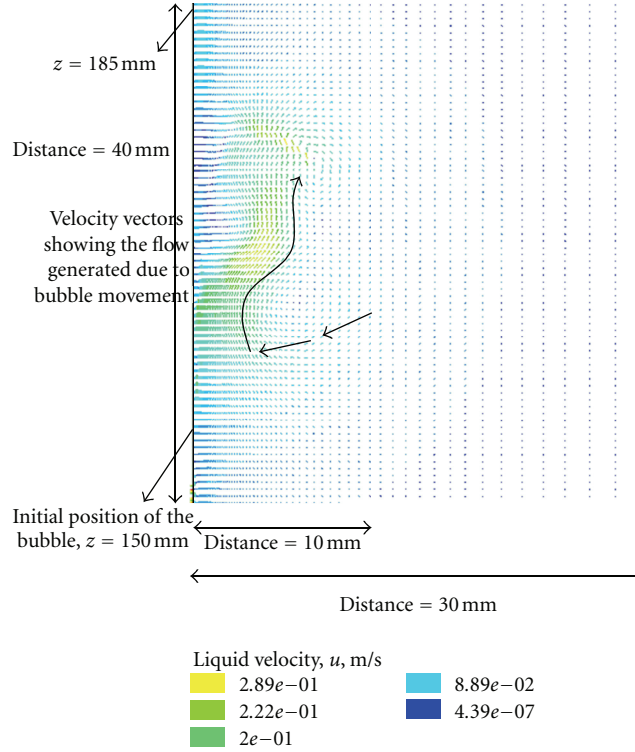


FIGURE 6: Velocity vectors showing the movement of the bulk fluid due to bubble movement.

$$S_{E_l} = -S_{E_v}. \quad (19)$$

Latent heat source for the energy equation becomes

$$S_E = -S_{E_v} \cdot \lambda_{cond}. \quad (20)$$

Turbulence equations are given by the SST k - ω model as follows.

Turbulent kinetic energy is

$$\begin{aligned} & \frac{\partial(\epsilon_q \rho K)}{\partial t} + \langle u_k \rangle \nabla \cdot \langle \epsilon_q \rho K \rangle \\ & = \nabla \cdot \left(\left(\mu + \frac{\mu_t}{\sigma_K} \right) \nabla K \right) \\ & \quad + G_K + G_b - Y_K. \end{aligned} \quad (21)$$

Turbulent kinetic energy is $G_K = \nu_t |\bar{S}|^2$ where $|\bar{S}| = \sqrt{2S_{ij}S_{ij}}$

$$|\bar{S}_{ij}| = \frac{1}{2} \left(\frac{\partial u_r}{\partial z} + \frac{\partial u_z}{\partial r} \right). \quad (22)$$

Energy dissipation rate equation is given as follows

$$\begin{aligned} & \frac{\partial(\epsilon_q \rho \omega)}{\partial t} + \langle u_k \rangle \nabla \cdot \langle \epsilon_q \rho \omega \rangle \\ & = \nabla \cdot \left(\left(\mu + \frac{\mu_t}{\sigma_K} \right) \nabla \omega \right) \\ & \quad + G_\omega - Y_\omega. \end{aligned} \quad (23)$$

Generation of turbulence due to buoyancy is given as:

$$G_b = -\beta g \frac{\mu_t}{\sigma_t} \frac{\partial \langle T \rangle}{\partial z}. \quad (24)$$

Dissipation of K and ω is given below:

$$Y_K = \epsilon_1 \rho_1 \beta_\infty^* f_{\beta^*} K \omega, \quad Y_\omega = \rho \beta_r \omega^2, \quad (25)$$

where,

$$\begin{aligned} \beta_\infty^* & = 0.09, f_{\beta^*} \\ & = \begin{cases} 1, & \chi_k \leq 0 \\ \left[\frac{1 + 680\chi_k^2}{1 + 400\chi_k^2} \right], & \chi_k > 0, \chi_k = \frac{1}{\omega^3} \frac{\partial K}{\partial z} \frac{\partial \omega}{\partial z}. \end{cases} \end{aligned} \quad (26)$$

Production of ω is given by:

$$G_\omega = \frac{\alpha_\infty}{\nu_t} G_K \quad (27)$$

Equations, (1) to (27) were solved using the commercial flow solver Fluent 6.2.

3.4. Solution Domain, Boundary Conditions, and Numerical Schemes. The spatial derivatives in (5), (8), (9), (21), and (23) were discretized using the QUICK scheme [13] while

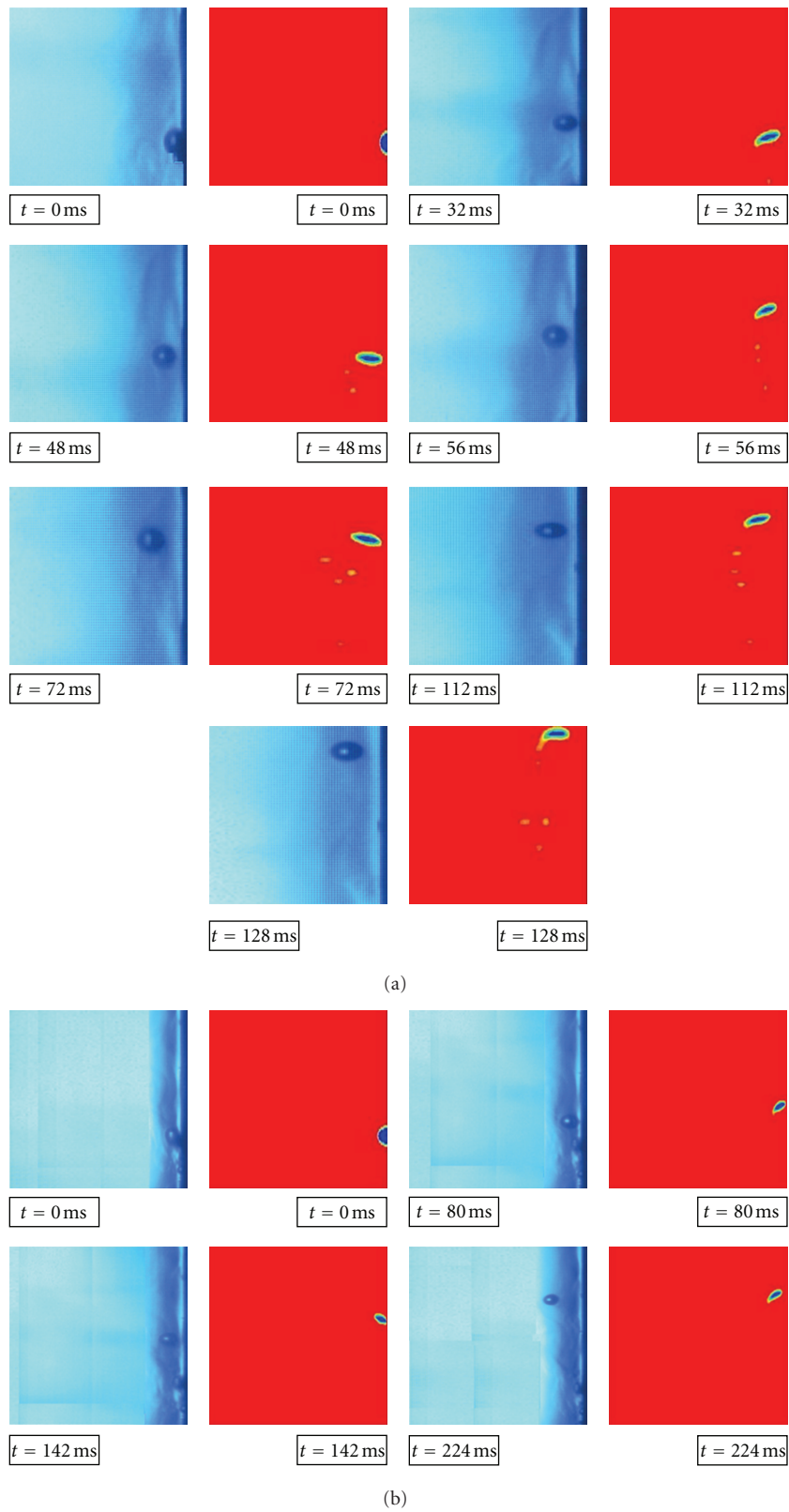


FIGURE 7: Comparison of bubble movement with high-speed photography and VOF simulations. (a) $Ra = 8 \times 10^{12}$ (b) $Ra = 1.8 \times 10^{13}$.

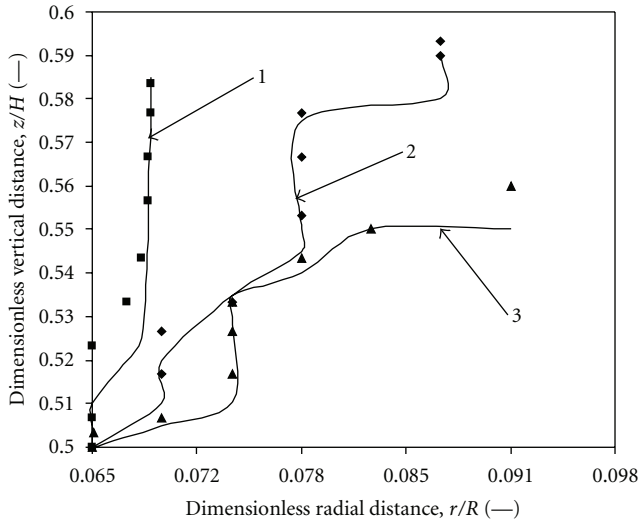


FIGURE 8: Dimensionless vertical distance v/s , Dimensionless radial distance.

a first-order implicit method was used for the discretization of the temporal derivatives. The pressure implicit with splitting of operator (PISO) algorithm [14] was used for the pressure-velocity coupling in the momentum equation.

A 2D rectangular solution domain ($H = 150$ mm, $R = 150$ mm) as shown in Figure 2 with nonuniform structured grid was used. A single phase simulation has been carried out for the first 20 seconds when the first bubble departs as observed in the experiments of $Ra = 1.88 \times 10^{13}$. A bubble of suitable diameter as calculated from the measured bubble size by high-speed camera has been patched as an initial condition and two-phase simulation using VOF method has been carried out. A no slip boundary condition was used at the stationary wall. A constant heat flux was given as a boundary condition, so that the spatially averaged heat flux can be monitored for longer times and the behavior of heat transfer coefficient can be monitored in time. The constant heat flux q_{cond} has been calculated by using (13).

The effect of time step on bubble size was investigated by performing the simulations with four different time steps (1×10^{-4} s, 1×10^{-5} s, 1×10^{-6} s, and 1×10^{-7} s) for $Ra = 1.8 \times 10^{13}$. The difference in predicted bubble sizes for 1×10^{-6} s and 1×10^{-7} s was about 2% and therefore all further simulations were carried out using a time step of 1×10^{-6} s.

4. Results and Discussion

In the present section we present the results of bubble movement and the lift force exerted on the bubble when a specific amount of heat input is provided. The present simulations have been provided after 60 seconds of run when the first bubble appears as per experimental observations. Rayleigh number (Ra) has been varied in the range $7.9 \times 10^{12} < Ra < 1.88 \times 10^{13}$. For formation of single bubbles only small part of the whole pipe (Area = 3 mm²) has been considered with interstices and the rest of the circumferential area has been buffed so that no bubbles can

form at the surface. Simulations have been performed as per experimental conditions and the vertical bubble motion has been compared. The effect of heat flux which influences the bubble diameter and distance from wall has been studied.

4.1. Grid Independence. The grid used for the simulations is shown in Figure 2. For single phase run the grid independence has been checked. It has been found that there is very little variation in the axial velocities at different axial locations as shown in Figure 3. Further, the grid independency has been tested for various grid size to bubble diameter ratio ((i) 1/10 and (ii) 1/20) for resolving the surface deformations. It has been observed that the deformation of the bubble surface is not much influenced by increasing the grid size. However, decreasing the number of cells caused divergence in the 2D simulations.

4.2. Variation of Axial Velocity with Radial Distance. Figure 4 shows the variation of axial velocity with dimensionless radial distance. As the heat flux increases the axial velocity increases for a distance of 1 mm, decreases upto a distance of 4 mm, and then remains constant. A reasonably good agreement with experimental data has been observed. The experimental data was obtained with a hot film anemometer probe at various vertical positions near the wall. The constant temperature anemometer mode has been used which gives velocity series with time.

4.3. Effect of Heat Flux on Bubble Diameter and Flow Patterns. In the case of subcooled boiling the effect of heat flux on the bubble diameter for a single bubble has been carried out in the present work. Figure 5 shows the variation in bubble diameter with increase in heat flux. It can be observed that, as the heat flux increases, the bubble diameter and the distance of the bubble from the wall after departure also increase. The increase in the bubble diameter is steep during the initial heat fluxes while the slope decreases as the flux increases. Figure 6 shows the velocity vectors due to the movement of the bubble at a time of 56 ms. As can be clearly seen significant amount of increase in flow is observed due to the bubble rise. The velocity vectors also match the photographs as in Figure 7(a). The rushing of the bulk fluid from the bulk can also be observed.

4.4. Bubble Tracking. Movement of the single bubble has been tracked both with the help of high-speed camera (125 frames/s) and 2D CFD simulations. For different heat inputs ($7.9 \times 10^{12} < Ra < 1.88 \times 10^{13}$) the bubble motion has been tracked. The bubble diameter was measured and the similar conditions (bubble diameter, heat input) were provided for the numerical runs. A single phase run was performed before the first bubble appeared and then a bubble of diameter as observed in the experimental run has been provided. Figure 7(a) shows the sequence of images of bubble movement ($d_B = 1.6$ mm, $Ra = 7.9 \times 10^{12}$) by both experimental and computational techniques. An area of liquid (30 mm \times 40 mm) of the total area has been chosen

for investigation. Initially bubble adheres to the tube wall after which it moves in the upward direction. The bubble departs from the surface and migrates away from the wall after which it moves steadily without any movement upto a certain distance and then moves away from the wall. The shear for this case was measured as 1.3 s^{-1} . It can be observed that in corresponding VOF simulations the bubble gets deformed into ellipsoidal-shaped bubbles after departing from the surface. This denotes the need for a surface-tracking mechanism better than VOF. However, in experimental photographs (Figure 7(a)) the bubble shape is spherical till 72 ms while at $t = 112 \text{ ms}$ and $t = 128 \text{ ms}$ the experimental photographs also show ellipsoidal shape. Similarly, Figure 7(b) shows the sequence of images for higher bubble diameters ($d_B = 2.2 \text{ mm}$). It can be seen that the movement away from the wall after bubble departure is much more pronounced for 2.2 mm bubble. The shear rate considered here is 2.5 s^{-1} . However, several other reasons like the use of better turbulence models (Large Eddy simulations (LES)) and three dimensional (3D) simulations may also be needed. The movement of the bubbles is; however, well matched with the experimental observations. The bubble trajectory as shown in Figure 8 depicts that a smaller diameter bubble for a low-heat input moves steadily along the wall while a higher diameter bubble moves steadily along the wall and departs away from the wall after a certain vertical distance has been traversed. Tomiyama et al. [15] found that, in bubble columns, larger bubbles depart away from the wall while smaller bubbles moved towards the wall. The shear in the case of Tomiyama et al. [15] was 3.8 s^{-1} while here the shear and bubble diameter both are function of heat flux. Experimental visualization showed that, for the same shear rate, when runs were carried out at prolonged time periods ($t = 120 \text{ s}$) the bubble tended to move towards the wall adhere to the surface and again depart. This process continued till it reached the top free surface of the pool. The analysis presented in this subsection suggests that a more detailed study of the dynamics occurring in the thermal boundary layer and the turbulent structures near the wall has a major role to play in the bubble movement. The study is; however, out of scope of the present work.

5. Conclusions

Bubble dynamics in subcooled pool boiling systems have been evaluated for ($7.9 \times 10^{12} < Ra < 1.88 \times 10^{13}$). The bubble movement has been found to be lateral for a certain vertical distance and bubbles departed when they approached the top surface. Bubble trajectories were plotted for the vertical distance in which the bubbles were found to be in the wall regime with a shift to the neutral regime as defined by Tomiyama et al. [15]. Bubble diameter increases steeply with increase in Ra number ($Ra < 1.5 \times 10^{13}$) with no significant increase with an increase in Ra number. The single bubble considered moves within the boundary layer until it is near the top surface where it departs. The developed CFD model can be extended to study various phenomena like (a) study the effect of multiple bubbles on hydrodynamics and

heat transfer in subcooled boiling systems, (b) calculation of non-drag forces like lift and virtual mass forces in such systems, and (c) studying coalescence and breakup phenomena in such systems.

Notation

d_B :	Equivalent bubble diameter, mm
E :	Total energy supplied to the system, kJ
E_q :	Energy of fluid, kJ
\vec{F}_q :	Force because of the pressure jump at the interface, N
g :	Gravitational constant, m s^{-2}
G_b :	Generation of turbulence due to buoyancy, $\text{m}^4 \text{ s}^{-1}$
G_K :	Generation of turbulent kinetic energy due to mean velocity gradients ($\text{kg} \cdot \text{m}^{-1} \text{ s}^3$)
H :	Column height, mm
H :	Specific enthalpy as in energy equation in (9), kJ/kg
I :	Identity matrix, (—)
K :	Turbulent kinetic energy as in (21), m^2/s^2
k :	Thermal conductivity, $\text{W m}^{-1} \text{ K}^{-1}$
k_{eff} :	Effective thermal conductivity, $\text{W m}^{-1} \text{ K}^{-1}$
k_l :	Thermal conductivity of liquid, W/mK
k_v :	Thermal conductivity of vapor, W/m K
\dot{m} :	Total mass flow rate of steam, kg/s
\dot{m}'_j :	Mass flow rate at the j th cell, kg/s
n :	Surface normal vector, (—)
\hat{n} :	Unit normal vector, (—)
p :	Total pressure, Pa
$\langle p \rangle$:	Time averaged of total pressure, Pa
q_{cond} :	Condensation heat flux in (18), W/m^2
q''_l :	Liquid heat flux across the interface, W/m^2
q''_v :	Vapor heat flux across the interface, W/m^2
R :	Radius of the tank, m
r :	Spatial co-ordinate in radial direction
S_{el} :	Mass source in liquid phase, kW/m^3
S_{eq} :	Mass source in qth phase, kW/m^3
S_{ev} :	Mass source in vapor phase, kW/m^3
S_E :	Source term for energy equation, $\text{kg m}^{-2} \text{ s}^{-1}$
S_{ij} :	Strain term in three spatial co-ordinates, N m^{-2}
S :	Strain term, N m^{-2}
$ \bar{S} $:	overall averaged strain term, N m^{-2}
$ \bar{S}_{ij} $:	Average of strain terms in two spatial co-ordinates, N m^{-2}
t :	Time, s
T :	Temperature, K
$\langle T \rangle$:	Time averaged value of temperature, K
u_k :	Velocity vector, m/s
$\langle u \rangle$:	Time average of velocity, m/s
V_j :	Volume of each cell, m^3
Y_K :	Dissipation of turbulent kinetic energy in K equation, $\text{m}^2 \text{ s}^{-3}$
Y_ω :	Dissipation of turbulent kinetic energy in ω equation, $\text{m}^2 \text{ s}^{-3}$
z :	Space co-ordinate in axial direction.

Greek Symbols

α_∞ : Constant used in (27)
 β_r : Is constant used in Y_ω equation
 β_∞^* : Constant
 μ_{eff} : Effective viscosity, kg/ms
 χ : Constant
 λ_q : Latent heat of condensation for qth phase, kJ/kg
 ϵ : Volume fraction
 ϵ_q : Volume fraction of fluid, (—)
 $\epsilon_{q,j}$: Volume fraction of fluid at jth cell, (—)
 ϵ_l : Volume fraction of the liquid phase, (—)
 κ : Surface curvature
 λ_{cond} : Latent heat of condensation kJ/kg
 λ_q : Term used to calculation of shear stress component
 μ : Molecular viscosity, $\text{kg m}^{-1} \text{s}^{-1}$
 μ_l : Viscosity of liquid, kg/ms
 μ_v : Viscosity of vapor, kg/ms
 ω : Specific dissipation rate, $\text{m}^{-2} \text{s}^{-1}$
 ρ : Density, kg m^{-3}
 ρ_l : Density of liquid, kg/m^3
 ρ_q : Density of fluid, kg/m^3
 ρ_v : Density of vapour, kg/m^3
 ν : Kinematics viscosity, m^2/s
 ν_t : Turbulent viscosity, m^2/s
 σ : Surface tension, N/m
 σ_t : Turbulent Prandtl number, (—)
 σ_k : Turbulent Prandtl number for kinetic energy equation, (—)
 τ_k : Shear stress, N m^{-2}
 $\bar{\tau}_k$: Averaged shear stress component, N/m^2
 χ_k : Constant used in (26), (—).

Subscripts and Superscripts

eff : Effective
 i, j, k : Axis indexes of spatial co-ordinates
 l : Liquid
 q : Phase
 v : Vapor
 r : Cylindrical space coordinate for radial direction
 t : Turbulent
 z : Cylindrical space coordinate for axial direction.

References

- [1] A. A. Voloshko and A. V. Vurgaft, "Investigation of the condensation of single vapor bubbles in a layer of underheated liquid," *Journal of Engineering Physics*, vol. 19, no. 2, pp. 936–939, 1973.
- [2] A. A. Ganguli, *Studies in heat transfer: role of phase change and non-condensable gases [Ph.D. thesis]*, Institute of Chemical Technology, Mumbai, India, 2009.
- [3] S. S. Jeon, S. J. Kim, and G. C. Park, "CFD simulation of condensing vapor bubble using VOF model," *Proceedings of World Academy of Science, Engineering and Technology*, vol. 60, pp. 209–215, 2009.
- [4] N. Nikolopoulos, A. Theodorakakos, and G. Bergeles, "A numerical investigation of the evaporation process of a liquid droplet impinging onto a hot substrate," *International Journal of Heat and Mass Transfer*, vol. 50, no. 1-2, pp. 303–319, 2007.
- [5] A. Tomiyama, A. Sou, H. Minagawa, and T. Sakaguchi, "Numerical analysis of a single bubble by VOF method," *JSME International Journal, Series B*, vol. 36, no. 1, pp. 51–56, 1993.
- [6] D. K. Agarwal, S. W. J. Welch, G. Biswas, and F. Durst, "Planar simulation of bubble growth in film boiling in near-critical water using a variant of the VOF method," *Journal of Heat Transfer*, vol. 126, no. 3, pp. 329–338, 2004.
- [7] D. L. Youngs, "Time-dependent multi-lateral flow with large fluid distortion," in *Numerical Methods for Fluid Dynamics*, K. Morton and M. Baines, Eds., pp. 273–285, Academic Press, New York, NY, USA, 1982.
- [8] M. H. Yuan, Y. H. Yang, T. S. Li, and Z. H. Hu, "Numerical simulation of film boiling on a sphere with a volume of fluid interface tracking method," *International Journal of Heat and Mass Transfer*, vol. 51, no. 7-8, pp. 1646–1657, 2008.
- [9] Z. Yang, X. F. Peng, and P. Ye, "Numerical and experimental investigation of two phase flow during boiling in a coiled tube," *International Journal of Heat and Mass Transfer*, vol. 51, no. 5-6, pp. 1003–1016, 2008.
- [10] A. A. Ganguli, M. J. Sathe, A. B. Pandit, J. B. Joshi, and P. K. Vijayan, "Hydrodynamics and heat transfer characteristics of passive decay heat removal systems: CFD simulations and experimental measurements," *Chemical Engineering Science*, vol. 65, no. 11, pp. 3457–3473, 2010.
- [11] C. W. Hirt and B. D. Nichols, "Volume of fluid (VOF) method for the dynamics of free boundaries," *Journal of Computational Physics*, vol. 39, no. 1, pp. 201–225, 1981.
- [12] J. U. Brackbill, D. B. Kothe, and C. Zemach, "A continuum method for modeling surface tension," *Journal of Computational Physics*, vol. 100, no. 2, pp. 335–354, 1992.
- [13] B. P. Leonard, "A stable and accurate convective modelling procedure based on quadratic upstream interpolation," *Computer Methods in Applied Mechanics and Engineering*, vol. 19, no. 1, pp. 59–98, 1979.
- [14] R. I. Issa, "Solution of the implicitly discretised fluid flow equations by operator-splitting," *Journal of Computational Physics*, vol. 62, no. 1, pp. 40–65, 1986.
- [15] A. Tomiyama, H. Tamai, I. Zun, and S. Hosokawa, "Transverse migration of single bubbles in simple shear flows," *Chemical Engineering Science*, vol. 57, no. 11, pp. 1849–1858, 2002.

Review Article

CFD Simulation of Annular Centrifugal Extractors

S. Vedantam,¹ K. E. Wardle,² T. V. Tamhane,³ V. V. Ranade,¹ and J. B. Joshi^{3,4}

¹ Chemical Engineering and Process Development Division, National Chemical Laboratory, Pune 411008, India

² Chemical Sciences and Engineering Division, Argonne National Laboratory, Lemont, IL 60439, USA

³ Department of Chemical Engineering, Institute of Chemical Technology, Matunga, Mumbai 400 019, India

⁴ Homi Bhabha National Institute, Anushakti Nagar, Mumbai 400 094, India

Correspondence should be addressed to K. E. Wardle, kwardle@anl.gov and J. B. Joshi, jbjoshi@gmail.com

Received 30 March 2012; Accepted 13 June 2012

Academic Editor: Mahesh T. Dhotre

Copyright © 2012 S. Vedantam et al. This is an open access article distributed under the Creative Commons Attribution License, which permits unrestricted use, distribution, and reproduction in any medium, provided the original work is properly cited.

Annular centrifugal extractors (ACE), also called annular centrifugal contactors offer several advantages over the other conventional process equipment such as low hold-up, high process throughput, low residence time, low solvent inventory and high turn down ratio. The equipment provides a very high value of mass transfer coefficient and interfacial area in the annular zone because of the high level of power consumption per unit volume and separation inside the rotor due to the high g of centrifugal field. For the development of rational and reliable design procedures, it is important to understand the flow patterns in the mixer and settler zones. Computational Fluid Dynamics (CFD) has played a major role in the constant evolution and improvements of this device. During the past thirty years, a large number of investigators have undertaken CFD simulations. All these publications have been carefully and critically analyzed and a coherent picture of the present status has been presented in this review paper. Initially, review of the single phase studies in the annular region has been presented, followed by the separator region. In continuation, the two-phase CFD simulations involving liquid-liquid and gas-liquid flow in the annular as well as separator regions have been reviewed. Suggestions have been made for the future work for bridging the existing knowledge gaps. In particular, emphasis has been given to the application of CFD simulations for the design of this equipment.

1. Introduction

Annular centrifugal extractors, also called annular centrifugal contactors [1–5], offer several advantages over the other conventional process equipment such as low holdup, high process throughput, low residence time, low solvent inventory, and high turndown ratio. The equipment provides a very high value of mass transfer coefficient and interfacial area in the annular zone because of the high level of power consumption per unit volume [6, 7] and separation inside the rotor due to the high g of centrifugal field. Annular centrifugal extractors find wide applications in nuclear fuel processing where safety is the main concern [2, 8, 9], in biological operations where controlled shear field and/or facilitated settling is important [10, 11] and polymerization [12, 13], excellent mixing, heat, and mass transfer [14–19]. Annular centrifugal extractors can also be used for a variety of chemical reactions such as synthesis of monodisperse silica particles, regeneration of spent activated carbon [20, 21],

esterification, and hydrolysis [22, 23], as cavitation reactor [24], and they have also been demonstrated for use with ionic liquids [25].

Depending upon the orientation of rotating cylinder, the equipment is classified as a horizontal or vertical contactor. In both types of contactors, the flow behavior can be broadly classified as either a homogeneous dispersion, banded dispersion, or stratified flow with both the phases retaining their individual integrity. To design this equipment, it is important to understand a priori the conditions under which the transition takes place from one type of flow regime to another. Industrial scale equipment typically has a vertical orientation [26–28]. Some published work is also available for horizontal orientation [4, 29, 30].

The annular centrifugal extractor (ACE) consists of coaxial cylinders ((1) and (2)) as shown schematically in Figure 1. The immiscible feed liquids enter at points (3A) and (3B) into the annular region between the two cylinders. The spinning of the rotor imparts power (in the range of

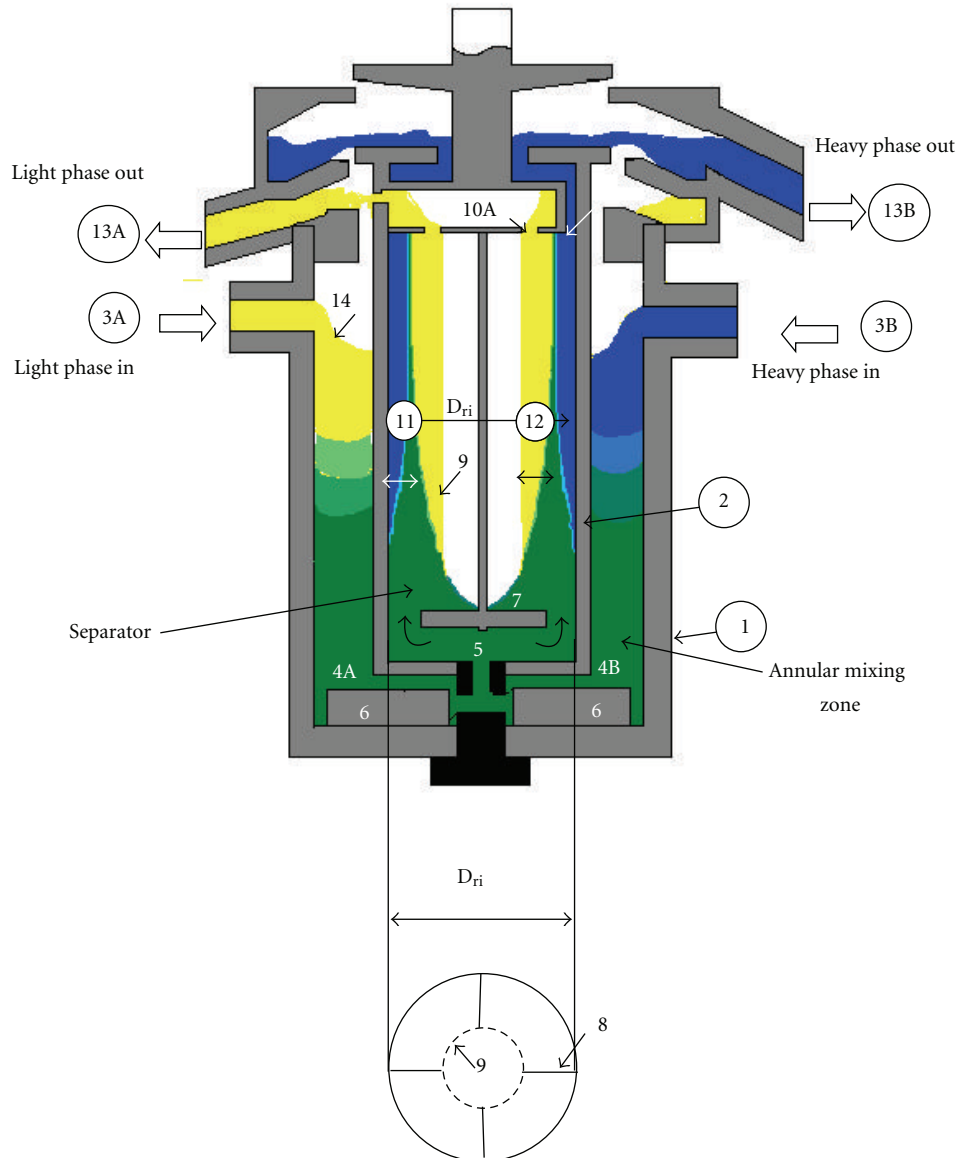


FIGURE 1: Schematic diagram of the annular centrifugal extractor (ACE) [6] (1) stationary cylinder, (2) rotating cylinder, (3A) light-phase inlet, (3B) heavy-phase inlet, (4A and B) Region below rotating cylinder, (5) central opening for rotating cylinder, (6) radial baffles on the stationary bottom plate, (7) deflecting baffle in the rotor, (8) vertical baffles in the rotor, (9) interface between air and light phase, (10A and B) overflow weirs for lighter and heavier phase, respectively, (11) clean width for heavy phase, (12) clean width for light phase, (13A and B) Outlets for light and heavy phases, respectively, (14) liquid level in the annulus.

20–600 kW/m³) which results into a very fine dispersion of the two immiscible liquids. The dispersion flows downwards in the annular region (where the mass transfer occurs) and then flows radially inwards in the region below the rotating cylinder (points (4A) and (4B) in Figure 1) and finally enters the central opening (orifice) of the rotating cylinder (point 5). Baffles (6) are provided in the bottom region which are attached to the base of the outer cylinder (or in rare cases to the bottom of the rotating cylinder). The dispersion entering the central orifice gets deflected toward the wall by the horizontal deflecting baffle (7) provided close to the entrance. Above the level of (7) the rotor is

provided with vertical baffles (8) so as to create several chambers ranging from 4 to 8. The rotating cylinder imparts to the liquid a practically rigid body rotation the inner surface of which has almost a vertical shape (9) because of high “*g*” (except a small parabolic portion at the bottom). The dispersion entering at the bottom gets separated as it moves upwards. The rate of separation depends upon the drop size distribution, their settling velocities under the centrifugal action ($r\Omega^2$), densities, viscosities, and coalescing behavior of the two phases. For complete separation (which is considered to be a flagship advantage of ACEs), adequate height needs to be provided for a given level of ($r\Omega^2$). After

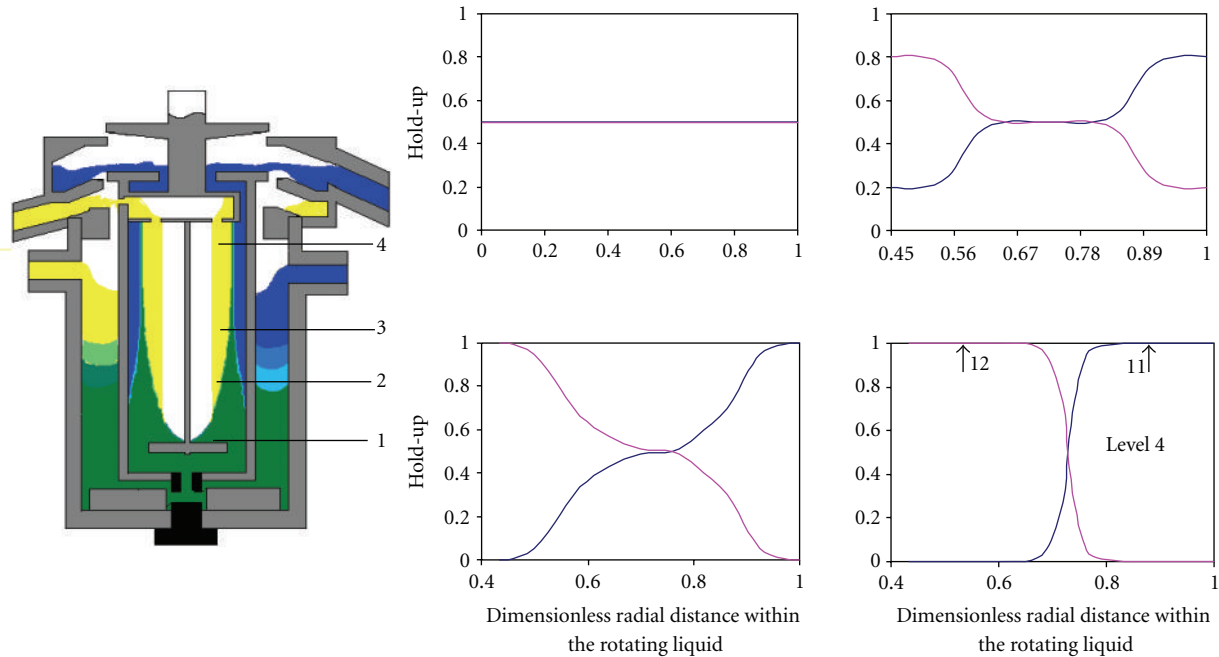


FIGURE 2: Variation of dispersion band in ACE [6].

complete separation, the overflow weirs [(10A) and (10B)] are provided in such a way that only very clean light and heavy phases pass over the respective weirs. The size and location of the weirs are provided in the hardware according to the relative flow rates of heavy and light phases and their corresponding clean widths (11) and (12). The flow of liquids from points (3A) and (3B) to (13A) and (13B) passes through the steps of extraction and separation.

Inside the rotor, the heavy and light phases are separated and the process of separation is schematically shown in Figure 2. It can be seen that, after the dispersion enters the rotor, the thickness of the dispersion band decreases as the dispersion flows upward. At point 4, complete separation can be seen to occur. The width of separation band at any location (say, point 3 in Figure 2) increases with an increase in flow rate and a decrease in interfacial tension. Further, the width decreases with an increase in the rotor speed and the density difference.

For a certain flow rate of aqueous phase, there is a maximum permissible flow rate of organic phase at which the dispersion band practically reaches the level of outflow weir (points 11 and 12 in Figure 1) and the carryover of mixed phase may occur in both or one of the outlet streams. This condition is known as flooding. The design of settler is based on the settling time of droplet of dispersed phase in the dispersion band. Hence, the characterization of dispersion band is very important in centrifugal extractors.

It is now known that the current practice of designing any process equipment (including annular centrifugal extractors) is closer to an art than the desired scientific procedures. Such a status is because of the complexity of fluid mechanics which includes three dimensional, turbulent, and multiphase nature of the flow in majority of process

equipment. Therefore, since 1980, computational fluid dynamics (CFD) is increasingly being used for understanding the fluid mechanics in process equipment [3, 18, 31–57] and many others. Joshi and Ranade [58] have brought out the perspectives of CFD in terms of expectations, current status, and path forward. The following stepwise procedure has been recommended for rational and reliable design.

- (1) Experimental measurements: flow visualization using particle image velocimetry (PIV), laser Doppler velocimetry (LDV), ultrasound Doppler velocimetry (UDV), tomography, phase Doppler particle analyzer (PDPA), and so forth.
- (2) Computational fluid dynamics (CFDs) for the simulation of single phase or multiphase three-dimensional turbulent flow.
- (3) Comparison between CFD predictions (step 1) and experimental measurements (step 2) for the validation of both the steps. The validation step is needed because the experimental technique as well as CFD have not reached stage of perfection.
- (4) Development of relationship between the fluid mechanics and the design objectives such as mixing, axial dispersion, heat transfer, solid suspension, degeneration of proteins, and enzymes.
- (5) Measurement of drop size distribution, effective interfacial area, mass and heat transfer coefficients, critical conditions for solid suspension, and so forth.
- (6) Extensive comparison of steps 4 and 5 for the validation of these steps.
- (7) Optimization: recommendations of design procedures and scaleup.

The above procedure has been used partially or fully by several investigators, for instance, for mixing [15, 19, 52, 53, 59–63], axial mixing [64–67], heat and mass transfer [68–73], gas induction [74–76], solid suspension [75, 77, 78], and enzyme deactivation [79].

In the present paper, we review the previous literature on CFD simulation of annular centrifugal extractors. In Section 2, qualitative description has been provided for the flow pattern in the annular and separator regions. Section 3 is concerned with the CFD formulation and the solution procedure. Further, the CFD simulation of single-phase flow in annular and separator regions has been described in Sections 4 and 6, respectively. The Sections 5 and 7 review the simulation of gas-liquid interface and two phase flow on the annular side whereas Section 8 is devoted for the simulation of multiphase flow on the separator side. An attempt has been made to bring out the current status of CFD simulations. Suggestions have been made for the future work in this area.

2. Hydrodynamic Characteristics

2.1. Centrifugal Instability and Taylor-Vortex Flow Regimes. At relatively low rotor speeds, the flow in the annular space is practically tangential because the viscous forces are dominant at low speeds. At high rotor speeds, when the centrifugal forces dominate the viscous forces, the flow patterns in the annular space results in an instability termed as the centrifugal instability, which leads to a wide and interesting scope of study into flow physics at micro-, meso- and macroscales. As the so-called Taylor-Couette flow attracts attention in the design and operation of efficient process equipment, nineteenth-century demonstrated ample studies that investigated the centrifugal instability occurring in these flows. Extensive reviews were presented by Koschmieder [80], Vedantam and Joshi [3]. A brief overview of the subject with some additional studies on this subject is presented here.

Couette [81] and Mallock [82] carried out drag experiments in concentric cylinder system and thus noted instability at certain rotational speeds. This was later explained by Rayleigh [83] for inviscid flows, wherein it was reported that flow is unstable only when the cylinders rotate in opposite directions. While, if they rotate in same directions, instability would result only when the angular momentum offered by the outer cylinder goes lower than the inner one. Taylor [84] theoretically analyzed the instability for viscous fluids, using linear theory of stability thus showing good agreement with experimental data. His analytical solution arrived at the definition of a dimension less number, which was later named after him as Taylor number (Ta). This number refers to the ratio of centrifugal forces to viscous forces and was expressed mathematically as

$$\begin{aligned} \text{Ta} &= \frac{4\Omega_i^2 d^4 (\vartheta - \eta^2)}{\nu^2 (\eta^2 - 1)}, \\ \text{Re} &= \frac{R_i \Omega_i^2 d}{\nu^2}. \end{aligned} \quad (1)$$

Various criteria for the onset of instability were arrived at and presented in the literature. A detailed discussion of all these criteria has been given by Vedantam and Joshi [3]. Jeffreys [85] used the linear theory of stability to study the analogy between Taylor-Couette flow and Rayleigh-Benard convection. These studies were limited to the narrow annular gaps. Then, wider gaps and a range of annular gaps were studied by many others [86–88]. Chandrasekhar [87] incorporated an axial flow in the linear theory of stability and thus found the transition from Couette flow (CF) to Taylor vortex flow (TVF) occurring at a number which was called as critical Taylor number (Ta_{Cr}). He showed that the introduction of axial flow delays the occurrence of instability as

$$\text{Ta}_{\text{Cr}} = 1708 + 27.15\text{Re}_z^2. \quad (2)$$

The case of wide gaps was also addressed by Roberts [89], and the Ta_{Cr} was found to vary with the radius ratio as

$$\text{Ta}_{\text{Cr}} = 1589.2\eta^{-1.0964}. \quad (3)$$

Stuart [90] used the nonlinear theory of instability for the first time to understand the variations in the formation of vortex patterns. This study was further followed by Davey [88], Coles [91], DiPrima and Eagles [92]. As the Ta increases beyond the Ta_{Cr} , the flow structure changes from Taylor vortex flow to a wavy vortex flow (WVF). Upon further increase of Ta, this leads to a chaotic vortex flow (CVF), followed by fully turbulent Taylor vortex flow (TTVF). These various vortex patterns presented previously by Deshmukh et al. [26] are reproduced here in Figure 3, for ready reference of the reader.

The wavy nature of the WVF was found to be dependent upon the way in which the inner cylinder rotation was varied. Similarly, number of vortices also depended upon the startup conditions of experimentation [91]. Burkhalter and Koschmeider [93] carried out experiments to study the end effects on the vortex pattern. They found that the size of the end vortices increases with an increase in Ta, and the number of vortices decreases with an increase in the annular gap. In the classic work of Andereck et al. [94], flow maps were shown to depict the various flow regimes. They carried out flow visualization experiments using laser light-scattering technique. However, did not consider the continuous operation and hence there was an absence of the net axial flow. Lueptow et al. [95] brought out a flow map in the Ta- Re_z plane incorporating the axial flow. Koschmieder [80] carried out the flow visualization experiments to measure the wavelength of vortices formed by TTVF, upto a Ta of 40000 Ta_{Cr} . It was also reported in his study that the vortex wavelength very much depended upon the experimental startup conditions.

Braun et al. [96] presented experimental and numerical results exploring various flow formations finally resulting into fully developed Taylor instability (500–1800 rpm). The experimental investigation uses the Full Flow Field Tracking (FFFT) method, to visualize the flow in longitudinal cross sections and at the same time correlate flow pattern observations to torque measurements. There experimental

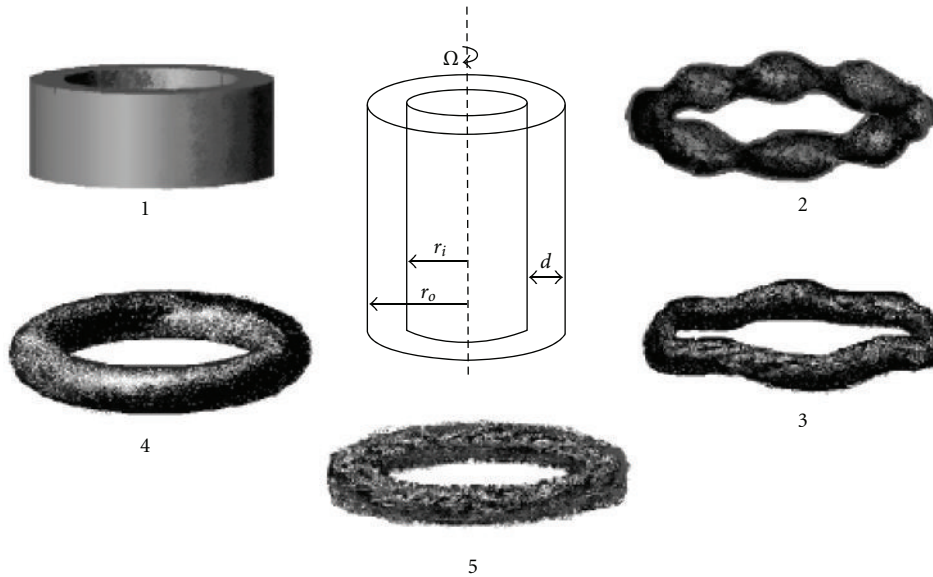


FIGURE 3: System of concentric cylinders and various vortex patterns in the absence of axial flow: (1) couette flow, (2) wavy vortex flow, (3) chaotic vortex flow, (4) Taylor vortex flow and, (5) turbulent Taylor vortex flow.

results indicated that incipient flow instabilities appear at lower speeds than the ones predicted by the Ta_{Cr} , and include formation of incipient Taylor cells that occupy only a part of the gap. The cells are separated by axially flowing narrow rope-like flowing streams that twist in a cork-screw fashion around the circumference, while separating the incipient cells. As the rotational velocities increase the Taylor cells keep growing until they occupy the entire gap. They also performed 3D CFD studies for the matching set of conditions and for the higher rotational velocities (1500–1800 rpm), where experimental studies were not possible. The torque computed by the numerical model was compared with the experimentally obtained torque and the two results were found to agree very favourably. Numerical simulation studies allowed an in-depth understanding of the flow mechanisms and trajectories inside the fully formed vortical Taylor instabilities (CFD simulations were performed using CFD-ACE+ commercial software).

Table 1 shows the geometrical details used for the CFD simulations in the past. Deshmukh et al. [26], in their paper on computational flow modeling and flow visualization in an annular centrifugal extractor, performed CFD simulations, and validated the modelled onset of centrifugal instability with the data of Rayleigh [83], Taylor [84], and Chandrasekhar [87]. They found that, as the rotation of outer cylinder increases, viscous forces become less important, as compared to the centrifugal forces and the Rayleigh criterion is arrived at, as an asymptote. In order to understand the effect of viscosity over a range of rotational speeds, they performed simulations over a wide viscosity range, thus capturing the gradual shift in stability curve from Taylor fluid towards the Rayleigh line.

Desevaux [97] studied the development of Taylor cells from Couette flow with a sudden start of the rotor, using a

transient 3D CFD model. He thus proved the utility of CFD modeling to understand the propagation of Taylor cells. He used the data of Varechon et al. [98], for validation. The data used was from the laser tomography. The results were proven in line with the established data that vortex formation occurred after a Ta of 1700.

Saqr et al. [99] carried out five numerical experiments at different angular velocities to study the non-isothermal Taylor-Couette flow. They reported an uncharacteristic discontinuity locus numerically observed in the 2D nonisothermal Taylor-Couette flow at $Re = 85$ to 622. The Navier-stokes equations were solved in the discretised X - Y space using a finite volume, pressure-based approach for the unsteady flow between two concentric cylinders. The inner cylinder was subjected to constant heat flux and constant angular velocity, while the outer cylinder was fixed and maintained at constant temperature. The ratio between the outer and inner cylinder diameters was restricted to the ratio of sum of the cylinder diameters to the outer cylinder diameter (Golden Ratio).

Considering the studies reported on both experimental as well as numerical investigations, it is clear that CFD modeling could be used to understand the flow transition of Taylor instability. One extension of these studies would be to the modeling and simulation of secondary instabilities such as formation of azimuthal waves.

2.2. Separation Characteristics. The process of separation of the heavy and light phases inside the rotor is conceptually shown in Figure 2. It can be seen that, after the dispersion enters the rotor, the thickness of the dispersion band decreases as the dispersion flows upward. At point 4, complete separation can be seen to occur. The width of separation band at any location (say, point 3 in Figure 2) increases with an increase in flow rate and a decrease in

TABLE 1: Summary of geometric parameters used in the previous work.

Serial number	Authors	ACE dimensions			d (mm)	Simulation of		Number of Phases		Range of speed, r/s
		D_i (mm)	D_o (mm)	H (mm)		Annular region	Separator region	One	Two	
1	Zhu and Vigil, [153]	22.2	25.4	235				LL		5–50
2	Wang et al., [170]	69.8	95.2	432						0.1–0.3
3	Vedantam et al., [5]	84	102	18	9					5–25
4	Wardle et al., [133]	50.8	63.4	37.76	6.3					50
5	Vedantam et al., [4]			16–225	1.5–15					0–15
6	Padial-Collins et al., [166]			150				LL		16.67–50
7	Deshmukh et al., [26]	39		10–1000	2–15					0–20
8	Deshmukh et al., [132]	39	52	72						0–20
9	Wardle et al., [141]	50.8	63.4	81.3	6.3			GL		60
10	Deshmukh et al., [119]		52	72						0–20
11	Wardle et al., [27]	50.8	63.4	81.3	6.3			GL		60
12	Wardle et al., [143]	47.4		106				GL		60
13	Sathe et al., [28]	39	49	57	5			LL		2–26
14	Deng et al., [123]	36.8	60	60	11.6					3.35
15	Wardle, [145]	50.8	63.4	81.3 (Annulus) 106 (Separator)	6.3			GLL (Annulus) GLL (Separator)		60
16	Gandhir and Wardle, [165]	47.4		106				GL		60

*The orifice diameter d_o has not been included in the table as most the authors above have simulated the annular and separator regions separately and hence not in specified the orifice diameter d_o .

interfacial tension. Further, the width decreases with an increase in the rotor speed and the density difference.

For a certain flow rate of aqueous phase, there is a maximum permissible flow rate of organic phase at which the dispersion band practically reaches the level of outflow weir (points 11 and 12 in Figure 1) and the carryover of mixed phase may occur in both or one of the outlet streams. This condition is known as flooding. The design of settler is based on the settling time of droplet of dispersed phase in the dispersion band. Hence, the characterization of dispersion band is very important in the study of liquid-liquid extraction equipment such as mixer settlers, centrifugal extractors, among others.

Several investigations have been carried out to study the separation mechanism of liquid-liquid dispersion in a gravity settler [100–103]. The structure of dispersion band and the drop concentration at various levels in the dispersion band in the settler was studied experimentally for a wide range of parameters. The characteristics of dispersion band in a continuous settler are a function of dispersion band thickness and dispersion throughput. The thickness shows the variation of volume fraction of dispersed phase against the vertical distance from the coalescence front for various throughputs. Obviously, the dispersion band thickness increases with an increase in the throughput. The experimental evidences published are limited to the type of settler and no unified correlation exists to design the liquid-liquid settler for both batch and continuous types. Some of the researchers [1] estimated the settling time to characterize

the interfacial area of liquid-liquid dispersion. However, this settling time did not fit into any of the existing dimensionless groups used in the interfacial area correlation to evaluate the separation capacity. Hence, there has been a need of a correlation for the design and scaleup of settling zone which is required to coalesce the liquid-liquid dispersions. This subject will be discussed in the following sections.

For correlating the separation data, Leonard [104] identified to characteristic time scales: (a) residence time of dispersion in separating zone of flow system (Q/V) or time for dispersion to break in batch systems (t_B); (b) time for a droplet to travel the thickness of the separating zone (settling time, T_S). If ΔZ is the thickness of dispersion band and V_S is the average hindered settling velocity of drops, the separation time is given by the following equation:

$$T_S = \frac{\Delta Z}{V_S}. \quad (4)$$

The value of V_S is proportional to g under creeping flow and \sqrt{g} under turbulent conditions. Barnea and Mizrahi [100–102] have reported that the settling time is proportional to square root of acceleration (either gravity or centrifugal):

$$T_S \propto \sqrt{\frac{\Delta Z}{a}}. \quad (5)$$

Using (5), Leonard [103] defined the dispersion number as follows:

$$N_D = \frac{1}{T_S} \sqrt{\frac{\Delta Z}{a}}, \quad (6)$$

where N_D was denoted as dispersion number by Leonard [103]. For a flow system, the definition of N_D takes the following form:

$$N_D = \frac{Q}{V} \sqrt{\frac{\Delta Z}{a}}. \quad (7)$$

By introducing the concept of residence time t_R , the dispersion number can be expressed in the more general form:

$$N_D = \frac{1}{t_R} \sqrt{\frac{\Delta Z}{a}}. \quad (8)$$

In a gravity settler, acceleration is simply the acceleration due to gravity, g , and in a centrifugal settler, acceleration is given by

$$a = r\omega^2. \quad (9)$$

Acceleration varies within the centrifugal settler. Hence, the volume average acceleration is given by

$$a = \bar{r}\omega^2, \quad (10)$$

where

$$\bar{r} = \frac{\int_{r_o}^{r_u} 2\pi r^2 dr}{\int_{r_o}^{r_u} 2\pi r dr} = \frac{2}{3} \left(\frac{r_u^3 - r_o^3}{r_u^2 - r_o^2} \right). \quad (11)$$

From (7), it can be seen that the dispersion number is proportional to throughput for a given equipment size and a given acceleration field. It includes both the dispersion band thickness and time required for dispersion to settle. It also reflects the fineness of the drop size depending upon the time taken for the droplet to settle. The size of droplet varies with the speed of agitation or mixing. Hence, the dispersion number is a measure of efficiency of separation in liquid-liquid extraction equipment. It has been shown to be practically constant for wide range liquid-liquid systems [103]. It includes time for emulsion to break in such a way that both batch and flow systems give the same value of dispersion number for a particular liquid-liquid system.

Recently, Tamhane et al. [105] have performed separation experiments under gravity and centrifugal conditions over a wide range of parameters ($120 < \Delta\rho < 600 \text{ kg/m}^3$, $3 < \sigma < 58.3 \text{ mN/m}$, $1 < \mu_C < 12.2 \text{ mPa}\cdot\text{s}$, $0.6 < \mu_D < 12.2 \text{ mPa}\cdot\text{s}$, $0.05 < D_i < 0.25 \text{ m}$, $0.005 < (D_o - D_i) < 0.025 \text{ m}$, $10 < N < 40 \text{ r/s}$). They have proposed the following correlations for the dispersion number:

Gravity settling

$$N_D = 0.0562 \left(\frac{\sigma^3 \Delta\rho}{\mu_C^4 g} \right)^{0.059} \left(\frac{C}{D} \right)^{-0.111} \times \left(\frac{\Delta\rho}{\rho_C} \right)^{0.101} \left(\frac{\mu_C}{\mu_D} \right)^{-0.211}; \quad (12)$$

Annular centrifugal extractor

$$N_D = 0.1 \left(\frac{\sigma^3 \Delta\rho}{\mu_C^4 g} \right)^{0.036} \left(\frac{C}{D} \right)^{0.019} \left(\frac{\Delta\rho}{\rho_C} \right)^{0.174} \times \left(\frac{\mu_C}{\mu_D} \right)^{0.074} \left(\frac{a}{g} \right)^{-0.086} \left(\frac{Q}{ND_i^3} \right)^{0.95}. \quad (13)$$

As an example of the use of dispersion number in design of ACE, let us fix the total throughput to $6.5 \text{ m}^3/\text{h}$. The rotor speed is kept to a typical value of 30 r/s . From (7), we can see that N_D depends on the variables Q , V , ΔZ , and a . V is in turn a function of the rotor height H . As a general thumb of rule, $H \sim 2.5R_i$, where R_i is the rotor radius. Now, $V = \pi R_i^2 H$. Thus, $V = 2.5\pi R_i^3$. Also, $a = \omega^2 R_i$. Hence, at 30 r/s , $a = 35495 R_i$. Further, while designing the dispersion band thickness at maximum throughput, the fluid is thought to occupy the entire rotor. Hence, ΔZ in this case is equal to R_i . Thus, (7) reduces to the form:

$$N_D = \frac{9.54 \times 10^{-6}}{R_i^3}. \quad (14)$$

Taking a value of N_D to be 0.00075 , we get the value of R_i equal to 0.119 m . Thus, D_i is equal to 0.238 m . The tested capacity of a 250 mm rotor ACE is indeed $6.5 \text{ m}^3/\text{h}$, which is consistent with the aforesaid procedure.

3. CFD Formulation and Solution Procedure

Performance of annular centrifugal extractors (ACEs) crucially depends on underlying fluid dynamics and mixing. Even single-phase flow through such ACEs exhibits rich physics and multitudes of flow regimes. Presence of multiple phases leads to even complex flow structures. The physical construction and operation of ACEs are discussed in previous two sections. On the face of it, the underlying complexities appear almost intractable and the task of computational modeling of ACEs looks truly daunting. Despite the apparent intractability, computational modeling has, however, potential to offer better insight and useful information for evolving design guidelines. Various investigators have attempted to develop computational fluid dynamics based models for carrying out simulations of flow in ACEs. The work done so far is critically reviewed in Sections 4 to 7. In this section, general approach and framework for examining such CFD models and simulations is discussed.

Some of the key aspects discussed in the Sections 1 and 2 are reexamined here in light of formulating appropriate modeling framework. Please note that typical power dissipation per unit mass in ACEs is significantly higher (in the range of $20\text{--}600 \text{ kW/m}^3$) than classical stirred tanks. The typical tip speed of inner rotating cylinder is in the range of 1 to 25 m/s . This results into a very fine dispersion of the two immiscible liquids. Flow in the annular space is turbulent and typical Kolmogorov length scales are in the range of 10^{-6} to 10^{-5} m . The ratio of Kolmogorov length scales to annular gap is, therefore, in the range of 10^{-5} to 10^{-3} . The flow within the annular space becomes unstable and exhibits

many diverse flow regimes. There may be a free surface in the annular space depending upon the flow rates, dispersion process, and specific construction of ACE. The presence of free surface makes the problem even more complex. For estimating the extraction, it is important to capture size of the dispersed phase particle, location of free surface and axial mixing within the annular space.

The dispersion enters the inner rotating cylinder from the bottom orifice. Baffles which guide the dispersion towards inner cylinder via orifice are one of the key design components. Computational flow models can provide useful insight on this. In this region, the flow is characterized as turbulent-dispersed multiphase flows. Usually there are baffles (horizontal as well as vertical) in the inner rotating cylinder. The rotation of inner cylinder creates strong body force and cause phase separation. The rate and extent of phase separation depends upon the drop size distribution, difference in densities and viscosities of two immiscible phases and coalescing behaviour. Appropriate sizing of inner cylinder and outflow weirs is critical for adequate separation of phases. Typically centrifugal acceleration experienced by dispersed phase particles in the inner rotating cylinder is in the range of 1000 to 5000 m/s^2 . This acceleration causes coalescence and separation leading to stratified flow regime in inner rotating cylinder. Flooding may occur if the phase separation does not occur adequately and may lead to the carryover of mixed phase in both or one of the outlet streams. It is important to gain better understanding of regime transition and phase separation for obtaining a handle on separation efficiency of ACEs.

Considering the large number of design variables available for tuning the performance of ACEs, it is useful to develop computational models to simulate fluid dynamics of ACEs and use the simulated flow fields for drawing useful design guidelines. Most of the early modeling efforts were primarily focused on descriptive correlations of experimental data. The dimensionless dispersion number described above was developed in order to predict the maximum throughput of a contactor for a given set of immiscible fluids and a fixed rotor speed. Significant effort was also put forth in the development of a computational model which could aid in the design of contactor weirs by calculating the necessary weir sizes given the properties of the two phases. A descriptive model for the height of the liquid in the annulus as a function of rotor speed was also developed. In recent years, significant efforts have been carried out to exploit recent advances in computational fluid dynamics (CFD) to gain better understanding of ACEs. CFD based models and simulations have in principle potential to provide qualitative as well as quantitative analyses of the flow within ACEs. Such analysis may enable greater understanding of and confidence in scaled-up designs which would be used in pilot and full-scale operational facilities. However, the potential benefits strongly depend on how well the key aspects briefly reviewed here are represented while formulating CFD models. Prevailing approaches for CFD modeling are briefly reviewed here along with an outline of the challenges to modeling these flows. The obtained results and observations from various studies are critically reviewed and discussed in

Sections 4 to 7. It will be useful to examine key design issues of ACEs and discuss possible CFD approaches to address those issues. It will be useful to begin the discussion from the inlets.

Two immiscible feed liquids enter ACE via two separate inlets connected to the annular region between the two cylinders (see Figure 4(a)).

The spinning of the rotor creates a dispersion of the two immiscible liquids. The dispersion flows downwards in the annular region (where the mass transfer occurs) and then eventually enters the inner rotating cylinder via bottom opening (point 5 in Figure 4(b)). The liquid height in the annular region is one of the critical design parameters. For a specific configuration, this liquid height in the annular region determines the throughput of the mixing zone. While the throughput of a given contactor is typically limited by the capacity for complete separation of the two phases within the rotor such that there is minimal other-phase contamination in the respective outlets, another limiting case is if the dispersion in the annulus fills the mixing zone and overflows into the organic collector ring. Even if the liquid height under nominal conditions is acceptable, flow transients and changes in liquid height due to phase inversion make the annular liquid height an important factor during operation.

Another important and relevant issue in the annular region is possible entrapment of air in the liquid-liquid dispersion. Since the region being open to air, air bubbles may get entrained and entrapped in the annular region. This will lead to reduction in drag, and thus a reduction in energy dissipation. Such entrapped bubbles have been observed in the flow visualization experiments. The liquid height as well as entrapped bubbles also influence flow characteristics in the annular region including axial mixing as well as mass transfer characteristics. It is, therefore, important to review CFD approaches needed to estimate these key desired characteristics in the annular region.

It can be seen that the fluid dynamics of annular region is very complex involving creation of dispersion in presence of multiple free surfaces (liquid-liquid and gas-liquid) and intense turbulence in a geometrically complex shape with moving boundaries. It is almost impossible to make "a priori" predictions of such a complex flow. However, judicious use of CFD models can provide very useful insights and guidelines for design purposes. The overall flow structures and axial mixing can be reasonably estimated by making a pseudohomogenous assumption to represent liquid-liquid dispersion. The first cut solution may be obtained by even ignoring the free surface and simply using single-phase flow simulations. These single-phase simulations will provide useful estimates of energy dissipation rates as well as axial mixing in the annular region. The estimates of energy dissipation rates may be then used to estimate representative droplet diameter to estimate mass transfer coefficients. The Eulerian-Eulerian (EE) approach can then be used to understand possible influence of slip between two liquid phases. Please note that more often than not effective drag in liquid-liquid dispersions will be a strong function of Kolmogorov length scale (energy dissipation rate). Appropriate correlations of effective drag coefficients

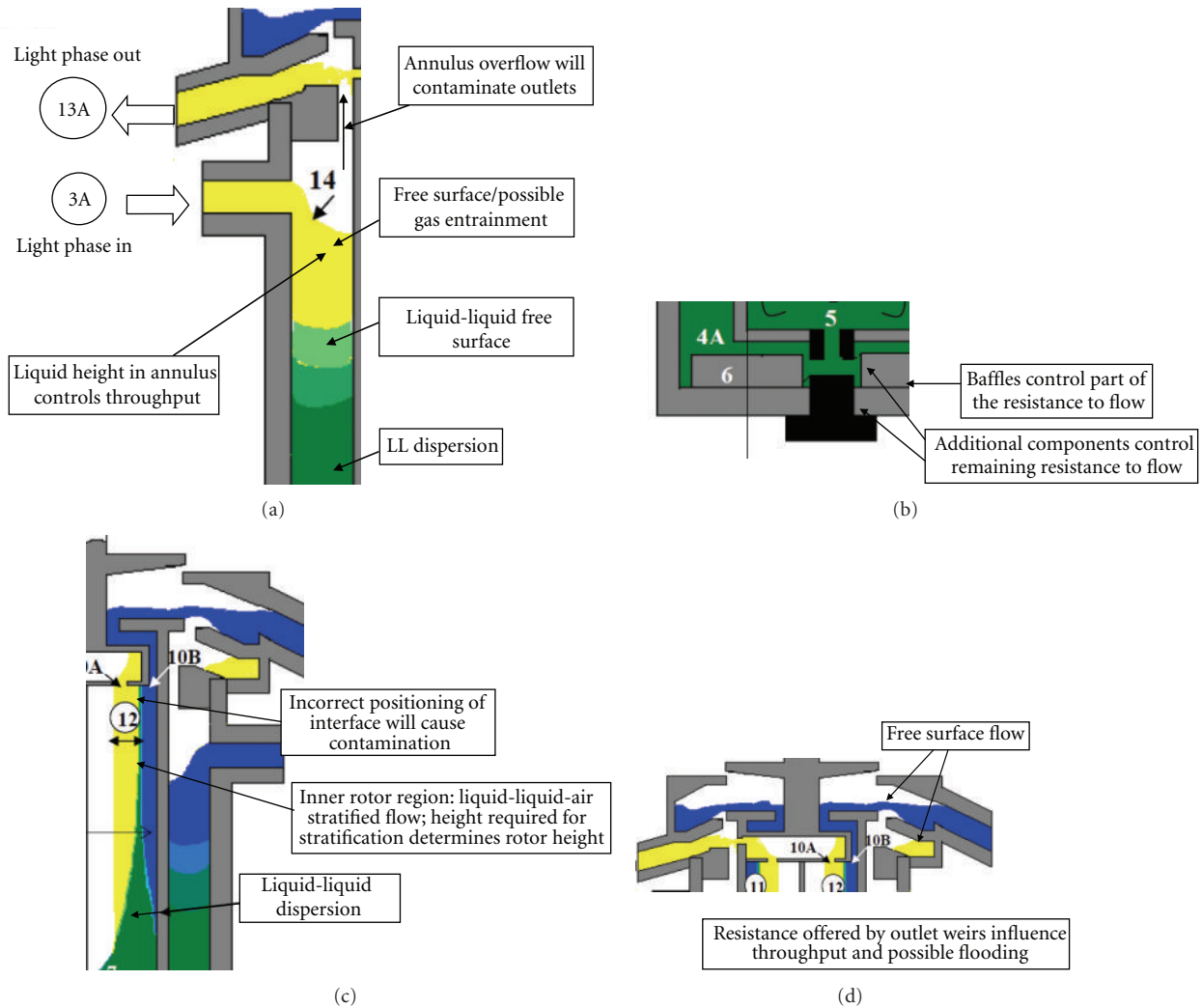


FIGURE 4: (a) Schematic representation of the inlet and outlet sections of ACE, (b) schematic representation of the bottom vanes and resistance, (c) dispersion band and sections tapping light and heavy phases in the separator region, (d) Heavy-phase weir and free surface flow at the top at the point of collection.

should, therefore, be used while developing EE based CFD models for ACE. These models can then be combined with volume of fluid (VOF) approach to capture free surface as well as possible entrainment of gas phase. This last approach invariably required 3D simulations and, therefore, is very compute intensive. The approach can, however, provide useful information on possibility of overflow of annular region (and contamination with the organic phase outlet) as well as entrainment of gas bubbles. More information about the EE and VOF approaches may be found in Ranade [106]. More information on hybrid approach (EE with VOF) may be obtained from the work of Kuipers and coworkers [37–41].

The flow in the bottom region of ACE is essentially controlled by the geometrical configuration of the bottom region (see Figure 4(b)).

The key design aspect of the bottom region is to provide appropriate resistance to flow from annular region to inner

rotating cylinder. This is realized by providing baffles (fixed in number, shape, size, and location for a given configuration of ACE) as well as additional moving components to realize ability to manipulate resistance during the ACE operation (position of these can be modified to realize better operating conditions in ACE). Since the key design issue is to estimate flow resistance or pressure drop offered by the bottom region, single-phase CFD simulations using the pseudohomogenous fluid (representing liquid-liquid dispersion) are adequate. The choice of turbulence models (since the geometry is quite complex) and use of adequate number of computational cells are crucial to obtain accurate estimated of flow resistance and key features of flow in the bottom region of ACE. Such CFD models can be used to evolve appropriate guidelines for manipulating flow characteristics of ACE by influencing flow in the bottom region of ACE.

The flow in the inner rotor region is again quite complex involving significant changes in the flow characteristics.

The liquid-liquid dispersion enters the rotor and eventually transitions to stratified flow regime because of the strong centrifugal action.

In liquid-liquid stratification studies, the two-phase flow is another variation of a single-phase flow that explores the effect of interface on the vortex flow. A significant challenge with free-surface modeling techniques is that they are inherently mesh dependent; only interfacial features that can be resolved on the mesh can be captured. As a further limitation, such methods are time dependent by nature and are limited by the Courant flow number, in turn showing the dependency of time step on mesh spacing. The regime transition is inherently a complex problem. The existing VOF based approach may, however, be used to obtain broad estimates of height required for realizing stratified layers. A combination of EE and VOF will be useful to simulate the flow in the inner rotor region of ACE.

Closely linked with the flow characteristics of the inner rotor, the flow in the outlets and associated weirs is equally crucial to understand for realizing stable operation of ACE. The key features of flow in the outlet region are as follows.

The pressure drop across outlet weirs influences number of design parameters of ACE. CFD-based studies help in understanding the flow in the weir region and, therefore, several other key design parameters of ACE. Until recently, CFD modeling techniques had not been applied to the rotor design in ACE. However, a useful analytical approach was demonstrated for determining the proper dimensions of the weirs based primarily on experimental correlations and hydrostatic balance arguments [107]. While this method has been generally quite successful for rotor sizing of contactors with an open upper weir (and the obsolete air-controlled upper weir), some experiments with “closed” upper weir systems have produced behavior which cannot fully be explained by the existing theoretical models. One such unexplained behavior is the elevated throughput that has been observed for large upper weir sizes in these units. This same behavior has also been observed in larger units of this design. VOF approach or even a single-phase approach may be used to estimate pressure drop across outlet weirs of ACE. CFD modeling can provide useful insights in resolving such issues.

Better understanding of the flow within the rotor and specifically the flow over the weirs requires full simulation of the complex rotor and weir geometries and analysis of the liquid free surface flow. Further, such hydraulic simulations can calculate important flow quantities which characterize the rotor and weirs such as the zero-point flow rate. Zero-point flow rate refers to the point wherein, due to excess flow rate coming into the rotor, the liquid volume maintained in the rotor increases so much that the liquid starts to come out of exit ports without getting separated. These kinds of studies are barely reported in a couple of papers until date. In practice, the zero-point flow rate is used to verify fabrication consistency of a set of rotors with the same specifications, such as might be used in a multistage bank of contactors.

This brief review of CFD approaches relevant to different aspects of ACE design and operation indicates the usefulness of computational flow models. Some of the applications

of these are discussed in the subsequent sections. The governing equations for single phase flows, the Eulerian-Eulerian approach and volume of fluid approach may be found in many text books (for example, Ranade [106], Ranade and coworkers [18, 19, 54, 108–110], and manuals of commercial CFD vendors). These are, therefore, not repeated and discussed here. Appropriate boundary conditions need to be formulated for connecting the generic CFD model to the specific configuration under consideration. It is often essential to make judicious use of constant pressure, velocity inlet and outlet boundary conditions to effectively represent various sections of ACE. The boundary conditions used by different investigators are reviewed in the subsequent sections while discussing the results available in the published literature.

The quality of simulated results using CFD models of course also crucially depends on numerical implementation of selected model equations. Table 2 gives a summary of key numerical parameters (like the number of grids used, method of discretization and the solution procedure) used by various investigators. It is essential that adequately fine mesh (compared to relevant space scales of the considered ACE) is used along with the higher order discretization schemes. The published CFD results are reviewed in the following sections in light of this brief review on formulation and solution of CFD models.

4. CFD Simulation of Single Phase Flow on the Annular Side

4.1. Velocity Profiles in Presences/Absence of Axial Flow. The earliest studies on velocity profiles date back to that of Taylor [84], who plotted radial velocity distribution against the onset of centrifugal instability and also determined the vortex spacing from both analytical and experimental studies. Most of the studies reported till date have presented results on flow field determination and flow regime classification. While the mixing zone in the annulus extends along the entire length of the annulus, initial studies focused on neglecting the end regions of the annulus, thus reporting the flow field for larger aspect ratios. The information typically obtained was the flow regimes and the vortex patterns. Later, with advances in methodology, end effects were also considered.

For highly turbulent regimes, Parker and Merati [111] used Laser Doppler Anemometry (LDA) to measure three components of mean velocity and turbulent intensity at various circumferential planes. They studied the end effects on vortices for aspect ratios of 4 and 20. Baier [112] carried out CFD modeling to determine vortex velocities for various operating conditions. Haut et al. [113], also carried out CFD simulations, in the annular region in a horizontal corotating cylinder system. They used the $k-\epsilon$ turbulence model to incorporate turbulence effects in wavy vortex flow and turbulent Taylor vortex flow. Particle image velocimetry (PIV) was used to determine average and instantaneous velocities.

TABLE 2: Some details of CFD simulations in previous work.

Serial number	Authors	Number of grids	Method of discretization*, **			Multiphase model used
			Momentum	Pressure-velocity coupling	Pressure equation	
1	Zhu and Vigil, [153]	30 (radial) × 300 (Axial)				ASM (Fluent 5.0)
2	Wang et al., [170]					(Fluent 6.0)
3	Vedantam et al., [5]	3D 70000 Hexahedral	First order upwind	PISO	PRESTO	VOF (Fluent 6.1)
4	Wardle et al., [133]	3D 588484 Tetrahedral	First order upwind	SIMPLE	Standard	(Fluent 6.1)
5	Vedantam et al., [4]	2D 20000	First order upwind	SIMPLE	Pressure staggering option (PRESTO)	(Fluent 6.1.2)
6	Padial-Collins et al., [166]					(EE) (CartaBlanca)
7	Deshmukh et al., [26]	2D 20000	QUICK upwind	PISO	Pressure staggering option (PRESTO)	(Fluent 4.5, 6.0)
8	Deshmukh et al., [132]	3D 600000 Hexahedral	QUICK	PISO	PRESTO	(Fluent 6.2.16)
9	Wardle et al., [141]	3D 286000	First order upwind	PISO		VOF (Fluent 6.3)
10	Deshmukh et al., [119]	3D 600000 Hexahedral	QUICK	PISO	PRESTO	(Fluent 6.2.16)
11	Wardle et al., [27]	3D 800000 Tetrahedral				VOF (Fluent 6.3)
12	Wardle et al., [143]	311000 Tetrahedral (Annulus) 160000 Tetrahedral (Separator)				VOF (Fluent 6.3)
13	Sathe et al., [28]	3D 600000 Hexahedral	Second order upwind	SIMPLE	PRESTO	(EE) (Fluent 6.3)
14	Deng et al., [123]	3D 600000 Tetrahedral	First order upwind	SIMPLE	Standard	(Fluent 6.3.06)
15	Wardle, [145]	650000—2.5 M Polyhedral	First order upwind	PISO		VOF (Open FOAM-1.6)
16	Gandhir and Wardle, [165]	3D 586846 Polyhedral	First order upwind	PISO		VOF (Open FOAM-1.6)

* Most of the authors, *except from the group of Joshi and coworkers*, have only specified that fluent (specific version) has been used for the CFD simulations. They have *Not* mentioned the various model parameters used for the simulations.

**The underrelaxation factors have Not been specified by most of the authors.

Deshmukh et al. [26] carried out both 3D CFD and experimental measurements, and made an extensive comparison with the data from the literature. They have covered a wide range of annular gaps, rotation ratios, and net axial liquid velocities. Energy balance also was established for various operating conditions. In case of counter-rotating cylinders, an additional set of vortices was found along the length of the annulus beyond a certain Ta_{Cr} . For the case of the annular centrifugal extractor, they observed elongated vortices at both the ends of the annulus; however, they concluded that the vortex at the lower end shows more elongation. Further, the flow was found to be tangential in the region below the rotating cylinder. Sathe et al. [28], in their study of two-phase liquid-liquid flow, carried out CFD simulations for single phase and compared the data with the PIV measurements for a vertical configuration. They compared their simulation data with the vortex spacing and found the comparison to be inline with measured data.

4.2. Axial Mixing and Residence Time Distribution. Axial dispersion in Taylor-Couette flow has been investigated

in the past and reported in the literature. Vedantam and Joshi [3] have summarized the axial dispersion studies in Taylor-Couette contactors for various flow regimes. In laminar flows, RTD experiments and the description of axial dispersion either by one parameter that includes dispersed plug flow model or tanks in series model has been used or a two parameter model has been used [114–116]. Normally, it has been shown in most studies that laminar Taylor vortex regime usually is depicted by well-defined vortices.

Kataoka et al. [114], for the first time provided a basis for treating each vortex as a well-mixed reactor. They performed two-point RTD measurements and concluded that there is no vortex intermixing. Thus, at a higher aspect ratio (implying that end effects could be neglected), the overall flow was expected to go close to plug flow behavior. Desmet et al. [117, 118] investigated mixing in laminar flows and concluded that under laminar flow conditions, intravortex transport is slow compared to intersvortex transport and indicated that a single vortex cannot be treated as a well-mixed reactor. However, as the Taylor-vortex flow reaches the flow regime of turbulent Taylor vortex flow, intravortex flow is prominent than the intervortex flow. Vedantam et al. [5] used

CFD for estimating the mixing time and RTD in a Taylor-Couette flow. They also obtained very good agreement with the experimental observation reported previously in the literature. However, their study was confined to a lower range of Ta , which is unlikely to be applied for highly turbulent regimes needed in the study of annular centrifugal extractors.

Deshmukh et al. [119] studied RTD for the annular region of the annular centrifugal extractor experimentally as well as computationally. They developed an experimental technique capable of picking quick response. The convective motion was shown to control the rate of mixing, and the role of turbulent diffusion was found to be small. They concluded that the RTD studies indicated the existence of a single-back-mixed stage, in spite of the presence of multiple vortices in the annulus. Further, the numbers of tanks in series were found to be dependent on the aspect ratio used in the geometry. Figure 5 shows the flow patterns and turbulent properties at 30 rev/s used by them, at the center of the annulus. Details of the reproduced figure are mentioned within the figure caption. Their work also indicated an attempt toward reducing the axial mixing by providing radial baffles, which practically leads to a plug flow kind of behavior.

4.3. Effect of Internals on the Flow Field. In general, baffles play a significant role in engineering devices. Baffles enhance mixing efficiency in a tank or a batch oscillatory column [120, 121] and they are used to increase permeate flux in membrane filtration [122]. Deng et al. [123] carried out characterization of Taylor vortex flow in a short column with a wide gap and concluded that the vortex flow was sensitive to boundary conditions. Several modified boundaries including end wall effects [124] were studied. Some studies included varying the radius of the inner cylinder [125] and also asymmetric boundary conditions [126]. All the above studies were seen to affect the vortex formation. However, there were very limited results which were presented in the above literature with regard to baffled devices in Taylor vortex flow or annular centrifugal extractor. The work in [127] introduced a baffle in the upper part of the rotating cylinder electrode cell. But this was done in order to avoid any bubble formation in the annular region noting that, up to a speed of 3000 rpm, no bubbles were formed. Some studies were reported on the rheology of slurries using a DeBex viscometer [128]. They also attributed the formation of Taylor vortices to the existence of baffles. Clark [129] carried out experiments in electrochemical reactor for electrodeposition in an eco-cell. Taylor vortices were also observed as a cascade of cells separated by baffles.

Sczechowski et al. [130], showed that the introduction of horizontal baffles does not change the axisymmetric feature of the Taylor-Couette flow. Instead, they are shown to provide additional surfaces to confine the vortex flow. Horizontal baffles were found to affect the vortex size. In an infinitely long column, the diameter of an individual vortex was found to be approximately equal to the annular gap.

Loureiro et al. [131], carried out both numerical and experimental studies to understand the Taylor-Couette instabilities in flows involving Newtonian fluids as well as power-law fluids. The flow inside a horizontal annulus due to the

inner cylinder rotation was studied. The bottom of the annular space was partially blocked by a plate parallel to the axis of rotation, thereby destroying the circumferential symmetry of the annular space geometry. This flow configuration was encountered in the drilling process of horizontal petroleum wells, where a bed of cuttings is deposited at the bottom part of the annulus. The velocity field for this flow was obtained both numerically and experimentally. In the numerical work, the equations which govern the three-dimensional, laminar flow of both Newtonian and power-law liquids were solved via a finite-volume technique. In the experimental research, the instantaneous and time-averaged flow fields over two-dimensional meridional sections of the annular space were measured employing the particle image velocimetry (PIV) technique, also both for Newtonian and power-law liquids. Their study was focused on the formation of secondary form of distorted Taylor vortices. Deshmukh et al. [132] examined flow patterns and axial back mixing in the presence of radial baffles in the annulus and concluded that the horizontal radial baffles can reduce the axial mixing in turbulent Taylor-Couette flow.

Deng et al. [123] presented a study on Taylor vortex flow in between a rotating inner cylinder and a stationary outer cylinder with vertical as well as horizontal baffles. They found that, upon the introduction of vertical baffles, the axisymmetric vortex nature is eliminated thus leading to a three dimensional flow pattern, including the recirculation flow in the radial-azimuthal plane and periodic variation of the vertical position of the vortices. The horizontal baffle was found to separate the original fluid column in compartments, and the length of the vortices inside was found to be a variable in a certain range to fit the compartment dimension. They found that the number, position, and width of the baffles do affect the vortex structure in the annulus. Figure 6 shows the Taylor vortices obtained in presence of horizontal baffles. With two horizontal baffles in the annulus, the flow pattern is largely affected by the baffle width and the distance between the two baffles. This study provided a better understanding of Taylor vortex flow in presence of internal baffles, which will be important for practical applications of Taylor vortex devices.

4.4. Challenges in Validation Data Generation for Flow Visualization. The flow in the ACE is generally turbulent, unsteady, and it most likely could consist of liquid-liquid-gas phases, thus increasing the complexity involved in the modeling as well as data generation. Under typical conditions, the flow in the mixing region opaque; thus, laser-based, optical techniques are limited to interrogation of the near-wall regions only. Optical access to the flow inside the rotor is also obviously restricted although transparent rotors have been fabricated.

Due to the challenges of quantitative measurement of flows in actual contactor configurations at typical operating conditions with multiple phases, the available experimental data in the literature tends to be for simplified geometries, single phase operation, and/or reduced rotor rotation rates. While this provides a means of more direct comparison with CFD simulations, if the test conditions are greatly varied

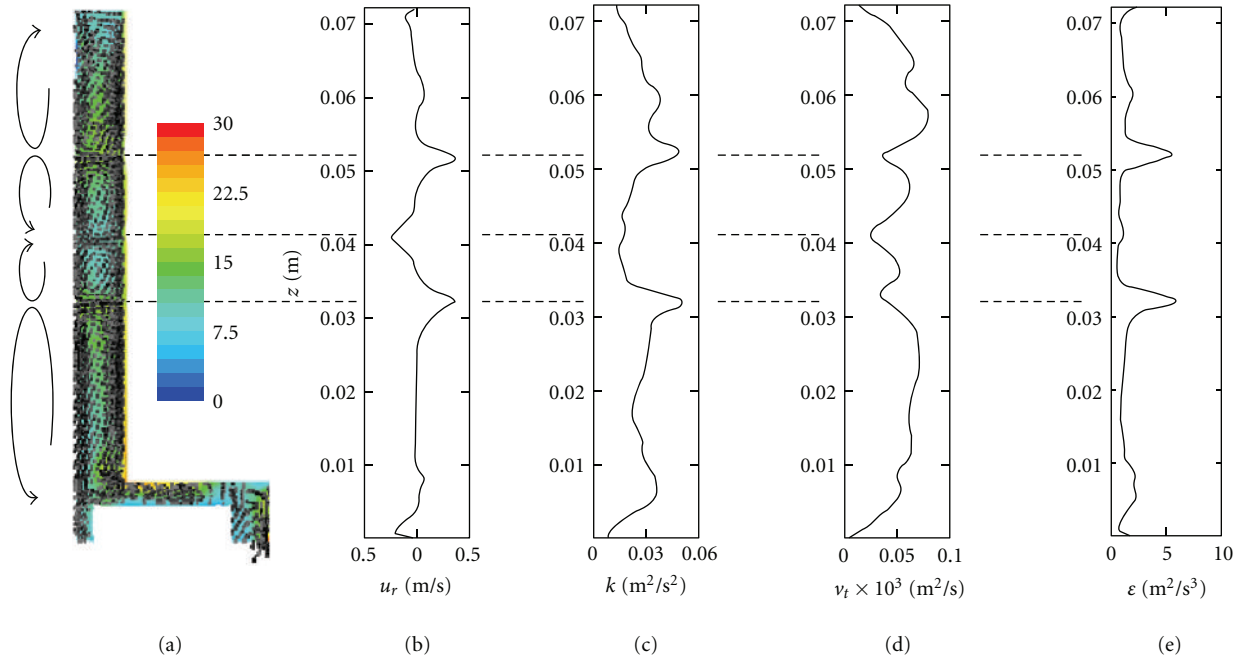


FIGURE 5: Flow patterns and turbulent properties at 30 r/s and total flow rate 4.16 mL/s at the center of annulus: (a) contours of turbulent intensities (%); (b) radial velocity profile; (c) turbulent kinetic energy profile; (d) turbulent viscosity profile; (e) turbulent kinetic energy dissipation profile [119].

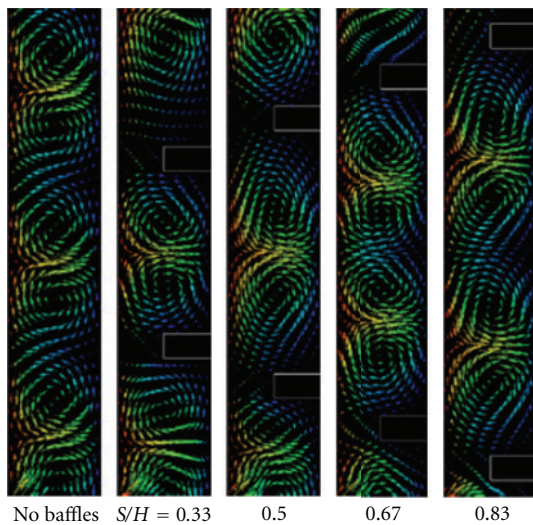


FIGURE 6: Flow patterns in presence of horizontal baffles in the annulus [123].

from realistic ones, there is the problem of extrapolating the “validation” of the simulation at reduced conditions to one at realistic conditions where the flow regime may be substantially different such that the models are no longer valid.

The issue of turbulence always requires attention. Though LES and full RSM modeling methods are available, RANS solution methods such as k - ϵ model are still widely

used owing to their less computational expense. Further, it was shown in the literature that unsteady RANS solution methods capture both qualitatively and quantitatively complex flows which are not statistically stationary with much more accuracy, as compared to steady RANS solutions [133–135].

5. CFD Simulation of Gas-Liquid Interface on the Annular Side

While a simplified, single-phase approximation of the flow in the annular zone of a centrifugal contactor as described in the previous Sections (4.1 to 4.4) yields some useful insights and provides a reduced complexity condition for both simulation and experiments, it is, nevertheless, unable to capture important characteristics of the flow in the actual device as it is typically configured. In particular, the annular region of the centrifugal contactor is not liquid full due to the upper end being open to the collector ring region and outlet channels which are maintained at zero gauge pressure to ensure steady flow between stages. Thus, even for hydraulic operation with a single liquid phase, the flow from the inlets into the annular region can be by droplets or rivulets down the housing wall or rotor depending on operational conditions. Thus, free surface effects dominate the annular region flow and make it quite different from standard closed system Taylor-Couette flow. While annular centrifugal extractor designs do exist [136] in which the effect of the free surface and air drawdown into the annular region has been reduced, the majority of available designs are subject to an “open” annulus with free surface flow.

The effect of an upper free surface on Taylor-Couette flow between vertically oriented concentric cylinders has been primarily studied for low to moderate Reynolds numbers [137–139]. For example, Watanabe et al. [137] explored—both experimentally and computationally—rotation rates up to $Re = 2000$ where free surface instabilities are present but extremely mild compared to those found under typical conditions ($Re > 50,000$) in centrifugal contactors. The influence of the free surface was seen as a slight variation in the shape of the upper most Taylor-Couette cell which was also found to be slightly larger than lower ones. As seen also in Deshmukh et al. [132], the number of cells was also found to be dependent on the startup procedure with a sudden start tending to result in a larger number of Taylor cells than a linear ramping of the rotation rate to the final state. Mahamdia et al. [138] experimentally explored the effect of a free surface on TC flow at low rotation rates and identified secondary instabilities near the free surface.

Due to the added complexity of the free surface at high rotation rates, experimental studies of flows in such conditions are few. Mujica and Lathrop [140] have experimentally observed the instabilities of turbulent free-surface flow in an annular device for high Reynolds numbers ($Re \sim 10^6$) and have observed large-scale “gravity-wave” oscillations in liquid height and tornado-like vortex motion about the spinning cylinder. However, these observations were for an “annular” device with a very large gap size—essentially a spinning rod in a tank. Thus the flow behavior and free surface motion is substantially different from that seen for Taylor-Couette flow with a narrow gap.

Wardle and coworkers were the first to attempt to apply free-surface capturing CFD methods to simulate gas-liquid free surface flow in the centrifugal contactor mixing zone at relevant conditions [27, 141]. Using volume of fluid (VOF) methods [142] and the commercial code Fluent, the free-surface flow in a lab-scale centrifugal contactor having a 50.8 mm rotor was explored [141]. Conditions were chosen for a low-moderate flow rate at a typical rotation rate for this size device (377 rad/s). It was discovered that the free surface is a critical characteristic of the flow in the annular region, with the result that contact between the fluid and the spinning rotor was both discontinuous and intermittent (see Figure 7 with images taken from Wardle et al. [143]). Entrained bubble velocity measurements from LDV are reported. In addition, time autocorrelation of the velocity data provided a quantitative measure of the periodic free surface oscillation that was observed in both visually (high-speed video) and computationally. Excellent quantitative comparison was achieved for the frequency of oscillation. Elsewhere [144], the frequency and magnitude of oscillation is reported as a function of flow rate and rotor speed and was observed to decrease with an increase in either parameter. This same experimental study reports additional data for PIV-measured velocities at several flow rates and high-speed imaging of bubble entrainment under the rotor in the vane region for two vane types (4 straight vanes and 8 straight vanes).

In a follow-on study [27], the methodology was applied to explore numerically the effect of the mixing vanes

(see Figure 8) on the annular liquid flow. As observed in companion experiments (see also [144]), the predicted liquid hold-up volume and height was found to be a strong function of the vane configuration. Vane configurations with four straight vanes (4V), eight straight vanes (8V), and eight curved vanes (CV) were tested. It was seen that fewer vanes resulted in greater liquid volume, liquid height, and fluid-rotor contact due to reduced “pumping” by the housing vanes with the ranking in order being $4V > 8V > CV$. A case with the addition of a gap between the vane and the outer wall and one with a narrower annular gap were also tested for the 8V case (additional images and analysis for these cases is reported in Wardle et al. [141]). It was found that the volume holdup (and consequently the residence time) could be increased by 54% by adding a vane-wall gap equal to half the annular gap. Comparison of mixing as characterized by the turbulent energy dissipation rate, which is directly correlated with droplet size for liquid-liquid systems, followed a similar trend. Despite the value of such relative comparisons, absolute prediction of the height of the liquid in the annulus and hold-up volume is difficult due to uncertainties in the boundary conditions at the rotor inlet; coupled solution of the two regions (annulus and rotor) can eliminate this problem and have recently been reported Wardle [145].

A significant challenge with free-surface modeling techniques is that they are inherently mesh dependent; only interfacial features that can be resolved on the mesh can be captured. As a further limitation, such methods are time dependent by nature and are limited by the Courant flow number:

$$Cr = \frac{\Delta t}{\Delta x/u} \approx 0.25. \quad (15)$$

Thus, the time step Δt is directly proportional to the mesh spacing Δx (u is the flow velocity)—that is if the mesh spacing is cut in half to increase interfacial resolution, the time step must essentially be decreased by the same margin. Consequently, such methods are quite computationally intensive when applied to large systems. A recent study by Wardle and Lee [146] explores the application of a computationally scalable technique using a finite element-based implementation of the lattice Boltzmann method to free surface flow in an annular mixer. While the methodology can be extended to turbulent flows, this study was limited to very low rotation rates and thus the effect of the free surface was small. Good comparison was found with the experimental results of Watanabe et al. [137] which explored a similar range of rotation speeds.

6. CFD Simulation of Single-Phase Flow in the Separator Zone

Patra et al. [147] have studied the hydrodynamics within the rotor using computational fluid dynamics with standard $k-\epsilon$ model. The rotor diameter has been varied over a wide range of 15 to 375 mm and the rotor speed 20 to 175 rad/s. A comparison has been presented between the CFD predictions and the experimental measurements reported in

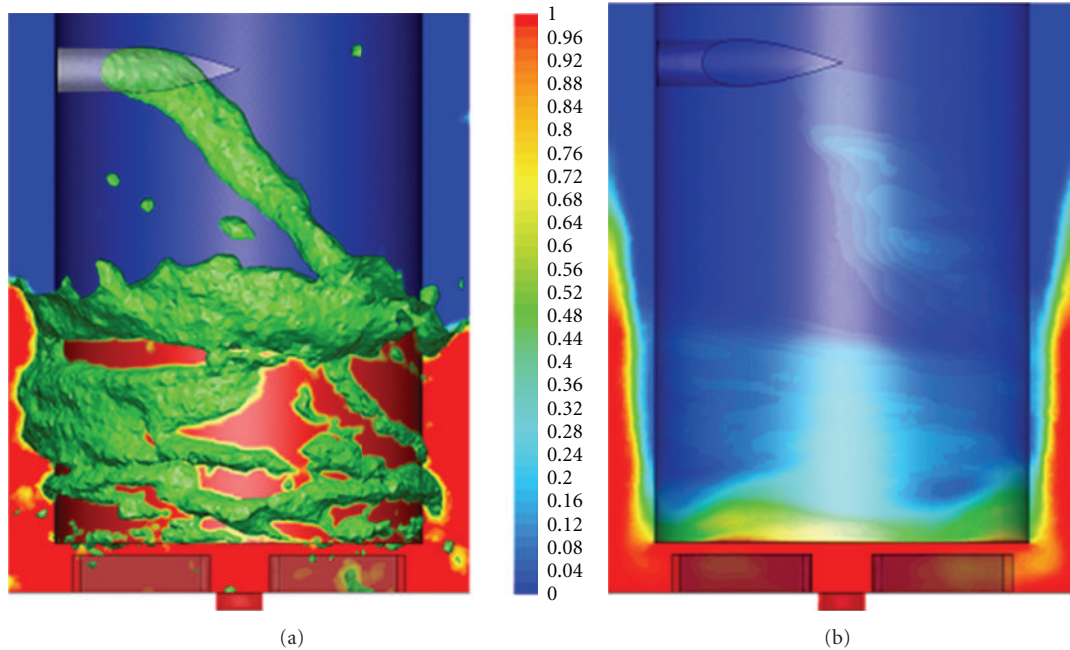


FIGURE 7: Snapshots of instantaneous (a) and time-averaged (b) liquid volume fraction for free-surface simulation of the annular mixing region with four straight housing vanes. Images are taken from Wardle et al. [143].

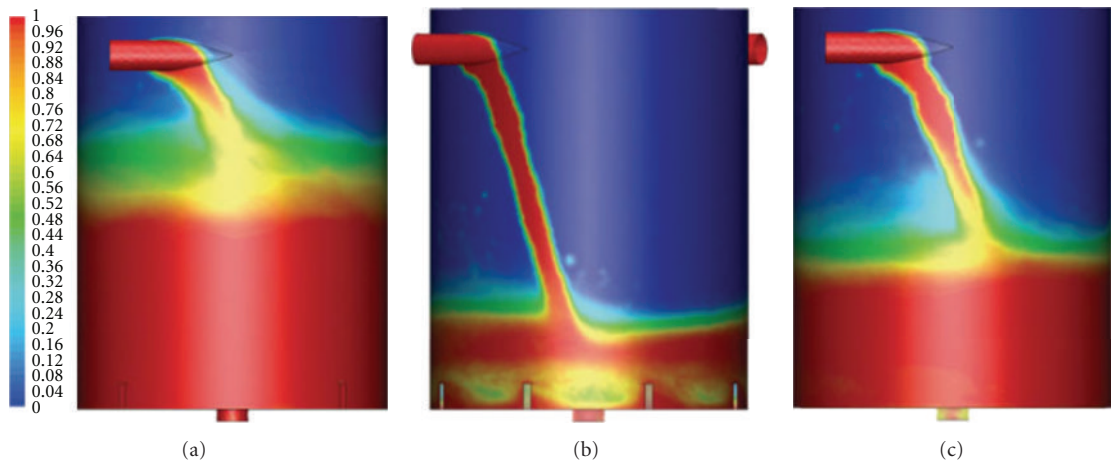


FIGURE 8: Time-averaged water volume fractions in the annular region from CFD for the 4-vane (a) 8-vane (b) and curved vane (c) geometries [27].

the published literature. The hydraulic performance of rotor as a centrifugal pump has been presented in terms of head, capacity and power consumption. The flow pattern in the suction and settling zones of the contactor has been presented with streamlines, static pressure distribution, and the velocity profiles.

The flow inside the rotor of ACE was found to be turbulent-forced vortex flow. The energy dissipation increased with an increase in the rotor speed. The CFD simulations satisfied the overall energy balance. The energy input rate by rotation was equal to the sum of the viscous and the turbulent energy dissipation rates. Such a balance was found to hold for all the rotational speeds and the rotor

sizes. As a consequence of rotation, zone of negative pressure was created at the rotor inlet resulting into a suction of liquid at the bottom center and delivering it at the top of the bowl. The pumping rate was found to increase with an increase in the rotor speed. The throughput system also increased with speed of rotor. Additionally, the available static pressure was found to help in interstage pumping. With an increase in the diameter of the rotor, the pumping capacity of rotor was found to increase. With an increase in the inlet orifice diameter, the pumping capacity of the system was found to increase initially at a faster rate. Further increase in orifice diameter had a nominal effect at relatively low rotational speeds, however, sizeable effect at high rotational speeds.

The trajectory of fluid inside the rotor was observed to follow a spiral helical path originating from the rotor inlet and coming out at rotor outlet. The method of CFD simulation in the work by Patra et al. [147] is expected to be useful for the estimation of pumping capacity while designing these equipment in practice.

7. CFD Simulation of Two Phase Flows on the Annular Side

As with the contactor as a whole, the flows in the annular mixing region include both phase segregated and dispersed flow regimes—“clean” fluids enter a stage and flow as rivulets down the housing wall or, if the feed velocity is high and the annular gap small, impinge on the rotor and are thrown off as droplets. The shear induced in the narrow annular gap by the spinning inner cylinder causes the two fluids to mix to some extent with one phase becoming dispersed into the other and the size of the dispersed phase droplets depending on the fluid properties and flow conditions [148, 149]. Traditional CFD modeling such as that which has been done to date and described in the following sections is flow regime dependent—that is different methods are used for segregated, sharp-interface flows than are used for dispersed flows. Recent promising work has been reported by Wardle and Pereira [150] on the development of hybrid methods as an extension of the techniques demonstrated for Eulerian multifluid—VOF coupling given in Štrubelj et al. [151].

7.1. Liquid-Liquid Stratification. In a recent paper [145], Wardle presents an attempt to simulate the multiphase flow in the annular mixing zone using interface capturing techniques to resolve large droplets and liquid-liquid structures. A model annular mixing zone with four straight housing vanes was used. As stated in the paper, this effort was primarily to demonstrate the limitations of a VOF-only formulation and the need for development of advanced methods which combine dispersed phase modeling with sharp interface capturing. It was found that while the incoming fluid streams did indeed breakup into smaller chunks and droplets, the majority of each fluid remained as large rivulets as shown in Figure 9 reproduced from that work. An additional observation from these simulations is the fact that in relation to air, the two liquids tend to behave as a single fluid. It is thus concluded, that a sharp interface is only required between either liquid phase and air in order accurately capture the physics of the fluid-rotor interaction and in order to capture liquid-liquid mixing dispersed phase modeling could be employed. Yet, the combination of these two techniques is not currently available in any commercial CFD packages.

In this same work [145], extension of the same sharp-interface, three-phase methods to the entire contactor was also performed and the results demonstrated the well-known tendency of VOF methods to overpredict coalescence of droplets. Once the “mixed” liquid-liquid flow entered the rotor, the two fluids were seen to promptly separate. Despite these limitations of a VOF-only methodology, this work

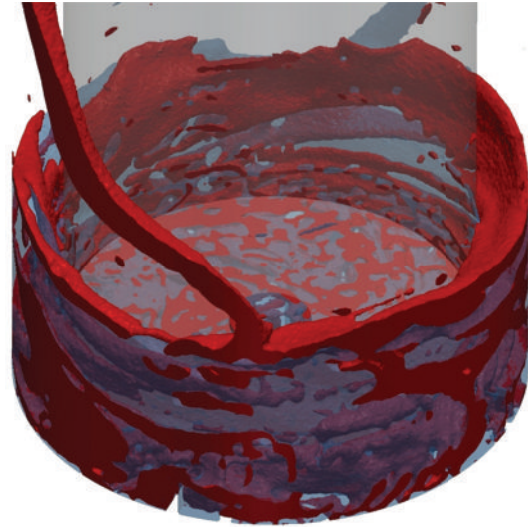


FIGURE 9: Snapshot of liquid phases for liquid-liquid-air simulation of a contactor mixing zone using VOF interface capturing methods taken from Wardle, [145]. Water is shown as transparent blue and oil is red while the air is not colored.

provides a foundation for further developments toward multiphase flow simulation and also demonstrated the applicability of the open-source package OpenFOAM to serve as the basic framework for future methods developments in this area.

7.2. Liquid-Liquid Dispersion. Just as for the single-phase regime, simplification of the mixing zone flow to look only at liquid-full (no air or free surface), liquid-liquid dispersed flow in the annular region has been explored by several researchers due to its broader application to general two-phase Taylor-Couette flow devices. As such, the majority of work to date in this area has primarily been focused on application to low shear, laminar liquid-liquid extraction [152]. Campero and Vigil [29] have examined experimentally various flow patterns for liquid-liquid Taylor-Couette-Poiseuille flow (TC with added axial flow) for several different liquid-liquid phase pairs including water-kerosene for a horizontally oriented annular device. They looked at Reynolds numbers up to ~ 5000 and identified three flow regimes: (1) translating banded flow, (2) spatially homogeneous flow, and (3) oscillatory/alternating combination of (1) and (2) depending on the Weber and Reynolds numbers of the flow. This same experimental setup was used by Zhu and Vigil [153] for further study of the kerosene-water system for both experimental and numerical studies of liquid-liquid flow in a horizontally oriented Taylor-Couette device. Building on the previous work, they proposed a mechanism for the formation of banded liquid-liquid flow—alternating aqueous-rich and organic-rich vortices—which occurs for the upper end of the range of relatively low Re studied ($Re = 300 \sim 5000$). A very useful recent study by Sathe and coworkers [28] explores a broader range of flow regimes both experimentally and computationally for

a vertically oriented Taylor-Couette mixer using a sodium iodide solution as the dispersed phase and kerosene as the continuous one. While no air- or air-liquid-free surface is present, a range of flow regimes spanning segregated to homogeneously dispersed liquid-liquid flows was explored. Data includes velocities and hold-up fraction from PIV and PLIF, respectively, and droplet size characterization using high-speed imaging. Droplet size measurements were made only for relatively low rotation rates where droplets sizes were in the range of 1-2 mm at a dispersed phase fraction of 0.5. PIV and PLIF were done for low rotation rates and dispersed phase fractions <0.1 . Simulations were done over a wider range of conditions using Fluent with an Eulerian two-fluid model and a 2D, axisymmetric annular geometry. A fixed dispersed phase droplet diameter as predicted using the correlation by Haas [148] was imposed. CFD simulations were conducted up to rotation rates where the predicted droplet size was 30 microns and homogeneous dispersion resulted. While comparison between simulation and experiment was generally good, it was concluded that the assumption of a constant diameter droplet size required by the methodology resulted in some unavoidable deviations. The droplet size was additionally found to have a significant affect on the overall flow appearance.

7.3. Gas-Liquid Dispersion. Due to the annular region being “open” to air, in addition to the formation and rotation of the free surface, there is also air that is entrained as bubbles in both single liquid and liquid-liquid flow conditions. Various researchers have looked at the effect of air bubbles and their distribution in turbulent Taylor-Couette flow. Unlike what was seen for a lighter liquid dispersed in a heavier continuous phase where droplets tended to go toward the vortex cores, it has been shown that bubbles migrate toward the inner cylinder and are most stably located in rings along the regions of outflow between toroidal TC vortices [154–157]. Numerical studies have also been able to predict this behavior [154, 158, 159]. Batten et al. [160] developed a method of using the average bubble distribution to identify the location of Taylor cells. Additionally, one effect of the bubbles accumulation near the inner cylinder is the reduction of drag and corresponding decrease in energy dissipation [161]. This is important as energy dissipation is a key measure of the mixing intensity and is consequently directly correlated to droplet size for liquid-liquid mixing.

Atkhen et al. [154] have observed the fluid mechanics of an annular contactor apparatus with radial vanes beneath the rotor directing the flow toward a downward axial exit (see also [149, 162]). The device used in this work had a very long aspect ratio (total height relative to annular gap)—hydrodynamic observations were made with a liquid height of ~ 50 cm and annular gaps of 5 mm and 10 mm. Thus, for this system under the range of conditions explored, the effect of the free surface was limited to the formation and distribution of air bubbles throughout the annulus. It was observed that at the high end of the range of rotation speeds explored ($Ta > 5 \times 10^4$) that spatial and temporal defects due to free surface agitation led to elimination of stable

Taylor vortices. Note that this is approximately an order of magnitude lower than the transition to fully turbulent Taylor vortex flow and several orders of magnitude lower than the Taylor number in typical annular centrifugal contactor flow.

8. CFD Simulation of Two-Phase Flows in the Separator Zone Including the Overflow Weirs

8.1. Flow Simulation for Gas-Liquid System inside the Rotor. As described earlier and shown in the general contactor sketch in Figure 1, the flow of the liquid-liquid dispersion enters the spinning rotor and is thrown towards the outer wall where the two fluids separate as they flow upward. As the upper section and outlet channels are open to air, a vertical column of air (which would be more of a typical vortex at lower rotation rates) also develops along the axis of the rotor. Thus, even in the rotor a complex, three-phase system exists. Further, the flow of the separated liquid streams over their respective weirs occurs as a free-surface and may exist as droplets or rivulets depending on the magnitude of flow and operating conditions. Proper sizing of the heavy-phase and light-phase weirs and outlet channels is essential for achieving optimum throughput with no other phase carryover (unseparated dispersed phase which leaves the stage with the continuous phase and degrades overall extraction efficiency) for a given liquid-liquid system. While non-CFD approaches (described in Section 2.2) to modeling the operation of the rotor using hydrostatic balance arguments and various flow correlations [107, 163] have been successful at providing a useful means for proper weir design, relatively few CFD-based studies have been conducted to help understand the flow in this region of the contactor and aid in more fundamental design and operational optimizations.

Wardle et al. [143] applied the same free surface simulation methodology mentioned above in the context of the mixing zone to exploration of the flow of a single liquid phase in the rotor of a lab-scale contactor. The actual rotor geometry from a contactor manufactured by CINC Industries (CINC-V2) was used and the solution was done within a rotating reference frame. The authors demonstrated that at normal operating speeds the liquid forms a vertical annulus on the outer wall with a stable air column in the center. A methodology for predicting the zero-point flow rate (single-phase feed rate at which flow begins to exit from the light-phase side) using CFD was developed. In addition, interesting flow phenomena in the region above the heavy-phase weir was identified which helped to explain experimentally observed behavior—namely, elevated and sometimes unstable heavy-phase throughput [164]. It was discovered that the narrow flow region above the upper weir formed by a cap, which in this design holds the changeable weir in place, could potentially seal with liquid forming a siphon and artificially elevating the throughput through the heavy phase side (Figure 10(a)). Simulations and experiments verified that venting of the cap could eliminate this siphon formation.

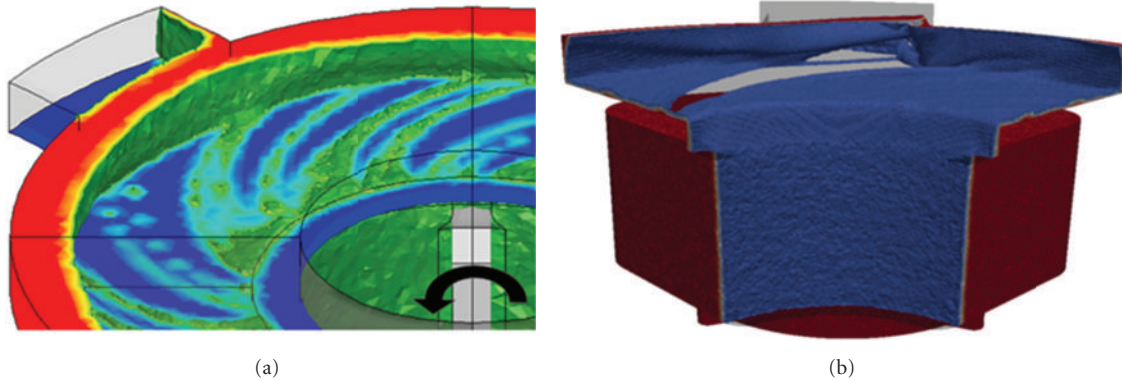


FIGURE 10: (a) Snapshot of free surface flow over the upper weir at high flow rate showing liquid accumulation under weir cap [143], (b) Snapshot of free surface flow over the upper weir at high flow rate showing liquid accumulation under weir cap [165].

Building on the previous simulations for the full rotor, Gandhir and Wardle [165] explored the flow in the aqueous underflow region (region on heavy phase side above item 10B in Figure 1) and above the upper weir using free-surface capturing, this time using the open-source CFD toolkit OpenFOAM as the CFD package. While significant liquid accumulation and some negative pressure buildup was observed, complete liquid sealing of the weir cap outlets was not found in this case (Figure 10(b)) and was attributed to the greater mesh resolution used in this study relative to the earlier one. The relative pressure drop in the underflow region was investigated and found to vary only slightly with different modifications to the weir cap. While cap design modifications were proposed which can smooth the outlet flow, as with the previous work on the full rotor [143], it was determined that a cap vent is required to regulate pressure and ensure smooth and predictable operation as seen with an open upper weir.

Using the open-source CFD package OpenFOAM, Wardle also reported the first coupled-region model simulations for the combined annulus and rotor zones using multiple moving reference frames and sharp interface capturing for gas-liquid flow and gas-liquid-liquid flow [145]. Figure 11 taken from that work shows a snapshot of the liquid flow for the two-phase, water-air case for this couple-zone model. As noted in that work, a coupled-zone model eliminates the need for difficult approximations of boundary conditions at the rotor inlet which make it challenging to independently predict annular liquid height or its effect on rotor flow.

8.2. Flow Simulation of a Liquid-Liquid System inside the Rotor. A 2006 study by Padiyal-Collins et al. [166] looked at the separation of a liquid-liquid mixture using an Eulerian multifluid framework (per-phase momentum equations for dispersed phase modeling of phases as interpenetrating continua). This work employed a simplified rotor geometry (2D and 3D) which was assumed to be entirely filled with the separating dispersion (no air core). For their dispersed phase modeling, the authors used a fixed dispersed phase diameter of 150 microns which reportedly mimicked the experimentally observed separation time. The influence of

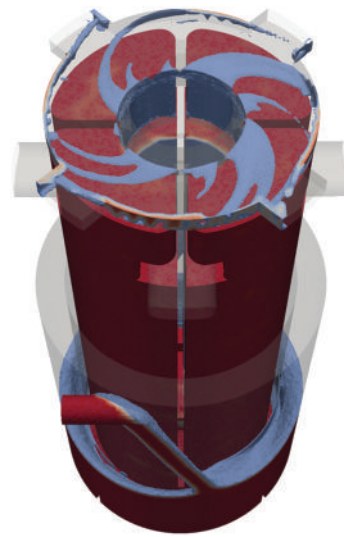


FIGURE 11: Simulation of free surface flow (water, air) in for a coupled annular mixer, rotor centrifugal contactor model taken from Wardle, [145]. The spiraling flow of liquid over the upper weir can be seen; rotor rotation is in the counter-clockwise direction.

“effective” mixture viscosity, which is greater than that of either phase alone, was explored and found to be important to the separability of the two phases. Additionally, it was suggested that an outward sloping rotor interior sidewall could potentially increase the phase separation capacity of the rotor for a given throughput.

8.3. Effect of Annulus Liquid Height on the Flow Profile Inside the Separator. Liquid height in the annulus is critical to the optimized design and operation of the ACE. While the throughput of a given contactor is typically limited by the capacity for complete separation of the two phases within the rotor, such that there is minimal other-phase contamination in the respective outlets, another limiting case is the understanding if the dispersion in the annulus fills the mixing zone, and overflows into the organic collector ring. Even if the liquid height under nominal conditions is

acceptable, flow transients and changes in the liquid height due to phase inversion make the annular liquid height an important factor during operation.

9. Conclusions

(1) The annular region of the annular centrifugal extractor (ACE) has been simulated using computational Fluid Dynamics over a wide range of design and operating conditions, such as (Table 1): $22.2 < D_i < 500$ mm, $1.5 < d < 25$ mm, $1.67 < N < 60$ r/s. This covers the Taylor number range of $50 < Ta < 3 \times 10^8$. In majority of the cases, single-phase flow has been simulated.

(2) For the simulation of annular region, k - ϵ , RSM and LES have been employed as turbulence models. Among k - ϵ and RSM, the latter has been found to give more reasonable predictions of three components of mean velocity, Reynolds stresses, k and ϵ . Extensive comparisons have been presented by Vedantam and Joshi [3], Wardle et al. [133], Deshmukh et al. [26, 132], and Deng et al. [123].

(3) Though LES has been employed by a few investigators, the grid size has been coarse.

(4) The CFD simulations give the value of turbulent energy dissipation rate (ϵ) at all the locations of simulation. The volume integral of ϵ gives the total energy dissipation in the simulation region. It has also been shown that the viscous dissipation is not negligible particularly in small scale equipment and where the velocity gradients are steep. The simulated energy dissipation rate needs to be equal to the energy supply rate by the impeller rotation. Such a complete energy balance has been established by Vedantam and Joshi [3], Deshmukh et al. [26, 132], Sathe et al. [28], and Tamhane et al. [105]. The establishment of such energy balance has been considered to be an important criterion for the validity of CFD simulation.

(5) Taylor [84] has experimentally measured the transition points from purely tangential flow to Taylor-Couette flow. These experiments were performed over a wide range of rotational speeds of inner and outer cylinders. The effects of corotation and counter-rotation have been examined. However, the gap between the cylinders was small. Therefore, Chandrasekhar [87] considered the case of large gaps and found the transition criterion analytically. Further, Rayleigh [83] has developed a criterion for inviscid fluids. For all these three cases of Taylor, Chandrasekhar and Rayleigh, the transition points can very well be predicted by the CFD simulations [26].

(6) The value of Ta at which the first transition occurs from Couette flow (CF) to Taylor vortex flow is designated as critical Taylor number (Ta_{Cr}). For the stationary outer cylinder, as Ta increases beyond Ta_{Cr} , the flow transition occurs to wavy vortex flow (WVF, $Ta_{Cr} < Ta < 100 Ta_{Cr}$), then to chaotic vortex flow (CVF, $100 Ta_{Cr} < Ta < 1000 Ta_{Cr}$) and finally to turbulent Taylor vortex flow (TTVF, $Ta > 1000 Ta_{Cr}$).

(7) The effects of operating parameters like rotor speed and axial flow rate on the number of Taylor vortices formed in the annular region have been observed by Deshmukh et al.

[26, 132]. They showed that the number of Taylor vortices decreases with an increase in rotor speed. Also, when an axial flow was imposed on the existing rotational flow, the number of vortices decreases with an increase in the net axial flow.

(8) Deshmukh et al. [119, 132] and Tamhane et al. [105] have also studied the flow patterns in presence of helical baffles in the annular region. They observed that each compartment contained a pair of counter-rotating Taylor vortices. This fact was shown to aid an approach to plug flow behaviour.

(9) Deng et al. [123] have investigated the Taylor vortex flow in a short column in presence of vertical and horizontal baffles on the outer cylinder. The calculation resulted from CFD simulation agreed well with the PIV measurements. The introduction of vertical baffles eliminated the axisymmetric vortex structure and resulted in a three-dimensional flow pattern, including the circulation flow in the radial-azimuthal plane and the periodic variation of the vertical position of vortices. The horizontal baffle separated the original fluid column in compartments, and the length of the vortices inside was variable in a certain range to fit the compartment dimension. It was found that the number, position, and width of the baffles affected the vortex structure in the annulus. This study could provide informative insight to many engineering applications of Taylor vortex devices.

(10) The computational methodology of Wardle et al. [27] has been further validated and applied to perform a detailed analysis and comparison of the flow and mixing for several possible housing vane configurations. In general, it has been seen that the housing vane geometry has a significant impact on the overall flow patterns, liquid height and liquid volume, fluid-rotor contact, and energy dissipation rate in the rotor region.

(11) The presence of vanes on the bottom plate, below the rotor, essential to direct the flow inside the rotor has been shown to enhance the back-mixing and turbulence [132]. The CFD results show that providing suitable internals such as radial baffles as well as the length of vanes on the bottom plate can reduce backmixing in the annulus.

(12) Wardle et al. [133] presented the results of CFD calculations of the flow in the mixing region of an annular centrifugal contactor applying various simplifying assumptions (i.e., steady-state, liquid full contactor, and single liquid phase) and using relatively simple CFD models. It was found that realistic, qualitatively accurate results could be obtained for the flow underneath the rotor.

(13) Wardle et al. [141] have presented a comparison of experimental measurements and computational modeling of the free surface flow in the mixing zone of an annular centrifugal contactor. It was found that CFD modeling using the LES turbulence simulation method even for a relatively coarse computational grid was able to qualitatively and quantitatively predict the actual dynamics of the flow in the contactor mixing zone. A comparison with LDV data showed that the mean and RMS velocities were captured with much better accuracy by LES modeling than for either RANS or DES on the same mesh. Thus, for transient modeling of the flow in the contactor using the VOF interface-tracking method, it appears that greater accuracy can be obtained

from LES without a significant increase in computational cost. More importantly, this study has shown that the velocity predictions and free surface dynamics from CFD modeling of the centrifugal contactor are experimentally verifiable.

(14) A comparison presented by Wardle et al. [27] has shown both qualitatively and quantitatively that the mixing vane geometry has a clear impact on the overall effectiveness of the mixing zone. The conclusions obtained from the simulations were compared with a variety of experimental observations and found to have generally good predictive accuracy for the flow of water in the mixing zone. From this, it is anticipated that the experimental analysis and modeling scheme set forth here can aid in the proper selection of contactor geometry as well as lend insight into ways to improve the design of existing contactor units with minimal modification. In particular, from this comparison, it can be concluded that among the given configurations, one might select the 4-vane geometry for better low flow rate operation as it maintains a predictable liquid volume with greater fluid-rotor contact; however, at high flow rates (1000 mL/min), the liquid level is such that nearly the entire mixing zone is filled and there is the risk of overflow into the lower phase collector ring and phase contamination. This marks a practical upper limit for this geometry. While high flow rates were not simulated, it has generally been observed that adequate operation can be achieved with either the curved vanes or 8-vanes at high flow rates. For some processes and phase pairs, there may be issues with overmixing and emulsification. In such cases, this type of analysis could certainly aid in selecting an appropriate geometry and targeting experiments for improving operation for the flow conditions specified by the process. It has also been demonstrated that a noticeable improvement, both in terms of mixing and residence time, can be achieved through the simple addition to the standard 8 vane geometry of a vane-wall gap with a width equal to half the annular gap (d).

(15) The flow in the separation zone of the annular centrifugal contactor has been explored [143] through the application of detailed computational flow simulations of the actual geometry of a model rotor of a CINC V-2 centrifugal contactor. It was found that there is indeed a vertical column of air that develops along the axis of the spinning rotor. For moderate flow rates, the heavy phase exit ports above the upper weir remain open and there is droplet flow over the weir. At high flow rates, the flow area above the upper weir becomes sealed with water and forms a siphon which increases the amount of flow that can pass over the upper weir. This was observed quantitatively through prediction of the zero-point flow rate for the standard sealed upper weir cap and for one with venting. Similar trends between the two weir caps were also observed experimentally. This research effort has viewed the contactor from the perspective of solvent extraction and has, therefore, deemed the zero-point elevation an undesirable quality. For operation of the contactor primarily as a dedicated separation device, it might be argued that a higher heavy phase throughput is advantageous. Even so, it can generally be concluded that a predictable throughput is preferable regardless of the application of the unit.

(16) The simulations by Wardle et al. [143] provide a detailed view of the flow structures within the rotor of the centrifugal contactor. In particular, specific details of the flow above the upper weir have helped to explain previously observed behaviors for this design of contactor rotors. As this commercial contactor design has been in general favorably evaluated for solvent extraction use by a number of studies [164, 167–169] the research presented here provides a tool for evaluating the design as well as a method for enabling greater general understanding of the flow and hydraulic operation of the separation zone of the annular centrifugal contactor.

(17) The CFD toolkit OpenFOAM was used by Wardle [145] to explore previously unreachable simulation space for multiphase flow in a model annular centrifugal contactor. In particular, liquid-liquid mixing simulations with a greater mesh refinement than the mesh number which was used earlier were performed. More importantly, mixing zone-separation zone were coupled. This package provides the necessary framework for developing advanced multiphase solvers specifically tailored to the physics of the problem at hand based on the limitations of existing methodologies as identified here. It is clear from these simulations that while the VOF methodology is capable of providing a general idea of the flow in both regions of the contactor, only underresolved simulations are possible because the mesh required for full resolution of the interphase mixing and resulting small droplets is computationally prohibitive even with massive HPC systems due to the fine meshing and very small time steps that are required.

(18) Wardle [145] have recommended that an interpenetrating (Eulerian-Eulerian), statistical multiphase modeling methodology coupled with VOF for the liquid-air interface(s) be employed to enable prediction of the physical effects of the unresolved droplet scales. Additional coupling of such a solver with droplet size distribution information is expected to a simulation framework capable of providing unique insight into the area of solvent extraction process simulation in a variety of process liquid-liquid contacting equipment including the annular centrifugal contactor.

(19) Zhu and Vigil [153] have investigated that banded distributions of disperse-phase droplets are characteristic of liquid-liquid Taylor-Couette flow with a fixed outer cylinder. These structures arise when centrifugal forces associated with the rotation of the vortices themselves, as opposed to the inner cylinder, are sufficiently strong to cause droplet migration to vortex cores ($\rho_p < \rho_C$) or to vortex inflow boundaries ($\rho_p > \rho_C$). For the case of a less dense disperse phase, the scaling relation provided by (6) (in their paper) appears to correctly predict the “bandedness” of liquid-liquid Taylor-Couette flow. However, its usefulness as a predictive tool is limited by the lack of prior knowledge concerning (1) the azimuthal velocity component u_θ , with respect to the vortex rotational axis in the core on the outer layer of a vortex, and (2) the turbulent viscosity in the vortex cores. Droplet diameters can be estimated by using Haas’s correlation, (2) [148]. As a first approximation, for small particle loadings one would expect u_θ to be independent of α

and d_p and to be proportional to the inner cylinder angular velocity so that $u_\theta/\Omega_i R_i = \text{constant}$.

Authors have also suggested that, a plot of this ratio against azimuthal Reynolds number results in

$$\frac{u_\theta}{\Omega_i R_i} = 0.14. \quad (16)$$

Calculation of the mixture turbulent viscosity at the vortex core is more difficult, as this quantity depends upon the local turbulent kinetic energy and turbulent dissipation, which in turn are composition-dependent quantities. Equation (6) is strongly dependent on the mean droplet diameter, which in turn depends more sensitively on We than on Re , according to (2) (Both equations from Zhu and Vigil [153]). A decrease in interfacial surface tension through the introduction of a surfactant, therefore, is a more effective means for reducing droplet size than is a proportional increase in the angular velocity of the inner cylinder. For fixed interfacial surface tension, experiments and FLUENT simulations show that the disperse phase becomes progressively more homogeneously distributed as the azimuthal Reynolds number is increased.

(20) An experimental facility for measuring orthokinetic aggregation has been developed by Wang et al. [170] and tested. By making use of a CCD camera and an in-line optical assembly, nonintrusive measurements of particle size distributions have been performed. The evolution of a surfactant-free polystyrene sphere aggregation process under various mean shear rates in the laminar Taylor vortex flow regime has been investigated.

The authors have made the following additional observations.

(i) The mean aggregate particle size, d_{43} , grows before reaching a steady-state value, which depends upon the value of the mean shear. Specifically, the steady-state value of d_{43} decreases with increasing shear rate, which suggests that aggregate breakup is the reason that particle growth ceases. Further evidence of this is provided by the fact that the steady-state value of d_{43} is independent of the total initial monomer concentration. In contrast, if the cessation of particle growth was due only to the presence of too few particles rather than to breakup of aggregates, one would expect the steady-state value of d_{43} to depend on the total initial monomer concentration. (ii) The two-dimensional perimeter based fractal dimension of the flocs, D_{pf} , was used to quantify aggregate structure. A comparison of time plots of the mean particle size d_{43} and D_{pf} shows that initially aggregates have a ramified, open structure that becomes more compact as breakup-induced restructuring occurs even after the mean aggregate size has reached steady state. Such restructuring is consistent with the observations of other investigators. (iii) Although the experiments described here were performed in a batch mode because of the slow growth of aggregates, the Taylor-Couette reactor could prove to be convenient for studying faster aggregation processes. In particular, by operating the Taylor-Couette reactor in a steady-state continuous mode so that a weak axial flow causes axial translation of the Taylor vortices with minimal disruption, optical PSD measurements can be obtained

at leisure at various axial locations in the reactor. (iv) If the reactor is operated in the laminar Taylor vortex regime, each axial location will sample particles with identical residence times. Such measurements are impossible with other common continuous flow devices, such as stirred tank reactors. Velocity field measurements obtained by PIV were used to validate the CFD model implemented on Fluent. Thus the shear field can be obtained accurately for the simulation of aggregation and breakage. The simulation of particle size enlargement can be done by using average shear, and it can provide useful information about the parameters in the model. However, use of CFD is necessary for accurate simulation of simultaneous aggregation and breakage processes, especially when reactions occur on short time scales.

(21) Padiyal-Collins et al., [166] have solved the momentum and mass conservation equations in the simulation of the separation of the aqueous and the organic components in the rotor zone of a centrifugal contactor. The authors have demonstrated a computational scheme and a tool which can be used to examine complex hydraulics, to explore effects of the geometry in the process, and to study the influence of different initial conditions, distinct rotor speeds, and diverse physical contributions. We have studied the importance of the effective viscosity. Its effect seems important at the low and high angular velocities, especially for the vertical contactor case. Since the objective is to reach very high extraction efficiency, the more accuracy in the modeling of effective viscosity in the simulations may be necessary. The calculations also show a potentially strong effect from mass transfer on the dynamics, indicating the need for realistic mass transfer parameters before more definitive statements can be made. Ultimately, these simulations aim at improving the efficiency of the centrifugal contactors by allowing, for example, investigation of alternative shapes for the devices or suggesting more appropriate initial conditions. Both of these had significant effects in our simulations. Future plans include the evaluation and optimization of advanced designs for contactors as well the investigation of the issue of scale to determine the minimum size for pilot units.

(22) The dispersion in a vertical Taylor-Couette contactor has been studied by Sathe et al. [28] experimentally as well as computationally. The experiments have been also carried out using high-speed imaging for getting the information about the drop sizes. The correlation by Hass was found to give comparable estimate of the drop sizes. The slight deviation observed was due to the dependence of holdup on the drop size in the annulus. The correlation by Hass does not contain the holdup of the dispersed phase, whereas the actual drop size depends on it. For this reason, the correlation seems to predict the drop size well at low-dispersed phase holdup values in the annular region.

(23) The PIV measurements have also been carried out [28] for the single-phase flow. A very good agreement has been found between the CFD predictions and experimental data in terms of mean velocity profiles as well as the number of vortices. The CFD simulations for the single-phase flow and also with multiphase flow have a limiting case of $\epsilon_D = 0$. The PIV images were processed to obtain the velocity vectors

under the similar conditions. It was found that the number of vortices and the spacing between them obtained with the PIV were in good agreement with those shown by the CFD simulations.

(24) Simultaneous measurements of flow field and dispersed phase holdup have been performed by Sathe et al. [28] using PIV and PLIF techniques, respectively. The experimental data were used to validate the CFD simulation. A good agreement has been observed for the mean velocities, number of vortices, and hold-up profiles within the acceptable limits. It was also observed that the results obtained with single-phase CFD simulations matched with those obtained with the simulations using the Eulerian multiphase model with $\epsilon_D = 0$. Thus, it was concluded that Eulerian multiphase model could be extrapolated to single-phase model when the holdup of the dispersed phase is taken as zero.

(25) The effect of physical properties like density difference and interfacial tension and the effect of geometrical parameters such as annular gap on the flow patterns have been studied by Sathe et al. [28] using CFD. The results have been represented in the form of regime maps with the Eotvos and Taylor number as the two coordinates. The results are independent of dispersed-phase hold-up for $\epsilon_D > 0.05$.

(26) At very low rotational speeds ($Ta > 2 \times 10^6$, $Eo < 0.046$), Sathe et al. [28] have shown that the two phases remain vertically stratified with a clear interface in between them. Further, these authors have shown that, at moderate rotational speeds, segregated flow can be observed when, $Eo > 0.046$, and $7 \times 10^6 > Ta > 2 \times 10^6$ or $Eo > [1.87 \times 10^{-7} Ta - 1.26]$, $Ta > 7 \times 10^6$. In such cases the light phase gets dispersed in the heavier phase at the bottom as well as heavy phase is observed to be dispersed in the light phase at the top.

(27) Sathe et al. [28] have shown that, when the drops are large, centrifugal force on the drops due to tangential rotation of fluid around the cylinder axis was found to be dominant which gives a banded dispersion such that $Ta > 7 \times 10^6$ and $Eo < [1.87 \times 10^{-7} Ta - 1.26]$ (for $Eo > 0.046$) or $Eo > 5.04 \times 10^{-2} - 6.23 \times 10^{-11} Ta$ (for $Eo < 0.046$). The dispersed phase in this case was found to mainly accumulate near either outflow or inflow region of Taylor vortices for $\rho_C > \rho_D$ or $\rho_C < \rho_D$, respectively. Also, when the drops are small and/or the density difference between the phases is small homogeneous dispersion can be observed, such that $2 \times 10^6 < Ta < 7 \times 10^6$, $Eo < 0.046$ or $Ta > 7 \times 10^6$, and $Eo < [5.04 \times 10^{-2} - 6.23 \times 10^{-11} Ta]$.

(28) A systematic investigation by Gandhir and Wardle [165] has shown that the design of the weir cap has a significant effect on the flow patterns above the weir as well as on the pressures generated in this region. In turn, the pressure drop will have an influence on the throughput as characterized by the zero point flow rate. A number of variations and modifications to the weir cap design were simulated and, combined with insight from the previous work. The authors have made a number of recommendations. These simulations all considered only for the CINC-V2 contactor design. While no relevant data has been published, it appears from available information

from preliminary tests at Argonne and elsewhere that the larger CINC units such as the V5 and V10 are equally effective if not more susceptible to negative pressure effects and siphon formation in the cap region and, therefore, the conclusions here should be equally applicable to those units. Measurements of the relative dimensions of the weir cap for the CINC-V5 contactor show that the heavy-phase outlet channel is much longer, with an aspect ratio of 1.25 compared to only 0.45 for the V2. This, in addition to minor underscaling of the channel width and the gap space above the weir, may indeed be the cause of the observed propensity for negative pressure effects and siphon formation.

Simulations are underway with a V2 cap scaled to the V5 relative dimensions to confirm this hypothesis and the overall effects of these differences on the flow profile and siphon susceptibility. The following work elements are progressive.

- (i) Recommendation (b) assumes that the recommendation (a) is complete and are aimed at modifications to existing contactor units in terms of (a) vent in the weir cap (with 2 or more holes), (b) orient the cap with the outlet channel aligned with the light phase outlet channel, (c) modify the cap according to design (b).
- (ii) If recommendation (a) is implemented, (b) requires no additional effort to also implement. Item (c) requires some additional machining of the weir cap but should correspondingly offer some measure of additional stability of flow through smoothing of the exit flow profile. Additional simulations and experiments for the recommended modifications in the larger CINC contactor units (V5 and V10) should be done to verify that these changes have the desired effect.

(29) Tamhane et al. [57] have carried out drop size measurement studies with the help of phase Doppler particle analyser (PDPA). A wide range of power consumption was employed in these studies. The measurements were taken at two different hold up values, namely 2.5% and 7.5%. It was found that, the mean drop size decreased with an increase in the power consumption in the annulus. The decrease in drop size was sharp in the initial stages while it was gradual in the latter part.

(30) Tamhane et al. [105] also observed that the drop sizes increased with increasing hold-up values of dispersed phase. In order to compare the experimental observations with the analytical solutions, Rosin-Rammler distribution function is used. Moreover, the effect of drop size on Weber number was studied. It was found that the exponent of Weber number is around -0.58 .

(31) A correlation for the drop diameter in the annular region of Annular centrifugal extractor has been proposed by Tamhane et al. [105], which takes into account the effect of operating parameters like fluid properties, power per unit volume, and hold-up. The correlation is based on their own measurements and all the results on drop size (in ACE) available in the published literature.

10. Suggestions for Future Work

(1) The subject of centrifugal instability has been discussed in Section 2.1. It consists of transition from purely circumferential flow to Taylor vortex flow. The subsequent transitions to (a) Couette flow ($Ta = Ta_{Cr}$), (b) wavy vortex flow (WVF) ($Ta_{Cr} < Ta < 100 Ta_{Cr}$), (c) then to chaotic vortex flow (CVF, $100 Ta_{Cr} < Ta < 1000 Ta_{Cr}$) and finally (d) to turbulent Taylor vortex flow (TTVF, $Ta > 1000 Ta_{Cr}$) were also described. However, the published work has been almost confined to single phase Newtonian fluids, small Taylor-Couette geometries with infinite length. The work needs to be extended to the practical cases of annular centrifugal extractors (ACEs) having gas-liquid interface at one end and the bottom baffled portion (Figure 1 (part 6)) at the other end. The work also needs to be extended to large size ACEs upto 1.5 m rotor diameter and 3 m rotor height. The work also needs to be extended to multistage counter-current ACEs.

As mentioned earlier, the reported work has been largely for single phase Newtonian fluids. The cases of liquid-liquid and gas-liquid dispersions together with a wide range of physical properties ($\rho_C, \rho_D, \mu_C, \mu_D, \sigma$, and nonNewtonian nature) need attention in future.

(2) The overall flow structures and axial mixing can be reasonably estimated by making a pseudohomogenous assumption to represent liquid-liquid dispersion. The first cut solution may be obtained by even ignoring the free surface and simply using single phase flow simulations. These single phase simulations will provide useful estimates of energy dissipation rates as well as axial mixing in the annular region. The estimates of energy dissipation rates may be then used to estimate representative droplet diameter to estimate mass transfer coefficients. The Eulerian-Eulerian (EE) approach can then be used to understand possible influence of slip between two liquid phases. Please note that more often than not effective drag in liquid-liquid dispersions will be a strong function of Kolmogorov length scale (energy dissipation rate). Appropriate correlations of effective drag coefficients should, therefore, be used while developing EE-based CFD models for ACE. These models can then be combined with volume of fluid (VOF) approach to capture free surface as well as possible entrainment of gas phase. This last approach invariably required 3D simulations and, therefore, is very compute intensive.

(3) The key design aspect of the bottom region is to provide appropriate resistance to flow from annular region to inner rotating cylinder. This is realized by providing baffles (fixed in number, shape, size, and location for a given configuration of ACE) as well as additional moving components to realize ability to manipulate resistance during the ACE operation (position of these can be modified to realize better operating conditions in ACE). Since the key design issue is to estimate flow resistance or pressure drop offered by the bottom region, single-phase CFD simulations using the pseudohomogenous fluid (representing liquid-liquid dispersion) are adequate. The choice of turbulence models (since the geometry is quite complex) and use of adequate number of computational cells are crucial to obtain

accurate estimate of flow resistance and key features of flow in the bottom region of ACE. Such CFD models can be used to evolve appropriate guidelines for manipulating flow characteristics of ACE by influencing flow in the bottom region of ACE.

(4) In liquid-liquid stratification studies, the two-phase flow is another variation of a single-phase flow that explores the effect of interface on the vortex flow. A significant challenge with free-surface modeling techniques is that they are inherently mesh dependent; only interfacial features that can be resolved on the mesh can be captured. As a further limitation, such methods are time dependent by nature and are limited by the Courant flow number, in turn, showing the dependency of time step on mesh spacing. The regime transition is inherently a complex problem. The existing VOF based approach may, however, be used to obtain broad estimates of height required for realizing stratified layers. A combination of EE and VOF will be useful to simulate the flow in the inner rotor region of ACE. Closely linked with the flow characteristics of the inner rotor, the flow in the outlets and associated weirs is equally crucial to understand for realizing stable operation of ACE.

(5) The pressure drop across outlet weirs influences number of design parameters of ACE. CFD-based studies help in understanding the flow in the weir region and therefore several other key design parameters of ACE. Until recently, CFD modeling techniques had not been applied to the rotor design in ACE. However, a useful analytical approach was demonstrated for determining the proper dimensions of the weirs based primarily on experimental correlations and hydrostatic balance arguments [107]. While this method has been generally quite successful for rotor sizing of contactors with an open upper weir (and the obsolete air-controlled upper weir), some experiments with "closed" upper weir systems have produced behavior which cannot fully be explained by the existing theoretical models. One such unexplained behavior is the elevated throughput that has been observed for large upper weir sizes in these units. This same behavior has also been observed in larger units of this design. VOF approach or even a single phase approach may be used to estimate pressure drop across outlet weirs of ACE. CFD modeling can provide useful insights in resolving such issues.

(6) Better understanding of the flow within the rotor and specifically the flow over the weirs requires full simulation of the complex rotor and weir geometries and analysis of the liquid free surface flow. Further, such hydraulic simulations can calculate important flow quantities which characterize the rotor and weirs such as the zero-point flow rate. Zero-point flow rate refers to the point wherein, due to excess flow rate coming into the rotor, the liquid volume maintained in the rotor increases so much that the liquid starts to come out of exit ports without getting separated. These kinds of studies are barely reported in a couple of papers until date. In practice, the zero-point flow rate is used to verify fabrication consistency of a set of rotors with the same specifications, such as might be used in a multistage bank of contactors.

(7) The quality of simulated results using CFD models of course also crucially depends on numerical implementation

of selected model equations. Table 2 gives a summary of key numerical parameters (like the number of grids used, method of discretization, and the solution procedure) used by various investigators. It is essential that adequately fine mesh (compared to relevant space scales of the considered ACE) is used along with the higher order discretization schemes. The published CFD results are reviewed in the following sections in light of this brief review on formulation and solution of CFD models.

(8) The suggestions (2) to (7) above in terms of CFD simulations need to cover a wide range of geometries such as $30 < D_i < 1500$ mm, $30 < H < 3000$ mm, $3 < d < 100$ mm. Various baffle designs [105, 119, 123] need to be analysed for reducing axial mixing. For all these geometrical cases, a wide range of physical properties ($\rho_C, \rho_D, \mu_C, \mu_D, \sigma$, and nonNewtonian nature) need to be studied.

(9) The simulation of rotor (separator region) has received scant attention in the past. The future work may be undertaken in the following steps: (a) pumping capacity of the rotor for single liquid phase without any internals, however over a wide range of rotor diameter and height, bottom orifice diameter and the rotor speed, (b) the work can be extended for the case of internals such as diversion plate and baffles and also the details pertaining to the outlet weirs. (c) In the third step, the existence of gas phase can be considered in the central core region. (d) Simulations are needed for the separation of liquid-liquid dispersion into clean individual phases.

(10) It has been brought out in Section 3 that the Kolmogorov length scale in the mixing zone is of the order of 1 to 10 microns. This range is order of magnitude smaller than the classical process equipment such as stirred tanks, bubble columns, fluidized beds, packed columns, plate columns, among others. Therefore, any future efforts of large eddy simulation need to take into account this small range of Kolmogorov length scale. The LES is known to predict the hydrodynamic parameters more accurately than the RANS, k - ϵ , and RSM models. The LES simulations also give information on turbulent structures in terms of their size, shape, velocity, and energy distributions [64, 171–180]. These structures properties can then be related to the mechanisms of heat, mass, and momentum transfer [70, 73, 181, 182].

(11) The mixing and the separation zones contain liquid-liquid dispersions with possibly a drop size distribution. A population balance approach may be combined with CFD (for instance, [55, 183, 184]).

(12) The performances of mixing and separation zones are strongly interlinked. The rotor height (H) and rotor speed (N) are selected for clean separation. The values H, N, D_i , do decide the pumping capacity which also depends upon the level in the mixing zone.

(13) Accurate prediction of stage extraction efficiency can allow optimization of operation and design as well as identification of issues which lead to poor extraction efficiency. Prediction of stage efficiency requires an accurate prediction of specific interfacial area as well as interphase mass transfer coefficients. Prediction of interfacial area is a nontrivial challenge as it requires accurate models for droplet

size variation and some method for capturing droplet size distribution (e.g., population balance modeling, interfacial area transport, etc.). While much can be drawn from similar efforts in the broader liquid-liquid mixing community, research evaluations of the many available correlations for droplet breakup and coalescence should be evaluated for applicability to annular contactors.

(14) While one key advantage of centrifugal contactors is their relatively short residence time and high throughput, for kinetically limited, processes this can be a drawback which necessitates use of a less efficient equipment type that can accommodate the required residence times. CFD-based design tools for design modifications aimed at increasing residence time in annular centrifugal contactors could be of great value for broadening the range of processes which can be successfully implemented using this technology.

(15) Computational work to date has primarily focused on the development of methods and models and their validation for controlled conditions in simplified geometries. Aside from a few specific efforts (e.g., [27]), little has been published on CFD-based efforts to explore the broad range of specific design elements (e.g., annular gap size, vane-rotor gap, etc.) though experimental observations have given some insight into several key features.

(16) As the rotor of the contactor is essentially a centrifuge, particulates can be problematic (even with filtering of feed streams) for long-term operation of certain processes and require periodic shutdown and cleaning of rotors. While shutdown and restart of contactors are easily and quickly accomplished and “clean in place” rotor designs are available [185], CFD tools offer a direct method of exploring particulate flow and evaluating operational limits and design and/or operational changes to mitigate particulate issues.

(17) This is a very challenging problem for computational modeling (and experimentation). However, it is known that the extraction efficiency for processes can be quite different depending on which phase is dispersed. Additionally, process upsets which lead to phase inversion can be problematic—particularly for very small contactors.

(18) Centrifugal contactors have been constructed over a very wide range of rotor sizes from 1 cm to many 10 s of centimeters [186]. Often very small contactors are used for process development and it is not always well understood how certain hydrodynamic effects (e.g., surface tension) differ between the various scales.

Notation

- a : Acceleration (gravitational or centrifugal, m/s^2)
 C/D : Flow rate ratio of continuous to dispersed phase (–)
 Cr : Courant number, $Cr = \Delta t / (\Delta x / \vec{u})$ (–)
 d : Annular gap (m)
 d_{43} : Mean aggregate particle size (m)
 D_i : Diameter of rotor (m)
 D_o : Diameter of stator (m)
 D_{pf} : Two-dimensional perimeter-based fractal dimension of the flocs (m)

$r_o E_o$: Eotvos number, $E_o = \Delta \rho g d_d^2 / \sigma$ (–)
 g : Acceleration due to gravity (m/s^2)
 H : Height of the annulus (m)
 N : Rotor speed (r/s)
 N_D : Dispersion number (–)
 Q : Volumetric flow rate of both phases through the settler (m^3/s)
 r : Radial position from the rotation axis (m)
 \bar{r} : Average radius of the dispersion band in ACE (m)
 r_o : Radius of the inner edge of the dispersion band (m)
 r_u : Radius of the outer edge of the dispersion band (m)
 Re : Reynolds number of rotor, $Re = Ri \Omega_i^2 d / \nu^2$ (–)
 Re_Z : Axial Reynolds number (–)
 R_i : Radius of rotor (m)
 t_B : Batch settling time of the dispersion (s)
 t_R : Residence time of the dispersion in settler (s)
 Δt : Time step (s)
 Ta : Taylor number, $Ta = 4 \Omega_i^2 d^4 (\vartheta - \eta^2) / \nu^2 (\eta^2 - 1)$ (–)
 Ta_{Cr} : Critical value of Taylor number, (–)
 T_S : Settling time (s)
 \vec{u} : Flow velocity (m/s)
 u_r : Radial velocity (m/s)
 u_θ : Tangential component of fluid velocity (m/s)
 V : Volume of the dispersion band in the settling zone (m^3)
 V_S : Settling velocity (m/s)
 We : Weber number (–)
 Δx : Mesh spacing (m)
 ΔZ : Thickness of dispersion band (m).

Greek Symbols

ϑ : Rotational speed ratio of inner cylinder to outer cylinder (–)
 ν : Kinematic viscosity (m^2/s)
 ν_t : Turbulent kinematic viscosity (m^2/s)
 η : Radius ratio, R_o/R_i (–)
 μ_C : Viscosity of continuous phase (Pa.s)
 μ_D : Viscosity of dispersed phase (Pa.s)
 ρ_C : Density of continuous phase (kg/m^3)
 ρ_D : Density of dispersed phase (kg/m^3)
 ρ_p : Density of droplets (kg/m^3)
 $\Delta \rho$: Density difference (kg/m^3)
 σ : Interfacial tension between continuous and dispersed phase (N/m)
 σ_ε : Turbulent Prandtl number for energy dissipation rate (–)
 σ_k : Turbulent Prandtl number for kinetic energy (–)
 ω : Angular velocity (rad/s)
 ϵ_D : Volume fraction of dispersed phase (–)

ε : Turbulent energy dissipation rate per unit mass (m^2/s^3)
 σ_ε : Turbulent Prandtl number for energy dissipation rate (–)
 σ_t : Turbulent Prandtl number for kinetic energy (–)
 τ : Reynolds stress (Pa)
 Ω_i : Rotor speed (r/s).

Subscript

C : Continuous phase
 D : Dispersed phase
 i : Property pertaining to inner cylinder.

References

- [1] D. S. Webster, A. S. Jennings, A. A. Kishbaugh, and H. K. Bethmann, "Performance of centrifugal mixer-settler in the reprocessing of nuclear fuel," in *Recent Advances in Reprocessing of Irradiated Fuel, Nuclear Engineering—Part XX*, W. A. Rodger and D. E. Ferguson, Eds., vol. 65 of *Chemical Engineering Progress Symposium Series*, no. 94, pp. 70–77, American Institute of Chemical Engineers, New York, NY, USA, 1969.
- [2] G. J. Bernstein, D. E. Grosvenor, J. F. Lenc, and N. M. Levitz, ANL-7698, 1973.
- [3] S. Vedantam and J. B. Joshi, "Annular centrifugal contactors—a review," *Chemical Engineering Research and Design*, vol. 84, no. 7, pp. 522–542, 2006.
- [4] S. Vedantam, J. B. Joshi, and S. B. Koganti, "Three-dimensional CFD simulation of stratified two-fluid Taylor-Couette flow," *The Canadian Journal of Chemical Engineering*, vol. 84, no. 3, pp. 279–288, 2006.
- [5] S. Vedantam, J. B. Joshi, and S. B. Koganti, "CFD simulation of RTD and mixing in the annular region of a Taylor-Couette contactor," *Industrial & Engineering Chemistry Research*, vol. 45, no. 18, pp. 6360–6367, 2006.
- [6] B. D. Kadam, J. B. Joshi, S. B. Koganti, and R. N. Patil, "Hydrodynamic and mass transfer characteristics of annular centrifugal extractors," *Chemical Engineering Research and Design*, vol. 86, no. 3, pp. 233–244, 2008.
- [7] B. D. Kadam, J. B. Joshi, S. B. Koganti, and R. N. Patil, "Dispersed phase hold-up, effective interfacial area and Sauter mean drop diameter in annular centrifugal extractors," *Chemical Engineering Research and Design*, vol. 87, no. 10, pp. 1379–1389, 2009.
- [8] C. S. Schlea, H. E. Henry, M. R. Caverly, and W. J. Jenkins, "Purex process performance with short-residence contactors," USAEC Report DP-809, 1963.
- [9] B. F. Roth, "Centrifugal extractors for the reprocessing of nuclear fuels with high burn up and plutonium content," Tech. Rep. KFK-862, 1969.
- [10] J. B. Joshi, C. B. Elias, and M. S. Patole, "Role of hydrodynamic shear in the cultivation of animal, plant and microbial cells," *Chemical Engineering Journal and the Biochemical Engineering Journal*, vol. 62, no. 2, pp. 121–141, 1996.
- [11] Y. M. D. Tsao, E. Boyd, G. J. Spaulding, and D. A. Wolf, "Fluid dynamics within a rotating bioreactor in space and earth environments," *Journal of Spacecraft and Rockets*, vol. 31, no. 6, pp. 937–943, 1994.

- [12] T. Imamura, K. Saito, and S. A. Ishikura, "New approach to continuous emulsion polymerization," *Polymer International*, vol. 30, no. 2, pp. 203–206, 1993.
- [13] K. Kataoka, N. Ohmura, M. Kouzu, Y. Simamura, and M. Okubo, "Emulsion polymerization of styrene in a continuous Taylor vortex flow reactor," *Chemical Engineering Science*, vol. 50, no. 9, pp. 1409–1416, 1995.
- [14] J. B. Joshi, M. M. Sharma, Y. T. Shah, C. P. P. Singh, M. Ally, and G. E. Klinzing, "Heat transfer in multiphase contactors," *Chemical Engineering Communications*, vol. 6, no. 4-5, pp. 257–271, 1980.
- [15] A. B. Pandit and J. B. Joshi, "Mixing in mechanically agitated gas-liquid contactors, bubble columns and modified bubble columns," *Chemical Engineering Science*, vol. 38, no. 8, pp. 1189–1215, 1983.
- [16] A. B. Pandit and J. B. Joshi, "Mass and heat transfer characteristics of three phase sparged reactors," *Chemical Engineering Research and Design*, vol. 64, no. 2, pp. 125–157, 1986.
- [17] S. Cohen and D. M. Marom, "Experimental and theoretical study of a rotating annular flow reactor," *The Chemical Engineering Journal*, vol. 27, no. 2, pp. 87–97, 1983.
- [18] V. V. Ranade, J. B. Joshi, and A. G. Marathe, "Flow generated by pitched blade turbines II: simulation using k-e model," *Chemical Engineering Communications*, vol. 81, pp. 225–248, 1989.
- [19] V. V. Ranade, J. R. Bourne, and J. B. Joshi, "Fluid mechanics and blending in agitated tanks," *Chemical Engineering Science*, vol. 46, no. 8, pp. 1883–1893, 1991.
- [20] T. Ogihara, G. Matsuda, T. Yanagawa, N. Ogata, K. Fujita, and M. Nomura, "Continuous synthesis of monodispersed silica particles using Couette-Taylor vortex flow," *Journal of the Ceramic Society of Japan*, vol. 103, pp. 151–154, 1995.
- [21] V. D. Mundale, H. S. Joglekar, A. Kalam, and J. B. Joshi, "Regeneration of spent activated carbon by wet air oxidation," *The Canadian Journal of Chemical Engineering*, vol. 69, no. 5, pp. 1149–1159, 1991.
- [22] N. N. Gandhi, S. B. Sawant, and J. B. Joshi, "Specificity of a lipase in ester synthesis: effect of alcohol," *Biotechnology Progress*, vol. 11, no. 3, pp. 282–287, 1995.
- [23] N. N. Gandhi, N. S. Patil, S. B. Sawant, J. B. Joshi, P. P. Wangikar, and D. Mukesh, "Lipase-catalyzed esterification," *Catalysis Reviews*, vol. 42, no. 4, pp. 439–480, 2000.
- [24] A. B. Pandit and J. B. Joshi, "Hydrolysis of fatty oils: effect of cavitation," *Chemical Engineering Science*, vol. 48, no. 19, pp. 3440–3442, 1993.
- [25] J. F. Birdwell Jr., J. McFarlane, R. D. Hunt et al., "Separation of ionic liquid dispersions in centrifugal solvent extraction contactors," *Separation Science and Technology*, vol. 41, no. 10, pp. 2205–2223, 2006.
- [26] S. S. Deshmukh, S. Vedantam, J. B. Joshi, and S. B. Koganti, "Computational flow modeling and visualization in the annular region of annular centrifugal extractor," *Industrial & Engineering Chemistry Research*, vol. 46, no. 25, pp. 8343–8354, 2007.
- [27] K. E. Wardle, T. R. Allen, M. H. Anderson, and R. E. Swaney, "Analysis of the effect of mixing vane geometry on the flow in an annular centrifugal contactor," *AIChE Journal*, vol. 55, no. 9, pp. 2244–2259, 2009.
- [28] M. J. Sathe, S. S. Deshmukh, J. B. Joshi, and S. B. Koganti, "Computational fluid dynamics simulation and experimental investigation: study of two-phase liquid-liquid flow in a vertical Taylor-Couette contactor," *Industrial & Engineering Chemistry Research*, vol. 49, no. 1, pp. 14–28, 2010.
- [29] R. J. Campero and R. D. Vigil, "Flow patterns in liquid-liquid Taylor-Couette-poiseuille flow," *Industrial & Engineering Chemistry Research*, vol. 38, no. 3, pp. 1094–1098, 1999.
- [30] X. Zhu, R. J. Campero, and R. D. Vigil, "Axial mass transport in liquid-liquid Taylor-Couette-Poiseuille flow," *Chemical Engineering Science*, vol. 55, no. 21, pp. 5079–5087, 2000.
- [31] T. Hong, L. S. Fan, and D. J. Lee, "Force variations on particle induced by bubble-particle collision," *International Journal of Multiphase Flow*, vol. 25, no. 3, pp. 477–500, 1999.
- [32] Y. Li, G. Q. Yang, L. P. Zhang, and L. S. Fan, "Numerical studies of bubble formation dynamics in gas-liquid-solid fluidization at high pressures," *Powder Technology*, vol. 116, no. 2-3, pp. 246–260, 2001.
- [33] Z. Cui and L. S. Fan, "Turbulence energy distributions in bubbling gas-liquid and gas-liquid-solid flow systems," *Chemical Engineering Science*, vol. 59, no. 8-9, pp. 1755–1766, 2004.
- [34] W. Warsito and L. S. Fan, "Dynamics of spiral bubble plume motion in the entrance region of bubble columns and three-phase fluidized beds using 3D ECT," *Chemical Engineering Science*, vol. 60, no. 22, pp. 6073–6084, 2005.
- [35] G. Q. Yang, D. Bing, and L. S. Fan, "Bubble formation and dynamics in gas-liquid-solid fluidization—a review," *Chemical Engineering Science*, vol. 62, no. 1-2, pp. 2–27, 2007.
- [36] M. Van Sint Annaland, N. Deen, and J. A. M. Kuipers, "Numerical simulation of gas bubbles behaviour using a three-dimensional volume of fluid method," *Chemical Engineering Science*, vol. 60, no. 11, pp. 2999–3011, 2005.
- [37] W. Dijkhuizen, I. Roghair, M. Van Sint Annaland, and J. A. M. Kuipers, "DNS of gas bubbles behaviour using an improved 3D front tracking model- Drag force on isolated bubbles and comparison with experiments," *Chemical Engineering Science*, vol. 65, no. 4, pp. 1415–1426, 2010.
- [38] M. A. Van der Hoef, J. A. M. Kuipers, and J. Wang, "Coarse grid simulation of bed expansion characteristics of industrial-scale gas-solid bubbling fluidized beds," *Chemical Engineering Science*, vol. 65, no. 6, pp. 2125–2131, 2010.
- [39] I. Roghair, Y. M. Lau, N. G. Deen et al., "On the drag force of bubbles in bubble swarms at intermediate and high Reynolds numbers," *Chemical Engineering Science*, vol. 66, no. 14, pp. 3204–3211, 2011.
- [40] M. A. Van der Hoef, J. A. M. Kuipers, and J. Wang, "CFD study of the minimum bubbling velocity of Geldart A particles in gas-fluidized beds," *Chemical Engineering Science*, vol. 65, no. 12, pp. 3772–3785, 2011.
- [41] D. Jain, N. G. Deen, J. A. M. Kuipers, S. Antonyuk, and S. Heinrich, "Direct numerical simulation of particle impact on thin liquid films using a combined volume of fluid and immersed boundary method," *Chemical Engineering Science*, vol. 69, no. 1, pp. 530–540, 2012.
- [42] R. A. Bakker and H. E. A. Van Den Akker, "A lagrangian description of micromixing in a stirred tank reactor using 1D-micromixing models in a CFD flow field," *Chemical Engineering Science*, vol. 51, no. 11, pp. 2643–2648, 1996.
- [43] R. F. Mudde and H. E. A. Van Den Akker, "2D and 3D simulations of an internal airlift loop reactor on the basis of a two-fluid model," *Chemical Engineering Science*, vol. 56, no. 21-22, pp. 6351–6358, 2001.
- [44] R. S. Oey, R. F. Mudde, L. M. Portela, and H. E. A. Van Den Akker, "Simulation of a slurry airlift using a two-fluid model," *Chemical Engineering Science*, vol. 56, no. 2, pp. 673–681, 2001.

- [45] H. Hartmann, J. J. Derksen, C. Montavon, J. Pearson, I. S. Hamill, and H. E. A. van den Akker, "Assessment of large eddy and RANS stirred tank simulations by means of LDA," *Chemical Engineering Science*, vol. 59, no. 12, pp. 2419–2432, 2004.
- [46] J. J. Derksen, K. Kontomaris, J. B. McLaughlin, and H. E. A. Van den Akker, "Large-eddy simulation of single-phase flow dynamics and mixing in an industrial crystallizer," *Chemical Engineering Research and Design*, vol. 85, no. 2, pp. 169–179, 2007.
- [47] B. C. H. Venneker, J. J. Derksen, and H. E. A. Van den Akker, "Turbulent flow of shear-thinning liquids in stirred tanks—the effects of Reynolds number and flow index," *Chemical Engineering Research and Design*, vol. 88, no. 7, pp. 827–843, 2010.
- [48] B. C. H. Venneker, J. J. Derksen, and H. E. A. Van den Akker, "Reply to comments on 'turbulent flow of shear-thinning liquids in stirred tanks—the effects of Reynolds number and flow index,'" *Chemical Engineering Research and Design*, vol. 89, no. 10, pp. 2194–2195, 2011.
- [49] V. V. Ranade and J. B. Joshi, "Flow generated by a disc turbine. I: experimental," *Chemical Engineering Research and Design*, vol. 68, no. 1, pp. 19–33, 1990.
- [50] V. V. Ranade and J. B. Joshi, "Flow generated by a disc turbine. II: mathematical modelling and comparison with experimental data," *Chemical Engineering Research and Design*, vol. 68, no. 1, pp. 34–50, 1990.
- [51] V. V. Ranade, V. P. Mishra, V. S. Saraph, G. B. Deshpande, and J. B. Joshi, "Comparison of axial flow impellers using a laser Doppler anemometer," *Industrial & Engineering Chemistry Research*, vol. 31, no. 10, pp. 2370–2379, 1992.
- [52] A. W. Patwardhan and J. B. Joshi, "Design of gas-inducing reactors," *Industrial & Engineering Chemistry Research*, vol. 38, no. 1, pp. 49–80, 1999.
- [53] A. W. Patwardhan and J. B. Joshi, "Relation between flow pattern and blending in stirred tanks," *Industrial & Engineering Chemistry Research*, vol. 38, no. 8, pp. 3131–3143, 1999.
- [54] J. B. Joshi, "Computational flow modelling and design of bubble column reactors," *Chemical Engineering Science*, vol. 56, no. 21–22, pp. 5893–5933, 2001.
- [55] M. R. Bhole, J. B. Joshi, and D. Ramkrishna, "CFD simulation of bubble columns incorporating population balance modeling," *Chemical Engineering Science*, vol. 63, no. 8, pp. 2267–2282, 2008.
- [56] R. K. Reddy, J. B. Joshi, K. Nandkumar, and P. D. Mineev, "Direct numerical simulations of a freely falling sphere using fictitious domain method: breaking of axisymmetric wake," *Chemical Engineering Science*, vol. 65, no. 6, pp. 2159–2171, 2010.
- [57] T. V. Tamhane, J. B. Joshi, K. Mudali, R. Natarajan, and R. N. Patil, "Measurement of drop size characteristics in annular centrifugal extractors using phase Doppler particle analyzer (PDPA)," *Chemical Engineering Research and Design*, vol. 90, no. 8, pp. 985–997, 2012.
- [58] J. B. Joshi and V. V. Ranade, "Computational fluid dynamics for designing process equipment: expectations, current status, and path forward," *Industrial & Engineering Chemistry Research*, vol. 42, no. 6, pp. 1115–1128, 2003.
- [59] J. B. Joshi, "Gas phase dispersion in bubble columns," *The Chemical Engineering Journal*, vol. 24, no. 2, pp. 213–216, 1982.
- [60] N. K. Nere, A. W. Patwardhan, and J. B. Joshi, "Liquid-phase mixing in stirred vessels: turbulent flow regime," *Industrial & Engineering Chemistry Research*, vol. 42, no. 12, pp. 2661–2698, 2003.
- [61] T. Kumaresan and J. B. Joshi, "Effect of impeller design on the flow pattern and mixing in stirred tanks," *The Chemical Engineering Journal*, vol. 115, no. 3, pp. 173–193, 2006.
- [62] A. K. Sahu, P. Kumar, A. W. Patwardhan, and J. B. Joshi, "CFD modelling and mixing in stirred tanks," *Chemical Engineering Science*, vol. 54, no. 13–14, pp. 2285–2293, 1999.
- [63] M. W. Haque, K. D. P. Nigam, and J. B. Joshi, "Hydrodynamics and mixing in highly viscous pseudo-plastic non-newtonian solutions in bubble columns," *Chemical Engineering Science*, vol. 41, no. 9, pp. 2321–2331, 1986.
- [64] J. B. Joshi, "Axial mixing in multiphase contactors—a unified correlation," *Chemical Engineering Research and Design*, vol. 58, pp. 155–165, 1980.
- [65] K. Ekambara and J. B. Joshi, "Axial mixing in pipe flows: turbulent and transition regions," *Chemical Engineering Science*, vol. 58, no. 12, pp. 2715–2724, 2003.
- [66] K. Ekambara and J. B. Joshi, "Axial mixing in laminar pipe flows," *Chemical Engineering Science*, vol. 59, no. 18, pp. 3929–3944, 2004.
- [67] O. Lorenz, A. Schumpe, K. Ekambara, and J. B. Joshi, "Liquid phase axial mixing in bubble columns operated at high pressures," *Chemical Engineering Science*, vol. 60, no. 13, pp. 3573–3586, 2005.
- [68] S. S. Thakre and J. B. Joshi, "CFD simulation of bubble column reactors: importance of drag force formulation," *Chemical Engineering Science*, vol. 54, no. 21, pp. 5055–5060, 1999.
- [69] S. S. Gulawani, J. B. Joshi, M. S. Shah, C. S. RamaPrasad, and D. S. Shukla, "CFD analysis of flow pattern and heat transfer in direct contact steam condensation," *Chemical Engineering Science*, vol. 61, no. 16, pp. 5204–5220, 2006.
- [70] C. S. Mathpati and J. B. Joshi, "Insight into theories of heat and mass transfer at the solid–fluid interface using direct numerical simulation and large eddy simulation," *Industrial & Engineering Chemistry Research*, vol. 46, no. 25, pp. 8525–8557, 2007.
- [71] M. T. Dhotre and J. B. Joshi, "Two-dimensional CFD model for the prediction of flow pattern, pressure drop and heat transfer coefficient in bubble column reactors," *Chemical Engineering Research and Design*, vol. 82, no. 6, pp. 689–707, 2004.
- [72] M. T. Dhotre, V. S. Vitankar, and J. B. Joshi, "CFD simulation of steady state heat transfer in bubble columns," *The Chemical Engineering Journal*, vol. 108, no. 1–2, pp. 117–125, 2005.
- [73] S. S. Deshpande, C. S. Mathpati, S. S. Gulawani, J. B. Joshi, and V. R. Kumar, "Effect of flow structures on heat transfer in single and multiphase jet reactors," *Industrial & Engineering Chemistry Research*, vol. 48, no. 21, pp. 9428–9440, 2009.
- [74] J. B. Joshi and M. M. Sharma, "Mass transfer and hydrodynamic characteristics of gas inducing type of agitated contactors," *The Canadian Journal of Chemical Engineering*, vol. 55, no. 6, pp. 683–695, 1977.
- [75] B. N. Murthy, N. A. Deshmukh, A. W. Patwardhan, and J. B. Joshi, "Hollow self-inducing impellers: flow visualization and CFD simulation," *Chemical Engineering Science*, vol. 62, no. 14, pp. 3839–3848, 2007.
- [76] B. N. Murthy, R. S. Ghadge, and J. B. Joshi, "CFD simulations of gas-liquid-solid stirred reactor: prediction of critical impeller speed for solid suspension," *Chemical Engineering Science*, vol. 62, no. 24, pp. 7184–7195, 2007.

- [77] K. S. M. S. R. Rao, V. B. Rewatkar, and J. B. Joshi, "Critical impeller speed for solid suspension in mechanically agitated contactors," *AIChE Journal*, vol. 34, no. 8, pp. 1332–1340, 1988.
- [78] V. B. Rewatkar, J. B. Joshi, and K. S. M. S. Raghava Rao, "Critical impeller speed for solid suspension in mechanically agitated three-phase reactors. 1. Experimental part," *Industrial & Engineering Chemistry Research*, vol. 30, no. 8, pp. 1770–1784, 1991.
- [79] J. B. Joshi, S. B. Sawant, A. W. Patwardhan, D. J. Patil, S. S. Kshatriya, and N. K. Nere, "Relation between flow pattern and de-activation of enzymes in stirred reactors," *Chemical Engineering Science*, vol. 56, no. 2, pp. 443–452, 2001.
- [80] E. L. Koschmieder, *Bénard Cells and Taylor Vortices*, Cambridge University Press, New York, NY, USA, 1993.
- [81] M. Couette, "Études sur le frottement des liquides," *Annales de Chimie et de Physique* 6, vol. 21, pp. 433–510, 1890.
- [82] A. Mallock, "Experiments on fluid viscosity," *Philosophical Transactions of the Royal Society A*, vol. 187, pp. 41–56, 1896.
- [83] L. Rayleigh, "On the dynamics of revolving fluids," *Proceedings of the Royal Society of London A*, vol. 93, no. 648, pp. 148–154, 1916.
- [84] G. I. Taylor, "Stability of a viscous liquid contained between two rotating cylinders," *Philosophical Transactions of the Royal Society A*, vol. 223, no. 605–615, pp. 289–343, 1923.
- [85] H. Jeffreys, "Some cases of instability in fluid motion," *Proceedings of the Royal Society A*, vol. 118, no. 779, pp. 195–208, 1928.
- [86] R. J. Donnelly, "Experiments on the stability of viscous flow between rotating cylinders. I. Torque measurements," *Proceedings of the Royal Society A*, vol. 246, no. 1246, pp. 312–325, 1958.
- [87] S. Chandrasekhar, "The stability of spiral flow between rotating cylinders," *Proceedings of the Royal Society A*, vol. 265, no. 1321, pp. 188–197, 1962.
- [88] A. Davey, "The growth of Taylor vortices in flow between rotating cylinders," *Journal of Fluid Mechanics*, vol. 14, pp. 336–368, 1962.
- [89] P. H. Roberts, "Appendix. The solution of the characteristic value problems," *Proceedings of the Royal Society A*, vol. 283, p. 550, 1965.
- [90] J. T. Stuart, "On the non-linear mechanics of hydrodynamic stability," *Journal of Fluid Mechanics*, vol. 4, pp. 1–21, 1958.
- [91] D. J. Coles, "Transition in circular Couette flow," *Journal of Fluid Mechanics*, vol. 21, pp. 385–425, 1965.
- [92] R. C. DiPrima and P. M. Eagles, "Amplification rates and torques for Taylor—vortex flows between rotating cylinders," *Physics of Fluids*, vol. 20, no. 2, pp. 171–175, 1977.
- [93] J. E. Burkhalter and E. L. Koschmeider, "Steady supercritical Taylor vortex flow," *Journal of Fluid Mechanics*, vol. 58, pp. 547–560, 1973.
- [94] C. D. Andereck, S. S. Liu, and H. L. Swinney, "Flow regimes in a circular Couette system with independently rotating cylinders," *Journal of Fluid Mechanics*, vol. 164, pp. 155–183, 1986.
- [95] R. M. Lueptow, A. Docter, and K. Min, "Stability of axial flow in an annulus with a rotating inner cylinder," *Physics of Fluids A*, vol. 4, no. 11, pp. 2446–2455, 1992.
- [96] M. J. Braun, R. K. Corder, and V. Kudriavtsev, "Flow visualization of the evolution of Taylor instabilities and comparison with numerical simulations," in *Proceedings of the ASME Pressure Vessels and Piping Conference (PVP '02)*, vol. 448-1 of *Computational Technologies for Fluid/Thermal/Structural/Chemical Systems With Industrial Applications*, pp. 45–54, August 2002.
- [97] P. Desevaux, "Numerical flow visualization of the formation of Taylor cells in a laminar Taylor-Couette flow," *Journal of Visualization*, vol. 12, no. 2, pp. 91–92, 2009.
- [98] E. Varchon, J. P. Prenel, and G. Cognet, "Visualization of Taylor cells formation," in *Proceedings of the 4th Triennial International Symposium on Fluid Control, Fluid Measurement, and Visualization (FLUCOME '94)*, pp. 577–582, Toulouse, France, 1994.
- [99] K. M. Saqr, N. A. C. Sidik, H. S. Aly, and Y. A. ElDrainy, "Uncharacteristic phenomenon in the nonisothermal Taylor-Couette flow," in *Proceedings of the International Conference on Signal Processing Systems (ICSPS '09)*, pp. 879–883, Singapore, May 2009.
- [100] E. Barnea and J. J. Mizrahi, "Separation mechanism of liquid-liquid dispersions in a deep later gravity settler: part I. The structure of the dispersion band," *Chemical Engineering Research and Design*, vol. 53, pp. 61–69, 1975.
- [101] E. Barnea and J. J. Mizrahi, "Separation mechanism of liquid-liquid dispersions in a deep later gravity settler: part II. Flow patterns of the dispersed and continuous phases within the dispersion band," *Chemical Engineering Research and Design*, vol. 53, pp. 70–74, 1975.
- [102] E. Barnea and J. J. Mizrahi, "Separation mechanism of liquid-liquid dispersions in a deep later gravity settler: part III. Hindered settling and drop to drop coalescence in the dispersion band," *Chemical Engineering Research and Design*, vol. 53, pp. 75–82, 1975.
- [103] R. A. Leonard, "Solvent characterization using the dispersion number," *Separation Science and Technology*, vol. 30, no. 7–9, pp. 1103–1121, 1995.
- [104] R. A. Leonard, "Recent advances in centrifugal contactor design," *Separation Science and Technology*, vol. 23, no. 12–13, pp. 1473–1487, 1988.
- [105] T. V. Tamhane, J. B. Joshi, U. K. Mudali, R. Natarajan, and R. N. Patil, "Axial mixing in annular centrifugal extractors," *The Chemical Engineering Journal*. In press.
- [106] V. V. Ranade, *Computational Flow Modelling For Chemical Reactor Engineering*, vol. 5, Academic Press, 2002.
- [107] R. S. Leonard, R. H. Pelto, A. A. Ziegler, and G. J. Bernstein, "Flow over circular weirs in a centrifugal field," *The Canadian Journal of Chemical Engineering*, vol. 58, no. 4, pp. 531–534, 1980.
- [108] V. V. Ranade and J. B. Joshi, "Flow generated by pitched blade turbines I: measurements using laser Doppler anemometer," *Chemical Engineering Communications*, vol. 81, no. 1, pp. 197–224, 1989.
- [109] J. B. Joshi, N. K. Nere, C. V. Rane et al., "CFD simulation of stirred tanks: comparison of turbulence models. Part I: radial flow impellers," *The Canadian Journal of Chemical Engineering*, vol. 89, no. 1, pp. 23–82, 2011.
- [110] J. B. Joshi, V. V. Ranade, S. D. Gharat, and S. S. Lele, "Sparged loop reactors," *The Canadian Journal of Chemical Engineering*, vol. 68, no. 5, pp. 705–741, 1990.
- [111] J. Parker and P. Merati, "An investigation of turbulent Taylor-Couette flow using laser Doppler velocimetry in a refractive index matched facility," *Journal of Fluids Engineering*, vol. 118, no. 4, pp. 810–818, 1996.
- [112] G. Baier, *Liquid-liquid extraction based on a new flow pattern: two-fluid Taylor-Couette flow [Ph.D. thesis]*, University of Wisconsin-Madison, Madison, Wis, USA, 2000.

- [113] B. Haut, H. B. Amor, L. Coulon, A. Jacquet, and V. Halloin, "Hydrodynamics and mass transfer in a Couette-Taylor bioreactor for the culture of animal cells," *Chemical Engineering Science*, vol. 58, no. 3–6, pp. 777–784, 2003.
- [114] K. Kataoka, H. Doi, T. Hongo, and M. Futagawa, "Ideal plug-flow properties of Taylor vortex flow," *Journal of Chemical Engineering of Japan*, vol. 8, no. 6, pp. 472–476, 1975.
- [115] J. Legrand and F. Coeuret, "Circumferential mixing in one-phase and two-phase Taylor vortex flows," *Chemical Engineering Science*, vol. 41, no. 1, pp. 47–53, 1986.
- [116] P. I. Pudijiono, N. S. Tavare, J. Garside, and K. D. P. Nigam, "Residence time distribution from a continuous Couette flow device," *The Chemical Engineering Journal*, vol. 42, no. 2, pp. 101–110, 1998.
- [117] H. Desmet, G. V. Verelst, and G. V. Baron, "Local and global dispersion effects in Couette-Taylor flow—I. Description and modeling of the dispersion effects," *Chemical Engineering Science*, vol. 51, no. 8, pp. 1287–1298, 1996.
- [118] H. Desmet, G. V. Verelst, and G. V. Baron, "Local and global dispersion effects in Couette-Taylor flow—II. Quantitative measurements and discussion of the reactor performance," *Chemical Engineering Science*, vol. 51, no. 8, pp. 1299–1309, 1996.
- [119] S. S. Deshmukh, M. J. Sathe, and J. B. Joshi, "Residence time distribution and flow patterns in the single-phase annular region of annular centrifugal extractor," *Industrial & Engineering Chemistry Research*, vol. 48, no. 1, pp. 37–46, 2009.
- [120] T. Kumaresan, N. K. Nere, and J. B. Joshi, "Effect of impeller design on the flow pattern and mixing in stirred tanks," *Industrial & Engineering Chemistry Research*, vol. 45, no. 3, pp. 173–193, 2006.
- [121] X. Ni and C. C. Stevenson, "On the effect of gap size between baffle outer diameter and tube inner diameter on the mixing characteristics in an oscillatory-baffled column," *Journal of Chemical Technology & Biotechnology*, vol. 74, no. 6, pp. 587–593, 1999.
- [122] B. B. Gupta, J. A. Howell, D. Wu, and R. W. Field, "A helical baffle for cross-flow microfiltration," *Journal of Membrane Science*, vol. 102, pp. 31–42, 1995.
- [123] R. Deng, D. Y. Arifin, M. Y. Chyn, and C. H. Wang, "Taylor vortex flow in presence of internal baffles," *Chemical Engineering Science*, vol. 65, no. 16, pp. 4598–4605, 2010.
- [124] O. Czarny, E. Serre, P. Bontoux, and R. M. Lueptow, "Interaction of wavy cylindrical Couette flow with endwalls," *Physics of Fluids*, vol. 16, no. 4, pp. 1140–1148, 2004.
- [125] M. A. Sprague and P. D. Weidman, "Continuously tailored Taylor vortices," *Physics of Fluids*, vol. 21, no. 11, Article ID 009912PHF, pp. 1–8, 2009.
- [126] R. Mullin and C. Bohm, "Bifurcation phenomena in a Taylor-Couette flow with asymmetric boundary conditions," *Physics of Fluids*, vol. 13, no. 1, p. 136, 2001.
- [127] J. H. Kim and L. S. Kim, "Flow-accelerated corrosion behavior of SA106 Gr.C steel in alkaline solution characterized by rotating cylinder electrode," *Journal of the Korean Nuclear Society*, vol. 32, no. 6, p. 595, 2000.
- [128] F. N. Shi and T. J. Napier-Munn, "Measuring the rheology of slurries using an on-line viscometer," *International Journal of Mineral Processing*, vol. 47, no. 3–4, pp. 153–176, 1996.
- [129] J. H. Clark, *Chemistry of Waste Minimization*, Blackie, Academic and Professional New York, 1995.
- [130] J. G. Sczechowski, C. A. Koval, and R. D. Noble, "A Taylor vortex reactor for heterogeneous photocatalysis," *Chemical Engineering Science*, vol. 50, no. 20, pp. 3163–3173, 1995.
- [131] B. V. Loureiro, P. R. De Souza Mendes, and L. F. A. Azevedo, "Taylor-Couette instabilities in flows of Newtonian and power-law liquids in the presence of partial annulus obstruction," *Journal of Fluids Engineering*, vol. 128, no. 1, pp. 42–54, 2006.
- [132] S. S. Deshmukh, J. B. Joshi, and S. B. Koganti, "Flow visualization and three-dimensional CFD simulation of the annular region of an annular centrifugal extractor," *Industrial & Engineering Chemistry Research*, vol. 47, no. 10, pp. 3677–3686, 2008.
- [133] K. E. Wardle, T. R. Allen, and R. Swaney, "Computational fluid dynamics (CFD) study of the flow in an annular centrifugal contactor," *Separation Science and Technology*, vol. 41, no. 10, pp. 2225–2244, 2006.
- [134] B. Wegner, A. Maltsev, C. Schneider, A. Sadiki, A. Dreizler, and J. Janicka, "Assessment of unsteady RANS in predicting swirl flow instability based on LES and experiments," *International Journal of Heat and Fluid Flow*, vol. 25, no. 3, pp. 528–536, 2004.
- [135] G. Iaccarino, A. Ooi, P. A. Durbin, and M. Behnia, "Reynolds averaged simulation of unsteady separated flow," *International Journal of Heat and Fluid Flow*, vol. 24, no. 2, pp. 147–156, 2003.
- [136] J. Rivalier, J. Duhamet, and F. Gandi, "Annular Centrifugal Extractor with Embedded Stirring Rotor," U.S. Patent 7, 134, 991, 2006.
- [137] T. Watanabe, Y. Toya, and I. Nakamura, "Development of free surface flow between concentric cylinders with vertical axes," *Journal of Physics*, vol. 14, no. 1, pp. 9–19, 2005.
- [138] A. Mahamdia, A. Bouabdallah, and S. E. Skali, "Effects of free surface and aspect ratio on the transition of the Taylor-Couette flow," *Comptes Rendus Mécanique*, vol. 331, no. 3, pp. 245–252, 2003.
- [139] M. Ammar, B. Ahcène, and S. S. Eddine, "Écoulement de Taylor-Couette en géométrie finie et à surface libre," *The Canadian Journal of Chemical Engineering*, vol. 83, no. 4, pp. 652–657, 2005.
- [140] N. Mujica and D. P. Lathrop, "Hysteretic gravity-wave bifurcation in a highly turbulent swirling flow," *Journal of Fluid Mechanics*, vol. 551, pp. 49–62, 2006.
- [141] K. E. Wardle, T. R. Allen, M. H. Anderson, and R. E. Swaney, "Free surface flow in the mixing zone of an annular centrifugal contactor," *AIChE Journal*, vol. 54, no. 1, pp. 74–85, 2008.
- [142] C. W. Hirt and B. D. Nichols, "Volume of fluid (VOF) method for the dynamics of free boundaries," *Journal of Computational Physics*, vol. 39, no. 1, pp. 201–225, 1981.
- [143] K. E. Wardle, T. R. Allen, and R. Swaney, "CFD simulation of the separation zone of an annular centrifugal contactor," *Separation Science and Technology*, vol. 44, no. 3, pp. 517–542, 2009.
- [144] K. E. Wardle, T. R. Allen, M. H. Anderson, and R. E. Swaney, "Experimental study of the hydraulic operation of an annular centrifugal contactor with various mixing vane geometries," *AIChE Journal*, vol. 56, no. 8, pp. 1960–1974, 2010.
- [145] K. E. Wardle, "Open-source CFD simulations of liquid-liquid flow in the annular centrifugal contactor," *Separation Science and Technology*, vol. 46, no. 15, pp. 2409–2417, 2011.
- [146] K. E. Wardle and T. Lee, "Finite element lattice Boltzmann simulations of free surface flow in a concentric cylinder," *Computers & Mathematics with Applications*. In press.
- [147] J. Patra, J. B. Joshi, N. K. Pandey, U. K. Mudali, and R. Natarajan, *Chemical Engineering Communications*. In press.

- [148] P. A. Haas, "Turbulent dispersion of aqueous drops in organic liquids," *AIChE Journal*, vol. 33, no. 6, pp. 987–995, 1987.
- [149] E. Tison, "Caractérisation de la zone de mélange d'un extracteur centrifuge annulaire à effet Couette utilisé en extraction liquide-liquide," [Ph.D. thesis], Institut National Polytechnique de Lorraine (INPL), 1996.
- [150] K. E. Wardle and C. Pereira, "Advanced multi-fluid simulations and experiments of flow in liquid-liquid contactors," *Transactions of the American Nuclear Society*, vol. 104, p. 168, 2011.
- [151] L. Štrubelj, I. Tiselj, and B. Mavko, "Simulations of free surface flows with implementation of surface tension and interface sharpening in the two-fluid model," *International Journal of Heat and Fluid Flow*, vol. 30, no. 4, pp. 741–750, 2009.
- [152] G. Baier and M. D. Graham, "Two-fluid Taylor-Couette flow: experiments and linear theory for immiscible liquids between corotating cylinders," *Physics of Fluids*, vol. 10, no. 12, pp. 3045–3055, 1998.
- [153] X. Zhu and R. D. Vigil, "Banded liquid-liquid Taylor-Couette-Poiseuille flow," *AIChE Journal*, vol. 47, no. 9, pp. 1932–1940, 2001.
- [154] K. Atkhen, J. Fontaine, and J. E. Wesfreid, "Highly turbulent Couette-Taylor bubbly flow patterns," *Journal of Fluid Mechanics*, vol. 422, pp. 55–68, 2000.
- [155] H. Djeridi, J. F. Fave, J. Y. Billard, and D. H. Fruman, "Bubble capture and migration in Couette-Taylor flow," *Experiments in Fluids*, vol. 26, no. 3, pp. 233–239, 1999.
- [156] Y. Murai, H. Oiwa, and Y. Takeda, "Bubble behavior in a vertical Taylor-Couette flow," *Journal of Physics*, vol. 14, no. 1, pp. 143–156, 2005.
- [157] Y. Shiomi, H. Kutsuna, K. Akagawa, and M. Ozawa, "Two-phase flow in an annulus with a rotating inner cylinder (flow pattern in bubbly flow region)," *Nuclear Engineering and Design*, vol. 141, no. 1-2, pp. 27–34, 1993.
- [158] E. Magere, M. O. Deville, K. Atkhen, and J. Fontaine, "Simulation of the pressure distribution in a spent nuclear fuel reprocessing Taylor-Couette device," in *Proceedings of the 4th Eccomas Conference on Computational Fluid Dynamics*, vol. 1, p. 1094, Athens, Greece, September 1998.
- [159] Y. Shiomi, S. Nakanishi, and H. Kutsuna, "CFD calculation for two-phase flow in concentric annulus with rotating inner cylinder," unpublished manuscript.
- [160] W. M. J. Batten, S. R. Turnock, N. W. Bressloff, and S. M. Abu-Sharkh, "Turbulent Taylor-Couette vortex flow between large radius ratio concentric cylinders," *Experiments in Fluids*, vol. 36, no. 3, pp. 419–421, 2004.
- [161] T. H. Van den Berg, S. Luther, D. Lathrop, and D. Lohse, "Drag reduction in bubbly Taylor-Couette turbulence," *Physical Review Letters*, vol. 94, Article ID 044501, 4 pages, 2005.
- [162] K. Atkhen, *Etude Hydrodynamique D'un Extracteur Centrifuge Utilisant les Propriétés des Écoulements de Couette-Taylor* [Ph.D. thesis], University of Paris, 1998.
- [163] R. A. Leonard, G. J. Bernstein, R. H. Peltó, and A. A. Ziegler, "Liquid-liquid dispersion in turbulent Couette flow," *AIChE Journal*, vol. 27, no. 3, pp. 495–503, 1981.
- [164] R. Leonard, M. S. Regalbutto, S. Aase, H. Arafat, and J. Falkenberg, "Hydraulic performance of a 5-cm contactor for caustic-side solvent extraction," Tech. Rep. ANL-02/18, Argonne National Laboratory, 2002.
- [165] A. Gandhir and K. E. Wardle, "CFD analysis of fluid flow above the upper weir of an annular centrifugal contactor," *Separation Science and Technology*, vol. 47, no. 1, pp. 1–10, 2012.
- [166] N. T. Padiál-Collins, D. Z. Zhang, Q. Zou, X. Ma, and W. B. VanderHeyden, "Centrifugal contactors: separation of an aqueous and an organic stream in the rotor zone (LA-UR-05-7800)," *Separation Science and Technology*, vol. 41, no. 6, pp. 1001–1023, 2006.
- [167] J. F. Birdwell Jr. and K. K. Anderson, "Evaluation of 5-cm centrifugal contactor hydraulic and mass transfer performance for caustic-side solvent extraction of cesium," Tech. Rep. ORNL/TM-2001/137, Oak Ridge National Laboratory, 2001.
- [168] J. Law, R. Tillotson, and T. Todd, "Evaluation of the hydraulic performance and mass transfer efficiency of the CSSX process with the optimized solvent in a single stage of 5.5-Cm diameter centrifugal Contactor," Tech. Rep. INEEL/EXT-02-01106, Idaho National Engineering and Environmental Laboratory, 2002.
- [169] J. Law, D. Meikrantz, T. Garn, N. Mann, S. Herbst, and T. Todd, "Testing of commercially available engineering- and plant-scale annular centrifugal contactors for the processing of spent nuclear fuel," Tech. Rep. INL/CON-06-11498, Idaho National Laboratory, 2002.
- [170] L. Wang, D. L. Marchisio, R. D. Vigil, and R. O. Fox, "CFD simulation of aggregation and breakage processes in laminar Taylor-Couette flow," *Journal of Colloid and Interface Science*, vol. 282, no. 2, pp. 380–396, 2005.
- [171] J. B. Joshi and M. M. Sharma, "Liquid phase backmixing in sparged contactors," *The Canadian Journal of Chemical Engineering*, vol. 56, no. 1, pp. 116–119, 1978.
- [172] J. B. Joshi and M. M. Sharma, "A circulation cell model for bubble columns," *Transactions of the Institution of Chemical Engineers*, vol. 57, pp. 244–251, 1979.
- [173] A. A. Kulkarni, J. B. Joshi, V. Ravikumar, and B. D. Kulkarni, "Wavelet transform of velocity-time data for the analysis of turbulent structures in a bubble column," *Chemical Engineering Science*, vol. 56, no. 18, pp. 5305–5315, 2001.
- [174] A. A. Kulkarni, J. B. Joshi, V. Ravikumar, and B. D. Kulkarni, "Identification of the principal time scales in the bubble column by wavelet analysis," *Chemical Engineering Science*, vol. 56, no. 20, pp. 5739–5747, 2001.
- [175] J. B. Joshi, V. S. Vitankar, A. A. Kulkarni, M. T. Dhotre, and K. Ekambara, "Coherent flow structures in bubble column reactors," *Chemical Engineering Science*, vol. 57, no. 16, pp. 3157–3183, 2002.
- [176] A. A. Kulkarni and J. B. Joshi, "Measurement of eddy diffusivity in bubble column and validation based on the intermittency models," *Chemical Engineering Science*, vol. 60, no. 22, pp. 6146–6159, 2005.
- [177] A. V. Kulkarni and J. B. Joshi, "Estimation of hydrodynamic and heat transfer characteristics of bubble column by analysis of wall pressure measurements and CFD simulations," *Transactions of the Institution of Chemical Engineers*, vol. 84, pp. 601–609, 2006.
- [178] M. V. Tabib and J. B. Joshi, "Analysis of dominant flow structures and their flow dynamics in chemical process equipment using snapshot proper orthogonal decomposition technique," *Chemical Engineering Science*, vol. 63, no. 14, pp. 3695–3715, 2008.
- [179] S. S. Deshpande, J. B. Joshi, V. R. Kumar, and B. D. Kulkarni, "Identification and characterization of flow structures in chemical process equipment using multiresolution techniques," *Chemical Engineering Science*, vol. 63, no. 21, pp. 5330–5346, 2008.

- [180] M. V. Tabib, M. J. Sathe, S. S. Deshpande, and J. B. Joshi, "A hybridized snapshot proper orthogonal decomposition-discrete wavelet transform technique for the analysis of flow structures and their time evolution," *Chemical Engineering Science*, vol. 64, no. 21, pp. 4319–4340, 2009.
- [181] J. B. Joshi, M. V. Tabib, S. S. Deshpande, and C. S. Mathpati, "Dynamics of flow structures and transport phenomena, 1. Experimental and numerical techniques for identification and energy content of flow structures," *Industrial & Engineering Chemistry Research*, vol. 48, no. 17, pp. 8244–8284, 2009.
- [182] C. S. Mathpati, M. V. Tabib, S. S. Deshpande, and J. B. Joshi, "Dynamics of flow structures and transport phenomena, 2. Relationship with design objectives and design optimization," *Industrial & Engineering Chemistry Research*, vol. 48, no. 17, pp. 8285–8311, 2009.
- [183] K. Ekambara, K. Nandakumar, and J. B. Joshi, "CFD simulation of bubble column reactor using population balance," *Industrial & Engineering Chemistry Research*, vol. 47, no. 21, pp. 8505–8516, 2008.
- [184] M. R. Bhole, J. B. Joshi, and D. Ramkrishna, "Population balance modeling for bubble columns operating in the homogeneous regime," *AIChE Journal*, vol. 53, no. 3, pp. 579–588, 2007.
- [185] L. L. Macaluso and D. H. Meikrantz, "Self-cleaning Rotor for a Centrifugal Separator," U.S. Patent 5,908,376, 1999.
- [186] R. A. Leonard, "Design principles and applications of centrifugal contactors for solvent extraction," in *Ion Exchange and Solvent Extraction: A Series of Advances*, chapter 10, pp. 563–616, CRC Press, 2010.

Research Article

CFD Modeling of Solid Suspension in a Stirred Tank: Effect of Drag Models and Turbulent Dispersion on Cloud Height

Shitanshu Gohel,¹ Shitalkumar Joshi,¹ Mohammed Azhar,²
Marc Horner,³ and Gustavo Padron⁴

¹ ANSYS Fluent India Pvt. Ltd., MIDC, Plot No. 34/1, Rajiv Gandhi IT Park, Hinjewadi, Pune 411057, India

² ANSYS UK Ltd., Sheffield Business Park, 6 Europa View, Sheffield S9 1XH, UK

³ ANSYS Inc., 1007 Church Street, Suite 250, Evanston, IL 60201, USA

⁴ BHR Group, The Fluid Engineering Centre, Cranfield, Bedfordshire MK43 0AJ, UK

Correspondence should be addressed to Shitanshu Gohel, shitanshu.gohel@ansys.com

Received 10 February 2012; Accepted 13 April 2012

Academic Editor: Nandkishor Nere

Copyright © 2012 Shitanshu Gohel et al. This is an open access article distributed under the Creative Commons Attribution License, which permits unrestricted use, distribution, and reproduction in any medium, provided the original work is properly cited.

Many chemical engineering processes involve the suspension of solid particles in a liquid. In dense systems, agitation leads to the formation of a clear liquid layer above a solid cloud. Cloud height, defined as the location of the clear liquid interface, is a critical measure of process performance. In this study, solid-liquid mixing experiments were conducted and cloud height was measured as a function of operating conditions and stirred tank configuration. Computational fluid dynamics simulations were then performed using an Eulerian-Granular multiphase model. The effects of hindered and unhindered drag models and turbulent dispersion force on cloud height were investigated. A comparison of the experimental and computational data showed excellent agreement over the full range of conditions tested.

1. Introduction

The suspension of solid particles in a liquid is a key requirement of many industrial processes. Examples relevant to this work include crystallisation, dissolution, and adsorption processes. Each of these can be characterized as complex multiphase processes that are often facilitated by mechanically stirred tanks. Maximizing contact between the solid and liquid phases facilitates mass transfer and reaction, therefore, assessing the ability of the process to suspend particles is a key objective. The quality of suspension can be quantified by three parameters: just suspension velocity, solids distribution, and cloud height. The latter is defined as the location of the interface between solids-rich liquid and clear liquid regions. Cloud height is critical because of limited mixing between the suspended solids and the upper clear liquid layer. The current study aims to develop and validate a computational model of a solids suspension process using experimental measurements of cloud height.

The hydrodynamics in stirred vessels are complex, three-dimensional, and turbulent. The interplay between solid and liquid materials, vessel design, impeller type and location, and level of agitation all determine the efficiency of the mixing process. Numerous empirical models have been developed to relate tank performance to operating conditions and geometry [1, 2]. However, these models lack wider application, owing to the complexity of the flow field. This has helped to motivate the need for more detailed analysis.

Computational fluid dynamics (CFD) methods are powerful tools for improving our understanding of mixing in stirred tanks. In the last few years, encouraging results have been obtained in the simulation of solid suspension systems [3]. The solids distribution has been traditionally simulated using either Lagrangian [4–6] or Eulerian multiphase modeling approaches [7–14]. The Lagrangian model treats solids as individual particles subject to hydrodynamic forces that are approximated using single-particle empirical models. The Eulerian model, on the other hand, treats the solids as an

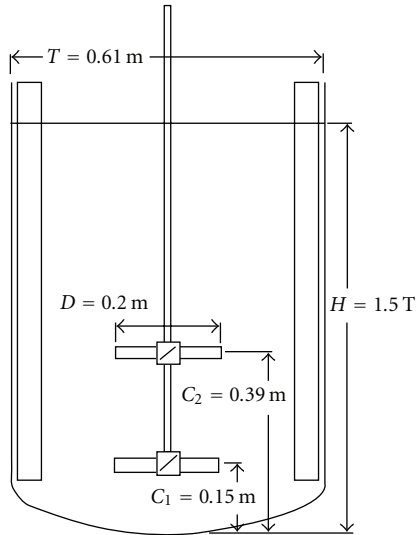


FIGURE 1: Schematic representation of the stirred tank reactor.

additional continuous phase. Interphase transport models are added to account for the interaction between the solids and the fluid phase.

The Granular model is an extension of the Eulerian model wherein the solids are modeled as a pseudo-fluid. The pseudo-fluid physical properties, such as viscosity, solids pressure and stress, are derived from the kinetic theory of granular flow. According to Montante et al. [15], the Granular model has been found to be more appropriate for modeling processes exhibiting high local solid concentrations.

Turbulence modeling is also critical to the success of CFD analysis in solid-liquid systems. Turbulence plays an important role in developing single-phase flow structures, and it is generally accepted that it will also have some influence on the solids distribution in stirred tanks. Previous CFD investigations have highlighted the importance of turbulence-assisted solids dispersion in stirred tanks [16–20]. However, a quantitative evaluation of the effect of turbulent dispersion on cloud height has not been considered in detail.

To address the above, this study aims to develop a CFD modeling strategy for predicting cloud height in a solid suspension process. An Eulerian-Granular multiphase model is used to model the particle suspension process. Experimental data is used to justify the selection of model inputs, specifically the drag model and turbulent dispersion force. Each of these were evaluated independently to illustrate their relative importance. Finally, a comparison of the model results with corresponding experimental data establishes the validity of the modeling approach across a wide range of experimental conditions.

2. Experimental Setup and Procedure

The experimental work was carried out at BHR Group as part of the fluid mixing processes (FMPs) industrial research

program. The tests were performed in a transparent Perspex tank with a diameter (T) of 0.61 m, equipped with four standard baffles and a torispherical base, as shown in Figure 1. The impellers were centrally mounted pitched blade turbines (PBTs) with a diameter (D) of 0.2 m and a blade width of 0.055 m. One set of tests was carried out with a single-impeller located at a distance from the tank bottom (C_1) of 0.15 m. For the dual impeller tests, a second impeller was installed on the same shaft at an off-bottom distance (C_2) of 0.39 m. The liquid height (H) was kept constant at $1.5T$ in all experiments.

The solid phase was comprised of sand particles with a nominal average diameter of $180\ \mu\text{m}$ and a density of $2,630\ \text{kg/m}^3$. The liquid phase was water with a density of $1,000\ \text{kg/m}^3$ and a viscosity of $0.001\ \text{Pa}\cdot\text{s}$. Solids concentrations of 10% (w/w) and 15% (w/w) were tested. These values correspond to 4% and 6.2% by volume, respectively.

The solids cloud height was obtained by measuring the distance from the bottom of the tank to the cloud surface. Measurements were determined visually from outside the tank. Given the turbulent nature of the flow, the cloud surface was not flat. Therefore, the minimum and maximum positions of the surface at a fixed radial position on the wall of the tank were recorded. The average cloud height (H_c) could then be calculated for each experimental condition. Measurements were carried out at impeller speeds (N) ranging from 150 to 450 RPM in 50 RPM increments.

For both impeller systems, the minimum impeller speed for just suspension (N_{JS}) was also determined at each solids loading. This is the minimum speed at which the impeller(s) operate to ensure that the solids are suspended, that is, not settled at the vessel bottom. N_{JS} was determined by placing a mirror underneath the tank and observing the bed of solids at the bottom while the impeller speed was increased in small increments. The criterion used to determine whether the solids were suspended followed that of Zwietering [1], who defined N_{JS} as “the impeller speed at which no material remains stationary on the vessel base for more than 1-2 seconds.”

Figure 2 shows the results for the fractional average cloud height (H_c/H) versus impeller speed normalized by N_{JS} . At impeller speeds below N_{JS} ($N/N_{JS} < 1$), the cloud height is considerably higher with the dual impeller system than with the single impeller system (up to about 70% higher). The difference becomes less significant at higher impeller speeds.

With the single-impeller system, there is no significant difference between the two different solid concentrations. There is a small difference at high impeller speeds with the dual-impeller system. However, this could be due to experimental error (typically 5 to 10%).

3. Modeling and Numerical Simulations

3.1. Euler-Granular Theory. The simulations were performed using the Euler-Granular multiphase model available in the commercial CFD software, ANSYS Fluent 13.0 (ANSYS Inc., Canonsburg, PA, USA). This model assumes that each phase coexists at every point in space in the form of

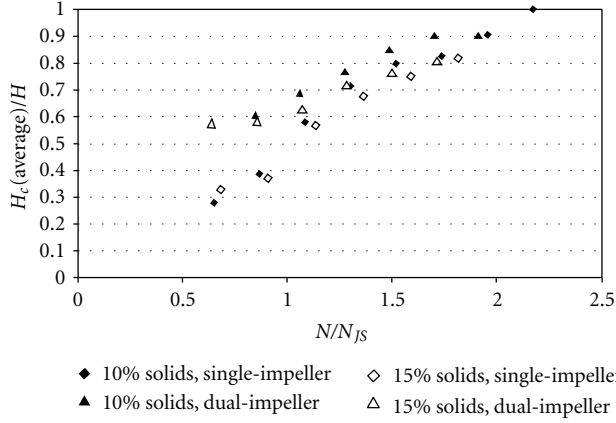


FIGURE 2: Fractional average cloud height (H_c/H) as a function of impeller speed normalized by N_{js} for the single- and dual-impeller configurations for 10% (w/w) and 15% (w/w) solids.

interpenetrating continua. The continuity and momentum equations are solved for all phases and the coupling between phases is obtained through pressure and interphase exchange coefficients.

The conservation equation for each phase q is [21]:

$$\frac{\partial}{\partial t}(\alpha_q \rho_q) + \nabla \cdot (\alpha_q \rho_q \vec{u}_q) = 0 \quad (1)$$

$$\begin{aligned} \frac{\partial}{\partial t}(\alpha_q \rho_q \vec{u}_q) + \nabla \cdot (\alpha_q \rho_q \vec{u}_q \vec{u}_q) = & -\alpha_q \nabla p + \nabla \cdot \bar{\tau}_q \\ & + \sum_{q=1}^n (R_{fs} + \dot{m}_{fs} \vec{u}_{fs}) + \vec{F}_q, \end{aligned} \quad (2)$$

where terms with the subscript “ fs ” account for exchange between the fluid and solid phases. One fluid phase and one solid phase were modeled in this work. They are denoted individually with subscripts f and s , respectively, in the rest of this section.

In the Eulerian-Granular model, the solid phase momentum equation includes an additional solid pressure term. The solids pressure and solids stress tensor terms ($\bar{\tau}_q$) are determined from the kinetic theory of granular flow as described by Ding and Gidaspow [22]. The Euler-Granular model also includes an additional transport equation for the granular temperature.

In (2), \vec{F}_q accounts for the effects of lift force, virtual mass force and any other external forces acting on the solid phase. The term R_{fs} represents fluid solid interphase momentum exchange which is expressed as:

$$R_{fs} = K_{fs}(\vec{u}_f - \vec{u}_s), \quad (3)$$

where K_{fs} is the interphase exchange coefficient, which is defined in terms of the drag model proposed by Ding and Gidaspow [22]:

$$K_{fs} = \frac{3}{4} C_D \frac{\alpha_s \alpha_f \rho_f |\vec{u}_f - \vec{u}_s|}{d_s} \alpha_f^{-2.65} \quad \text{for } \alpha_f > 0.8,$$

$$\begin{aligned} K_{fs} = 150 \frac{\alpha_s (1 - \alpha_f) \mu_f}{\alpha_f d_s^2} \\ + 1.75 \frac{\alpha_s \rho_f |\vec{u}_f - \vec{u}_s|}{d_s} \quad \text{for } \alpha_f \leq 0.8 \end{aligned}$$

$$C_D = \frac{24}{\text{Re} \alpha_f} \left(1 + 0.15 (\text{Re} \alpha_f)^{0.687} \right), \quad \text{Re} = \frac{\rho_f |\vec{u}_f - \vec{u}_s| d_s}{\mu_f}. \quad (4)$$

For turbulent flows, the drag force (C_D) is a function of average velocity. A correction term is included in the interphase momentum exchange equation to account for the effect of turbulent dispersion due to instantaneous fluctuations, as proposed by Deutsch and Simonin [23]. The resulting interphase momentum exchange term is then given by:

$$R_{fs} = K_{fs}(\vec{U}_f - \vec{U}_s) - K_{fs} \vec{v}_{dr}. \quad (5)$$

Here \vec{U} represents phasic average velocities and \vec{v}_{dr} is the drift velocity:

$$\vec{v}_{dr} = - \left(\frac{D_f}{\sigma_{fs} \alpha_f} \nabla \alpha_f - \frac{D_s}{\sigma_{fs} \alpha_s} \nabla \alpha_s \right). \quad (6)$$

In this expression, $D_f = D_s = D_{i,fs}$ are the fluid-solid turbulent dispersion coefficients, and σ_{fs} is the dispersion Prandtl number (which is set equal to 0.75 in this study).

3.2. Simulation Setup

3.2.1. Geometry and Mesh. The geometric models and meshes were constructed in the commercial software, GAMBIT 2.4 (ANSYS, Inc., Canonsburg, PA, USA). Full hexahedral meshes were constructed for each of the two tank configurations (Figure 3). The computational mesh for the single impeller tank had 47, 72, and 122 cells in the radial, angular, and axial directions, respectively; while the mesh for the dual impeller configuration had 47, 72, and 177 cells in the respective directions. These settings resulted in 402k hexahedral elements for the single-impeller tank and 576k hexahedral elements for the dual-impeller tank. (Note that multiplying the mesh sizings in each direction will result in a mesh count that is higher than the final mesh count quoted in the text. This is because there is no mesh at impeller and shaft locations and because there are small regions of paved mesh which are not regularly spaced.) The mesh spacing was more or less uniform in each direction, with mesh refinement on wall surfaces and in the impeller zones.

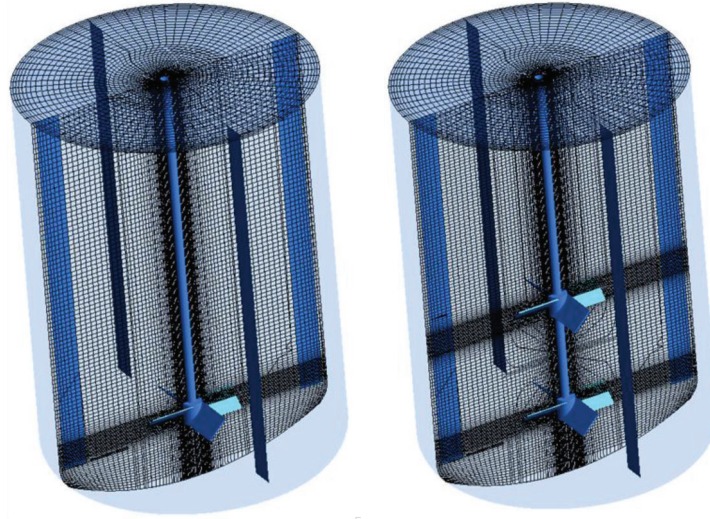


FIGURE 3: CFD meshes for the single- and dual-impeller stirred tanks.

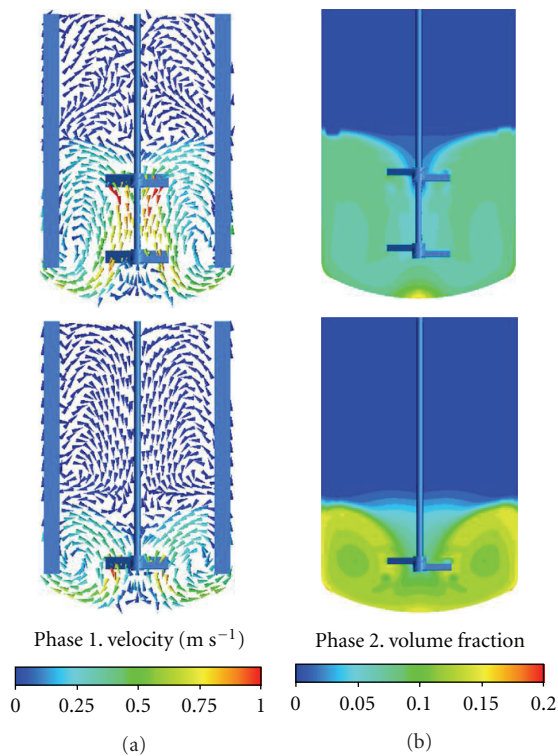


FIGURE 4: Contour plots for 200 RPM, 10% (w/w) loading for single- and dual-impeller configurations on a midplane. (a) Velocity vector of liquid phase. (b) Volume fraction of solid phase.

A grid-dependency study was carried out to evaluate mesh suitability for the single impeller configuration. The procedure involved comparing results from the baseline mesh to a refined grid with 3.2 million hexahedral cells, representing an almost 8-fold increase over the baseline mesh. The effects on one flow parameter—impeller

TABLE 1: Grid dependency study for the single-impeller tank. (A) 10% (w/w) solids loading and 300 RPM, (B) 15% (w/w) solids loading and 250 RPM.

Test case	Baseline	Refined mesh	Difference (%)	
Case A	Normalized Cloud Height (H_c/H)	0.655	0.644	1.68
	Power Number	1.762	1.760	0.11
Case B	Normalized Cloud Height (H_c/H)	0.492	0.501	1.83
	Power Number	1.837	1.767	3.80

power number—and one multiphase model output—cloud height—were extracted and compared (see Table 1). The Gidaspow drag model and turbulent dispersion force were included in all cases. The maximum difference in the impeller power numbers was less than 4%, and the maximum difference in the predicted cloud height was less than 2%. Therefore, the resolution of the baseline mesh was deemed satisfactory.

3.2.2. Physical Models and Boundary Conditions. The realizable $k-\epsilon$ turbulence model was used to resolve the turbulent solid-liquid flow field. For comparison purposes, inter-phase momentum exchange terms were calculated using the Gidaspow (hindered) and Schiller-Naumann (unhindered) drag models. The effect of including turbulence-assisted solids dispersion in the interphase exchange term was also evaluated [23, 24].

The multiple reference frame (MRF) approach was used to model impeller rotation. Although an approximation, this approach has been shown to produce satisfactory results,

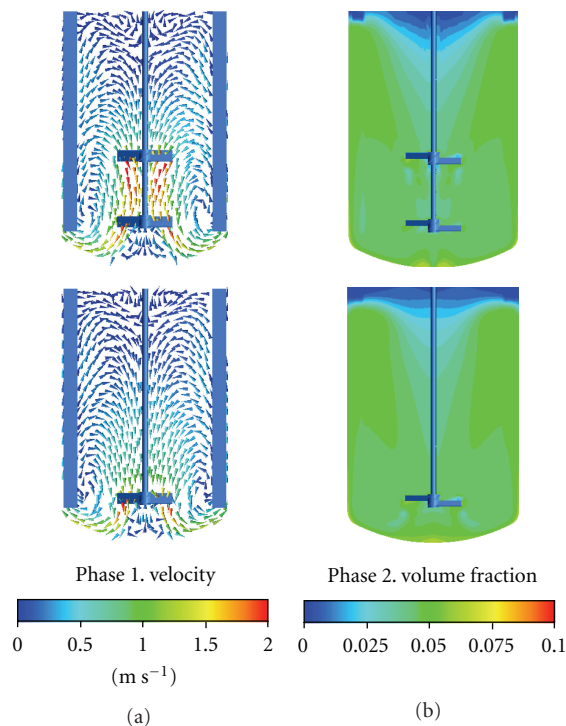


FIGURE 5: Contour plots for 400 RPM, 10% (w/w) loading for single- and dual-impeller configurations on a midplane. (a) Velocity vector of liquid phase. (b) Volume fraction of solid phase.

especially when the interaction between baffles and impellers is weak. The free surface was assumed to be fixed, thus a symmetry boundary condition was prescribed. A no-slip boundary condition was applied for all other wall surfaces.

High-order discretization schemes were chosen to minimize numerical diffusion. The Green-Gauss Node Based Gradient option was used for gradient calculations at cell interfaces and the QUICK discretization scheme was used for momentum, volume fraction and turbulence equations. All cases were initialized with a uniformly distributed solid phase. The steady state solver was utilized to solve for all flow variables.

4. Results

4.1. Flow and Solid Distributions. Liquid velocities provide insight into the mixing processes occurring inside stirred tanks. Figures 4 and 5 show model results for liquid velocities and solid phase volume fraction on a tank midplane. Recirculation zones are evident near the tank bottom. These recirculation zones are predicted to be larger in the dual impeller configuration and increase in size with RPM. A distinct interface between clear liquid at the top of the tank and the cloudy region is observed at low RPM. The model also predicts that solids are more uniformly distributed throughout the entire reactor at higher RPM.

4.2. Effect of Drag. Drag forces induce significant interphase momentum transfer and tend to dominate other interphase processes. Therefore, drag force model selection is critical

to the accuracy of the solid-liquid suspension model. The Gidaspow and Schiller-Naumann drag models were investigated. The Gidaspow drag model has been specifically tailored to take into consideration particle induced hindrance. For this reason, it is expected to give good predictions for high solid volume fractions (as was observed under certain operating conditions studied here). Additional simulations with the Schiller-Naumann model were performed to help elucidate the importance of particle hindrance in this system.

Figure 6 shows volume rendered (volume rendered post-processing permits visualization of the solid-phase distribution throughout the entire domain by increasing the opacity of the foreground results) contour plots of solids concentration and cloud height for the single and the dual impeller configurations. The double-headed arrows marked “EXP” represent the location of the experimentally observed cloud height with the arrow thickness representing the observed $\pm 8\%$ variation in the experimental data. When post-processing the CFD model, the cloud height was defined as the maximum z -coordinate of an isosurface of solid phase volume fraction (note that the shaft axis is aligned with z -axis). Following Kasat et al. [12], the location of this isosurface is defined as the average solid phase volume fraction. It can be seen from Figure 6 that the Gidaspow model is a better predictor of cloud height versus the Schiller-Naumann model. Experimental results further substantiate the Gidaspow drag model as a better predictor of cloud height (see Figure 7). These results suggest that particle hindrance effects are an important aspect of the model, even at the relatively low solids loading studied here.

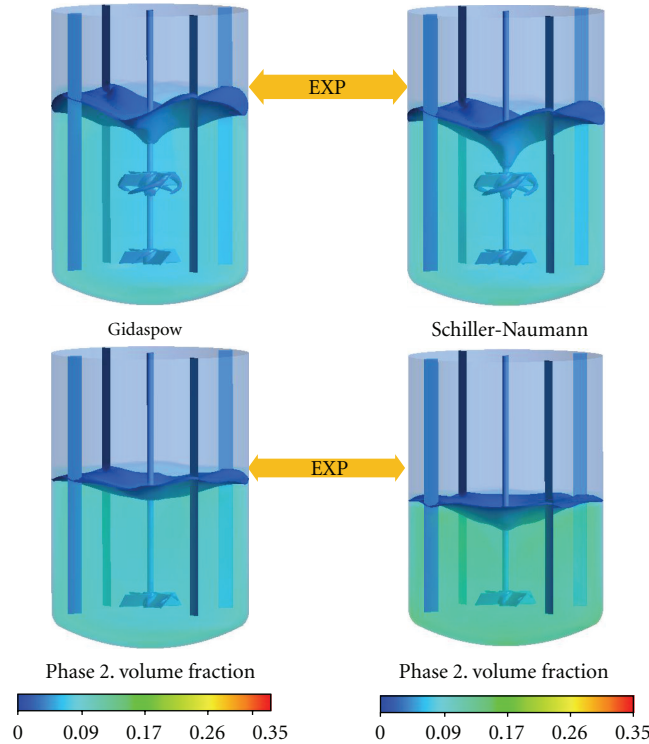


FIGURE 6: Effect of drag model. Volume rendered plots with isosurface for single- and dual-impeller configurations, 15% (w/w) loading, 300 RPM. The double-headed arrows marked “EXP” represent the location of experimental observation with arrow thickness representing the observed 8% spread in the experimental data.

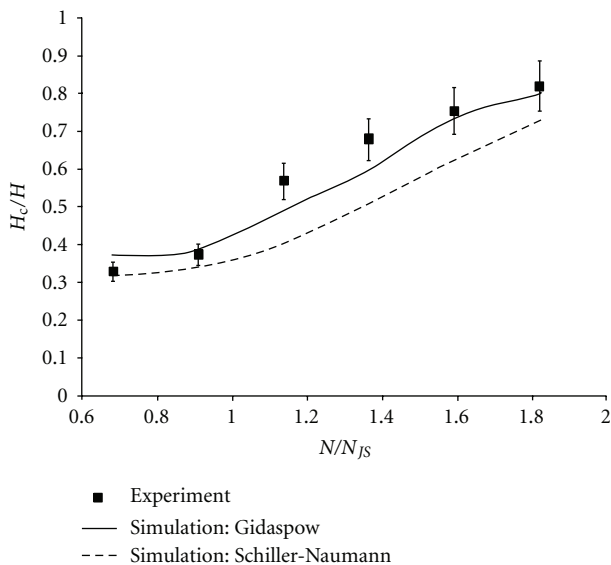


FIGURE 7: Effect of drag model. Plot of normalized cloud height against normalized impeller speed for 15% (w/w) loading and single-impeller.

4.3. Effect of the Turbulent Dispersion Force (TDF). The contribution of the turbulent dispersion force is significant when the size of the turbulent eddies is larger than the particle size [12]. Figure 8 shows how the inclusion of

TDF substantially increases the cloud height. Moreover, the predicted cloud heights give better comparison with the experimental data when TDF is included. In an extreme example, it was observed that omitting TDF leads to a 250% difference in the cloud height prediction (see Figure 8(b)). Similar studies performed with the Schiller-Naumann drag model showed an identical trend, although the predicted cloud heights were observed to be slightly lower than that predicted by the Gidaspow. Therefore, TDF must be included in the model for the reactor configuration and conditions studied here.

4.4. Experimental Validation. Results from the previous sections establish the model requirements based on a limited set of experiments. Applying the modeling strategy over the full range of experimental operating conditions establishes model validation. The experimental study included single- and dual-impeller tanks operating at six to seven speeds and for two different solids concentrations (10% (w/w) and 15% (w/w)), resulting in a total of 26 experimental measurements. Numerical simulations were performed for each of these experimental points.

The profiles of the normalized cloud heights are plotted in Figures 9(a) and 9(b). It can be seen that the predicted cloud height for all operating conditions are in good agreement with the experimental data. For the single-impeller system, the simulations overpredict cloud height at lower RPM for both 10% (w/w) and 15% (w/w) solids loading.

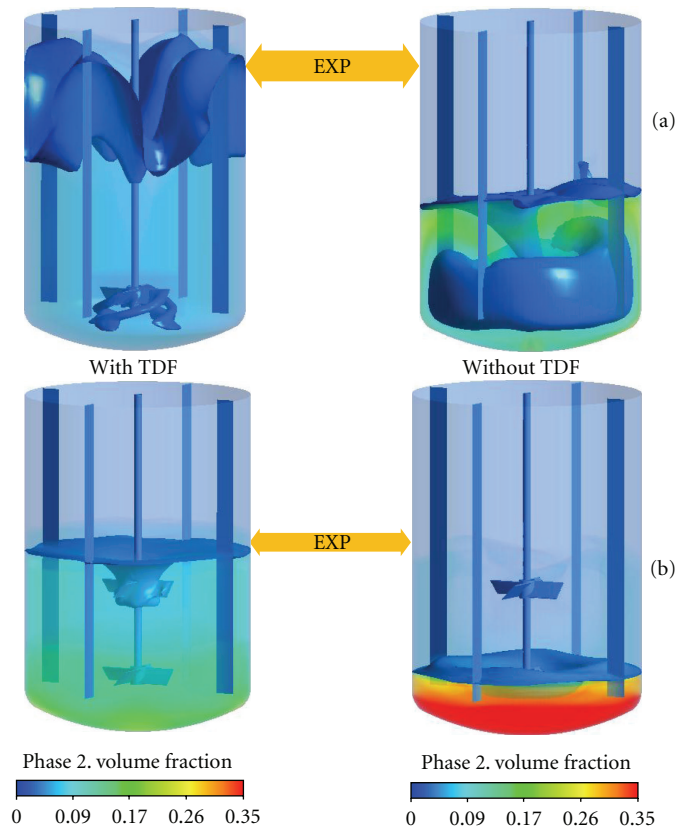


FIGURE 8: Effect of turbulent dispersion force (TDF). Volume rendered plots with isosurface for (a) single-impeller, 10% (w/w) loading, 400 RPM and (b) dual-impeller, 15% (w/w) loading, 150 RPM. The double-headed arrows marked “EXP” represent the location of experimental observation with arrow thickness representing the observed 8% spread in the experimental data. Gidaspow drag model.

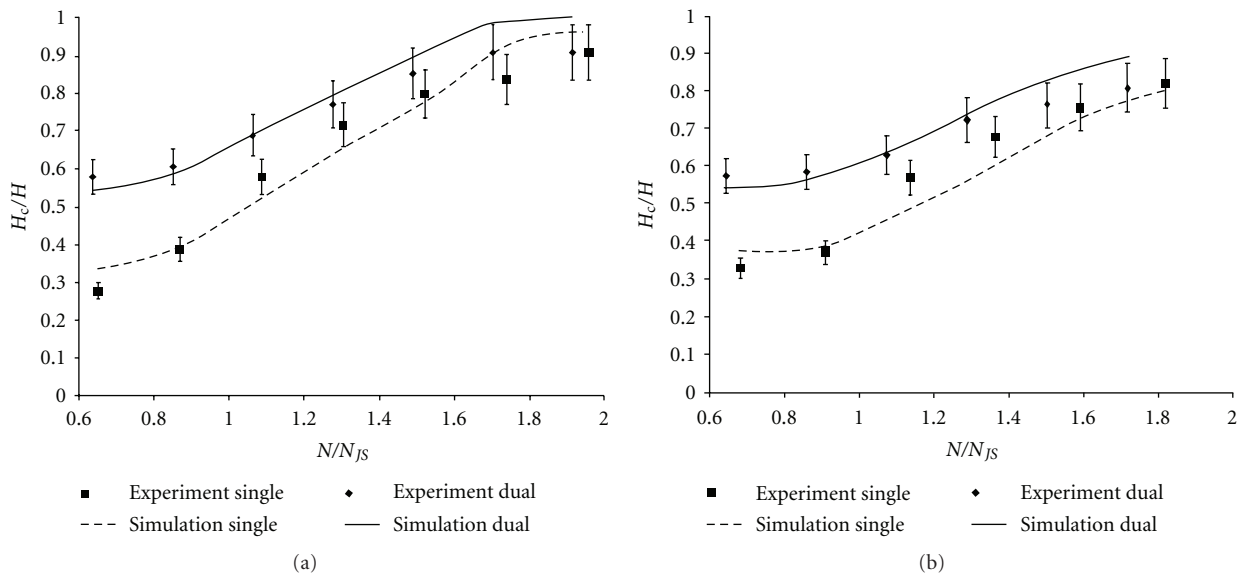


FIGURE 9: (a) Plot of normalized cloud height against normalized impeller speed for 10% (w/w) loading; (b) plot of normalized cloud height against normalized impeller speed for 15% (w/w) loading.

This may be due to the fact that the single impeller may be not able to fully suspend solids at low RPM. Modifications to the TDF model to include effect of local solid concentration may overcome this difficulty. This analysis is left for future study.

5. Conclusion

A CFD modeling strategy was developed to predict cloud height in stirred tanks with single- and dual-axial PBT impellers. The CFD model was based on Eulerian-Granular multiphase theory. The effects of two different drag models, Gidaspow and Schiller-Naumann, and a drift velocity-based turbulent dispersion force were analyzed. The modeling strategy was developed for a limited set of experimental conditions and then applied across the full range solids loading, agitation rates, and reactor configurations. It was determined that the inclusion of turbulent dispersion force was critical to accurate prediction of cloud height for the conditions studied. The drag model was observed to have a much lower influence. The resulting modeling strategy was then compared to the full experimental range of cloud height measurements. The model was found to be predictive of cloud height across a broad range of experimental conditions, the exception being the single-impeller configuration at low agitation rates. It is the authors' opinion that solids concentration-based inclusion of the TDF can be studied further to improve the model prediction at lower agitation rates.

Nomenclature

C_1 :	Distance of lower impeller from the tank bottom, m
C_2 :	Distance of upper impeller from the tank bottom, m
C_D :	Drag coefficient
D :	Impeller diameter, m
d_s :	Particle diameter, m
$D_{t,fs}$:	fluid-solid turbulent dispersion coefficient, m^2/s
\vec{F}_q :	Lift, virtual mass, and any other external forces acting on the solid phase, N/m^3
H :	Liquid fill level, m
H_c :	Cloud height, m
K_{fs} :	Interphase exchange coefficient, kg/m^3-s
\dot{m}_{fs} :	Fluid-solid interphase mass exchange, kg/m^3-s
N :	Impeller rotational speed, rpm
N_{JS} :	Just suspension speed, rpm
p :	Pressure shared by all phases, N/m^2
Re:	Relative Reynolds number
R_{fs} :	Fluid-solid interphase momentum exchange, N/m^3
T :	Tank diameter, m
\vec{u}_f :	Velocity of fluid phase, m/s
\vec{u}_{fs} :	Interphase velocity, m/s
\vec{u}_q :	Velocity of q th phase, m/s
\vec{u}_s :	Velocity of solid phase, m/s

\vec{U}_f :	Phasic average velocity of fluid phase, m/s
\vec{U}_s :	Phasic average velocity of solid phase, m/s
\vec{v}_{dr} :	Drift velocity, m/s.

Greek letters

α_q :	Volume fraction of phase q
$\vec{\tau}_q$:	Stress-strain tensor for phase q , N/m^2
μ_f :	Kinematic viscosity of liquid phase, $kg/m-s$
σ_{fs} :	Dispersion Prandtl number
ρ_q :	Density of phase q , kg/m^3 .

Subscripts

f :	Fluid phase
fs :	Exchange between fluid and solid phases
q :	Phase number
s :	Solid phase
t :	Turbulent.

Acknowledgments

The authors gratefully acknowledge the invaluable help provided by Prem Andrade and Mohan Srinivasa (ANSYS, Pune) for their guidance during the CFD simulations.

References

- [1] T. N. Zwietering, "Suspending of solid particles in liquid by agitators," *Chemical Engineering Science*, vol. 8, no. 3-4, pp. 244–253, 1958.
- [2] K. J. Bittorf and S. M. Kresta, "Prediction of cloud height for solid suspensions in stirred tanks," in *Proceedings of the CHISA Conference*, Prague, Czech Republic, August 2002.
- [3] A. Ochieng and M. S. Onyango, "CFD simulation of solids suspension in stirred tanks: review," *Hemijiska Industrija*, vol. 64, no. 5, pp. 365–374, 2010.
- [4] S. Decker and M. Sommerfeld, "Calculation of particle suspension in agitated vessels with the Euler-Lagrange approach," in *Proceedings of the IChemE Symposium Series*, no. 140, pp. 71–82, July 1996.
- [5] J. J. Derksen, "Numerical simulation of solids suspension in a stirred tank," *AIChE Journal*, vol. 49, no. 11, pp. 2700–2714, 2003.
- [6] H. Barrue, C. Xureb, and J. Bertrand, "A computational study on solid suspension in stirred reactor," in *Proceedings of the ECCE 1*, p. 1843, Florence, Italy, 1997.
- [7] G. Montante and F. Magelli, "Modelling of solids distribution in stirred tanks: analysis of simulation strategies and comparison with experimental data," *International Journal of Computational Fluid Dynamics*, vol. 19, no. 3, pp. 253–262, 2005.
- [8] G. Micale, F. Grisafi, L. Rizzuti, and A. Brucato, "CFD simulation of particle suspension height in stirred vessels," *Chemical Engineering Research and Design*, vol. 82, no. 9, pp. 1204–1213, 2004.
- [9] A. R. Khopkar, G. R. Kasat, A. B. Pandit, and V. V. Ranade, "Computational fluid dynamics simulation of the solid suspension in a stirred slurry reactor," *Industrial and Engineering Chemistry Research*, vol. 45, no. 12, pp. 4416–4428, 2006.

- [10] M. Spidla, M. Mostek, V. Sinevic, M. Jahoda, and V. Machon, "Experimental assessment and CFD simulations of local solid concentration profiles in a pilot-scale stirred tank," *Chemical Papers*, vol. 59, no. 6, pp. 386–393, 2005.
- [11] G. Micale, G. Montante, F. Grisafi, A. Brucato, and J. Godfrey, "CFD simulation of particle distribution in stirred vessels," *Transactions of IChemE, Part A, Chemical Engineering Research and Design*, vol. 78, no. 3, pp. 435–444, 2000.
- [12] G. R. Kasat, A. R. Khopkar, A. B. Pandit, and V. V. Ranade, "CFD simulation of liquid-phase mixing in solid-liquid stirred reactor," *Chemical Engineering Science*, vol. 63, no. 15, pp. 3877–3885, 2008.
- [13] M. V. Sardeshpande, V. A. Juvekar, and V. V. Ranade, "Hysteresis in cloud heights during solid suspension in stirred tank reactor: experiments and CFD simulations," *AIChE Journal*, vol. 56, no. 11, pp. 2795–2804, 2010.
- [14] M. Ljungqvist and A. Rasmuson, "Numerical simulation of the two-phase flow in an axially stirred vessel," *Chemical Engineering Research and Design*, vol. 79, no. 5, pp. 533–546, 2001.
- [15] G. Montante, D. Rondini, A. Bakker, and F. Magelli, "CFD predictions of solid concentration distributions in a baffled stirred vessel agitated with multiple PBT impellers," in *Proceedings of the CHISA Conference*, Prague, Czech Republic, August 2002.
- [16] A. Ochieng and A. E. Lewis, "CFD simulation of solids off-bottom suspension and cloud height," *Hydrometallurgy*, vol. 82, no. 1-2, pp. 1–12, 2006.
- [17] R. Angst, E. Harnack, M. Singh, and M. Kraume, "Grid and model dependency of the solid/liquid two-phase flow CFD simulation of stirred reactors," in *Proceedings of the 11th European Conference of Mixing*, p. 347, Bamberg, Germany, 2003.
- [18] A. Ochieng and A. E. Lewis, "Nickel solids concentration distribution in a stirred tank," *Minerals Engineering*, vol. 19, no. 2, pp. 180–189, 2006.
- [19] D. F. Fletcher and G. J. Brown, "Numerical simulation of solid suspension via mechanical agitation: effect of the modelling approach, turbulence model and hindered settling drag law," *International Journal of Computational Fluid Dynamics*, vol. 23, no. 2, pp. 173–187, 2009.
- [20] H. Barrue, J. Bertrand, B. Cristol, and C. Xuereb, "Eulerian simulation of dense solid-liquid suspension in multi-stage stirred vessel," *Journal of Chemical Engineering of Japan*, vol. 34, no. 5, pp. 585–594, 2001.
- [21] ANSYS FLUENT 13.0 Documentation, ANSYS, Inc., Canonsburg, Pa, USA.
- [22] J. Ding and D. Gidaspow, "Bubbling fluidization model using kinetic theory of granular flow," *AIChE Journal*, vol. 36, no. 4, pp. 523–538, 1990.
- [23] E. Deutsch and O. Simonin, "Large eddy simulation applied to the motion of particles in stationary homogeneous fluid turbulence," in *Turbulence Modifications in Multiphase Flows*, vol. 110, pp. 35–42, ASME Fluids Engineering Division, 1991.
- [24] O. Simonin, E. Deutsch, and J. P. Minier, "Eulerian prediction of the fluid/particle correlated motion in turbulent two-phase flows," *Advances in turbulence 4, Applied Scientific Research*, vol. 51, no. 1-2, pp. 275–283, 1993.

Research Article

A Priori Direct Numerical Simulation Modelling of the Curvature Term of the Flame Surface Density Transport Equation for Nonunity Lewis Number Flames in the Context of Large Eddy Simulations

Mohit Katragadda and Nilanjan Chakraborty

School of Mechanical and Systems Engineering, Newcastle University, Claremont Road, Newcastle-upon-Tyne NE1 7RU, UK

Correspondence should be addressed to Nilanjan Chakraborty, nilanjan.chakraborty@newcastle.ac.uk

Received 15 March 2012; Accepted 8 May 2012

Academic Editor: Mahesh T. Dhotre

Copyright © 2012 M. Katragadda and N. Chakraborty. This is an open access article distributed under the Creative Commons Attribution License, which permits unrestricted use, distribution, and reproduction in any medium, provided the original work is properly cited.

A Direct Numerical Simulation (DNS) database of freely propagating statistically planar turbulent premixed flames with Lewis numbers Le ranging from 0.34 to 1.2 has been used to analyse the statistical behaviours of the curvature term of the generalised Flame surface Density (FSD) transport equation, in the context of the Large Eddy Simulation (LES). Lewis number is shown to have significant influences on the statistical behaviours of the resolved and sub-grid parts of the FSD curvature term. It has been found that the existing models for the sub-grid curvature term C_{sg} do not capture the qualitative behaviour of this term extracted from the DNS database for flames with $Le \ll 1$. The existing models of C_{sg} only predict negative values, whereas the sub-grid curvature term is shown to assume positive values within the flame brush for the $Le = 0.34$ and 0.6 flames. Here the sub-grid curvature terms arising from combined reaction and normal diffusion and tangential diffusion components of displacement speed are individually modelled, and the new model of the sub-grid curvature term has been found to capture C_{sg} extracted from DNS data satisfactorily for all the different Lewis number flames considered here for a wide range of filter widths.

1. Introduction

Flame Surface Density (FSD) based reaction rate closure is well established in the context of Reynolds Averaged Navier-Stokes (RANS) simulations of turbulent premixed flames [1, 2]. The increased affordability of high performance computing has made Large Eddy Simulation (LES) an alternative simulation tool, where the large-scale physical processes are resolved, but modelling is still required for the subgrid quantities. The FSD-based reaction rate closure has recently been successfully extended for the purpose of LES [3–14]. In LES simulation of premixed combustion, a Favre-filtered reaction progress variable transport equation is solved alongside other filtered conservation equations. The reaction progress variable is defined as $c = (Y_{R0} - Y_R)/(Y_{R0} - Y_{R\infty})$, where Y_R is the mass fraction of a suitable reactant and the subscripts 0 and ∞ denote the values in the fully unburned and burned gases, respectively. The generalised

FSD is defined as $\Sigma_{gen} = \overline{|\nabla c|}$ [3–14], where the overbar indicates the LES filtering process. The Favre-filtered reaction progress variable transport equation takes the following form:

$$\bar{\rho} \frac{\partial \tilde{c}}{\partial t} + \bar{\rho} \tilde{u}_j \frac{\partial \tilde{c}}{\partial x_j} = \overline{\left(\rho D \frac{\partial c}{\partial x_j} \right)} + \bar{w} - \frac{\partial}{\partial x_j} \left(\bar{\rho} (\tilde{u}_j \tilde{c} - \tilde{u}_j \tilde{c}) \right), \quad (1)$$

where $\tilde{Q} = \overline{\rho Q / \bar{\rho}}$ indicates the Favre filtered value of a general variable Q , u_j is the velocity component in the j th direction, ρ is the density, D is the molecular diffusivity, and \bar{w} is the filtered reaction rate. The first two terms on right hand side of (1) denote the filtered molecular diffusion and reaction rates, respectively, and their combined contribution can be modelled using Σ_{gen} in the following manner:

$$\overline{w + \nabla \cdot (\rho D \nabla c)} = \overline{(\rho S_d)_s} \Sigma_{gen}, \quad (2)$$

where $\overline{(\overline{Q})}_s = \overline{Q|\nabla c|}/\Sigma_{\text{gen}}$ indicates the surface-weighted filtered value of a general quantity Q and $S_d = Dc/Dt/|\nabla c|$ is the displacement speed, which denotes the speed at which a given c isosurface moves normal to itself with respect to an initially coincident material surface. The generalised FSD Σ_{gen} is an unclosed quantity and is closed either by using an algebraic expression or by solving a modelled transport equation alongside other conservation equations. The algebraic closure is valid when the generation rate of flame surface area remains in equilibrium with its destruction rate, but this assumption is rendered invalid under unsteady conditions (e.g., combustion instabilities). Under unsteady conditions, it is often advantageous to solve a modelled transport equation of Σ_{gen} . The exact transport equation for the generalised FSD Σ_{gen} is given as [1, 4–7, 9, 10, 12]:

$$\begin{aligned} \frac{\partial \Sigma_{\text{gen}}}{\partial t} + \frac{\partial(\tilde{u}_j \Sigma_{\text{gen}})}{\partial x_j} \\ = - \frac{\partial \left[\overline{((u_i)_s - \tilde{u}_i) \Sigma_{\text{gen}}} \right]}{\partial x_i} + \overline{\left(\frac{(\delta_{ij} - N_i N_j) \partial u_i}{\partial x_j} \right)} \Sigma_{\text{gen}} \\ - \frac{\partial \left[\overline{(S_d N_i)_s \Sigma_{\text{gen}}} \right]}{\partial x_i} + \overline{\left(S_d \left(\frac{\partial N_i}{\partial x_i} \right) \right)} \Sigma_{\text{gen}}, \end{aligned} \quad (3)$$

where $N_i = -(\partial c/\partial x_i)/|\nabla c|$ is the i th component of flame normal vector. The terms on the left hand side of (3) denote transient and mean advection effects, respectively. The first three terms on the right hand side of (3) denote the effects of subgrid convection, flame surface area generation due to fluid-dynamic straining, and flame normal propagation, respectively. The last term of (3) describes the production/destruction of Σ_{gen} due to flame curvature $\kappa_m = (\partial N_i/\partial x_i)/2$ and thus referred to as the FSD curvature term [4–7, 9, 10, 12]. It has been found in several previous studies [5–7, 9, 14] that the FSD curvature term remains a leading order contributor to the FSD transport for both unity and nonunity Lewis number turbulent premixed combustion. As the curvature term remains a leading order contributor to the FSD transport, the modelling of $\overline{(S_d \nabla \cdot \vec{N})}_s \Sigma_{\text{gen}}$ is crucial for the transport equation-based FSD closure. The statistical behaviour of $\overline{(S_d \nabla \cdot \vec{N})}_s \Sigma_{\text{gen}}$ is significantly affected by curvature dependence on S_d [9, 10, 12]. Earlier *a priori* Direct Numerical Simulation (DNS) analyses [9, 10, 12] showed that existing models for the subgrid curvature term C_{sg} do not adequately capture the qualitative behaviour of this term obtained from DNS data. Moreover, the model parameters for the existing subgrid curvature term C_{sg} models are found to be strong functions of the LES filter width Δ [9, 10, 12].

To date, most existing FSD-based models have been proposed for unity Lewis number flames where the differential diffusion of heat and mass has been ignored. The Lewis number is defined as the ratio of thermal diffusivity α_T to mass diffusivity D (i.e., $Le = \alpha_T/D$).

The effects of Le on the statistical behaviour of the FSD curvature term $\overline{(S_d \nabla \cdot \vec{N})}_s \Sigma_{\text{gen}}$ are yet to be analysed in detail, and this paper aims to bridge this gap in the existing literature. It is worth noting that, in a premixed flame, different species have different values of Lewis number. Thus, specifying a global Lewis number Le characterising the whole combustion process is not straightforward. The Lewis number of the deficient reactant is often considered to be the characteristic Le of the combustion process in question [15, 16]. Moreover, several previous studies [16–29] analysed the effects of differential diffusion of heat and mass by modifying the characteristic Lewis number in isolation, and the same procedure has been adopted here. In the present study, a simplified chemistry-based DNS database of statistically planar turbulent premixed flames with global Lewis numbers ranging from 0.34 to 1.2 has been considered to analyse the statistical behaviour of the FSD curvature term $\overline{(S_d \nabla \cdot \vec{N})}_s \Sigma_{\text{gen}}$ in the context of LES. In this context, the main objectives of this study are as follows:

- (1) to analyse the statistical behaviours of the subgrid FSD curvature term in the context of LES, for flames with different values of Lewis number;
- (2) to propose models for different components of the subgrid FSD curvature terms and assess their performances in comparison to the corresponding quantities extracted from DNS data.

The rest of the paper will be organised as follows. The necessary mathematical background will be provided in the next section. This will be followed by a brief description of the numerical implementation related to the DNS database. Following this, results will be presented and subsequently discussed. The main findings will be summarised, and conclusions will be drawn in the final section.

2. Mathematical Background

The curvature term of the FSD $\overline{(S_d \nabla \cdot \vec{N})}_s \Sigma_{\text{gen}}$ is often decomposed in the following manner [4–7, 9, 10, 12]:

$$\overline{(S_d \nabla \cdot \vec{N})}_s \Sigma_{\text{gen}} = C_{\text{mean}} + C_{\text{sg}}, \quad (4)$$

where C_{mean} and C_{sg} are the resolved and subgrid components of the FSD curvature term, respectively. The resolved curvature term C_{mean} can be expressed in three different manners [5, 9, 10, 12]:

$$C_{\text{mean}} = \overline{(S_d)_s} \left[\frac{\partial \overline{(N_i)_s}}{\partial x_i} \right] \Sigma_{\text{gen}} \quad (5a)$$

$$C_{\text{mean}} = \overline{(S_d)_s} \left[\frac{\partial M_i}{\partial x_i} \right] \Sigma_{\text{gen}}, \quad (5b)$$

$$C_{\text{mean}} = (\delta_{ij} - n_{ij}) \frac{\partial \left[\overline{(S_d)_s (N_i)_s} \right]}{\partial x_j} \Sigma_{\text{gen}}, \quad (5c)$$

where $M_i = -(\partial \bar{c}/\partial x_i)/|\nabla \bar{c}|$ is the i th component of the resolved flame normal vector. It was demonstrated

by Chakraborty and Cant [10, 12] that (5a) provides the best option for the resolved curvature term C_{mean} , as it gives rise to the smallest magnitude of C_{sg} among all the possibilities shown in (5a)–(5c). Equation (5a) was found to perform the best among the three possibilities shown in (5a), (5b), (5c) for this database. This is advantageous from the perspective of efficient modelling of the FSD curvature term $(S_d \nabla \cdot \vec{N})_s \Sigma_{\text{gen}}$ as most of the modelling uncertainty is associated with C_{sg} . Moreover, (5a) has also been used for the modelling of $(S_d \nabla \cdot \vec{N})_s \Sigma_{\text{gen}}$ in previous LES simulations [5–7, 13]. For the present analysis (5a), (i.e., $C_{\text{mean}} = (S_d)_s [\partial(N_i)_s / \partial x_i] \Sigma_{\text{gen}}$) will be considered for the resolved curvature term C_{mean} .

It is often useful to decompose the flame displacement speed $S_d = (Dc/Dt)/|\nabla c| = [\dot{w} + \nabla \cdot (\rho D \nabla c)]/\rho |\nabla c|$ in the following manner for the purpose of modelling the FSD curvature term [9–12, 30, 31]:

$$S_d = S_r + S_n + S_t, \quad (6a)$$

$$S_r = \frac{\dot{w}}{\rho |\nabla c|}, \quad (6b)$$

$$S_n = \frac{\vec{N} \cdot \nabla (\rho D \vec{N} \cdot \nabla c)}{\rho |\nabla c|}, \quad (6c)$$

$$S_t = -D \nabla \cdot \vec{N} = -2D \kappa_m, \quad (6d)$$

where S_r and S_n are the reaction and normal diffusion components of displacement speed and S_t is the tangential diffusion component of displacement speed. The following expression for C_{sg} can be obtained using (6a)–(6d) and (5a) (i.e., $C_{\text{mean}} = (S_d)_s [\partial(N_i)_s / \partial x_i] \Sigma_{\text{gen}}$):

$$C_{\text{sg}} = C_{\text{sg1}} + C_{\text{sg2}} = \left(S_d \frac{\partial N_i}{\partial x_i} \right)_s \Sigma_{\text{gen}} - \overline{(S_d)_s} \frac{\partial \overline{(N_i)_s}}{\partial x_i} \Sigma_{\text{gen}}, \quad (7)$$

where

$$C_{\text{sg1}} = \left[\overline{\left((S_r + S_n) \frac{\partial N_i}{\partial x_i} \right)_s} \Sigma_{\text{gen}} - \overline{(S_r + S_n)_s} \frac{\partial \overline{(N_i)_s}}{\partial x_i} \Sigma_{\text{gen}} \right], \quad (8a)$$

$$C_{\text{sg2}} = - \left[\overline{\left(D \left(\frac{\partial N_i}{\partial x_i} \right)^2 \right)_s} \Sigma_{\text{gen}} - \overline{\left(D \frac{\partial N_i}{\partial x_i} \right)_s} \frac{\partial \overline{(N_i)_s}}{\partial x_i} \Sigma_{\text{gen}} \right]. \quad (8b)$$

Equation (8a) indicates that curvature ($\kappa_m = \nabla \cdot \vec{N}/2$) dependences of $(S_r + S_n)$ and $|\nabla c|$ significantly influence the statistical behaviour of C_{sg1} . Equation (8b) suggests that C_{sg2} is expected to assume negative values throughout the flame brush.

Hawkes and Cant [6, 7] modified a version of the Coherent Flamelet Model (CFM) by Candel et al. [2] for the purpose of LES as:

$$C_{\text{sg}} = - \frac{\alpha_N \beta_1 S_L \Sigma_{\text{gen}}^2}{(1 - \bar{c})}, \quad (9)$$

where $\alpha_N = 1 - \overline{(N_k)_s} \overline{(N_k)_s}$ is a resolution parameter which vanishes when the flow is fully resolved and β_1 is a model parameter. Hawkes [5] discussed a possibility of modifying a RANS model proposed by Cant et al. [1] for the purpose of LES as:

$$C_{\text{sg}} = - \frac{C_H S_L \Sigma_{\text{gen}}^2}{(1 - \bar{c})}, \quad (10)$$

where $C_H = \alpha_N \beta_2 [1 - (1/3)[1 - \exp(-10(1 - \bar{c})\sqrt{\tilde{k}/\Sigma_{\text{gen}} S_L \Delta})]$, $A = 10.0$, $u'_{\Delta} = \sqrt{2\tilde{k}/3}$ is the subgrid turbulent velocity fluctuation, $\tilde{k} = (\overline{\rho u_i u_i} - \overline{\rho} \tilde{u}_i \tilde{u}_i)/2\overline{\rho}$ is the subgrid kinetic energy, and β_2 is a model parameter. Another model of C_{sg} was proposed by Charlette et al. [4]:

$$C_{\text{sg}} = - \frac{\beta_3 S_L (\Sigma_{\text{gen}} - |\nabla \bar{c}|) \Sigma_{\text{gen}}}{\bar{c}(1 - \bar{c})}, \quad (11)$$

where β_3 is a model parameter. The models given by (9)–(11) (henceforth will be referred to as CSGCFM, CSGCPB, and CSGCHAR, resp.) ensure that C_{sg} vanishes when the flow is fully resolved (i.e., $\overline{(N_k)_s} \overline{(N_k)_s} = 1.0$ and $\Sigma_{\text{gen}} = |\nabla \bar{c}|$). *A priori* DNS assessment of the CSGCFM, CSGCPB, and CSGCHAR models and the modelling of C_{sg1} and C_{sg2} will be addressed in Section 4 of this paper.

3. Numerical Implementation

In principle combustion, DNS should account for both three dimensionality of turbulence and detailed chemical mechanism. However, until recently, most combustion DNS studies were carried out either in two dimensions with detailed chemistry or in three dimensions with simplified chemistry due to the limitation of computer storage capacity. Although it is now possible to carry out three-dimensional DNS with detailed chemistry, they remain extremely expensive (e.g., millions of CPU hours and thousands of processors [32]) and the cost of an extensive parametric analysis based on three-dimensional detailed chemistry-based DNS often becomes prohibitive. As the present analysis concentrates on an extensive parametric variation in terms of Lewis number, the chemical mechanism is simplified here by an Arrhenius-type irreversible single-step chemical reaction (i.e., Reactants \rightarrow Products) following several previous studies [1–12, 14]. It has been found that the strain rate and curvature dependences of S_d and $|\nabla c|$ obtained from three-dimensional simplified chemistry DNS [25–27, 33, 34] are found to be qualitatively similar to the corresponding behaviours obtained from detailed chemistry-based DNS simulations [16, 30, 31, 35]. As the statistical behaviours of the FSD curvature term $(S_d \nabla \cdot \vec{N})_s \Sigma_{\text{gen}}$ are strongly dependent on the curvature dependences of S_d and $|\nabla c|$, the results for this analysis are expected to be valid even for detailed chemistry based simulations at least in a qualitative sense without much loss of generality. Several studies [3–7, 9–12] have concentrated on *a priori* DNS modelling of FSD based on simplified chemistry in the past and the same approach has been adopted here.

A compressible three-dimensional DNS code SENGAs [36] was used for the simulations where the conservation equations of mass, momentum, energy, and species are solved in nondimensional form. A cubic domain of each side equal to $24.1\delta_{th}$ is considered for the present DNS database where δ_{th} is the thermal flame thickness, which is defined as $\delta_{th} = (T_{ad} - T_0)/\text{Max}|\nabla\hat{T}|_L$, and the subscript L refers to quantities in an unstrained planar laminar flame with T_{ad} , T_0 , and \hat{T} being the adiabatic flame, unburned gas, and instantaneous gas temperatures, respectively. The computational domain was discretised using a Cartesian grid of $230 \times 230 \times 230$ with equal grid spacing in each direction. The grid spacing Δx is determined based on the flame resolution, and about 10 grid points are kept within the thermal flame thickness δ_{th} for all the cases considered here. This grid spacing Δx corresponds to 0.73η , where η is the Kolmogorov length scale. The boundaries in the mean flame propagation were taken to be partially nonreflecting and were implemented using the Navier-Stokes Characteristic Boundary Conditions (NSCBC) technique [37]. The boundary conditions in the transverse direction were taken to be periodic. The spatial derivatives for the internal grid points were evaluated using a tenth-order central differencing scheme, and the order of differentiation gradually decreases to a one-sided 2nd order scheme at the partially nonreflecting boundaries. The time advancement was carried out using an explicit low storage third-order Runge-Kutta scheme [38].

For the current DNS database, the turbulent velocity field was initialised using a pseudospectral method [39] following the Batchelor-Townsend turbulent kinetic energy spectrum [40]. The flame is initialised using a steady planar unstrained laminar flame solution. The initial values of normalised root mean square (rms) turbulent velocity fluctuation u'/S_L , integral length scale to thermal flame thickness ratio l/δ_{th} , heat release parameter $\tau = (T_{ad} - T_0)/T_0$, Damköhler number $Da = lS_L/u'\delta_{th}$, and Karlovitz number $Ka = (u'/S_L)^{3/2}(l/\delta_{th})^{-1/2}$ are listed in Table 1. According to Peters [41], all the cases considered here can be taken to represent the thin reaction zone regime combustion, as Ka remains greater than unity. Standard values are considered for Prandtl number Pr and the Zeldovich number β (i.e., $Pr = 0.7$ and $\beta = T_{ac}(T_{ad} - T_0)T_{ad}^2 = 6.0$, where T_{ac} is the activation temperature).

Under decaying turbulence, DNS simulations should be carried out for a simulation time $t_{sim} \geq \max(t_f, t_c)$ [42], where $t_f = l/u'$ is the initial eddy turn over time and $t_c = \delta_{th}/S_L$ is the chemical time scale. For this database, the statistics were extracted after about three eddy turn over times (i.e., $3t_f = 3l/u'$), which corresponded to one chemical time scale (i.e., $t_c = \delta_{th}/S_L$). This simulation time remains small but comparable to several studies [3, 24, 28, 43–47] which contributed significantly to the FSD-based modelling in the past. The statistics presented in this paper did not change significantly since halfway through the simulation (i.e., $1.5t_f = 1.5l/u'$). The value of u'/S_L in the unburned gas ahead of the flame had decayed by 50% of its initial value when the statistics were extracted. By this time, the

TABLE 1: Initial values of the simulation parameters and non-dimensional numbers relevant to the DNS database.

Case	Le	u'/S_L	l/δ_L	l/δ_{th}	δ_{th}/η	τ	Re_t	Da	Ka
A	0.34	7.5	1.13	2.45	7.32	4.5	47.0	0.33	34.3
B	0.6	7.5	1.76	2.45	7.32	4.5	47.0	0.33	19.40
C	0.8	7.5	2.13	2.45	7.32	4.5	47.0	0.33	14.70
D	1.0	7.5	2.45	2.45	7.32	4.5	47.0	0.33	11.75
E	1.2	7.5	2.72	2.45	7.32	4.5	47.0	0.33	9.80

normalised integral value l/δ_{th} had increased to around 1.7 times of its initial value. The values of u'/S_L and l/δ_{th} at the time statistics were extracted are also representative of the thin reaction zones regime combustion [41]. This DNS database was used extensively earlier for the purpose of RANS modelling [27, 28, 48, 49], and the interested readers are referred to these papers for further details.

The DNS data was explicitly LES filtered using a Gaussian filter kernel in physical space for the purpose of *a priori* analysis. The filtered quantity $\overline{Q}(\vec{x}, t)$, is given by

$$\overline{Q}(\vec{x}, t) = \int Q(\vec{x} - \vec{r})G(\vec{r})d\vec{r}, \quad (12)$$

where $G(\vec{r})$ is the Gaussian filter kernel, which is defined in the following manner:

$$G(\vec{r}) = \left(\frac{6}{\pi\Delta^2}\right)^{3/2} \exp\left(\frac{-6\vec{r} \cdot \vec{r}}{\Delta^2}\right). \quad (13)$$

The filtered quantities of interest were extracted for filter widths Δ ranging from $0.4\delta_{th}$ to $2.4\delta_{th}$ in steps of $0.4\delta_{th}$. These filter sizes are comparable to the range of Δ used in several previous studies [3, 4, 9–12, 14] for *a priori* DNS analysis and span a useful range of length scales (i.e., from $\Delta \approx 0.4\delta_{th}$, where the flame is partially resolved, up to $2.4\delta_{th}$, where the flame becomes fully unresolved and Δ is comparable to the integral length scale).

4. Results and Discussion

The instantaneous isosurfaces of c ranging from 0.01 to 0.99 at $t_c = \delta_{th}/S_L$ are shown in Figure 1, which indicates that the flame wrinkling increases with decreasing Lewis number and this tendency is particularly prevalent for the $Le \ll 1$ flames due to thermodiffusive instabilities [17–29]. The unburned reactants diffuse into the reaction zone at a faster rate than the rate at which heat diffuses out in the $Le < 1$ flames. This gives rise to simultaneous presence of high temperature and reactant concentration in the reaction zone for the $Le < 1$ flames, which in turn leads to greater burning rate and flame surface area generation in comparison to the unity Lewis number flame. By contrast, heat diffuses faster than the diffusion rate of reactants into the reaction zone in the case of $Le > 1$, which reduces the burning rate and the rate of flame area generation in comparison to the unity Lewis number flame. The increase in burning rate and flame area generation with decreasing Lewis number can be substantiated by the values of normalised turbulent

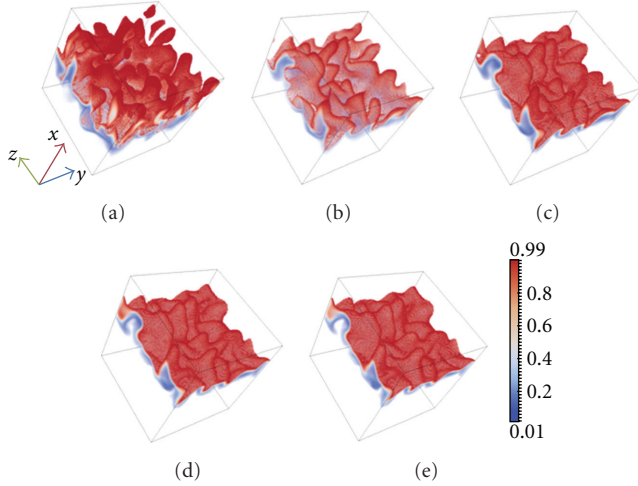


FIGURE 1: Instantaneous isosurfaces of c ranging from 0.01 to 0.99 at $t = 3t_f = t_c$ for cases (a) $Le = 0.34$; (b) $Le = 0.6$; (c) $Le = 0.8$; (d) $Le = 1.0$; (e) $Le = 1.2$. The domain size is $24.1\delta_{th} \times 24.1\delta_{th} \times 24.1\delta_{th}$.

flame speed S_T/S_L and normalised flame surface area A_T/A_L which are presented in Table 2. The values of S_T/S_L have been evaluated by volume integrating the reaction rate \dot{w} using the expression $S_T = (1/\rho_0 A_P) \int_V \dot{w} dV$, where A_P is the projected area of the flame in the direction of mean flame propagation, while the values of A_T/A_L have been evaluated by volume integrating $|\nabla c|$ (i.e., $\int_V |\nabla c| dV$) under both turbulent and laminar conditions. Table 2 shows that both S_T/S_L and A_T/A_L increase with decreasing Lewis number, and this effect is particularly prevalent in the flames with $Le < 1$ due to the presence of thermodiffusive instabilities [17–29]. The increase in flame wrinkling with decreasing Lewis number is also visually evident from the c isosurfaces presented in Figure 1.

The variations of $(S_d \nabla \cdot \vec{N})_s \Sigma_{gen}$, C_{mean} , and C_{sg} conditionally averaged in bins of \tilde{c} isosurfaces for cases (a)–(e) are shown in Figure 2 for filter widths $\Delta = 8\Delta_m \approx 0.8\delta_{th}$ and $\Delta = 24\Delta_m \approx 2.4\delta_{th}$, where Δ_m is the DNS grid size. It is evident from Figure 2 that Le significantly affects the statistical behaviours of the curvature terms. The filter widths $\Delta = 8\Delta_m \approx 0.8\delta_{th}$, and $\Delta = 24\Delta_m \approx 2.4\delta_{th}$ span a useful range of length scales (i.e., from $\Delta \approx 0.8\delta_{th}$, where the flame is partially resolved, up to $2.4\delta_{th}$ where the flame becomes fully unresolved and Δ is comparable to the integral length scale). In the $Le \ll 1$ flames (e.g., cases (a) and (b)), the FSD curvature term $(S_d \nabla \cdot \vec{N})_s \Sigma_{gen}$ behaves as a source term for the major part of the flame brush before assuming negative values towards the burned gas side for $\Delta = 8\Delta_m \approx 0.8\delta_{th}$. For $\Delta = 24\Delta_m \approx 2.4\delta_{th}$, the FSD curvature term $(S_d \nabla \cdot \vec{N})_s \Sigma_{gen}$ acts as a source (sink) term towards the unburned (burned) gas side of the flame brush in the $Le \ll 1$ flames. In the case of $Le \approx 1.0$ flames (i.e., cases (c)–(e)) the curvature term $(S_d \nabla \cdot \vec{N})_s \Sigma_{gen}$ behaves as a sink type term throughout the flame brush for all filter widths. It can be seen from Figure 2 that C_{mean} acts as a source (sink) term for cases (a)–(b) ((c)–(e)). The magnitude of C_{mean} (C_{sg}) decreases

TABLE 2: The effects of Lewis number on normalised turbulent flame speed S_T/S_L and normalised flame surface area A_T/A_L after 3.0 initial eddy turn over times.

Case	Le	S_T/S_L	A_T/A_L
A	0.34	13.70	3.93
B	0.6	4.58	2.66
C	0.8	2.53	2.11
D	1.0	1.83	1.84
E	1.2	1.50	1.76

(increases) with increasing Δ in all cases, and for large filter widths $(S_d \nabla \cdot \vec{N})_s \Sigma_{gen}$ is principally made up of C_{sg} . The LES filtering is a convolution process, and the weighted averaging involved in the filtering process leads to a decrease in the magnitude of C_{mean} with increasing filter width Δ . The flow becomes increasingly unresolved with increasing filter width Δ , and this is reflected in the rise in C_{sg} magnitude with increasing filter width Δ .

The resolved curvature term $C_{mean} = \overline{(S_d)_s \partial(\vec{N}_i)_s / \partial x_i \Sigma_{gen}}$ can be seen to capture the behaviour of the curvature term $(S_d \nabla \cdot \vec{N})_s \Sigma_{gen}$, well at small filter widths (i.e., $\Delta \leq \delta_{th}$) for flames with $Le \approx 1.0$ (i.e., cases (c)–(e)). However, the magnitude of C_{mean} decreases with increasing Δ and it does not capture the behaviour of the FSD curvature term $(S_d \nabla \cdot \vec{N})_s \Sigma_{gen}$ for the $Le \ll 1.0$ flames (i.e., cases (a) and (b)). The subgrid curvature term, C_{sg} follows the qualitative behaviour of the FSD curvature term $(S_d \nabla \cdot \vec{N})_s \Sigma_{gen}$ for all filter widths. The subgrid curvature term C_{sg} almost entirely makes up the FSD curvature term $(S_d \nabla \cdot \vec{N})_s \Sigma_{gen}$ for $\Delta \gg \delta_{th}$, and this is especially true for the $Le \ll 1.0$ cases (i.e., cases (a) and (b)). It can further be observed from Figure 2 that C_{sg} assumes positive values towards the unburned gas side of the flame brush in the $Le \ll 1$ flames (e.g., cases (a) and (b)), whereas the existing models for C_{sg} allow for only negative values (see (9)–(11)). This suggests that new models for C_{sg} are warranted to account for the influences of nonunity Lewis number (i.e., $Le \neq 1.0$).

In order to be able to model the subgrid curvature term C_{sg} , the decomposition prescribed in (8a)–(8b) has been used here. The variations of $((S_r + S_n) \nabla \cdot \vec{N})_s \Sigma_{gen}$, $-(D(\nabla \cdot \vec{N})^2)_s \Sigma_{gen} = -4(D\kappa_m^2)_s \Sigma_{gen}$, C_{sg1} and C_{sg2} conditionally averaged in bins of \tilde{c} isosurfaces for cases (a)–(e) are shown in Figure 3 for filter widths $\Delta = 8\Delta_m \approx 0.8\delta_{th}$ and $\Delta = 24\Delta_m \approx 2.4\delta_{th}$. It is evident from Figure 3 that C_{sg2} remains negative throughout the flame brush for all cases and follows the qualitative behaviour of $-(4(D\kappa_m^2)_s \Sigma_{gen})$. A comparison between $((S_r + S_n) \nabla \cdot \vec{N})_s \Sigma_{gen}$ and $-4(D\kappa_m^2)_s \Sigma_{gen}$ reveals that $-4(D\kappa_m^2)_s \Sigma_{gen}$ remains the major contributor to $(S_d \nabla \cdot \vec{N})_s \Sigma_{gen}$ for all the flames at all values of Δ , which is consistent with the expected behaviour in the thin reaction zones regime [41]. The contribution of $((S_r + S_n) \nabla \cdot \vec{N})_s \Sigma_{gen}$ remains significant for the $Le < 1$ cases (i.e., cases (a), (b) and (c)), but its contribution remains weak in comparison

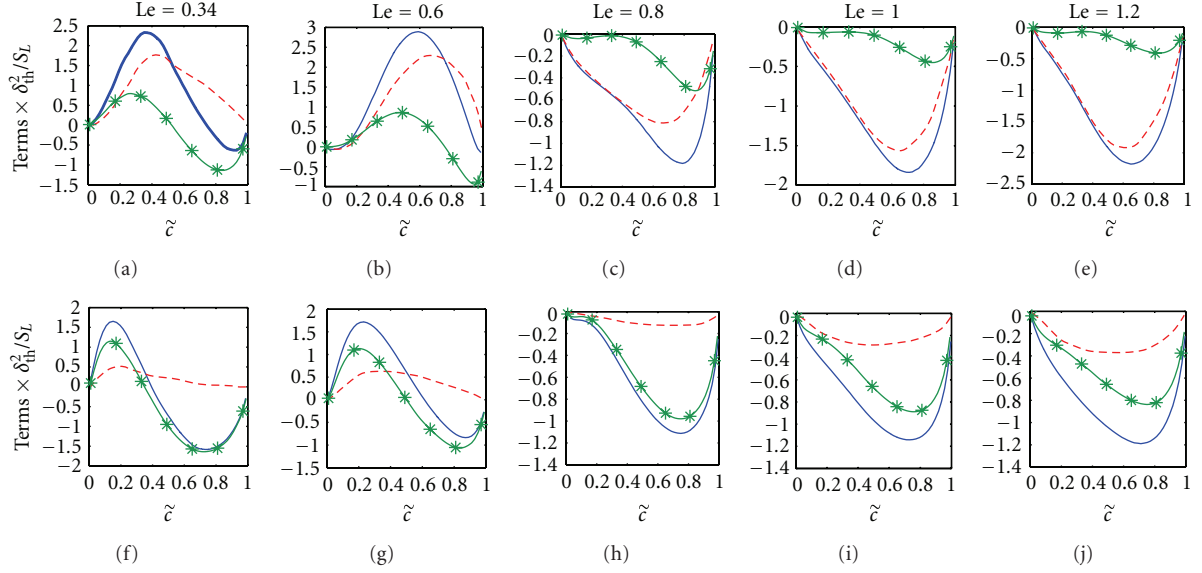


FIGURE 2: Variation of $(S_d \nabla \cdot \vec{N})_s \Sigma_{gen}$ (solid line), $C_{mean} = \overline{(S_d)_s} \partial \overline{(N_i)_s} / \partial x_i \Sigma_{gen}$ (dashed line) and C_{sg} (asterisk line) conditionally averaged in bins of \tilde{c} across the flame brush for filter sizes $\Delta = 8\Delta_m \approx 0.8\delta_{th}$ (top row): (a) $Le = 0.34$ (1st column); (b) $Le = 0.6$ (2nd column); (c) $Le = 0.8$ (3rd column); (d) $Le = 1.0$ (4th column); (e) $Le = 1.2$ (5th column) and for filter size $\Delta = 24\Delta_m \approx 2.4\delta_{th}$ (bottom row): (f) $Le = 0.34$ (1st column); (g) $Le = 0.6$ (2nd column); (h) $Le = 0.8$ (3rd column); (i) $Le = 1.0$ (4th column); (j) $Le = 1.2$ (5th column). All terms are ensemble averaged on \tilde{c} isosurfaces in Figure 2 and subsequent cases. All the curvature terms in this and subsequent figures are normalised by S_L / δ_{th}^2 .

to the magnitude of $-4\overline{(D\kappa_m^2)_s} \Sigma_{gen}$ in the $Le = 1.0$ and 1.2 flames (i.e., cases (d) and (e)). Figure 3 demonstrates that C_{sg1} remains close to the magnitude of $((S_r + S_n) \nabla \cdot \vec{N})_s \Sigma_{gen}$ for all Δ for the $Le = 1.0$ flame (i.e., case (d)), indicating that $\overline{(S_r + S_n)_s} \partial \overline{(N_i)_s} / \partial x_i \Sigma_{gen}$ does not play a major role in capturing the behaviour of $((S_r + S_n) \nabla \cdot \vec{N})_s \Sigma_{gen}$. However, there is a significant difference in magnitudes of $((S_r + S_n) \nabla \cdot \vec{N})_s \Sigma_{gen}$ and C_{sg1} for small values of Δ (i.e., $\Delta < \delta_{th}$) in the nonunity Lewis number flames (i.e., cases (a)–(c) and (e)), which indicates that $\overline{(S_r + S_n)_s} \partial \overline{(N_i)_s} / \partial x_i \Sigma_{gen}$ plays a key role for small values of filter width in these flames. For large values of filter width (i.e., $\Delta \gg \delta_{th}$) C_{sg1} remains the major contributor to $((S_r + S_n) \nabla \cdot \vec{N})_s \Sigma_{gen}$ for all cases considered here, indicating that $\overline{(S_r + S_n)_s} \partial \overline{(N_i)_s} / \partial x_i \Sigma_{gen}$ plays progressively less important role for increasing values of Δ .

Figure 3 shows that there is a significant difference between $-4\overline{(D\kappa_m^2)_s} \Sigma_{gen}$ and C_{sg2} for all cases for small values of Δ , and the difference between these quantities decreases with increasing Δ . As most of the contribution of $-4\overline{(D\kappa_m^2)_s} \Sigma_{gen}$ remains unresolved for large values of Δ , the subgrid curvature term C_{sg2} remains the major contributor to $-4\overline{(D\kappa_m^2)_s} \Sigma_{gen}$, indicating that $(-D\partial N_i / \partial x_i)_s \partial \overline{(N_i)_s} / \partial x_i \Sigma_{gen}$ plays progressively less important role for increasing values of Δ where the flame is fully unresolved. However, the contribution of $(-D\partial N_i / \partial x_i)_s \partial \overline{(N_i)_s} / \partial x_i \Sigma_{gen}$ remains significant for small values of Δ , where the flame is partially resolved. Figure 3 further shows that the order of magnitudes of both C_{sg1} and C_{sg2} remains comparable and thus accurate modelling of C_{sg1} and C_{sg2} is necessary for precise predictions of C_{sg} .

As the range of κ_m values obtained on a flame surface increases with increasing flame wrinkling, the magnitude of $-4\overline{(D\kappa_m^2)_s}$ increases with decreasing Le , which in turn leads to increasing magnitude of $-4\overline{(D\kappa_m^2)_s} \Sigma_{gen}$ and C_{sg2} (see Figure 3). The positive contribution of C_{sg1} overcomes the negative contribution of C_{sg2} towards the unburned gas side of the flame brush for the $Le = 0.34$ and 0.6 flames (i.e., cases (a) and (b)) and yields a net positive contribution of C_{sg} towards the reactant side of the flame brush (see Figure 2).

The statistical behaviours of $((S_r + S_n) \nabla \cdot \vec{N})_s \Sigma_{gen}$ and C_{sg1} depend on the nature of the curvature $\kappa_m = \nabla \cdot \vec{N} / 2$ dependences of $(S_r + S_n)$ and $|\nabla c|$, and the variation of $(\kappa_m)_s$ across the flame brush. The correlation coefficients for $(S_r + S_n) - \kappa_m$ and $|\nabla c| - \kappa_m$ for five different c isosurfaces across the flame brush for all the cases are shown in Figures 4(a) and 4(b), respectively. For all cases, $S_t = -2D\kappa_m$ remains negatively correlated with κ_m with a correlation coefficient close to (-1.0) . However, Figures 4(a) and 4(b) demonstrate that Le significantly affects the curvature κ_m dependences of $(S_r + S_n)$ and $|\nabla c|$. It can be seen from Figures 4(a) and 4(b) that $(S_r + S_n)$ and $|\nabla c|$ remain positively (negatively) correlated with κ_m for the $Le < 1.0$ ($Le > 1.0$) flames, whereas both $(S_r + S_n)$ and $|\nabla c|$ show weak curvature dependences in the unity Lewis number flame. The positive correlations between $(S_r + S_n)$ and κ_m , and between $|\nabla c|$ and κ_m strengthen with decreasing Le for the $Le < 1$ flames. The physical explanations for the observed influences of Lewis number on the curvature dependence of $(S_r + S_n)$ and $|\nabla c|$ have been discussed elsewhere [25–27] and thus will not be discussed in this paper.

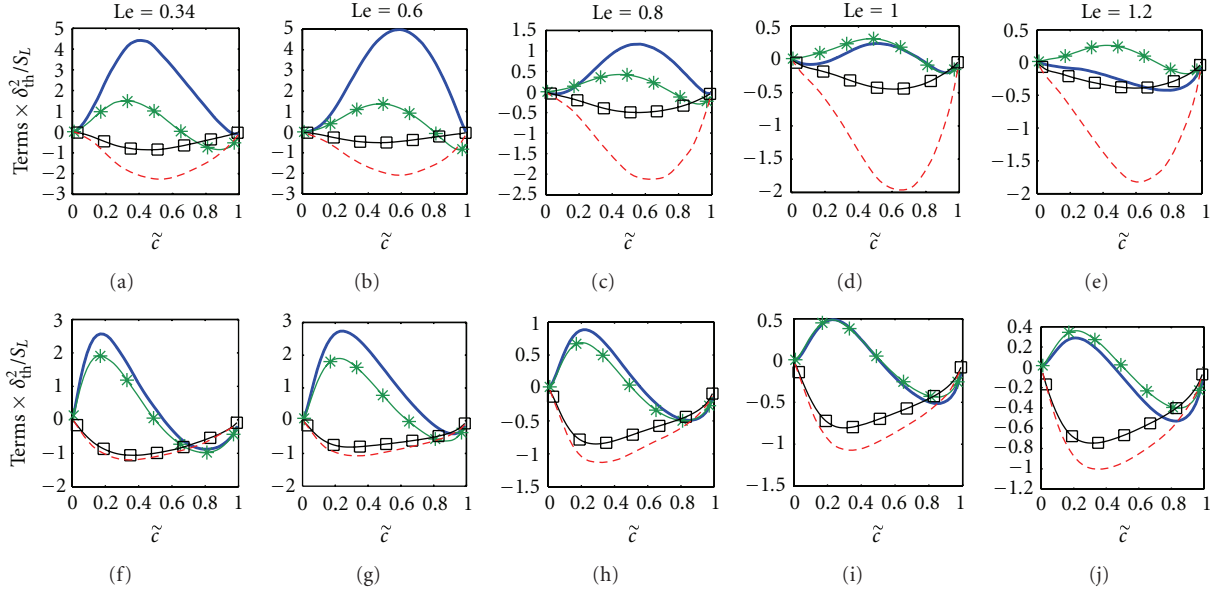


FIGURE 3: Variation of $\overline{((S_r + S_n) \nabla \cdot \vec{N})_s \Sigma_{\text{gen}}}$ (solid line), $-4\overline{(D\kappa_m^2)_s \Sigma_{\text{gen}}}$ (dashed line), C_{sg1} (asterisk line), and C_{sg2} (squared line) conditionally averaged in bins of \tilde{z} across the flame brush for $\Delta = 8\Delta_m \approx 0.8\delta_{\text{th}}$ (top row): (a) $Le = 0.34$ (1st column); (b) $Le = 0.6$ (2nd column); (c) $Le = 0.8$ (3rd column); (d) $Le = 1.0$ (4th column); (e) $Le = 1.2$ (5th column) and for filter size $\Delta = 24\Delta_m \approx 2.4\delta_{\text{th}}$ (bottom row): (f) $Le = 0.34$ (1st column); (g) $Le = 0.6$ (2nd column); (h) $Le = 0.8$ (3rd column); (i) $Le = 1.0$ (4th column); (j) $Le = 1.2$ (5th column).

The variations of $\overline{(\kappa_m)_s}$ conditionally averaged in bins of \tilde{z} isosurfaces for cases A–E are shown in Figures 4(c) and 4(d) for filter widths $\Delta = 8\Delta_m \approx 0.8\delta_{\text{th}}$ and $\Delta = 24\Delta_m \approx 2.4\delta_{\text{th}}$, respectively. It is evident from Figures 4(c) and 4(d) that $\overline{(\kappa_m)_s}$ assumes positive (negative) values towards the unburned (burned) gas side of the flame brush. For small values of Δ , the surface-weighted filtered value of curvature $\overline{(\kappa_m)_s}$ approaches to κ_m (i.e., $\lim_{\Delta \rightarrow 0} \overline{(\kappa_m)_s} = \kappa_m |\nabla c| / |\nabla c| = \kappa_m$) and thus the ensemble averaged value of $\overline{(\kappa_m)_s}$ remains small for small values of filter width as the ensemble averaged value of κ_m remains negligible for statistically planar flames. The difference between the ensemble averaged values of $\overline{(\kappa_m)_s}$ and κ_m increases with increasing filter width Δ , as flame wrinkling increasingly takes place at the subgrid level. For the $Le = 1.0$ flame (i.e., case D), the combination of positive (negative) value of $\overline{(\kappa_m)_s}$ and weak $(S_r + S_n) - \kappa_m$ and $|\nabla c| - \kappa_m$ correlations gives rise to positive (negative) values of the ensemble averaged values of $\overline{((S_r + S_n) \nabla \cdot \vec{N})_s \Sigma_{\text{gen}}}$ and C_{sg1} towards the unburned (burned) gas side of the flame brush for all values of Δ . The predominant positive $(S_r + S_n) - \kappa_m$ and $|\nabla c| - \kappa_m$ correlations give rise to positive values of the ensemble averaged values of $\overline{((S_r + S_n) \nabla \cdot \vec{N})_s \Sigma_{\text{gen}}}$ and C_{sg1} throughout the flame brush for small values of Δ in the $Le = 0.34, 0.6,$ and 0.8 flames. By contrast, negative $(S_r + S_n) - \kappa_m$ and $|\nabla c| - \kappa_m$ correlations (see Figures 4(a) and 4(b)) give rise to negative values of the ensemble averaged values of $\overline{((S_r + S_n) \nabla \cdot \vec{N})_s \Sigma_{\text{gen}}}$ and C_{sg1} throughout the flame brush for small values of Δ in the $Le = 1.2$ flame. These local dependences are progressively smeared with increasing Δ because of the convolution operation associated with LES filtering process, and this leads to positive (negative) values

of $\overline{((S_r + S_n) \nabla \cdot \vec{N})_s \Sigma_{\text{gen}}}$ and C_{sg1} towards the unburned (burned) gas side of the flame brush for all cases considered here, including the nonunity Lewis number flames where the curvature dependences of $(S_r + S_n)$ and $|\nabla c|$ are particularly strong.

The dependences of $\overline{(S_r + S_n)_s}$ and Σ_{gen} on $0.5 \times \partial \overline{(N_i)_s} / \partial x_i \Sigma_{\text{gen}}$ are likely to capture some of κ_m dependences of $(S_r + S_n)$ and $|\nabla c|$ at small values of filter widths Δ (i.e., $\Delta < \delta_{\text{th}}$), where the flame is partially resolved. This effect is particularly prevalent in the nonunity Lewis number flames where both $(S_r + S_n)$ and $|\nabla c|$ are strongly correlated with curvature κ_m even though the flames are statistically planar in nature. As a result of this, the contribution of $\overline{(S_r + S_n)_s \partial \overline{(N_i)_s} / \partial x_i \Sigma_{\text{gen}}}$ remains close to that of $\overline{((S_r + S_n) \nabla \cdot \vec{N})_s \Sigma_{\text{gen}}}$ for small filter widths (i.e., $\Delta < \delta_{\text{th}}$) for the non-unity Lewis number flames, which is reflected in the small contribution of C_{sg1} (see $\Delta = 0.8\delta_{\text{th}}$ variations in Figures 3(a)–3(c) and Figure 3(e)). The correlation between the resolved quantities (e.g., dependences of $\overline{(S_r + S_n)_s}$ and Σ_{gen} on $0.5 \times \partial \overline{(N_i)_s} / \partial x_i \Sigma_{\text{gen}}$) weakens with increasing filter width Δ due to smearing of local information. Moreover, physical processes take place increasingly at the subgrid level for $\Delta \gg \delta_{\text{th}}$, and thus $\overline{(S_r + S_n)_s \partial \overline{(N_i)_s} / \partial x_i \Sigma_{\text{gen}}}$ does not capture the behaviour of $\overline{((S_r + S_n) \nabla \cdot \vec{N})_s \Sigma_{\text{gen}}}$ for large filter widths in all cases considered here, including the nonunity Lewis number flames where the curvature dependences of $(S_r + S_n)$ and $|\nabla c|$ are particularly strong. This leads to $C_{\text{sg1}} \approx \overline{((S_r + S_n) \nabla \cdot \vec{N})_s \Sigma_{\text{gen}}}$ for $\Delta \gg \delta_{\text{th}}$ in all cases considered here (see $\Delta = 2.4\delta_{\text{th}}$ variations in Figures 3(f)–3(j)). It can be seen from Figure 3 that the positive contribution of

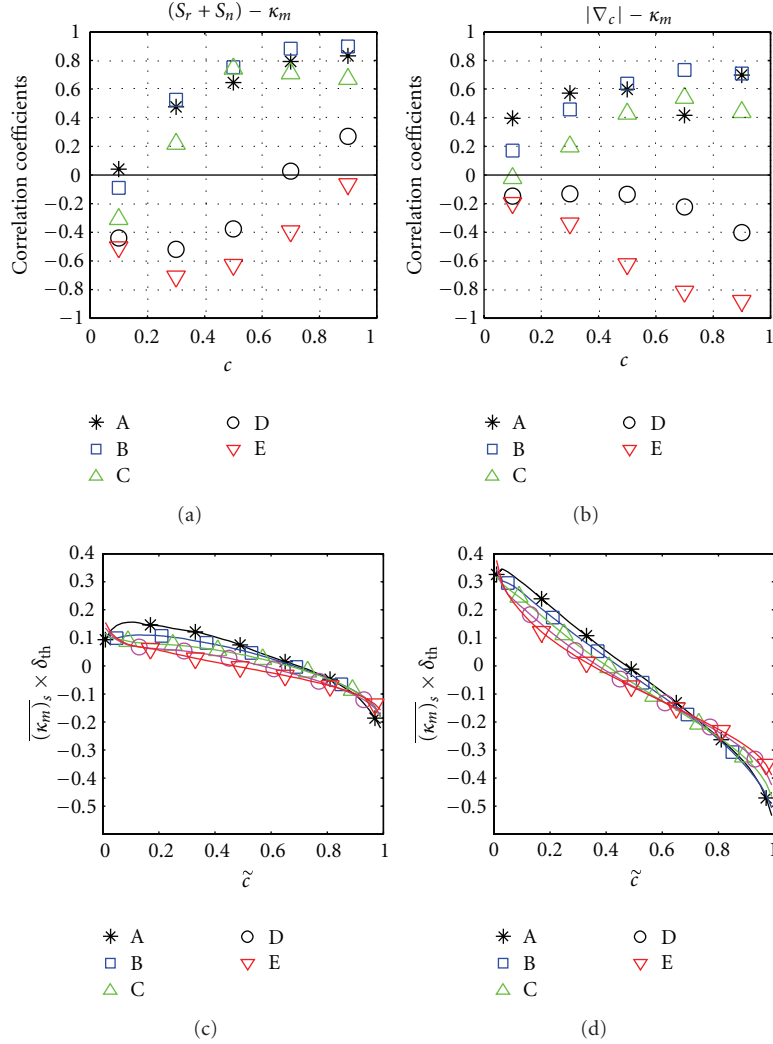


FIGURE 4: Correlation coefficients between (a) $(S_r + S_n)$ and κ_m , and between (b) $|\nabla c|$ and κ_m correlations on $c = 0.1, 0.3, 0.5, 0.7,$ and 0.9 isosurfaces for cases A–E. Variation of $(\kappa_m)_s \times \delta_{th}$ with \tilde{c} across the flame brush for (c) $\Delta = 8\delta_{th} \approx 0.8\delta_{th}$ and (d) $\Delta = 24\delta_{th} \approx 2.4\delta_{th}$ for cases A–E.

C_{sg1} overcomes the negative contribution of C_{sg2} towards the unburned gas side of the flame brush in the $Le = 0.34$ and 0.6 flames, which lead to positive value of $C_{sg} = C_{sg1} + C_{sg2}$ towards the unburned gas side for all values of Δ in these cases (see Figure 2). By contrast, negative values of C_{sg2} overcome the positive contributions of C_{sg1} towards the unburned gas side of the flame brush in the $Le = 0.8, 1.0,$ and 1.2 flames, which lead to negative values of $C_{sg} = C_{sg1} + C_{sg2}$ throughout the flame brush in these cases (see Figure 2).

The subgrid fluctuations of the surface-weighted contributions of $(S_r + S_n)$ and $\nabla \cdot \vec{N}$ are scaled here using S_L and $(\Sigma_{gen} - |\nabla \bar{c}|)$, respectively, to propose the following model for C_{sg1} :

$$C_{sg1} = -\frac{\beta_4 (\Sigma_{gen} - |\nabla \bar{c}|) (\bar{c} - c^*) S_L \Sigma_{gen}}{\{\exp[-a_\Sigma (1 - \bar{c})] \bar{c} (1 - \bar{c})^m\}}, \quad (14)$$

where $\beta_4, c^*, a_\Sigma,$ and m are the model parameters. The function $(\bar{c} - c^*) / \{\exp[-a_\Sigma (1 - \bar{c})] \bar{c} (1 - \bar{c})^m\}$ in (14)

is used to capture the correct qualitative behaviour of C_{sg1} throughout the flame brush. In a compressible, LES simulation \tilde{c} is readily available and \bar{c} needs to be extracted from \tilde{c} . The methodology of extracting \bar{c} from \tilde{c} in the context of LES was discussed elsewhere [9, 10, 12] and will not be discussed in detail in this paper. The model parameter c^* ensures that the transition from positive to negative value of C_{sg1} takes place at the correct location within the flame brush. The quantity $(\Sigma_{gen} - |\nabla \bar{c}|)$ vanishes when the flow is fully resolved (i.e., $\lim_{\Delta \rightarrow 0} (\Sigma_{gen} - |\nabla \bar{c}|) = \lim_{\Delta \rightarrow 0} (|\nabla \bar{c}| - |\nabla \bar{c}|) = |\nabla c| - |\nabla c| = 0$), and thus C_{sg1} becomes exactly equal to zero when the flow is fully resolved (i.e., $\Delta \rightarrow 0$) according to (14). It has been found that $m = 1.85$ enables (14) to capture the qualitative behaviour of C_{sg1} when the optimum values of c^* and a_Σ are chosen. The optimum values of $c^* (a_\Sigma)$ tend to increase with decreasing (increasing) Δ . The curvature κ_m dependences of $(S_r + S_n)$ and $|\nabla c|$ are influenced by Le (see Figures 4(a) and 4(b)), and

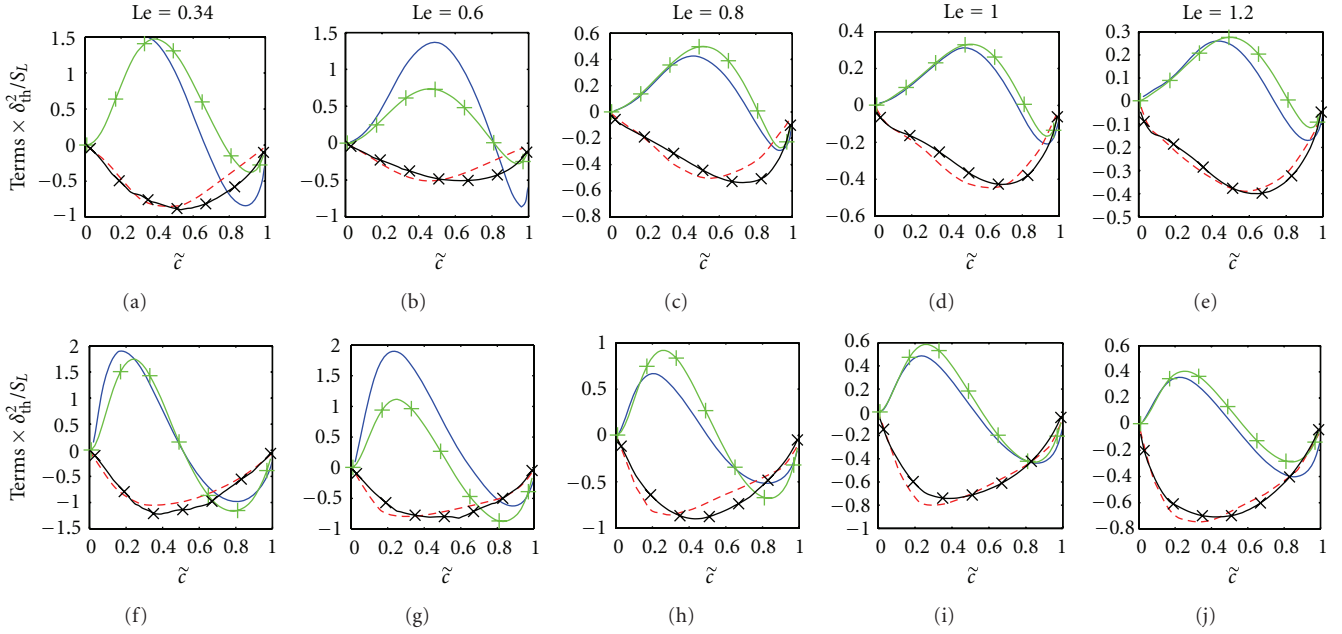


FIGURE 5: Variations of C_{sg1} (solid line) and C_{sg2} (dashed line) conditionally averaged in bins of \tilde{z} across the flame brush along with the predictions of (14) (vertical line) and (16) (crosses line) for $\Delta = 8\Delta_m \approx 0.8\delta_{th}$ (top row): (a) $Le = 0.34$ (1st column); (b) $Le = 0.6$ (2nd column); (c) $Le = 0.8$ (3rd column); (d) $Le = 1.0$ (4th column); (e) $Le = 1.2$ (5th column) and for filter size $\Delta = 24\Delta_m \approx 2.4\delta_{th}$ (bottom row): (f) $Le = 0.34$ (1st column); (g) $Le = 0.6$ (2nd column); (h) $Le = 0.8$ (3rd column); (i) $Le = 1.0$ (4th column); (j) $Le = 1.2$ (5th column).

these local dependences also appear in the resolved scale but their strength diminishes with increasing Δ due to filtering operation. As the resolved and subgrid curvature terms are closely related [9, 10, 12], the qualitative behaviour of C_{sg1} is also affected by the curvature dependences of displacement speed components and scalar gradient at the resolved scale, which leads to the variation of the optimum values of a_Σ , β_4 , and c^* with Le and Δ . The model parameter β_4 needs to be decreased for decreasing values of Σ_{gen} for satisfactory prediction of (14). The prediction of (14) ensemble averaged on \tilde{z} isosurfaces is compared with the ensemble averaged values of C_{sg1} in Figure 5 for all cases considered here for the optimum values of β_4 , c^* , and a_Σ for $\Delta = 0.8\delta_{th}$ and $\Delta = 2.4\delta_{th}$ when m is taken to be $m = 1.85$. The optimum values of β_4 , c^* , and a_Σ are estimated by calibrating the prediction of (14) with respect to the ensemble averaged values of C_{sg1} obtained from DNS data and the variation of the optimum values of β_4/Σ_{gen} , c^* , and a_Σ with Δ/δ_{th} for all cases are shown in Figure 6. The optimum values of β_4/Σ_{gen} , c^* , and a_Σ are parameterised here as

$$\frac{\beta_4}{\Sigma_{gen}} = 9.81\delta_{th} \left[l_1 + \frac{(l_2 - l_1)}{\{1.0 + \exp[-10.0(Le - 1)]\}^{1/2}} \right], \quad (15a)$$

where

$$l_1 = 1.2 \frac{[\Delta^{2.79} + 1.2(\Delta + \delta_{th})^{2.79}]}{(\Delta + \delta_{th})^{2.79}}; \quad (15b)$$

$$l_2 = 1.34 \frac{[\Delta^{0.67} + 0.53(\Delta + \delta_{th})^{0.67}]}{[3.1\Delta^{0.67} + 0.1(\Delta + \delta_{th})^{0.67}]},$$

$$c^* = k_1 + \left[\frac{(k_2 - k_1)}{\{1.0 + \exp(-2.0(\Delta/\delta_{th} - 1.5))\}} \right]; \quad (15c)$$

$$a_\Sigma = \frac{k_4}{(1.0 + \exp(-5.0(\Delta/\delta_{th} - 1.0)))},$$

where

$$k_1 = 0.75 + \frac{0.15}{[1.0 + \exp(-5.0(k_3 - 4.6))]}; \quad (15d)$$

$$k_2 = 0.65 + \frac{0.05}{[1.0 + \exp(-9.0(k_3 - 4.0))]},$$

$$k_4 = 0.81 - \frac{0.67}{[1.0 + \exp(-5.0(k_3 - 4.6))]}; \quad (15e)$$

$$k_3 = \frac{(\text{Re}_\Delta^{0.83} + 0.1)}{[(\Delta/\delta_{th})^{1.73} + 0.1]}; \quad \text{Re}_\Delta = \frac{4\rho_0\Delta}{\mu_0} \sqrt{\left(\frac{2\tilde{k}}{3}\right)}.$$

Figure 5 shows that (14) satisfactorily predicts C_{sg1} when m is taken to be $m = 1.85$, and the optimum values of β_4 , c^* , and a_Σ are used. According to the parameterisation given by (15a)–(15e), β_4 increases with decreasing Le , as the effects of chemical reaction strengthen with decreasing values of Lewis number (see Table 2). Moreover, β_4/Σ_{gen} , c^* , and a_Σ approach to asymptotic values for large values of Δ and turbulent Reynolds number based on LES filter width $\text{Re}_\Delta = 4\rho_0\sqrt{2\tilde{k}/3\Delta}/\mu_0$, where ρ_0 and μ_0 are the unburned gas density and viscosity, respectively.

Here, the contribution of $(D\kappa_m^2)_s - (D\partial N_i/\partial x_i)_s \partial(N_i)_s/\partial x_i$ is scaled with $(\Xi_\Delta - 1)^n S_L \Sigma_{gen}$ (i.e., $(D\kappa_m^2)_s - (D\partial N_i/\partial x_i)_s \partial(N_i)_s/\partial x_i \sim (\Xi_\Delta - 1)^n S_L \Sigma_{gen}$) where the

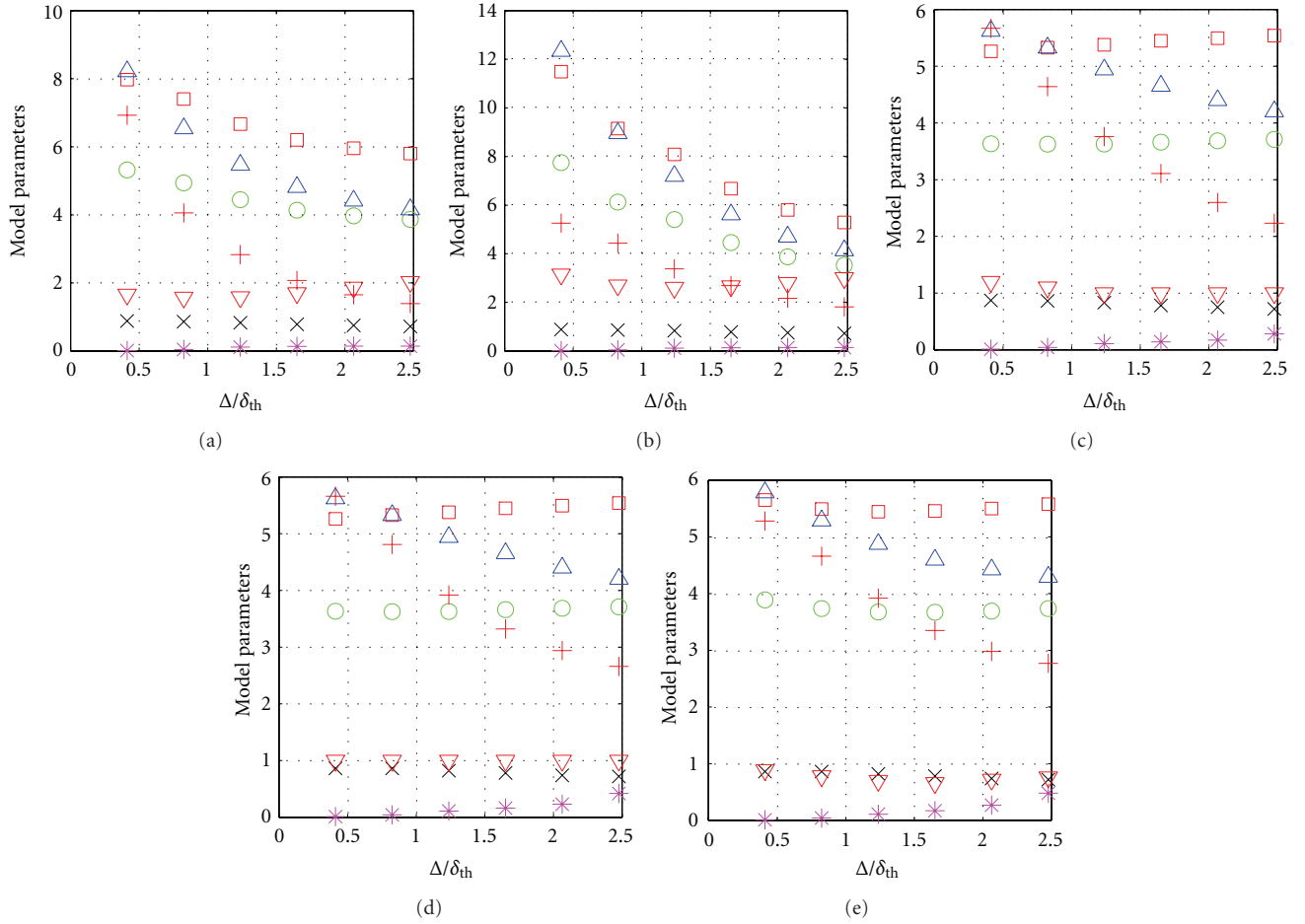


FIGURE 6: Variations of the model parameters β_1 (\circ), β_2 (\square), β_3 (\triangle), β_4/Σ_{gen} (down-pointing triangle), β_5 (+), a_2 (*), and c^* (\times) with Δ for: (a) $Le = 0.34$; (b) $Le = 0.6$; (c) $Le = 0.8$; (d) $Le = 1.0$; (e) $Le = 1.2$.

sub-grid fluctuations of D are taken to scale with S_L/Σ_{gen} . The above relations are utilised here to propose a model for C_{sg2} in the following manner:

$$C_{sg2} = -\frac{\beta_5 S_L (\Xi_\Delta - 1)^n \Sigma_{gen}^2}{\bar{c}(1 - \bar{c})}, \quad (16)$$

where $\Xi_\Delta = \Sigma_{gen}/|\nabla \bar{c}|$ is the wrinkling factor [8, 11, 43, 50, 51], β_5 and n are the model parameters, and $\bar{c}(1 - \bar{c})$ is used to capture the correct qualitative behaviour of C_{sg2} . The subgrid curvature term C_{sg2} vanishes when the flow is fully resolved according to (16), (i.e., $\lim_{\Delta \rightarrow 0} \Xi = \lim_{\Delta \rightarrow 0} \Sigma_{gen}/|\nabla \bar{c}| = \lim_{\Delta \rightarrow 0} |\nabla \bar{c}|/|\nabla \bar{c}| = |\nabla \bar{c}|/|\nabla \bar{c}| = 1.0$). It has been found that (16) satisfactorily captures the behaviour of C_{sg2} throughout the flame brush for $n = 1.0$ in all cases when a suitable value of β_5 is used. The variation of the global mean optimum values of β_5 with Δ/δ_{th} is shown in Figure 6 for all cases considered here. The optimum values of β_5 have been parameterised here in the following manner:

$$\beta_5 = m(Le) \left\{ \frac{Re_\Delta}{(Re_\Delta + 1.0)} \right\} \times \left[r_1 + \left\{ \frac{(r_2 - r_1)}{(1.0 + \exp(-5.0(Re_\Delta - r_3)))} \right\} \right], \quad (17a)$$

where

$$r_1 = 1.6 \frac{(r_4^{1.23} + 6.24)}{(7.17r_4^{1.23} + 0.26)}; \quad (17b)$$

$$r_2 = 1.88 \frac{(r_4^{2.27} + 5.92)}{(8.47r_4^{2.27} + 0.47)}$$

$$r_3 = 35.0 \operatorname{erf}[\exp\{5.3(r_4 - 1.0)\}]; \quad (17c)$$

$$r_4 = \frac{\Delta}{(\Delta + \delta_{th})}$$

$$m(Le) = \left(r_5 + \frac{(1.0 - r_5)}{\{1.0 + \exp[-10.0(Le - 1.0)]\}^{1/4}} \right); \quad (17d)$$

$$r_5 = 0.46 \frac{[r_4^{5.22} + 4.53]}{[8.0r_4^{5.22} + 2.96]}.$$

The predictions of (16) ensemble averaged on \tilde{c} isosurfaces are compared with ensemble averaged values of C_{sg2} in Figure 5 for all cases at $\Delta = 0.8\delta_{th}$ and $\Delta = 2.4\delta_{th}$, which show that (16) satisfactorily predicts the statistical behaviour of C_{sg2} when n is taken to be $n = 1.0$ and the optimum value of β_5 is used. According to (17a)–(17d), β_5 approaches to asymptotic values for large values of Δ and $Re_\Delta = 4\rho_0\sqrt{2k/3}\Delta/\mu_0$.

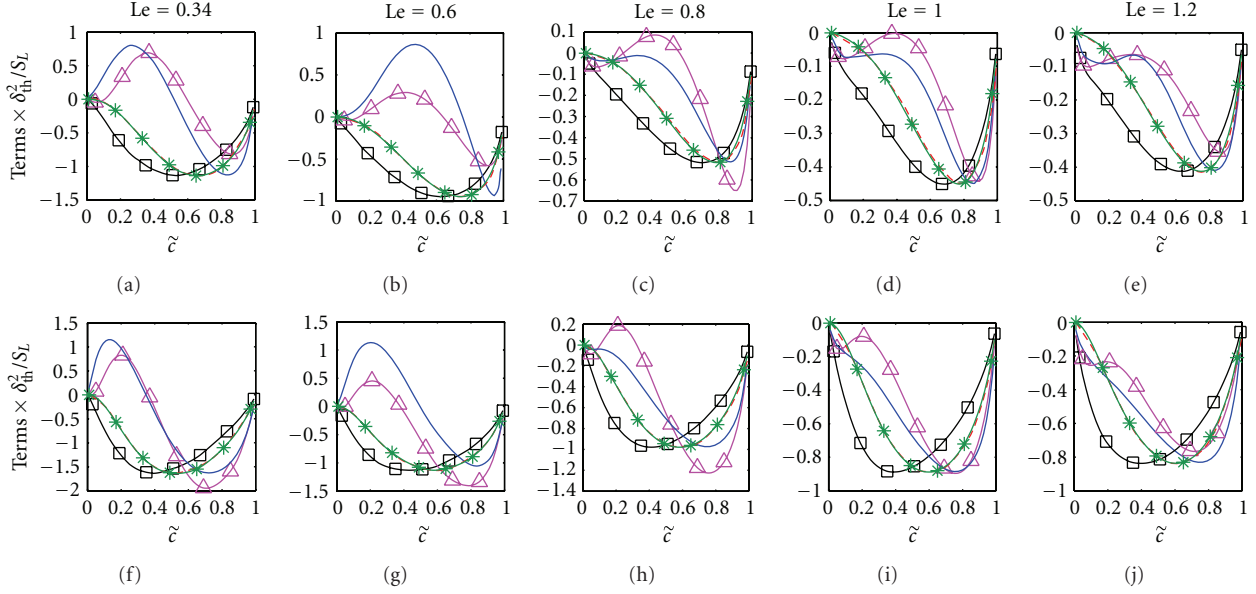


FIGURE 7: Variation of C_{sg} (solid line) conditionally averaged in bins of \tilde{z} across the flame brush along with the predictions of CSGCAND (asterisk line), CSGCANT (dashed line), CSGCHAR (squared line) and CSGNEW (triangle line) for filter sizes $\Delta = 8\Delta_m \approx 0.8\delta_{th}$ (top row): (a) $Le = 0.34$ (1st column); (b) $Le = 0.6$ (2nd column); (c) $Le = 0.8$ (3rd column); (d) $Le = 1.0$ (4th column); (e) $Le = 1.2$ (5th column) and for filter size $\Delta = 24\Delta_m \approx 2.4\delta_{th}$ (bottom row): (f) $Le = 0.34$ (1st column); (g) $Le = 0.6$ (2nd column); (h) $Le = 0.8$ (3rd column); (i) $Le = 1.0$ (4th column); (j) $Le = 1.2$ (5th column).

Equations (13) and (15a)–(15e) can be combined to propose a model for C_{sg} in the following manner:

$$C_{sg} = \frac{-\beta_4 (\Sigma_{gen} - |\nabla \tilde{c}|) (\tilde{c} - c^*) S_L \Sigma_{gen}}{\{\exp[-a_\Sigma (1 - \tilde{c})] \tilde{c} (1 - \tilde{c})^m\}} - \frac{\beta_5 S_L (\Xi_\Delta - 1)^n \Sigma_{gen}^2}{\tilde{c} (1 - \tilde{c})}. \quad (18)$$

The above model will henceforth be referred to CSGNEW model in this paper. Equation (18) allows for a positive contribution of C_{sg} through the contribution of $-\beta_4 (\Sigma_{gen} - |\nabla \tilde{c}|) (\tilde{c} - c^*) S_L \Sigma_{gen} / \{\exp[-a_\Sigma (1 - \tilde{c})] \tilde{c} (1 - \tilde{c})^m\}$, which is absent in the CSGCAND, CSGCANT, and CSGCHAR models. The predictions of the CSGCAND, CSGCANT, CSGCHAR, and CSGNEW models for $\Delta = 0.8\delta_{th}$ and $\Delta = 2.4\delta_{th}$ are compared with C_{sg} obtained from DNS in Figure 7 for the optimum values of β_1 , β_2 , β_3 , and β_5 . The optimum values of β_1 , β_2 , and β_3 are estimated by calibrating the models based on the ensemble averaged value of C_{sg} obtained from DNS data. The variations of the optimum values of β_1 , β_2 , and β_3 with Δ for all cases are also shown in Figure 6. It is evident from Figure 6 that β_1 , β_2 , β_3 , and β_5 remain greater than unity for all cases. This is found to be consistent with the realisability analysis by Hawkes and Cant [52]. Figure 6 further demonstrates that the optimum values of β_1 , β_2 , and β_3 change appreciably with increasing Δ , which is consistent with earlier findings [9, 10, 12]. Moreover, optimum values of β_1 , β_2 , and β_3 for a given Δ are affected by Le (see Figure 6). It is worth noting that parameterisation of the optimum values of β_1 , β_2 and β_3 also yields complex relations similar to (15a)–(15e) and (17a)–(17d). However, such parameterisation is

not presented here because the CSGCAND, CSGCANT, and CSGCHAR models do not capture the qualitative behaviour of C_{sg} for the $Le = 0.34$ and 0.6 flames.

It can further be seen from Figure 7 that the CSGCHAR model tends to overpredict the negative values of C_{sg} towards the unburned gas side in cases C–E ($Le = 0.8, 1.0$ and 1.2 flames), and this behaviour becomes more prominent with increasing filter size. It is clear from Figure 7 that for $\Delta = 24\Delta_m = 2.4\delta_{th}$, the CSGCHAR model predicts the maximum magnitude of C_{sg} near the middle of the flame whereas the actual maximum magnitude of C_{sg} is attained slightly towards the burned gas side. The CSGCAND and CSGCANT models give comparable performance for optimum values of β_1 and β_2 in cases C–E. However, the CSGCAND and CSGCANT models do not satisfactorily capture the qualitative behaviour of C_{sg} and underpredict (overpredict) the magnitude of C_{sg} towards the burned gas side (middle) of the flame brush in the $Le = 0.8, 1.0$ and 1.2 flames. Figure 7 demonstrates that the CSGNEW model captures the qualitative behaviour of C_{sg} in a better manner than the CSGCAND and CSGCANT models and the quantitative agreement between C_{sg} and the CSGNEW model remains better than the CSGCAND, CSGCANT, and CSGCHAR models in all cases for all values of Δ when optimum values of β_4 , β_5 , a_Σ , and c^* are used.

5. Conclusions

The LES modelling of the curvature term $(S_d \nabla \cdot \vec{N})_s \Sigma_{gen}$ of the generalised FSD Σ_{gen} transport equation has been addressed here using a simplified chemistry-based DNS database of freely propagating statistically planar turbulent

premixed flames with Lewis number Le ranging from 0.34 to 1.2. The statistical behaviours of the subgrid curvature term C_{sg} for a range of different values of Δ have been analysed in terms of its contributions C_{sg1} and C_{sg2} arising from the combined reaction and normal diffusion component and tangential diffusion components of displacement speed (i.e., $(S_r + S_n)$ and $S_t = -2D\kappa_m$), respectively. The Lewis number is shown to have significant influences on the statistical behaviours of the resolved and subgrid components of the FSD curvature term. Detailed physical explanations have been provided for the observed filter size and Lewis number dependences of the different components of $(S_d \nabla \cdot \vec{N})_s \Sigma_{gen}$. Models have been identified for individual components of the subgrid curvature term (i.e., C_{sg1} and C_{sg2}), and the performances of these models have been compared to the corresponding quantities extracted from DNS data. It has been found that the new models for C_{sg1} and C_{sg2} satisfactorily capture the statistical behaviours of the corresponding terms extracted from DNS data. It has been found that the existing models for the subgrid curvature term C_{sg} do not satisfactorily capture the qualitative behaviour of the corresponding quantity extracted from DNS data for all the flames considered here. This problem is particularly prevalent for flames with small values of Lewis number (e.g., $Le = 0.34$ and 0.6) where C_{sg} locally assumes positive values, whereas the existing models can only predict negative values of C_{sg} . The performance of the newly proposed model for C_{sg} has been found to be better than the existing models, and it has been shown to capture positive contributions of C_{sg} for the $Le \ll 1$ flames. The present analysis has been carried out using a DNS database with moderate value of Re_t in the absence of the effects of detailed chemistry and transport. As simplified chemistry-based DNS qualitatively captures the curvature $\kappa_m = \nabla \cdot \vec{N}/2$ and strain rate dependences of S_d and $|\nabla c|$ obtained from detailed chemistry based simulations, it can be expected that the statistical behaviours of the curvature term $(S_d \nabla \cdot \vec{N})_s \Sigma_{gen}$ presented in this paper will be valid at least in a qualitative sense in the context of detailed chemistry. However, the quantitative values of the model parameters (i.e., β_4 , β_5 , a_Σ , and c^*) may need to be altered in the presence of detailed chemistry. Thus, three-dimensional DNS data with detailed chemistry and experimental data at higher values of Re_t will be necessary for more comprehensive modelling of $(S_d \nabla \cdot \vec{N})_s \Sigma_{gen}$ and C_{sg} in the context of LES. Moreover, the newly proposed models need to be implemented in LES simulations for the purpose of *a posteriori* assessments. However, this is kept beyond the scope of this paper. Several previous studies [3–7, 9–12, 43–49] concentrated purely on the model development based on *a priori* analysis of DNS data and the same approach has been adopted here. Implementation of the newly developed models in LES simulations will form the basis of future investigations.

Acknowledgment

The financial support by EPSRC, UK, is gratefully acknowledged.

References

- [1] R. S. Cant, S. B. Pope, and K. N. C. Bray, "Modelling of flamelet surface-to-volume ratio in turbulent premixed combustion," *Proceedings of the Combustion Institute*, vol. 23, no. 1, pp. 809–815, 1991.
- [2] S. Candel, D. Veynante, F. Lacas, E. Maistret, N. Darabhia, and T. Poinot, "Coherent flamelet model: applications and recent extensions," in *Recent Advances in Combustion Modelling*, B. E. Larrouturou, Ed., pp. 19–64, World Scientific, Singapore, 1990.
- [3] M. Boger, D. Veynante, H. Boughanem, and A. Trouvé, "Direct numerical simulation analysis of flame surface density concept for large eddy simulation of turbulent premixed combustion," *Proceedings of the Combustion Institute*, vol. 27, no. 1, pp. 917–925, 1998.
- [4] F. Charlette, A. Trouvé, M. Boger, and D. Veynante, "A flame surface density model for large eddy simulations of turbulent premixed flames," in *Proceedings of the Joint Meeting of the British, German and French Sections of the Combustion Institute*, Nancy, France, 1999.
- [5] E. R. Hawkes, *Large eddy simulation of premixed turbulent combustion [Ph.D. thesis]*, Cambridge University Engineering Department, Cambridge, U.K., 2000.
- [6] E. R. Hawkes and R. S. Cant, "A flame surface density approach to large-eddy simulation of premixed turbulent combustion," *Proceedings of the Combustion Institute*, vol. 28, no. 1, pp. 51–58, 2000.
- [7] E. R. Hawkes and R. S. Cant, "Implications of a flame surface density approach to large eddy simulation of premixed turbulent combustion," *Combustion and Flame*, vol. 126, no. 3, pp. 1617–1629, 2001.
- [8] R. Knikker, D. Veynante, and C. Meneveau, "A dynamic flame surface density model for large eddy simulation of turbulent premixed combustion," *Physics of Fluids*, vol. 16, no. 11, pp. L91–L94, 2004.
- [9] N. Chakraborty, *Fundamental study of turbulent premixed combustion using direct numerical simulation (DNS) [Ph.D. thesis]*, Cambridge University Engineering Department, Cambridge, U.K., 2005.
- [10] N. Chakraborty and R. S. Cant, "A priori analysis of the curvature and propagation terms of the flame surface density transport equation for large eddy simulation," *Physics of Fluids*, vol. 19, no. 10, Article ID 105101, 2007.
- [11] N. Chakraborty and M. Klein, "A priori direct numerical simulation assessment of algebraic flame surface density models for turbulent premixed flames in the context of large eddy simulation," *Physics of Fluids*, vol. 20, no. 8, Article ID 085108, 2008.
- [12] N. Chakraborty and R. S. Cant, "Direct numerical simulation analysis of the flame surface density transport equation in the context of large eddy simulation," *Proceedings of the Combustion Institute*, vol. 32, no. 1, pp. 1445–1453, 2009.
- [13] F. E. Hernandez-Perez, F. T. C. Yuen, C. P. T. Groth, and O. L. Gulder, "LES of a laboratory-scale turbulent premixed Bunsen flame using FSD, PCM-FPI and thickened flame models," *Proceedings of the Combustion Institute*, vol. 33, no. 1, pp. 1365–1371, 2011.
- [14] M. Katragadda and N. Chakraborty, "Effects of Lewis number on flame surface density transport in the context of large eddy simulation," in *Proceedings of the 5th European Combustion Meeting*, Cardiff University, Cardiff, UK, June 2011.
- [15] M. Mizomoto, Y. Asaka, S. Ikai, and C. K. Law, "Effects of preferential diffusion on the burning intensity of curved

- flames," *Proceedings of the Combustion Institute*, vol. 20, no. 1, pp. 1933–1939, 1985.
- [16] H. G. Im and J. H. Chen, "Preferential diffusion effects on the burning rate of interacting turbulent premixed hydrogen-air flames," *Combustion and Flame*, vol. 131, no. 3, pp. 246–258, 2002.
- [17] G. I. Sivashinsky, "Instabilities, pattern formation, and turbulence in flames," *Annual Review of Fluid Mechanics*, vol. 15, pp. 179–199, 1983.
- [18] P. Clavin and F. A. Williams, "Effects of molecular diffusion and thermal expansion on the structure and dynamics of turbulent premixed flames in turbulent flows of large scale and small intensity," *Journal of Fluid Mechanics*, vol. 116, pp. 251–282, 1982.
- [19] P. A. Libby, A. Linan, and F. A. Williams, "Strained premix laminar flames with nonunity Lewis numbers," *Combustion Science and Technology*, vol. 34, no. 1–6, pp. 257–293, 1983.
- [20] R. G. Abdel-Gayed, D. Bradley, M. N. Hamid, and M. Lawes, "Lewis number effects on turbulent burning velocity," *Proceedings of the Combustion Institute*, vol. 20, no. 1, pp. 505–512, 1985.
- [21] W. T. Ashurst, N. Peters, and M. D. Smooke, "Numerical simulation of turbulent flame structure with non-unity Lewis number," *Combustion Science and Technology*, vol. 53, no. 4–6, pp. 339–375, 1987.
- [22] D. C. Haworth and T. J. Poinso, "Numerical simulations of Lewis number effects in turbulent premixed flames," *Journal of Fluid Mechanics*, vol. 244, pp. 405–436, 1992.
- [23] C. J. Rutland and A. Trouvé, "Direct simulations of premixed turbulent flames with nonunity Lewis numbers," *Combustion and Flame*, vol. 94, no. 1–2, pp. 41–57, 1993.
- [24] A. Trouvé and T. Poinso, "The evolution equation for the flame surface density in turbulent premixed combustion," *Journal of Fluid Mechanics*, vol. 278, pp. 1–31, 1994.
- [25] N. Chakraborty and R. S. Cant, "Influence of Lewis number on curvature effects in turbulent premixed flame propagation in the thin reaction zones regime," *Physics of Fluids*, vol. 17, no. 10, Article ID 105105, 2005.
- [26] N. Chakraborty and R. S. Cant, "Effects of Lewis number on turbulent scalar transport and its modelling in turbulent premixed flames," *International Journal of Heat and Mass Transfer*, vol. 49, no. 13–14, pp. 2158–2172, 2006.
- [27] N. Chakraborty and M. Klein, "Influence of Lewis number on the surface density function transport in the thin reaction zone regime for turbulent premixed flames," *Physics of Fluids*, vol. 20, no. 6, Article ID 065102, 2008.
- [28] N. Chakraborty and R. S. Cant, "Effects of Lewis number on turbulent scalar transport and its modelling in turbulent premixed flames," *Combustion and Flame*, vol. 156, no. 7, pp. 1427–1444, 2009.
- [29] N. Chakraborty and R. S. Cant, "Effects of Lewis number on flame surface density transport in turbulent premixed combustion," *Combustion and Flame*, vol. 158, no. 9, pp. 1768–1787, 2011.
- [30] N. Peters, P. Terhoeven, J. H. Chen, and T. Echekeki, "Statistics of flame displacement speeds from computations of 2-D unsteady methane-air flames," *Proceedings of the Combustion Institute*, vol. 27, no. 1, pp. 833–839, 1998.
- [31] T. Echekeki and J. H. Chen, "Analysis of the contribution of curvature to premixed flame propagation," *Combustion and Flame*, vol. 118, no. 1–2, pp. 308–311, 1999.
- [32] J. H. Chen, A. Choudhary, B. de Supinski et al., "Terascale direct numerical simulations of turbulent combustion using S3D," *Computational Science & Discovery*, vol. 2, no. 1, Article ID 015001, 2009.
- [33] N. Chakraborty and S. Cant, "Unsteady effects of strain rate and curvature on turbulent premixed flames in an inflow-outflow configuration," *Combustion and Flame*, vol. 137, no. 1–2, pp. 129–147, 2004.
- [34] N. Chakraborty and R. S. Cant, "Effects of strain rate and curvature on surface density function transport in turbulent premixed flames in the thin reaction zones regime," *Physics of Fluids*, vol. 17, no. 6, Article ID 065108, pp. 1–15, 2005.
- [35] N. Chakraborty, E. R. Hawkes, J. H. Chen, and R. S. Cant, "The effects of strain rate and curvature on surface density function transport in turbulent premixed methane-air and hydrogen-air flames: a comparative study," *Combustion and Flame*, vol. 154, no. 1–2, pp. 259–280, 2008.
- [36] K. W. Jenkins and R. S. Cant, "DNS of turbulent flame kernels," in *Proceedings of the 2nd AFOSR Conference on DNS and LES*, pp. 192–202, Kluwer Academic Publishers, 1999.
- [37] T. J. Poinso and S. K. Lele, "Boundary conditions for direct simulations of compressible viscous flows," *Journal of Computational Physics*, vol. 101, no. 1, pp. 104–129, 1992.
- [38] A. A. Wray, "Minimal storage time advancement schemes for spectral methods," Technical Report MS 202 A-1, NASA Ames Research Center, California, Calif, USA, 1990.
- [39] R. S. Rogallo, "Numerical experiments in homogeneous turbulence," NASA Technical Memorandum 91416, NASA Ames Research Center, California, Calif, USA, 1981.
- [40] G. K. Batchelor and A. A. Townsend, "Decay of turbulence in final period," *Proceedings of the Royal Society A*, vol. 194, no. 1039, pp. 527–543, 1948.
- [41] N. Peters, *Turbulent Combustion*, Cambridge University Press, Cambridge, UK, 2000.
- [42] D. C. Haworth, R. J. Blint, B. Cuenot, and T. J. Poinso, "Numerical simulation of turbulent propane-air combustion with nonhomogeneous reactants," *Combustion and Flame*, vol. 121, no. 3, pp. 395–417, 2000.
- [43] F. Charlette, C. Meneveau, and D. Veynante, "A power-law flame wrinkling model for LES of premixed turbulent combustion—part I: non-dynamic formulation and initial tests," *Combustion and Flame*, vol. 131, no. 1–2, pp. 159–180, 2002.
- [44] N. Swaminathan and K. N. C. Bray, "Effect of dilatation on scalar dissipation in turbulent premixed flames," *Combustion and Flame*, vol. 143, no. 4, pp. 549–565, 2005.
- [45] N. Swaminathan and R. W. Grout, "Interaction of turbulence and scalar fields in premixed flames," *Physics of Fluids*, vol. 18, no. 4, Article ID 045102, 2006.
- [46] I. Han and K. Y. Huh, "Roles of displacement speed on evolution of flame surface density for different turbulent intensities and Lewis numbers in turbulent premixed combustion," *Combustion and Flame*, vol. 152, no. 1–2, pp. 194–205, 2008.
- [47] R. W. Grout, "An age extended progress variable for conditioning reaction rates," *Physics of Fluids*, vol. 19, no. 10, Article ID 105107, 2007.
- [48] N. Chakraborty and N. Swaminathan, "Effects of Lewis number on scalar dissipation transport and its modeling in turbulent premixed combustion," *Combustion Science and Technology*, vol. 182, no. 9, pp. 1201–1240, 2010.
- [49] N. Chakraborty and N. Swaminathan, "Effects of Lewis number on scalar variance transport in premixed flames," *Flow, Turbulence and Combustion*, vol. 87, no. 2–3, pp. 261–292, 2010.

- [50] H. G. Weller, G. Tabor, A. D. Gosman, and C. Fureby, "Application of a flame-wrinkling LES combustion model to a turbulent mixing layer," *Proceedings of the Combustion Institute*, vol. 27, no. 1, pp. 899–907, 1998.
- [51] G. Tabor and H. G. Weller, "Large eddy dimulation of pre-mixed turbulent combustion using Ξ flame surface wrinkling model," *Flow, Turbulence and Combustion*, vol. 72, no. 1, pp. 1–27, 2004.
- [52] E. R. Hawkes and R. S. Cant, "Physical and numerical realizability requirements for flame surface density approaches to large-eddy and Reynolds averaged simulation of premixed turbulent combustion," *Combustion Theory and Modelling*, vol. 5, no. 4, pp. 699–720, 2001.

Research Article

Analysis of Hydrodynamics of Fluid Flow on Corrugated Sheets of Packing

Kumar Subramanian and Günter Wozny

Berlin Institute of Technology, StraÙ des 17 Juni 135 Berlin, Germany

Correspondence should be addressed to Günter Wozny, guenter.wozny@tu-berlin.de

Received 10 February 2012; Revised 7 May 2012; Accepted 16 May 2012

Academic Editor: Sreepriya Vedantam

Copyright © 2012 K. Subramanian and G. Wozny. This is an open access article distributed under the Creative Commons Attribution License, which permits unrestricted use, distribution, and reproduction in any medium, provided the original work is properly cited.

Modelling of the hydrodynamics behaviour of the liquid on the corrugated sheets of packing is studied using three-dimensional, volume-of-fluid (VOF) model that is incorporated in Ansys Fluent 12.0. The flow of three different liquids with different physical properties is modelled. A domain of corrugated sheets of packing resembling the real structured packing with little modifications in the elementary geometry is constructed using ICEM CFD 12.0. The quantitative comparisons of the wetting behavior from the simulations are in good agreement with experiments. Further, the study has been extended to understand the influence of the second corrugated sheet on the flow behavior. The contours from the simulations indicate the liquid hold-up in the crimp of two corrugated sheets, and these results are in good agreement with the earlier experimental studies performed using X-ray tomography in the literature. The result from the simulation shows that even for the high flow rate of around 811 mL/min for silicon-oil (DC5), only 60% of the corrugated sheet has been wetted. Hence, the efficiency of the existing packing can be further increased by increasing the wetted area in the corrugated sheet of packing.

1. Introduction

The key to success in separation of liquid mixtures by distillation depends on the creation and utilization of vapor-liquid contact area. The three major types of distillation equipments are trays, random packing, and structured packing. The corrugated sheet of packing, introduced in the late 1970s, became competent by claiming higher capacity and lower sensitivity to solids while retaining the high efficiency. Hence, by 1980s, the corrugated sheets of structured packing have drawn increased attention in industry [1]. The reason for the increased efficiency with structured packing is reported as additional mass transfer due to the increase in interfacial area created by spreading liquid over the packing surface [1]. Even though the structured packing is well established, the local flow behavior inside the packing is still not well understood. Various efforts have been exerted by researchers around the world using different approaches to know about the local flow behavior that helps to design the packed column and in terms of increasing their efficiency.

Geometrical features of corrugated sheets of packing play a crucial role in flow behavior of fluid inside the packing.

Geometrical modifications of the packing are possible in three different ways: (1) varying surface of the corrugated sheet with grooved, lanced, textured, or smoothened surface, (2) changing the size of small elemental geometry like corrugation size and angle, and (3) with or without perforations.

1.1. Elementary Geometry. An elementary geometry of the corrugated sheet of packing is shown in Figure 1. The corrugation size defines the opening between adjacent corrugated layers. The ratio of B to h and S to h and the crimp angle (β) define the geometry of flow channel and of the vapor-liquid contact zone, respectively. Packing can be classified based on the specific surface area. Crimp angle varies from 28° to 45° , and base-to-height ratios range from 2 : 1 to 4 : 1. Most of the packing is not strictly triangle as shown below but is rounded top apex. The corrugation angle (α) also plays important role in deciding the capacity of the packing.

The element height is relatively low (typically 20 to 28 cm), and the angle of rotation is around 90° . Corrugation angle of 45° to the vertical enables good flow of liquid and avoids liquid accumulation.

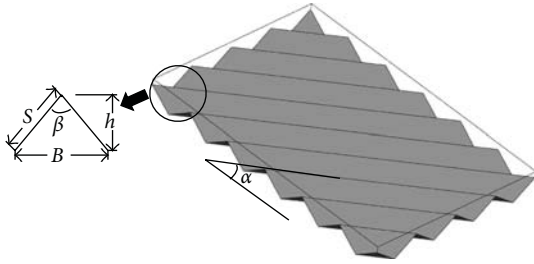


FIGURE 1: Elementary geometry details of the corrugated sheet of packing.

The effect of the opening angle on the performance of the structured packing was studied earlier [2]. Two different opening angles of 90° and 20° were both studied numerical- and experimental-wise. It was also presented that when the opening angle was decreased from 90 to 20° , pressure drop of the packing could reduce by 35% and mass transfer could increase by 13% compared to Mellapak packing having the same specific surface area [2].

The results of two different packing series from Montz GmbH namely, B1 (embossed sheet metal, nonperforated) and BSH (expanded metal, perforated), were studied. In total, six different packings with two different corrugation angles of 45° and 60° and two different specific surfaces of 250 and $400 \text{ m}^2/\text{m}^3$ were investigated. The outcome showed that with increasing corrugation angle the pressure drop decreases, the capacity increases, and the mass transfer decreases. The holes on the surface could be the reason behind the slightly larger capacity of BSH packing in comparison with B1 packing. The influence of the corrugation angle on the performance of the packing was also presented [3].

1.2. Surface Features. Most of the structured packing surfaces have roughened or enhanced surfaces that assist the lateral spread of liquid, promote film turbulence, and enhance the area available for mass transfer. Measurements performed in the laboratory scale showed that mass transfer efficiency and wetter area are enhanced by textured surfaces. Texturing is of various types like grooving, lancing, shallow embossing, and deep embossing. Some different surface textures available in corrugated sheet of packing is shown in Figure 2. Figure 2(a) shows the corrugated sheet of packing without any surface textures but with perforations. Figures 2(b) and 2(c) show the three-dimensional surface textures on the packing. Various research studies have contributed exclusively to the study of the influence of surface textures on flow behavior and their further impact on mass transfer. The effect of 2-dimensional roughnesses on the flow behavior followed by gas-liquid absorption was reported [4]. The rate of absorption of CO_2 into water flowing over a plate with large-scale roughness can go up to 3.5 times faster than a smooth plate. The results were also compared with theoretical correlations. Similarly, various research contributions were presented to know the influence of film flow on complex and periodic surfaces [5–7]. The surface of most of the structured packing contains perforations.

1.3. CFD Studies. The geometry representing the column of 960 mm height with 288 mm inner diameter was meshed. Four elements of packing, rotated against each other by 90° with effective corrugation angle of 19° , were used. The model of packing of MELLAPAK 250Y made from polypropylene was employed. Simulations are carried out using CFX 10.0 to study the countercurrent two-phase flow [8]. Numerical result of the liquid flow shows the flow of liquid phase through the packing as well as the redistribution of liquid phase when liquid meets the joint of the packing elements. The flow behavior was also studied experimentally using X-ray tomographic visualization technique with contrast agent tracer [9].

An exclusive investigation was performed to study the flow behavior of liquid film and rivulets on inclined planes. The volume-of-fluid-like model in CFX 5.0 was utilized to study the same. The influence of surface tension was taken into account, and the simulation studies were validated with experimental work [10–13].

A direct numerical simulation to study physical and reactive absorption in gas-liquid flow on structured packing was recently published. It also showed that the liquid side mass transfer is well predicted by the Higbie theory. The numerical results were compared to approximate solution presented in the literature [14, 15]. Van Baten and Krishna [16] studied the gas and liquid mass transfer in katapak-S structures using CFD simulations, and gas phase mass transfer was in good agreement with the theoretical correlation of Viva et al. [17], whereas the liquid phase mass transfer was onefold lesser than the correlation.

In the present work, the three-dimensional volume-of-fluid (VOF) model is presented to study the flow of liquid on the corrugated sheet of packing. The surface tension of the liquid has been taken into consideration using continuum surface (CSF) model. The transient simulations are performed using the geometric reconstruction scheme for interpolation near the interface, and SIMPLEC-based solver was utilized. The comparison between the simulation and experimental studies is also presented. Further, the study was extended to study the wetting behavior for two corrugated sheets of packing.

2. Numerical Details

2.1. Details of the Model. The simulations are carried out with the commercial tool ANSYS Fluent 12.0, ANSYS Inc [18].

2.1.1. Volume-of-Fluid (VOF) Model. The volume-of-fluid (VOF) model, which is one of the limiting cases of Euler-Euler homogenous model, is considered in this work. The VOF model considers that the gas and liquid phases are not interpenetrating. For each phase that is added, a variable is introduced. In each control volume, the volume fractions of all phases sum to unity.

The tracking of the interface(s) between the phases is accomplished by the continuity equation for the volume

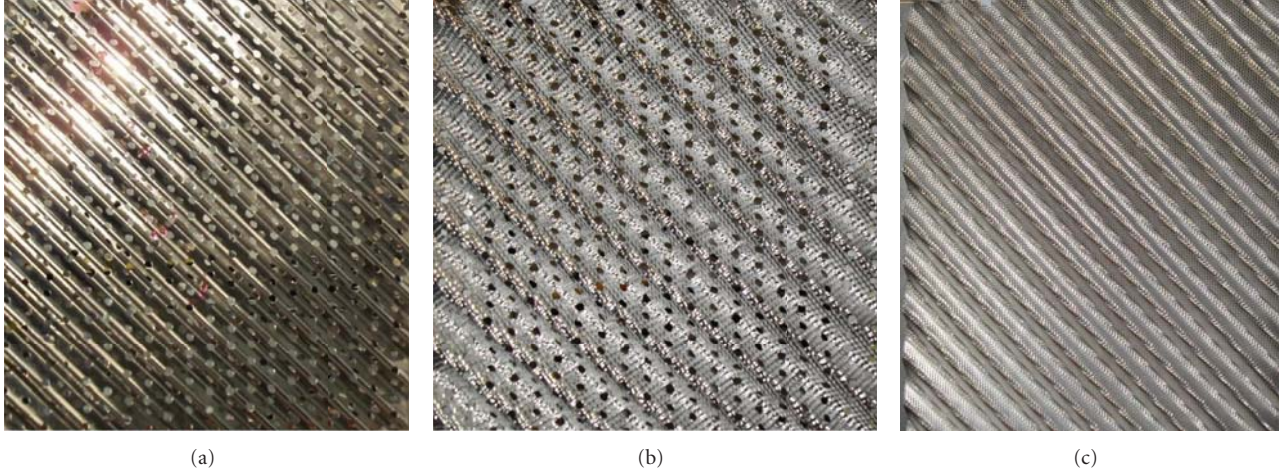


FIGURE 2: Different packings used in industrial applications: (a) smooth, perforated; (b) 3D grooved, perforated; (c) 3D embossed, unperforated.

TABLE 1: Details of different geometries utilized in this work.

S. no.	No. of sheets	Crimp apex	Perforations	Surface textures	Crimp angle
C1	One	Sinusoidal	No	Smooth	45°
C2	One	Sinusoidal	Yes	Smooth	45°
C3	Two	Sinusoidal	No	Smooth	45°

fraction of one (or more) of the phases. For the q th phase, this equation has the following form:

$$\frac{1}{\rho_Q} \left[\frac{\partial}{\partial t} (\alpha_q \rho_q) + \nabla \cdot (\alpha_q \rho_q \vec{v}_q) = S_{\alpha_q} + \sum_{p=1}^n (\dot{m}_{pq} - \dot{m}_{qp}) \right], \quad (1)$$

where α_q is the volume fraction of the q th phase, ρ is the density, and S is the source term.

The volume fraction equation will not be solved for the primary phase; the primary-phase volume fraction will be computed based on the following constraint:

$$\sum_{q=1}^n \alpha_q = 1. \quad (2)$$

The volume fraction equation can be solved using explicit time discretization.

2.1.2. Explicit Discretization. In the explicit approach, finite difference interpolation schemes are applied to the volume fraction values that were computed at the previous time step:

$$\frac{\alpha_q^{n+1} \rho_q^{n+1} - \alpha_q^n \rho_q^n}{\Delta t} V + \sum_f (\rho_q U_f^n \alpha_{q,f}^n) = \left[\sum_{p=1}^n (\dot{m}_{pq} - \dot{m}_{qp}) + S_{\alpha_q} \right] V, \quad (3)$$

where $(n + 1)$ is the index of the new (current) time step, n is the previous time step, $\alpha_{q,f}$ is the face value of the q th fraction, V is the volume of the cell, and U_f is the volume flux through the face, based on normal velocity.

2.1.3. Interpolation near the Interface. Geometric reconstruction scheme was utilized in this work to interpolate variables near the interface between two phases.

In time-dependent VOF calculations, the time step used for the volume fraction calculation will not be the same as the time step used for the rest of the transport equations. ANSYS FLUENT will refine the time step for VOF automatically, based on the input for maximum Courant number allowed near the free surface. The Courant number (Co) is a dimensionless number that compares the time step in a calculation to the characteristic time of transit of a fluid element across a control volume:

$$Co = \frac{\Delta t}{\Delta x_{\text{cell}} / \nu_{\text{fluid}}}, \quad (4)$$

where Δx_{cell} is the minimum cell dimension, ν_{fluid} is the kinematic viscosity of the fluid, and Δt is the time step. The time step used in the simulation is 1×10^{-5} sec. In the region near the fluid interface, ANSYS FLUENT divides the volume of each cell by sum of the outgoing fluxes. The resulting time represents the time it would take the fluid to empty out of the cell.

2.1.4. Surface Tension. The VOF model can also include the effects of surface tension along the interface between each pair of phases. The influence of surface tension source

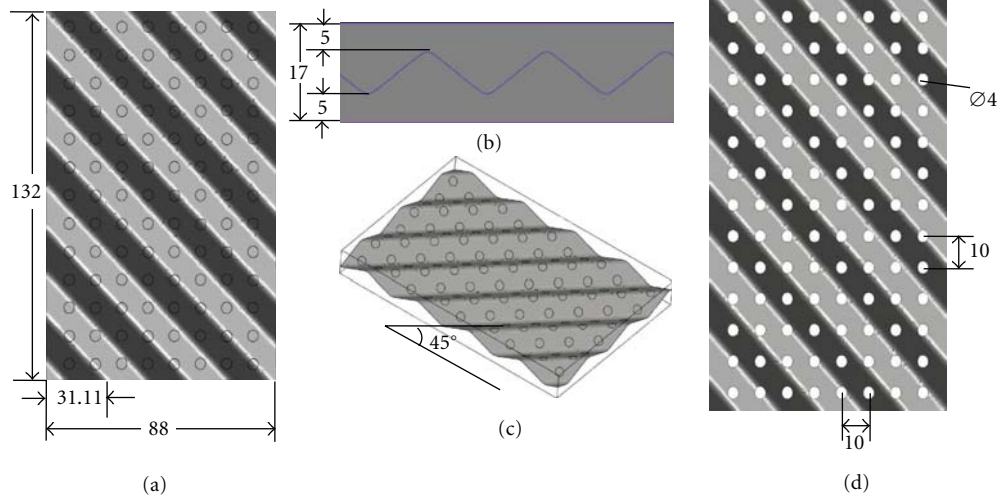


FIGURE 3: Schematic view of geometry of corrugated sheet of packing. (a) Top view: geometry without holes. (b) Side view. (c) Isometric view (d) Top view: geometry with holes. All dimensions are in mm.

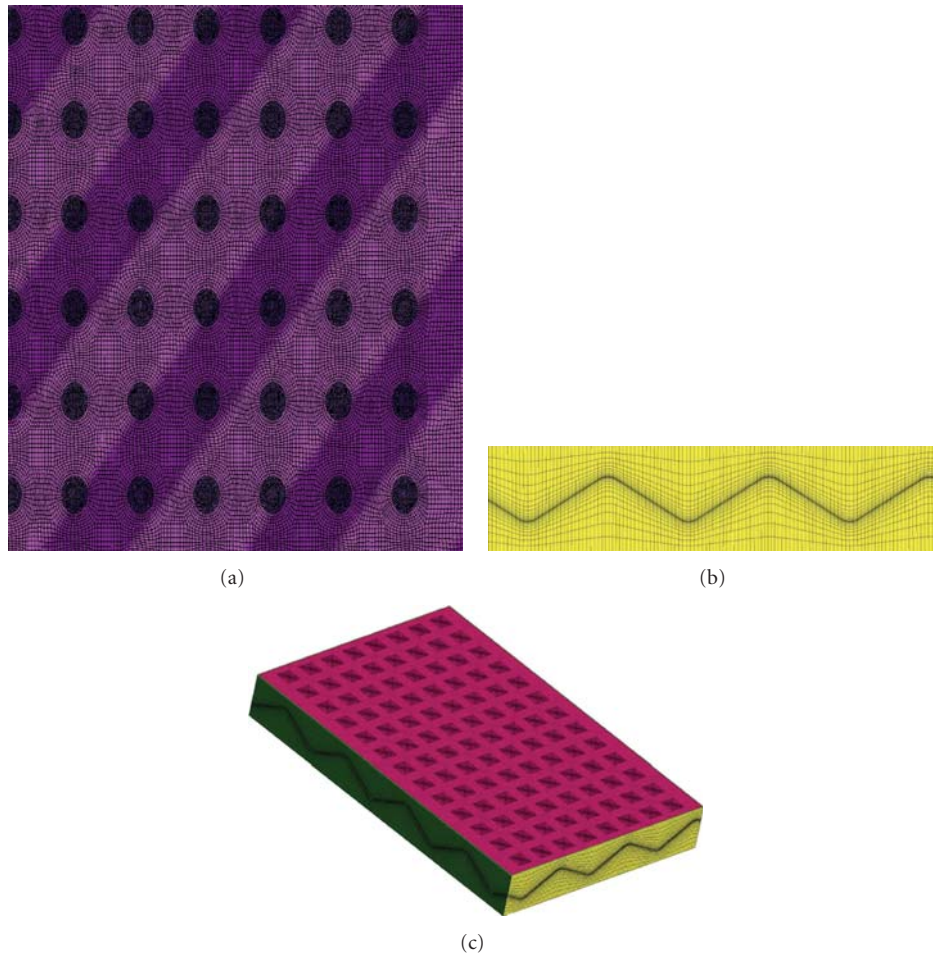


FIGURE 4: Meshes shown in detail for corrugated sheet of packing used in this work. (a) Top view. (b) Side view. (c) Isometric view.

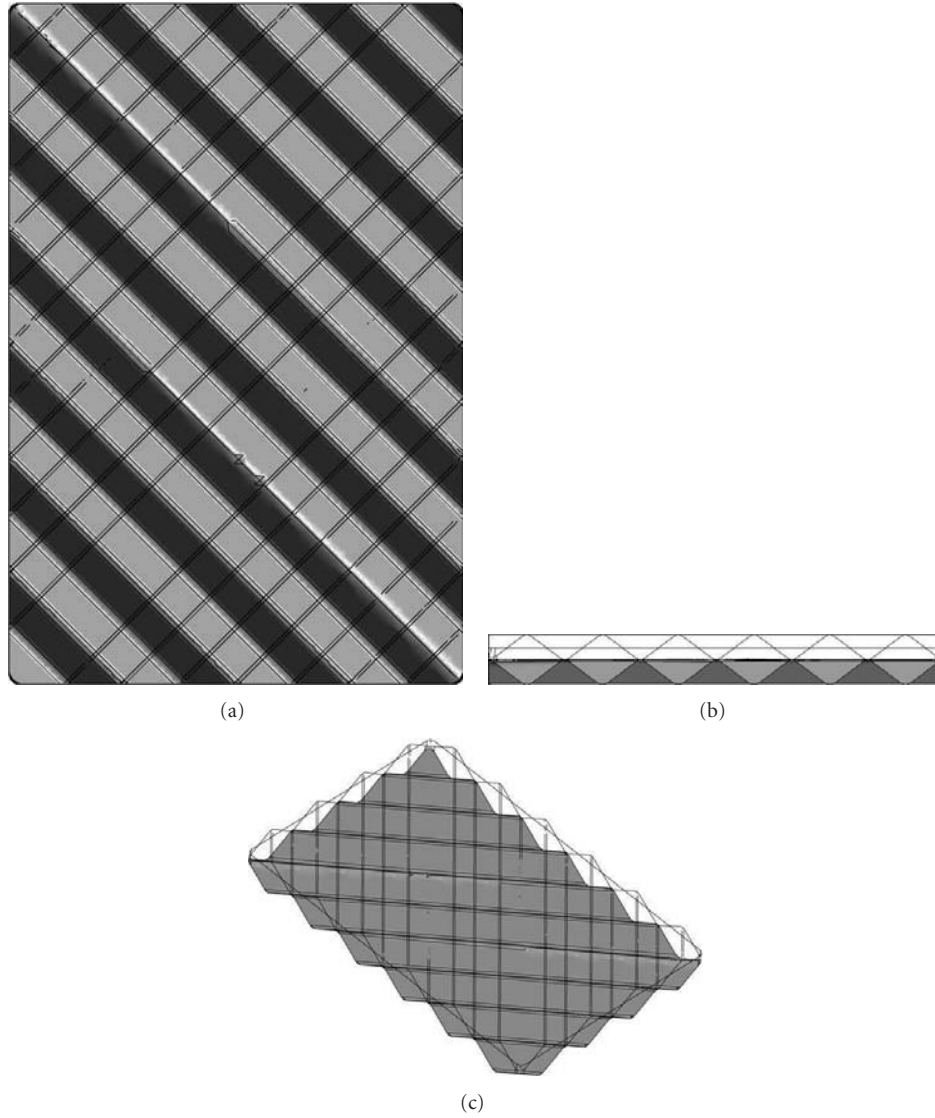


FIGURE 5: Schematic view of two corrugated sheets of packing with smooth crimp. (a) Top views (b) Side view. (c) Isometric view.

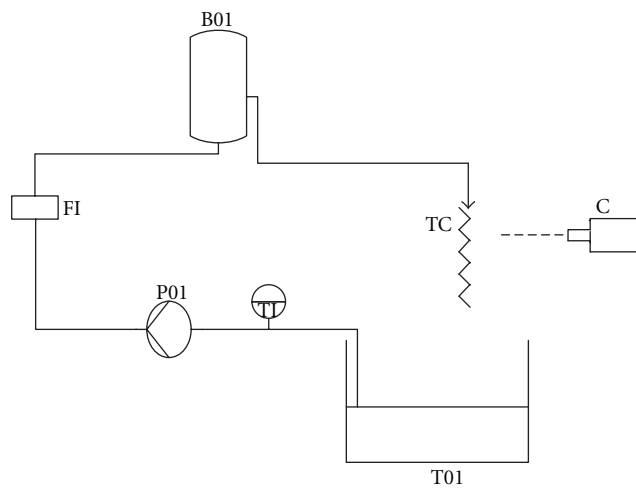


FIGURE 6: Experimental setup used in wetting studies. Sample picture from Water-Glycerol study. P01: pump; B01: buffer tank; TC: test cell; C: camera; FI: flow indicator; TI: thermocouple; T01: solution tank.

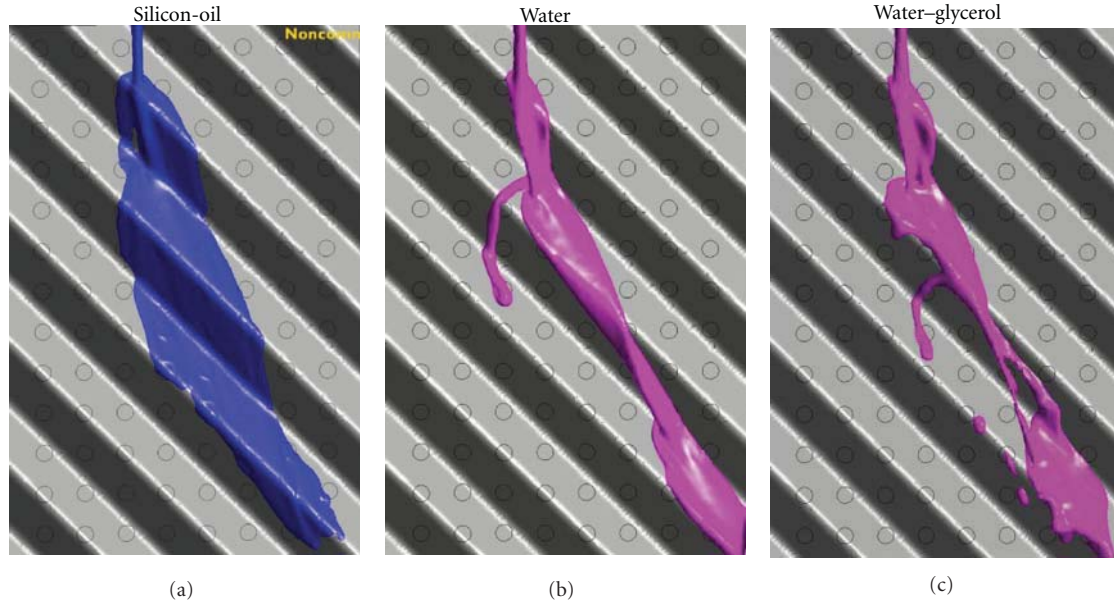


FIGURE 7: Snapshot from simulation for wetting behaviour of silicon-oil (DC5) and water and water-glycerol on corrugated sheet of packing without holes.

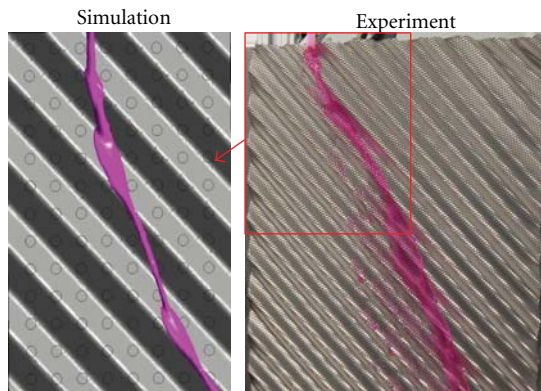


FIGURE 8: Comparison between simulation and experiment for flow of water on corrugated sheet of packing without holes. Flow rate: 386 mL/min. Rectangular box shown in red colour is the geometry considered in simulation studies.

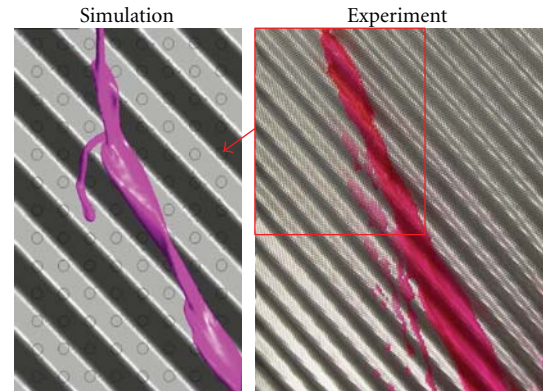


FIGURE 9: Comparison between simulation and experiment for flow of water-glycerol on corrugated sheet of packing without holes. Flow rate: 387 mL/min.

term is taken into account by the continuum surface model (CSF) proposed by Brackbill [19]. The addition of surface tension to the VOF calculation results in a source term in the momentum equation.

All the simulations are performed under transient and laminar conditions. Detailed description of the equation and other assumptions has been already presented [20]. All the simulations are performed on IBM pSeries 690 supercomputers with SGI Altix XE 250 and in 32 parallel nodes of the HLRN (High Performance Computing Network of Northern Germany) at regional computing clusters available at Berlin.

2.2. Geometry and Dimensions. In order to study the flow behaviour in corrugated sheet of packing, three major geometries are considered in this work. Geometries are

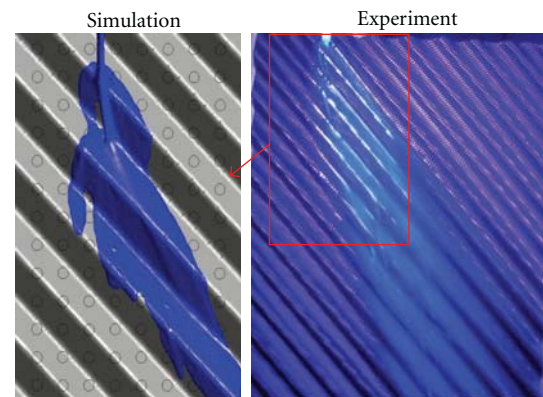


FIGURE 10: Comparison between simulation and experiment for flow of silicon-oil (DC5) on corrugated sheet of packing without holes. Flow rate: 241 mL/min.

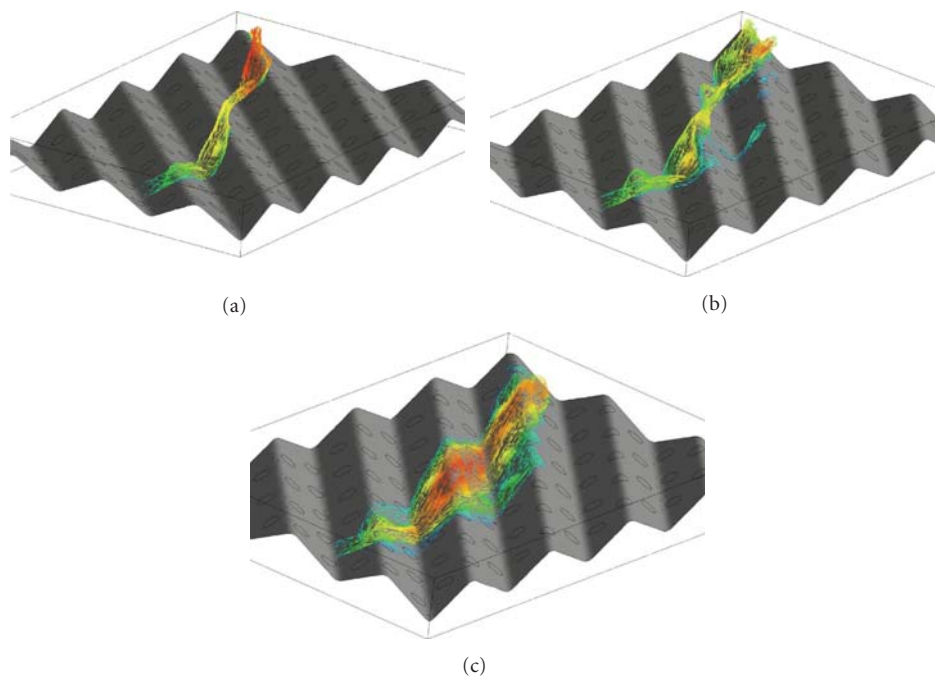


FIGURE 11: Velocity vectors for three liquids flowing through corrugated sheet of packing smooth crimp apex. (a) Water. (b) Water-glycerol. (c) Silicon-oil.

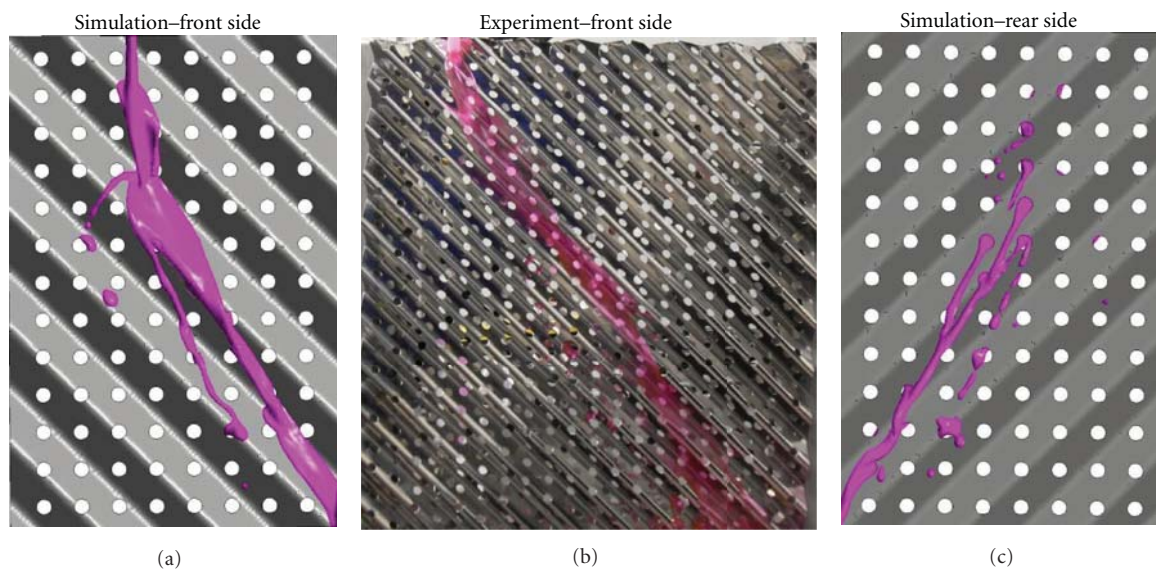


FIGURE 12: Comparison between simulation and experiment for flow of water on corrugated sheet of packing with perforations. Flow rate: 623 mL/min.

developed and meshed using ICEM CFD 12.0 [21]. List of geometries used in this work is presented in Table 1.

The detailed geometries with sinusoidal crimp are shown in Figure 3. Overall dimensions of the geometrical domain are $132 \text{ mm} \times 88 \text{ mm} \times 17 \text{ mm}$. The corrugation angle used in all the geometries is 45° , and the perforation is of 4 mm diameter with pitch of 10 mm along the length and width of the geometry, which is shown in Figure 3(d). The influence of the perforations was taken into consideration by changing the boundary conditions as described in Table 2.

Figure 4 shows the detailed meshing of the geometry shown in Figure 3, and the mesh consists of 1143600 cells. Figure 5 shows the geometry in which two corrugated sheets are arranged as in practical applications, one corrugated sheet is turned 90° to the other.

2.3. Boundary Conditions. Details of the boundary conditions used in the simulations are listed in Table 2. The influence of perforations has been brought in simulation by changing the boundary conditions of holes in the geometry.

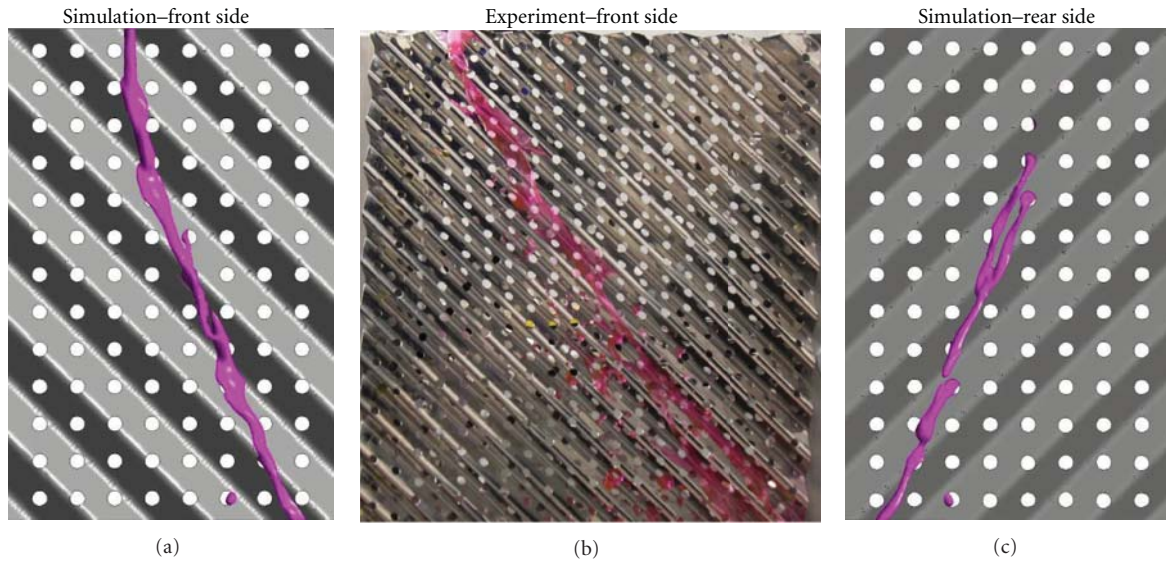


FIGURE 13: Comparison between simulation and experiment for flow of water on corrugated sheet of packing with perforations. Flow rate: 386 mL/min.

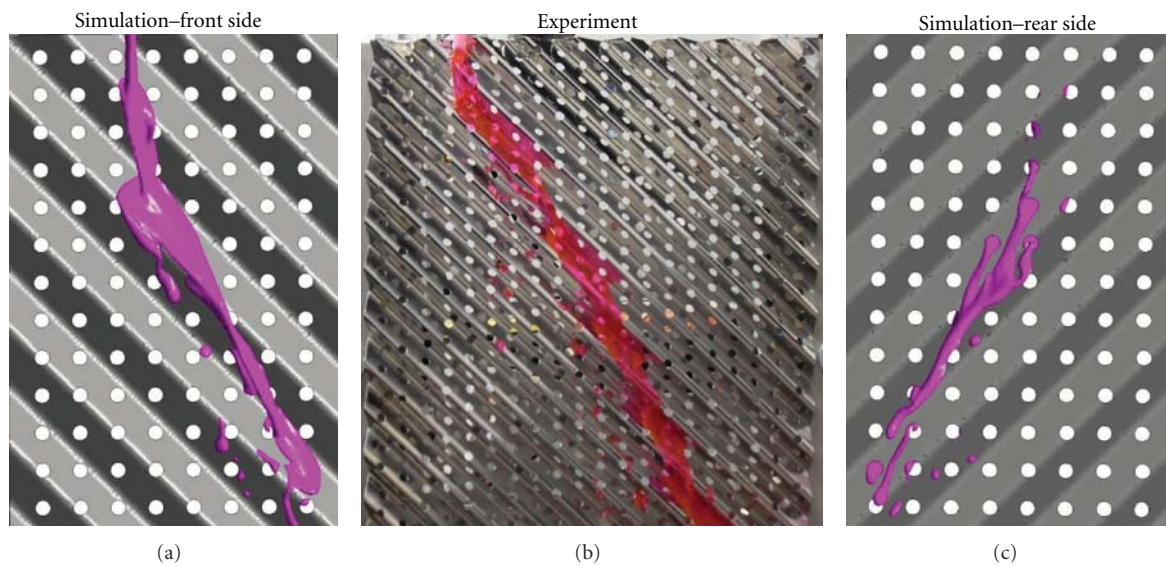


FIGURE 14: Comparison between simulation and experiment for flow of water-glycerol on corrugated sheet of packing with perforations. Flow rate: 590 mL/min.

For the simulation with perforations, boundary conditions of the perforations will be assigned as interior, otherwise it will be assigned as wall. This method helps in using the same geometry for both the simulations and helps in comparing the influence later.

As described in Section 2.1, simulations are performed on three major geometries. For geometry C1 and C2, one inlet of 4 mm pipe was considered just to resemble real flow distributors used in industries. Three different flow rates are studied for each testing system. The details of the flow rates and Reynolds number presented in this work are shown in Table 3.

For simulation using geometry C3, 4 inlets each of 4 mm diameter were considered for study. The aim of using these

4 inlets is to study the maximum wetting possibility in the corrugated sheet of packing. Hence, very high flow rate of 811 mL/min was studied. Two major inlet positions as described in Section 3.3 are also considered.

2.4. Testing Systems. Three different fluids with difference in viscosity and contact angle were selected for this study. The details of the liquids are listed in Table 4. Water-glycerol (45 wt%) and water have similar contact angle but Water-glycerol has higher viscosity than water. Silicon-oil (DC5) has very low contact angle but similar viscosity to that of Water-glycerol (45 wt%). To capture the wetting, Rhodamine-B was used as coloring pigment in water and

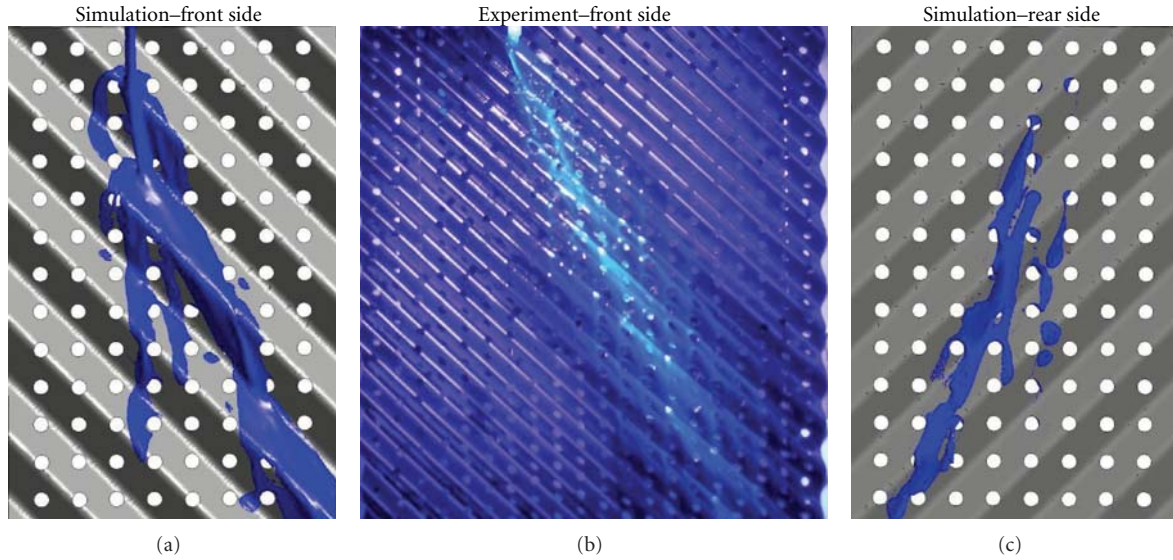


FIGURE 15: Comparison between simulation and experiment for flow of silicon-oil on corrugated sheet of packing with perforations. Flow rate: 508 mL/min.

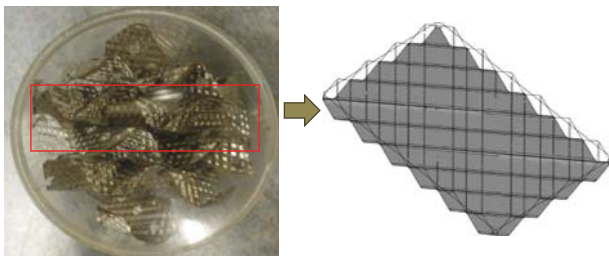
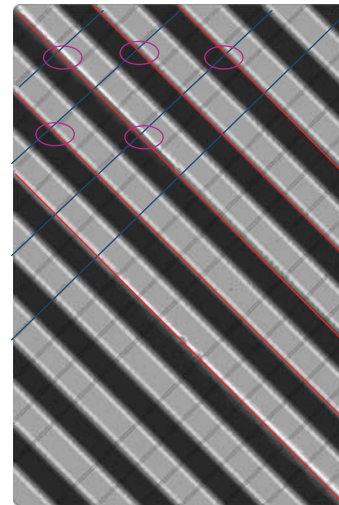


FIGURE 16: Comparison of domains used in simulation from real packing geometry.

TABLE 2: Boundary conditions used in the simulations.

	Simulation without perforations	Simulation with perforations
Inlet	Velocity inlet	Velocity inlet
Outlet	Pressure outlet	Pressure outlet
Top	Pressure outlet	Pressure outlet
Bottom	Pressure outlet	Pressure outlet
Corrugation—base	Wall (CA)	Wall (CA)
Corrugation—holes	Wall (CA)	Interior
Sides	Symmetry	Symmetry



- Crimp in bottom sheet
- Crimp in top sheet
- Meeting points of two sheets

FIGURE 17: Explanation of meeting points from two corrugated sheets of packing and interest of our study.

water-glycerol solution. As the color of the testing system is pink, the wetting can be studied without the help of UV-light. The usage of this coloring pigment has been studied earlier [22], and this will not influence any of the physical parameters of the testing system. For silicon-oil (DC5), Coumarin was used as a coloring agent, which gives blue reflections when studied with the help of UV-light. But the corrugated sheet must be coated with black color to capture the UV light.

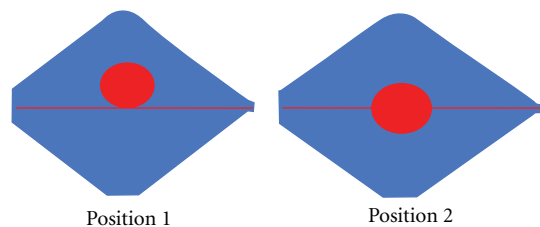


FIGURE 18: Two inlet positions used in the simulation.

TABLE 3: Details of the flow rate and Reynolds number presented in this work.

	Flow rate (mL/min.)	Re
Water	386	2033
	623	3291
Water-glycerol (45%)	386	486
	590	743
Silicon-oil (DC5)	241	230
	508	486

TABLE 4: Properties of the testing system.

	Viscosity η (mPa s)	Density ρ (kg/m ³)	Surface tension σ (mN/m)	Contact angle θ (°)
Water	1	997	72.7	76.6
Water-glycerol (45 Wt%)	4.6	1113	70	69
Silicon-oil (DC5)	4.6	915	18.5	≈ 7

TABLE 5: Wetted area for bottom and top of the packing in % for silicon-oil (DC5).

	Position 1 (%)	Position 2 (%)
Bottom sheet	5.07	15.36
Top sheet	54.42	39.06
Total	59.49	54.42

2.5. Experimental Setup. The flow diagram of the experimental setup is shown in Figure 6. Test liquids were pumped using pump (P01) from the solution tank (T01) to flow through the test cell (TC). Before flowing through the test cell, it passes through the flow indicator (FI) and buffer tank (B01). Buffer tank is used in order to avoid pulsations arising from the pump. A camera (C) is placed in the stand opposite to the corrugated sheet, which enables taking pictures.

3. Results and Discussion

3.1. Flow on Corrugated Sheet with Smooth Crimp Surface without Holes. In this section, comparison between experiment and simulation for flow of three different liquids on corrugated sheet of packing is presented. In Figure 7, a snapshot from simulation for a qualitative comparison of wetting behavior of silicon-oil (DC5), water, and water-glycerol on corrugated sheet is presented. It can be seen that the fluid with low contact angle, that is, silicon-oil (DC5), has more wetting in comparison to water and water-glycerol (45 wt%), which has very high contact angle. In other words, water, and water-glycerol system with high contact angle has a tendency to change its direction towards the corrugation than silicon-oil.

In Figures 8, 9, and 10, the flow and wetting behavior of water, water-glycerol, and silicon-oil (DC5) over corrugated sheet without perforations are shown in comparison with experimental studies. Geometry utilized in the simulation is similar to Figure 3. Liquid flows through circular inlets of

4 mm diameter, which reflects the distributors utilizing in real-time industrial applications, which stands at 90° from base. Experiments are performed on Montz B1-300 packing, which has textured surface. However, geometry used in the simulations is without microstructure on the surface. Hence, the differences are needed to be considered while comparing the simulation and experiments.

As seen in Figures 8–11, the direction of the flow of liquid changes in the direction of corrugation, which helps to utilize the packing surface effectively and hence the wetting area increases. When the liquid flows inside corrugation, the width of the liquid flow is more while it is lesser in the crimp of packing. In turn, the thickness of the liquid is more in the crimp of packing, which can be seen in Figures 8–11. This phenomenon is also in accordance with earlier experimental studies where the liquid hold-up is reported to be more around the crimp [23].

While comparing Figures 8 and 9 with Figure 10, the influence of contact angle can be noticed. The wetting of liquid with low contact angle, that is, silicon-oil (DC5), is higher than the wetting of water and water-glycerol Figures 9 and 10.

In Figure 11, closer view of the velocity vector is shown to understand the smooth flow of the liquid over the crimp of the corrugated sheet of packing. It is clear from this section that the liquid with low contact angle has very good wetting behaviour, which is also in accordance with our earlier studies with smooth inclined plate. The corrugation in the packing sheets helps the fluid to flow longer by changing the direction along the corrugation. This increases the contact time of the liquid-gas inside the packing.

3.2. Flow on Corrugated Sheet of Packing with Holes. In this section, the flows of different testing liquids on the corrugated sheet of packing with holes are shown. Figure 12–Figure 15 show the wetting on corrugated sheet of packing with smooth crimp surface and with holes for water, water-glycerol and silicon-oil. Figures 12 and 13 show the hydrodynamics of flow of water at two different flow rates. Figures 14 and 15 show the flow behavior of water-glycerol, and silicon-oil (DC5).

The influence of perforations can be clearly seen while comparing Figure 8–Figure 10 with Figure 12–Figure 15. Due to perforations, both sides of the corrugated sheet are wetted. However, the wetting area on the front side of the corrugated sheet considerably reduced in comparison to the sheet without perforations.

In Figure 12–Figure 15, comparison between experiment and simulation is also shown. The flow on the front side of the sheet is shown in comparison with simulation and experiment. It is very tedious to capture the flow on the rear side of the corrugated sheet experimentally. Hence, the flow on the rear of the packing is shown from CFD simulations.

By comparing Figures 12 and 13, the change in wetting due to change in flow rate can be observed. The wetting of water at high flow is more (Figure 12) compared to at low flow rate (Figure 13). On the other hand, it should be noticed that holes are utilized more in the low flow rate. Hence,

the wetting on the rear side of the packing is more for low flow rate. So it looks like flow rate and holes play a contradictory role while wetting.

While comparing Figures 13 and 15, it can be understood that for high viscous fluids the flow wetting behavior has no big difference.

As seen in Section 3.1, silicon-oil has shown better wetting in the corrugated sheet of packing with perforations as well (Figure 16). The wetting on the front side of the packing is less in comparison with the packing without perforations. But the wetting on the rear side is considerably high. For silicon-oil, the change in flow rate did not make a huge difference in wetting the rear side of the sheet (not shown here).

Overall, the presence of perforations plays a key role in wetting and hence increases the contact area for the liquid gas interaction. Hence, in recent times, almost all the industrial packings have perforations. Now with this study, the wetting on the rear side of the packing can also be understood, which is usually cumbersome with experiments.

3.3. Two Corrugated Sheets of Packing. The major aim of this section is to study the extent of wetting on two corrugated sheets of packing. In reality, corrugated sheets of packing are arranged in such a way that one, sheet is placed 90° opposite to the other one, that is, corrugation lies in the opposite direction, helping the fluid to change its direction. Figure 16 shows the domain of the geometry used for simulation in comparison with real packing segment. As shown, only part of the packing segment is considered for simulation in order to understand the influence of the second sheet in the liquid hold-up and in the wetting pattern. The main region to be considered is the meeting points where two corrugated sheets touch each other, which are explained in Figure 17.

Simulations are performed with the inlet conditions described as follows.

- (i) Inlets are 4 mm diameter liquid distributors as seen in Section 3.1
- (ii) Four inlet distributors are considered to understand the maximum wetting possible with two corrugated sheets of packing.
- (iii) Two different inlet positions are considered as shown in Figure 18. Two inlet positions are chosen in such a way that one position is inside the corrugation of bottom sheet (Position 1) and the other position is outside the corrugation of bottom sheet (Position 2). By this, the influence of the meeting point due to the second corrugated sheet on the flow of liquid can be clearly seen.
- (iv) Silicon-oil with volumetric flow rate of 811 mL/min showed the maximum wetting in our earlier studies.

Figures 19 and 20 show the isometric view of volume fraction of silicon-oil at different heights of the corrugated sheet of packing along the flow direction. It can be clearly seen that the liquid holds up near the criss-cross junction, that is, around the meeting point of the two sheets. Moreover,

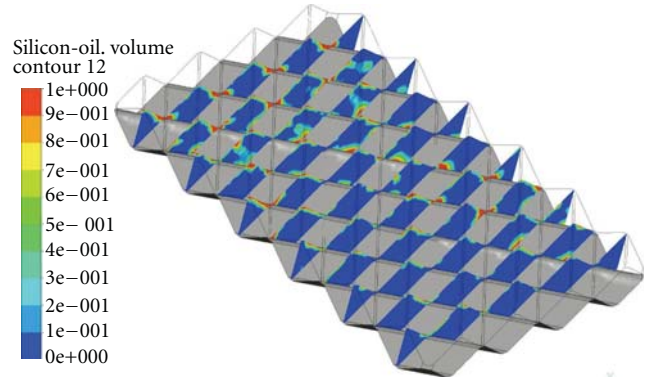


FIGURE 19: Contour of silicon-oil volume fraction at different heights of corrugated sheet of packing simulated along the flow direction for inlet position 1. Vol. Flow rate = 811 mL/min.

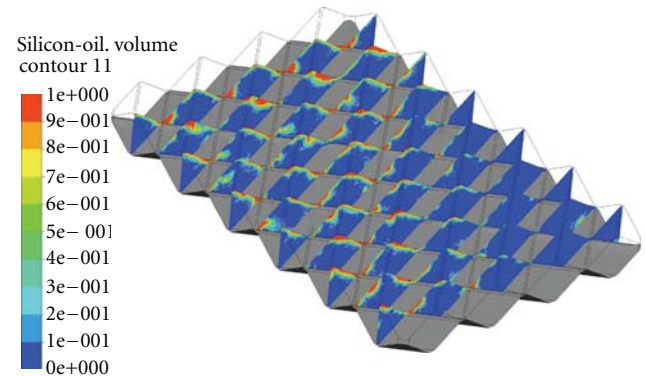


FIGURE 20: Contour of silicon-oil volume fraction at different heights of corrugated sheet of packing simulated in the flow direction for inlet position 2. Vol. Flow rate = 811 mL/min.

the hold-up is more near the inlet than in the outlet. This phenomenon of liquid holding up near this junction is seen in experimental study [23] performed using X-ray tomography for Mellapak 752.Y.

Figures 21 and 22 show the wetting of bottom and top sheets for simulation with two corrugated sheets of packing and for two different inlet positions mentioned earlier but for the same flow rate. It is very interesting to note that along with the liquid hold-up, small change in inlet positions makes a huge impact on wetting of the corrugated sheet. For position 1, where most of the portion of inlet lies inside the corrugation of top sheets wets only the top packing sheet and the bottom sheets remain without wetting. For position 2, where the inlet lies equally to both the corrugated sheets, wets more of the bottom sheet and considerably less of the top sheet compared to position 1.

In Table 5, the wetted areas of bottom and top corrugated sheets are shown. It is clear from position 1 that only 54% and 5.07% of top and bottom sheets are wetted, respectively. Moreover, in case of position 2, the wetted area is 15.36% and 39.06% for bottom and top sheets, respectively. Overall, only 55 to 60% of the packing area is utilized.

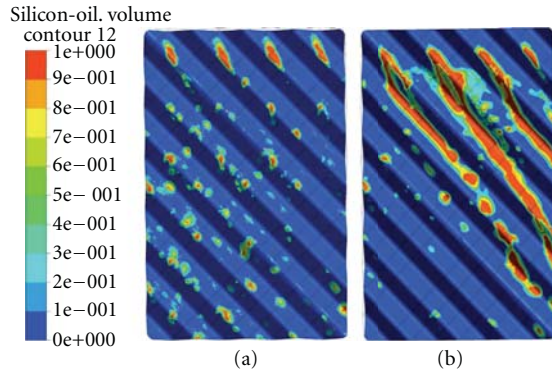


FIGURE 21: Wetted area on the bottom packing for two inlet positions. (a) Position 1. (b) position 2. Vol. Flow rate = 811 mL/min.

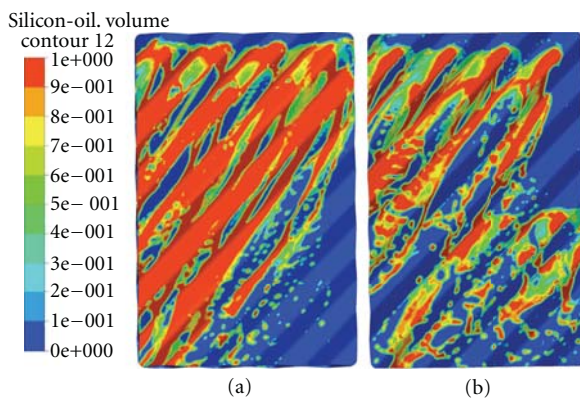


FIGURE 22: Wetted area on the top packing for two inlet positions. (a) Position 1. (b) Position 2. Vol. Flow rate = 811 mL/min.

As shown, only maximum of 60% of the packing area is utilised for wetting of testing system with low contact angle (which usually wets easily), for maximum inlet possible, that is, four inlets through four corrugations and relatively high flow rate of around 811 mL/min. It is very clear that around 40% of the area can be utilised and hence efficiency of the packing can be further improved. The influences of surface textures are not considered in the simulation, which can be considered further in simulation studies to understand the wetting behaviour better.

4. Conclusions

The three-dimensional VOF model is presented in this work in order to study the flow of liquid on the corrugated sheets of packing. Geometries with three different modifications in the element of the geometry have been studied. Three different testing fluids with different physical properties were considered. The simulations are performed in the 3D geometry resembling the corrugated sheet of packing. The simulations are compared with quantitative experimental studies. The corrugation changes the direction of the flow of fluid, and this increases the contact time of gas-liquid in the packing. As expected, the increase in flow rate also increased

the wetting area. Testing mixture with low contact angle had better wetting.

The influence of perforations on wetting of the corrugated sheet was also shown. The wetting area on the front side of the sheet decreases while the liquid wets the rear side of the packing. Liquids flowing at low flow rate utilize the perforations more and wet both sides of the sheets. The increase in flow rate counter affects the presence of perforations. Due to high flow rate, perforations are not utilized completely hence the wetting on the rear side of packing was lesser compared to low flow rate.

The second corrugated sheet was introduced to simulation domain to understand the influence of criss-cross junctions where both the sheets touch each other. Liquid hold-up near the junctions of two sheets was high, as noticed in some experimental studies performed using X-ray tomography [17]. It is also shown that the minor change in position of the inlet distributors considerably changes the wetting area and the flow direction of the liquid. Even for the simulation performed with the maximum number of inlets and for liquid with low contact angle, the complete area of packing was not utilized. This clearly proves that the efficiency of the existing packing can be further increased. The wetting of the corrugated sheet of packing can be further increased by textures on the surface. This theoretical work can be extended to study the wetting behavior on the corrugated sheet with microstructures on the surface of the packing. Various surface textures are possible as explained earlier in Section 1.2. The influence of the different 2D and 3D microstructures can be studied. Considering the validity of this model, dimension (nm to mm) of the microstructure can be optimized to achieve maximum wetting and hence high mass transfer. It is highly recommended to study the influence of microstructures using the CFD simulations, which will help to develop new surface textures to utilize the surface of packing completely. With the validated model, experiment efforts can be reduced but cannot be avoided completely. This study can also be further extended to study the transport processes in distillation and absorption.

Acknowledgments

The authors thank the management committee of Evonik Stiftung for funding this project and are grateful to HLRN Berlin for using parallel computing in clusters. They also thank Mr. Martin Kohrt for his technical assistance in experimental study and Dr. Ilja Ausner for supplying the packing sheets for experiments.

References

- [1] H. Kister, *Distillation Design*, McGraw-Hill, 1992.
- [2] S. J. Luo, W. Y. Fei, X. Y. Song, and H. Z. Li, "Effect of channel opening angle on the performance of structured packings," *Chemical Engineering Journal*, vol. 144, no. 2, pp. 227–234, 2008.
- [3] Ž. Olujić, A. F. Seibert, and J. R. Fair, "Influence of corrugation geometry on the performance of structured packings: an experimental study," *Chemical Engineering and Processing*, vol. 39, no. 4, pp. 335–342, 2000.

- [4] J. T. Davies and K. V. Warner, "The effect of large-scale roughness in promoting gas absorption," *Chemical Engineering Science*, vol. 24, no. 2, pp. 231–240, 1969.
- [5] L. Zhao and R. L. Cerro, "Experimental characterization of viscous film flows over complex surfaces," *International Journal of Multiphase Flow*, vol. 18, no. 4, pp. 495–516, 1992.
- [6] S. Shetty and R. L. Cerro, "Flow of a thin film over a periodic surface," *International Journal of Multiphase Flow*, vol. 19, no. 6, pp. 1013–1027, 1993.
- [7] S. Shetty and R. L. Cerro, "Spreading of a liquid point source over a complex surface," *Industrial and Engineering Chemistry Research*, vol. 37, no. 2, pp. 626–635, 1998.
- [8] B. Mahr, "Numerisches Berechnen und tomographisches Messen zwei-phasiger Strömungsfelder in geordneten Schichtungen," in *Institut für Verfahrenstechnik*, Leibnitz Universität Hannover, Hanover, Germany, 2007.
- [9] B. Mahr and D. Mewes, "X-ray tomographic visualization of liquid spreading in structured packings using contrast-agent tracer," in *Proceedings of the 13th International Heat Transfer Conference (IHTC '06)*, Sydney, Australia, 2006.
- [10] J. U. Repke, I. Ausner, S. Paschke, A. Hoffmann, and G. Wozny, "On the track to understanding three phases in one tower," *Chemical Engineering Research and Design*, vol. 85, no. 1, pp. 50–58, 2007.
- [11] A. Hoffmann, I. Ausner, J. U. Repke, and G. Wozny, "Fluid dynamics in multiphase distillation processes in packed towers," *Computers and Chemical Engineering*, vol. 29, no. 6, pp. 1433–1437, 2005.
- [12] A. Hoffmann, I. Ausner, J. U. Repke, and G. Wozny, "Detailed investigation of multiphase (gas-liquid and gas-liquid-liquid) flow behaviour on inclined plates," *Chemical Engineering Research and Design*, vol. 84, no. 2, pp. 147–154, 2006.
- [13] Y. Xu, S. Paschke, J. U. Repke, J. Yuan, and G. Wozny, "Portraying the countercurrent flow on packings by three-dimensional computational fluid dynamics simulations," *Chemical Engineering and Technology*, vol. 31, no. 10, pp. 1445–1452, 2008.
- [14] Y. Haroun, D. Legendre, and L. Raynal, "Direct numerical simulation of reactive absorption in gas-liquid flow on structured packing using interface capturing method," *Chemical Engineering Science*, vol. 65, no. 1, pp. 351–356, 2010.
- [15] Y. Haroun, D. Legendre, and L. Raynal, "Volume of fluid method for interfacial reactive mass transfer: application to stable liquid film," *Chemical Engineering Science*, vol. 65, no. 10, pp. 2896–2909, 2010.
- [16] J. M. van Baten and R. Krishna, "Gas and liquid phase mass transfer within KATAPAK-S structures studied using CFD simulations," *Chemical Engineering Science*, vol. 57, no. 9, pp. 1531–1536, 2002.
- [17] A. Viva, S. Aferka, D. Toye, P. Marchot, M. Crine, and E. Brunazzi, "Determination of liquid hold-up and flow distribution inside modular catalytic structured packings," *Chemical Engineering Research and Design*, vol. 89, no. 8, pp. 1414–1426, 2011.
- [18] Ansys Fluent 12.0 User Guide, 2009.
- [19] J. U. Brackbill, "A continuum method for modeling surface tension," *Journal of Computational Physics*, vol. 100, no. 2, pp. 335–354, 1992.
- [20] K. Subramanian, S. Paschke, J. U. Repke, and G. Wozny, "Drag force modelling in CFD simulation to gain insight of packed columns," in *Proceedings of the 9th International Conference on Chemical and Process Engineering, (ICheaP '09)*, pp. 561–566, May 2009.
- [21] Ansys ICEM CFD Manual 12.1, 2009.
- [22] S. Paschke, *Experimentelle Analyse ein- und zweiphasiger Filmströmungen auf glatten und strukturierten Oberflächen*, TU Berlin, Berlin, Germany, 2011.
- [23] A. Viva, S. Aferka, E. Brunazzi, P. Marchot, M. Crine, and D. Toye, "Processing of X-ray tomographic images: a procedure adapted for the analysis of phase distribution in MellapakPlus 752.Y and Katapak-SP packings," *Flow Measurement and Instrumentation*, vol. 22, no. 4, pp. 279–290, 2011.

Research Article

Mixing Study in an Unbaffled Stirred Precipitator Using LES Modelling

**Murielle Bertrand,¹ Delphine Parmentier,¹ Olivier Lebaigue,²
Edouard Plasari,³ and Frédéric Ducros²**

¹*Nuclear Energy Division, Radiochemistry and Processes Department, French Alternative Energies and Atomic Energy Commission, 30207 Bagnols sur Ceze, France*

²*Nuclear Energy Division, Reactor Studies Department, French Alternative Energies and Atomic Energy Commission, 34054 Grenoble, France*

³*Reactions and Process Engineering Laboratory, CNRS, 54001 Nancy, France*

Correspondence should be addressed to Murielle Bertrand, murielle.bertrand@cea.fr

Received 9 December 2011; Revised 8 March 2012; Accepted 14 March 2012

Academic Editor: Nandkishor Nere

Copyright © 2012 Murielle Bertrand et al. This is an open access article distributed under the Creative Commons Attribution License, which permits unrestricted use, distribution, and reproduction in any medium, provided the original work is properly cited.

This paper describes the CFD modelling of a reactor operating in the nuclear industry using LES approach. The reactor consists of an unbaffled stirred tank reactor in which plutonium precipitation reactions are carried out. The flow generated in such a precipitator is complex and there is very little information available in the literature about unbaffled reactors stirred with magnetic rod. That is why a hydrodynamic modelling has been developed using computational fluid dynamics (CFD) in order to get accurate description of mixing phenomena inside the precipitator and therefore to be able to predict the solid particle properties. Due to the strong turbulence anisotropy, the turbulence transport simulation is achieved by a large eddy simulation (LES) approach which gives unsteady solutions. The numerical simulations are performed in 3D using the Trio.U code developed at the Commissariat à l'Énergie Atomique. The predictive performances of the modelling are analysed through a mixing phenomena study. Both experimental and numerical studies are performed. This work shows how hydrodynamics inside the reactor can have a noticeable effect on the precipitate properties and how LES modelling is a very effective tool for the process control.

1. Introduction

Owing to the manipulation of radioactive materials at large scale, nuclear industry has to implement reactors with unusual design. An unbaffled magnetic rod-stirred reactor thus has been developed in the spent nuclear fuel reprocessing industry for use as a precipitator [1, 2]. Precipitation reactions being very fast are well known to be highly sensitive to mixing effects. That is why an accurate knowledge of the hydrodynamics inside the reactor is particularly essential to control the quality of the solid particles formed, on the one hand, and to develop a global modelling of the precipitation process, on the other hand.

Flows in stirred unbaffled vessels have not been widely discussed in the literature, unlike stirred baffled vessels, because they are less frequently used in processes [2–4]. Their mixing performance is significantly lower due to the

predominance of the tangential velocity over the axial and radial velocity components. Without counterimpellers, however, fluid rotation leads to the formation of a vortex that distorts the free surface; some applications can take advantage of this vortex. In the precipitator considered here, this configuration limits scaling by maintaining potentially adhering particles away from the walls and thus facilitates maintenance procedures that are particularly demanding in nuclear industry.

Moreover, all the studies described in the literature concern conventional impellers, either radial (turbines, flat- or pitched-blade stirrers) or axial (helical impellers), none of which corresponds to a magnetic rod rotating at the bottom of the vessel.

According to Rankine's combined vortex description, the hydrodynamics in an unbaffled reactor is characterized by the presence of two macromixing zones. The liquid near

the axis rotates as a solid cylinder with an angular velocity closed to the agitator one, whereas the outside liquid behaves as a free vortex [5]. The presence of these two different mixing zones highly impacts the distribution of reagent concentrations and the powder quality.

Knowing how important it is to entirely control the properties of actinide precipitates, a hydrodynamic modelling of the vortex precipitator has been undertaken using computational fluid dynamics (CFD). Due to the predominance of the circulation flow around the impeller axis, the turbulence is highly anisotropic. Then, the classical statistical turbulence models (Reynolds-Average-Navier-Stokes- (RANS-) like models) cannot be applied. The turbulence transport simulation can be achieved using the Large Eddy Simulation (LES) approach which resolves the largest scales using filter and gives the unsteady flow field taking into account the real movement of the stirrer. LES appears to be a very promising alternative to RANS techniques and direct numerical simulations (DNSs) [6–8]. The first ones present many limitations especially when solving complex flows with highly anisotropic turbulence while the latter one remains still far too expensive for industrial applications. Recently several chemical engineering studies based on the large eddy simulation approach have been published in the literature, to describe flows in baffled and unbaffled stirred tank reactor [9–13]. Results obtained are overall very satisfactory.

The objective of this work is to check the potential of LES approach to describe mixing in the vortex reactor and then to be applied to model the precipitation process.

2. Precipitation Experiments

2.1. Experimental Setup. In order to highlight the influence of the presence of two macromixing zones on the precipitation mechanisms, different reagent feeding positions are tested in the vortex reactor. Due to obvious experimental constraints, experiments are performed using neodymium to simulate the actinide behaviour [14] at laboratory scale in a geometric similarity reactor, shown in Figure 1. It consists of an unbaffled glass cylindrical vessel stirred by a cylindrical magnetic rod and equipped with a thermostated loop and an overflow nozzle.

The ratios between the tank diameter T , the tank height H , and the rod length D are as follows:

$$\begin{aligned} \frac{D}{T} &= 0.47, \\ \frac{H}{T} &= 1.5. \end{aligned} \quad (1)$$

The precipitations are carried out at room temperature by mixing continuously a neodymium III nitrate solution to an oxalic acid solution, according to the following equilibrium:

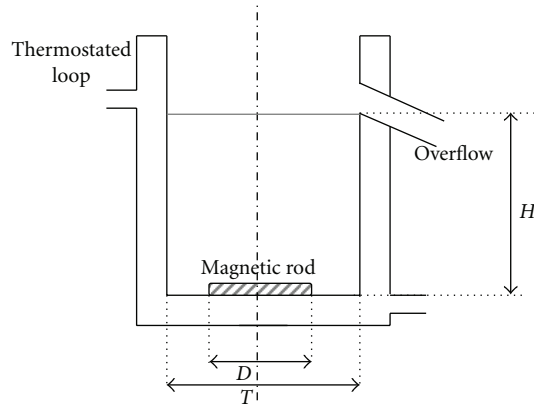
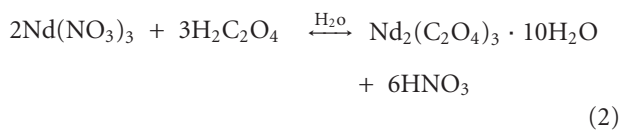


FIGURE 1: Experimental precipitator diagram.

TABLE 1: Operating parameters of precipitation experiments.

Temperature T ($^{\circ}\text{C}$)	25
Residence time τ (min)	30
$[\text{Nd}^{3+}]$ (mol.L^{-1})	0.2
$[\text{C}_2\text{O}_4^{2-}]$ (mol.L^{-1})	0.7
Acidity in the reactor (mol.L^{-1})	1

They are performed under stoichiometric conditions and in nitric acid medium.

The rotation speed is adjusted so that the volume power consumption is the same one as for the industrial feature. The flow is fully turbulent as the impeller Reynolds number is greater than 10^4 [15]:

$$\text{Re}_a = \frac{ND^2}{\nu} \approx 2 \cdot 10^4, \quad (3)$$

where N is the stirrer speed and ν the kinematic viscosity.

Precipitation experimental conditions are detailed in Table 1.

Samples taken at the reactor outlet are analyzed using a particle size analyzer (Malvern Mastersizer) and observed by scanning electron microscopy (SEM).

Two feeding point positions are investigated as shown in Figure 2: one located into the free vortex (a) and the other located into the forced vortex (b). The reagents are injected above the surface of the liquid.

2.2. Experimental Results. Experimental results point out a sensible influence of the feeding location on the crystal size. Figure 3 shows the SEM photos of neodymium III oxalate which has a lengthened platelets shape and Table 2 compares the mean particle sizes which vary by a factor of 1.5 to 2. Larger crystals are obtained when the reagents are injected into the free vortex.

2.3. Mixing Phenomena Observations. These two operating conditions lead to different hydrodynamic behaviours of the system. In the first case, the precipitate appears into

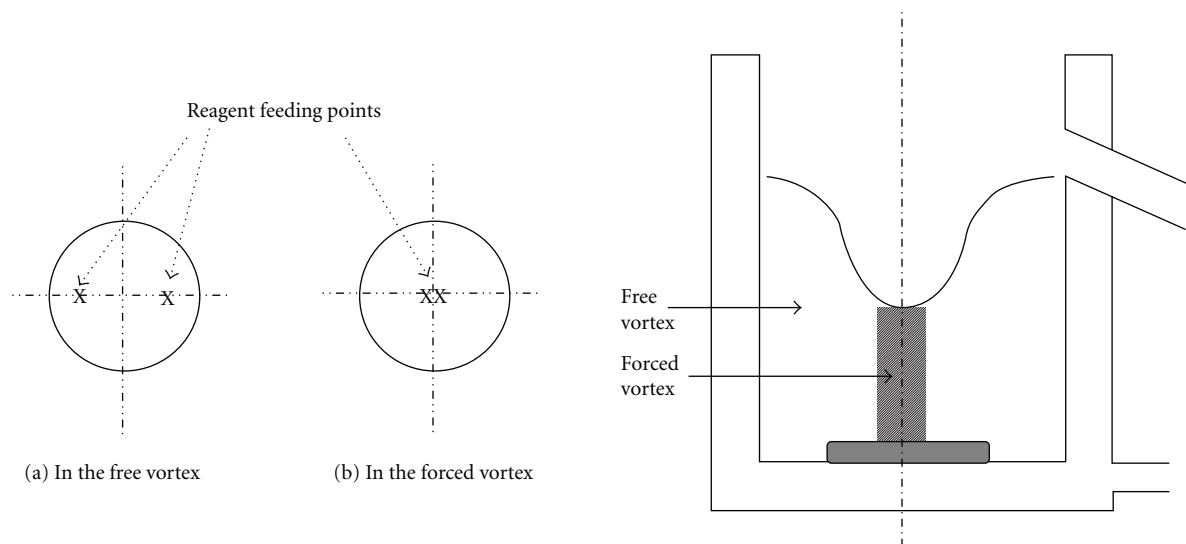


FIGURE 2: Feeding positions in the precipitator.

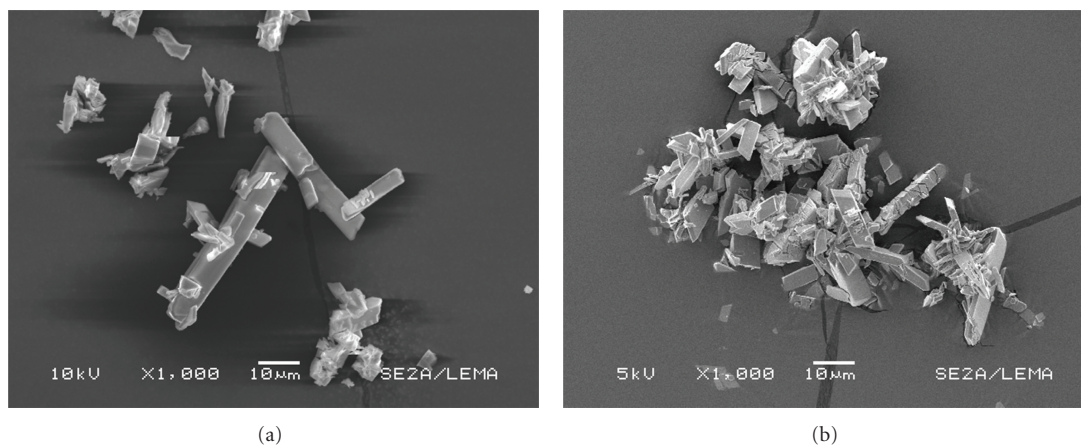


FIGURE 3: Neodymium III oxalate crystals obtained in the free vortex (a) and in the forced vortex (b).

TABLE 2: Mean volume crystal size depending on the feeding position.

Feeding point localisation	L_{43} (μm)
Forced vortex	80–100
Free vortex	160–180

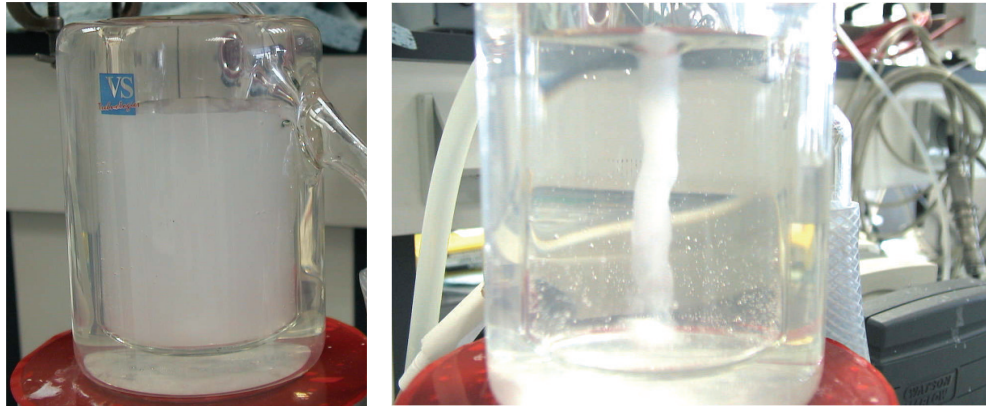
the whole of the reactor as shown in Figure 4(a). On the contrary, for a reagent inlet located into the forced vortex, a coloured column appears at the reactor centre (see Figure 4(b)), and then the precipitate diffuses progressively inside the free vortex from the reactor bottom upwards.

This experimental study proves the major role of flows which characterise an unbaffled precipitator and points out the need for an accurate hydrodynamic description in order to quantify this influence and to guarantee a better control of the process. That is why the flow pattern inside the precipitator is studied using computational fluid dynamics (CFD).

3. Hydrodynamic Modelling

Unbaffled reactors are characterised by a strong turbulent anisotropy as the tangential component is largely predominant. The turbulence models based on the eddy viscosity concept (k - ϵ -like models), classically used in chemical engineering, cannot take into account the turbulence anisotropy. That is why a hydrodynamic modelling has been developed at industrial scale using the large eddy simulation (LES) approach which gives unsteady solutions. In LES approach, the large scales are solved while the small ones are modelled by applying a space filter [16] so that the unsteady flow field can be reached according the real movement of the magnetic rod. The numerical simulations are performed in 3D with the trio_U code developed at the French Atomic Energy Commission [17–20].

3.1. Calculation Parameters. The computational field is based on the geometry shown in Figure 1. Inlet and outlet



(a) In the free vortex

(b) In the forced vortex

FIGURE 4: Reagent feeding position influence during the precipitation process.

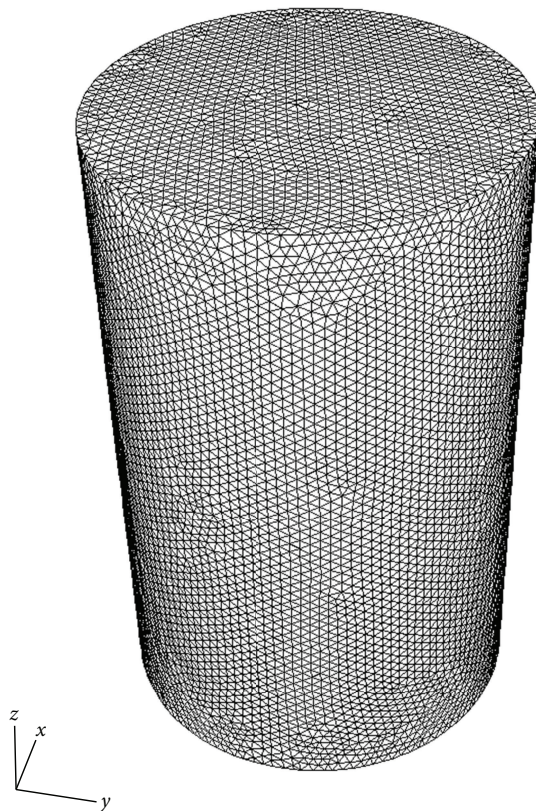


FIGURE 5: Homogeneous unstructured grid with tetrahedral elements.

flows are not taken into account. A fixed homogeneous unstructured grid is realised with about 650 000 tetrahedral elements of approximately the same volume (see Figures 5 and 6).

The ratio between the cell length scale Δx and the tank diameter T is about $\Delta x = T/40$. The ratio of cell volume to mean cell volume ranges from 0.101 and 3.16. The histogram of the largest angle of each tetrahedral element (see Figure 6) shows the good quality of the mesh.

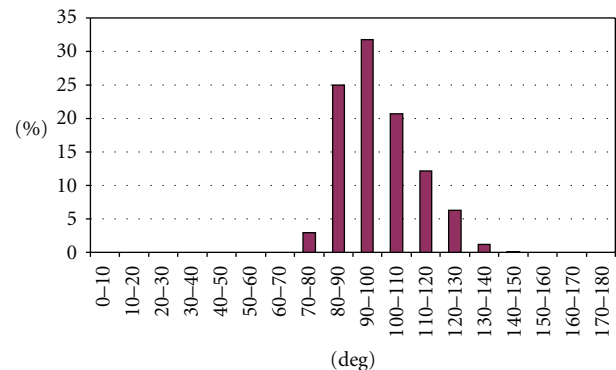


FIGURE 6: Histogram of the largest angle of tetrahedra.

The tank is supposed to be filled with water. The initial conditions of this calculation consider a fluid at rest with a horizontal free surface. At the initial instant the magnetic rod is driven to the required constant rotation speed with a Reynolds number of about $7 \cdot 10^4$.

The air/water interface is simulated by the Discontinuous Front Tracking method [21] and defined by a moving Lagrangian mesh independent of the Eulerian finite element mesh of the computational field. This two-phase gas/liquid model presents the advantage of simulating the free surface motion according to the flow.

The magnetic rod is taken into account by an Immersed Boundary Condition model [22]. It is defined by an independent Lagrangian mesh which rotates at an imposed constant speed [23] and its action on the surrounding fluid results in additional momentum source terms (forcing terms). Navier-Stokes equations are then solved in the fixed frame of the tank.

Characterised by an impeller Reynolds number equal to $7 \cdot 10^4$, the flow is fully turbulent.

The eddy viscosity is modelled according to the Wall-Adaptating Local Eddy-Viscosity concept (the WALE model) [24]. This subgrid turbulence model, which is a functional-modelling-like unsteady model, improves the system behaviour near walls, in shear layers, and in turbulence transition process.

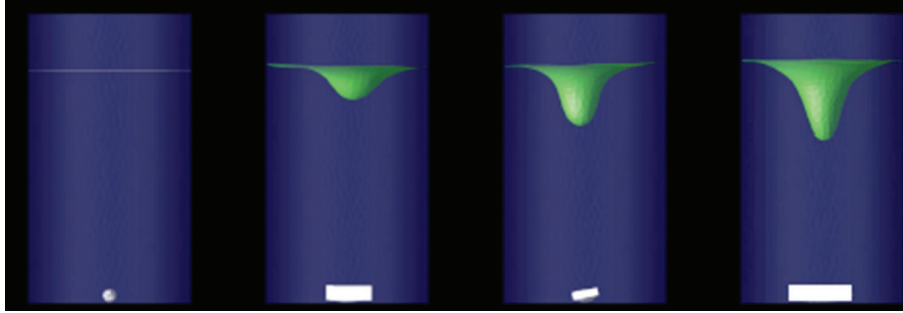


FIGURE 7: Vortex formation after stirrer startup.

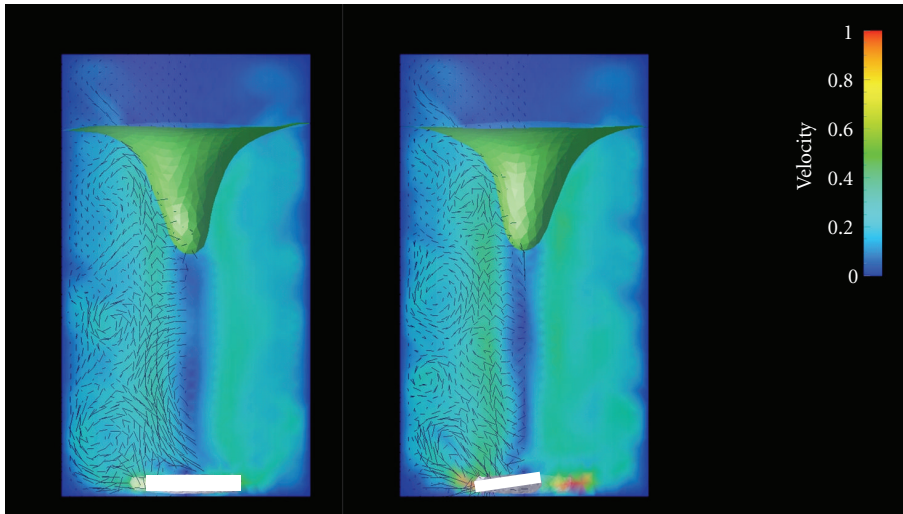


FIGURE 8: Vector velocity field at two different rod positions on a reactor midplane.

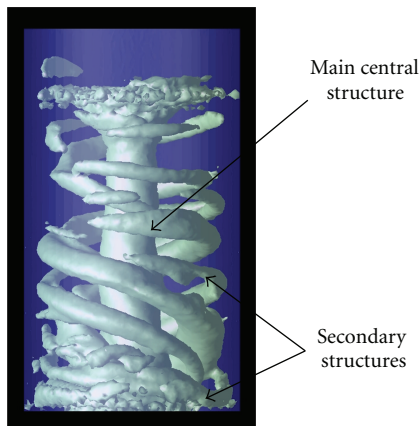


FIGURE 9: Representation of instantaneous turbulent flow structures using Q criterion.

The top of the tank is an open boundary with an imposed pressure. The walls are modelled with standard law-of-the-wall boundary conditions, as boundary layers are not resolved by the mesh.

3.2. *Inducing Fluid Flow.* The stirring action at the bottom of the vessel imparts a rotating movement to the fluid and forms a vortex at the surface. The entire fluid volume cannot be placed in movement instantaneously: 15 seconds are necessary for the volume fluid to reach steady-state kinetic energy conditions. Figure 7 shows this progressive vortex formation following the stirrer startup.

The unsteady gas/liquid interface simulation method allows us to observe the continuous movement of the free surface after formation of the vortex, unlike statistical approaches that give the time averaged fields and then cannot capture the time fluctuations [2]. The vortex follows the main rotational movement of the flow, and the interface is therefore not exactly axisymmetric in the vortex zone: its tip exhibits slight precessional motion with a vertical.

3.3. *LES Instantaneous Velocities.* In agreement with Nagata's model [25], the main flow comprises fluid rotation around the vessel symmetry axis, in which the tangential velocity component predominates. However, the tangential velocity norm varies in space and time with the rod position. The fluid is periodically discharged radially by the rod, forming swirling structures superimposed on one other over the full height of the reactor. These moving structures

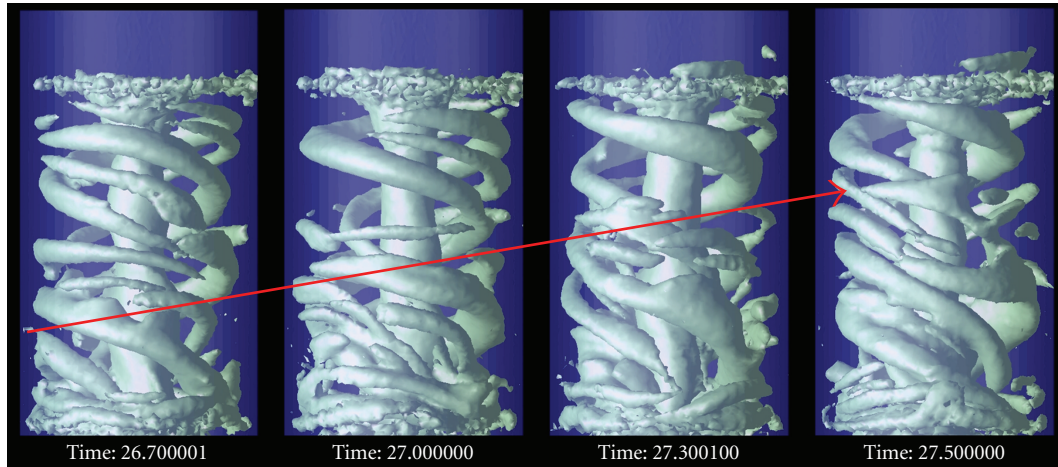
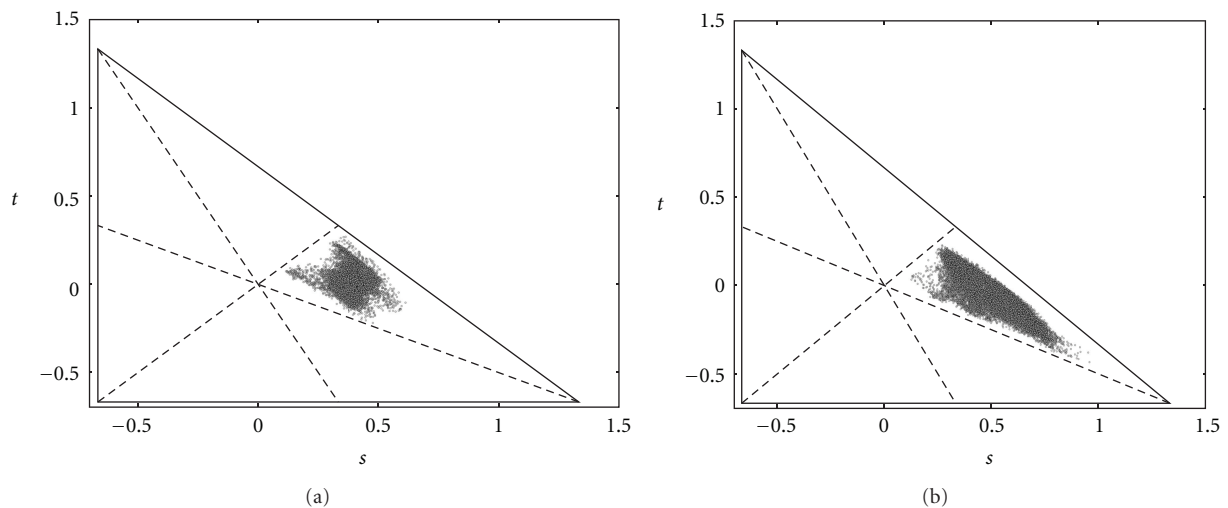


FIGURE 10: Upwards movement of the secondary structures.

FIGURE 11: Values of (s, t) in the Lumley triangle for the forced (a) and the free vortex zone (b).TABLE 3: Comparison of CFD r_c^* value with Nagata's and Le Lan's models ($Re_a = 7 \cdot 10^4$).

	LES	Nagata's correlation	Le Lan's correlation
r_c^*	0.5	0.53	0.51

of smaller magnitude vary approximately synchronously with the movement of the stirrer. The velocity vector field shown in Figure 8 on a reactor mid-plane at different times demonstrates the displacement of these structures.

The turbulent structures can be observed using the level-sets of the Q criterion which is the commonly used Eulerian criteria for coherent vortices [26]. Representing the eddy structures based on this turbulence criterion shows a dominant vertical central structure (see Figure 9) surrounded by smaller secondary structures that exhibit not only helical rotational movement around the vessel centreline but also upward motion from the bottom toward the vortex (see

Figure 10). The secondary structures are in the free vortex zone.

As LES solution holds most of the turbulent fluctuations (those solved by the grid), it is possible to have access in each control volume to good estimates of Reynolds tensor and then to build the Lumley triangle [27]. The (s, t) values in the Lumley triangle, obtained in the forced and in the free vortex zones, are shown in Figure 11 (s and t are the first and second eigenvalues of the anisotropy tensor [27]). They clearly highlight the strong turbulence anisotropy in most of regions of the precipitator, as no dots are situated close to the origin.

3.4. Comparison with Experimental Results. Experimental velocity measurements have been performed in the vortex reactor using Laser Doppler Velocimetry. Figure 12 provides a comparison between the tangential, radial, and axial velocities measured experimentally and calculated with LES. Velocities are dimensionalized using a reference velocity $V_\theta = \pi ND$ and their evolution is given with respect to the

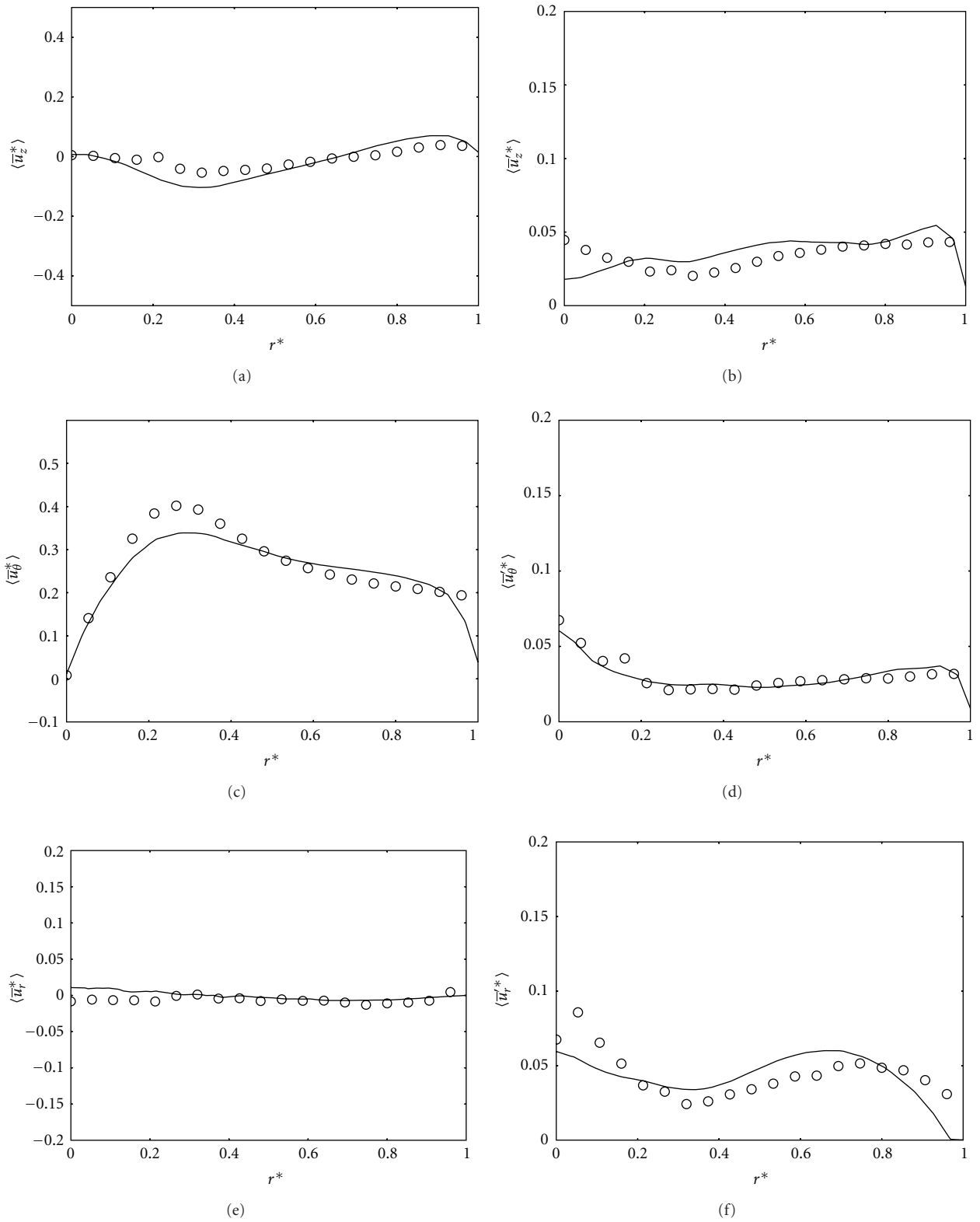


FIGURE 12: Mean (\bar{u}) and fluctuating parts (u') of the velocity field along the radius at the same height $z^* = 0.35$. Solid lines: LES results; symbols: experiments.

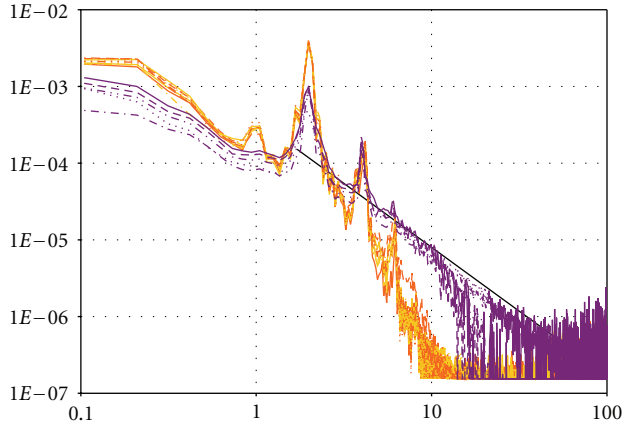


FIGURE 13: Energy spectrum of the vertical velocity fluctuations in the forced vortex ($z^* = 0.11$ and $r^* = 0.18$). Violet line: experiments (measured at 0, 90, 180, and 270° at the same z^* and r^*); orange lines: LES computations (measured at 0, 45, 90, ..., 315°) at the same z^* and r^*). The black straight line is a $k^{-5/3}$ slope.

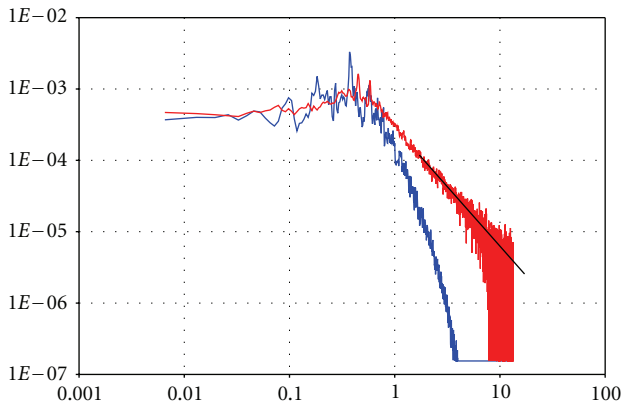


FIGURE 14: Energy spectrum of the radial velocity fluctuations in the free vortex ($z^* = 0.35$ and $r^* = 0.89$). Red line: experiments; blue lines: LES computations. The black straight line is a $k^{-5/3}$ slope.

nondimensionalized radius r^* for the height $z^* = Z/H = 0.35$:

$$\begin{aligned} u_i^* &= \frac{u_i}{\pi ND}, \\ r^* &= \frac{2r}{D}. \end{aligned} \quad (4)$$

where u is the velocity vector and r the radial distance.

We can notice that fluctuations are very intense for all components, especially at the bottom of the tank (See Figure 12). Mean and fluctuating axial velocity are of the same order. Moreover, radial fluctuations are much stronger than the mean counterparts (with the very exception of the region close to the impeller). This indicates a strong unsteadiness of the flow. Additional comparisons, at different heights can be found in a previous publication [28] which shows that most of the mean and fluctuating velocities are well described by our LES simulation.

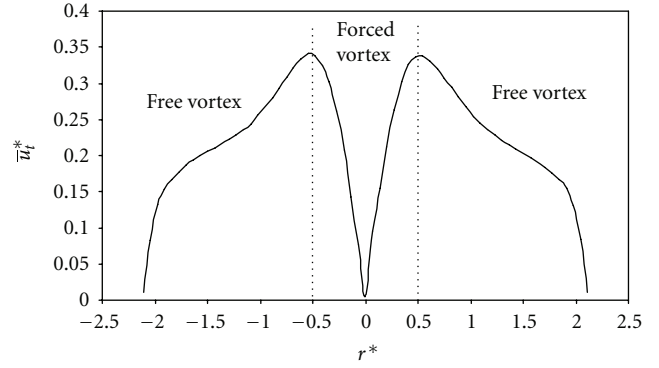


FIGURE 15: Computational mean tangential velocity profile.

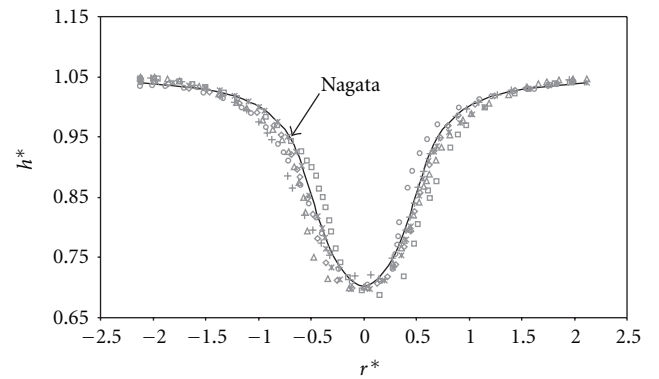


FIGURE 16: Comparison between computational vortex profiles (points) and Nagata's theory (black line).

A more detailed analysis of the flow inside the vortex reactor can be provided by a spectral analysis. In order to be compared with experimental results, spectra are computed from temporal signals whose duration exceeds 7000 rod rotations for experimental signals and 200 rod rotations for LES computations.

Figure 13 shows a typical spectrum of the vertical velocity fluctuations in the forced vortex region ($z^* = 0.11$ and $r^* = 0.18$) and Figure 14 in the free vortex region ($z^* = 0.35$ and $r^* = 0.89$). The frequencies are converted to nondimensional ones with the impeller rotation speed N used as a reference frequency. The spectral analysis points out the most obvious signature: the signature of the rod motion. Close to the impeller, the dominant frequency is of course twice the impeller rotation rate (i.e., $f^* = 2$).

These figures show that the dispersion of the experimental lines (3) versus angular position in the tank is moderate, except for very low frequencies. Similarly, the dispersion of the curves in the LES computation (6) is very limited, even at low frequencies. In Figure 13, several harmonics of the main frequency are observed, especially in the LES computation, namely, $f^* = 2, 4,$ and 6 . The real experimental signal exhibits more damped harmonics, for the harmonic $f^* = 6$ is barely present in the real fluid. The peak close to $f^* = 1$ in the simulation results is an artefact of an overestimated epitrochoidal motion superimposed to the rod rotation to

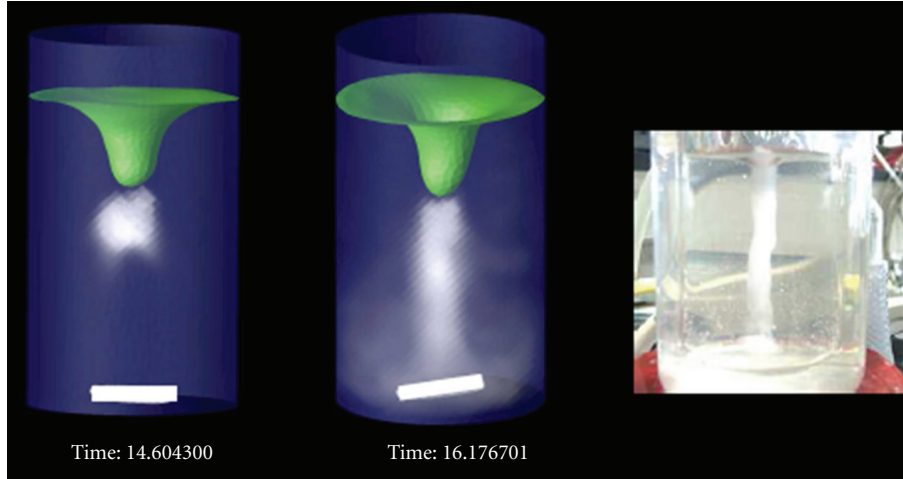


FIGURE 17: Tracer path-injection into the forced vortex.

mimic an off-axis precession of the centre of gravity of the rod. This motion has been observed for low height of liquid in the tank and postulated to exist when the tank is properly filled. The absence of such a $f^* = 1$ peak in the experimental results shows that the real precession motion is more limited with nominal liquid height. Figure 13 points out also an unsatisfactory agreement between the high-frequency trends. The simulation seems to be overdissipating for the highest frequencies in several locations in the tank. This is probably due to a lack of resolution. The cutoff frequency in the calculation is a little too low, and as a consequence, the nonlinear convection scheme too much stabilizes the flow in those regions. However, this behaviour does not seem to affect the overall energy of the fluctuations: the agreement between experimental and computational lower frequency levels is fairly good.

Finally, we can conclude that here is globally a good agreement between LES and experiments, which validates the numerical simulations and its LES model. The LES hydrodynamic modelling can thus be applied to the precipitation process modelling.

3.5. Mean Velocity Fields. According to Nagata's theory, the mean tangential velocity increases linearly with the radius in the forced vortex zone (see Figure 15):

$$0 < r < r_c : \bar{u}_t = r\omega_c, \quad (5)$$

where r_c is the radius of the boundary between the forced vortex and the free vortex.

The angular velocity of the fluid near the centre ω_c was found to be slightly lower than the agitator velocity ω_a : $\omega_c/\omega_a = 93\%$

In the free vortex zone, tangential velocity is inversely proportional to the radius:

$$r_c < r < \frac{T}{2} : \bar{u}_t r^{0.6} = \text{constant}. \quad (6)$$

The computational values of the forced vortex radius are of the same order than those calculated with both Nagata et al.'s [25] and Le Lan and Angelino's [29] correlations. For instance, for an impeller Reynolds number of $7 \cdot 10^4$, Table 3 presents the following different dimensionless radius $r_c^* = 2r_c/D$.

Figure 16 compares vortex profiles calculated at different moments with Nagata's theory. The computational-free surface is in good agreement with Nagata's relations:

$$\begin{aligned} h &= h_a + \frac{1}{2}\pi^2(R_c)^2 D \text{Fr} \left(\frac{r_c}{r}\right)^2 & \text{for } 0 \leq r \leq r_c, \\ h &= h_a + \frac{1}{2}\pi^2(R_c)^2 D \text{Fr} \left[2 - \left(\frac{r_c}{r}\right)^2\right] & (7) \\ & & \text{for } r_c \leq r \leq \frac{T}{2}, \end{aligned}$$

where Fr is the Froude number and h_a the height between the bottom of the tank and the bottom of the vortex.

Using the results of the LES simulations, the radius of the boundary between the forced vortex and the free vortex can be accurately determined according to the operating conditions. This information is crucial to control the reagent feeding point.

3.6. Mixing Phenomena. The hydrodynamic modelling is used to enhance the mixing phenomena inside the vortex reactor. The injection of a tracer is simulated in order to visualize the preferential path followed by a fluid particle depending on the initial feed location. The computational simulations reproduce the previous experimental observations.

When the tracer is injected into the forced vortex, it remains confined inside until it reaches the stirrer; then it diffuses into the free vortex (see Figure 17).

On the contrary, when the passive tracer is supplied in the free vortex, the tracer is diluted into the whole volume of the reactor (see Figure 18).

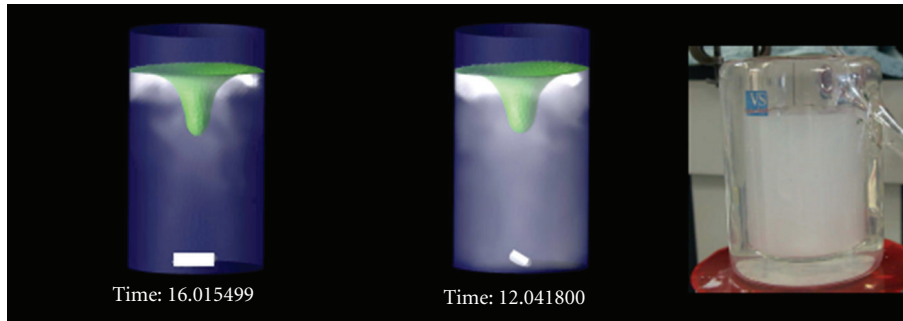


FIGURE 18: Tracer path-injection into the free vortex.

Mixing phenomena are completely different in both studied cases and influence highly precipitation mechanisms: nucleation, growth, and agglomeration processes. In the free vortex, the reagents injected are beforehand diluted into the surrounding fluid and precipitation takes place in the whole volume. On the contrary, in the forced vortex, inlet flows imprisoned in a very low volume remain concentrated so that high supersaturation gradients appear in the reactor. Thus, the free vortex enhances the growth process leading to the larger crystals, whereas the forced vortex characterised by high supersaturations enhances nucleation phenomena leading to smaller crystals. The supersaturation profile inside the precipitator is highly dependent on the reagent feeding position.

4. Conclusions

The LES approach using Trio_U code has been successfully applied to simulate with a high accuracy degree the flow in a vortex precipitator. The LES simulations allow the unsteady velocity and turbulence fields according to the agitator position to be calculated. The spectral analysis points out that the most significant frequencies are retrieved. Mixing phenomena are accurately described. Both numerical and experimental studies point out the major role of the flow pattern inside the precipitator. Indeed the mean crystal size can vary by a factor of 1.5 to 2 times only by modifying the reagent injection position. During the process precipitation, the position of the reagent feeding has to be controlled carefully; otherwise the precipitate properties vary. Using the results of the LES simulations, it is possible to get a good estimation of the radius of the forced vortex.

A global modelling of actinide precipitation processes is under development by combining this hydrodynamic model with kinetic laws in order to solve the population balance. Nucleation, crystal growth, and agglomeration kinetics are taken into account [30, 31]. The computer simulation is an important tool for the design, the optimisation, and scale-up of new geometries, especially in nuclear environment where experiments are limited.

Nomenclature

L_{43} : Mean volume particle diameter (m)
 D : Magnetic rod length (m)

h_a : Height between the bottom of the tank and the bottom of the vortex (m)
 H : Reactor height (m)
 N : Stirrer speed (rpm)
 r : Radius (m)
 r_c : Forced vortex radius (m)
 s, t : First and second eigenvalues of the anisotropy tensor ($\text{m}^2 \cdot \text{s}^{-1}$)
 t : Time (s);
 T : Reactor diameter (m)
 u : Velocity vector, ($\text{m} \cdot \text{s}^{-1}$)
 V_θ : Reference velocity, ($\text{m} \cdot \text{s}^{-1}$)
 z : Height m
 ω : Angular velocity ($\text{m} \cdot \text{s}^{-1}$)
 ν : Kinematic viscosity ($\text{m}^2 \cdot \text{s}^{-1}$)

Subscript

*: Nondimensionalized variable.

References

- [1] P. Auchapt and A. Ferlay, "Appareil à effet vortex pour la fabrication d'un procédé," Patent FR 1 556 996, 1981.
- [2] T. Mahmud, J. N. Haque, K. J. Roberts, D. Rhodes, and D. Wilkinson, "Measurements and modelling of free-surface turbulent flows induced by a magnetic stirrer in an unbaffled stirred tank reactor," *Chemical Engineering Science*, vol. 64, no. 20, pp. 4197–4209, 2009.
- [3] P. Armenante, C. C. Chou, and R. B. Hemrajani, "Comparison of experimental and numerical velocity distribution profiles in an unbaffled mixing vessel provided with a pitched-blade turbine," *ICHEME Symposium Series*, vol. 136, pp. 349–356, 1994.
- [4] M. Kagoshima and R. Mann, "Development of a networks-of-zones fluid mixing model for an unbaffled stirred vessel used for precipitation," *Chemical Engineering Science*, vol. 61, no. 9, pp. 2852–2863, 2006.
- [5] S. Nagata, N. Yoshioka, and T. Yokoyama, "Studies on the power requirement of mixing impellers," *Memoirs of the Faculty of Engineering, Kyoto University*, vol. 17, pp. 175–185, 1955.
- [6] H. Hartmann, J. J. Derksen, and H. E. A. van den Akker, "Macroinstability uncovered in a Rushton turbine stirred tank by means of LES," *AIChE Journal*, vol. 50, no. 10, pp. 2383–2393, 2004.

- [7] B. N. Murthy and J. B. Joshi, "Assessment of standard k - ϵ model, RSM and LES turbulence models in a baffled stirred vessel agitated by various impeller designs," *Chemical Engineering Science*, vol. 63, no. 22, pp. 5468–5495, 2008.
- [8] A. Delafosse, A. Line, J. Mochain, and P. Guiraud, "LES and URANS simulations of hydrodynamics in mixing tank: comparison to PIV experiments," *Chemical Engineering Research and Design*, vol. 86, no. 12, pp. 1322–1330, 2008.
- [9] J. J. Derksen, M. S. Doelman, and H. E. A. van den Akker, "Three-dimensional LDA measurements in the impeller region of a turbulently stirred tank," *Experiments in Fluids*, vol. 27, no. 6, pp. 522–532, 1999.
- [10] J. Derksen and H. E. A. van den Akker, "Large eddy simulations on the flow driven by a Rushton turbine," *AIChE Journal*, vol. 45, no. 2, pp. 209–221, 1999.
- [11] R. Alcamo, G. Micale, F. Grisafi, A. Brucato, and M. Ciofalo, "Large-eddy simulation of turbulent flow in an unbaffled stirred tank driven by a Rushton turbine," *Chemical Engineering Science*, vol. 60, no. 8-9, pp. 2303–2316, 2005.
- [12] S. L. Yeoh, G. Papadakis, and M. Yianneskis, "Determination of mixing time and degree of homogeneity in stirred vessels with large eddy simulation," *Chemical Engineering Science*, vol. 60, no. 8-9, pp. 2293–2302, 2005.
- [13] H. S. Yoon, S. Balachandar, and M. Y. Ha, "Large eddy simulation of flow in an unbaffled stirred tank for different Reynolds numbers," *Physics of Fluids*, vol. 21, no. 8, Article ID 085102, 2009.
- [14] B. Chapelet-Arab, L. Duvieubourg, G. Nowogrocki, F. Abraham, and S. Grandjean, "U(IV)/Ln(III) mixed site in polymetallic oxalato complexes. Part III: structure of $\text{Na}[\text{Yb}(\text{C}_2\text{O}_4)_2(\text{H}_2\text{O})] \cdot 3\text{H}_2\text{O}$ and the derived quadratic series $(\text{NH}_4^{+})_{1-x}[\text{Ln}_{1-x}\text{U}_x(\text{C}_2\text{O}_4)_2(\text{H}_2\text{O})] \cdot (3+x)\text{H}_2\text{O}$, Ln = Y, Pr-Sm, Gd, Tb," *Journal of Solid State Chemistry*, vol. 179, no. 12, pp. 4029–4036, 2006.
- [15] R. Perry and C. Chilton, *Chemical Engineer's Handbook*, McGraw-Hill, New York, NY, USA, 5th edition, 1973.
- [16] S. B. Pope, *Turbulent Flows*, Cambridge University Press, Cambridge, UK, 2000.
- [17] Y. Benarafa, O. Cioni, F. Ducros, and P. Sagaut, "RANS/LES coupling for unsteady turbulent flow simulation at high Reynolds number on coarse meshes," *Computer Methods in Applied Mechanics and Engineering*, vol. 195, no. 23-24, pp. 2939–2960, 2006.
- [18] C. Calvin and P. Emonot, "The Trio_U project: a parallel CFD 3-dimensional code," in *Proceedings of the Scientific Computing in Object-Oriented Parallel Environments (ISCOPE '97)*, Y. Ishikawa, R. R. Oldehoeft, J. Reynders, and M. Tholburn, Eds., Lecture Notes in Computer Science, pp. 169–176, Springer, Marina del Rey, Calif, USA, December 1997.
- [19] C. Calvin, O. Cueto, and P. Emonot, "An object-oriented approach to the design of fluid mechanics software," *Mathematical Modelling and Numerical Analysis*, vol. 36, no. 5, pp. 907–921, 2002.
- [20] <http://www-trio-u.cea.fr/>.
- [21] B. Mathieu, O. Lebaigue, and L. Tadrist, "Dynamic contact line model applied to single bubble growth," in *Proceedings of the 41st European Two-Phase Flow Group Meeting*, Trondheim, Norway, 2003.
- [22] E. A. Fadlun, R. Verzicco, P. Orlandi, and J. Mohd-Yusof, "Combined immersed-boundary finite-difference methods for three-dimensional complex flow simulations," *Journal of Computational Physics*, vol. 161, no. 1, pp. 35–60, 2000.
- [23] B. Mathieu, "A 3D parallel implementation of the front-tracking method for two-phase flows and moving bodies," in *Proceedings of the 177ème Session Société Hydrotechnique de France, Advances in the Modelling Methodologies of Two-Phase Flows*, Lyon, France, November 2004.
- [24] F. Nicoud and F. Ducros, "Subgrid-scale stress modelling based on the square of the velocity gradient tensor," *Flow, Turbulence and Combustion*, vol. 62, no. 3, pp. 183–200, 1999.
- [25] S. Nagata, K. Yamamoto, and M. Ujhara, "Studies on the power requirement of mixing impellers," *Memoirs of the Faculty of Engineering, Kyoto University*, pp. 336–349, 1958.
- [26] J. Jeong and F. Hussain, "On the identification of a vortex," *Journal of Fluid Mechanics*, vol. 285, pp. 69–94, 1995.
- [27] R. Escudié and A. Liné, "Analysis of turbulence anisotropy in a mixing tank," *Chemical Engineering Science*, vol. 61, no. 9, pp. 2771–2779, 2006.
- [28] N. Lamarque, B. Zoppé, O. Lebaigue, Y. Dolias, M. Bertrand, and F. Ducros, "Large-eddy simulation of the turbulent free-surface flow in an unbaffled stirred tank reactor," *Chemical Engineering Science*, vol. 65, no. 15, pp. 4307–4322, 2010.
- [29] A. Le Lan and H. Angelino, "Etude du vortex dans les cuves agitées," *Chemical Engineering Science*, vol. 27, no. 11, pp. 1969–1978, 1972.
- [30] M. Bertrand-Andrieu, E. Plasari, and P. Baron, "Determination of nucleation and crystal growth kinetics in hostile environment—application to the tetravalent uranium oxalate $\text{U}(\text{C}_2\text{O}_4)_2 \cdot 6\text{H}_2\text{O}$," *Canadian Journal of Chemical Engineering*, vol. 82, no. 5, pp. 930–938, 2004.
- [31] S. Lalleman, M. Bertrand, and E. Plasari, "Physical simulation of precipitation of radioactive element oxalates by using the harmless neodymium oxalate for studying the agglomeration phenomena," *Journal of Crystal Growth*, vol. 342, no. 1, pp. 42–49, 2012.

Research Article

Chemical Kinetic Study of Nitrogen Oxides Formation Trends in Biodiesel Combustion

Junfeng Yang,¹ Valeri I. Golovitchev,¹ Pau Redón Lurbe,² and J. Javier López Sánchez²

¹ Department of Applied Mechanics, Chalmers University of Technology, 412-96 Göteborg, Sweden

² CMT-Motores Térmicos, Universidad Politécnica de Valencia, 46022 Valencia, Spain

Correspondence should be addressed to Junfeng Yang, jungfeng@chalmers.se

Received 6 December 2011; Accepted 28 February 2012

Academic Editor: Mahesh T. Dhotre

Copyright © 2012 Junfeng Yang et al. This is an open access article distributed under the Creative Commons Attribution License, which permits unrestricted use, distribution, and reproduction in any medium, provided the original work is properly cited.

The use of biodiesel in conventional diesel engines results in increased NO_x emissions; this presents a barrier to the widespread use of biodiesel. The origins of this phenomenon were investigated using the chemical kinetics simulation tool: CHEMKIN-2 and the CFD KIVA3V code, which was modified to account for the physical properties of biodiesel and to incorporate semidetached mechanisms for its combustion and the formation of emissions. Parametric ϕ -T maps and 3D engine simulations were used to assess the impact of using oxygen-containing fuels on the rate of NO formation. It was found that using oxygen-containing fuels allows more O₂ molecules to present in the engine cylinder during the combustion of biodiesel, and this may be the cause of the observed increase in NO emissions.

1. Introduction

Biodiesel fuels consist of long-chain monoalkyl esters derived from vegetable oils and expected to be increasingly important alternatives or supplements to conventional diesel fuel for use in diesel engines. However, in many studies, as summarized in [1], it was observed that the use of biodiesel in engines causes more NO_x emissions than are generated when using conventional diesel fuel. Numerous experimental and numerical studies have been conducted in order to better understand the origins of the increased NO_x emissions, and various explanations have been proposed on the basis of their results; the literature in this area has been reviewed by Mueller et al. [2]. Broadly speaking, two classes of explanation have been put forward: engine calibration effects [3] and combustion effects, such as higher flame temperatures [4, 5], injection timing shifting due to high bulk modulus [6], shorter autoignition delays, or combinations of these factors [2]. While these studies indicate that the increased NO_x emissions have multiple causes, it is generally accepted that the specific combustion chemistry of biodiesel is probably a major factor. Some of the factors listed have already been shown to have only minor effects on the amount of NO_x produced, including the adiabatic flame temperature [4]

and the high-bulk modulus of biodiesel [7]. However, the fundamental principles underpinning these increased NO_x emissions remain elusive, and current experimental techniques have not yet proven to be sufficient for their identification. Consequently, computational modeling of biodiesel spray combustion is an attractive tool for obtaining new insights into the origins of the elevated NO_x emissions observed when using biodiesel fuels in conventional diesel engines.

To determine the equilibrium compositions and dominant thermal mechanism of NO_x formation during high-temperature combustion of biodiesel fuels in diesel engines, equilibrium calculations and sensitivity analyses were performed using the EQUIL and PSR codes of the CHEMKIN-2 package [8, 9].

Chemical mechanisms for the combustion of diesel oil surrogate (DOS) and rapeseed methyl ester (RME) have previously been constructed and validated [10, 11]. In order to model the formation of NO_x, the extended N₂O/NO/NO₂ submechanism (26 reactions) [12] and the NCN pathway of prompt NO formation (27 reactions) [13] were incorporated into these combustion mechanisms; the modified mechanisms were used in CFD engine simulations of biodiesel spray combustion. The physical and chemical aspects of

the combustion process were simulated using the KIVA3V, Rel. 2 code [14], which couples turbulent flow dynamics with spray atomization described in terms of the Kelvin-Helmholtz/Rayleigh-Taylor, KH-RT, model [15], and accounts for gas and fuel droplets interactions, including droplet collision, evaporation, and mixture formation.

To understand the origins of the increased NO_x emissions, dynamic ϕ - T parametric maps were constructed for specific species of interest and used in conjunction with data from 3D engine simulations. Analyses of O_2 and NO_x concentrations revealed that more O_2 (and O atoms) are available during biodiesel decomposition than during that of diesel oil. This is due to the presence of O-atoms in the fuel molecules and indicates that biodiesel combustion tends to occur under more lean mixture conditions than is the case for conventional diesel oil. The calculations indicate that NO concentrations peak at the equivalence ratio of approximately 0.78 exist for both diesel and biodiesel fuels; as such, the slightly leaner fuel/air mixture in the combustion region during combustion of RME might be largely responsible for the increased NO emissions relative to those observed during the combustion of diesel oil.

A similar observation was reported by Adi et al. [16], who claimed that the use of oxygen-containing fuels increases the combustible oxygen mass fraction in the diffusion flame front; this in turn would increase the temperature of combustion, favoring the formation of NO.

Present work addresses to a comparative study between pure diesel oil and neat biodiesel fuel combustion using a numerical method. On the basis of our observations and analyses, we propose the following alternative hypothesis: the use of oxygen-containing fuels such as biodiesel (rather than a pure hydrocarbon fuel such as conventional diesel oil) generates a leaner fuel/air mixture, favoring NO formation. Future studies in this area will focus on analyzing the physical processes involved in the combustion of biodiesel in order to allow for the combustion of this important fuel under lean conditions without the drawback of elevated NO_x emissions.

2. Formulation of the Model

The numerical simulation of combustion phenomena is based on four separate, but coupled topics involving in multiphase combustion systems: the fluid mechanics described by the conservation equation of continuum mechanics, the chemical reactions between species making up the fluid, and spray and droplet dynamics which are the consequence of interaction between liquid fuel and gas. Finally, the systems referred as a set of turbulence modeling equations. The main conservation equations are taken in a form as they are implemented in the 3-D CFD KIVA-3 V code [14]. KIVA, a transient, three-dimensional, multiphase, multicomponent code for the analysis of chemically reacting flows with sprays, has been developed at the Los Alamos National Laboratory. The code uses an arbitrary Lagrangian Eulerian (ALE) methodology on a staggered grid, which discretizes a space using the finite-volume technique. The code uses an implicit time advancement with the exception of the convection

terms that are cast in an explicit, second-order monotone scheme. Also, the convection calculations are sub-cycled in the desired regions to avoid the time step restriction due to Courant conditions. Arbitrary numbers of species and chemical reactions are allowed. A stochastic particle method is used to calculate evaporating liquid sprays, including the effects of droplet collisions and aerodynamics breakups. Although specifically designed for performing ICE calculations, the modularity of the code allows it for easy modifications for solving a variety of combustion problems.

2.1. The Model Formulation: Main Conservation Laws. The conservation equations listed below are given in “advective form” rather than in “conservative form” that requires approximations of both the conservative and nonconservative terms:

Conservation of mass:

$$\frac{\partial \rho}{\partial t} + \nabla \cdot (\rho \mathbf{u}) = \dot{\rho}^s. \quad (1)$$

Conservation of momentum (a vector equation with three components):

$$\begin{aligned} \frac{\partial (\rho \mathbf{u})}{\partial t} + \nabla \cdot (\rho \mathbf{u} \mathbf{u}) = & \rho \mathbf{g} + \mathbf{F}^s - \frac{1}{a^2} \nabla p \\ & + \nabla \cdot \bar{\sigma} - A_o \nabla \left(\frac{2}{3} \rho k \right). \end{aligned} \quad (2)$$

Conservation of energy:

$$\begin{aligned} \frac{\partial (\rho I)}{\partial t} + \nabla \cdot (\rho \mathbf{u} I) = & -\nabla \cdot \mathbf{J} + \dot{Q}^c + \dot{Q}^s - p \nabla \cdot \mathbf{u} \\ & + (1 - A_o) \bar{\sigma} : \nabla \mathbf{u} + A_o \rho \epsilon. \end{aligned} \quad (3)$$

Conservation of mass for chemical species m (one equation for each of the N_s species)

$$\frac{\partial \rho_m}{\partial t} + \nabla \cdot (\rho_m \mathbf{u}) = \nabla \cdot \left[\rho D \nabla \left(\frac{\rho_m}{\rho} \right) \right] + \dot{\rho}_m^c + \dot{\rho}_m^s \delta_{m1}, \quad (4)$$

where m is species index, N_s is the species numbers; superscripts “c” and “s” denote the terms associated with the chemical reaction and spray, respectively, δ_{i1} is the Kronecker delta function, that is, species 1 is the species of which the sprays are composed. The main variable definitions are given in the notations.

The system of conservation laws (1)–(4) is supplemented by equations of state and the algebraic equations specifying the models of fluid, see, for example, [17]. The turbulence was described by the k - ϵ model with the velocity dilatation and spray interaction terms.

2.2. Turbulent Combustion Modeling. To simulate turbulent combustion, the partially stirred reactor (PaSR) method [18] has been employed. To outline the main features of the approach, let us consider the average gas phase equations (4) for a chemically reacting species. Since the KIVA-3 V code is based on the operation-splitting procedure applied to

the mass conservation equations for species participating in any multistep reaction mechanism, the third step of the computational procedure accounts for chemical kinetics coupled with species micromixing. This step can be interpreted as representing combustion in a constant volume partially stirred reactor of a computational cell size, where reactions occur in a fraction of its volume described in the term of the ODE system:

$$\frac{dc^1}{dt} = \frac{c^1 - c^0}{\tau} = f_r(\dots, c, \dots), \quad (5)$$

where τ is a time integration step, $f_r(\dots, c, \dots) \equiv \rho^c$ is the chemical source term calculated at some unknown (virtual) concentrations, c , parameters of a subgrid scale reaction zone. The model distinguishes between the concentration (in mean molar density) at the reactor exit, c^1 , the concentration in the reaction zone, c , and in the feed, c^0 . When time proceeds, c^1 trades place for c^0 . The species indices are omitted for simplicity.

To close the model, the additional equation for the reaction volume can be engaged, that is,

$$\frac{dc}{dt} = -\frac{c - c^1}{\tau_{\text{mix}}} + f_r(c), \quad (6)$$

where τ_{mix} is the micromixing time, the expression for $f_r(\dots, c, \dots)$ is formally simplified.

The difference between (6) and that from the PSR perfectly stirred reactor (PSR) [9] model is that the residence time in the reactor equation of the PSR model is replaced by the micromixing time. Taking this equation in a steady-state form, one can get the basic equations of the PaSR model (6) as follows:

$$\frac{dc^1}{dt} = f_r(c) = \frac{c - c^1}{\tau_{\text{mix}}}. \quad (7)$$

There are a number of micromixing models based on different principles; the review of these can be found in [19]. One of the simplest and widely used micromixing models is the ‘‘interaction by exchange with the mean’’ (IEM) approach [19]. In this approach, the scalar variable c relaxes to its mean c^1 value according to the linear term in (7). Then, rewriting the reaction rate in (7), $f_r(c)$, in terms of reactor exit parameters, one can get

$$f_r(c^1) + \left(\frac{\partial f_r}{\partial c} \right)_{|c=c^1} (c - c^1) = f_r(c^1) - \frac{c - c^1}{\tau_c} \quad (8)$$

using the Taylor’s expansion at the value c^1 , assuming that the reaction times can be estimated as reciprocal values of the Jacobian matrix diagonal elements evaluated at the grid resolved values $c = c^1$, that is, $\tau_c \sim [\partial f_r / \partial c]^{-1}$ and accounting for that $(\partial f_r / \partial c)_{|c=c^1} < 0$. Algebraic manipulation with the second pair of (4) leads to the relation:

$$f_r(c^1) - \frac{c - c^1}{\tau_c} = \frac{c - c^1}{\tau_{\text{mix}}}. \quad (9)$$

and, finally, to the main relation of the PaSR model:

$$f_r(c) = f_r(c^1) \frac{\tau_c}{\tau_c + \tau_{\text{mix}}}. \quad (10)$$

This means the chemical source terms can be calculated using the averaged species concentrations, if multiplied by the model rate parameters ratio $\tau_c / (\tau_c + \tau_{\text{mix}})$. The application of (10) is applicable to the chemical mechanisms of an arbitrary complexity. The model parameters such as τ_{mix} and τ_c are calculated as described in [20, 21], for example,

$$\tau_{\text{mix}} = \left(\frac{k}{\varepsilon} \right) \cdot \left(\frac{c_\mu}{\text{Re}_t} \right)^{0.621}, \quad (11)$$

where Re_t is the turbulence Reynolds number, c_μ is the parameter of the k - ε model.

It is instructive to note that the rate expression (10) treats the reactions in a full complexity on the contrary to the expression used in the ‘‘characteristic time’’ of combustion [22]:

$$f_{r,i}(c) = -\frac{Y_i - Y_i^*}{\tau_{c,i} + f\tau_{\text{mix}}}, \quad (12)$$

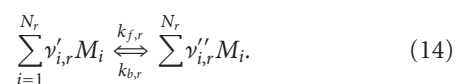
where Y_i and Y_i^* are current and equilibrium concentrations, f is a multiplier ranging from 0 to 1 switching from kinetic to turbulent regime of combustion, and characteristic chemical time is taken as the ignition delay time calculated using detailed chemical mechanism.

Sometimes, on the ignition stage of combustion, the shell ignition model which operates with artificial species representing low-temperature chemistry is used. The review of turbulence combustion models can be found in [23], but if the ignition is formally considered as the process preceding the combustion stage, such models are not used in the ignition description. The most effective separation of ignition and combustion stages is realized in [24] based on the usage of ignition integral calculated with the help of an artificial neural network (ANN) and KIVA-3 V (or KIVA4) code. The ignition integral:

$$I(t) = \int_0^t \frac{1}{\tau_{\text{ign}}(T, p, \phi)} dt \quad (13)$$

predicts the ignition onset as $I(t) = 1$ using a time history of ignition delays during the process development. The ignition delays are calculated and stored in a special library using the detailed chemical mechanisms for particular fuels.

2.3. Finite-Rate Formulation for Reaction Model. If the effects of turbulent fluctuations are ignored, the reaction rates can be determined by the Arrhenius rate expressions. Consider the r -reaction written in a form as follows:



The molar rate of creation/destruction of i -species in to r -reaction is given by

$$\hat{R}_{i,r} = \Gamma (\nu'_{i,r} - \nu''_{i,r}) \left(k_{f,r} \prod_{j=1}^{N_r} [C_{j,r}]^{\eta'_{j,r}} - k_{b,r} \prod_{j=1}^{N_r} [C_{j,r}]^{\eta''_{j,r}} \right). \quad (15)$$

Above, Γ represents the net effect of inert collision partners in the third body reactions on the reaction rate. This term is read as

$$\Gamma = \sum_j^{N_r} \gamma_{j,r} C_j, \quad (16)$$

where $\nu'_{i,r}$ are stoichiometric coefficients for reactants in r -reaction, $\nu''_{i,r}$ are stoichiometric coefficients for product in r -reaction, M_i denoting i -species, $k_{f,r}$ is a rate parameter for the forward stage of reaction r , $k_{b,r}$ is a rate parameter for the backward stage of reaction r , C_j are molar concentrations of reactants and products in r -reaction. $\eta'_{j,r}$ are forward rate exponents for reactant and product species, $\eta''_{j,r}$ are backward rate exponents for reactant and product species, and $\gamma_{j,r}$ are the third body efficiencies of the r -reaction. For elementary reactions, η_{jr} are equal to $\nu_{j,r}$; for global reactions, these values are specified based on the experiment rate data.

The formulation of chemical kinetics problem must be supplemented by the equation of stages for ideal and thermally perfect gas. The thermodynamic properties required for the calculations are available from the database [25].

2.4. Mechanisms of NO_x Formation. In order to understand the increased emissions of NO_x during biodiesel combustion, it is necessary to understand the key reactions in the formation of NO_x . Over the last few decades, many scientific and technical articles concerning the formation of NO_x have been published. On the basis of these studies, four main processes that form nitric oxides have been identified, as summarized by Miller and Bowman [26]: the thermal, prompt, N_2O , and fuel-bound nitrogen mechanisms.

The thermal mechanism of NO formation was proposed by Zeldovich et al. and involves a series of elementary reactions [27, 28] with high activation energies due to the strength of the triple bond in the N_2 molecule, which can only be broken at an appreciable rate at very high temperatures. This mechanism is generally accepted to play a major role in the formation of NO_x . Obviously, the rate of the Zeldovich mechanism is highly sensitive to the temperature of the reactants in flames, and to the concentrations of O and N atoms. In diesel engines, the in-cylinder and flame temperatures are determined by the properties of the liquid fuel (such as its bulk modulus and cetane number), the thermal-physical properties of the vapor (enthalpy, heat capacity), and the rate of heat loss, which is primarily due to radiation from soot particles. The radical O could originate from the oxidizer (O_2) and oxygenated fuel molecules; the only possible source of nitrogen is the air. An extended Zeldovich mechanism that takes all of these key factors into

account was used in this study; the key elementary steps in this mechanism are reactions 1–4 in Table 1, which were supplemented with the reactions of the N_2O pathways (reactions 5–9) and elementary steps corresponding to the “catalytic” interaction between NO and NO_2 (reactions 10–14). Data on the rates of these reactions were taken from the literature [12] and used without modification.

The nitrous oxide (N_2O) mechanism, first postulated by Wolfrum [29], is analogous to the Zeldovich mechanism in that its key step involves an O atom attacking molecular nitrogen in the presence of third body to form N_2O , which can subsequently react with O to produce NO . This mechanism is generally considered to play a minor role in the overall formation of NO [30]. Initially, Tomeczek and Gradon [31, 32] proposed rate parameters much higher than those that are currently used, resulting in the overprediction of NO concentrations in $\text{CH}_4\text{-O}_2\text{-Ar}$ flames [33]; more experimental data will be needed in order to obtain accurate rates for this process. The nitrous oxide mechanism is typically regarded as being a thermal NO formation mechanism; the combination of this mechanism with the Zeldovich mechanism is referred to as the thermal $\text{NO}/\text{N}_2\text{O}$ route.

The prompt NO mechanism was suggested by Fenimore [34]. Its main feature is that the CH radical (methylidyne), which is formed exclusively at the flame front, reacts with nitrogen in the air to form hydrocyanic acid (HCN), which reacts further to form NO [34]. However, predictions of the rate of NO formation via processes that involve HCN are typically relatively inaccurate. NCN -based prompt NO formation has recently been observed in gaseous jet combustion [35] and has been proposed to play a role in the combustion of methane [36, 37]; it was subsequently incorporated into a detailed mechanism for methane combustion [13]. The NCN pathway of prompt NO formation involves the 27 elementary steps that are listed in Table 2, along with the relevant rate parameters. It is important to note that both the HCN and the NCN -based prompt NO mechanisms are favored in rich flames. However, because the only available data on the rates of the relevant reactions had been obtained at atmospheric pressure, the prompt NO mechanism was not considered in previous studies [2]; little is known about the rates of these processes under the conditions that prevail during the combustion of diesel oil. Moreover, the prompt NO mechanism was considered to be unimportant because combustion in diesel engines generally occurs under lean conditions, which suppress the formation of CH_x radicals and are thus unfavorable to the prompt NO mechanism. However, while the combustion process in diesel engines is lean on the overall, localized regions of rich combustion occur in non-premixed fuel/air flames. As such, to properly understand the production of NO_x in diesel engines, it is necessary to determine the contribution of the prompt NO mechanism. To the best of our knowledge, the work described herein was the first study on the impact of the prompt NO mechanism on the production of NO_x during the combustion of biodiesel fuels.

Fuel-bound nitrogen has been shown to affect the formation of NO_x during the combustion of nitrogen-containing compounds. For example, during the gasification process,

TABLE 1: Elementary steps in the thermal mechanism of NO and N₂O. The forward reaction rate is given by $k_f = A_f T^{n_f} \exp(-E_f/RT)$ [12].

		A_f	n_f	E_f
1	$N + NO = N_2 + O$	$3.50E + 13$	0.0	330
2	$N + O_2 = NO + O$	$2.65E + 12$	0.0	6400
3	$N + OH = NO + H$	$7.33E + 13$	0.0	1120
4	$N + CO_2 = NO + CO$	$1.90E + 11$	0.0	3400
5	$N_2O + O = N_2 + O_2$	$1.40E + 12$	0.0	10810
6	$N_2O + O = NO + NO$	$2.90E + 13$	0.0	23150
7	$N_2O + H = N_2 + OH$	$4.40E + 14$	0.0	18880
8	$N_2O + OH = N_2 + HO_2$	$2.00E + 12$	0.0	21060
9	$N_2O + M = N_2 + O+M$	$1.30E + 11$	0.0	59820
10	$NO + HO_2 = NO_2 + OH$	$2.11E + 12$	0.0	-480
11	$NO_2 + O = NO + O_2$	$3.90E + 12$	0.0	-240
12	$NO_2 + H = NO + OH$	$1.32E + 14$	0.0	360
13	$NO + O + M = NO_2 + M$	$1.06E + 20$	-1.41	0.0
14	$NO_2 + CH_3 = CH_3O + NO$	$1.50E + 13$	0.0	0.0
15	$NO + CH_3O_2 = NO_2 + CH_3O$	$2.53E + 12$	0.0	-358

TABLE 2: Elementary steps in the NCN pathway of prompt NO formation. The forward reaction rate is given by $k_f = A_f T^{n_f} \exp(-E_f/RT)$ [13].

		A_f	n_f	E_f
1	$CH + N_2 = CN + H$	$3.0E + 12$	0.0	22155
2	$CN + N_2O = CN + NO$	$6.0E + 13$	0.0	15360
3	$CN + N_2O = NCN + NO$	$1.80E + 10$	0.0	1450
4	$CN + NCO = CN + CO$	$1.8E + 13$	0.0	0.0
5	$C_2O + N_2 = CN + CO$	$7.0E + 11$	0.0	17000
6	$CH + N_2 = HNCN$	$1.65E + 21$	-3.62	14196
7	$HNCN + M = H + CN + M$	$1.79E + 28$	-3.44	64502
8	$HNCN + O = NO + HCN$	$1.22E + 14$	0.05	73.5
9	$HNCN + O = NH + NCO$	$5.6E + 13$	0.05	73.5
10	$HNCN + O = CN + HNO$	$9.36E + 12$	0.05	73.5
11	$HNCN + OH = CN + H_2O$	$8.28E + 03$	2.78	3135
12	$HNCN + O_2 = HO_2 + CN$	$1.26E + 08$	1.28	24240
13	$NCN = N + CN$	$2.95E + 30$	-5.29	117090
14	$NCN = C + N_2$	$2.66E + 28$	-5.23	83110
15	$NCN = CNN$	$3.69E + 29$	-5.84	78410
16	$NCN + H = HCN + N$	$1.89E + 14$	0.0	8425
17	$NCN + O = CN + NO$	$2.54E + 13$	0.15	-34
18	$NCN + O = CO + N_2$	$2.42E + 02$	2.32	-1135
19	$NCN + O = N + NCO$	$2.2E + 09$	0.42	-157
20	$NCN + N = N_2 + CN$	$1.0E + 13$	0.0	0.0
21	$NCN + C = CN + CN$	$1.0E + 13$	0.0	0.0
22	$NCN + OH = HCN + NO$	$3.32E + 10$	-0.97	7290
23	$NCN + OH = HCN + NO$	$4.69E + 10$	0.44	4000
24	$NCN + O_2 = NO + NCO$	$3.8E + 09$	0.51	24590
25	$NCN + CH = HCNCN$	$3.21E + 13$	0.0	-860
26	$NCN + CN = C_2N_2 + N$	$1.25E + 14$	0.0	8020
27	$NCN + CH_2 = H_2CN + CN$	$7.99E + 13$	0.0	4630

nitrogenous compounds in coal give rise to ammonia (NH₃) and hydrocyanic acid (HCN), which are then oxidized to NO [30]. However, biodiesel fuels are mixtures of long-chain methyl esters and as such are considered to be nitrogen free, meaning that it is not necessary to consider the effects of fuel-bound nitrogen when modeling their combustion. Moreover, contemporary manufacturing techniques make it possible to ensure that the fuel's nitrogen content remains negligible.

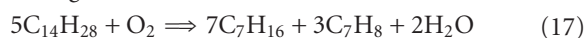
In addition to these four major routes for NO_x formation, there are several unverified mechanisms, for example, diazomethane, CH₂N₂, [38], NNH [39], and stepwise N₂H₃ [40] routes. Since all of these mechanisms either require further experimental validation or have yet to demonstrate their relevance experimentally, they were not considered in the study reported herein.

This article describes a study of the contributions of two verified mechanisms of NO formation (the thermal NO/N₂O and NCN-based prompt NO mechanisms) to the elevated NO_x emissions observed during the combustion of biodiesel, using numerical methods. In particular, calculations of the chemical kinetics of combustion and simulations of diesel engine behavior were performed. Parametric ϕ - T maps were constructed on the basis of the simulated results, leading to a plausible explanation for the increased NO_x emissions.

2.5. Combustion Mechanisms. The combustion mechanisms of real hydrocarbon fuels involve a lot of species and chemical reactions. In order to accurately model complex chemical phenomena, it is necessary to use validated detailed and reduced mechanisms. The reduced chemical mechanisms used in CFD studies are simplifications of the (more realistic) detailed mechanisms. The earliest models used a series of one-step reactions to describe the conversion of fuel to products (water and carbon dioxide in the simplest case). This mechanism is normally called the global reaction mechanism, and it is not widely used nowadays because of its poor accuracy. However, some elements of the approach are retained in the mechanisms based on so-called surrogate fuel components, which are used to represent real fuels.

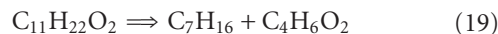
The work described herein focused on three surrogate fuel components and their associated combustion mechanisms: diesel oil surrogate (DOS) [10], rapeseed methyl ester (RME) [11], and palm-oil methyl ester (PME) [41].

2.5.1. The Diesel Oil Surrogate Mechanism. The practical diesel oil consist of a great number of aliphatic, cyclic, and aromatic compounds, and their combustion is too complex to be modeled using a comprehensive set of chemical reaction mechanism for each constituent. Consequently, a diesel oil surrogate model was proposed, as is a 70/30% mixture of *n*-heptane (C₇H₁₆) and toluene (C₇H₈) to achieve the same C/H proportion and cetane number as real diesel oil [10]. Both components of the mixture can be formed by the pyrolysis of C₁₄H₂₈, which is taken to be representative of a "real" diesel molecule; a global oxidative pyrolysis step, shown in (17), was added to the combustion mechanism to account for the decomposition of this molecule into the components of the surrogate mixture:



The *n*-heptane and toluene represent the aliphatic and aromatic compounds of real diesel oil, respectively. The DOS combustion mechanism involves 68 species participating in 280 reactions. The physical properties of DOS are assumed to the combination as real diesel oil heat of formation, density, vapor pressure, and thermal conductivity; the enthalpy is set equal to that of *n*-dodecane, and the critical temperature, latent heat, liquid viscosity, and surface tension are set equal to those for *n*-hexadecane [13]. The DOS mechanism has been validated against shock-tube autoignition delays measured at different pressures, temperatures, and equivalence ratios [10]. It has been used in 3D CFD simulations of diesel engines that generated predictions of the in-cylinder parameters which were in a good agreement with experimental data [10].

2.5.2. The RME Combustion Mechanism. The RME combustion mechanism was generated by combining the DOS, reduced mb (methyl butanoate), and md (methyl decanoate) submechanisms [11, 42, 43]. The first step of the mechanism involves the decomposition of methyl oleate (C₁₉H₃₆O₂), a major component of real RME fuel, into md (C₁₁H₂₂O₂), mb (C₅H₁₀O₂), and allene (C₃H₄) in a molar ratio of 1 : 1 : 1; see (18). The md then decomposes into *n*-heptane and mp2d (C₄H₆O₂), an intermediate in the combustion of md and mb, as as follows:



The oxidation pathway for the above substituent component was illustrated in Figure 1. The route for mb oxidation involves a series of hydrogen-abstract, oxygen-addition to the radical methyl esters, isomerization and ketohydroperoxide decomposition, Figure 1(a). The md decomposes into mp2d and *n*-heptane, see Figure 1(b). The submechanism of mp2d was already considered in the mb mechanism. The oxidation of *n*-heptane was only depicted for the pathway of H-abstraction and the decomposition of *n*-heptyl radical for clarity. The oxidation of allene is in a more straightforward way to the final products and low level intermediates (e.g., CH₂O, H₂O, C₂H₄) but less subbranch reactions, Figure 1(c).

The physical and thermal properties of RME are taken to be identical to those of methyl oleate [25, 44]. The final reduced RME combustion mechanism features 98 species and 450 reactions and was validated against experimental data obtained using a Volvo D12C diesel engine [11].

2.5.3. The PME Combustion Mechanism. PME oxidation is represented by the detailed methyl palmitate, MP, mechanism, which features 4222 species and 41573 reactions and was automatically generated using the EXGAS software package [41]. It has been validated against the measured conversion rates of methyl dodecanoate in a jet-stirred reactor, and the rules used when generating it have been described in detail [41]. The skeletal reaction diagram shown in Figure 2 illustrates the main pathway in the oxidation of PME.

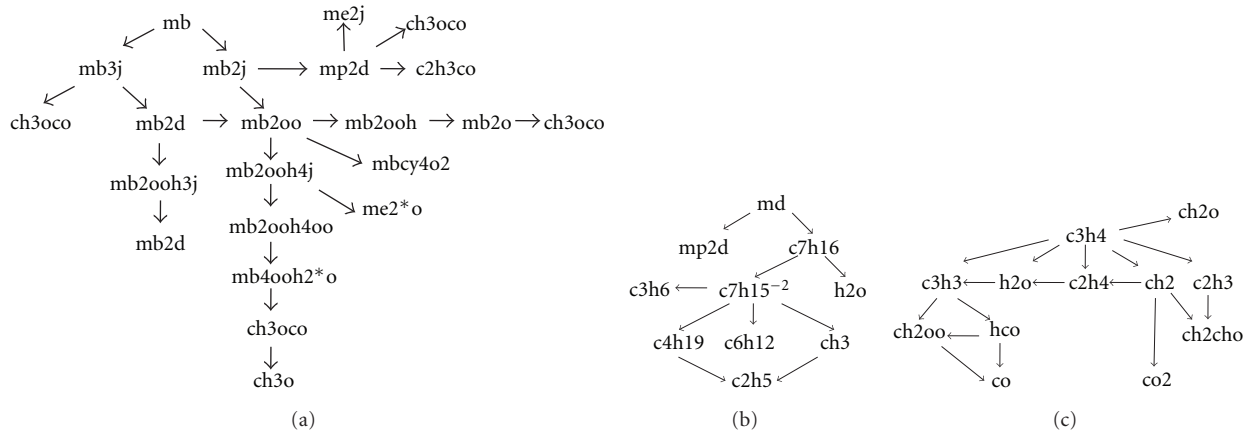


FIGURE 1: The oxidation pathway analysis for substituent components (a) methyl butanoate, $C_5H_{10}H_2$, (b) methyl decanoate, $C_{11}H_{22}O_2$, (c) allene, C_3H_4 .

As shown, the MP molecule decomposes into low level methyl esters and olefin radicals directly via β -scission of the C–C bonds at high temperatures. Conversely, under low-temperature conditions, oxidation is initiated by hydrogen atom abstraction caused by collisions between fuel and small radicals such as O, H, or OH. The addition of oxygen allows fuel radicals to form the peroxy methyl ester radical, which can undergo isomerization reactions and then decompose into ketones or cyclic ethers or undergo another addition of oxygen to form ketohydroperoxides. Ketohydroperoxides decompose then into two radicals providing chain branching to consume the C_{17} molecules. The thermodynamic properties of the most species involved were calculated using the THERGAS code and stored in CHEMKIN-2 format [45]. Properties of some species were taken from Burcat's data compilation [25]. The kinetic data for the chemical reactions, for example, isomerizations, combinations, and unimolecular decompositions, are calculated using KINGAS sub-package [45]. The detailed PME combustion mechanism is too large, that prevents its use in 3D CFD studies. The mechanism has been used in 0D calculations only, for example, for the analysis of autoignition and chemical equilibrium.

In order to study NO_x formation, the all thermal NO and N_2O submechanisms and the NCN pathway of prompt NO_x formation were incorporated into each of these three mechanisms. The prompt NCN-based NO_x mechanism, which features 24 elementary steps, was adapted from Konnov's mechanism number 0.6 [13] without modification.

2.6. Chemical Equilibrium/Kinetics Calculations. At equilibrium, the reactant concentrations do not change over time and the state parameters (temperature, pressure, and mixture composition) are determined by the species' thermal properties, that is, their enthalpies, entropies, and heat capacities. The equilibrium temperature (and thus, by definition, the adiabatic flame temperature) and equilibrium NO concentration can be predicted using 0D calculations, which are sufficiently fast to be performed using detailed mechanisms and provide an overview of the correlations between

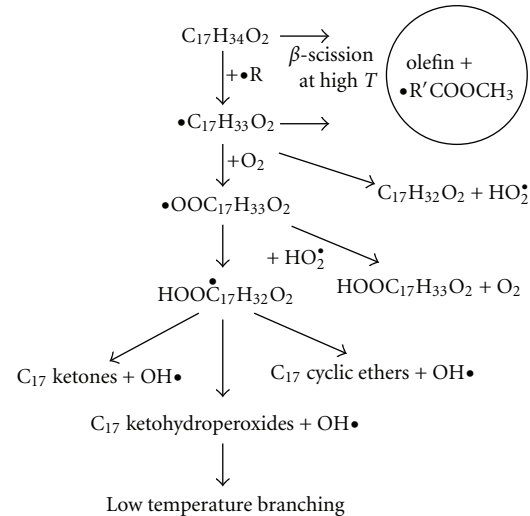


FIGURE 2: The skeletal reaction pathways for the oxidation of PME.

the factors that affect NO formation. To this end, the EQUIL code [8] of the CHEMKIN-2 package was used to calculate the composition and temperature of the equilibrium mixture, in terms of the concentrations of species such as NO, CH_2 , and CH. The flame temperature is a particularly useful property because of the pronounced temperature dependence of thermal NO formation. Particular attention was paid to the concentrations of the methylidyne/methylene radicals (CH and CH_2) because they are involved in the initiation of the prompt NO reactions. For illustrative purposes, the EQUIL analysis was performed for the DOS, RME, and PME fuels, assuming an initial pressure of 3000 kPa, an initial temperature of $626.84^\circ C$, and allowing the equivalence ratio to vary in the range $\phi = 0.1-9$, in a constant volume system.

To identify the reactions that have the most significant effects on the rate of NO formation, 0-D calculations were performed using the perfectly stirred reactor (PSR) model [9] as implemented in the CHEMKIN-2 package. The PSR model assumes the mixing of the oxidant and fuel to be

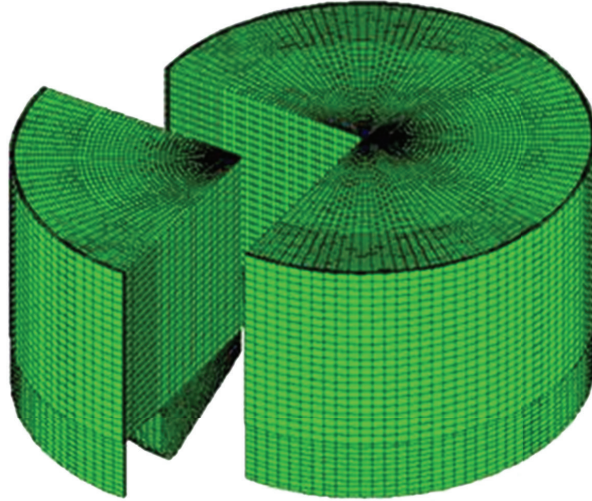


FIGURE 3: The full computational mesh for the Volvo D12C diesel engine, comprising 400,774 cells, and a 72-degree sector mesh with ~80,000 cells at BDC.

infinitely fast and the reactor parameters to be spatially uniform. Therefore, during the mixture's residence time in the reactor, combustion proceeds under chemical control. This assumption provides a convenient platform for studying the formation and emission of species such as NO using inherent sensitivity analysis. The sensitivity coefficients indicate the most sensitive chemical reactions in the various NO-forming pathways that are operational at different temperatures. To simulate the isothermal system used in experiments, a diluted fuel mixture (fuel:N₂, 0.3:99.7) and an oxidizer mixture (O₂:N₂, 21:79) were injected through the inlet port at constant ambient pressure and different initial temperatures (1226.84°C, 1526.84°C, and 2026.84°C). The equivalence ratio was assumed to be 0.5 that is regarded as a typical averaged ϕ value for the diesel engine combustion.

2.6.1. 3D Diesel Engine Modeling. 3D CFD diesel engine modeling was used to investigate the impact of biodiesel fuel on the amount of NO_x emitted via the exhaust during normal operation of the engine. The engine modeled in this paper is the one-cylinder, direct injection Volvo D12C research engine with a displacement volume of 2 L. The engine has an axisymmetric bowl-in-piston geometry with a peak at the centre of the bowl and a five-hole injector placed vertically in a central region of the cylinder. The relevant engine specifications (geometry and operating conditions) are listed in Table 3. A full 360° mesh comprised nearly 400,000 cells and a 72° sector mesh consisting of ~80,000 cells at Bottom Dead Center, BDC, was used in the modeling studies, as shown in Figure 3. The full- and sector-engine meshes were constructed using the K3PREP preprocessor embedded in the KIVA3V code. A partial engine cycle (starts from Inlet Valve Close, ~-160 CAD ATDC (Crank Angle Degree After Top Dead Center), up to 120 CAD ATDC, by which point the combustion process has gone to completion) was analyzed using the 3D CFD model based on the KIVA3V

TABLE 3: The specifications and operating conditions of the Volvo D12C diesel engine.

Bore	131 mm
Stroke	150 mm
Squish	1.85 mm
Connecting rod	260 mm
Injector nozzle dia (\varnothing)	0.235 mm
Engine speed	1000 rpm
Start of injection	-5.5 CAD ATDC
Injection duration	9.2 CAD
Injection mode	Main
Injected mass/stroke	60.8×10^{-6} kg
Initial pressure	103 kPa
Initial temp	56.84°C
Included angle of spray	145 deg
Spray cone 1/2 angle	12.5 deg
Initial droplet temp	76.84°C

code coupled with semidetailed combustion chemistry kinetics for DOS and RME fuels. The computational submodels implemented in the code to treat diesel spray combustion processes are listed in Table 4.

2.6.2. Parametric ϕ -T Maps. The use of static ϕ -T maps [46] and simplified combustion models in 3D engine simulations makes the results of such analyses more comprehensive. We present the results of an extended analysis based on detailed chemical modeling of the combustion of biodiesel fuels. These maps can be described as being "dynamic" [47], because the pressures and elapsed times after fuel injection used when plotting the parametric regions are continuously updated and correspond to the values calculated by the 3D

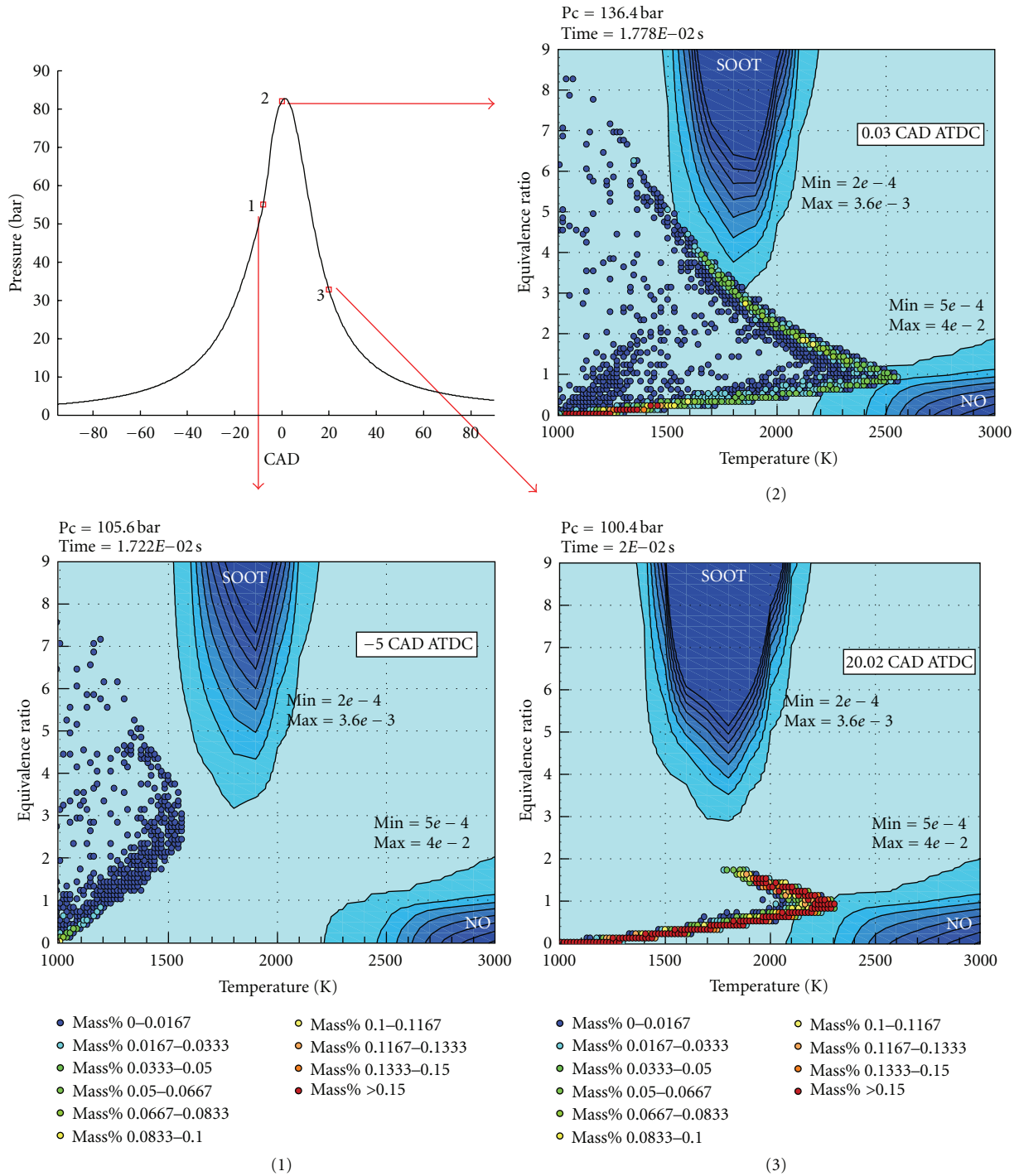


FIGURE 4: Schematic showing the construction of parametric ϕ -T dynamic maps. Maps 1–3 correspond to different points on the compression/expansion pressure curve.

engine simulation (see Figure 4). The points plotted on the maps represent the ϕ -T values of in-cylinder cells, while the species mass fraction corresponding to each ϕ -T region is labeled by its color. The positions of these points on the emissions maps provide useful insights into the complex relationships between combustion and the formation of emissions. The kinetic calculations were carried out using a special

option, TTIM, of the SENKIN code [48] of the CHEMKIN-2 package.

The equivalence ratio, one of the key parameters in the map, needs to be treated carefully when dealing with oxygenated fuels such as biodiesel. The approach used when calculating the value of ϕ for hydrocarbon fuels such as DOS is straightforward, as discussed elsewhere [47, 49]. When

TABLE 4: The computational submodels encoded in the KIVA3V, Rel. 2 code.

Turbulence model	RNG k - ϵ model
Breakup model	Hybrid KH-RT model
Collision model	Coalescence/grazing
Turbulent dispersion model	Gaussian probability distribution
Spray/wall interaction model	Particle method
Heat transfer model	Improved Law-of-Wall model
Evaporation model	Single component fuel
Combustion model	Detailed Arrhenius kinetics
Turbulence/chemistry interaction	PaSR model
Soot model	HACA pathway and simplified surface kinetics
NO _x formation model	Thermal and prompt NO

TABLE 5: Oxidation numbers of elements of interest in the saturated stoichiometric products [49].

Element	Oxidation number
Carbon, C	+4
Hydrogen, H	+1
Oxygen, O	-2
Nitrogen, N	0

dealing with oxygenated fuels, however, it is necessary to consider the oxygen atoms present in the fuel molecules. The chemical equivalence ratio was defined on the basis of the oxidation states of the elements in the fuel [49]:

$$r = - \frac{\left[\sum_{i=1}^{\text{NLM}} V_i^+ b_i \right]}{\left[\sum_{i=1}^{\text{NLM}} V_i^- b_i \right]}, \quad (20)$$

where V_i^+ and V_i^- are positive and negative oxidation states of the i th element in the relevant species (see Table 5). At least one of these states must be zero.

For example, if the negative oxidation state for oxygen is equal to -2 , its positive oxidation state is zero. The values of b_i in expression (20) are given by

$$b_i = \sum_{k=1}^{\text{NS}} a_{ik} n_k \quad (i = 1, \dots, \text{NLM}, k = 1, \dots, \text{NS}), \quad (21)$$

where NLM is the number of elements, NS is the number of species, a_{ik} is the number of kg-atoms of element per kg-mole of species k , and n_k is the kg-mole number of species k in the mixture, (kg-mole)/kg.

Equation (20) thus differs from the conventional fuel to oxygen equivalence ratio:

$$\phi = \frac{f/o}{(f/o)_{\text{st}}}, \quad (22)$$

where $(f/o)_{\text{st}}$ is the fuel/oxygen mass ratio under stoichiometric conditions.

Equation (22) is applicable to hydrocarbon-air mixtures before combustion has begun. When dynamic maps are constructed, the initial mixture composition is always represented by reactants and combustion products exported from the previous stages. Under such conditions, (22) is not applicable, but (20) can be used to characterize the mixture's stoichiometry. It can be shown that the two equivalence ratios r and ϕ are identical under stoichiometric conditions. They also take the identical values when considering the initial mixture consisting of only fuel and oxygen; this can be demonstrated by considering the example of RME, C₁₉H₃₆O₂, for which

$$\begin{aligned} r &= - \frac{\left[\sum_{i=1}^{\text{NLM}} V_i^+ \sum_{k=1}^{\text{NS}} a_{ik} n_k \right]}{\left[\sum_{i=1}^{\text{NLM}} V_i^- \sum_{k=1}^{\text{NS}} a_{ik} n_k \right]} \\ &= \frac{4 \cdot 19 \cdot n_{\text{fu}} + 1 \cdot 36 \cdot n_{\text{fu}} - 2 \cdot 2 \cdot n_{\text{fu}}}{2 \cdot 2 \cdot n_{\text{ox}}} \quad (23) \\ &= 27 \frac{n_{\text{fu}}}{n_{\text{ox}}} = \frac{n_{\text{fu}}/n_{\text{ox}}}{(n_{\text{fu}}/n_{\text{ox}})_{\text{st}}}. \end{aligned}$$

Here, $(n_{\text{fu}}/n_{\text{ox}})_{\text{st}} = 1/27$ for the RME fuel due to the stoichiometric relationship:



The subscripts fu and ox denote the fuel and the oxidizer, respectively.

In a contrast to (22), the formula (20) holds the initial mixture stoichiometry true in the course of all stages of combustion, that is, $dr/dt = 0$, and product concentrations can be used to calculate the chemical equivalence ratio.

Unlike (22), the equivalence ratio defined by (20) remains unchanged at every stage of the combustion process, that is, $dr/dt = 0$, and so the measured or calculated product concentrations can always be used to calculate the chemical equivalence ratio. This facilitates the construction of dynamic maps, see Figures 4 and 10–13. Before constructing a map, each species in the mixture must be classified as a fuel, an oxidizer, or a species with zero valency (also known as SSPs, saturated stoichiometric products) [49]. It is important to account for the effects of SSP species that may be present in the initial mixture when determining the chemical equivalence ratio; for example, mixtures containing recirculated exhaust gases are enriched by CO₂ and H₂O. In this way, it is able to distinguish between chemical species originated as products of the combustion process and those introduced as the EGR species.

When a cluster of cells intersects the peninsulas in which emissions (NO_x or soot) are formed, it characterizes the processes that lead to their formation. Another advantage of this analytical technique is that it is possible to simultaneously obtain maps for multiple different chemical species that are involved in a process of interest. For example, in the case of NO formation, it is interesting to study oxygen molecules and atoms (O₂ and O) and the hydroxyl radical, OH. This facilitates the quantitative analysis of emission-forming processes.

3. Modeling Results and Discussion

3.1. Results of the Chemical Equilibrium/Kinetics Calculation.

The predicted equilibrium adiabatic temperatures for different fuel/air mixtures are shown in Figure 5(a). For lean mixtures ($\phi < 1.0$), the temperature curves for three different fuel/air mixtures coincide with one another. Under rich conditions ($\phi > 1.0$), PME generates consistently lower ($\sim 70^\circ\text{C}$) temperatures than DOS when $\phi < 3.0$. This difference increases drastically for richer mixtures ($\phi > 3.0$) and reaches 110°C for $\phi = 9.0$. In a contrast, RME generates only slightly higher ($< 10^\circ\text{C}$) temperatures than DOS in rich mixtures ($\phi < 2.0$) and generates lower temperatures than DOS as the mixture becomes increasingly rich, reaching a maximum value of 60°C under the richest conditions examined.

The mole fraction of NO at equilibrium for mixtures with equivalence ratios between $0.1 < \phi < 2.5$ is plotted in Figure 5(b). At higher equivalence ratios, the NO concentration was extremely small and is not presented. It can be seen that the peak NO concentration occurs at an equivalence ratio of 0.78 for all three fuels. Over the equivalence ratios considered, RME and DOS generate the same equilibrium concentrations of NO aside from in a very narrow range (0.75–0.80), in which RME generates a slightly higher peak value. Under the similar ϕ range, the curve for PME gives slightly lower NO value and mirrors that of DOS for other ϕ values. These two pictures illustrate that the temperature difference between DOS and RME is relatively modest and so cannot be responsible for the large ($\sim 10\%$) increase in NO_x emissions described in the EPA report. On the other hand, RME and PME generated a lower ($< 20^\circ\text{C}$) adiabatic temperature and a similar NO concentration for rich mixtures ($1.0 < \phi < 2.0$). This unexpected result demonstrates that, when using PME, NO formation is not governed by thermal factor alone.

The equilibrium concentrations of methylidyne/methylene radicals (CH and CH_2), which are essential for the initiation of prompt NO formation, are shown (as functions of the equivalence ratio) in Figures 5(c) and 5(d), respectively.

In general, DOS/air mixtures contain less CH under slightly rich ($\phi < 1.8$) conditions and more CH under much richer ($1.8 < \phi < 6.0$) conditions than do the corresponding RME/air mixtures. The maximum CH concentration occurs at equivalence ratios of 1.7 for both DOS and RME. With PME, the CH concentration keeps a similar value as that of DOS at the region $\phi < 1.6$. Above this point, the CH level deviates from DOS curve and goes underneath it.

The absolute CH_2 concentration under any given set of conditions is typically about an order of magnitude greater than that of CH under the same conditions. For these three fuel/air mixtures, the CH_2 concentration increases rapidly from $\phi \approx 1.2$, reaching a plateau that spans the region between $\phi \approx 2.0$ and $\phi \approx 3.0$. Above $\phi \approx 3.0$, the concentration of CH_2 increases further, peaking at around $\phi \approx 3.4$. Beyond this point, the CH_2 concentration falls very slightly. The CH_2 concentration curves for RME and DOS coincide in the range $1.2 < \phi < 3$. When $\phi > 3$, the CH_2 concentration generated using DOS is $\sim 25\%$ higher than that generated with RME. The CH_2 concentration for PME takes the same

value as for DOS and RME under sub-stoichiometric conditions till $\phi \approx 2.0$. For a more rich mixture, the CH_2 concentration starts to fall down from the level observed with RME. These two separate peaks in the CH_2 plot are related to the formation/reduction of NO ($\phi < 2$) and soot ($\phi > 3$) [50]. The similar trend in CH plot is just a consequence of CH_2 distribution.

By correlating these four plots, it was found that the noticeable equilibrium NO concentrations occurred in the $0.1 < \phi < 2.0$ region, where RME and DOS afforded very similar temperatures and concentrations of CH/ CH_2 and NO (although the peak CH/ CH_2 concentration was slightly higher for RME for $\phi \approx 1.8$). It was expected that since DOS and RME generated very similar adiabatic temperature profiles, they would also generate similar NO concentration profiles. However, the higher CH concentration observed with RME should favor prompt NO formation a little bit thus resulting in RME generating a higher NO concentration at rich mixture regime. As such, the fact that DOS and RME have near-identical NO emission profiles cannot be explained by considering adiabatic temperature factors and prompt NO formation alone. The nearly identical adiabatic temperature for all fuels in a full ϕ range are indicative that lower LHV's for biodiesels are mostly due to fuel-bound oxygen atoms, but not a particular structure of the fuel molecules.

3.2. PSR Modeling Results. The normalized sensitivity coefficients for NO with respect to important reactions rate generated by PSR modeling are shown in Figure 6 for (a) DOS and (b) RME, focusing on the most sensitive reactions in the NO formation process. Three different temperatures (1226.84°C , 1526.84°C , and 2026.84°C) were examined. A positive sensitivity coefficient, as observed for the thermal NO formation reactions, indicates that increasing temperatures accelerate the formation of NO, while negative sensitivity coefficients indicate the opposite. Reactions for which no bar is shown do not significantly affect the rate of NO formation at the indicated temperature. The plots indicate that the most sensitive reactions (of both the Zeldovich and the NCN-based prompt NO mechanisms) had significant effects on both the combustion of RME and that of DOS.

This means that NO formation is dominated by the same reactions for both RME and DOS. As shown, the prompt NO reactions (R434, R439, R449, R459, R460) are important at low-temperature, 1226.84°C . Their influence decreases as the temperature rises. Once the temperature reaches 2026.84°C , NO formation becomes governed by the Zeldovich mechanism (R336, R338). The branching reactions (R140, R141, R142) that consume the active species O and O_2 compete with those involved in NO formation in both the thermal and prompt mechanisms and thus have the largest negative sensitivity coefficients.

3.3. Diesel Engine Modeling Results. The predicted in-cylinder parameters for the Volvo D12C diesel engine fueled by DOS and RME are plotted in Figures 7 and 8. The detailed

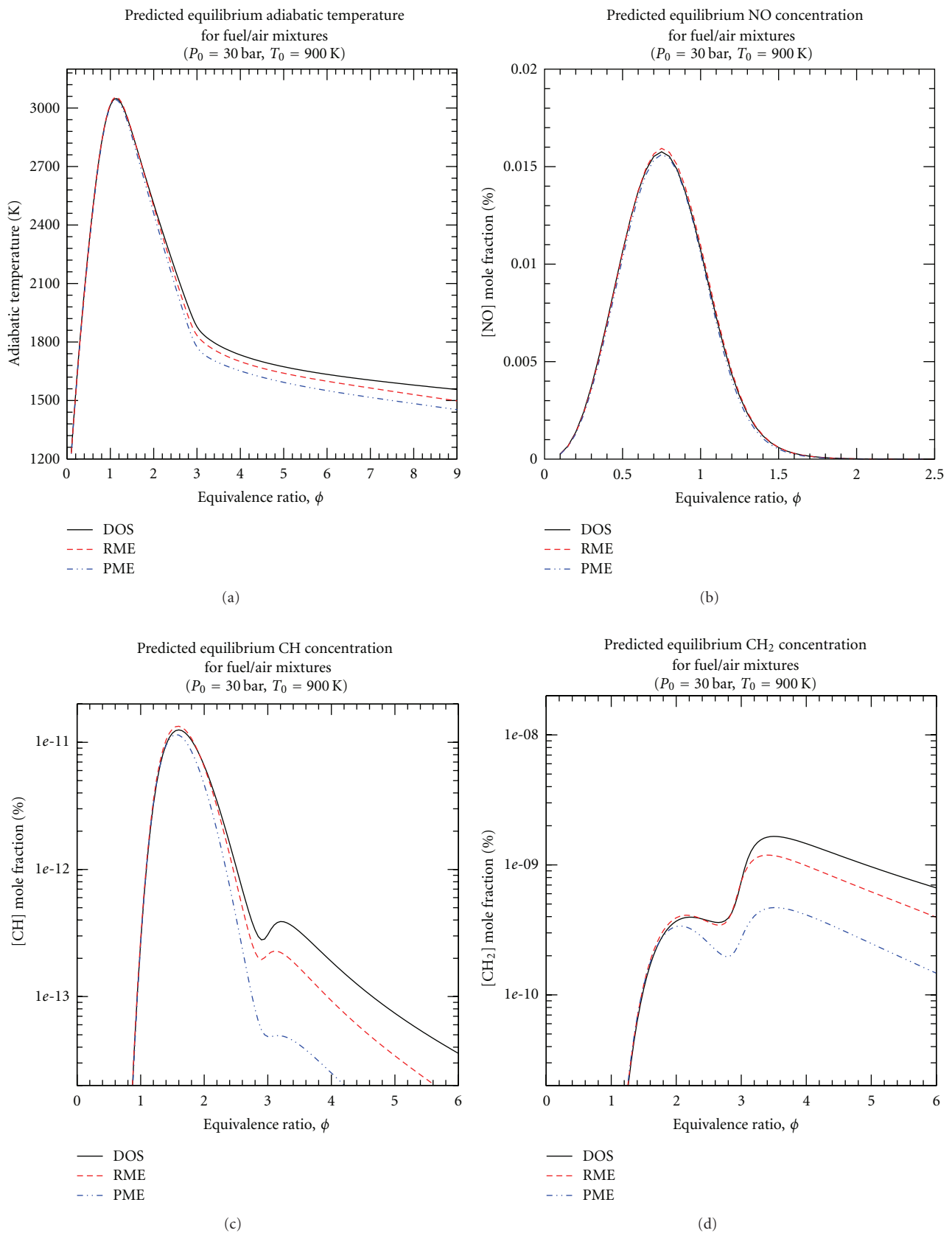


FIGURE 5: Predicted equilibrium (a) adiabatic temperature, (b) NO concentration (c) CH concentration, (d) CH₂ concentration for DOS/air (black line), RME/air (red dash line), and PME/air (blue dash line with dots) mixtures. $T_0 = 626.84^\circ\text{C}$, $P_0 = 3000$ kPa.

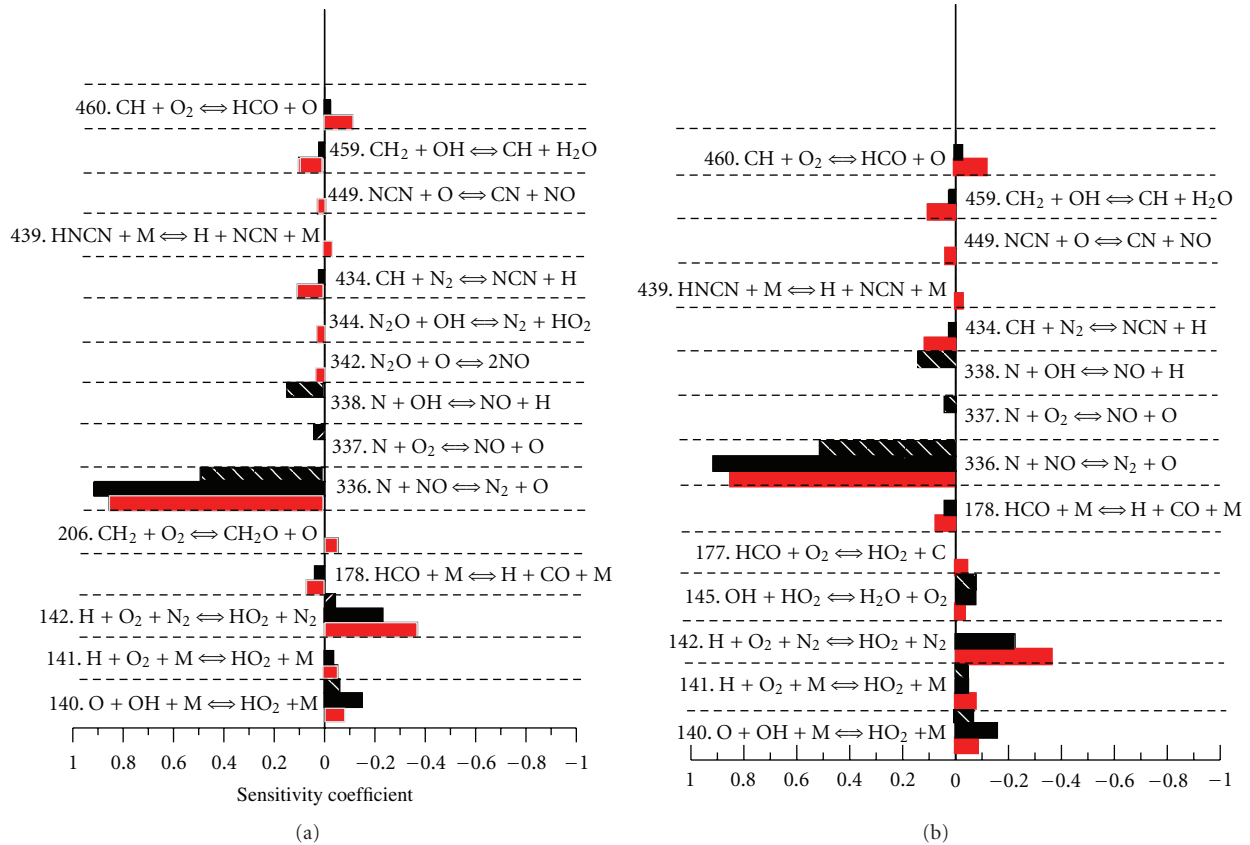


FIGURE 6: The normalized sensitivity coefficients for NO with respect to the important reaction rates, (a) DOS, (b) RME at different temperatures (red bars indicate sensitivity coefficients at 1226.84°C, black bars at 1526.84°C, and hatched bars at 2026.84°C).

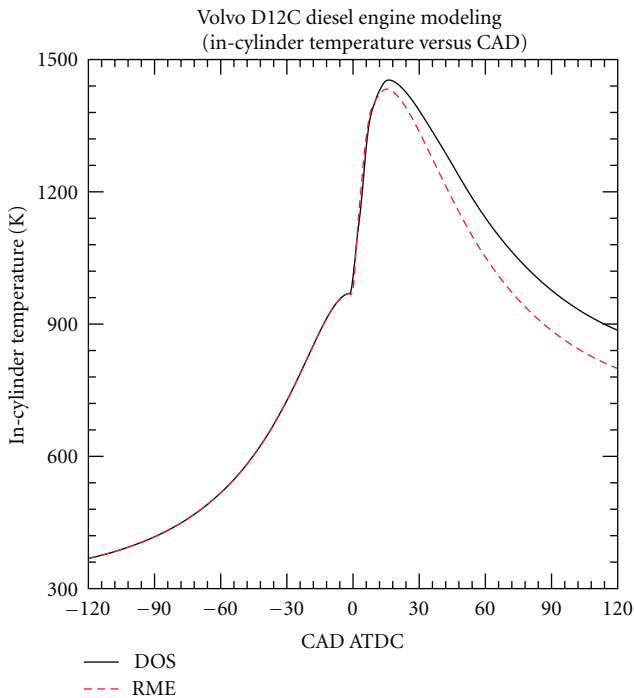


FIGURE 7: Averaged in-cylinder temperatures for the Volvo D12C diesel engine fuelled by DOS (solid line) and RME (dash line), without EGR.

PME oxidation mechanism was not used in the 3D engine simulation because of its size. Instead, the reduced mechanism based on the surrogate components was used. Since this study was focused on the formation of NO, only parameters relevant to this process (averaged in-cylinder temperature, NO concentrations) are discussed; parameters such as the in-cylinder pressure and energy release rate are ignored as illustrations even though they are important in characterizing engine performance. As shown in Figure 7, before the onset of combustion, the average in-cylinder temperature curves for DOS and RME are identical. The main combustion starts around top dead center (TDC). The heat released by the chemical reactions causes the in-cylinder temperature to increase, peaking after TDC. DOS gives a higher temperature due to its greater lower heat value (LHV), (44 MJ/Kg) compared to RME (37 MJ/Kg). This temperature difference increases during the expansion stroke.

The in-cylinder NO concentrations were plotted as functions of CAD ATDC. Both DOS and RME fuels were tested with the NCN prompt NO mechanism and without to assess the contribution of each NO formation mechanism. As shown, the NO concentration increases sharply after the initiation of combustion and remains high until combustion is complete. The NO curves explicitly show that most of the NO is formed during the early stages of combustion. The combustion temperature during the late expansion stroke does not affect the final NO concentration.

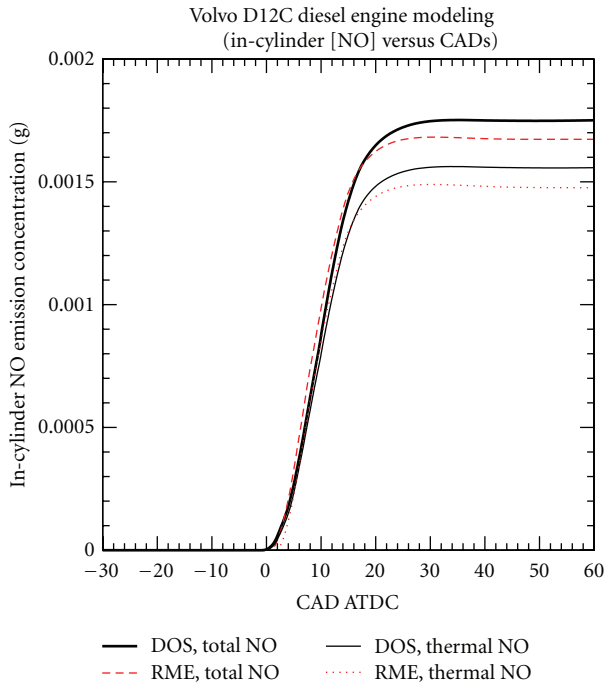


FIGURE 8: Averaged in-cylinder NO concentrations (total value indicated by bold line, thermal NO by the thin line) for the Volvo D12C diesel engine fuelled by DOS (solid line) and RME (dashed line), without EGR.

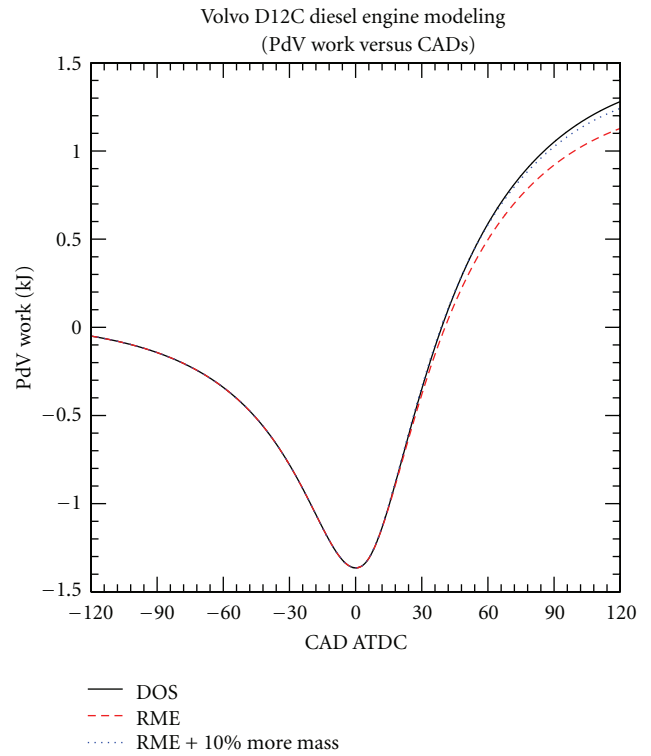


FIGURE 10: Predicted PdV work for the Volvo D12C diesel engine fuelled by DOS (black solid line), RME (red dashed line) and RME+ (dash-dot line), without EGR.

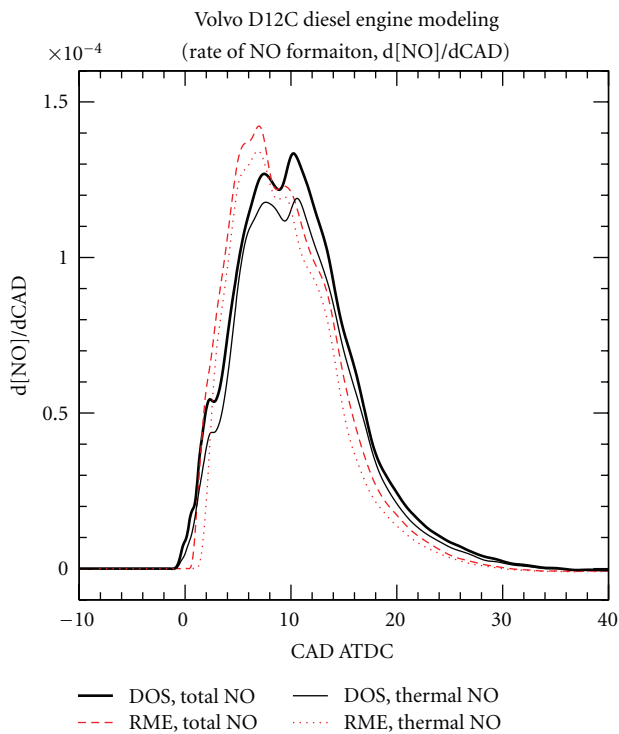


FIGURE 9: Averaged in-cylinder rates of NO formation for the Volvo D12C diesel engine fuelled by DOS (black solid line) and RME (red dashed line), without EGR.

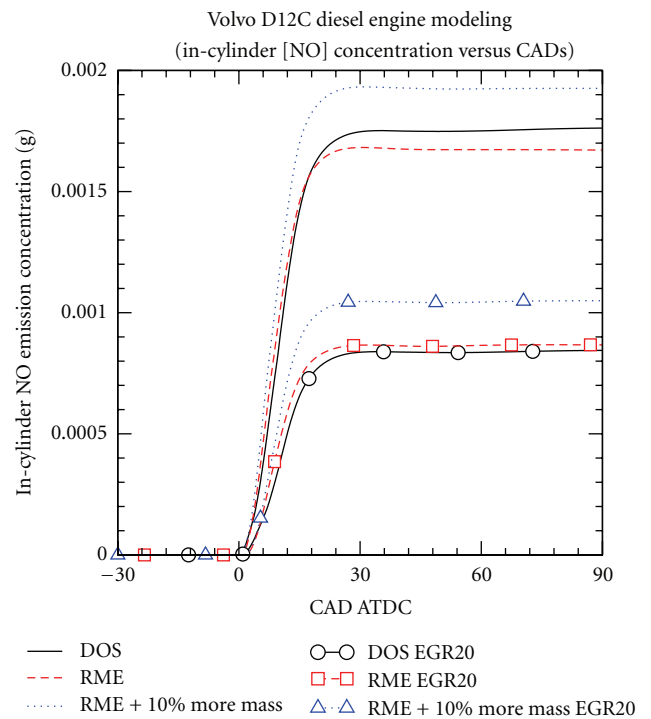


FIGURE 11: Impact of EGR level on the averaged in-cylinder NO concentrations (total value) for the Volvo D12C diesel engine fuelled by DOS (solid line), RME (dash-dot line), and RME+ (dotted line) without EGR; the same line style with symbols was the results for 20% EGR level condition.

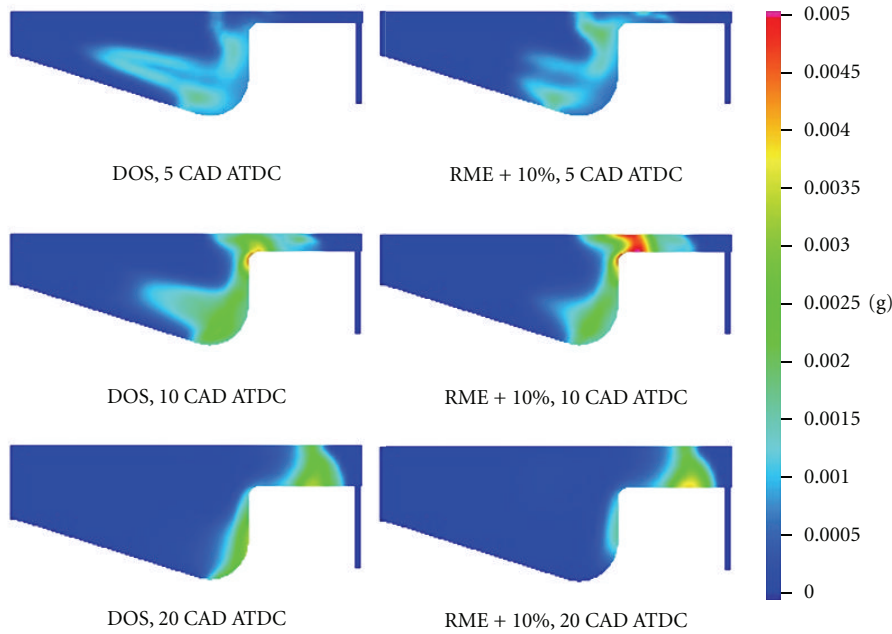


FIGURE 12: In-cylinder NO concentration distribution for the Volvo D12C diesel engine fuelled by DOS and RME+ 10% at 5, 10, 20 CAD ATDC without EGR.

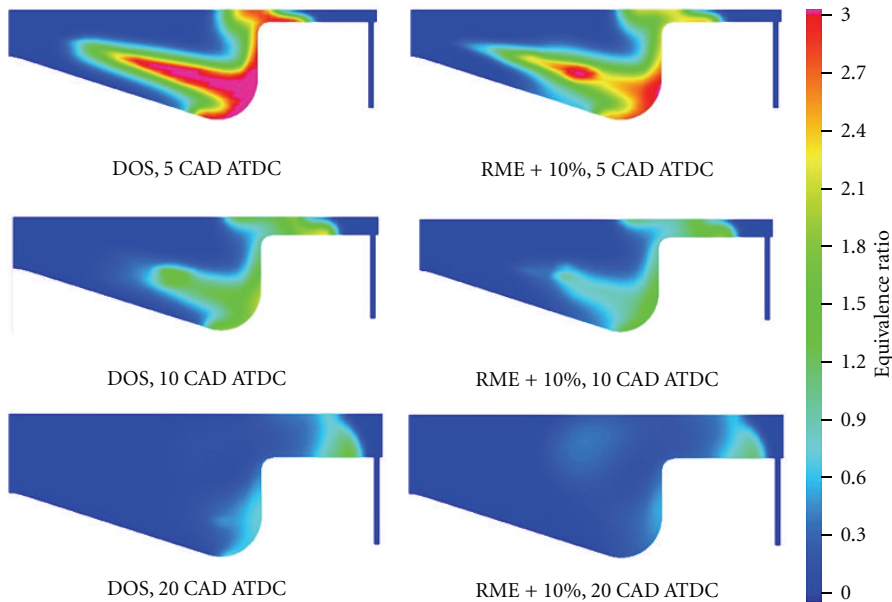


FIGURE 13: In-cylinder equivalence ratio distribution for the Volvo D12C Diesel engine fuelled by DOS and RME+ 10% at 5, 10, 20 CAD ATDC without EGR.

The peculiarities of NO formation are illustrated by the data on the rate of NO formation shown in Figure 9. It is observed that when using RME, the rate of NO formation begins to rise at a later stage than is the case of DOS. But once the NO formation was initiated, it goes beyond that of DOS immediately.

To compensate the reduced energy content of biodiesel fuel, extra RME (67×10^{-6} kg, which is 10% more in mass relative to the original value), called RME+, was injected

into the engine cylinder, that, on the other hand, keeps the engine operating on a constant power delivery basis. In general, the indicated engine work is represented by the pressure-volume work, or PV work, which is the integration of differential component PdV work on the CADs. Hence, by comparing the PdV work, one can examine if the combustion of different fuels gives the same indicated engine work (see Figure 10), in other words, a constant power delivery. Figure 10 illustrates that RME combustion (dot/dash line)

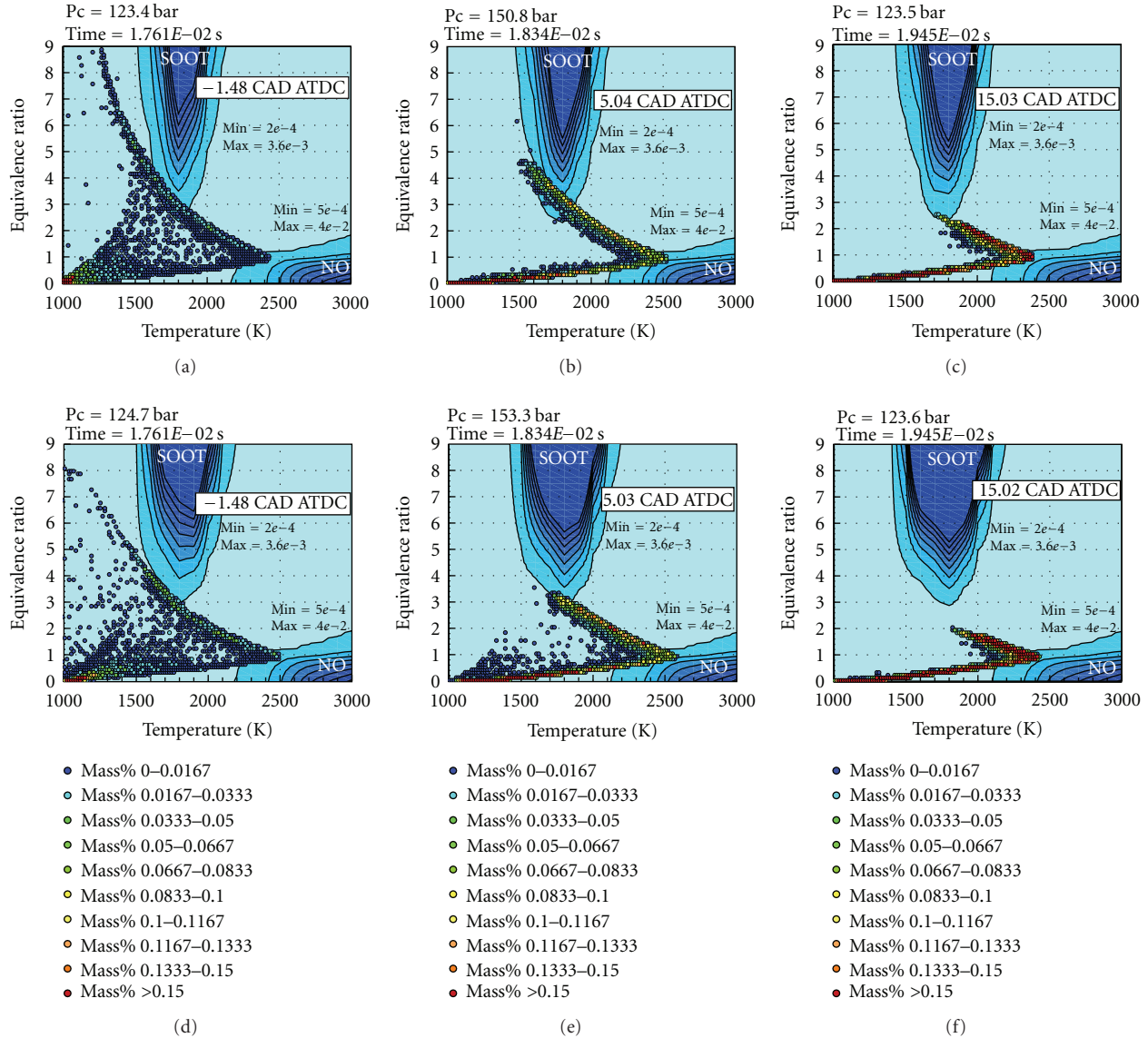


FIGURE 14: Parametric ϕ - T emission maps for instant soot and NO concentrations in the Volvo D12C Diesel engine fuelled by DOS (a–c) and RME (d–f) at different CADs (–1.5, 5.0, and 15.0, resp.); the engine was operated under 50% load with 30% EGR.

gives identical PdV value as diesel oil combustion (solid line) at the compression stroke, slightly lower PdV value at the expansion stroke. The RME+ produces exactly the same PdV value as diesel oil during the whole calculating engine cycle.

The predicted total in-cylinder NO concentration of the Volvo D12C diesel engine fuelled by diesel oil, RME, and RME+ was presented in Figure 11 for two different EGR levels: 0% and 20%. It shows the RME+ produce more NO emission compared to the pure diesel oil. This was observed for both EGR levels and represented the emission trends under the real engine operating conditions. Aside from this, one can also conclude that the cooling impact of EGR on the reduction of NO emission is more noticeable for the combustion of diesel oil, since the difference of NO value between 0% EGR (solid line) and 20% EGR (solid line

sampled by circles) is larger than that of RME. Such a less-effective EGR behavior of RME fuel is ascribed that the fuel-bound oxygen in RME fuel molecular (approx. 11% in mass fraction) and the additional oxygen in the EGR gas following biodiesel combustion results in less inert species (CO_2 , H_2O , etc.) which are present to absorb the heat of combustion, hence less cooling effect [16].

The final absolute NO concentrations for the combustion of these three fuels under two different EGR levels are shown in Table 6. As shown in Table 6, for 0% EGR level, the prompt NCN pathway accounts for 11.1% and 12.1% of the NO formation with DOS and RME, respectively. These data demonstrate that the prompt NO mechanism cannot explain the increased NO_x emissions described in the EPA report, since the mechanism is relevant in both RME

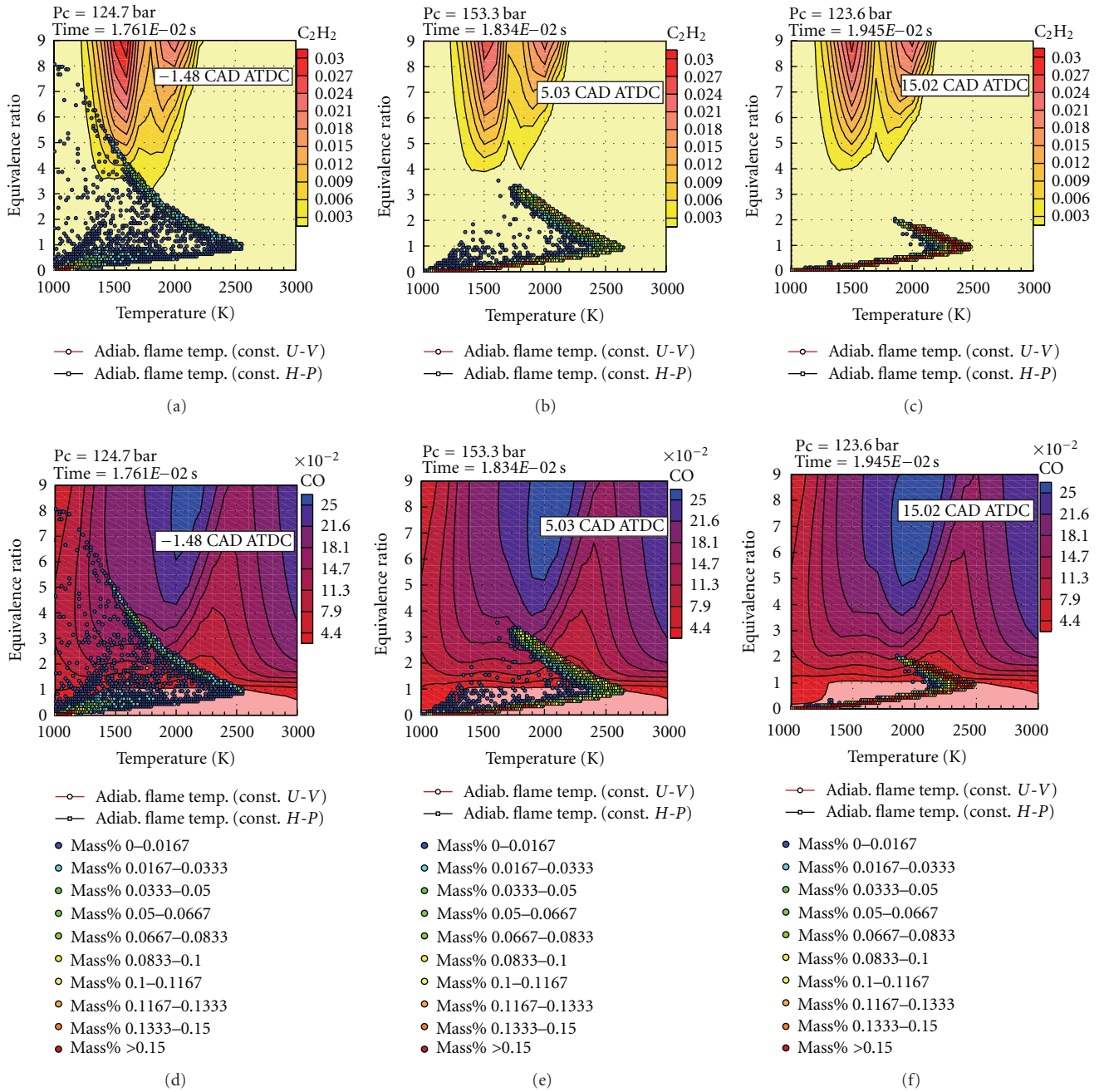


FIGURE 15: Parametric ϕ - T emission maps for instant acetylene, C_2H_2 concentrations (upper three plots) and carbon monoxide, CO concentrations (a, b, and c) in the Volvo D12C Diesel engine fuelled by RME at different CADs (-1.5, 5.0 and 15.0, resp.); the engine was operated under 50% load with 30% EGR.

and diesel combustion. Moreover, the contribution of the thermal NO mechanism is also similar for RME and DOS. However, for RME+, the thermal NO was promoted ~4% and the prompt NO was suppressed ~4% in proportion. The total NO increases ~10% compared with that of diesel oil combustion. This modeling result corroborated the similar emission trend reported by EPA.

Once a 20% EGR level was charged for the Volvo D12C diesel engine, the thermal NO formation is drastically reduced more than 50% for all fuels due to the suppressing

effect of lower-temperature combustion. The prompt NO emission for diesel oil and RME decreased only slightly but is kept nearly constant for RME+. Thereby, the proportion of prompt NO in the total NO concentration goes up generally for all fuels with EGR conditions.

To achieve deeper insights for the biodiesel NO_x increases, the in-cylinder NO concentration contour was visualized at difference crank angle instants for diesel oil and RME+, see Figure 12. One can see that the NO is mainly formed around the periphery of the reacting mixture. RME+

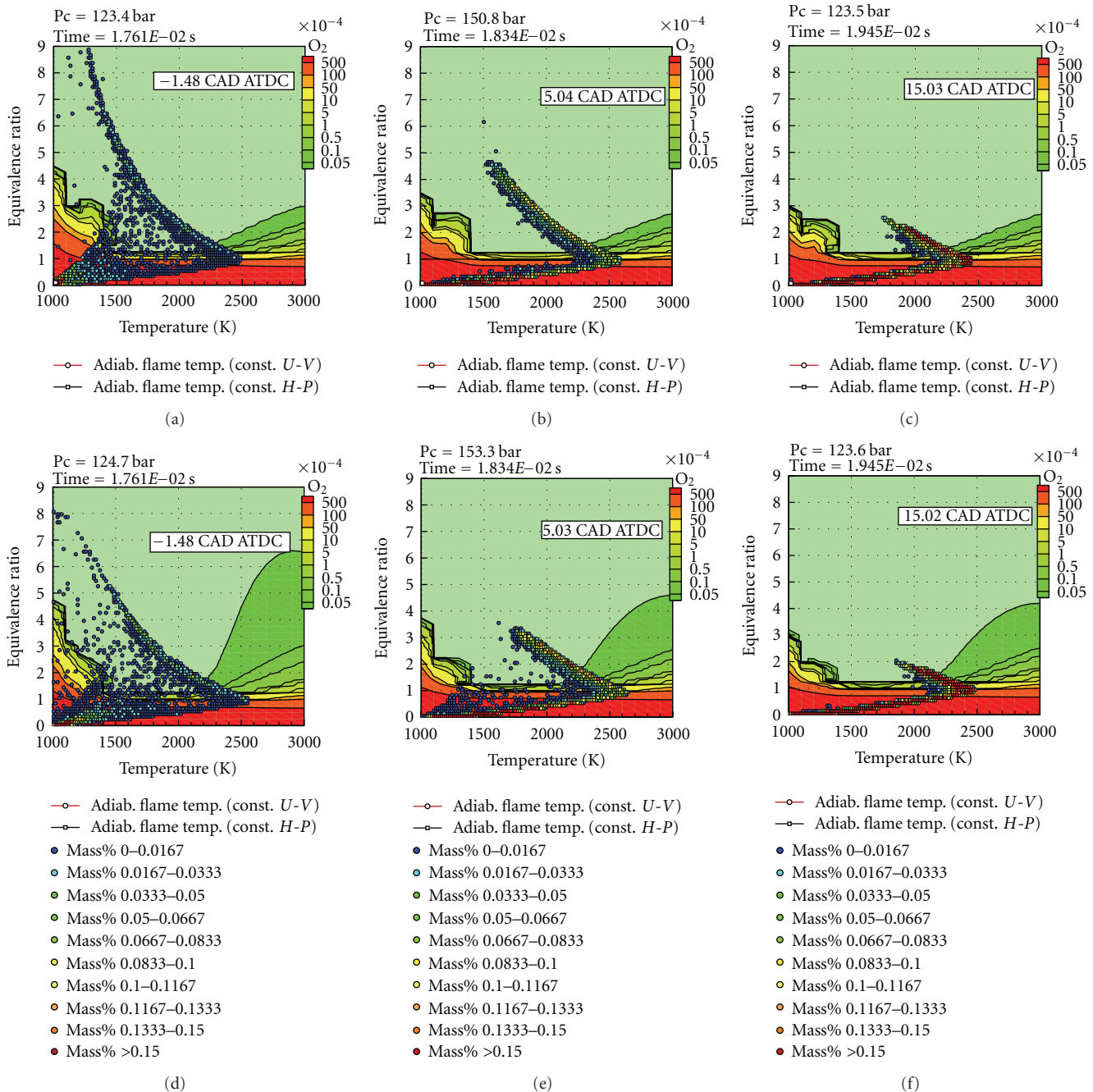


FIGURE 16: Parametric ϕ - T maps for instant O_2 concentrations in the Volvo D12C Diesel engine fuelled by DOS (a, b, and c) and RME (d, e, and f) at different CADs (-1.5, 5.0, and 15.0, resp.); the engine was operated under 50% load with 30% EGR.

combustion has a much wider and deeper colored (red and yellow) region around the periphery of the reacting mixing compared to diesel oil combustion, which means more NO was formed at this region.

3.4. ϕ - T Parametric Maps. Thus, neither the chemical equilibrium/kinetics calculations nor the 3D engine modeling provided any evident clues as to the origin of the increased NO_x emissions observed when using biodiesel. However, Figure 5(b) shows that NO is formed in a rather narrow

equivalence ratio range. As such, a small variation in ϕ could have a significant effect on the NO concentration. If combustion with RME will typically occur under leaner conditions than is the case with DOS, say with a 10% smaller value of ϕ , the quantity of NO formed during the combustion of RME would be $\sim 15\%$ greater than that formed with DOS, assuming that, in both cases, combustion was to proceed with an equivalence ratio between 0.78 and 1.5. This alone could, in principle, explain why biodiesel produces more NO_x during combustion. To verify if biodiesel

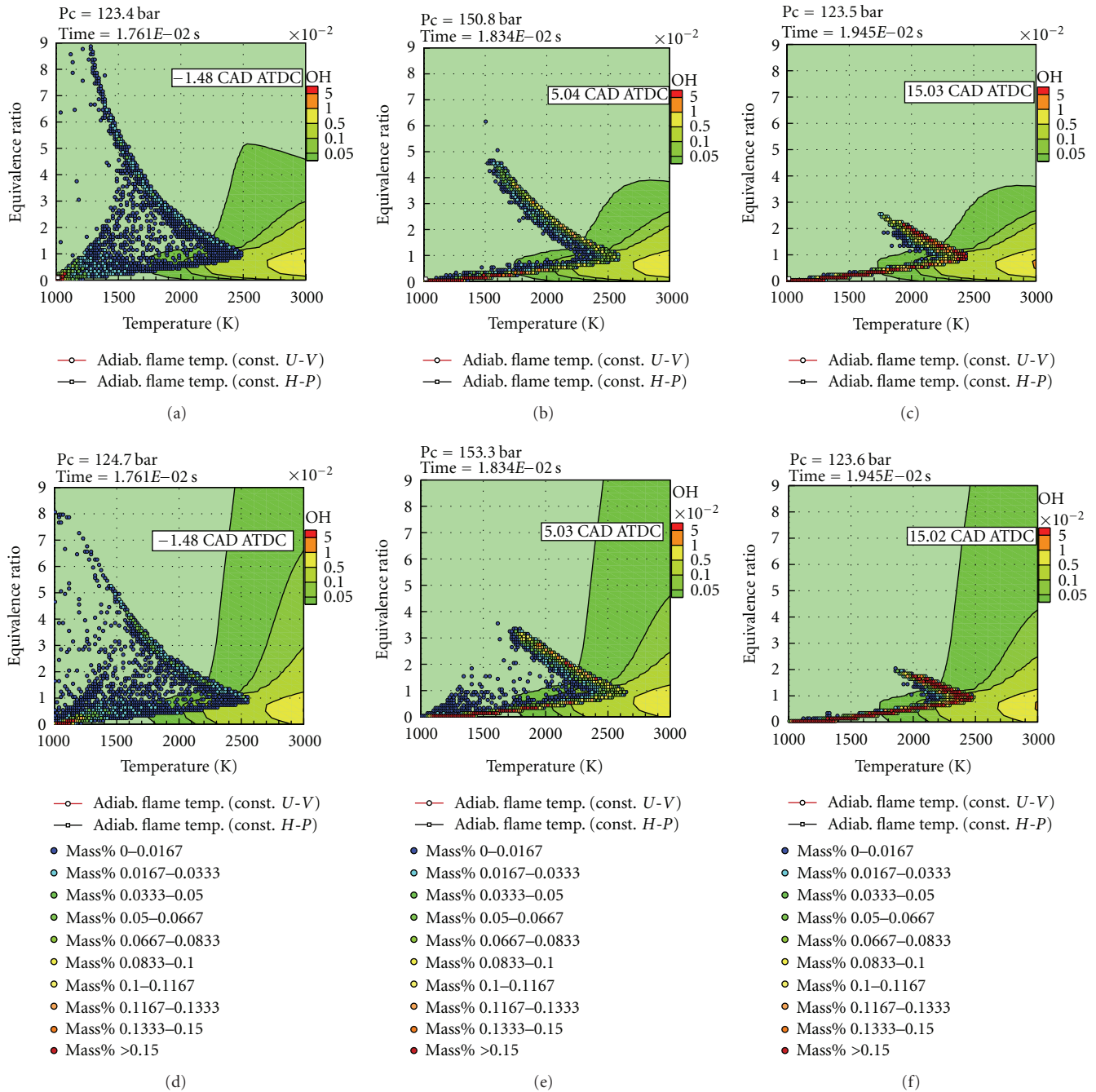


FIGURE 17: Parametric ϕ - T maps for instant OH concentrations in the Volvo D12C Diesel engine fuelled by DOS (a, b, and c) and RME (d, e, and f) at different CADs (-1.5, 5.0, and 15.0, resp.); the engine was operated under 50% load with 30% EGR.

combustion really has a leaner combustion, the equivalence ratio distribution in the diesel engine cylinder was presented for both diesel oil and RME at the same CADs instants as Figure 12, see Figure 13.

One can overlap the NO contour and equivalence contour and find out the highest NO concentration region locates at $\phi(0.6 \sim 1.8)$ under the diesel engine operating conditions. For the too high (red color) or too low (blue) equivalence ratio region, there is no NO formed (colored by blue) in Figure 12.

Furthermore, a convincing proof would be required to support the above conjecture. Such proof was obtained by analysis of dynamic ϕ - T maps for relevant in-cylinder species NO, O, and OH. The maps provide explicit visualizations of the conditions under which NO was formed and the distributions of the relevant species. The maps presented in Figures 14–17 were constructed for the Volvo D12C engine fuelled by DOS and RME operating under 50% load with 30% EGR, at the same indicated engine work for the tested fuels. Under these conditions, increased biodiesel NO_x

TABLE 6: The absolute NO concentration values contributed by different mechanisms for DOS, RME, and RME+ under 0% and 20% EGR level conditions.

Fuel	NO			
	Thermal NO ppm	Prompt NO ppm	Total NO ppm	Proportion % : %
DOS	551.0	68.6	619.6	88.9 : 11.1
RME	516.0	71.0	587.0	87.9 : 12.1
RME+ 10% more mass	617.49	57.86	675.35	91.4 : 8.6
DOS EGR20	244.32	52.58	296.9	82.3 : 17.7
RME EGR20	251.05	52.95	304.0	82.6 : 17.4
RME+ 10% mass EGR20	309.0	58.91	367.91	86.0 : 14.0

emissions consistent with the EPA report were observed in both experiments and simulations [11].

Figure 14 illustrates the instantaneous abundance of two in-cylinder species, soot and NO, for DOS and RME at different crank angles. It shows that NO formation occurs with relatively lean mixtures ($\phi < 2.0$) at high temperatures ($1927^\circ\text{C} < T < 2727^\circ\text{C}$), while soot was formed in rich mixtures ($\phi > 3$) at moderate temperatures ($1227^\circ\text{C} < T < 1727^\circ\text{C}$). These emission formation trends are not fuel specific, but by comparing Figures 14(a)–14(c) with 14(d)–14(f), it is apparent that, for RME combustion, the soot peninsula extends further in both the low- ($<1227^\circ\text{C}$) and high- ($>1727^\circ\text{C}$) temperature directions. That is to say, when using RME, soot formation occurs under a wider range of temperatures; in DOS combustion, these temperatures are either too low to allow soot formation or so high as to oxidize the soot as it forms. However, under these conditions, the area of intersection between the cluster points and the soot peninsula is narrower for RME (see Figures 14(d) and 14(f)) than for DOS (see Figures 14(a) and 14(c)), which is consistent with the observation that less soot is formed during RME combustion. Quantitative data on these processes can be obtained from the results of the 3D engine modeling.

The other intermediates, acetylene, C_2H_2 as a major soot precursor, and carbon monoxide, CO, for RME, are presented in Figure 15 to illustrate soot formation at incomplete combustion conditions. However, soot formation and oxidation are not the primary focus of this work, and they are not discussed further herein.

In terms of the formation of NO, the cell points show that for RME, the gaseous mass intersecting the NO formation region is larger than for DOS, in terms of both size (compare Figures 14(b) and 14(d)) and cell mass (compare the red areas in Figures 14(c) and 14(f)). This means that more NO is produced in the instant captured in the plots with RME than with DOS. The hypothesis that the leaner combustion that occurs when using biodiesel is responsible for the observed increase in NO emissions can be evaluated by constructing maps for the oxygen molecules or other oxidizing species at different crank angles. Because the equivalence ratio is determined by the O_2 concentration in the air and in the structure of the fuel molecules, it is interesting to study the effect of fuel-bound oxygen atoms on NO formation.

The ϕ - T O_2 species maps at different CADs are shown in Figure 16 for DOS (upper three plots) and RME (lower three plots). The different colors indicate the concentration of O_2 , with red denoting the highest concentrations, yellow denoting the intermediate value, and green denoting low concentrations. At temperatures between 1226.84°C and 2726.84°C , the highest O_2 level occurs under very lean conditions. A transition from the highest concentration to the lowest occurs within a narrow $\phi \approx 1$ region. One can see that a small amount of O_2 is observed even for the rich mixtures ($\phi \approx 3$). However, the green color occupies a very narrow area. This may be due to the fact that combustion requires the temperature to be sufficiently high to overcome the activation barriers of the reactions that initiate combustion. Under low-temperature conditions, the low rate of fuel oxidation means that more O_2 is available. Once again, the O_2 contour is not fuel specific.

It is apparent that, in RME combustion, more O_2 is present in the high temperature region ($T > 1726.84^\circ\text{C}$); see the green regions in the lower three plots of Figure 16. This is because RME is an oxygenated fuel that requires less external O_2 in order for combustion to occur. In the low-temperature range ($T < 1726.84^\circ\text{C}$), slightly less O_2 was retained with RME than with DOS due to its lower oxidation threshold. NO species are formed by the reaction of molecular nitrogen with oxidizing species at high temperatures; when using RME, the amount of available O_2 at these high temperatures with equivalence ratios between 0 and 5 is noticeably greater than is the case with DOS. As such, the fact that RME undergoes relatively lean combustion because of its oxygen content may explain increased NO emissions shown in Figure 14.

The hydroxyl (OH) radical also plays a significant role in thermal NO formation; maps for this species are shown in Figure 17. The same colors as were used previously are used to indicate the OH concentrations. It was observed that more OH radicals are formed during RME combustion, as shown by the greater width of the yellow regions in lower three plots of Figure 17. However, as discussed above, thermal NO formation alone cannot fully account for the increased NO_x emissions observed with biodiesel.

The approach developed herein also forecasts that the short-chain biodiesel, for example, mb, with a relatively

higher oxygen content can form too lean combusting mixture ($\phi < 0.78$) and produce less NO_x emissions.

4. Conclusion

Chemical equilibrium and kinetics calculations show that similar flame temperatures are achieved with RME and DOS, giving rise to comparable NO mole fractions under equilibrium conditions. The adiabatic temperature was predicted to be lower when using PME, but the NO concentrations generated using this fuel were nevertheless similar to those predicted for the other two over a wide range of equivalence ratios. In terms of the species involved in the formation of NO, it was predicted at low and moderate equivalence ratios ($\phi < 1.6$). RME/air mixtures have the coincident equilibrium concentrations of the CH radical, but for richer mixtures, the CH radical is more abundant in DOS/air mixtures. Only at a very narrow region ($1.6 < \phi < 2$), a slightly higher CH concentration was observed for RME/air mixture. Both DOS and RME generate similar concentrations of CH_2 at equivalence ratios that most strongly favor the formation of NO ($\phi < 3.0$). Under lean conditions, the levels of CH and CH_2 generated using PME are similar to those observed with DOS, but with rich mixtures, PME generates far fewer of these radicals. Sensitivity analysis showed that both the thermal and the prompt NO mechanisms are involved in the formation of NO during the combustion of DOS and RME, and that the thermal mechanism is dominant.

Diesel engine modeling was established for DOS, RME and RME+ for both without and with 20% EGR levels. Without EGR the thermal and prompt NO formation mechanisms account for approximately ~89% and ~11% of the total NO produced, respectively. The 20% EGR level could cause more than 50% reduction of thermal NO, but less pronounced effects on the prompt NO formation. Consequently, the increased NO emissions generated by the combustion of biodiesel cannot be attributed to a greater importance of the prompt mechanism. It was also observed that RME+ produces 10% more NO than DOS for both EGR levels. Aside from this, the cooling effect of EGR on the thermal NO reduction is less effective for RME combustion than DOS due to the less inert species in the EGR composition. The 3D CFD modeling results also illustrate that most NO was formed at the region whose equivalence ratio range $0.6 \sim 1.8$, and the RME combustion presents a leaner combusting condition relative to that of diesel oil.

Analysis of ϕ - T maps demonstrated that more O_2 molecules is available during RME combustion than was the case with DOS due to the presence of oxygen atoms within the RME molecules. Consequently, less external oxygen is required for combustion with RME, and RME combustion occurs under comparatively lean conditions, which favor NO formation when combustion occurs under conditions corresponding to the right-hand side of the NO- ϕ correlation curve.

In light of these data, it was proposed that the increased NO emissions observed when using biodiesel in conventional diesel engines are attributable to combustion effectively

occurring under leaner conditions when using oxygen-containing fuels. To test this hypothesis more rigorously, it will be necessary to conduct experiments aimed at analyzing the spatial distribution of the equivalence ratio within the cylinder of a diesel engine.

Acknowledgments

The support of the Engine Research Center, CERC, for Chalmers University of Technology and help of the Spanish Ministry of Science and Research for Universidad Politécnic de Valencia are gratefully acknowledged.

References

- [1] The US Environmental Protection Agency, "A comprehensive analysis of biodiesel impacts on exhaust emissions," Tech. Rep. EPA420-P-02001, 2002.
- [2] C. J. Mueller, A. L. Boehman, and G. C. Martin, "An experimental investigation of the origin of increased NO_x emissions when fueling a heavy-duty compression-ignition engine with soy biodiesel," SAE Paper 2009-01-1792, 2009.
- [3] W. A. Eckerle, E. J. Lyford-Pike, D. Stanton, J. Wall, L. La-Pointe, and S. Whitacre, "Effects of methyl-ester biodiesel blends on NO_x production," SAE Paper 2008-01-0078, 2008.
- [4] S. K. Jha, S. Fernando, and S. D. F. To, "Flame temperature analysis of biodiesel blends and components," *Fuel*, vol. 87, no. 10-11, pp. 1982-1988, 2008.
- [5] G. A. Ban-Weiss, J. Y. Chen, B. A. Buchholz, and R. W. Dibble, "A numerical investigation into the anomalous slight NO_x increase when burning biodiesel; A new (old) theory," *Fuel Processing Technology*, vol. 88, no. 7, pp. 659-667, 2007.
- [6] A. L. Boehman, D. Morris, J. Szybist, and E. Esen, "The impact of the bulk modulus of diesel fuels on fuel injection timing," *Energy & Fuels*, vol. 18, no. 6, pp. 1877-1882, 2004.
- [7] P. Ye and A. L. Boehman, "Investigation of the impact of engine injection strategy on the biodiesel NO_x effect with a common-rail turbocharged direct injection diesel engine," *Energy & Fuels*, vol. 24, no. 8, pp. 4215-4225, 2010.
- [8] W. C. Reynolds, *Element Potential Method for Chemical Equilibrium Analysis: Implementation in the Interactive Program STANJAN*, Department of Mechanical Engineering, Stanford University, 1986.
- [9] P. Glarborg, J. F. Grcar, and J. A. Miller, "PSR: a fortran program for modeling well-stirred reactors," Gov Pub SAND86-8209, 1992.
- [10] J. Gustavsson and V. I. Golovitchev, "Spray combustion simulation based on detailed chemistry approach for diesel fuel surrogate model," SAE Paper 2003-01-1848, 2003.
- [11] V. I. Golovitchev and J. Yang, "Construction of combustion models for rapeseed methyl ester bio-diesel fuel for internal combustion engine applications," *Biotechnology Advances*, vol. 27, no. 5, pp. 641-655, 2009.
- [12] D. L. Baulch, C. J. Cobos, R. A. Cox et al., "Summary table of evaluated kinetic data for combustion modeling," *Combustion and Flame*, vol. 98, no. 1-2, pp. 59-79, 1994.
- [13] A. A. Konnov, "Implementation of the NCN pathway of prompt-NO formation in the detailed reaction mechanism," *Combustion and Flame*, vol. 156, no. 11, pp. 2093-2115, 2009.
- [14] A. A. Amsden, "KIVA-3V: a block-structured KIVA program for engines with vertical or canted valves," Tech. Rep. LA-13313-MS, Los Alamos, NM, USA, 1997.

- [15] J. C. Beale and R. D. Reitz, "Modeling spray atomization with the Kelvin-Helmholtz/Rayleigh-Taylor hybrid model," *Atomization and Sprays*, vol. 9, no. 6, pp. 623–650, 1999.
- [16] G. Adi, C. Hall, D. Snyder et al., "Soy-biodiesel impact on NO_x emissions and fuel economy for diffusion-dominated combustion in a turbo—diesel engine incorporating exhaust gas recirculation and common rail fuel injection," *Energy & Fuels*, vol. 23, no. 12, pp. 5821–5829, 2009.
- [17] M. J. Holst, *Notes on The KIVA-II Software and Chemically Reactive Fluid Mechanics*, Lawrence Livermore National Laboratory, 1992.
- [18] V. I. Golovitchev, N. Nordin, R. Jarnicki, and J. Chomiak, "3-D diesel spray simulation using new detailed chemistry turbulent combustion model," SAE Paper 2000-01-1891, 2000.
- [19] R. O. Fox, "On the relationship between Lagrangian micro-mixing models and computational fluid dynamics," *Chemical Engineering and Processing: Process Intensification*, vol. 37, no. 6, pp. 521–535, 1998.
- [20] U. Frisch, *Turbulence*, Cambridge University Press, Cambridge, UK, 1995.
- [21] V. I. Golovitchev, K. Atarashiya, K. Tanaka, and S. Yamada, "Towards universal EDC-based combustion model for compression ignition engine simulation," SAE Paper 2003-01-1849, 2003.
- [22] S. C. Kong, C. D. Marriott, C. J. Rutland, and R. D. Reitz, "Experiments and CFD modeling of direct injection gasoline HCCI engine combustion," SAE Paper 2002-01-1925, 2002.
- [23] D. Veynante and L. Vervisch, "Turbulent combustion modeling," *Progress in Energy and Combustion Science*, vol. 28, no. 3, pp. 193–266, 2002.
- [24] S. M. Aceves, D. L. Flowers, J.-Y. Cheng, and A. Babajimopoulos, "Fast prediction of HCCI combustion with an artificial neural network linked to a fluid mechanics code," SAE Paper 2006-01-3298, 2006.
- [25] <ftp://ftp.technion.ac.il/pub/supported/aetdd/thermodynamics/BURCAT.THR>.
- [26] J. A. Miller and C. T. Bowman, "Mechanism and modeling of nitrogen chemistry in combustion," *Progress in Energy and Combustion Science*, vol. 15, no. 4, pp. 287–338, 1989.
- [27] Y. B. Zeldovich, P. Y. Sadvnikov, and D. A. Frank-Kamenetskii, *Oxidation of Nitrogen in Combustion*, Academy of Sciences of the USSR, Moscow, Russia, 1947.
- [28] Y. B. Zeldovich, G. I. Barenblatt, V. B. Librovich, and G. M. Makhviladze, *The Mathematical Theory of Combustion and Explosion*, Consultants Bureau, New York, NY, USA, 1985.
- [29] J. Wolfrum, "Bildung von stickstoffoxiden bei der verbrennung," *Chemie-Ingenieur-Technik*, vol. 44, no. 10, pp. 656–659, 1972.
- [30] J. Warnatz, U. Maas, and R. W. Dibble, *Combustion. Physical and Chemical Fundamentals, Modeling and Simulation, Experiments, Pollutant Formation*, Springer, 4th edition, 2006.
- [31] J. Tomeczek and B. Gradon, "The role of nitrous oxide in the mechanism of thermal nitric oxide formation within flame temperature range," *Combustion Science and Technology*, vol. 125, pp. 159–180, 1997.
- [32] J. Tomeczek and B. Gradoń, "The role of N₂O and NNH in the formation of NO via HCN in hydrocarbon flames," *Combustion and Flame*, vol. 133, no. 3, pp. 311–322, 2003.
- [33] A. A. Konnov and I. V. Dyakov, "Nitrous oxide conversion in laminar premixed flames of CH₄ + O₂ + Ar," *Proceedings of the Combustion Institute*, vol. 32, no. 1, pp. 319–326, 2009.
- [34] C. P. Fenimore, "Studies of fuel-nitrogen species in rich flame gases," in *Proceedings of the 17th Symposium (International) on Combustion*, pp. 661–670, The Combustion Institute, Pittsburgh, Pa, USA, 1979.
- [35] G. P. Smith, "Evidence of NCN as a flame intermediate for prompt NO," *Chemical Physics Letters*, vol. 367, no. 5-6, pp. 541–548, 2003.
- [36] L. V. Moskaleva and M. C. Lin, "The spin-conserved reaction CH + N₂ → H + NCN: a major pathway to prompt NO studied by quantum/statistical theory calculations and kinetic modeling of rate constant," *Symposium (International) on Combustion*, vol. 28, no. 2, pp. 2393–2402, 2000.
- [37] B. A. Williams and J. W. Fleming, "Experimental and modeling study of NO formation in 10 torr methane and propane flames: evidence for additional prompt-NO precursors," *Proceedings of the Combustion Institute*, vol. 31, no. 1, pp. 1109–1117, 2007.
- [38] B. A. Williams, J. A. Sutton, and J. W. Fleming, "The role of methylene in prompt NO formation," *Proceedings of the Combustion Institute*, vol. 32, no. 1, pp. 343–350, 2009.
- [39] J. W. Bozzelli and A. M. Dean, "O + NNH: a possible new route for NO_x formation in flames," *International Journal of Chemical Kinetics*, vol. 27, p. 1097, 1995.
- [40] A. A. Konnov and J. D. Ruych, "A possible new route forming NO via N₂H₃," in *Proceedings of the 28th Symposium (International) on Combustion*, Edinburgh, UK, 2000.
- [41] P. A. Glaude, O. Herbinet, S. Bax, J. Biet, V. Warth, and F. Battin-Leclerc, "Modeling of the oxidation of methyl esters—Validation for methyl hexanoate, methyl heptanoate, and methyl decanoate in a jet-stirred reactor," *Combustion and Flame*, vol. 157, no. 11, pp. 2035–2050, 2010.
- [42] J. L. Brakora, Y. Ra, R. D. Reitz, M. Joanna, and C. D. Stuart, "Development and validation of a reduced reaction mechanism for biodiesel-fueled engine simulations," SAE Paper 2008-01-1378, 2008.
- [43] O. Herbinet, W. J. Pitz, and C. K. Westbrook, "Detailed chemical kinetic oxidation mechanism for a biodiesel surrogate," *Combustion and Flame*, vol. 154, no. 3, pp. 507–528, 2008.
- [44] T. E. Daubert and R. P. Danner, "Physical and Thermodynamic Properties of Pure Chemicals," Part 4, 1989.
- [45] F. Battin-Leclerc, R. Bounaceur, G. M. Côme et al., *EXGAS-Alkanes, A Software for the Automatic Generation of Mechanisms for the Oxidation of Alkanes*, User Guide, Cedex, France, 2004.
- [46] K. Akihama, Y. Takatori, K. Inagaki, S. Sasaki, and A. M. Dean, "Mechanism of the smokeless rich diesel combustion by reducing temperature," SAE Paper 2001-01-0655, 2001.
- [47] V. I. Golovitchev, A. T. Calik, and L. Montorsi, "Analysis of combustion regimes in compression ignited engines using parametric ϕ -T dynamic maps," SAE Paper 2007-01-1838, 2007.
- [48] A. E. Lutz, R. J. Kee, and J. A. Miller, "SENKIN: a fortran program for predicting homogeneous gas phase chemical kinetics with sensitivity analysis," Sandia Report SAND87-8248, 1994.
- [49] C. J. Mueller, "The quantification of mixture stoichiometry when fuel molecules contain oxidizer elements or oxidizer molecules contain fuel elements," SAE Paper 2005-01-3705, 2005.
- [50] S. Cheski, I. Derzy, V. A. Lozovsky, A. Kachanov, and F. Stoeckel, "Intracavity laser absorption spectroscopy detection of singlet CH₂ radicals in hydrocarbon flames," *Chemical Physics Letters*, vol. 277, no. 5-6, pp. 423–429, 1997.

Research Article

Computational Fluid Dynamics of Two-Opposed-Jet Microextractor

Pritam V. Hule, B. N. Murthy, and Channamallikarjun S. Mathpati

Department of Chemical Engineering, Institute of Chemical Technology, Matunga, Mumbai 400 019, India

Correspondence should be addressed to Channamallikarjun S. Mathpati, cs.mathpati@ictmumbai.edu.in

Received 28 October 2011; Accepted 21 February 2012

Academic Editor: Sreepriya Vedantam

Copyright © 2012 Pritam V. Hule et al. This is an open access article distributed under the Creative Commons Attribution License, which permits unrestricted use, distribution, and reproduction in any medium, provided the original work is properly cited.

Liquid-liquid extraction is an important unit operation in chemical engineering. The conventional designs such as mixer settler have lower-energy efficiency as the input energy is dissipated everywhere. Experimental studies have proved that the novel designs such as two-opposed-jet contacting device (TOJCD) microextractor allow energy to be dissipated close to the interface, and major part of energy is used for drop breakup and enhancement of surface renewal rates. It is very difficult to estimate the local variation of energy dissipation (ε) using experiments. Computational fluid dynamics (CFD) has been used to obtain ε at different rotating speed of the top disc and nozzle velocity. In this work, performance analysis of TOJCD microextractor has been carried out using Reynolds stress model. The overall ε value was found in the range of 50 to 400 W/kg and shear rate in the range of 100000 1/s. A semiempirical correlation for $k_{L,a}$ is proposed, and parity plot with experimental data has been plotted.

1. Introduction

Liquid-liquid extraction (LLE) is an important unit operation in chemical engineering. Typical applications of the LLE are in metal extraction, aromatics nitration and sulfonation, polymer processing, waste water treatment as well as food and petroleum industries. LLE is a mass transfer operation in which a liquid solution (the feed) is contacted with an immiscible or nearly immiscible liquid (solvent) that exhibits preferential affinity or selectivity towards one or more of the components in the feed. Two streams result from this contact: the extract, which is the solvent-rich solution containing the desired extracted solute, and the raffinate, the residual feed solution containing little solute. The conventional designs such as mixer settler often have lower energy efficiency as the input energy is dissipated everywhere in the extractor.

The transfer of solute from one phase to another is controlled by diffusion across the interface and often rate limiting. The process can be intensified and energy efficiency can be improved by novel designs such as two-opposed-jet contact device [1, 2], annular centrifugal extractors [3], impinging jet contactors [4], pulsed sieve plate extraction columns [5], and so forth. Experimental studies have proved

that these novel designs offer higher energy efficiency. High energy dissipation and shear rates are used for breakup and enhancement of surface renewal rates. However, it is very difficult to estimate the local variation of energy dissipation using experiments. Computational fluid dynamics (CFD) can be used in such cases to estimate the local variation of energy dissipation and optimize the hardware configuration and selection of operating conditions [6].

The present work deals with Reynolds stress modelling of two-opposed-jet contact device designed by Dehkordi [1, 2]. This equipment can also be classified as microextractor and hence termed as “two-opposed-jet microextractor” in the present study. The principle of opposed jets is to bring the two jets flowing along the same axis in the opposite direction into collision. As the result of such a collision, a relatively narrow zone, called the impingement zone of high turbulence intensity, is created which offers excellent conditions for intensifying heat- and mass-transfer rates. The extensive details of impinging jet technique and applications for various processes can be found in Tamir [7] and Saien et al. [4].

Impinging jet system offers lot of complexities in modelling due to stagnation point, significant variations, and redistribution of Reynolds stress and highly anisotropic flow.

The standard $k-\varepsilon$ model will not work in simulating these types of flow accurately due to inherent assumption of isotropy. As the stagnation point is approached, there is a significant redistribution of energy between various stress components and hence Reynolds stress modelling (RSM) with appropriate pressure strain model is required. It is well known that for single-phase cases CFD tool is proven to be reliable; for instance, flow pattern in stirred tank [8], jet reactor [9], and centrifugal extractor [10] was well predicted. In view of this, in the present work a very fine and structured mesh with good quality has been employed to ensure better predictions.

The main objectives of present work were to obtain energy dissipation rate and shear rate distributions in two-opposed-jet microextractor for various geometric and operating conditions. Further, the energy dissipation from CFD data has been used to develop a semiempirical model for overall mass transfer coefficient which takes into account fundamental basis of turbulence phenomena. The energy supplied in the extractor is utilized for (i) creating liquid motion, (ii) creation of new surface, that is, drop breakup and increasing interfacial area, and (iii) turbulent fluctuations at liquid-liquid interface which improve true mass transfer coefficient (k_L). Point (ii) contributes to major utilization of energy input in case of microextractor. To quantify this, two-phase simulations with interphase forces need to be carried out; however, CFD tool is still not reliable for realistic predictions of immiscible mixing behaviour. Therefore, in the present work, an attempt has been made to understand this system using single phase simulations. The experimental mass transfer coefficient is correlated with total energy dissipated in the microextractor. The focus is not on getting individual components of energy utilization (i), (ii), and (iii), but to get overall dissipation rate. This can be obtained using single-phase simulations. In the present work, single-phase CFD simulation using Reynolds stress model has been carried out for preliminary analysis of microextractor.

2. Previous Work

In this section, numerical and experimental efforts to understand hydrodynamics and turbulent statistics of impinging jet have been discussed. Wang and Mujumdar [11–13] studied mixing characteristics of multiple and multiset turbulent opposing jets using standard $k-\varepsilon$ model. The effects of turbulence models, model constants, operating conditions, geometric parameters, flow conditions at the nozzle exit, turbulent Schmidt number as well as unequal opposing jets on mixing in the three-dimensional confined turbulent opposing jet flow were examined systematically. They observed that multiple opposing jets achieve better mixing than single opposing jets in the mixer studied. Compared to the single opposing jets, the multiple opposing jets yield mixing which is poorer in the dome, the impingement zone, and its vicinity, but better in the downstream zones after a critical value of axial distance. The total pressure drop for $n = 2$ is roughly 3.5 times higher than that for $n = 4$ due largely to the higher inlet velocity in the former at a given total mass flow rate. This demonstrates a significant power reduction without

detriment to mixing performance for multiple opposing jets ($n \geq 3$) compared to single opposing jets ($n = 2$) and thus the economic benefits of such mixers.

Abdel-Fattah [14] studied two-dimensional impinging circular twin-jet flow numerically (standard $k-\varepsilon$ model) and experimentally. The parameters studied were jet Reynolds number, nozzle to plate spacing, nozzle to nozzle centerline spacing, and jet angle. It was concluded that the stagnation primary point moves away in the radial main flow direction by increasing the jet angle. This shift becomes stronger by increasing the nozzle to nozzle centerline spacing. A secondary stagnation point was set up between two jets. The value of pressure at this point decreases by decreasing Reynolds number and/or increasing the jet angle. Turbulent kinetic energy increases within each vortex region; this increment decreases by increasing of jet angle and/or the nozzle to plate spacing.

Gavi et al. [15] carried out CFD study and scale-up of confined impinging jet reactors for precipitation of nanoparticles. Mixing at the molecular level is modelled with a presumed probability density function approach: the direct quadrature method of moments coupled with the interaction by exchange with the mean (DQMOM-IEM) model. Comparison between experimental data and simulations in a wide range of operating conditions showed excellent agreement. Best agreement with experimental data was found when the RSM and the Standard $k-\varepsilon$ model coupled with enhanced wall treatment were used.

Kleingeld et al. [16] carried out numerical modelling of impinging jet reactor. The model for the prediction of the interfacial area production in IJ reactor was developed and implemented in the form of a Monte Carlo simulation, based on the fact that bubble breakup in a turbulent environment is governed by the interactions of bubbles with turbulent eddies. Due to this intimate contact between phases, mass transfer coefficients (k_L) of up to 1.5×10^{-3} m/s have been realised, which, coupled with values of the specific interfacial area (a) of 8–18000 m^2/m^3 , have yielded volumetric mass transfer coefficients ($k_L a$) of up to 22 s^{-1} which are orders of magnitude higher than typical values obtained by conventional systems.

Marchisio [17] carried out LES of mixing and reaction in confined IJ reactor. Subgrid-scale mixing is described with a presumed PDF approach, namely, DQMOM-IEM. Model predictions compare well with experimental data (and Reynolds averaged Navier Stokes equation predictions from our previous work); comparison was carried out for two sets of initial concentration and two different reactor geometry. The analysis shows that CIJRs are indeed interesting devices, because of the high mixing efficiency and because of the absence of stagnant and recirculation zones. Niamnuy and Devahastin [18] have studied the effects of geometry and operating conditions on the mixing behavior of IJ mixer. For a fixed value of d/D , an increase in the value of the jet Reynolds number led to a better mixing in the impingement zone and its vicinity. This mixing behavior persisted until a critical value of dimensionless axial distance (x/D) was reached beyond which the mixing quality changed. For a mixer with two sets of inlet jets, it was found that a larger

spacing between the two sets of inlet jets (higher S/D) resulted in a better mixing in the region between the sets of inlet jets but yielded no significant difference in the required main flow channel length to obtain a well-mixed condition.

Li et al. [19] studied the stagnation point offsets of turbulent opposed jets at various exit velocity ratios, and nozzle separations were experimentally studied by a hot-wire anemometer, smoke-wire technique, and numerically simulated by Reynolds stress model (RSM). Results show that, for $2D \leq L \leq 4D$ (where L is nozzle separation and D is nozzle diameter), the position of the impingement plane is unstable and oscillates within a region between two relative stable positions when the exit velocities are equal. The instability and sensitivity of the stagnation point offset to the small difference of the exit velocities of opposed jets may ascribe to the instability of the large-scale vortices in the boundary layers of opposed jets. The study of the stagnation point offset of impinging streams is crucial for the effective use of such flow in industrial applications because imbalance of the exit flux of impinging streams is inevitable practically. The most important find of our study is that there exists a region of $2D \leq L \leq 8D$, in which the stagnation point of opposed jets is very sensitive to the exit velocity ratio, and small difference (3% or less) of exit velocity can cause the stagnation point to deviate obviously.

Unger and Muzzio [20] have measured concentration profiles and mixing performance in IJ reactors using laser-induced fluorescence (LIF) technique. Flow structures were visualized by imaging concentration distributions at five vertical planes throughout the mixers. Mixing is quantified for each Reynolds number examined by calculating the overall intensity of segregation. Mixing performance varies substantially as a function of Reynolds number. The results demonstrated the ability of laser-induced fluorescence to quantitatively capture small- and large-scale flow structures and accurately and reproducibly quantify mixing performance in real time for industrially relevant mixing devices. For unsteady-laminar flows $80 < Re_j < 300$, the jet oscillations which occur in the standard geometry result in better mixing than the swirling motion of the asymmetric jets; flow for the asymmetric jets is mostly steady and similar to flow for $Re_j < 80$. For more highly unsteady flows $Re_j > 300$, efficient mixing occurs in both geometries although the asymmetric eliminates the dead region in the bottom of the mixer and results in slightly greater overall homogeneity.

Sun et al. [21] studied velocity distribution of two opposed jets using hot film anemometry and CFD. The radial velocities of opposed jets with various exit velocities, nozzle diameters, and nozzle separations were measured experimentally. The normalized radial velocities are self-similar across various radial sections at $r \geq 1.5D$, and the radial velocity profiles can be described by a Gaussian distribution function. The half-width increases linearly with increasing radial distance at $r \geq 1.5D$, and spreading rates of radial jet are about 0.121. The normalized radial velocity at impingement plane increases firstly and then decreases with the increasing normalized radial distance. The normalized radial velocity is independent on nozzle diameter, nozzle separation, and exit velocity. The maximum radial velocity

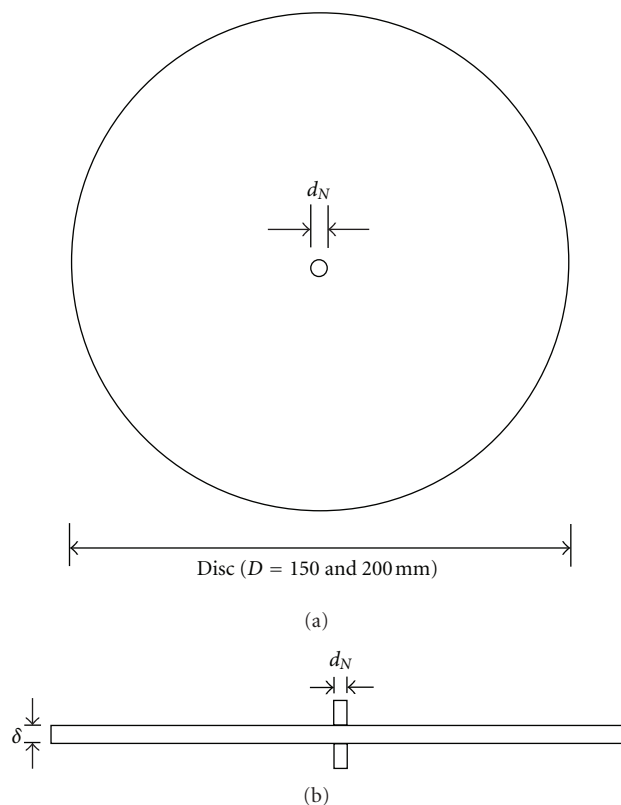


FIGURE 1: Geometric details. (a) Top view and (b) side view.

at impingement plane is proportional to the exit velocity, and it is inversely proportional to the 0.551th power of the normalized nozzle separation. The position of the maximum radial velocity increases with the nozzle separation at $L/D < 1$ and keeps invariant at $L/D \geq 1$.

It can be pointed out from the above-mentioned literature survey that impinging jet technique has been studied widely, and knowledge about the transport phenomena under turbulent conditions has been improved to satisfactory level using experimental and computational fluid dynamics. This understanding can be effectively utilized for design of various equipments as well as performance optimization. In this work, two-opposed-jet microextractor has been studied using Reynolds stress model. The Reynolds stress model is very effective in solving stagnation flows with very strong anisotropy.

3. Systems under Consideration

The microextractor geometry is shown in Figures 1(a) and 1(b). It consists of the following parts: (1) two circular disks with dimension of $D \text{ (m)} \times \delta \text{ (m)} = 0.15 \times 0.0015$ and 0.2×0.00015 , where D and δ are disk diameter and the distance between disks, respectively. The upper disk was rotated at various speeds (600, 1000, and 1400 rpm), and the lower disk was fixed. The aqueous and organic phases were fed into the lower and upper disks, respectively, through nozzle of 0.001 m diameter. Thus, the contact between the

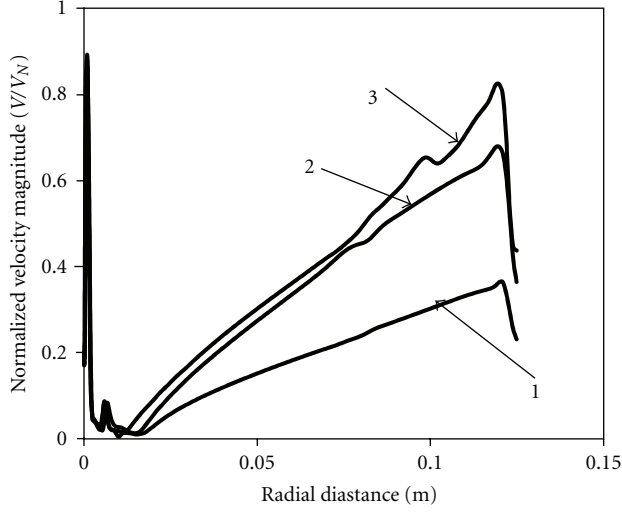


FIGURE 2: Variation of normalized velocity magnitude (V/V_N) along radial coordinate [$z = 0.00075$ m] disc diameter: 0.15 m, flow rate: 300 mL/min, line 1: 600 rpm, line 2: 1000 rpm, and line 3: 1400 rpm.

TABLE 1: Simulation details and results of two-opposed-jet microextractor using RSM.

Sr. no.	RPM	Aq flow rate Q_A (mL per min.)	Disc diameter (m)	Nozzle velocity m/s
1	600	300	0.15	6.36
2	1000	300	0.15	6.36
3	1400	300	0.15	6.36
4	600	190	0.15	4.03
5	1000	190	0.15	4.03
6	1400	190	0.15	4.03
7	600	110	0.15	2.33
8	1000	110	0.15	2.33
9	1400	110	0.15	2.33
10	600	300	0.20	6.36
11	1000	300	0.20	6.36
12	1400	300	0.20	6.36
13	600	190	0.20	4.03
14	1000	190	0.20	4.03
15	1400	190	0.20	4.03
16	600	110	0.20	2.33
17	1000	110	0.20	2.33
18	1400	110	0.20	2.33

two phases took place within the extraction compartment only. The present study is restricted to single phase using water as working fluid. The reason for using single phase simulations has already been explained in introduction. The ratio of flow rates through the top and bottom nozzles was kept unity for all the simulations. Flow rates considered in the present work were (i) $5 \times 10^{-5} \text{ m}^3/\text{s}$ (300 mL/min), (ii) $3.2 \times 10^{-5} \text{ m}^3/\text{s}$ (190 mL/min), and (iii) $1.8 \times 10^{-5} \text{ m}^3/\text{s}$ (110 mL/min). The geometric and operating parameters

are taken from the experimental work of Dehkordi [1]. Dehkordi [1] has considered a system where iso-butyric acid in aqueous solution was getting transferred to organic phase (cumene). The objective of present work was to study the hydrodynamics in such microextractors which predict the mass transfer rates. The mass transfer rate is strongly dependent on the energy dissipation profile. The performance of extractor is dependent on (i) jet velocity, (ii) disc rotation speed, (iii) density, and (iv) viscosity of the phase. In the work, effects of disc rotation speed and jet velocity are analyzed.

4. Governing Equations and Boundary Conditions

The standard $k-\epsilon$ model inherently fails to predict properly the anisotropic flow situations (Reynolds [22], Launder [23], and Hanjalić [24]). Reynolds stress model, in theory, can circumvent most of the deficiencies of standard $k-\epsilon$ model and also it has an ability to predict more accurately each individual stress. A Reynolds stress model solves continuity equation (1), momentum equation (2) six equations for the Reynolds stress (3), and another equation for the dissipation rate (4). The pressure strain term (Π_{ij}) in (3) is the most uncertain term in the RSM. This term is responsible for making turbulence isotropic and redistribution of energy between components $\langle u_1'^2 \rangle$, $\langle u_2'^2 \rangle$, and $\langle u_3'^2 \rangle$. This improves the accuracy of prediction of turbulence production rate as well as local turbulent kinetic energy dissipation rate (ϵ). One has the following:

$$\frac{\partial \rho}{\partial t} + \frac{\partial \langle u_i \rangle}{\partial x_i} = 0, \quad (1)$$

$$\rho \frac{\partial \langle u_i \rangle}{\partial t} + \rho \langle u_j \rangle \frac{\partial \langle u_i \rangle}{\partial x_j} = -\frac{\partial \langle p \rangle}{\partial x_i} + \frac{\partial}{\partial x_j} \left(\mu \frac{\partial \langle u_i \rangle}{\partial x_j} - \rho \langle u_i' u_j' \rangle \right), \quad (2)$$

$$\begin{aligned} & \left\{ \rho \frac{\partial \tau_{ij}}{\partial t} \right\} + \left\{ \rho \langle u_k \rangle \frac{\partial \tau_{ij}}{\partial x_k} \right\} \\ & = \left\{ -\rho \left(\tau_{ik} \frac{\partial \langle u_j \rangle}{\partial x_k} + \tau_{jk} \frac{\partial \langle u_i \rangle}{\partial x_k} \right) \right\} + \left\{ \frac{\partial}{\partial x_k} \left(\frac{\mu_t}{\sigma_k} \frac{\partial \tau_{ij}}{\partial x_k} \right) \right\} \\ & + \left\{ \frac{\partial}{\partial x_k} \left(\mu \frac{\partial \tau_{ij}}{\partial x_k} \right) \right\} + \left\{ -\frac{2}{3} \epsilon \delta_{ij} \right\} + \left\{ \Pi_{ij} \right\}, \end{aligned} \quad (3)$$

$$\begin{aligned} & \left\{ \rho \frac{\partial \epsilon}{\partial t} \right\} + \left\{ \rho \langle u_j \rangle \frac{\partial \epsilon}{\partial x_j} \right\} \\ & = \left\{ \rho C_{\epsilon 1} \frac{\epsilon}{k} \tau_{ij} \frac{\partial \langle u_i \rangle}{\partial x_j} \right\} + \left\{ \frac{\partial}{\partial x_j} \left(\frac{\mu_t}{\sigma_\epsilon} \frac{\partial \epsilon}{\partial x_j} \right) \right\} \\ & + \left\{ \frac{\partial}{\partial x_j} \left(\mu \frac{\partial \epsilon}{\partial x_j} \right) \right\} + \left\{ -C_{\epsilon 2} \rho \frac{\epsilon^2}{k} \right\}. \end{aligned} \quad (4)$$

4.1. Boundary Conditions. The top disc has been given rotational boundary condition whereas bottom disc is stationary.

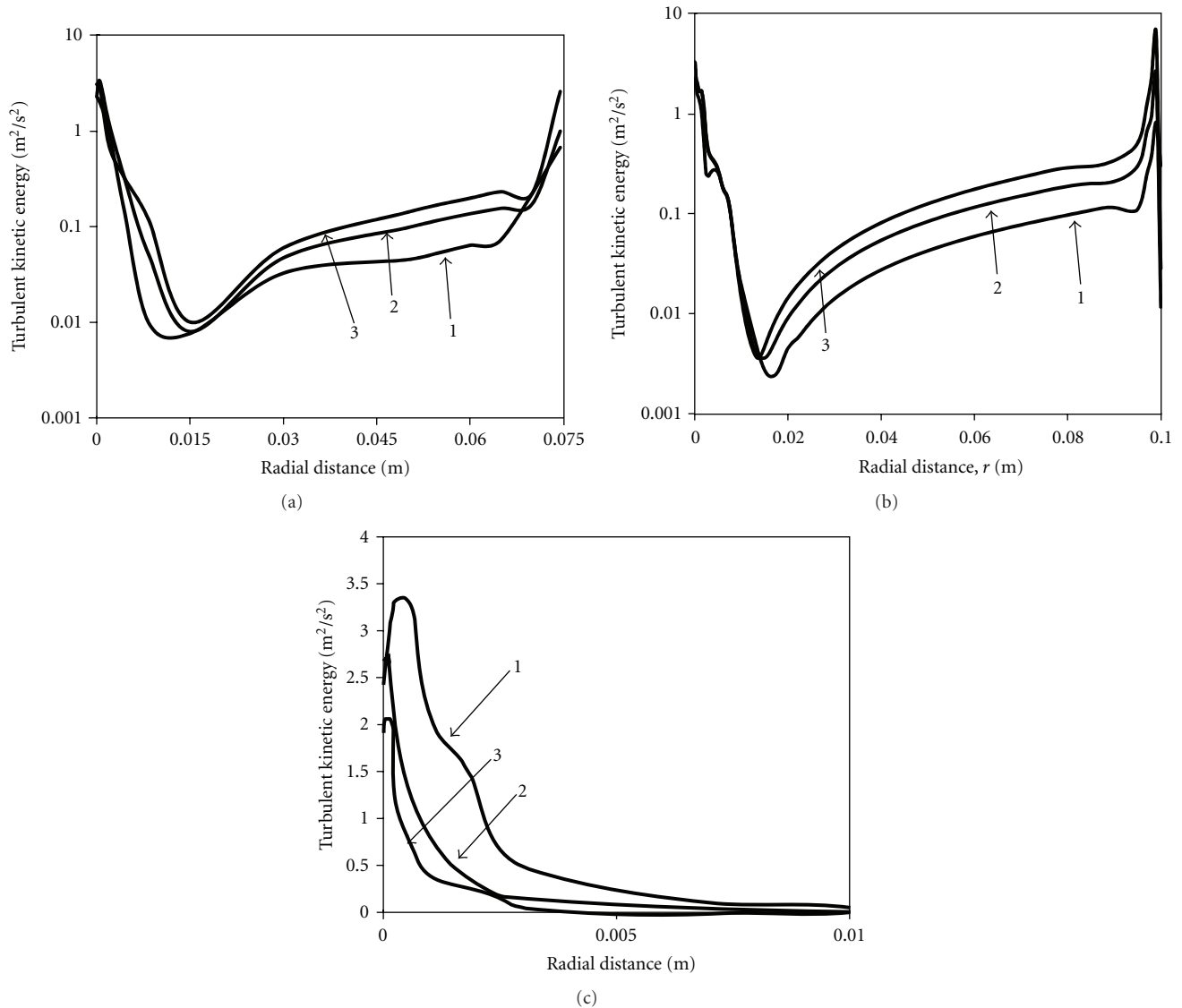


FIGURE 3: Variation of turbulent kinetic energy (k) along radial coordinate [$z = 0.00075$ m]. (a) Disc diameter: 0.15 m, flow rate: 300 mL/min, line 1: 600 rpm, line 2: 1000 rpm, line 3: 1400 rpm. (b) Disc diameter: 0.20 m, flow rate: 300 mL/min, line 1: 600 rpm, line 2: 1000 rpm, line 3: 1400 rpm. (c) Disc diameter: 0.15 m, rotation speed: 1000 rpm, line 1: 300 mL/min, line 2: 190 mL/min, line 3: 110 mL/min.

No slip condition is imposed on both the discs. Velocity inlet boundary condition is used at top and bottom nozzles. The opening at the end of the discs is given pressure outlet condition.

5. Simulation Details

Table 1 summarizes all the cases considered in this study. Hexahedral elements were used for meshing the geometry, and a good quality of mesh was ensured throughout the computational domain using GAMBIT mesh generation tool. In this work, all the computational work has been carried out with finite volume approach using the commercially available software FLUENT 6.2. Further, the second-order upwind scheme was used for continuity, momentum,

and turbulence equations. All the discretised equations were solved in a segregated manner with the Semi-Implicit Method for Pressure Linked Equations (SIMPLEs) algorithm. In the present work, all the solutions were considered to be fully converged when repeated iterations do not decrease the sum of residuals below 1×10^{-4} . Default model constants have been used for all the RSM parameters. For each case, grid independency study has been carried out using 0.8, 1.2, and 1.5 million cells for disc diameter of 0.15 m and 1.2, 1.4, and 1.6 million cells for another disc diameter of 0.20 m. The predicted mean shear and turbulent kinetic energy dissipation rate profiles were found to be same for all the three cases. Therefore, the present study employed 1.2 to 1.4 million cells. Further, the clearance between the discs; that is, 0.0015 m was resolved using 30 elements.

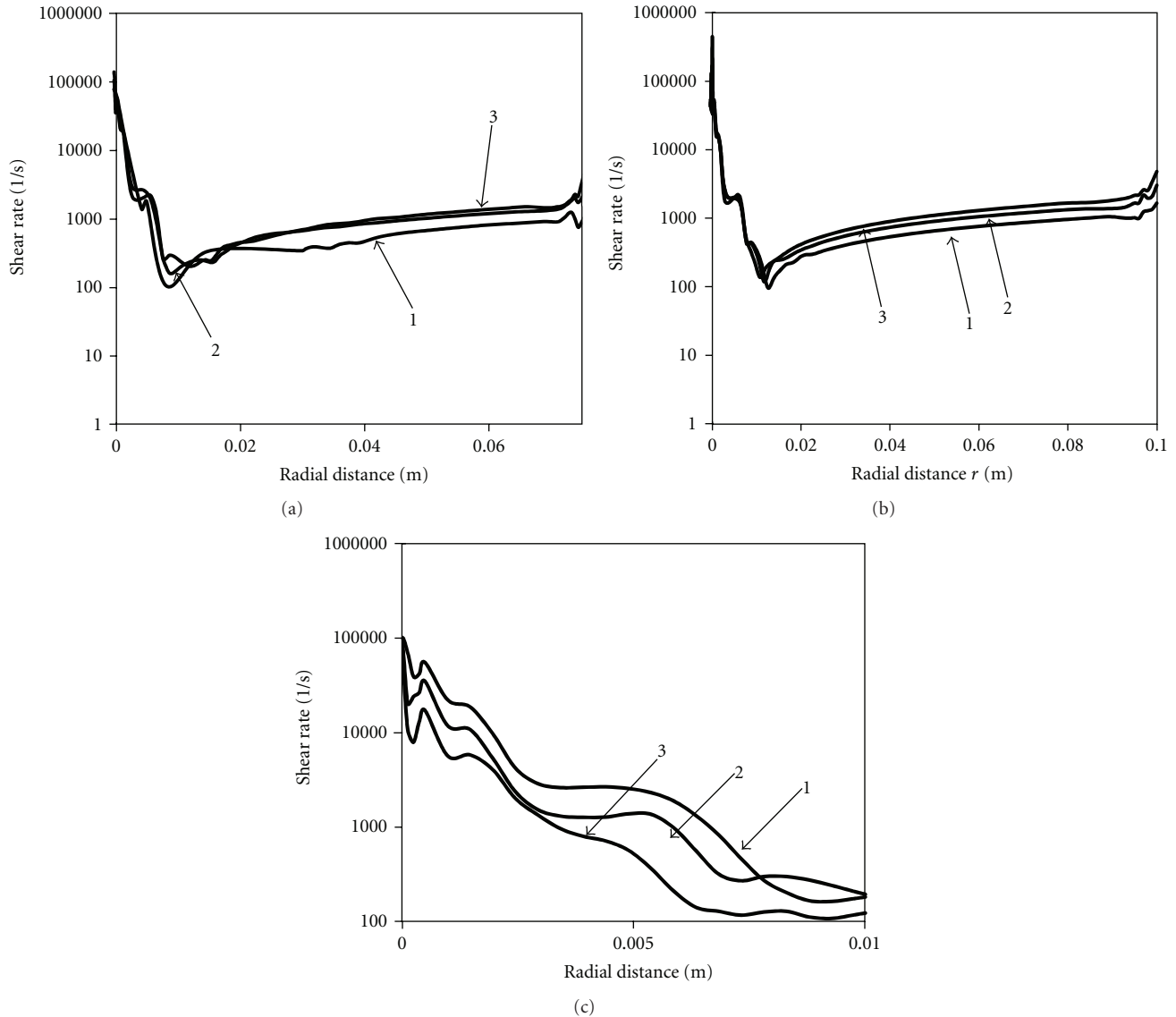


FIGURE 4: Variation of shear rate along radial coordinate [$z = 0.00075$ m]. (a) Disc diameter: 0.15 m, flow rate: 300 mL/min, line 1: 600 rpm, line 2: 1000 rpm, line 3: 1400 rpm. (b) Disc diameter: 0.20 m, flow rate: 300 mL/min, line 1: 600 rpm, line 2: 1000 rpm, line 3: 1400 rpm. (c) Disc diameter: 0.15 m, rotation speed: 1000 rpm, line 1: 300 mL/min, line 2: 190 mL/min, line 3: 110 mL/min.

The simulations were performed on desktop machines with i3 processor and 4 GB RAM. Each simulation took 20 hours on single processor.

6. Results and Discussion

In the present study, as stated earlier water flow rates were same through both the top and bottom nozzles which are of the same diameter. Therefore, the jets collide each other at exact mid plane. Hence, all the results are provided at the midplane ($z = 0.00075$ m). CFD results are presented in the form of velocity, shear rate, turbulence kinetic energy, and its dissipation rate with respect to various geometric (disc diameters) and operating parameters (flow rate = 110 mL/min to 300 mL/min and rotational speed = 600 to 1400 rpm).

Figure 2 shows zero velocity at the point of collision. The velocity shows a maxima close to the point of collision and suddenly drops down, then it gradually increased till $r = D/2$. This strong variation of velocity generates high shearing action which is in turn responsible for rate of surface renewal as well as drop breakup. It can be seen that flow rate significantly affects the velocity and shear in the central region, and rotation of top disc plays important role away from the centre. For $D = 0.15$ m and flow rate of 300 mL/min, Figure 3(a) shows the turbulent kinetic energy profiles at various disc rotational speeds (600, 1000, and 1400 rpm). The turbulent kinetic energy shows maxima at the centre (collision point) and periphery of the disc (due to highest centrifugal force). At the periphery it is a strong function of rotation speed and disc diameter (Figures 3(a) and 3(b)).

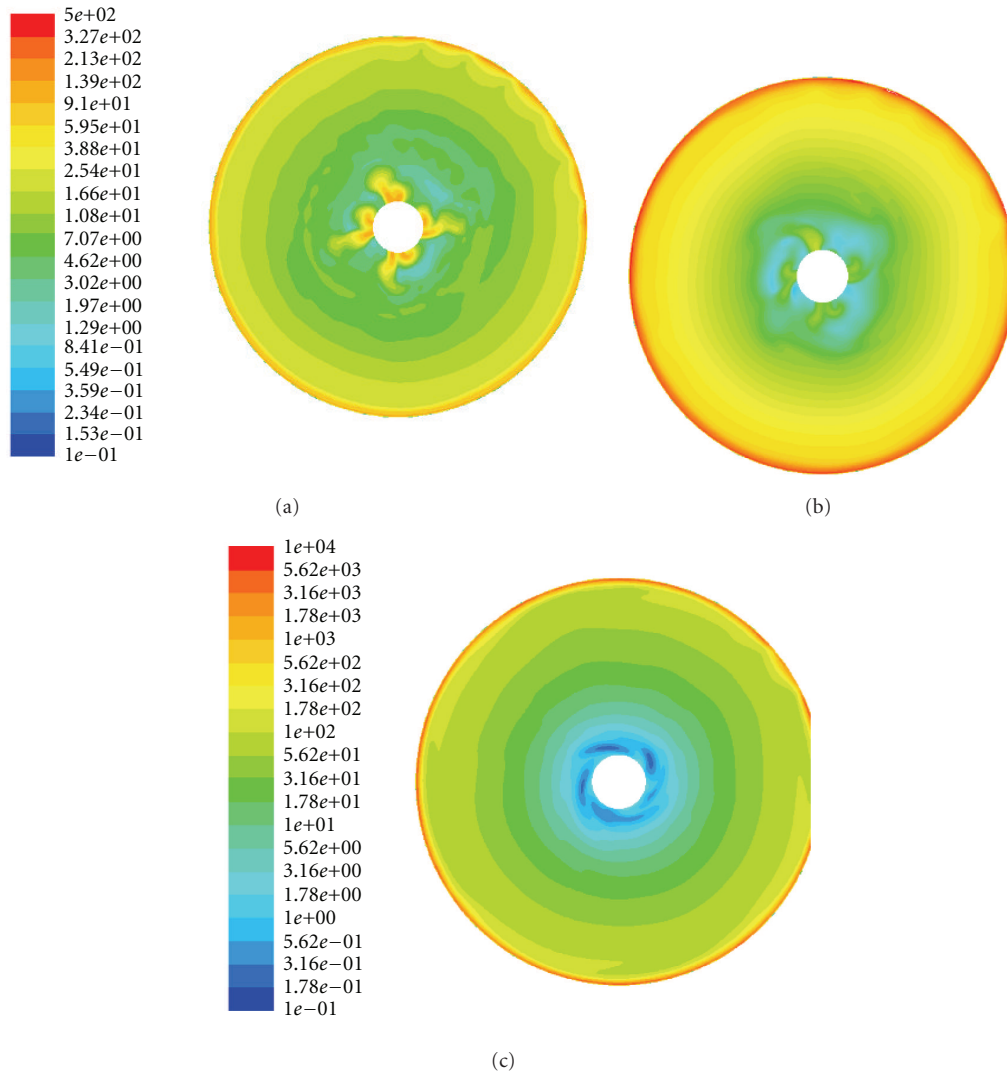


FIGURE 5: Contour plot of turbulent dissipation rate (ϵ) outer region ($r = 0.01$ m to $r = 0.075$ m) [$D = 0.2$ m] [$z = 0.00075$ m]. Flow rate: 300 mL/min, (a) 600 rpm, (b) 1000 rpm, and (c) 1400 rpm.

Figure 3(c) shows the variation of turbulent kinetic energy as a function of flow rate, and it can be observed that the maximum kinetic energy value decreases with decrease in flow rate. Combination of both the high shear and turbulent fluctuations in the central region is responsible for highest turbulence production (turbulence stress \times shear rate) which in turn provides very high dissipation rate. Figures 4(a)–4(c) shows variation of shear rate with flow rate and rotational speed. Change in flow rate from 110 mL/min ($\sim 10,000$ s^{-1}) to 300 mL/min ($\sim 100,000$ s^{-1}) has marked effect on shear rate. Figures 5 and 6 show the contour plot of turbulent dissipation rate. Figures 5(a)–5(c) show the effect of rotational speed at constant flow rate of 300 mL/min for $D = 0.2$ m. A very high dissipation is obtained at the periphery of the disc. At the flow rate of 300 mL/min, the average turbulent kinetic energy dissipation rate (TKED) of 10000 W/kg is obtained for 1400 rpm and about 500 W/kg for 600 rpm. In case of 110 mL/min, the average TKED rates

for 600, 1000, and 1400 rpm are 58, 150, and 377 W/kg, respectively. Figures 6(a)–6(c) show contour plots of the TKE, and it is observed that, with increasing flow rate, the region experiencing high dissipation rate is found to increase.

Figures 7(a) and 7(b) show the effect of rotational speed for $D = 0.15$ and 0.2 m, respectively. For a given flow rate, dissipation in the central region does not have any effect of rotational speed. At $r > 0.02$ m, effect of rotational speed is prominent. Figure 7(c) shows the effect of flow rate on dissipation rate in central region. The central zone ($\sim 10^5$ W/kg) has almost order of magnitude higher turbulent dissipation rate compared to periphery. The increase of flow rate from 110 mL/min to 300 mL/min increased the dissipation rate from 13,000 to 37,000 W/kg. This value is comparable to those obtained in high shear mixers and emulsifiers used in chemical and allied industries to get microemulsions. Typical correlation for droplet diameter in

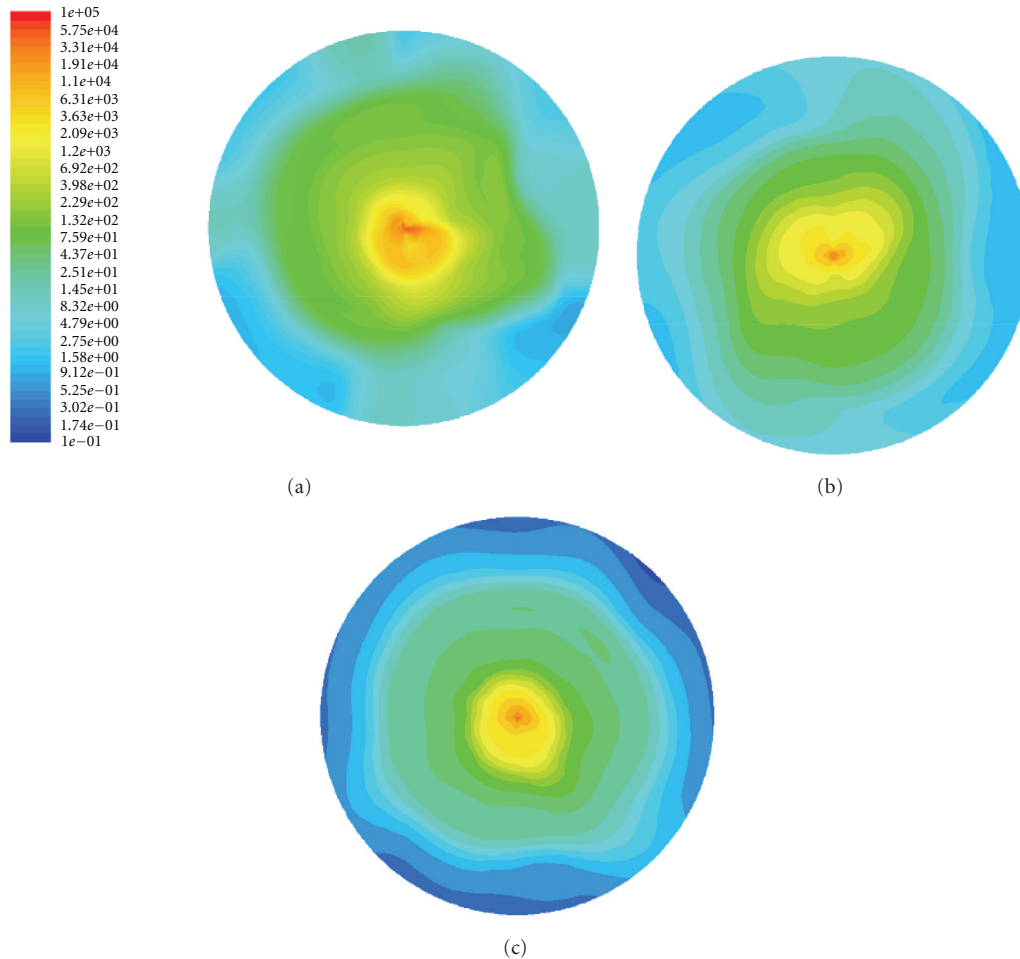


FIGURE 6: contour plot of turbulent dissipation rate (ϵ) inner region ($r = 0$ to $r = 0.01$ m) [$z = 0.00075$ m] [$D = 0.2$ m]. Upper disk rotation speed = 1000 rpm, (a) 300 mL/min, (b) 190 mL/min, (c) 110 mL/min.

high shear is provided by Davies [25]. Many of the qualitative observations made by Dehkordi [1] can be explained in quantitative manner by present CFD simulations. Some of their observations are reported below

“An increase in extraction efficiency may be noticed by increasing the upper disk speed. Such a behavior is the consequence of increasing the mixing and turbulence, which control the present extraction process.”

“In addition, an increase in the upper disk speed, N , increases the overall volumetric mass transfer coefficient, $k_L a$. This behavior may be explained by increasing the shear forces exerted on the phases and the turbulence that leads to an increase in the surface renewal mechanism and, hence, an increase in the interfacial mass-transfer area, a .”

The volume average dissipation rate as a function of rotation speed shows 550% increase in dissipation rate from 600 to 1400 rpm. In case of very high shear flows, the transfer coefficients are observed to be proportional to square root

of local turbulent dissipation rate. The interfacial area (i.e., drop size) is governed by the flow rate compared to rotation speed as maximum shearing takes place in the central region and drop breakup as well. The upper disk rotation stabilizes the drops to certain extent and overall dissipation may not have a control on the interfacial area. Hence, overall $k_L a$ varies as 0.5 power of turbulent dissipation rate. Hence the expected improvement in extraction efficiency is $(377/58)^{0.5} = 2.55$. The ratio of experimental $k_L a$ at 1400 and 600 rpm is $(13.5/8) = 1.7$.

Dehkordi [1] fitted a correlation based on experimental data for overall mass transfer coefficient is given by (5). V_d is microextractor volume in liter, Q_A is the flow rate in liter/min, D is disc diameter in m, and N is rotational speed in rpm

$$k_L a \text{ (s}^{-1}\text{)} = 0.003 D^{-0.1} V_d^{-0.6} Q_A^{0.59} N^{0.41}. \quad (5)$$

It can be seen from this correlation that aqueous and organic phase flow rate has significant effect on the overall mass transfer coefficient (as it governs droplet breakup rate and hence interfacial area) and followed by rotation speed (affects true mass transfer coefficient in the domain and

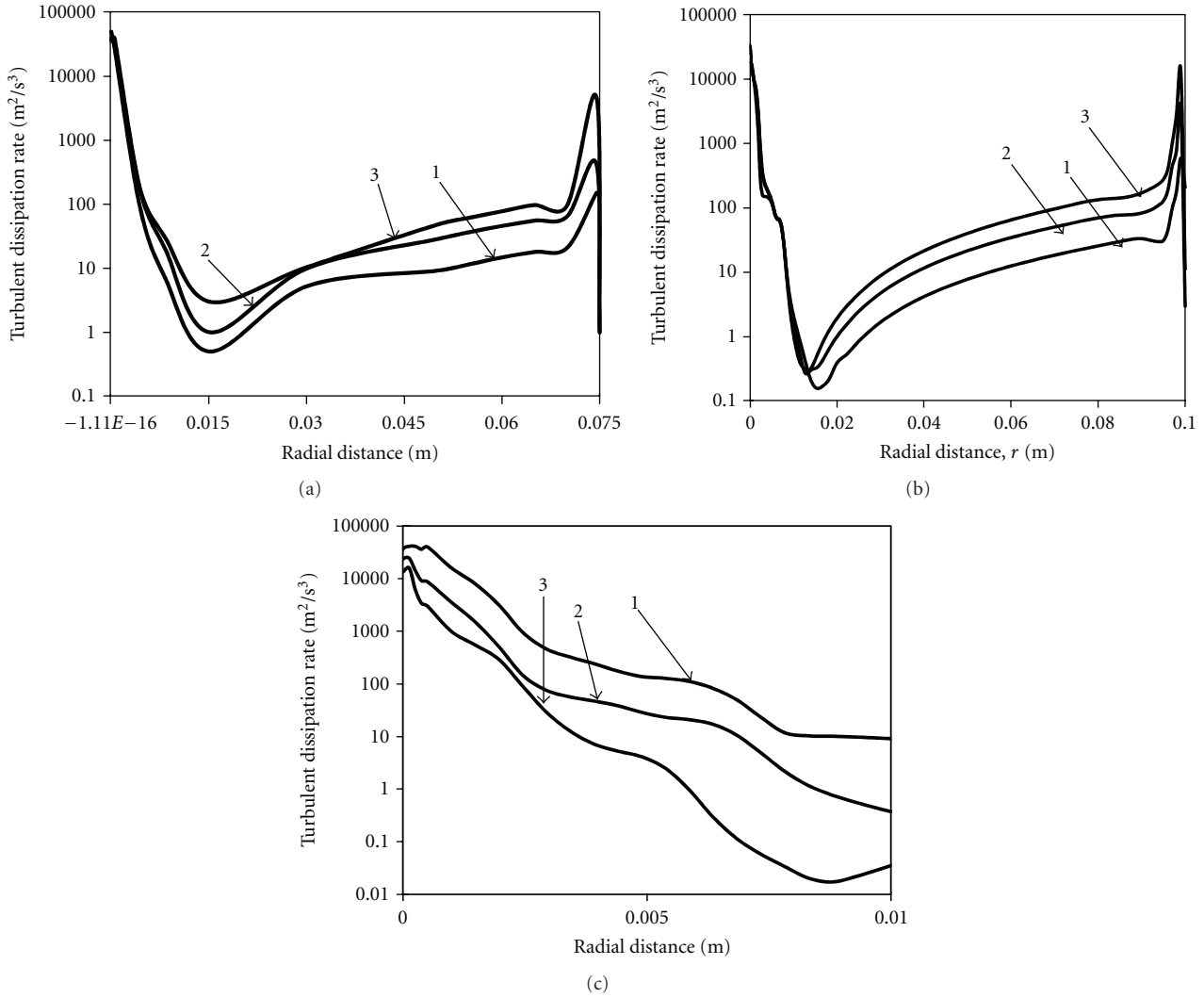


FIGURE 7: Variation of turbulent dissipation rate (ϵ) along radial coordinate [$z = 0.00075$ m]. (a) Disc diameter: 0.15 m, flow rate: 300 mL/min, line 1: 600 rpm, line 2: 1000 rpm, line 3: 1400 rpm. (b) Disc diameter: 0.20 m, flow rate: 300 mL/min, line 1: 600 rpm, line 2: 1000 rpm, line 3: 1400 rpm. (c) Disc diameter: 0.15 m, rotation speed: 1000 rpm; line 1: 300 mL/min, line 2: 190 mL/min, line 3: 110 mL/min.

stabilizing the drops). Experimental observations in various conventional contactors such as bubble columns, stirred vessels, jet mixers, high shear mixers, annular centrifugal extractors, and so forth suggest that the overall mass transfer coefficient is a function of power input per unit volume under turbulent conditions. However, in case of TOJCD, the power input per unit volume affects the true mass transfer coefficient (k_L), and the interfacial area is governed by the impinging jets which have energy proportional to nozzle velocity. Equation (6) is modified correlation to incorporate this theory of turbulence for microextractor. Table 2 shows the power consumed (P) per unit mass (M) for different cases along with the experimental mass transfer coefficient obtained by Dehkordi [1, 2]. We have

$$k_{L\alpha} \text{ (s}^{-1}\text{)} = A \left(\frac{P}{M} \right)^B V_N^C \quad (6)$$

MATLAB software is used to estimate the best fit values of A , B , and C based on the data provided in Table 2. The best fit values obtained are $A = 0.018$, $B = 0.22$, and $C = 0.78$. The revised correlation is provided as (7). These values clearly indicate that the nozzle velocity plays much more important role compared to the rotation speed of upper disc. We have

$$k_{L\alpha} \text{ (s}^{-1}\text{)} = 0.018 \left(\frac{P}{M} \right)^{0.22} V_N^{0.78} \quad (7)$$

The parity plot of experimental and predicted (from (7)) mass transfer coefficient is shown in Figure 8. It can be seen that the predictions are in very good agreement with the experimental mass transfer coefficient. Figure 9 shows the variation of mass transfer coefficient with rotation speed and jet velocity. Jet velocity has significant impact on mass transfer than rotation speed. The CFD simulation has provided valuable information about the power dissipation

TABLE 2: Power consumption per unit mass from CFD and experimental $k_{L,a}$ [1, 2].

Sr. no.	RPM	Aq flow rate Q_A (mL per min)	D (m)	V_N (m/s)	P/M W/kg (present CFD)	$k_{L,a}$ (s^{-1}) $\times 10^4$ (Dehkordi [1, 2])
1	600	300	0.20	6.36	58	1837
2	1000	300	0.20	6.36	149	2275
3	1400	300	0.20	6.36	376	2819
4	600	190	0.20	4.03	50	1354
5	1000	190	0.20	4.03	180	1520
6	1400	190	0.20	4.03	370	2005
7	600	110	0.20	2.33	50	837
8	1000	110	0.20	2.33	177	1033
9	1400	110	0.20	2.33	397	1328

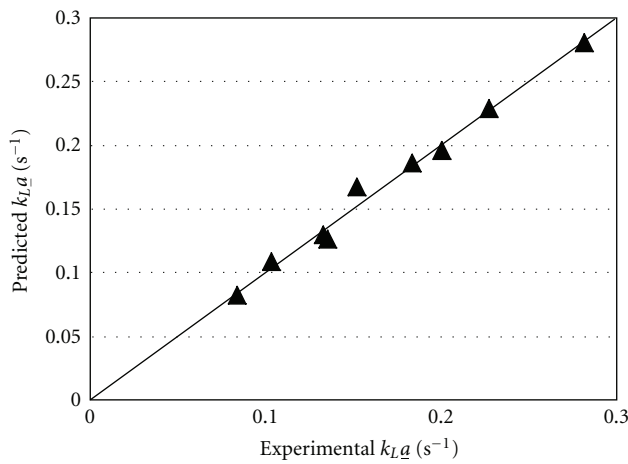


FIGURE 8: Parity plot of overall mass transfer coefficient prediction from proposed correlation with experimental data of Dehkordi [1, 2].

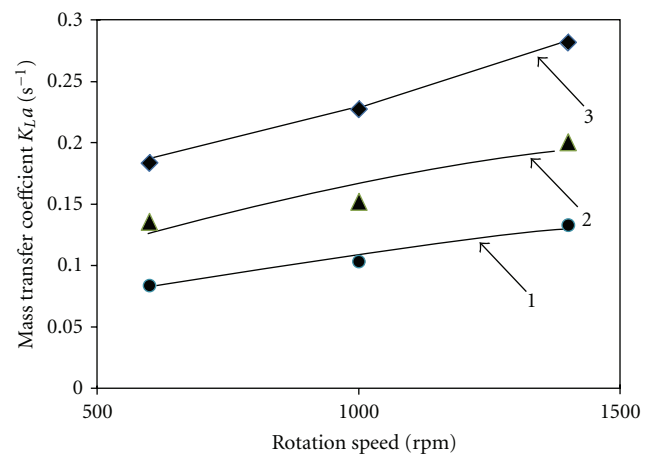


FIGURE 9: Variation of mass transfer coefficient with disk rotation speed; Prediction (correlation using CFD data); Line 1: 110 mL/min; Line 2: 190 mL/min; Line 3: 300 mL/min, • EXPT 110 mL/min, ▲ EXPT 190 mL/min, ◆ EXPT 300 mL/min.

per unit mass, which can be used to obtain semiempirical models with deeper insight into transport phenomena.

7. Conclusion

Microreactor technology is becoming popular in chemical process industries due to ease of scale-up and better energy efficiency. The microextractor design considered in the present work gives almost one theoretical stage with excellent extraction efficiency. The major turbulence generation (subsequent breakup of drops and mass transfer) is dominated by the rotation of top disc in peripheral region and jet velocity in the central region. The inertial force of the jet and the centrifugal force are going to be few orders of magnitude higher than the viscous forces. In this work, two-opposed-jet microextractor has been studied using Reynolds stress model. The Reynolds stress model is very effective in solving stagnation flows with very strong anisotropy. The average turbulent dissipation rate for 600, 1000, and 1400 rpm was 58, 150, and 377 W/kg, respectively. The CFD simulation with small eddy model is capable of predicting transport phenomena in this microextractor. The transport

phenomena are governed by small-scale eddies, and drop size is controlled by the shear in extractor volume. The understanding gained from the single phase CFD simulation can give very useful insights into two-phase extraction processes. CFD simulations clearly bring out the fact that the extractor efficiency is strongly dependent on the jet velocity and rotation speed of the upper disc. However, the effect of change of the disc diameter is not significant.

Notations

a :	Interfacial area (m^2/m^3)
d_N :	Nozzle diameter (m)
D :	Disc diameter (m)
D_t :	Turbulent diffusion coefficient (m^2/s)
k :	Turbulent kinetic energy (m^2/s^2)
k_L :	True mass transfer coefficient (m/s)
M :	Mass of fluid in extractor, kg
N :	Rotation speed of upper disc, rpm
p_i :	Pressure (N/m^2)
$\langle p_i \rangle$:	Time-averaged pressure (N/m^2)
P :	Power dissipated (W)

Q_A : Volumetric flow rate (m^3/s)
 S_{ki} : Shear rate (s^{-1}) =
 $1/2(\partial\langle u_k \rangle / \partial x_i + \partial\langle u_i \rangle / \partial x_k)$
 $\langle u_i \rangle$: Time average of velocity (m/s)
 V_d : Extractor volume, m^3
 V_N : Nozzle velocity, m/s
 x_i : Coordinate distances in i direction where
 $i = 1, 2, 3$ (m).

Greek Letters

δ_{ij} : Kronekar delta = 1 if $i = j$; = 0 if $i \neq j$
 δ : Gap width (m)
 ε : Energy dissipation rate (m^2/s^3)
 μ : Dynamic viscosity (kg/ms)
 μ_t : Turbulent viscosity (kg/ms)
 ν : Kinematic viscosity (m^2/s)
 ν_t : Eddy viscosity (m^2/s)
 Π_{ij} : Pressure strain tensor, ($\text{N/m}^2 \text{ s}$)
 ρ : Density of liquid (kg/m^3)
 σ_ε : Parameter in ε equation in RSM
 τ_{ij} : Reynolds Stress (m^2/s^2) = $-\langle u'_i u'_j \rangle$.

Abbreviations

CFD: Computational fluid dynamics
RSM: Reynolds stress modelling
TOJCD: Twin-opposed-jet contacting device.

References

- [1] A. M. Dehkordi, "Application of a novel-opposed-jets contacting device in liquid-liquid extraction," *Chemical Engineering and Processing*, vol. 41, no. 3, pp. 251–258, 2002.
- [2] A. M. Dehkordi, "Liquid-liquid extraction with chemical reaction in a novel impinging-jets reactor," *AIChE Journal*, vol. 48, no. 10, pp. 2230–2239, 2002.
- [3] B. D. Kadam, J. B. Joshi, S. B. Koganti, and R. N. Patil, "Hydrodynamic and mass transfer characteristics of annular centrifugal extractors," *Chemical Engineering Research and Design*, vol. 86, no. 3, pp. 233–244, 2008.
- [4] J. Saien, S. A. E. Zonouzian, and A. M. Dehkordi, "Investigation of a two impinging-jets contacting device for liquid-liquid extraction processes," *Chemical Engineering Science*, vol. 61, no. 12, pp. 3942–3950, 2006.
- [5] R. L. Yadav and A. W. Patwardhan, "Design aspects of pulsed sieve plate columns," *Chemical Engineering Journal*, vol. 138, no. 1–3, pp. 389–415, 2008.
- [6] C. S. Mathpatii, M. V. Tabib, S. S. Deshpande, and J. B. Joshi, "Dynamics of flow structures and transport phenomena, 2. Relationship with design objectives and design optimization," *Industrial and Engineering Chemistry Research*, vol. 48, no. 17, pp. 8285–8311, 2009.
- [7] A. Tamir, *Impinging Streams Reactors: Fundamentals and Applications*, Elsevier, Amsterdam, The Netherlands, 1994.
- [8] B. N. Murthy and J. B. Joshi, "Assessment of standard $k-\varepsilon$, RSM and LES turbulence models in a baffled stirred vessel agitated by various impeller designs," *Chemical Engineering Science*, vol. 63, no. 22, pp. 5468–5495, 2008.
- [9] C. S. Mathpatii, S. S. Deshpande, and J. B. Joshi, "Computational and experimental fluid dynamics of jet loop reactor," *AIChE Journal*, vol. 55, no. 10, pp. 2526–2544, 2009.
- [10] S. S. Deshmukh, S. Vedantam, J. B. Joshi, and S. B. Koganti, "Computational flow modeling and visualization in the annular region of annular centrifugal extractor," *Industrial and Engineering Chemistry Research*, vol. 46, no. 25, pp. 8343–8354, 2007.
- [11] S. J. Wang and A. S. Mujumdar, "Mixing characteristics of 3D confined turbulent opposing jets," in *International Workshop and Symposium on Industrial Drying*, pp. 309–316, Mumbai, India, December 2004.
- [12] S. J. Wang, S. Devahastin, and A. S. Mujumdar, "Effect of temperature difference on flow and mixing characteristics of laminar confined opposing jets," *Applied Thermal Engineering*, vol. 26, no. 5-6, pp. 519–529, 2006.
- [13] S. J. Wang and A. S. Mujumdar, "Flow and mixing characteristics of multiple and multi-set opposing jets," *Chemical Engineering and Processing*, vol. 46, no. 8, pp. 703–712, 2007.
- [14] A. Abdel-Fattah, "Numerical and experimental study of turbulent impinging twin-jet flow," *Experimental Thermal and Fluid Science*, vol. 31, no. 8, pp. 1061–1072, 2007.
- [15] E. Gavi, D. L. Marchisio, and A. A. Barresi, "CFD modelling and scale-up of Confined Impinging Jet Reactors," *Chemical Engineering Science*, vol. 62, no. 8, pp. 2228–2241, 2007.
- [16] A. W. Kleingeld, L. Lorenzen, and F. G. Botes, "The development and modelling of high-intensity impinging stream jet reactors for effective mass transfer in heterogeneous systems," *Chemical Engineering Science*, vol. 54, no. 21, pp. 4991–4995, 1999.
- [17] D. L. Marchisio, "Large Eddy Simulation of mixing and reaction in a Confined Impinging Jets Reactor," *Computers and Chemical Engineering*, vol. 33, no. 2, pp. 408–420, 2009.
- [18] C. Niamnuy and S. Devahastin, "Effects of geometry and operating conditions on the mixing behavior of an in-line impinging stream mixer," *Chemical Engineering Science*, vol. 60, no. 6, pp. 1701–1708, 2005.
- [19] W. Li, Z. Sun, H. Liu, F. Wang, and Z. Yu, "Experimental and numerical study on stagnation point offset of turbulent opposed jets," *Chemical Engineering Journal*, vol. 138, no. 1-3, pp. 283–294, 2008.
- [20] D. R. Unger and F. J. Muzzio, "Laser-induced fluorescence technique for the quantification of mixing in impinging jets," *AIChE Journal*, vol. 45, no. 12, pp. 2477–2486, 1999.
- [21] Z. G. Sun, W. F. Li, and H. F. Liu, "Study on the radial jet velocity distribution of two closely spaced opposed jets," *International Journal of Heat and Fluid Flow*, vol. 30, no. 6, pp. 1106–1113, 2009.
- [22] W. C. Reynolds, "Fundamentals of Turbulence for Turbulence Modeling and Simulation," Report No. 755, Lecture Notes for Von Karman Institute, Agard., 1987.
- [23] B. E. Launder, "Second-moment closure and its use in modelling turbulent industrial flows," *International Journal for Numerical Methods in Fluids*, vol. 9, no. 8, pp. 963–985, 1989.
- [24] K. Hanjalić, "Advanced turbulence closure models: a view of current status and future prospects," *International Journal of Heat and Fluid Flow*, vol. 15, no. 3, pp. 178–203, 1994.
- [25] J. T. Davies, "Drop sizes of emulsions related to turbulent energy dissipation rates," *Chemical Engineering Science*, vol. 40, no. 5, pp. 839–842, 1985.

Research Article

Numerical Studies on Heat Release Rate in Room Fire on Liquid Fuel under Different Ventilation Factors

N. Cai and W. K. Chow

Department of Building Services Engineering, Research Centre for Fire Engineering, The Hong Kong Polytechnic University, Hong Kong

Correspondence should be addressed to W. K. Chow, beelize@polyu.edu.hk

Received 9 January 2012; Accepted 6 March 2012

Academic Editor: Mahesh T. Dhotre

Copyright © 2012 N. Cai and W. K. Chow. This is an open access article distributed under the Creative Commons Attribution License, which permits unrestricted use, distribution, and reproduction in any medium, provided the original work is properly cited.

Heat release rate (HRR) of the design fire is the most important parameter in assessing building fire hazards. However, HRR in room fire was only studied by computational fluid dynamics (CFD) in most of the projects determining fire safety provisions by performance-based design. In contrast to ten years ago, officers in the Far East are now having better knowledge of CFD. Two common questions are raised on CFD-predicted results on describing free boundaries; and on computing grid size. In this work, predicting HRR by the CFD model was justified with experimental room pool fire data reported earlier. The software fire dynamics simulator (FDS) version 5 was selected as the CFD simulation tool. Prescribed input heating rate based on the experimental results was used with the liquid fuel model in FDS. Five different free boundary conditions were investigated to predict HRR. Grid sensitivity study was carried out using one stretched mesh and multiple uniform meshes with different grid sizes. As it is difficult to have the entire set of CFD predicted results agreed with experiments, macroscopic flow parameters on the mass flow rate through door opening predicted by CFD were also justified by another four conditions with different ventilation factors.

1. Introduction

There are many big construction projects [1] with difficulties to comply with the fire codes while developing in the Far East. Performance-based design (PBD) was then applied to determine fire safety provisions. However, budget allocated on fire safety used to be small, resulting in a lack of full-scale burning tests to measure heat release rate. There are even no resources allocated in some places like Hong Kong to compile a database of heat release rate for local products including train compartments of the railway system [2] as in Japan, China, and Korea. Consequently, wrong concept was adopted in estimating the heat release rate, taking “average value” as “peak value” in many projects submitted to be evaluated by the principal author [1]. At most, computational fluid dynamics (CFD) was applied [3, 4] in hazard assessment. Fire behavior involves complex dynamics driven by critical events, such as the ignition of secondary items, flashover, window breakage, and falling down of glass systems. All these phenomena have not yet been modeled realistically without

using empirical parameters. Authorities having jurisdictions (AHJ) are now more knowledgeable in fire science and engineering. Taking Hong Kong as an example, a huge percentage of senior officers approving fire projects are well trained and have a master degree. CFD-predicted results are, therefore, evaluated more in depth. Two questions [5, 6] on free boundaries and grid size are commonly raised in using CFD. The hazard assessment is normally rejected, and this is very different from fifteen years ago in accepting high-cost projects but the fire engineering reports had no in-depth experimental justification released to the public [7–9]. Therefore, very tight inspection scheme was implemented or proposed to implement in the Far East on those existing projects accepted 20 years ago. Most of the new project applications based on CFD are only accepted by AHJ for designing smoke control design in big and tall buildings [10]. Even so, field tests with hot smoke are required to justify the CFD predictions.

In fire safety design, the most important parameter is the heat release rate (HRR), which is the single most important

variable in characterizing the “flammability” of products and their consequent fire hazard. It gives information on fire size, fire growth rate, available egress time, and suppression system impact [11]. The potential for ignition of nearby items, flashover potential in a room, and the rate of water needed to extinguish the fire can be estimated [12]. The evolution of HRR with time becomes the most important input variable [13] which must be estimated properly to fire simulations. However, HRR used to be predicted by CFD without experimental justification.

The CFD software fire dynamics simulator (FDS) was selected to study fire driven fluid flow. It was developed [4] by National Institute of Standards and Technology (NIST), used in solving practical fire problems. The Navier-Stokes equations were derived to study low-speed, thermally driven flow with an emphasis on smoke and heat transport from fires. Large eddy simulation (LES) was used in simulating turbulence. The FDS version 5 was applied in this study.

These two questions on predicting HRR by CFD will be justified in this paper. HRR is predicted by FDS under different free boundary conditions and grid sensitivities. Results measured from full-scale burning test in gasoline fuel in a room calorimeter [14, 15] were used. Five boundary conditions were used to evaluate free open boundary conditions in applying CFD to predict HRR. Effect of grid size was investigated using one stretched mesh and multiple uniform meshes with different grid sizes.

As raised by Chen [16], it is difficult to have the whole set of CFD-predicted results agreed with experiments. However, macroscopic flow parameters predicted by CFD are very useful [17]. Four other fire scenarios with different ventilation conditions were investigated in this paper with empirical equations on HRR with ventilation factor. Four ventilation factors were used to predict HRR.

2. Earlier Experimental Results

Experimental data with heat release rates measured in a room calorimeter at Lanxi, Harbin, Heilongjiang, China [14, 15] were taken used in justifying CFD predictions. The room was constructed of brick with a cement finish of length 3.6 m, width 2.4 m, and height 2.4 m as shown in Figure 1. The thickness of the brick wall was 0.25 m, with the cement finish of thickness 20 mm. The ceiling was constructed with 0.2 m reinforced concrete. There was a door of height 2.0 m and width 0.8 m.

Three thermocouple trees, each with six thermocouples were placed at the center of the room, near the wall, and the center of the door as shown in Figure 1. The uppermost thermocouple was placed below the ceiling and the other five thermocouples were placed at 0.4 m intervals. A heat flux meter was placed 0.6 m from the door to measure the radiative heat flux received at the floor level. The ambient temperature was 15°C.

A gasoline pool fire of 0.46 m diameter was placed at the center of the room. The HRR was measured by oxygen consumption calorimeter. The measured HRR shown in Figure 2 is used to carry out grid sensitivity study in this paper.

3. Pyrolysis Model for Liquid Fuel

Pyrolysis of solids and liquids can be predicted in FDS by different models [4] depending on the availability of material properties. Evaporation rate of liquid fuel is determined by the Clausius-Clapeyron equation [18] through the liquid temperature and the concentration of fuel vapor above the pool surface. The volume fraction of the fuel vapor above the surface (X_f) is taken as a function of the liquid boiling temperature (T_b), the heat of vaporization (h_v) and the molecular weight (W_f) by:

$$X_f = \exp\left[-\frac{h_v W_f}{R}\left(\frac{1}{T_s} - \frac{1}{T_b}\right)\right]. \quad (1)$$

At the start of simulation, the fuel vapor mass flux m_i was generated first by the initial vapor volume flux V_i specified by the user:

$$m_i = \frac{V_i W_f}{RT_a/\rho_0}. \quad (2)$$

The evaporation mass flux will be updated in the simulation by inspecting the difference between the predicted close-to-the surface volume fraction of fuel vapor with the equilibrium value estimated by (1).

For simplicity, the liquid fuel itself is treated as a thermally thick solid in simulating thermal conduction. Convection within the liquid pool is not considered. The fuel mass flux cannot be expected as an explicit function of temperature, the value can only be estimated by iteration. Temperature and flow conditions would affect the result. Furthermore, estimation of the evaporation rate depends strongly on grid size and distribution. The material properties cannot be traced with measurement.

In applying FDS to study smoke spread and heat transfer, the heat release rate can be taken as an input parameter by the user. The desired value of HRR is transformed [18] into a mass flux for fuel (m_f) at a given solid surface given in terms of the heat release rate per unit area (q) and a specified time ramp function $f(t)$ by:

$$m_i = \frac{f(t)q}{\Delta H}. \quad (3)$$

The mass loss rate can then be computed according to the input q in FDS simulation. Typical values concerned are shown in the example calculation of the manual as listed in the following sections.

4. Free Open Boundary

There is an open boundary on the exterior boundary of the computational domain to let bi-directional flow with hot gas flowing out and cool air coming into the room through the openings. In FDS [18], the geometry as shown in Figure 3 is used to evaluate free open boundary. The hydrodynamic pressure (head) H_1 under the outflow condition at OPEN boundary is specified by point A_1 at pressure P_1 , velocity \mathbf{u}_1

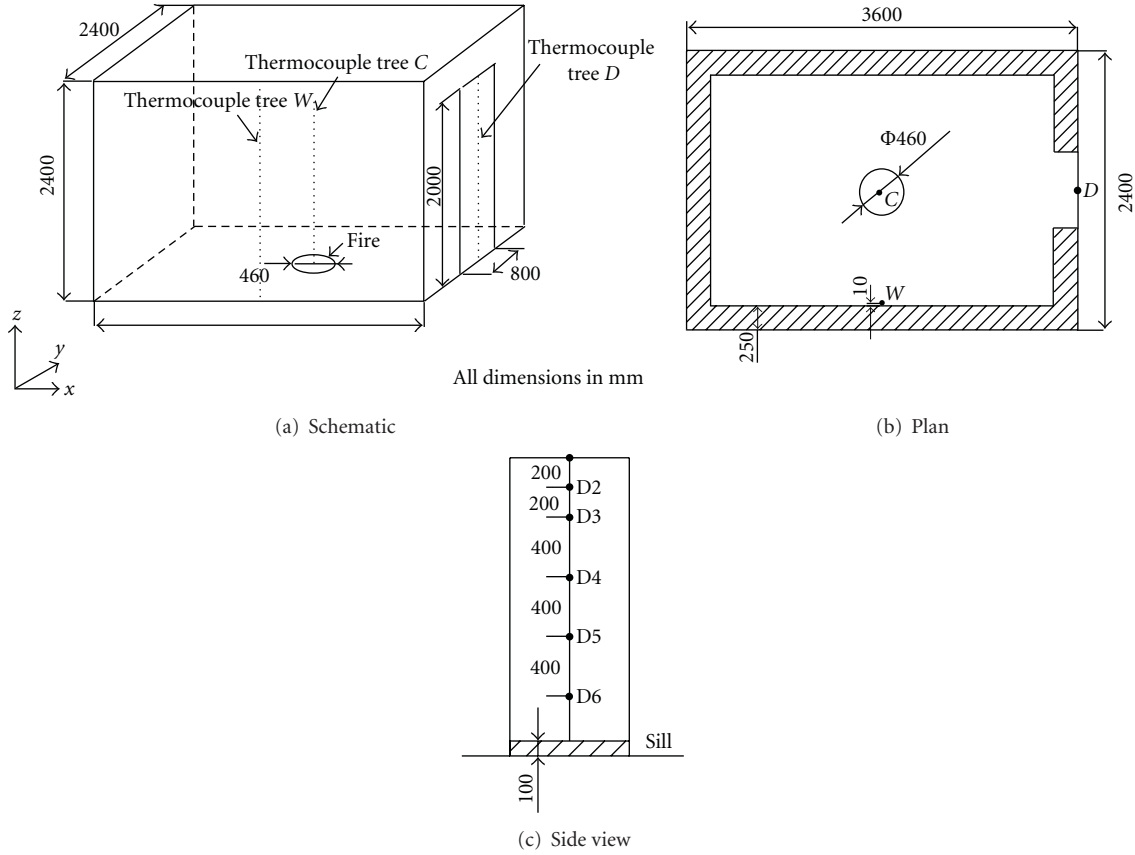


FIGURE 1: Experiment room (in mm).

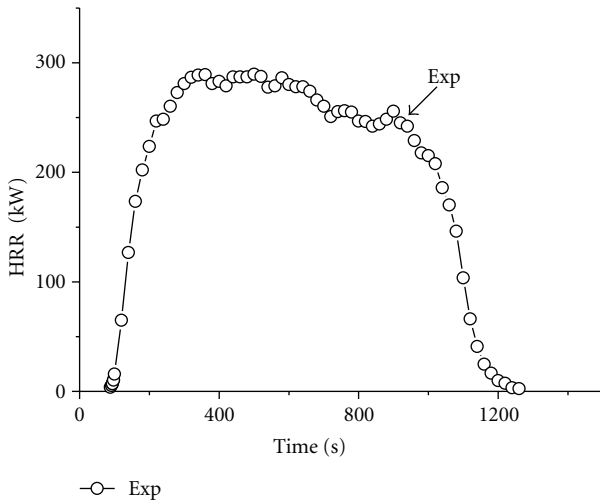


FIGURE 2: Measured curve of HRR by experiment.

and density ρ_1 to a point P_∞ far away from the outflow line at pressure P , velocity 0, and density ρ_∞ as:

$$H_1 = \frac{1}{2} \mathbf{u}_1^2 + \frac{P}{\rho_\infty}. \quad (4)$$

The pressure P is set to ambient pressure P_{ext} , ρ_∞ is the ambient density.

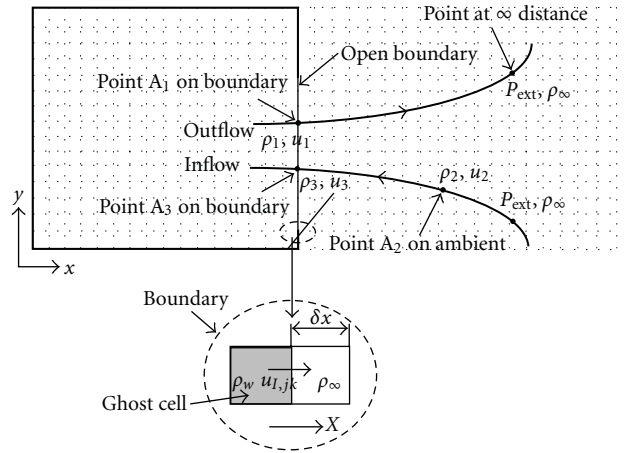


FIGURE 3: Free open boundary.

The Bernoulli theorem was applied to the inflow condition at an OPEN vent by taking the flow as inviscid, steady, and incompressible. Taking the point A_2 to A_3 of the inflow streamline, the fluid element on the boundary accelerated from point A_2 at pressure P_2 , density ρ_2 , and velocity \mathbf{u}_2 to point A_3 at state pressure P_3 , density ρ_3 , and velocity \mathbf{u}_3 :

$$P_2 + \frac{1}{2} \rho_2 \mathbf{u}_2^2 = P_3 + \frac{1}{2} \rho_3 \mathbf{u}_3^2. \quad (5)$$

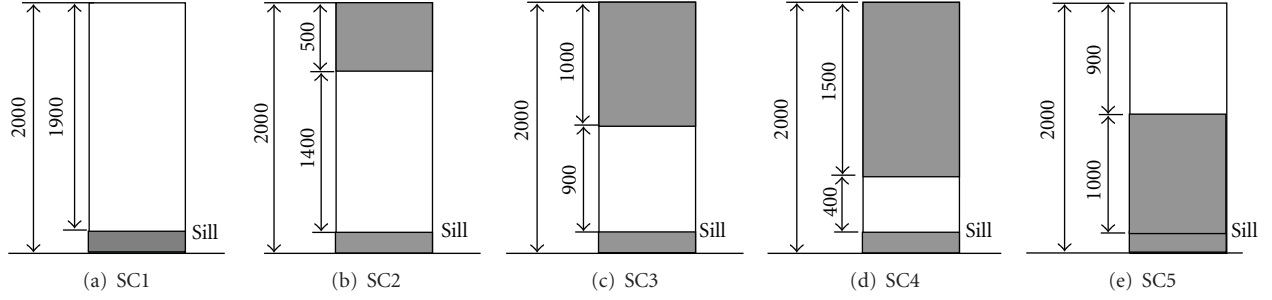


FIGURE 4: Ventilation dimensions of the door (in mm).

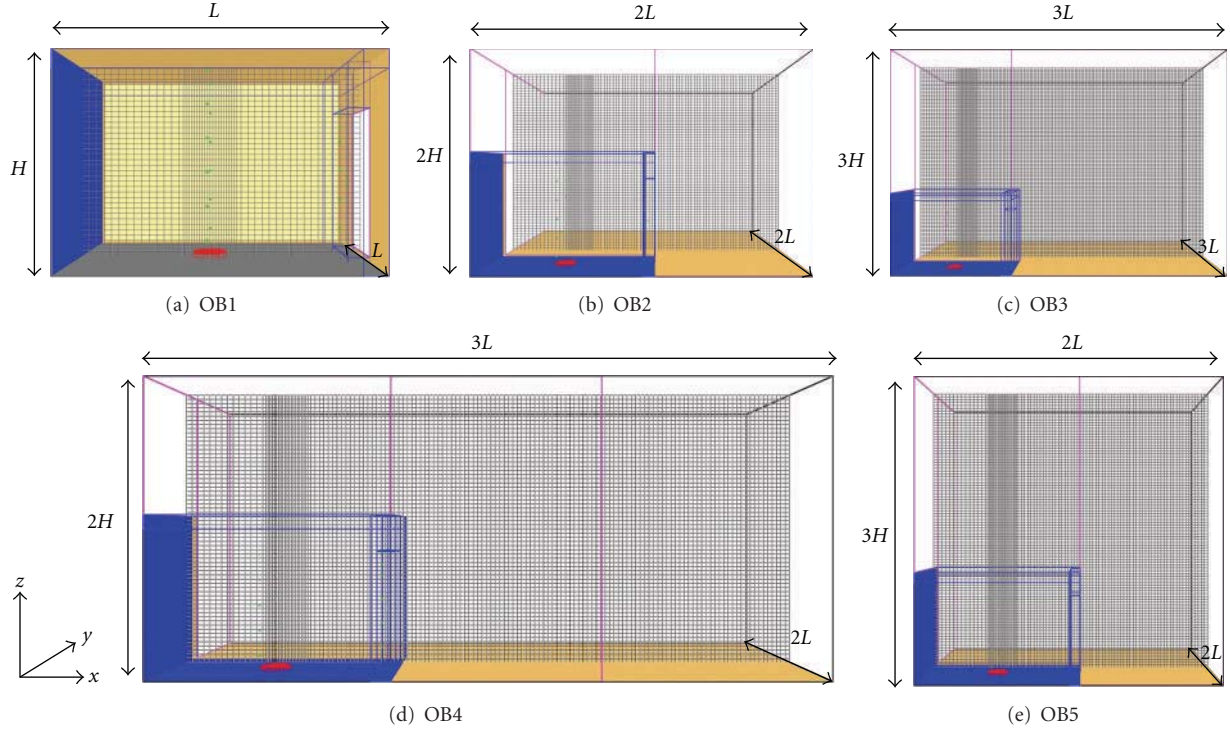


FIGURE 5: Plan OB1 to OB5.

The kinetic energy at A_2 is $(1/2)\rho_2\mathbf{u}_2^2$ with ambient pressure $P = P_{\text{ext}}$. The fluid accelerates to \mathbf{u}_3 at point A_3 which is on an inflow boundary.

The hydrodynamic pressure (head) H_3 at point 3 can be obtained by:

$$H_3 = \frac{1}{2}\mathbf{u}_3^2 + \frac{P_3}{\rho_\infty}. \quad (6)$$

Substituting (6) to (5) would give:

$$P_{\text{ext}} + \frac{1}{2}\rho_2\mathbf{u}_2^2 = \rho_\infty\left(H_3 - \frac{1}{2}\mathbf{u}_3\right) + \frac{1}{2}\rho_3\mathbf{u}_3^2. \quad (7)$$

Rearranging gives

$$H_3 = \frac{P_{\text{ext}}}{\rho_\infty} + \frac{1}{2}\mathbf{u}_2^2\frac{\rho_2}{\rho_\infty} + \frac{1}{2}\mathbf{u}_3\left(1 - \frac{\rho_3}{\rho_\infty}\right). \quad (8)$$

The density ρ_3 is taken as the average density between the gas-phase and ghost cells. Note that such ghost cells are

assigned with the same size as their neighbor cells to establish gradients of various quantities at the boundary as shown in the figure.

Taking I as the index of the last gas phase cell in the x direction, $u_{I,jk}$, $v_{I,jk}$, and $w_{I,jk}$ are the x , y , and z components of velocity at the boundary, respectively. At open boundaries (say $i = I$), H depends on whether the flow is incoming or outgoing. Defining \mathbf{u} at the I th cell as:

$$\mathbf{u}^2 = u_{I,jk}^2 + v_{I,jk}^2 + w_{I,jk}^2. \quad (9)$$

The density at the boundary wall is denoted by ρ_w . The background density used in defining H is ρ_∞ . \mathbf{u} is the velocity component at the boundary. The boundary condition on H is:

$$H_{I+1/2+jk} = H_{\text{ext}} + \frac{1}{2}\mathbf{u}^2 \quad \text{for } u_{I,jk} > 0,$$

$$H_{I+1/2+jk} = H_{\text{ext}} + H_0 + \frac{1}{2}\mathbf{u}^2\left(1 - \frac{\rho_w}{\rho_\infty}\right) \quad \text{for } u_{I,jk} \leq 0. \quad (10)$$

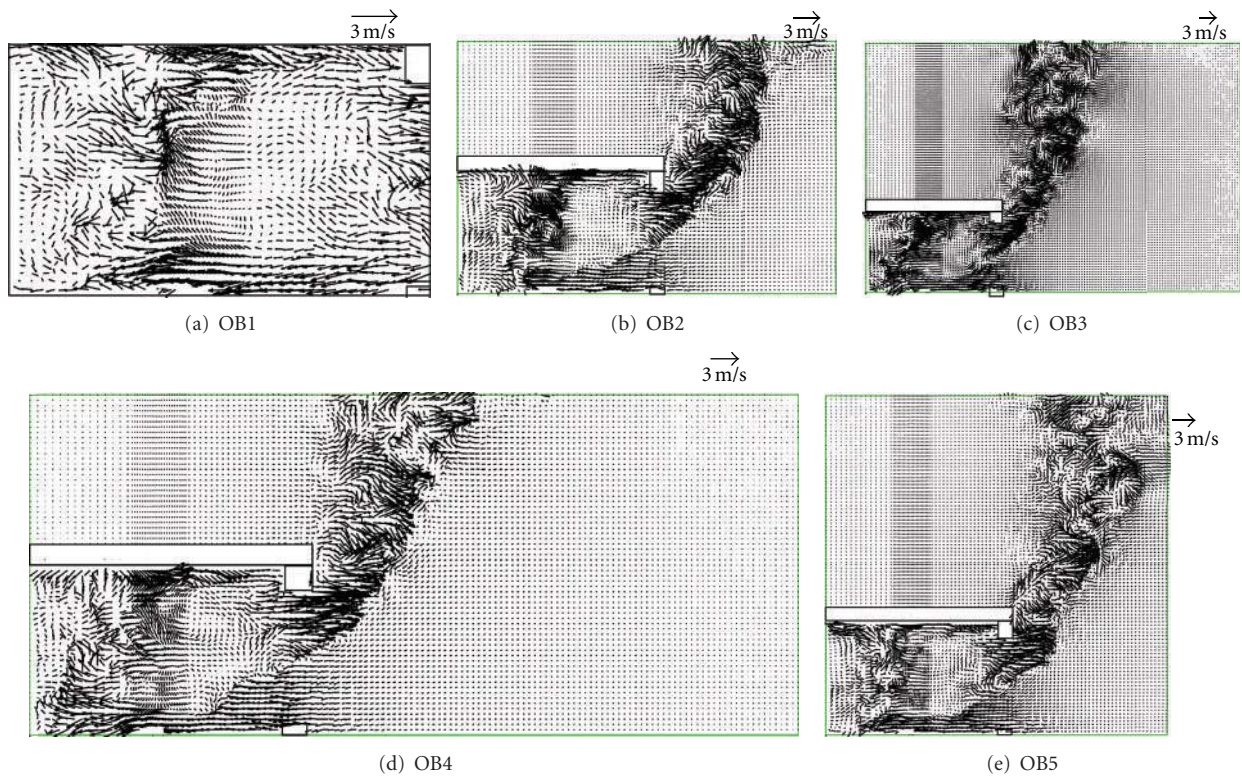


FIGURE 6: Velocity vectors of central plane for different cases at 600 s.

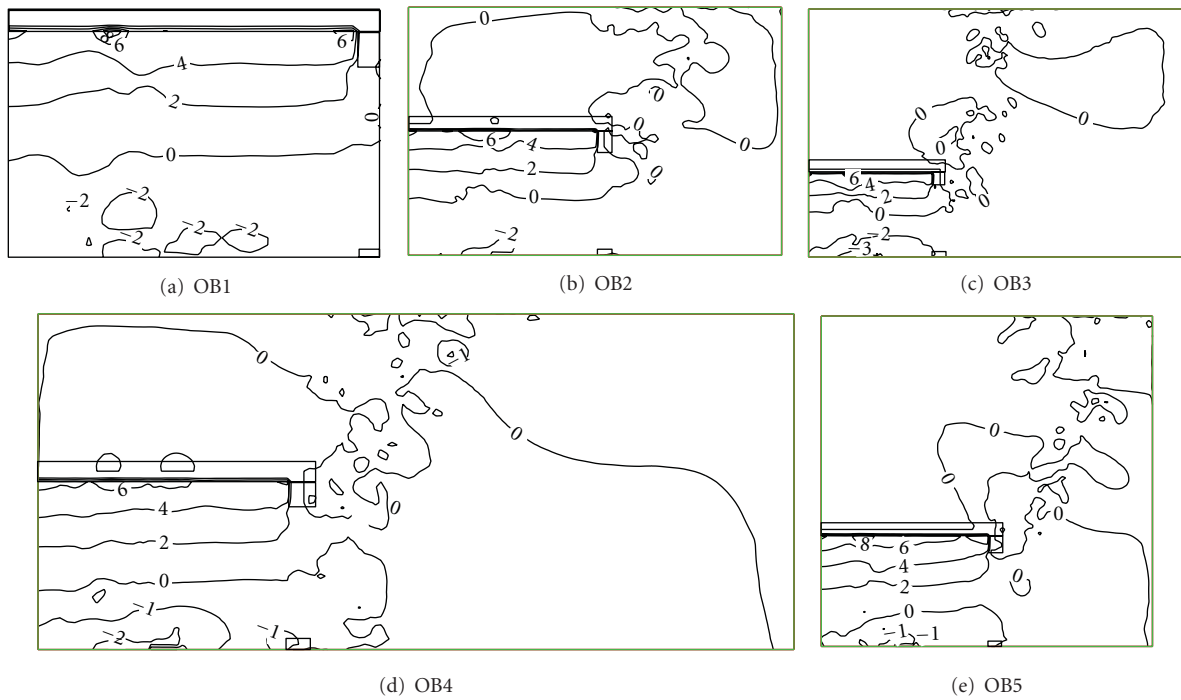


FIGURE 7: Pressure contours of central plane for different cases at 600 s.

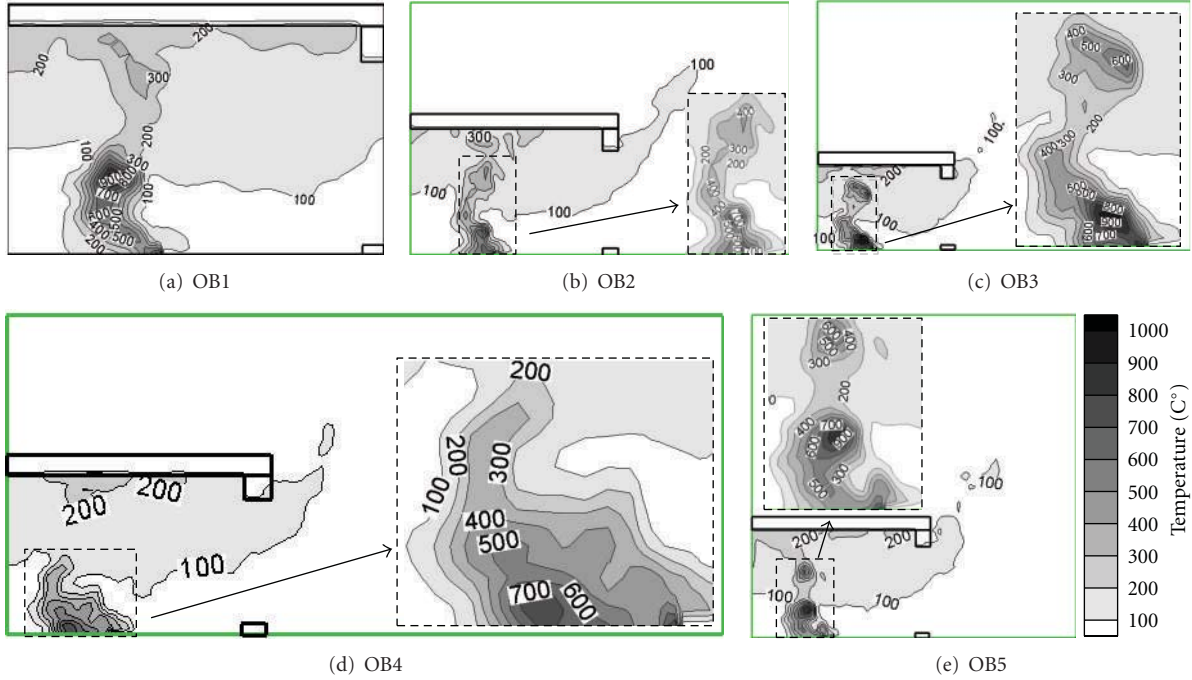


FIGURE 8: Temperature contours of central plane for different cases at 600 s.

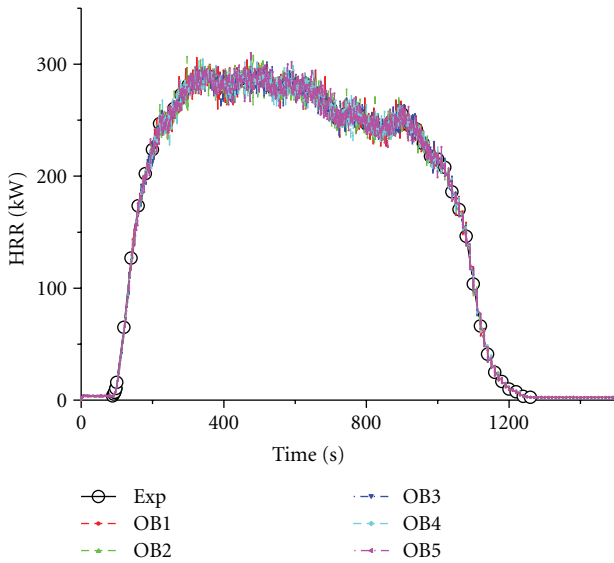


FIGURE 9: Comparison of the curves of HRR of Exp and OB1 to OB5.

The external dynamic pressure H_{ext} is:

$$H_{\text{ext}} = \frac{P_{\text{ext}}}{\rho_{\infty}}. \quad (11)$$

The initial dynamic pressure H_0 is:

$$H_0 = \frac{1}{2} \frac{(u_0^2 + v_0^2 + w_0^2) P_{\text{ext}}}{\rho_{\infty}}. \quad (12)$$

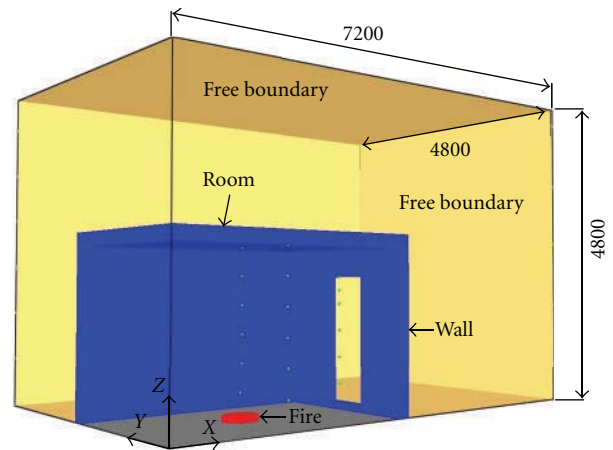


FIGURE 10: FDS model setup.

Both external and internal dynamic pressures are specified by the user (P_{ext} is set with DYNAMIC_PRESSURE for a specific VENT in FDS). The condition that (8) follows from prescribing the fluctuating hydrodynamic pressure P_{ext} at an outflow vent (zero by default) and assuming the Bernoulli equation applies to an inflow vent where the fluid accelerates from the state $\{P_{\text{ext}}; \rho_0; u_0; v_0; w_0\}$ along a streamline. Note that the background density ρ_{∞} is usually equal to the initial ambient density ρ_0 at the start of a calculation, but may change in time if the baroclinic correction term is included.

There are different views on specifying free open boundary conditions in applying CFD and these views should be watched carefully [19]. There have been some attempts to

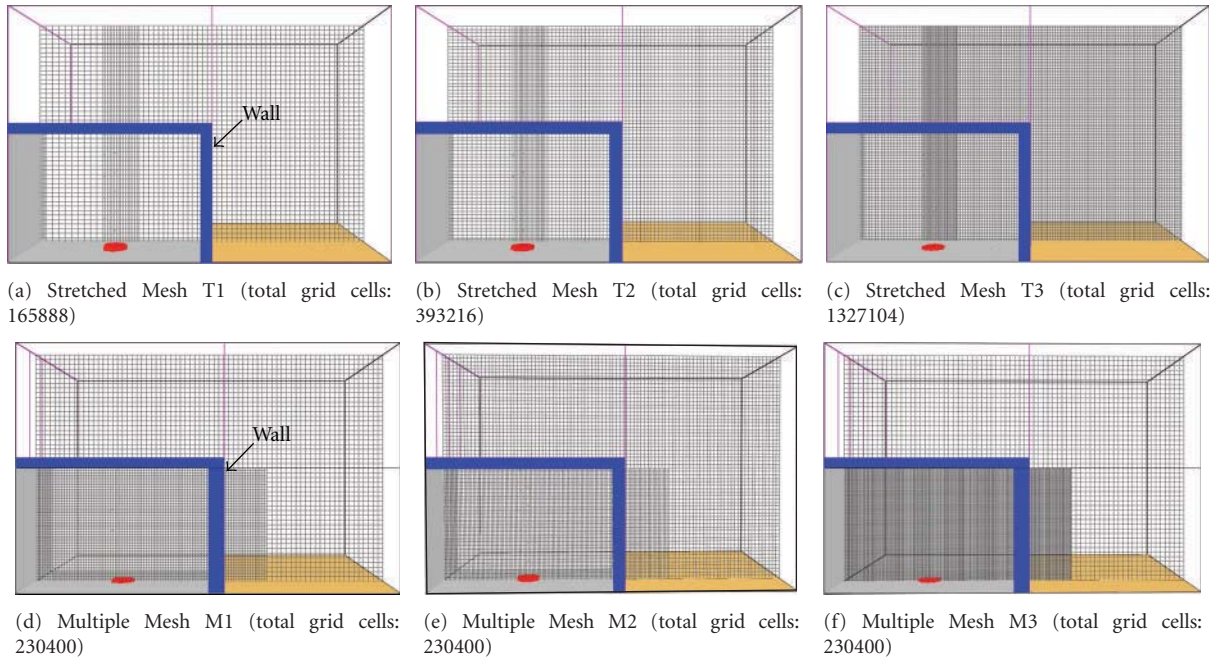


FIGURE 11: Computing mesh.

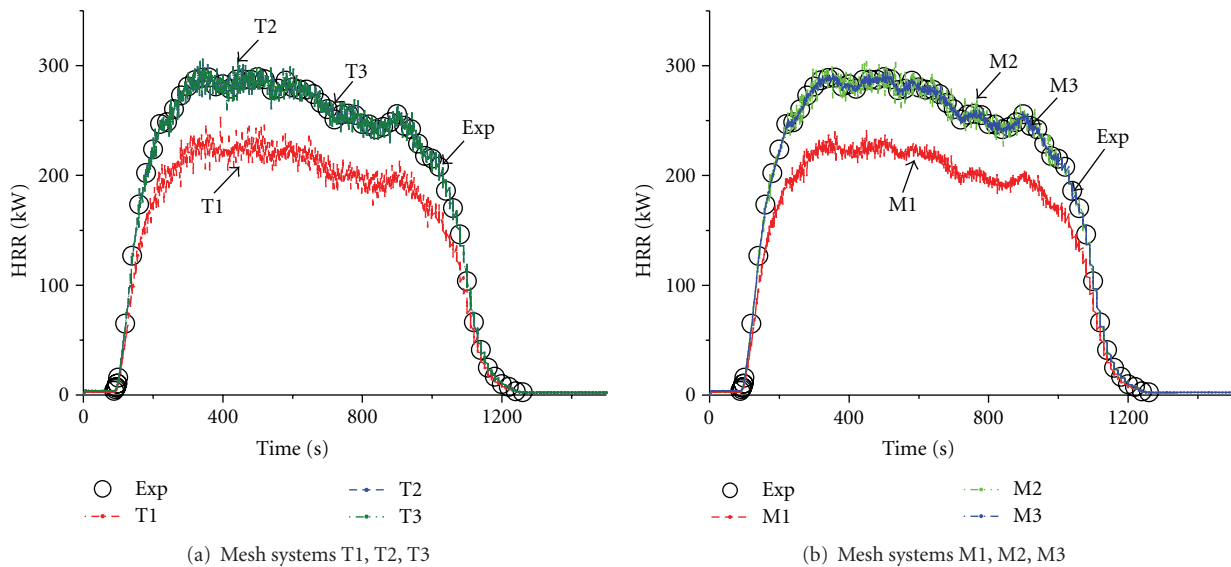


FIGURE 12: Predicted HRR profiles for different meshes.

solve the problem with free boundary. Markatos and co-workers [20, 21] extended the flow domain to the “free boundary” region outside the doorway when studying the smoke flow in enclosures and obtained results that agreed reasonably with experimental data. Schaelin and co-workers [22] pointed out that extending the computing domains outside was a better approach when simulating plume flow. Galea and Markatos [23] pointed out in their case study on simulating fire development in an aircraft that it is desirable to extend the solution domain outside the fire compartment in order to find physically realistic behaviour in the vicinity

of the open doors. Some pioneering work on fire modelling [19–21, 23] demonstrated that the flow pattern in the vicinity of doorway was entirely different if the free boundary had not been extended sufficiently. However, in applying FDS, Hadjisophocleous and Ko [24] suggested that the impact of the open boundary at the exterior of the computational domain was minor when the boundary had been extended up to 2 m outside a geometry of width 10 m. Therefore, it may not be necessary to extend the computational domain to some distance beyond the opening to obtain good results while using FDS version 4.07. They also pointed out that

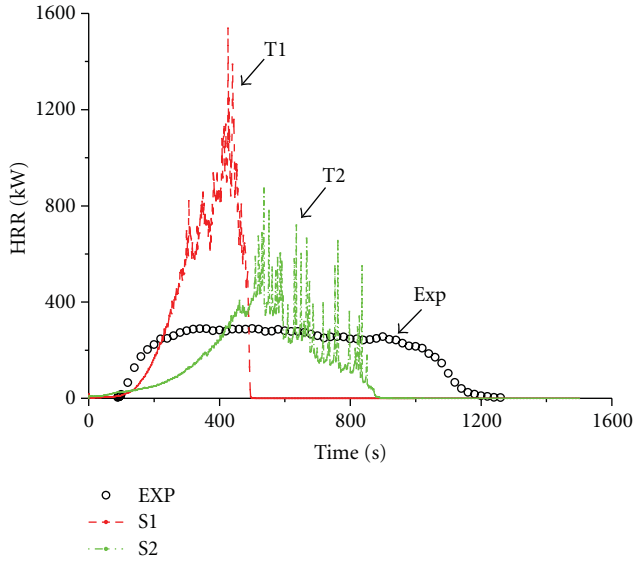


FIGURE 13: Comparison between the curves of predicted HRR and HRR of experiment.

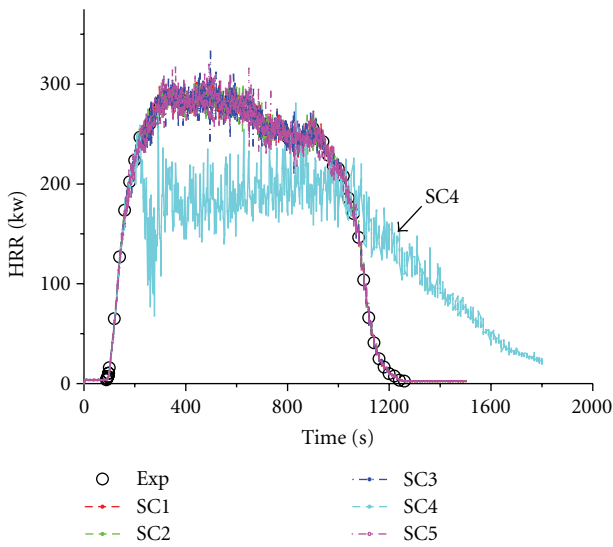


FIGURE 14: Comparison of the curves of HRR of SC1 to SC5.

this situation is rather complicated and should be evaluated for different cases. Note that different results were predicted by different simulation software packages. Further, strongly buoyant flow should be predicted more carefully. It is useful to compare the prediction with the Reynolds Averaged Navier Stokes equation method (RANS). However, this is quite labour intensive to develop a new CFD software and no resources to renew commercial CFD license. Earlier studies on thermal plume suggested that results are similar [25].

5. Numerical Simulations

The FDS version 5 was used to predict the HRR in a room fire. A three-dimensional Cartesian coordinate system was assumed with length along the x -direction, width along the

y -direction, and height along the z -direction. Free boundary conditions were imposed on the outside part between the computational domain and the external environment. Fluid can enter or leave the computational domain freely. Pressure at the boundary was taken as the same as the ambient pressure.

The physical properties of the brick wall and cement were taken as thermal conductivity $1.0 \text{ Wm}^{-1} \text{ K}^{-1}$, density 1700 kgm^{-3} , specific heat capacity $1000 \text{ Jkg}^{-1} \text{ K}^{-1}$. The physical properties of the ceiling were taken as constant values [26] with a thermal conductivity of $1.6 \text{ Wm}^{-1} \text{ K}^{-1}$, density of 2400 kgm^{-3} , and specific heat capacity of $920 \text{ Jkg}^{-1} \text{ K}^{-1}$.

The molecular formula of gasoline is C_8H_{18} , complete combustion with oxygen gives water vapor (H_2O) and carbon dioxide (CO_2) as:



Input parameters in FDS are the boiling temperature, heat of reaction and specific heat, values are found to be 155°C , 338.9 kJkg^{-1} and $2.22 \text{ kJkg}^{-1} \text{ K}^{-1}$, respectively, in the literature [5].

The pool fire was simulated by a polygon with equally calculated area to the circular pan in the experiment. The volume of gasoline was 8 liters. The initial air temperature was 15°C .

The Smagorinsky subgrid-scale turbulence model was used in large eddy Simulation (LES) of FDS. In this study, the value of the Smagorinsky coefficient C_s is 0.2, the value of the turbulent Prandtl number Pr_t is 0.5, and the value of the turbulent Schmidt number Sc_t is 0.5 as recommended [4].

A scenario SC1 with the same experimental condition with a door of width 0.8 m and height 2.0 m as shown in Figure 4 was used. Five free open boundary conditions labeled as OB1, OB2, OB3, OB4, and OB5 with the computational domain extended to different distances beyond the room, as shown in Figure 5, were examined first. Stretched mesh with cubic grids of size 0.075 m by 0.075 m by 0.075 m; and finer grids of size 0.0375 m by 0.0375 m by 0.0375 m were used in these simulations as listed in Table 1. Simulation results were compared with experimental data. Appropriate boundary conditions were then used for sensitivity analysis on grid. The total time for each simulation is taken to be 1500 s. The time step is determined by the Courant-Friedrichs-Lewy (CFL) condition to satisfy the stability criteria [4, 18].

In order to quantify this comparison precisely, functional analysis proposed by Peacock et al. [27] on zone modeling was applied to evaluate the CFD results [6, 28]. Transient predicted and measured data are expressed as vectors \vec{P} and \vec{M} . The Euclidean norm and secant inner product cosine between \vec{P} and \vec{M} are calculated:

$$\begin{aligned} \text{Norm} &= \frac{|\vec{P} - \vec{M}|}{|\vec{P}|}, \\ \text{Cosine} &= \frac{\langle \vec{P}, \vec{M} \rangle}{|\vec{P}| \cdot |\vec{M}|}. \end{aligned} \quad (14)$$

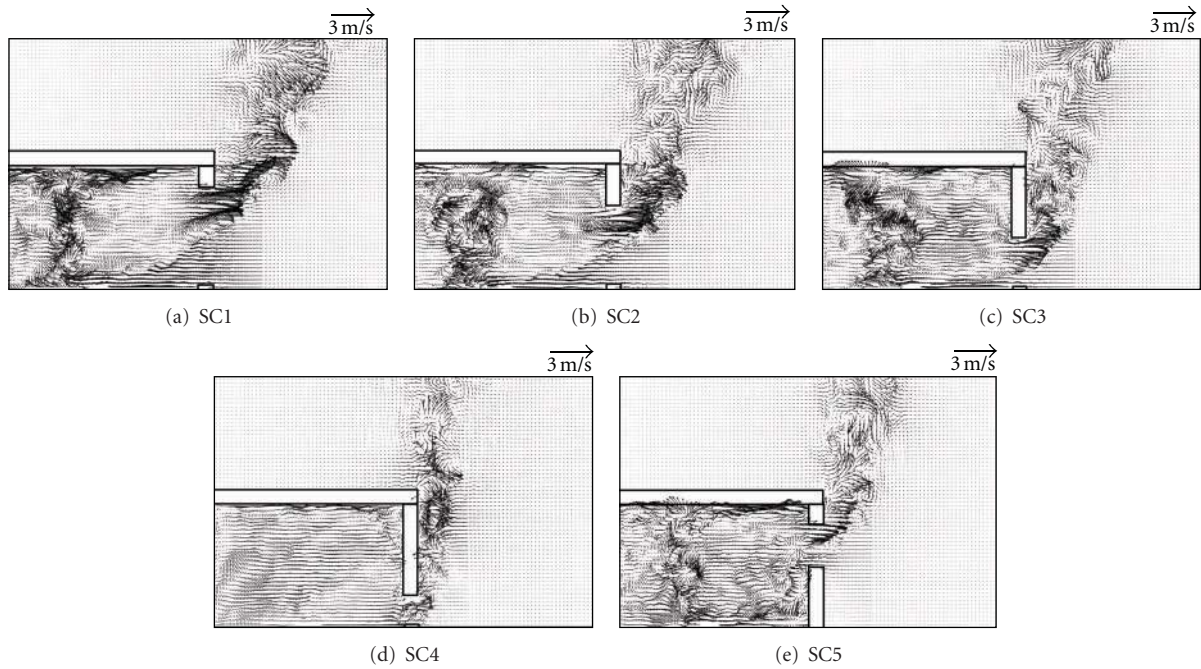


FIGURE 15: Velocity vectors of central plane for different cases at 600 s.

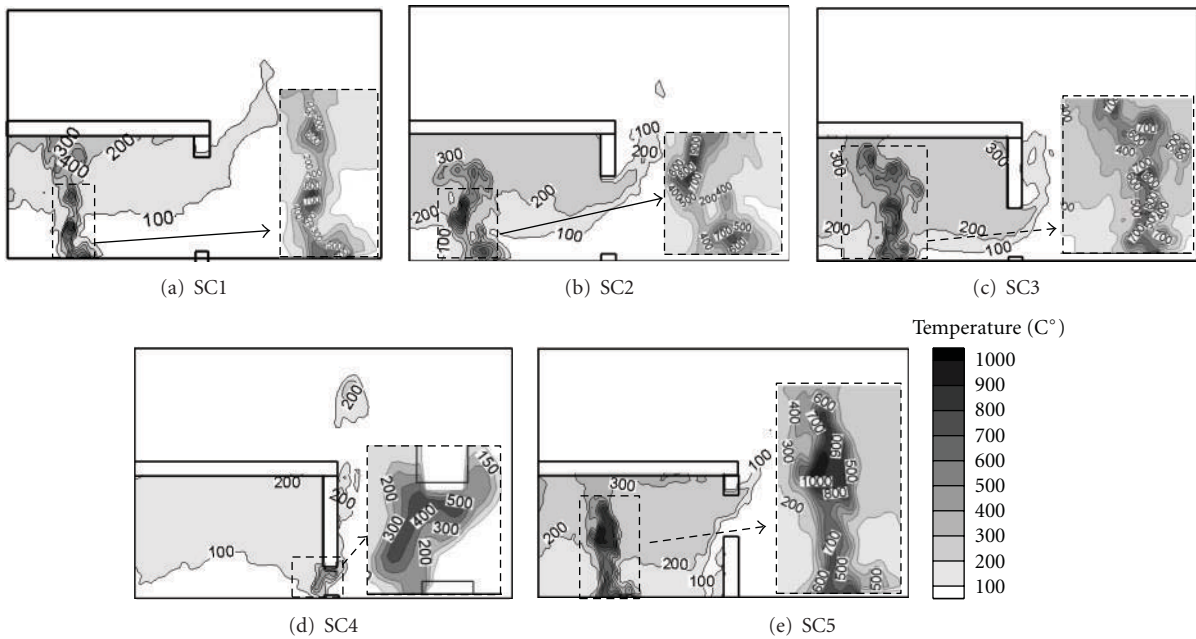


FIGURE 16: Temperature contours of central plane for different cases at 600 s.

Values of norm and cosine are used to compare CFD-predicted results with measured data. Values of norm should be close to 0, and cosine should be close to 1 for good agreement.

6. Open Boundary Conditions

Predicted HRR results for all five simulations OB1, OB2, OB3, OB4, and OB5 are compared with each other in Figure 9. The functional analysis results on norm and cosine

are shown in Table 1. Small norm values of 0.03 indicate that the predicted HRR curves are almost identical in magnitude with the experiment curve. Cosine values lying between 0.95 to 0.97 indicate that the curve shapes are very similar.

Velocity vectors, temperature contour, and the pressure contour at the central vertical plane of each condition at 600 s are shown from Figures 6, 7, and 8. The flow pattern of OB1 is very different from those of other four free boundary conditions. This suggests that extending the free

TABLE 1: Functional analysis results for different boundary conditions.

Boundary conditions	Computational domain			Norm	Cosine
	x/m	y/m	z/m		
OB1	3.6	2.4	2.4	0.03	0.96
OB2	7.2	4.8	4.8	0.03	0.96
OB3	10.8	7.2	7.2	0.03	0.95
OB4	10.8	4.8	4.8	0.03	0.97
OB5	7.2	4.8	7.2	0.03	0.95

boundary to outside is significant. The pressure contours indicate the location of the neutral plane in the room of OB5 was different from those of the rest. The predicted air temperature contours are similar to all five boundary conditions. The highest predicted temperature of OB2 was similar to that of OB4. Both OB3 and OB5 got the same value of the highest predicted temperature. These results indicate that the height of extending distance would affect the predicted results on velocity pattern, temperature, and pressure contour, though the HRR curves are similar. Further investigations on why the HRR curves are similar should be carried out by simulating the combustion process.

Taking both computing accuracy and the computing time required into consideration, the boundary condition OB2 was selected for further simulation in this paper. Computing domain was extended to 7.2 m length, 4.8 m width and 4.8 m height in the Cartesian co-ordinate system to simulate air movement and distribution of combustible gases. The size of computing domain was twice of the chamber along the x , y and z directions respectively as shown in Figure 10.

7. Grid Size Variation

In LES, transient larger eddies are solved and smaller unresolvable eddies are modeled with a time averaged component and a fluctuating perturbation about that average [3]. The fineness of the numerical grid would determine the size of eddies that can be solved. The nominal size of the mesh cell δx and the characteristic fire diameter D^* given by fire power \dot{Q} , air density ρ_∞ , temperature T_∞ , specific heat of air C_p , and gravitational acceleration g are important in simulating buoyant plumes [18]:

$$D^* = \left(\frac{\dot{Q}}{\rho_\infty C_p T_\infty \sqrt{g}} \right)^{2/5}. \quad (15)$$

The ratio $D^*/\delta x$ can be taken as the number of computational cells spanning the characteristic diameter of the fire. A refined grid system can improve the accuracy of results of LES. It was suggested by McGrattan et al. [29] that the value of $D^*/\delta x$ should be larger than 10 to guarantee a reliable operation of FDS. This value has been confirmed by Merci and Van Maele [30] to be acceptable for FDS simulation. Zou and Chow [31] got reasonable FDS

predictions of temperature and radiation data with $D^*/\delta x$ of about 14. Study by Hietaniemi et al. [32] on pool fire showed that having at least 20 cells within the diameter of the pool would give predictions agreed with experiments.

One stretched mesh (stretched in x - and y -directions and uniform in z -direction) and multiple uniform meshes (finer mesh in the vicinity of the fire and door) as shown in Figure 11 were applied to study grid sensitivity in this paper. Different nominal grid size systems varying from relatively coarse mesh to fine mesh were tested to study the effect of different grid systems on predicting HRR. Systems T1, T2, T3 are results predicted under stretched mesh; and M1, M2, M3 are results predicted under stretched mesh with different grid sizes as shown in Table 2. Under each mesh system, the grid size was reduced gradually. The predicted HRR was compared with experimental data [14, 15].

At first, the curve of heat release rates from the experiment was taken as the input function. The experimental HRR profile was compared with calculated HRR profiles for different grid sizes of stretched mesh as shown in Figure 12. As shown in Figure 12(a), there were significant changes when the grid system had changed from T1 to T2. Changing the grid system from T2 to T3 gives little change in the predicted HRR profile. However, a longer computation time of over 180 hours is required. The same conclusion can be applied to multiple mesh system file M2 as shown in Figure 12(b). Functional analysis results of the point-to-point comparison for grid size file T1, T2, T3, M1, M2, and M3 are presented in Table 2.

Grid system T1 give lower values than experiment as shown in Figure 12(a). Grid systems T2 and T3 have identical shape compared with experimental curve(s). Functional analysis results give a cosine of T1 (of 0.74). Values of cosine from T2 and T3 are 0.96 and 0.99, respectively. These values are very close to unity. Fining the system from T2 to T3 gives little changes in both curve shape and magnitude. Based on the functional analysis results, fining grid size than a certain value might not result in a better prediction.

Grid system M2 in the core area is the same as that of grid size file T2. Though the comparison, as shown in Figure 12, suggests that agreement would not be better for both the multiple meshes system and the stretched mesh system, the functional analysis, as shown in Table 2, confirms that grid system M2 agrees better with experiment. The results from finer grid file M3 for multiple meshes system agree well with experiment, as shown in Figure 12(b). Functional analysis in M3 confirms this. However, M3 required a 430-hour computing time, which is much longer than M2. And the changes in results triggered by M3 are not significant.

Within the grid size file T1 and T2, HRR was simulated by the liquid fuel model in FDS. The fuel was allowed to burn by itself. Predicted HRR by both systems did not agree with experiment as shown in Figure 13. The fuel was burnt up in a much shorter period than measured experimentally. Functional analysis indicates that better results can be predicted by finer grid system T2. However, predicted curves of both systems did not agree with experiment. The burning rate in a room fire is strongly affected by radiative heat feedback which might not be well simulated in the FDS

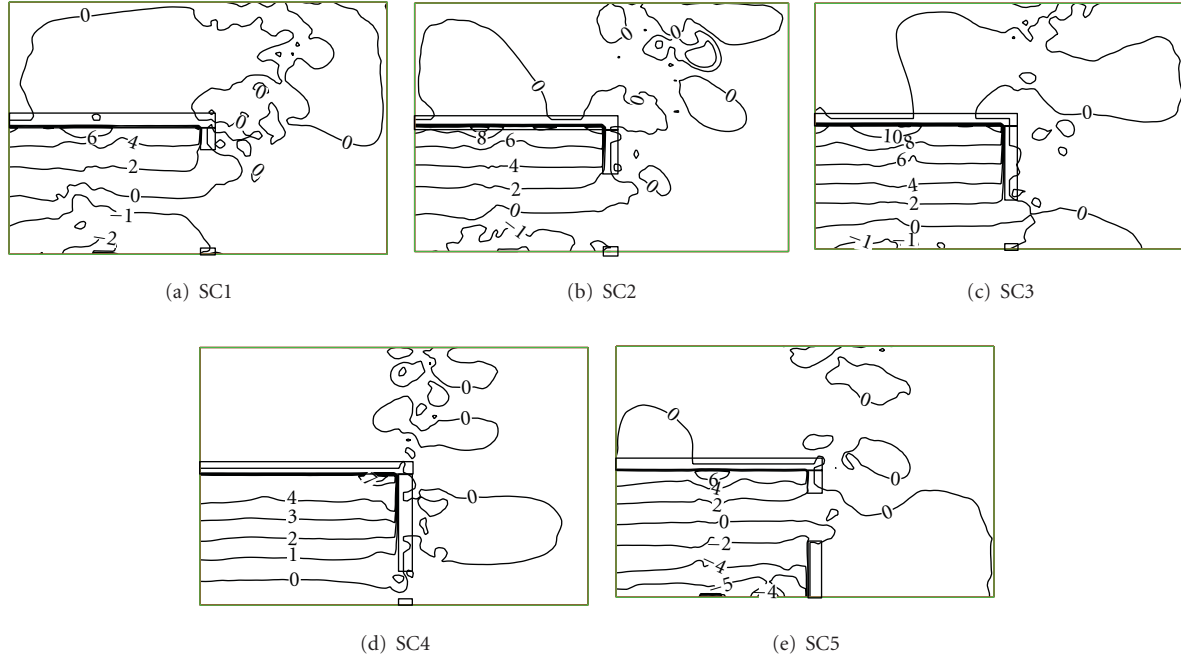


FIGURE 17: Pressure contour of central plane for different cases at 600 s.

TABLE 2: Grid conditions and functional analysis results on grid sensitivity.

Mesh type	Simulation number	Grid size in the fire room (mm)	Grid size in the extended domain (mm)	$D^*/\delta X$	Total number of grid cells	Norm	Cosine
Stretched mesh	T1	5	10	11	165,888	0.31	0.74
	T2	3.75	7.5	15	393,216	0.03	0.96
	T3	2.5	5	23	1,327,104	0.01	0.99
Multiple meshes	M1	5	10	11	262,656	0.27	0.95
	M2	3.75	7.5	15	466,944	0.02	0.97
	M3	2.5	5	23	746,496	0.01	0.99

model. As pointed out by the program developers [4], inherited limitations in the FDS liquid fuel model would generate problems. This limitation was also incorporated based on other research studies conducted by Smardz [33], Moghaddam et al. [34], and Thomas et al. [35]. Therefore, it is suggested that liquid fuel model should be applied carefully to engineering application. Further investigation to work on the accuracy of CFD prediction should be conducted.

Therefore, the heat release rate of a fire is better taken as an input parameter by ramped heating rate based on the experimental results. This will be shown in the following simulations with different ventilation factors. As pointed out by the program developers [4], inherited limitations in the FDS liquid fuel model would generate problems.

8. Ventilation Factors

Different ventilation scenarios were investigated by adjusting the door height from sill to upper boundary. In addition to SC1 with door height 2.0 m from the floor, four different

ventilation conditions SC2 to SC5 with a fixed door of width 0.8 m but different heights, as shown in Figure 4 were used in this study:

- (i) SC2: door height 1.5 m from the floor,
- (ii) SC3: door height 1.0 m from the floor,
- (iii) SC4: door height 0.5 m from the floor,
- (iv) SC5: door height 0.9 m from the ceiling.

In SC1, the four simulations SC2 to SC5 on different ventilation factors were conducted for 1500 s, using the grid size profile M2 and boundary condition OB2.

Predicted curve of the HRR in different scenarios by the FDS are compared with experiment in Figure 14. It is observed that, except SC4, all predicted HRR curves agree with the input HRR. SC4 has the lowest ventilation factor. Velocity vectors, temperature contour, and pressure contour of the central vertical plane at 600 s are shown in Figures 15, 16 and 17. Prediction in oxygen supply with the decreased opening area would decrease the heat release rate.

The macroscopic flow parameter transient net air flow of mass through the door predicted by FDS is used to justify CFD predictions. Four different ventilation factors V_f defined in terms of the openings A_0 and the opening height H_0 are changed:

$$V_f = A_0 \sqrt{H_0}. \quad (16)$$

An empirical equation was derived by Babrauskas and Williamson [36] to express the air flow rate \dot{m}_a through V_f :

$$\dot{m}_a = 0.5V_f. \quad (17)$$

Based on the predicted results by FDS, integrated mass flux through the door, and averaged (noun) over the computing period can give the intake airflow rate \dot{m}_a . Figure 18 shows the intake airflow rate \dot{m}_a for all ventilation scenarios. With the fire load located in the center of the room, increasing the size of the ventilation openings would increase the averaged intake airflow rate \dot{m}_a . Under the same ventilation condition, the averaged intake airflow rate \dot{m}_a would be increased by higher HRR value. This relationship can be described by linear correlation:

$$\dot{m}_a = 0.44V_f. \quad (18)$$

This equation is very close to the empirical equation given by (17).

It has to be pointed out that, for scenario SC5, though the ventilation area was similar to SC3, the amount of outtake air caused by convection was not as much as in scenario SC3 due to the different locations of opening. Buoyancy of the hot air might be a factor. Velocity vectors in Figures 15(c) and 15(e) show that ventilation rate increases if the opening is closer to the top of the room.

9. Conclusion

Heat release rate of a room pool fire was studied by FDS version 5 with different free open boundary conditions. A sensitivity study was carried out to compare predicted results with the experiment results under different grid systems. Predictions with the coarse grid have deviated more away from the experimental data. The predictions with a medium grid were found to agree with the experiment well, and selected for this study. In general, the prediction of HRR by FDS is good. Although the computational domain outside did not give much difference to the predicted HRR, predicted velocity patterns are very different.

Free opening boundary condition should be evaluated before being applied in CFD simulations, especially when the combustion process is included while simulating fires in tall or supertall buildings. Extending the computational domain to a sufficient distance beyond the opening is recommended.

The effects of ventilation factor on HRR and mass flow rate through the door opening were analyzed by FDS. On the five fire scenarios with different ventilation conditions investigated in this paper, air intake rate might be higher to give more oxygen for combustion under higher ventilation factor. Linear correlations can be fitted for the relationship

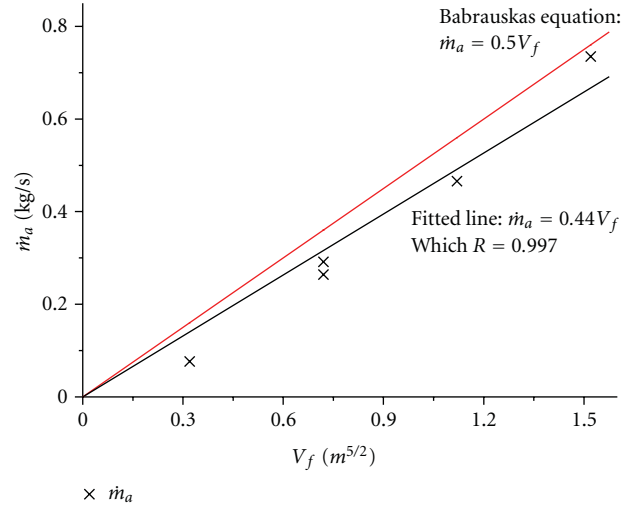


FIGURE 18: The curve of averaged intake airflow rate \dot{m}_a against ventilation factor V_f .

between the intake airflow rate and the ventilation factor, with results very close to those equations derived from simple hydraulic theory. Averaged predicted HRR by the liquid fuel model in FDS did not agree with the experimental results. The burning rate in a room fire is strongly affected by radiative heat feedback which might not be well simulated in the FDS model. This result was incorporated with other studies [4, 33–35]. It is suggested that liquid fuel model should be applied carefully to engineering application. Further related work on validation and verification of liquid fuel model in FDS should be conducted.

Acknowledgments

The work described in this paper was supported by a grant from the Research Grants Council of the Hong Kong Special Administrative Region, China for the project “Appropriate Safety for Lift shafts and Adjacent Lobbies of Evacuation Elevator Systems for Supertall Buildings under Big Fires” (PolyU 5148/08E) with account number B-Q11T.

References

- [1] W. K. Chow, “Performance-based design on fire safety provisions in the Far East,” in *Professional Development Conference and Exposition, Engineering Technology Conference*, Portland, Ore, USA, October 2011.
- [2] W. K. Chow, “A discussion on fire safety for subway systems in Hong Kong,” in *Exchange Meeting for SFPE Asia-Oceania Chapters – Transportation Fire Safety*, Korea Railroad Research Institute & SFPE Korean Chapter, Seoul, Korea, April 2011.
- [3] G. Cox and S. Kumar, “Modelling enclosure fires using CFD,” in *SFPE Handbook of Fire Protection Engineering*, pp. 3-194–3-218, Natl Fire Protection Assn, Quincy, Mass, USA, 4th edition, 2008.
- [4] K. B. McGrattan, B. Klein, S. Hostikka, and J. E. Floyd, “Fire Dynamics Simulator (Version 5), User’s Guide,” NIST Special Publication 1019-5, National Institute of Standards and Technology, Gaithersburg, Md, USA, 2009.

- [5] S. S. Li and W. K. Chow, "Application of computational fluid dynamics in simulating fire-induced air flow in large halls," in *8th Asia-Oceania Symposium on Fire Science and Technology*, Melbourne, Australia, December 2010.
- [6] W. K. Chow, C. L. Chow, and S. S. Li, "Simulating smoke filling in big halls by computational fluid dynamics," *Modelling and Simulation in Engineering*, vol. 2011, Article ID 781252, 16 pages, 2011.
- [7] W. K. Chow, "Fire safety desired in the new airport terminal," Lecture for 40th Anniversary, University of Science and Technology of China, Hefei, Anhui, China, September 1998.
- [8] W. K. Chow, "On the "cabins" fire safety design concept in the new Hong Kong airport terminal buildings," *Journal of Fire Sciences*, vol. 15, no. 5, pp. 404–423, 1997.
- [9] J. C. Jones, "Comment on fire load densities," *International Journal on Engineering Performance-Based Fire Codes*, vol. 10, no. 3, p. 75, 2011.
- [10] J. H. Klote, "Computer modeling for smoke control design," *Fire Safety Journal*, vol. 9, no. 2, pp. 181–188, 1985.
- [11] D. Madrzykowski and D. W. Stroup, "Flammability Hazard of Materials," in *Fire Protection Handbook*, A. E. Cote, C. C. Grant, J. R. Hall Jr., and R. E. Solomon, Eds., vol. 1, Chapter 3. Section 2, pp. 31–48, National Fire Protection Assoc., Quincy, Mass, USA, 20th edition, 2008.
- [12] J. G. Quintiere, *Principles of Fire Behavior*, Delmar Cengage Learning, 1998.
- [13] V. Babrauskas and R. D. Peacock, "Heat release rate: the single most important variable in fire hazard," *Fire Safety Journal*, vol. 18, no. 3, pp. 255–272, 1992.
- [14] W. K. Chow, Y. Gao, H. Dong, G. Zou, and L. Meng, "Full-scale burning tests on heat release rate of gasoline fire with water mist," *Journal of Applied Fire Science*, vol. 11, no. 1, pp. 21–40, 2002.
- [15] W. K. Chow, Y. Gao, H. Dong, G. W. Zou, Z. Luo, and L. Meng, "Experimental studies on minimum heat release rates for flashover with oxygen consumption calorimetry," *Architectural Science Review*, vol. 46, no. 3, pp. 291–296, 2003.
- [16] Q. Chen, "CFD for simulating air distribution in buildings: The state of the art, challenges, and opportunities," in *Proceedings of the 11th International Conference on Air Distribution in Rooms (ROOMVENT '09)*, pp. 23–31, Busan, Korea, May 2009.
- [17] C. L. Chow, "Air flow rate across vertical opening induced by room heat sources," *International Journal on Architectural Science*, vol. 8, no. 1, pp. 11–16, 2011.
- [18] K. McGrattan, S. Hostikka, J. Floyd et al., "Fire Dynamics Simulator (Version 5): Technical Reference Guide," NIST SP 1018, NIST Special Publication 1018-5, National Institute of Standards and Technology, Gaithersburg, Md, USA, 2009.
- [19] C. L. Chow and W. K. Chow, "A brief review on applying computational fluid dynamics in building fire hazard assessment," in *Fire Safety*, I. Sogaard and H. Krogh, Eds., Nova Science, 2009.
- [20] N. C. Markatos, M. R. Malin, and G. Cox, "Mathematical modelling of buoyancy-induced smoke flow in enclosures," *International Journal of Heat and Mass Transfer*, vol. 25, no. 1, pp. 63–75, 1982.
- [21] N. C. Markatos and G. Cox, "Hydrodynamics and Heat Transfer in enclosures containing a fire source," *PCH. Physico-chemical Hydrodynamics*, vol. 5, no. 1, pp. 53–66, 1984.
- [22] A. Schaelin, J. van der Maas, and A. Moser, "Simulation of airflow through large openings in buildings," in *Proceedings of the ASHRAE Winter Meeting*, pp. 319–328, Anaheim, Calif, USA, January 1992.
- [23] E. R. Galea and N. C. Markatos, "The mathematical modelling and computer simulation of fire development in aircraft," *International Journal of Heat and Mass Transfer*, vol. 34, no. 1, pp. 181–197, 1991.
- [24] G. Hadjisophocleous and Y. J. Ko, "Impact of various parameters on the CFD predictions of atrium smoke management systems," *ASHRAE Transactions*, vol. 115, pp. 263–270, 2009.
- [25] R. Yin and W. K. Chow, "Building fire simulation with a field model based on large eddy simulation," *Architectural Science Review*, vol. 45, no. 2, pp. 145–153, 2002.
- [26] *ASHRAE Handbook—Fundamentals*, American Society of Heating, Refrigerating and Air-Conditioning Engineers (ASHRAE), Atlanta, Ga, USA, 2001.
- [27] R. D. Peacock, P. A. Reneke, W. D. Davis W., and W. W. Jones, "Quantifying fire model evaluation using functional analysis," *Fire Safety Journal*, vol. 33, no. 3, pp. 167–184, 1999.
- [28] W. K. Chow and G. W. Zou, "Numerical simulation of pressure changes in closed chamber fires," *Building and Environment*, vol. 44, no. 6, pp. 1261–1275, 2009.
- [29] K. B. McGrattan, H. R. Baum, and R. G. Rehm, "Large Eddy simulations of smoke movement," *Fire Safety Journal*, vol. 30, no. 2, pp. 161–178, 1998.
- [30] B. Merci and K. Van Maele, "Numerical simulations of full-scale enclosure fires in a small compartment with natural roof ventilation," *Fire Safety Journal*, vol. 43, no. 7, pp. 495–511, 2008.
- [31] G. W. Zou and W. K. Chow, "Evaluation of the field model, fire dynamics simulator, for a specific experimental scenario," *Journal of Fire Protection Engineering*, vol. 15, no. 2, pp. 77–92, 2005.
- [32] J. Hietaniemi, S. Hostikka, and J. Vaari, "FDS simulation of fire spread comparison of model results with experimental data," VTT Working Papers 4, 2004.
- [33] P. Smardz, *Validation of Fire Dynamics Simulator (FDS) for forced and natural convection flows*, M.S. thesis, University of Ulster, 2006.
- [34] A.Z. Moghaddam, K. Moinuddin, I. R. Thomas, I. D. Bennetts, and M. Culton, "Fire behaviour studies of combustible wall linings applying FDS," in *Proceedings of the 15th Australasian Fluid Mechanics Conference*, Sydney, Australia, 2004.
- [35] I. R. Thomas, K. A. M. Moinuddin, and I. D. Bennetts, "The effect of fuel quantity and location on small enclosure fires," *Journal of Fire Protection Engineering*, vol. 17, no. 2, pp. 85–102, 2007.
- [36] V. Babrauskas and R. B. Williamson, "Post-flashover compartment fires: basis of a theoretical model," *Fire and Materials*, vol. 2, no. 2, pp. 39–53, 1978.

Research Article

Effects of Gravity and Inlet Location on a Two-Phase Countercurrent Imbibition in Porous Media

M. F. El-Amin,^{1,2} Amgad Salama,¹ and Shuyu Sun¹

¹ Computational Transport Phenomena Laboratory (CTPL), Division of Physical Sciences and Engineering (PSE), King Abdullah University of Science and Technology (KAUST), Thuwal 23955-6900, Saudi Arabia

² Department of Mathematics, Aswan Faculty of Science, South Valley University, Aswan 81528, Egypt

Correspondence should be addressed to M. F. El-Amin, mohamed.elamin@kaust.edu.sa

Received 28 December 2011; Accepted 26 February 2012

Academic Editor: Mandar Tabib

Copyright © 2012 M. F. El-Amin et al. This is an open access article distributed under the Creative Commons Attribution License, which permits unrestricted use, distribution, and reproduction in any medium, provided the original work is properly cited.

We introduce a numerical investigation of the effect of gravity on the problem of two-phase countercurrent imbibition in porous media. We consider three cases of inlet location, namely, from, side, top, and bottom. A 2D rectangular domain is considered for numerical simulation. The results indicate that gravity has a significant effect depending on open-boundary location.

1. Introduction

Oil recovery by imbibition mechanism, from fractured reservoirs, is a significant research area in multiphase flow in porous media especially for water-flooding process in fractured oil reservoirs. Fractured reservoirs are composed of the fracture network and matrix. Fractures have a higher permeability and relatively low volume compared to the matrix, whose permeability is very low but it contains the majority of the oil. Water flooding is used to increase oil recovery by increasing water pressure in fractures since water quickly surrounds oil-saturated matrices of lower permeability. The process of water flooding works well when the matrix is water-wet, and imbibition can lead to significant recoveries, while poor recoveries and early water breakthrough occur with oil-wet matrix conditions. Imbibition is defined as the displacement of the nonwetting phase (oil) by the wetting phase (water) with dominant effect of capillary forces. Imbibition can occur in both countercurrent and cocurrent flow modes, depending on the fracture network and the water injection rates. In cocurrent imbibition, water displaces oil out of the matrix; thus both water and oil flows are in the same direction. Countercurrent imbibition, on the other hand, is whereby a wetting phase imbibes into the porous matrix (rock), displacing the nonwetting phase out from one open boundary. In spite of the fact that cocurrent imbibition is faster and more efficient

than countercurrent imbibitions, the latter is often the only possible displacement mechanism for cases where a region of the matrix is exposed from one side to water filling the fracture [1–4]. Imbibition has also been investigated by several other authors either for cocurrent or countercurrent flows or both of them together (e.g., [5–8]). Reis and Cil [9] introduced one-dimensional model for oil expulsion by countercurrent water imbibition in rocks. An examination of countercurrent capillary imbibition recovery from single matrix blocks and recovery predictions by analytical matrix/fracture transfer functions was introduced by Cil et al. [10]. Lee and Kang [11] have introduced an experimental analysis of oil recovery in a fracture of variable aperture with countercurrent imbibition. Scaling of countercurrent imbibition was estimated by many authors in terms of fluid and rock properties (e.g., [12, 13]). Morrow and Mason [14] introduced a comprehensive review on recovery of oil by spontaneous imbibition. Kashchiev and Firoozabadi [15] gave analytical solutions for 1D countercurrent imbibition in water-wet media. Analytical analysis of oil recovery during countercurrent imbibition in strongly water-wet system was given by Tavassoli et al. [16]. The Barenblatt model of spontaneous countercurrent imbibition was investigated by Silin and Patzek [17]. Behbahani et al. [18] have performed a simulation of countercurrent imbibition in water-wet fractured reservoirs.

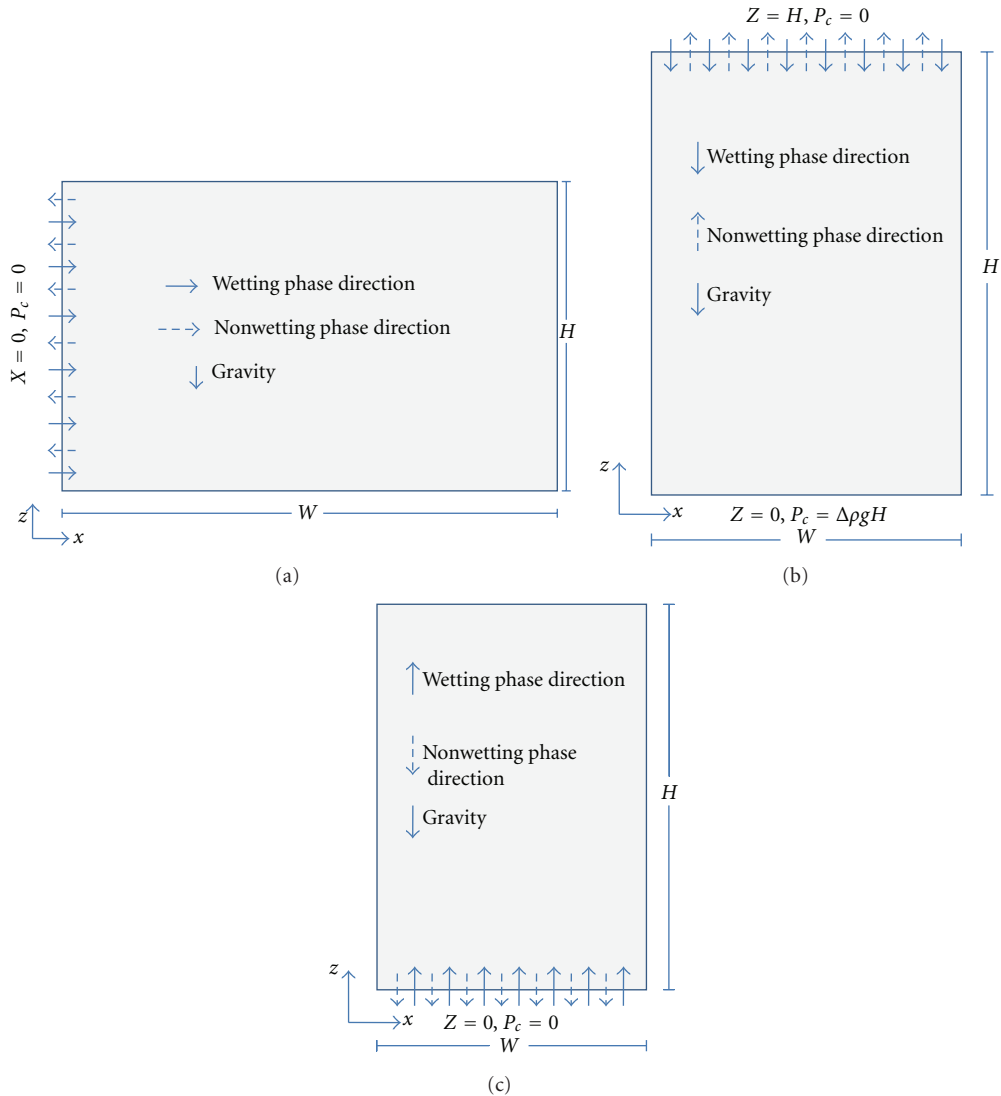


FIGURE 1: Schematic diagram of countercurrent imbibition with gravity effect for different locations of the open boundary: (a) side, (b) top, and (c) bottom.

In most of the previously mentioned imbibition studies, researchers have neglected the gravity force effect by dropping the gravity force term from the flow equations especially for the oil-water modeling. Wilkinson [19] studied the percolation model of immiscible displacement in the presence of buoyancy forces. Analytical and numerical solutions of gravity-imbibition and gravity-drainage processes were given by Bech et al. [20]. Tavassoli et al. [21] have introduced analysis of countercurrent imbibition with gravity in weakly water-wet system. A pore-scale study of gravity, capillary and viscous forces during drainage in a two-dimensional porous medium, was introduced by Løvoll et al. [22]. Effect of injection rate, initial water saturation, and gravity on water injection in slightly water-wet fractured porous media was examined experimentally by Karimaie and Torsæter [23]. Ruth et al. [24] provided an approximate analytical solution for countercurrent spontaneous imbibition. The problems of buoyancy-driven vertical migration of fluids have been

treated analytically or numerically by some researchers. For example, Silin et al. [25] have introduced simple analytical solutions in a model of gas flow driven by a combination of buoyancy, viscous and capillary forces for the problem of two-phase countercurrent fluid flow.

This study is devoted to numerically investigate the influences of gravity and open-boundary location on the countercurrent imbibition of two immiscible phases in a 2D porous medium domain.

2. Formulations, Results, and Discussion

The purpose of this study is to investigate the influence of gravity for different locations of the open boundary of an incompressible, two-phase, immiscible, countercurrent imbibition in a 2D homogenous porous medium domain. In this work both buoyancy and capillarity are considered. Figures 1(a), 1(b), and 1(c) show schematic diagrams of

the problem domain for different locations of the open boundary (side, top, and bottom). Wetting phase imbibes inwards in the porous medium domain of height H and width W with zero capillary pressure at the open boundary and no-flow boundary at the other boundaries.

Consider a rectangular core saturated with oil with irreducible water saturation, closed all around except at one face that is open to flow (countercurrent imbibition). The flow is governed by the combined Darcy law and the equations of mass conservation for each phase in 2D as follows:

$$\begin{aligned} \varphi \frac{dS_w}{dP_c} \left(\frac{\partial P_o}{\partial t} - \frac{\partial P_w}{\partial t} \right) &= \nabla \cdot \left(\frac{Kk_{rw}}{\mu_w} (\nabla P_w - \rho_w g \nabla z) \right), \\ \varphi \frac{dS_w}{dP_c} \left(\frac{\partial P_o}{\partial t} - \frac{\partial P_w}{\partial t} \right) &= -\nabla \cdot \left(\frac{Kk_{ro}}{\mu_o} (\nabla P_o - \rho_o g \nabla z) \right), \end{aligned} \quad (1)$$

where $\nabla \equiv (\partial/\partial x, \partial/\partial z)$, subscripts w and o designate wetting phase (water) and nonwetting phase (oil), respectively. P is the phase pressure, S_w is the water saturation, k_r is relative permeability, μ is phase viscosity, ρ is phase density, and g is gravity acceleration. K is permeability and φ is porosity of the porous medium.

The capillary pressure functions are dependent on the pore geometry, fluid physical properties, and phase saturations. The two-phase capillary pressure can be expressed by the Leverett dimensionless function $J(S)$; see, for example, Chen [26], which is a function of the normalized saturation S :

$$P_c = P_o - P_w = \gamma \left(\frac{\varphi}{K} \right)^{1/2} J(S), \quad (2)$$

where γ is the interfacial tension.

In order to consider a certain case of study, we may use a specified empirical formula of the capillary pressure in terms of normalized saturation function. The $J(S)$ function typically lies between two limiting (drainage and imbibition) curves which can be obtained experimentally. Correlation of the imbibition capillary pressure data depends on the type of application. Since our current research is concerned with the water-oil system, we use the correlation by Firoozabadi and coworkers [3, 15], in which the capillary pressure and the normalized wetting phase saturation are correlated as follows:

$$P_c = -B \ln S, \quad (3)$$

where B is the capillary pressure parameter, which is equivalent to $\gamma(\varphi/K)^{1/2}$ in (2); thus, $B \equiv -\gamma(\varphi/K)^{1/2}$ and $J(S) \equiv \ln S$. Note that $J(S)$ is a scalar nonnegative function.

Also,

$$S = \frac{S_w - S_{iw}}{1 - S_{or} - S_{iw}}, \quad 0 \leq S \leq 1, \quad (4)$$

where S_{iw} is the irreducible water saturation and S_{or} is the residual oil saturation.

For the countercurrent imbibition in which the only open end is initially in contact with oil, the ambient pressure

is considered zero. The water pressure in the core is given by the capillary pressure relationship, (2) and (3), which at $t = 0$ leads to

$$\begin{aligned} P_o &= 0, \quad t = 0, \quad 0 \leq x \leq W, \quad 0 \leq z \leq H, \\ P_w &= P_o - P_c(S_{wi}) = -P_c(S_{wi}), \\ t &= 0, \quad 0 \leq x \leq W, \quad 0 \leq z \leq H. \end{aligned} \quad (5)$$

In this study we consider three different locations of the open boundary, at side, top, or bottom, namely, Case A, Case B, and Case C, as follows.

Case A. Side open-boundary

$$\begin{aligned} P_w &= P_o = 0, \quad t > 0, \quad x = 0, \quad 0 \leq z \leq H, \\ q_w &= q_o = 0, \quad t > 0, \quad 0 \leq x \leq W, \quad z = 0, \\ q_w &= q_o = 0, \quad t > 0, \quad 0 \leq x \leq W, \quad z = H, \\ q_w &= q_o = 0, \quad t > 0, \quad x = W, \quad 0 \leq z \leq H, \end{aligned} \quad (6)$$

where q_w and q_o are the water and oil flow rate, respectively.

Case B. Top open-boundary:

$$\begin{aligned} q_w &= q_o = 0, \quad t > 0, \quad x = 0, \quad 0 \leq z \leq H, \\ q_w &= q_o = 0, \quad t > 0, \quad 0 \leq x \leq W, \quad z = 0, \\ P_w &= P_o = 0, \quad t > 0, \quad 0 \leq x \leq W, \quad z = H, \\ q_w &= q_o = 0, \quad t > 0, \quad x = W, \quad 0 \leq z \leq H. \end{aligned} \quad (7)$$

Case C. Bottom open-boundary

$$\begin{aligned} q_w &= q_o = 0, \quad t > 0, \quad x = 0, \quad 0 \leq z \leq H, \\ P_w &= P_o = 0, \quad t > 0, \quad 0 \leq x \leq W, \quad z = 0, \\ q_w &= q_o = 0, \quad t > 0, \quad 0 \leq x \leq W, \quad z = H, \\ q_w &= q_o = 0, \quad t > 0, \quad x = W, \quad 0 \leq z \leq H. \end{aligned} \quad (8)$$

Case A represents a domain of size (0.2, 0.2) m which is meshed by 10439 nodes and 19968 triangle elements, corresponding to more than 81690 DOF (quadratic Lagrange elements), while Cases B and C are meshed by 10591 nodes and 20272 triangle elements, corresponding to more than 82906 DOF (quadratic Lagrange elements). All computations have been performed using the commercial software COMSOL version 3.5a with the direct solver UMFPACK and were running on multi(7)-core workstation using SMP mode of parallel computation. Figures 2(a) and 2(b) show mesh distributions for Case A and Cases B and C, respectively, with fine mesh on the inlet side and the opposite side.

The simulation was running for imbibition time of 40 days so that it may be compared with the study of Pooladi-Darvish and Firoozabadi [3]. We use the same values of physical properties used by Pooladi-Darvish and Firoozabadi [3] as given in Table 1. Figure 3 shows distributions of water saturation and velocity vectors of the case of incorporating

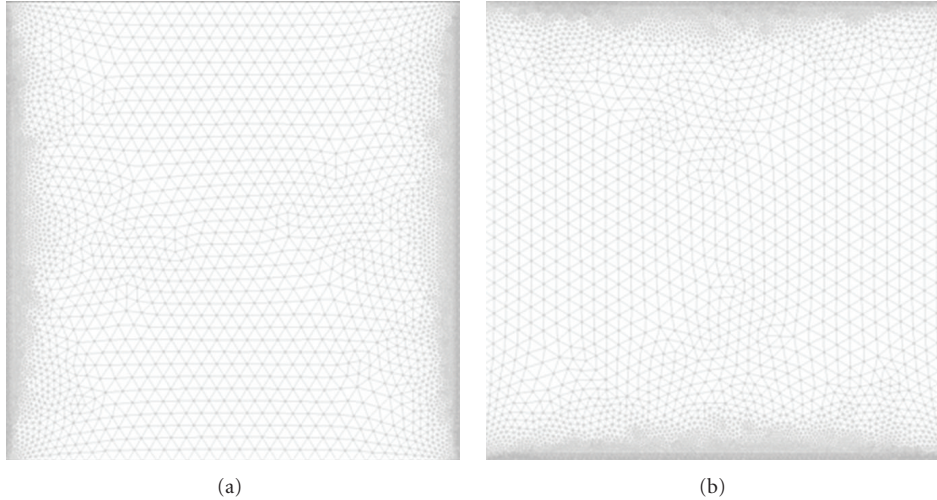


FIGURE 2: (a) Mesh distributions for the 2D dimensional Cases A. (b) Mesh distributions for the 2D dimensional Cases B and C

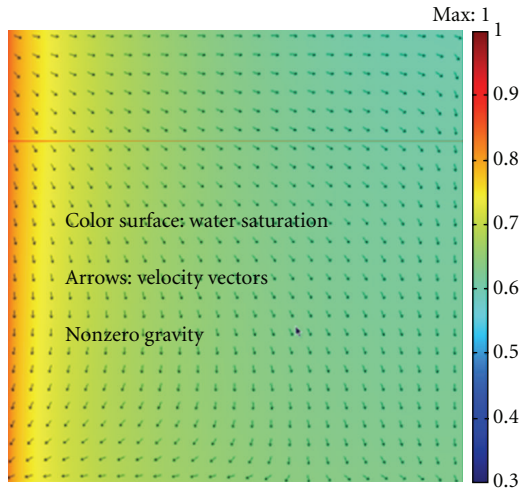


FIGURE 3: Distributions of water saturation and velocity vectors of nonzero gravity of Case A, at time imbibition of 40 days.

gravity in the flow equations. The zero-gravity case may be matched well by 1D simulation, while the opposite is true for the case of nonzero gravity which shows a nonuniform distribution of water velocity as shown in Figure 3. Additionally, a comparison between considering and neglecting gravity effect on water saturation against x -axis of Case A is plotted in Figure 4. It can be seen from this figure that considering the gravity term in the flow equations results in a slight increase in water saturation. Also, from the same figure we may note that the saturation profiles are comparable to the 1D case as shown by Pooladi-Darvish and Firoozabadi [3]. Comparison between considering and neglecting gravity effect on water and oil pressure against distance with considering gravity effect of Case A is plotted in Figure 5. From this figure, one may note that water and oil pressure vary downstream of the saturation front with time and location. Also, it can be seen that oil pressure reaches the

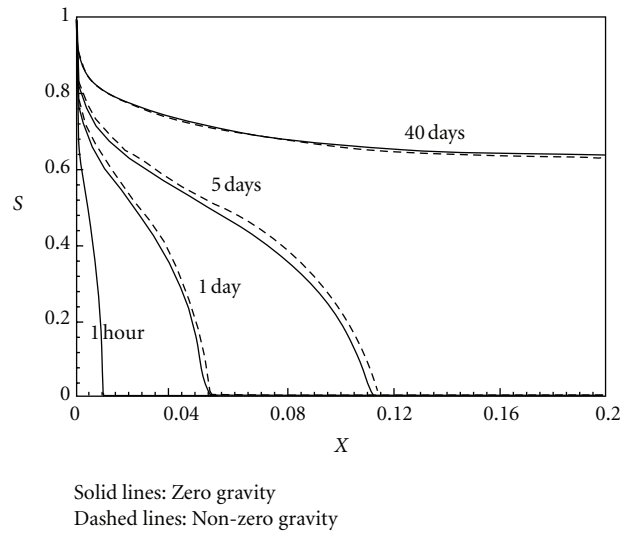


FIGURE 4: Comparison between considering and neglecting gravity effect on water saturation against x -axis of Case A, at $z = 0.15$ m.

TABLE 1: Primary parameters from Pooladi-Darvish and Firoozabadi [3].

a	b	B	K	k_{ro}^0	k_{rw}^0	L	S_{wi}	φ	$\mu_{w,o}$
4	4	10 kPa	$0.02 \mu\text{m}$	0.75	0.2	0.2 m	0.001	0.3	1 mPa

maximum in the two-phase region. It is interesting to note that gravity has a slight effect on water and oil pressures.

Figure 6 shows a comparison between considering and neglecting gravity effect on water x -velocity profiles against the horizontal distance for Case A. This figure indicates that at the beginning of the imbibition time the velocity is higher while after longer time of imbibition the velocity slows down as water imbibes inside the matrix. This may be interpreted based on the fact that the flow in this system is dominated by capillarity which reduces with the increase in saturation.

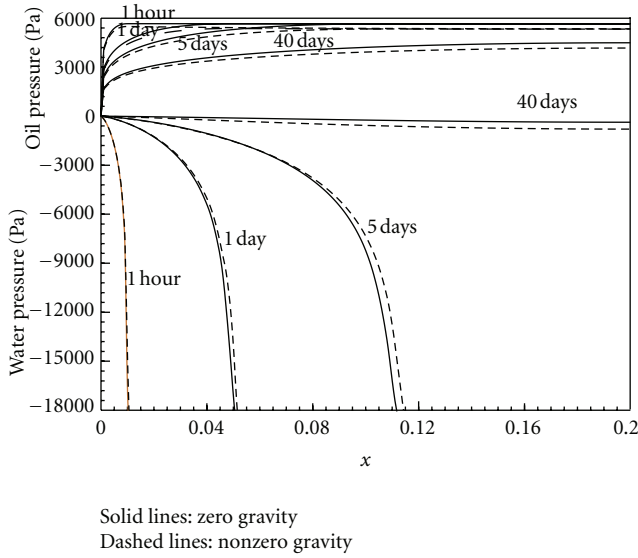


FIGURE 5: Comparison between considering and neglecting gravity effect on water and oil pressure against x -axis of Case A, at $z = 0.15$ m.

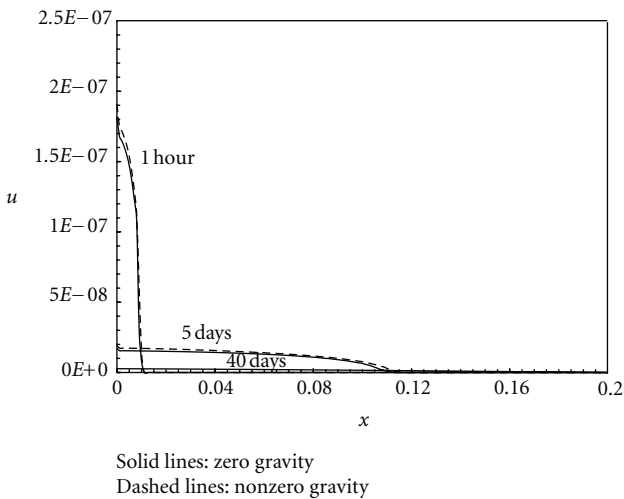


FIGURE 6: Comparison between considering and neglecting gravity effect on water x -velocity against x -axis of Case A, at $z = 0.15$ m.

In this figure, it is apparent that gravity has, generally, slight effect at early time of imbibition. However, this effect is seen to be more pronounced at later time of imbibition (e.g., after 40 days).

A comparison between considering and neglecting gravity effect on water saturation against z -axis for Case B is plotted in Figure 7. It is obvious that in the case of considering gravity the water saturation is slightly higher than that without gravity particularly after longer period of time (e.g., after 40 days of imbibition). A comparison between considering and neglecting gravity effect on water and oil pressure against z -axis of Case B is plotted in Figure 8. It is interesting to note that, for this case, both water and oil pressures are assisted by the gravity force.

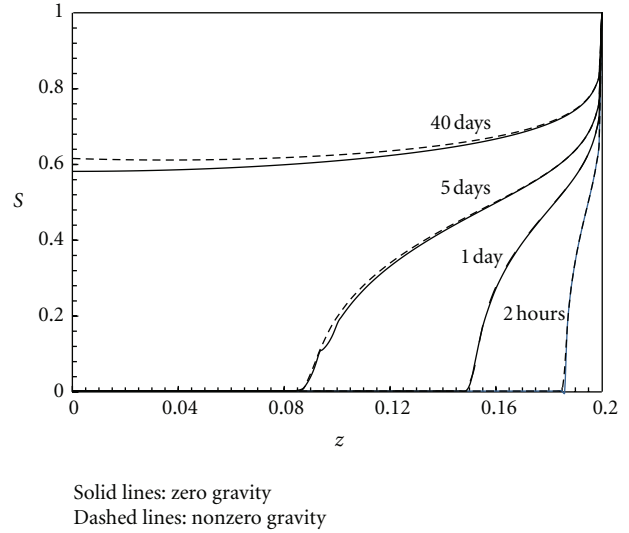


FIGURE 7: Comparison between considering and neglecting gravity effect on water saturation against z -axis of Case B, at $x = 0.15$ m.

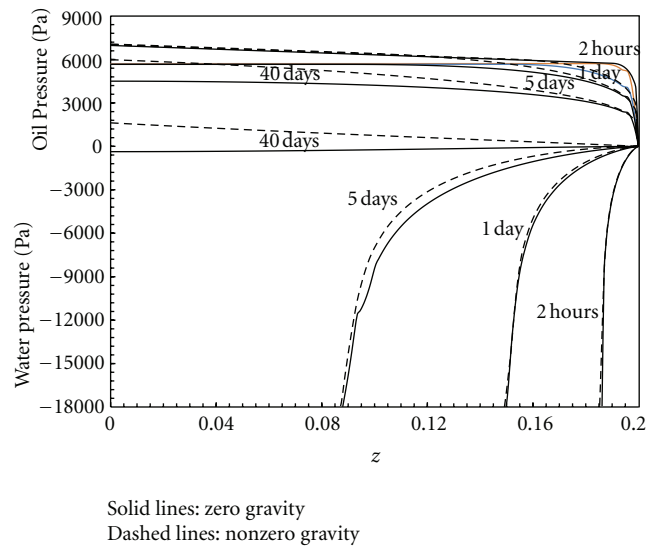


FIGURE 8: Comparison between considering and neglecting gravity effect on water and oil pressure against z -axis of Case B, at $x = 0.15$ m.

Figure 9 shows a comparison between considering and neglecting gravity effect on water saturation against z -axis of Case C. It can be seen from Figure 9 that considering the gravity force in the flow equations reduces water saturation. In this case the gravity works in the opposite direction of the water flow so it resists water imbibition. Also, considering the gravity force reduces both water and oil pressures as illustrated in Figure 10.

3. Conclusions

The aim of this work is to examine the influence of gravity on countercurrent imbibition of two-phase flow in porous

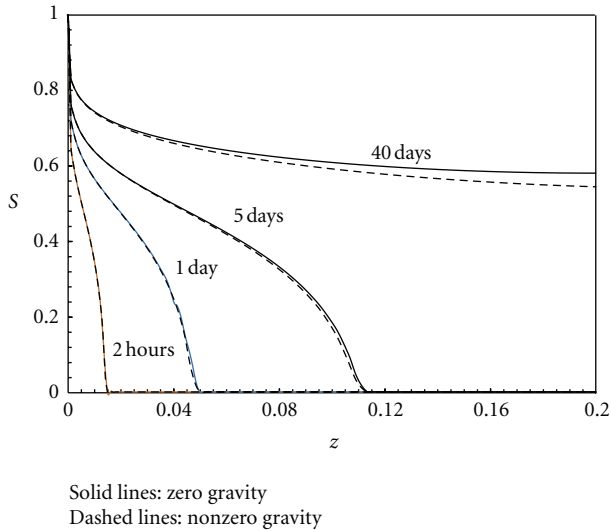


FIGURE 9: Comparison between considering and neglecting gravity effect on water saturation against z -axis of Case C, at $x = 0.15$ m.

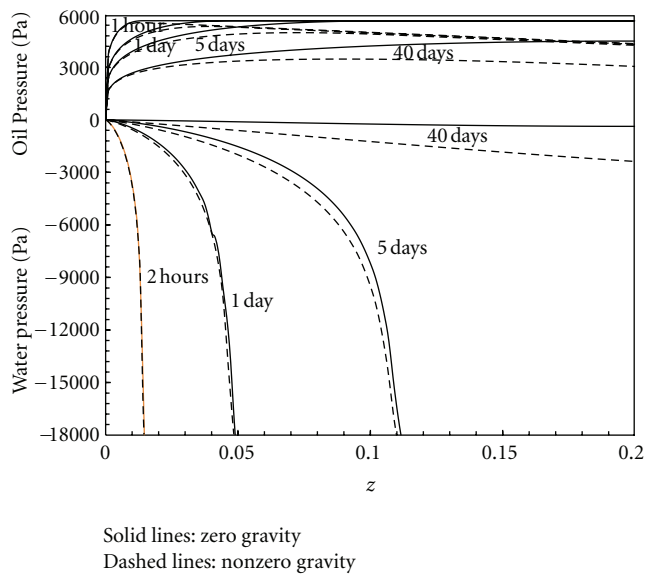


FIGURE 10: Comparison between considering and neglecting gravity effect on water and oil pressure against z -axis of Case C, at $x = 0.15$ m.

media for different locations of the open boundary. A 2D simulation for three different locations of the open boundary (side, top, and bottom) is considered. A comparable study of considering and neglecting gravity in the model is done for the three different open-boundary locations. From this work one may conclude that the bottom open-boundary reduces the water imbibition in the rock matrix and therefore decreases the oil recovery, while the opposite is true for both top and side open-boundary. The results indicate that the buoyancy effects due to gravity force take place depending on the location of the open boundary.

Acknowledgment

The work was supported by the KAUST-UT Austin AEA Project (ID 7000000058).

References

- [1] B. J. Bourblaux and F. J. Kalaydjian, "Experimental study of cocurrent and countercurrent flows in natural porous media," *SPE Reservoir Engineering*, vol. 5, no. 3, pp. 361–368, 1990.
- [2] M. E. Chimienti, S. N. Illiano, and H. L. Najurieta, "Influence of temperature and interfacial tension on spontaneous imbibition process," in *Proceedings of the Latin American and Caribbean Petroleum Engineering Conference*, vol. 53668, SPE, Caracas, Venezuela, 1999.
- [3] M. Pooladi-Darvish and A. Firoozabadi, "Cocurrent and countercurrent imbibition in a water-wet matrix block," *SPE Journal*, vol. 5, no. 1, pp. 3–11, 2000.
- [4] H. L. Najurieta, N. Galacho, M. E. Chimienti, and S. N. Illiano, "Effects of temperature and interfacial tension in different production mechanisms," in *Proceedings of the Latin American and Caribbean Petroleum Engineering Conference*, vol. 69398, Buenos Aires, Argentina, 2001.
- [5] R. W. Parsons and P. R. Chaney, "Imbibition model studies on water-wet carbonate rocks," *SPE Journal*, pp. 26–34, 1996.
- [6] R. Iffly, D. C. Rousselet, and J. L. Vermeulen, "Fundamental study of imbibition in fissured oil fields," in *Proceedings of the Annual Technical Conference*, vol. 4102, SPE, Dallas, Tex, USA, 1972.
- [7] G. Hamon and J. Vidal, "Scaling-up the capillary imbibition process from laboratory experiments on homogeneous samples," in *Proceedings of the European Petroleum Conference*, vol. 15852, SPE, London, UK, October 1986.
- [8] S. Al-Lawati and S. Saleh, "Oil recovery in fractured oil reservoirs by low IFT imbibition process," in *Proceedings of the Annual Technical Conference and Exhibition*, vol. 36688, SPE, Denver, Colo, USA, 1996.
- [9] J. C. Reis and M. Cil, "A model for oil expulsion by counter-current water imbibition in rocks: one-dimensional geometry," *Journal of Petroleum Science and Engineering*, vol. 10, no. 2, pp. 97–107, 1993.
- [10] M. Cil, J. C. Reis, M. A. Miller, and D. Misra, "An examination of countercurrent capillary imbibition recovery from single matrix-blocks and recovery predictions by analytical matrix/fracture transfer functions," in *Proceedings of the Annual Technical Conference and Exhibition*, vol. 49005, SPE, New Orleans, La, USA, September 1998.
- [11] J. Lee and J. M. Kang, "Oil recovery in a fracture of variable aperture with countercurrent imbibition: experimental Analysis," in *Proceedings of the Annual Technical Conference and Exhibition*, vol. 56416, Houston, Tex, USA, October 1999.
- [12] T. Babadagli, "Scaling of cocurrent and countercurrent capillary imbibition for surfactant and polymer injection in naturally fractured reservoirs," *SPE Journal*, vol. 6, no. 4, pp. 465–478, 2001.
- [13] D. Zhou, L. Jia, J. Kamath, and A. R. Kovscek, "Scaling of counter-current imbibition processes in low-permeability porous media," *Journal of Petroleum Science and Engineering*, vol. 33, no. 1–3, pp. 61–74, 2002.
- [14] N. R. Morrow and G. Mason, "Recovery of oil by spontaneous imbibition," *Current Opinion in Colloid and Interface Science*, vol. 6, no. 4, pp. 321–337, 2001.

- [15] D. Kashchiev and A. Firoozabadi, "Analytic solutions for 1D countercurrent imbibition in water-wet media," *SPE Journal*, vol. 8, no. 4, pp. 401–408, 2003.
- [16] Z. Tavassoli, R. W. Zimmerman, and M. J. Blunt, "Analytic analysis for oil recovery during counter-current imbibition in strongly water-wet systems," *Transport in Porous Media*, vol. 58, no. 1-2, pp. 173–189, 2005.
- [17] D. Silin and T. Patzek, "On Barenblatt's model of spontaneous countercurrent imbibition," *Transport in Porous Media*, vol. 54, no. 3, pp. 297–322, 2004.
- [18] H. S. Behbahani, G. Di Donato, and M. J. Blunt, "Simulation of counter-current imbibition in water-wet fractured reservoirs," *Journal of Petroleum Science and Engineering*, vol. 50, no. 1, pp. 21–39, 2006.
- [19] D. Wilkinson, "Percolation model of immiscible displacement in the presence of buoyancy forces," *Physical Review A*, vol. 30, no. 1, pp. 520–531, 1984.
- [20] N. Bech, O. K. Jensen, and B. Nielsen, "Modeling of gravity-imbibition and gravity-drainage processes: analytic and numerical solutions," *SPE Reservoir Engineering*, vol. 6, no. 1, pp. 129–136, 1991.
- [21] Z. Tavassoli, R. W. Zimmerman, and M. J. Blunt, "Analysis of counter-current imbibition with gravity in weakly water-wet systems," *Journal of Petroleum Science and Engineering*, vol. 48, no. 1-2, pp. 94–104, 2005.
- [22] G. Løvoll, Y. Méheust, K. J. Måløy, E. Aker, and J. Schmittbuhl, "Competition of gravity, capillary and viscous forces during drainage in a two-dimensional porous medium, a pore scale study," *Energy*, vol. 30, no. 6, pp. 861–872, 2005.
- [23] H. Karimaie and O. Torsæter, "Effect of injection rate, initial water saturation and gravity on water injection in slightly water-wet fractured porous media," *Journal of Petroleum Science and Engineering*, vol. 58, no. 1-2, pp. 293–308, 2007.
- [24] D. W. Ruth, Y. Li, G. Mason, and N. R. Morrow, "An approximate analytical solution for counter-current spontaneous imbibition," *Transport in Porous Media*, vol. 66, no. 3, pp. 373–390, 2007.
- [25] D. Silin, T. Patzek, and S. M. Benson, "A model of buoyancy-driven two-phase countercurrent fluid flow," *Transport in Porous Media*, vol. 76, no. 3, pp. 449–469, 2009.
- [26] Z. Chen, *Reservoir Simulation: Mathematical Techniques in Oil Recovery*, SIAM, Philadelphia, Pa, USA, 2007.

Research Article

Numerical Simulation of LVAD Inflow Cannulas with Different Tip

Guang-Mao Liu,¹ Hai-Bo Chen,¹ Fu-Liang Luo,² Yan Zhang,² Han-Song Sun,²
Jian-Ye Zhou,¹ and Sheng-Shou Hu¹

¹ Key Laboratory of Cardiovascular Regenerative Medicine, Ministry of Health, State Key Laboratory of Cardiovascular Disease, Fuwai Hospital, National Center for Cardiovascular Diseases, Chinese Academy of Medical Sciences and Peking Union Medical College, Beijing 100037, China

² Cardiovascular Surgery, State Key Laboratory of Cardiovascular Disease, Fuwai Hospital, National Center for Cardiovascular Diseases, Chinese Academy of Medical Sciences and Peking Union Medical College, Beijing 100037, China

Correspondence should be addressed to Jian-Ye Zhou, jianyehou@yahoo.com

Received 23 December 2011; Accepted 29 February 2012

Academic Editor: Mandar Tabib

Copyright © 2012 Guang-Mao Liu et al. This is an open access article distributed under the Creative Commons Attribution License, which permits unrestricted use, distribution, and reproduction in any medium, provided the original work is properly cited.

The tip structure of LVAD inflow cannula is one of major factors to lead adverse events such as thrombosis and suction leading to obstruction. In this research, four kinds of tips that had been used in inflow cannulas were selected and designed. The flow field of the four inflow cannulas inserted into the apex of left ventricle (LV) was numerically computed by computational fluid dynamics. The flow behavior was analyzed in order to compare the blood compatibility and suction in left ventricle and cannulas after the inflow cannulas with different tips were inserted to the apex of LV. The results showed that the cannula tip structure affected the LVAD performance. Among these four cannulas, the trumpet-tipped inflow cannula owned the best performance in smooth flow velocity distribution without backflow or low-velocity flow so that it was the best in blood compatibility. Nevertheless, the caged tipped cannula was the worst in blood compatibility. And the blunt-tipped and beveled tipped inflow cannulas may obstruct more easily than trumpet and caged tipped inflow cannulas because of their shape. The study indicated that the trumpet tip was the most preferable for the inflow cannula of long-term LVAD.

1. Introduction

LVADs have been widely applied to assist the circulation of heart failure (HF) patients. Some LVADs can prolong HF patients' lives for more than two years [1–5]. Now, most LVADs are equipped with complete accessories such as designed inflow and outflow cannulas to ensure that the LVADs can work safely and longer. The inflow cannula is the connection between left ventricle and LVAD. The inflow cannulas are mainly made of good blood compatibility materials such as titanium alloy, silicon rubber, or polythene. The shapes of inflow cannulas include blunt, beveled, caged, trumpet, and beak [6]. For example, the inflow cannula of Berlin Heart INCOR is made of silicon rubber with beak-shaped tip [7, 8]. And the inflow cannula of DeBakey LVAD is made of titanium alloy with trumpet shaped tip [9, 10].

The tip shape is a critical factor to fluid dynamic performance. The flow field and stress distribution in left ventricle and cannulas depend on the inflow cannulas tip structure at a certain flow rate and operative procedures such as insertion depth and insertion angle. Different tip structures of inflow cannulas can cause various degree of thrombosis and suction leading to obstruction that may further influence the LVAD's service life and the survival of the patients [11, 12]. Thrombosis is mainly caused by static and/or vortical flow in the inflow cannulas.

Mechanical hemolysis is another important aspect of the inflow cannulas. The hemolysis in the inflow cannulas is mainly caused by the high shear stress of flow in the inflow cannulas. The effective numerical prediction of mechanical hemolysis has been built [13–15]. In vitro and in vivo mechanical hemolysis tests have been studied previously [16–18].

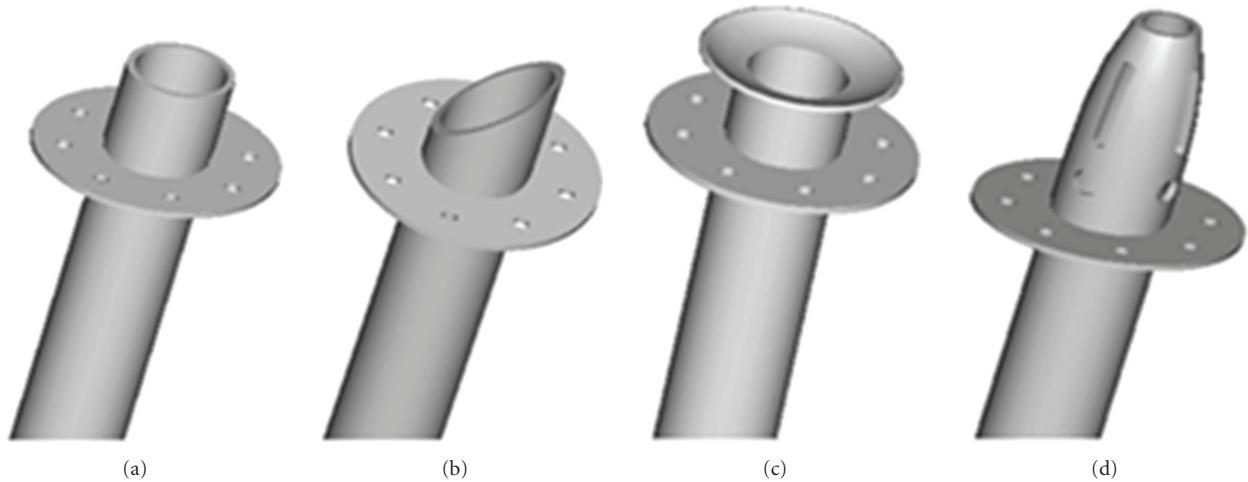


FIGURE 1: 3D model of inflow cannula tip: (a) blunt, (b) beveled, (c) trumpet, and (d) caged.

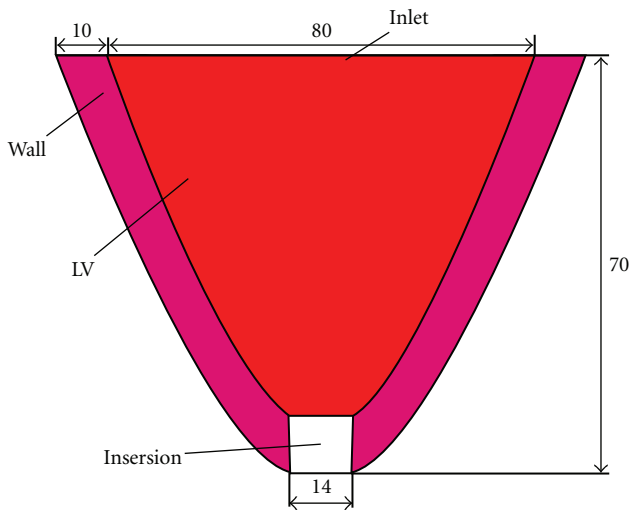


FIGURE 2: LV geometry model used to compare the inflow cannula tip.

To obtain a good performance in blood compatibility, the tip shape is the crucial factor to reduce static and vortical flow area in an inflow cannula design. The objective of this paper is to find which kind of tip shape is better for LVAD inflow cannula. The fluid dynamics of the inflow cannula are studied with numerical simulation or test in a mock loop model. Numerical simulation can simulate and analyze the flow velocity, stress distribution, and wall shear stress of cannula insertion [19, 20]. In this paper, we built the numerical model of blunt, beveled, caged, and trumpet-tipped cannulas inserted into left ventricle, respectively. The velocity distribution and stress distribution around the cannula tips and in cannulas were calculated. The blood compatibility and risk of suction leading to obstruction [21] of the four insertions were compared. The analysis results can help us select tip shape and design an inflow cannula which is suitable for long-term LVAD.

2. Materials and Methods

2.1. Geometry Model. Figure 1 illustrated the 3D model of four kinds of inflow cannulas with different tip shapes built by Pro-E software. The cannulas were made of titanium alloy. The four cannulas were assumed to be in the same size where the inner diameter was $d = 12$ mm, and the wall thickness was $s = 1$ mm. And they were considered as straight pipes to eliminate effects of curved portion. The cannulas' length out of ventricle is $l = 46$ mm.

Figure 2 showed the geometry model of LV for calculation. According to Fraser et al. and Tsukiya et al. [19, 22], the geometry of the left ventricle was simplified without regarding the heart real geometry, insertion depth, and insertion angle. The insertion point was assumed the apex of left ventricle. The inlet surface diameter of LV was set to 80 mm. The LV wall thickness was 10 mm and uniform. The depth from the inlet surface to the apex was 70 mm.

2.2. Computational Model. Four computational models of cannula inserted into LV were built by computational fluid dynamics software Workbench (ANSYS, Inc, Canonsburg, Pennsylvania, United States) according to the geometry models in Figures 1 and 2. Figure 3 demonstrated the typical unstructured computational grid for the four inflow cannulas. We adopted unstructured numeric grid. Furthermore, blood was assumed to be Newtonian with density of $\rho = 1059$ kg/m³ and viscosity of $\mu = 0.0035$ kg/m·s. The average flow rate was set to $Q = 5$ L/min. Thus the inlet mass flow was 0.0088 kg/s. The static outlet pressure was set to 0 Mpa. The LV wall and cannula wall were considered to be stiffness boundary and immobile. The fluid-structure interaction simulation was complicated, so the interaction was not involved in this study [19, 20, 22].

The Reynolds number was used as the index to estimate the flow to be laminar or turbulent. When the index is greater

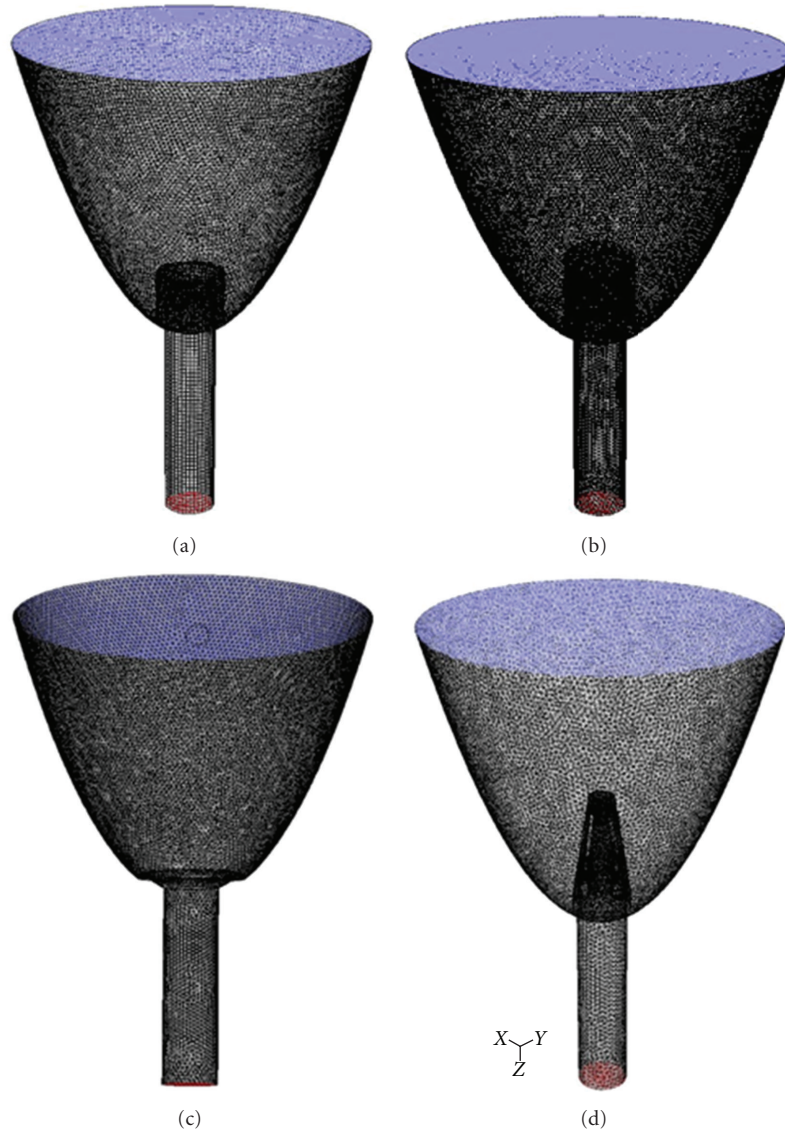


FIGURE 3: Numerical models of inflow cannulas insertion: (a) blunt, (b) beveled, (c) trumpet, and (d) caged.

than the critical Reynolds number, the flow is regarded as turbulent. The Reynolds number definition is

$$\text{Re} = \frac{VL}{\nu}, \quad (1)$$

where V is the mean velocity of the section (m/s), L is the characteristic length (m), and ν is fluid dynamic viscosity (m^2/s). For circular tube flow, the circular tube diameter d is the characteristic length L . The Reynolds number of inflow cannula blood flow is

$$\begin{aligned} \text{Re} &= \frac{VL}{\nu} = \frac{Q/(60 * 1000 * \pi(d/2000)^2) \cdot d/1000}{\mu/\rho} \\ &= \frac{Q\rho}{15\pi\mu d} = 2658. \end{aligned} \quad (2)$$

It is generally acknowledged that the critical Reynolds number of tube flow is 2320 [23]. So the flow in inflow cannula was turbulent flow. Therefore, $K-\varepsilon$ standard turbulence model was employed in numerical computation. The computational grid was generated by Workbench Fluent software. The unstructured numeric grid was generated from cannula surface.

3. Results

3.1. Velocity Distribution. Figure 4 showed velocity contour from inflow cannulas tip to outlet of four insertions. The flow velocity altered around the cannula tips and in cannulas. The flow velocity in ventricle was well distributed in the model of blunt and trumpet-tipped cannula. The maximal flow velocity was lower than 1 m/s. The velocity distribution was uniform and symmetrical along the z -axis after the blood flowed

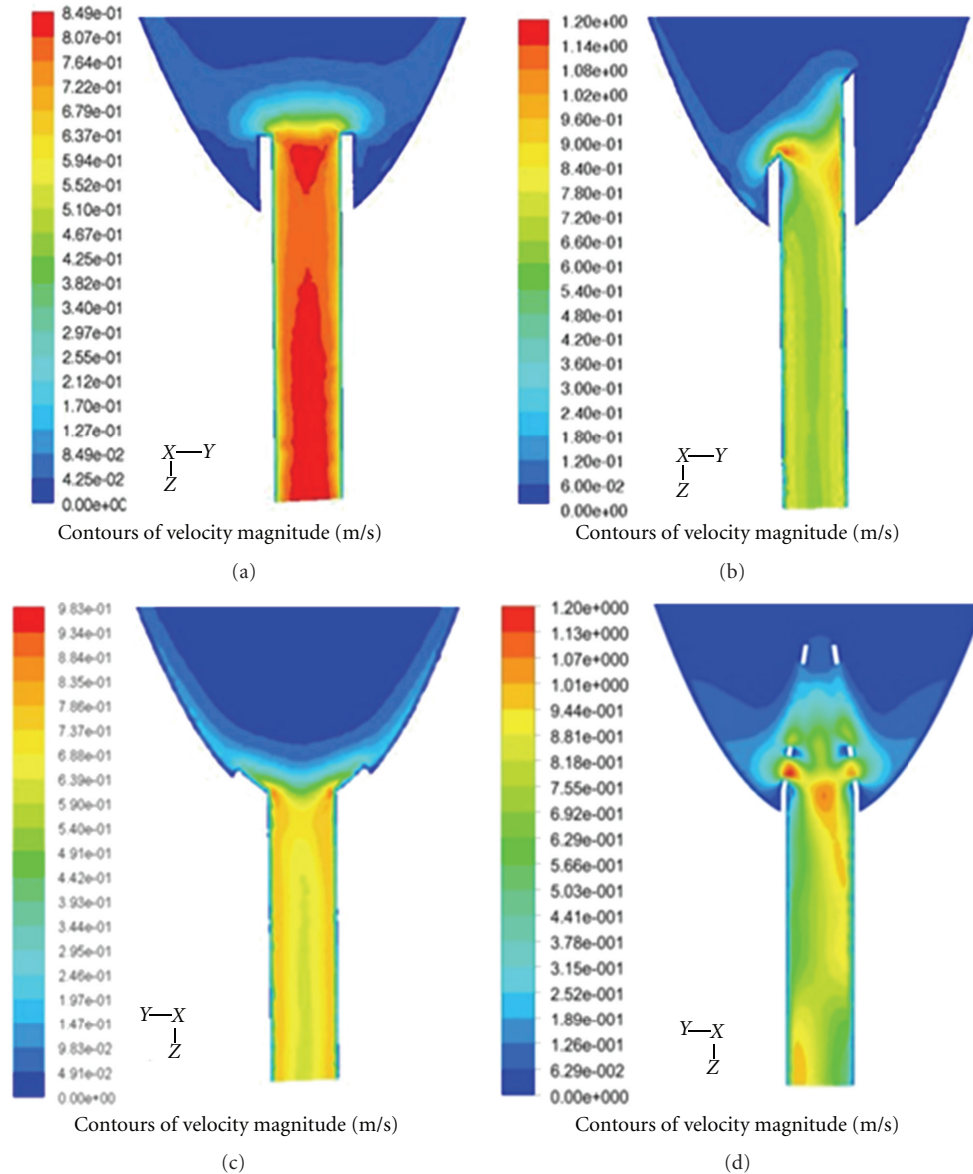


FIGURE 4: Velocity contour from tip to outlet: (a) blunt, (b) beveled, (c) trumpet, and (d) caged.

into the cannulas (Figures 4(a) and 4(c)). The uniform distribution velocity in cannulas could improve the flow field in LVADs because the blood flows into LVAD from inflow cannulas directly. That meant the blood compatibility of LVADs was advanced. The beveled and caged tips disturbed the flow in left ventricle. The maximal flow velocity reached to 1.2 m/s. The velocity distribution was not even or symmetrical along the z-axis in the cannulas flow (Figures 4(b) and 4(d)). The uneven velocity distribution in these two cannulas adversely effected flow in LVAD.

Figure 5 showed velocity vectors around inflow cannulas tips. There was obvious vortex region between the blunt-tipped cannula outer wall and ventricular inner wall near the insertion point (Figure 5 (a)). The flow velocity in the region was slower than 0.1 m/s. So this area could be potential of thrombosis. Nevertheless, the area in blunt-tipped cannula

was not likely to form thrombus because the flow in it was smooth. There were six obvious vortex regions near the caged tip (Figure 5(b)). Four of the six vortex regions were in caged tipped cannula and the minimum velocity was lower than 0.07 m/s. Additionally, turbulent flow was obvious near the inlet holes areas. Therefore these regions were likely to form clot. Figure 5(c) showed the velocity vector of beveled tipped inflow cannula. There were two vortex regions near insertion. One region was in left ventricle, and the other was in beveled tipped cannula. Both of these two regions were likely to form clot because the velocity was lower than 0.08 m/s. There was not vortex or flow stasis field in the trumpet tipped cannula (Figure 5(d)). The even velocity was 0.7 m/s and well distributed. Thus trumpet-tipped cannula had good blood compatibility and was not likely to form thrombosis.

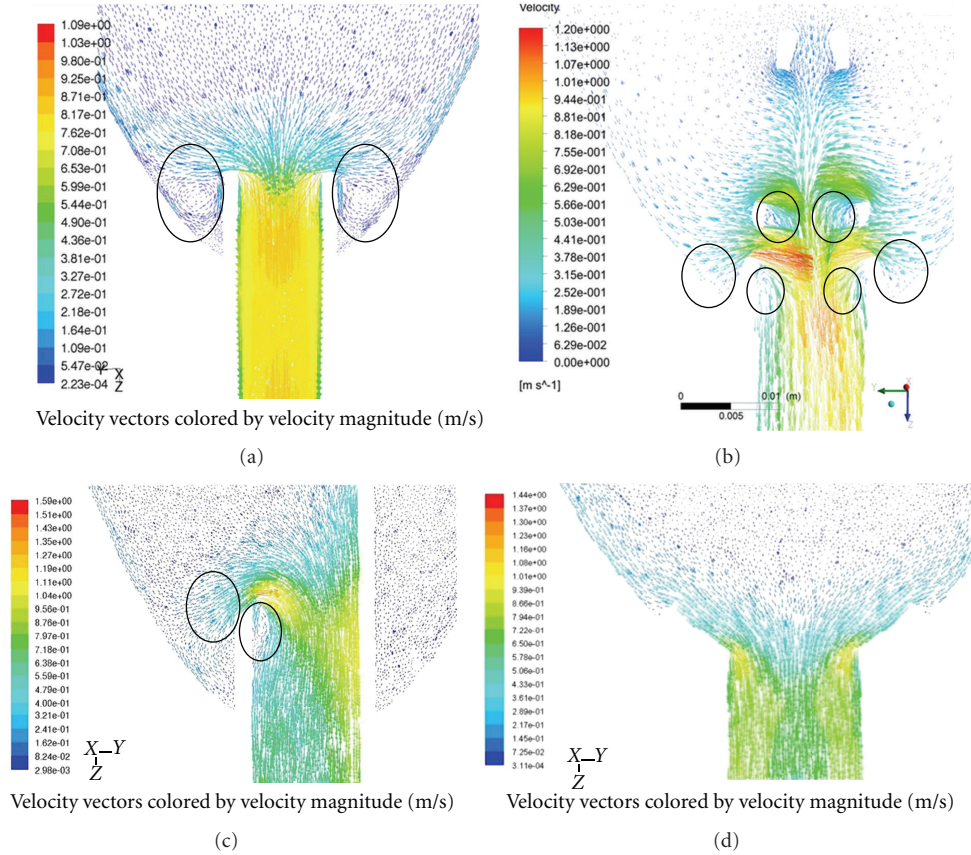


FIGURE 5: Velocity vector near tip: (a) blunt, (b) caged, (c) beveled, and (d) trumpet.

3.2. Static Pressure Distribution. Ventricular collapse and suction may occur when negative or low-pressure fields appeared. Furthermore, obstruction may happen if the tip could not resist the suction. Figure 6 showed static pressure distribution of four inflow cannulas insertion. The blunt tipped cannula did not create low-pressure field near the ventricular inner wall (Figure 6(a)). The beveled tipped cannula created one low-pressure field near the inflow bevel which was likely to ventricular collapsing (Figure 6(b)). The trumpet-tipped cannula had uniform low-pressure distribution around inlet (Figure 6(c)) which may cause ventricular collapse. Nevertheless, obstruction may not happen because the trumpet structure can resist suction. The caged tipped cannula created serious low-pressure field near inlet holes (Figure 6(d)). Ventricular collapse and suction were likely to occur. But the inlet could not be obstructed completely because not all the nine inlet holes could be obstructed at the same time.

3.3. Wall Shear Stress Distribution. Shear stress distribution was analyzed to evaluate hemolytic potential. Hemolysis is related to wall shear stress (WSS) value and blood exposure time [13–15, 24–26]. The computational fluid dynamics model with Eulerian formulation to estimate hemolysis in prosthesis device had been studied by Lacasse et al. [13], Song et al. [14], and Arvand et al. [15].

We estimated the damage to red cells with (3) [14]:

$$D = \int_{\text{outlet}}^{\text{inlet}} 1.8 \times 10^{-6} \cdot \tau^{1.991} \cdot dT^{0.765} \quad (3)$$

$$= \sum_{\text{outlet}}^{\text{inlet}} 1.8 \times 10^{-6} \cdot \tau^{1.991} \cdot \Delta T^{0.765},$$

where D symbolizes the blood damage index, τ is shear stress (Pa), and T is blood exposure time (s). The particle displacement is calculated using forward Euler integration of the particle velocity over time step (δt) as (4):

$$x_i^n = x_i^o + \frac{dx_i^o}{dt} \delta t, \quad (4)$$

where x denotes the displacement and the superscripts o and n refer to old and new values, respectively.

The blood damage index of the four inflow cannulas was shown in Figure 7. The estimation value of blood damage was between $5 \times 10^{-5}\%$ to $20 \times 10^{-5}\%$. The acceptable estimation value of blood damage for LVAD was $10^{-3}\%$ [27, 28]. So the blood damage in inflow cannula was negligible. The shear stress in inflow cannula was not able to cause hemolysis.

3.4. Limitations. This study eliminated the factors of real ventricle geometry, insertion depth, and insertion angle. But

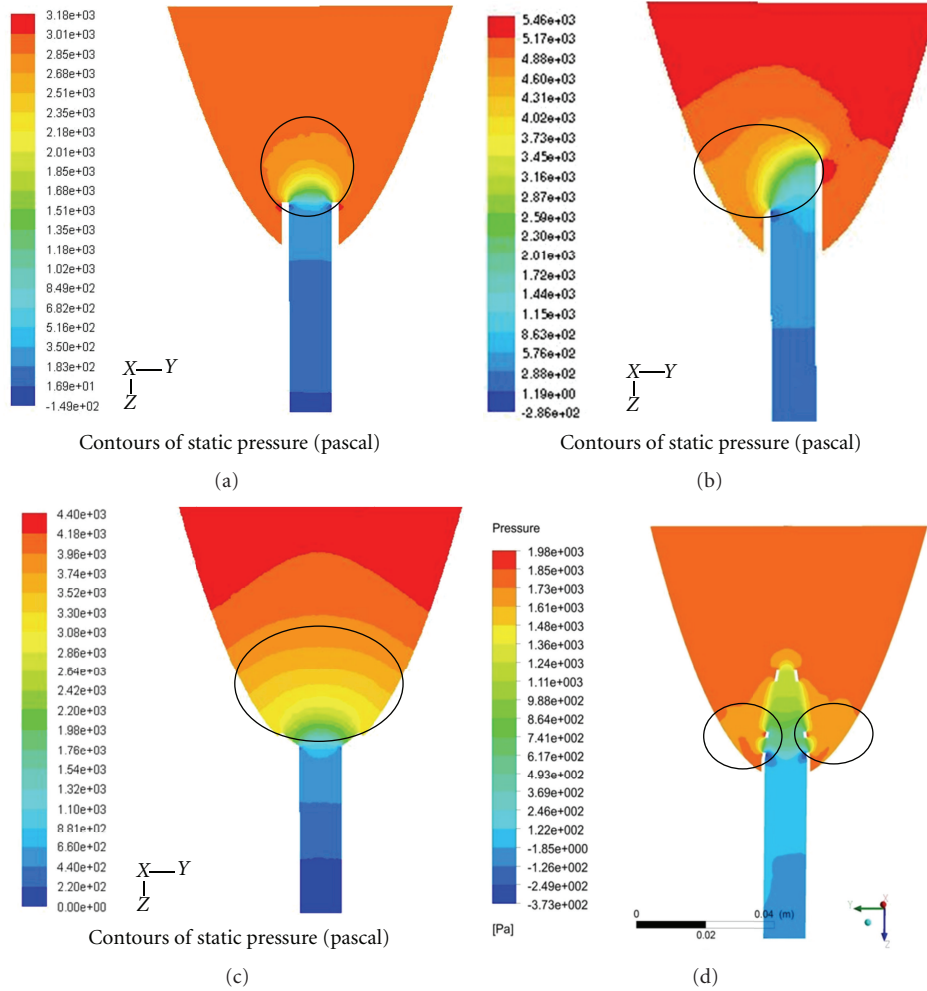


FIGURE 6: Contour of static pressure: (a) blunt, (b) beveled, (c) trumpet, and (d) caged.

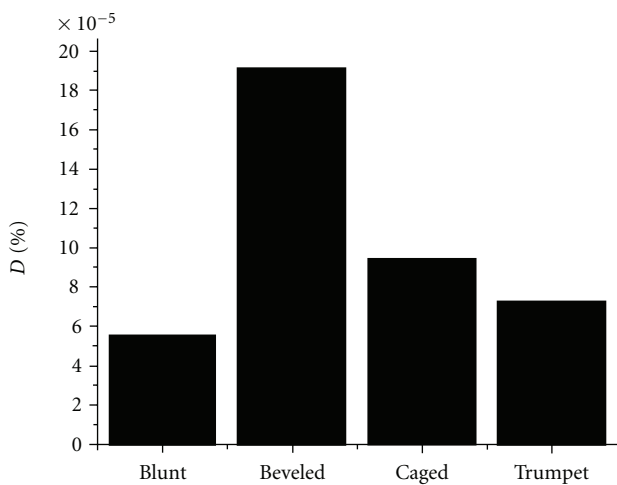


FIGURE 7: Blood damage index of inflow cannula.

actually, these factors may change the flow distribution in LV and inflow cannula and eventually cause the suction, and

obstruction. So the effect of insertion depth and angle on thrombosis potential, suction and obstruction should be further studied in the future.

The other limitation in this study is the simplified boundary conditions with rigid cavity and uniform flow inlet assumption. In reality, the flow in LV is much more complicated. The flow and pressure in ventricle change all the time with the beating. As the purpose of this study is to compare the tip shapes of the inflow cannulas, we think that the simplified boundary conditions are acceptable. Of course, the final outcome should be verified in animal test. And based on the results, profound study with more exact conditions is need in the future.

4. Conclusions

Despite the limitation, trumpet tip structure had the best effect on blood compatibility and was hard to generate suction. So trumpet-tipped inflow cannula was the best inflow cannula for LVAD. The caged tip structure had the worst impact on blood compatibility. The thrombosis potential of caged tipped cannula for long-term use was substantial.

Acknowledgments

This paper was supported by grants from National High-tech R&D Program of China (863 Program) (no. 2006AA-02Z4D3) and from state-level public service research institutes fund of basic research (2010-F08). The authors appreciated Mr. Lian-Hua Ma, from College of Mechanical Engineering and Applied Electronics Technology of Beijing University of Technology, for his great help in numerical calculation.

References

- [1] E. A. Rose, A. C. Gelijns, A. J. Moskowitz et al., "Long-term use of a left ventricular assist device for end-stage heart failure," *The New England Journal of Medicine*, vol. 345, no. 20, pp. 1435–1443, 2001.
- [2] M. C. Deng, L. B. Edwards, M. I. Hertz et al., "Mechanical circulatory support device database of the International Society for Heart and Lung Transplantation: third annual report—2005," *Journal of Heart and Lung Transplantation*, vol. 24, no. 9, pp. 1182–1187, 2005.
- [3] J. A. Morgan, R. John, V. Rao et al., "Bridging to transplant with the HeartMate left ventricular assist device: the Columbia Presbyterian 12-year experience," *Journal of Thoracic and Cardiovascular Surgery*, vol. 127, no. 5, pp. 1309–1316, 2004.
- [4] S. Salzberg, M. Lachat, G. Zünd et al., "Left ventricular assist device as bridge to heart transplantation—lessons learned with the MicroMed DeBakey axial blood flow pump," *European Journal of Cardio-thoracic Surgery*, vol. 24, no. 1, pp. 113–118, 2003.
- [5] G. P. Noon, D. Morley, S. Irwin, and R. Benkowski, "Development and clinical application of the MicroMed DeBakey VAD," *Current Opinion in Cardiology*, vol. 15, no. 3, pp. 166–171, 2000.
- [6] A. S. Curtis, Z. J. Wu, R. L. Kormos, B. P. Griffith, and J. F. Antaki, "Novel ventricular apical cannula: in vitro evaluation using transparent, compliant ventricular casts," *ASAIO Journal*, vol. 44, no. 5, pp. M691–M695, 1998.
- [7] T. Komoda, Y. Weng, and R. Hetzer, "Technique for insertion of the inflow cannula of the INCOR left ventricular assist device," *Annals of Thoracic Surgery*, vol. 85, no. 4, pp. 1466–1467, 2008.
- [8] A. Tschirkov, D. Nikolov, and V. Papantchev, "New technique for implantation of the inflow canula of Berlin Heart INCOR system," *European Journal of Cardio-Thoracic Surgery*, vol. 30, no. 4, pp. 678–679, 2006.
- [9] G. P. Noon, D. L. Morley, S. Irwin, S. V. Abdelsayed, R. J. Benkowski, and B. E. Lynch, "Clinical experience with the MicroMed DeBakey ventricular assist device," *Annals of Thoracic Surgery*, vol. 71, no. 3, pp. S133–S138, 2001.
- [10] G. M. Wieselthaler, H. Schima, and E. Wolner, "Special considerations on the implantation technique for the MicroMed-DeBakey ventricular assist device axial pump," *Annals of Thoracic Surgery*, vol. 76, no. 6, pp. 2109–2111, 2003.
- [11] T. Akimoto, K. Yamazaki, P. Litwak et al., "Continuously maintaining positive flow avoids endocardial suction of a rotary blood pump with left ventricular bypass," *Artificial Organs*, vol. 24, no. 8, pp. 606–610, 2000.
- [12] C. Schmid, M. Jurmann, D. Birnbaum et al., "Influence of inflow cannula length in axial-flow pumps on neurologic adverse event rate: results from a multi-center analysis," *Journal of Heart and Lung Transplantation*, vol. 27, no. 3, pp. 253–260, 2008.
- [13] D. Lacasse, A. Garon, and D. Pelletier, "Mechanical hemolysis in blood flow: user-independent predictions with the solution of a partial differential equation.," *Computer Methods in Biomechanics and Biomedical Engineering*, vol. 10, no. 1, pp. 1–12, 2007.
- [14] X. Song, A. L. Throckmorton, H. G. Wood, J. F. Antaki, and D. B. Olsen, "Computational fluid dynamics prediction of blood damage in a centrifugal pump," *Artificial Organs*, vol. 27, no. 10, pp. 938–941, 2003.
- [15] A. Arvand, M. Hormes, and H. Reul, "A validated computational fluid dynamics model to estimate hemolysis in a rotary blood pump," *Artificial Organs*, vol. 29, no. 7, pp. 531–540, 2005.
- [16] T. N. Bachman, J. K. Bhamma, J. Verkaik, S. Vandenberghe, R. L. Kormos, and J. F. Antaki, "In vitro evaluation of ventricular cannulation for rotodynamic cardiac assist devices," *Cardiovascular Engineering and Technology*, vol. 2, no. 3, pp. 203–211, 2011.
- [17] J. K. Bhamma, T. N. Bachman, R. L. Kormos, H. Borovetz, and J. F. Antaki, "Development of an ex vivo ovine ventricular assist device model for intraventricular visualization of the inflow cannula," *Journal of Heart and Lung Transplantation*, vol. 28, no. 8, pp. 860–861, 2009.
- [18] Y. Ootaki, D. Saeed, C. Ootaki et al., "Development of the Dex-Aide right ventricular assist device inflow cannula," *ASAIO Journal*, vol. 54, no. 1, pp. 31–36, 2008.
- [19] K. H. Fraser, T. Zhang, M. E. Taskin, B. P. Griffith, and Z. J. Wu, "Computational fluid dynamics analysis of thrombosis potential in left ventricular assist device drainage cannulae," *ASAIO Journal*, vol. 56, no. 3, pp. 157–163, 2010.
- [20] M. Grigioni, C. Daniele, U. Morbiducci et al., "Computational model of the fluid dynamics of a cannula inserted in a vessel: incidence of the presence of side holes in blood flow," *Journal of Biomechanics*, vol. 35, no. 12, pp. 1599–1612, 2002.
- [21] D. V. Amin, J. F. Antaki, P. Litwak, D. Thomas, Z. J. Wu, and M. Watach, "Induction of ventricular collapse by an axial flow blood pump," *ASAIO Journal*, vol. 44, no. 5, pp. M685–M690, 1998.
- [22] T. Tsukiya, K. Toda, and H. Sumikura, "Computational fluid dynamic analysis of the flow field in the newly developed inflow cannula for a bridge-to-decision mechanical circulatory support," *Artificial Organs*, vol. 14, no. 4, pp. 381–384, 2011.
- [23] H. Zhan-Zhong, W. Jing, and L. Xiao-Ping, *FLUENT Fluid Engineering Simulation Example and Apply*, Beijing Institute of Technology Press, 2007.
- [24] M. Giersiepen, L. J. Wurzing, R. Opitz, and H. Reul, "Estimation of shear stress-related blood damage in heart valve prostheses—in vitro comparison of 25 aortic valves," *International Journal of Artificial Organs*, vol. 13, no. 5, pp. 300–306, 1990.
- [25] R. Cheng, Y. G. Lai, and K. B. Chandran, "Three-dimensional fluid-structure interaction simulation of bileaflet mechanical heart valve flow dynamics," *Annals of Biomedical Engineering*, vol. 32, no. 11, pp. 1471–1483, 2004.
- [26] L. Goubergrits and K. Affeld, "Numerical estimation of blood damage in artificial organs," *Artificial Organs*, vol. 28, no. 5, pp. 499–507, 2004.

- [27] J. Wu, B. E. Paden, H. S. Borovetz, and J. F. Antaki, "Computational fluid dynamics analysis of blade tip clearances on hemodynamic performance and blood damage in a centrifugal ventricular assist device," *Artificial Organs*, vol. 34, no. 5, pp. 402–411, 2010.
- [28] G. Song, L. P. Chua, and T. M. Lim, "Numerical study of a bio-centrifugal blood pump with straight impeller blade profiles," *Artificial Organs*, vol. 34, no. 2, pp. 98–104, 2010.

Research Article

Optimization of Wind Turbine Airfoil Using Nondominated Sorting Genetic Algorithm and Pareto Optimal Front

Ziaul Huque,^{1,2} Ghizlane Zemmouri,^{1,2} Donald Harby,^{1,2} and Raghava Kommalapati^{2,3}

¹Department of Mechanical Engineering, Prairie View A&M University, P.O. Box 519, Mail Stop 2525, Prairie View, TX 77446, USA

²Center for Energy and Environmental Sustainability, Prairie View A&M University, P.O. Box 519, Mail Stop 2500, Prairie View, TX 77446, USA

³Department of Civil and Environmental Engineering, Prairie View A&M University, P.O. Box 519, Mail Stop 2510, Prairie View, TX 77446, USA

Correspondence should be addressed to Ziaul Huque, zihuque@pvamu.edu

Received 9 January 2012; Revised 13 February 2012; Accepted 13 February 2012

Academic Editor: Mahesh T. Dhotre

Copyright © 2012 Ziaul Huque et al. This is an open access article distributed under the Creative Commons Attribution License, which permits unrestricted use, distribution, and reproduction in any medium, provided the original work is properly cited.

A Computational Fluid Dynamics (CFD) and response surface-based multiobjective design optimization were performed for six different 2D airfoil profiles, and the Pareto optimal front of each airfoil is presented. FLUENT, which is a commercial CFD simulation code, was used to determine the relevant aerodynamic loads. The Lift Coefficient (C_L) and Drag Coefficient (C_D) data at a range of 0° to 12° angles of attack (α) and at three different Reynolds numbers ($Re = 68,459, 479,210, \text{ and } 958,422$) for all the six airfoils were obtained. Realizable $k-\epsilon$ turbulence model with a second-order upwind solution method was used in the simulations. The standard least square method was used to generate response surface by the statistical code JMP. Elitist Nondominated Sorting Genetic Algorithm (NSGA-II) was used to determine the Pareto optimal set based on the response surfaces. Each Pareto optimal solution represents a different compromise between design objectives. This gives the designer a choice to select a design compromise that best suits the requirements from a set of optimal solutions. The Pareto solution set is presented in the form of a Pareto optimal front.

1. Introduction

According to the US Department of energy, the combustion of fossil fuels results a net increase of 10.65 billion tones of atmospheric carbon dioxide every year [1] which deteriorates the environmental balance. Fossil fuels also give out sulfur dioxide into the air, which, after reacting with the moisture in air, produces sulfuric acid and leads to acid rain. Furthermore, depletion of these nonrenewable sources of energy is taking place at a rapid pace because of the increasing demands of energy, with the modernization of our society. Estimates from the US Department of Energy predict that the years of production left in the ground for oil are 43 years, gas 167 years, and coal 417 years [2]. Therefore, it is critical that we start looking for some renewable sources of energy that can be used as alternatives to fossil fuels. Renewable energy resources can play a key role in producing local, clean,

and inexhaustible energy to supply the growing demand for electricity, heat, and transportation fuel. Wind energy as a source of energy to produce electricity is favoured widely as an alternative to fossil fuels. It is plentiful, renewable, widely distributed, and clean and produces no greenhouse gas emissions. Wind turbines convert kinetic energy from the wind into mechanical energy which can be used to generate electricity. When the wind blows and flows around the blades of the wind turbines, which have essentially airfoil cross sections, it generates lift forces which makes the blades spin. These blades are connected to a drive shaft that turns an electric generator to produce electricity which therefore can be sent through a cable down the turbine tower to a transmission line. The blades of a wind turbine rotor are generally regarded as the most critical component of the wind turbine system [3]. The aerodynamic profiles of wind turbine blades have crucial influence on aerodynamic

efficiency of wind turbines. Even minor alterations in the shape of the profile can greatly alter the power curve and noise level. Some of the important design parameters include the number of blades, blade solidity, blade taper, and twist as well as tip-speed ratio. The aerodynamic theory of the wind turbines gradually developed, starting with the simple one-dimensional momentum analysis [4] of the actuator disc to the more commonly used BEM theory.

The BEM theory is based on the assumption that the flow at a given annulus does not affect the flow at adjacent annuli [5]. This allows the rotor blade to be analysed in sections, where the resulting forces are summed over all sections to get the overall forces of the rotor. The theory uses both axial and angular momentum balances to determine the flow and the resulting forces at the blade. BEM methods are very fast and reliable in the design process, nevertheless these are limited due to their two dimensional nature. These codes require tabulated data for the lift, drag and moment distributions versus the angle of attack to calculate the blade aerodynamic loads. Furthermore, empirical corrections are necessary to account for rotational effects near the root and three dimensional flows around the tip region [6].

Over the last several years, the wind turbine community has started to look at CFD methods to complement wind tunnel [7] and in field tests on the understanding of the complex flow physics around rotating wind turbine blades. CFD codes can be very useful on the calculation of aerodynamic coefficients required by engineering methods and on the explicit determination of loads since no corrections are necessary as in BEM method.

The overall goal of this study is to perform a response surface-based multiobjective optimization of selected 2D airfoil profiles using Elitist Nondominated Sorting Genetic Algorithm (NSGA). In order to achieve this overall goal, several specific objectives were determined. The first specific objective was to identify several airfoil profiles with their geometric coordinates. The second objective was to perform CFD simulations around the airfoils. Simulations for each airfoil were performed for several values of Re and α . The third objective was to determine response surfaces for lift and drag coefficients as a function of Re and α . The fourth and final objective was to perform the optimization using genetic algorithm to determine a set of nondominated solution for each airfoil. Based on the optimization results, designers can opt choose multiple airfoils for a single blade depending on Re and α variation along the length of the blade after appropriate twist and taper is applied. It is also worth to mention other interesting works [8, 9] that are reported where numerical models are used to design turbines specifically in the wave energy area.

2. Approaches

2.1. CFD Modelling. In this work, we consider the flow around six different airfoil shapes (NACA 63-218, E387, FX63-137, NACA 63-421, NACA 64-421, and NACA 65-421) at 3 different Reynolds number ($Re = 68,459$, $Re = 479,210$, and $Re = 958,422$) for a range of 0° to 12° angles of attack. These airfoils are created from a set of vertices generated

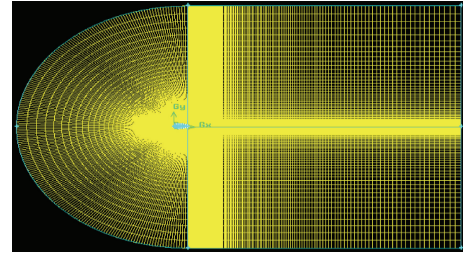


FIGURE 1: 2D mesh of the entire domain using a map scheme with around 50,000 quadrilateral elements.

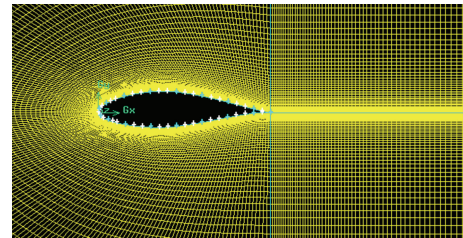


FIGURE 2: Mesh generated around the airfoil.

from the University of Illinois at Urbana Champagne (UIUC) airfoil database [10]. These vertices are connected using a smooth curve, creating the surface of the airfoil. A flow domain is created surrounding the airfoil and this domain is split for meshing purposes.

The CFD data of the 15 simulated cases for each airfoil were used to generate a response surface. The response surfaces were fit using standard least-square regression with quadratic polynomial using JMP. These response surfaces are obtained between design variable (Re and α) and objective functions (C_L and C_D) for each airfoil profile. All the design variables and the objective functions are normalized between 0 and 1 based on their maximum and minimum values in order to determine the response surface.

2.2. Grid Description. Grid generation is the most important step in the CFD simulations. The quality of the grid plays a direct role on the quality of the analysis, regardless of the flow solver used. Additionally, the solver will be more robust and efficient when using a well-constructed mesh. In this work, structured grids were generated using the commercial code GAMBIT. Figure 1 shows a 2D mesh of the entire domain using a map scheme with around 50,000 quadrilateral elements (the number varies slightly for different airfoils) while Figure 2 shows the blowup of the mesh generated around the airfoil.

In order to have a stable solution, the generated grids had the least number of elements with high aspect ratios. To be able to resolve adequately the boundary layer along the airfoil wall, grid points were clustered near the wall. The grids were also clustered near the trailing edge in order to catch the flow separation.

2.3. Boundary Conditions. Boundary conditions specify the flow and thermal variables on the boundaries of the physical

model. They are, therefore, a critical component of the CFD simulations, and it is important that they are specified appropriately. In this work, 3 different types of boundary conditions were used: no-slip boundary condition over the airfoil surface, inlet boundary condition for free stream flow, and pressure outlet. The outlet boundary of the domain was set to a constant pressure value. It was set to be atmospheric pressure. The object in the computational domain (i.e., the airfoil surface), around which the flow was simulated, was set to be no-slip boundary (wall). The no-slip boundary condition sets the stream wise velocity to zero. The velocity Inlet boundary condition was used to define the flow velocity at the flow inlet. Figure 3 shows the different assigned boundary conditions for all the CFD simulations as follows.

In Gambit, the boundary conditions were declared (i.e., wall, velocity inlet, and pressure outlet), but actual values for these boundaries were defined in fluent. For velocity inlet, we used 3 different velocities for each airfoil at every angle of attack. We set $v = 1$ m/s (for $Re = 68,459$), $v = 7$ m/s (for $Re = 479,210$), and $v = 14$ m/s (for $Re = 958,422$). The Realizable k -epsilon turbulence model and a second-order upwind solution method were used to get more accurate results.

2.4. Response Surface Methodology. The response surface method fits an approximate function to a set of experimentally or numerically evaluated design data points [11]. There are various response surface approximation methods available in the literature [11, 12], with the polynomial-based approximations being the most popular. In this technique, an appropriate ordered polynomial is fitted to a set of data points, such that the adjusted RMS error σ_a is minimized and quality parameter R_{adj}^2 is made as close as possible to one [12]. The σ_a and R_{adj}^2 are defined as follows.

Let N be the number of data points and let N_p be the number of coefficients, and error e_i at any point i is defined:

$$e_i = f_i^a - f_i^p, \quad (1)$$

where f_i^p is the actual value of the function at the design point and f_i^a is the predicted value. Hence,

$$\sigma_a = \sqrt{\frac{\sum_{i=1}^N e_i^2}{(N - N_p)}}, \quad (2)$$

$$R_{adj}^2 = 1 - \frac{\sigma_a^2 (N_p - 1)}{\sum_{i=1}^N (y_i - \bar{y})^2}, \quad (3)$$

where

$$\bar{y} = \frac{\sum_{i=1}^N y_i}{N_p}. \quad (4)$$

The number of data N has to be greater than the number of coefficients N_p so that the denominator of (2) is always positive and well posed. Since R_{adj}^2 needs to be as close as possible to 1 to represent a good fit, the terms in the numerator of (3) $(\sigma_a^2 (N_p - 1))$ should be less than or equal

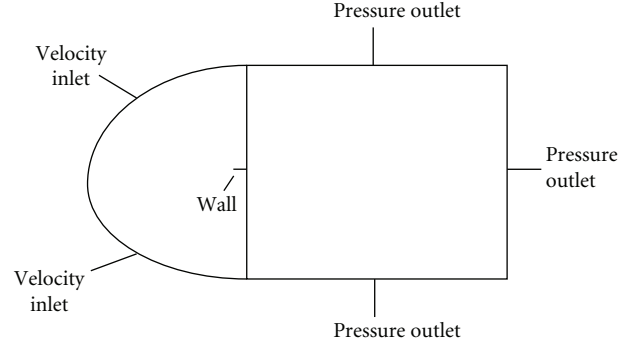


FIGURE 3: The flow domain with the boundary conditions.

to the denominator $\sum_{i=1}^N (y_i - \bar{y})^2$ so that R_{adj}^2 will always be positive. In this study, the response surface method is applied with two objectives, namely, to generate response surface from the CFD simulation results and to approximate the global Pareto optimal front by representing one objective in terms of others. Both aspects will be discussed in upcoming sections.

2.5. Optimization Approach. The methodology used for generating Pareto optimal front is a multiobjective evolutionary algorithm (MOEA). The specific algorithm used is the Elitist Nondominated Sorting Genetic Algorithm (NSGA-II) [13]. All genetic algorithm codes use some form of sorting scheme to get nondominated solutions. Nondominated solutions are the best solutions. Among the nondominated solutions one cannot be said to be better than the other. NSGA-II uses an explicit diversity-preserving mechanism. The starting point is the identification of constraints, performance criteria, design variables, and allowable range of design variables. The response surfaces generated from the results of the CFD simulations are incorporated into the NSGA-II code. In running the code input values for several parameters must be provided. These parameters and their best values, as suggested by Deb [11, 13] after their extensive parametric study, are as follows:

- (i) Population size: 100,
- (ii) Generations: 250,
- (iii) Crossover probability (P_{cross}): 1.00,
- (iv) Distribution parameter (for crossover): 20,
- (v) Mutation probability (P_{mut}): 0.250,
- (vi) Distribution parameter (for mutation): 200.

Where the population size is the size of the non-dominated solutions and the generations are equivalent to the number of iterations. Crossover probability, mutation probability, distribution parameter for crossover, and distribution parameter for mutation are used to create the offspring population from the parent population. The crossover probability is mainly responsible for the search aspect of the genetic algorithm while mutation probability keeps the diversity in the population. The distribution parameter for crossover controls the diversity of the children solutions obtained after

crossover while distribution parameter for mutation controls the spread of the solutions after mutation.

In NSGA-II algorithm, the code first creates a parent population of P_t of size N . From the parent set it then creates an offspring population Q_t of size N . The NSGA-II algorithm, instead of finding the non-dominated front of Q_t only, uses the combined population of P_t and Q_t to form R_t of size $2N$. Then, a nondominated sorting is used to classify the entire population R_t . Although this requires more effort compared to performing a non-dominated sorting on Q_t alone, it allows a global non-domination check among the offspring and parent solutions. Once the non-dominated sorting is over, the new population is filled by solutions of different non-dominated fronts, F_i , one at a time. The filling starts with the best non-dominated front and continues with solutions of the second non-dominated front and so on. Since the overall population size of R_t is $2N$, not all fronts may be accommodated in N slots available in the new population. All fronts which could not be accommodated are simply deleted. When the last allowed front is being considered, there may exist more solutions in the last front than the remaining slots in the new population. Instead of arbitrarily discarding some members from the last front, a niching strategy [13] is used to choose the members of the last front based on crowding distance. The solutions kept in the population are those which have the largest crowding distance thus keeping the diversity of the solution. This new set of solutions is now the parent set for the next generation. The procedure is then repeated till the best non-dominated set is obtained.

3. Results and Discussions

3.1. Flow Field Overview. The CFD validation is a very important part of computational fluid dynamics. It is used to evaluate the accuracy of CFD results. We compared the CFD results of Lift Coefficient of E387 airfoil for 5 different angles of attack with National Renewable Energy Laboratory (NREL) experimental data [14] for $Re = 479,210$ as shown in Figure 4. The CFD results of Lift Coefficient show good agreement with NREL experimental results.

Colour contours of static pressure and velocity vectors by velocity magnitude of NACA 64-421 airfoil at an angle of attack of 6° and at $Re = 479,210$ are shown in Figures 5 and 6. The static pressure plot clearly shows the higher pressure (indicated by red, yellow, and green colours) on the bottom surface and lower pressure (indicated by blue colour) on the top surface. In the velocity vector plot, higher velocity corresponding to lower pressure and lower velocity corresponding to higher pressure can be clearly observed.

3.2. Performance Trend

3.2.1. C_p Distribution. Figures 7(a)–7(c) show the C_p distribution for NACA 63-421 for the three Reynolds numbers. In each figure and for each angle of attack (uniform colour), the bottom line represents the C_p distribution at the top surface of the airfoil, indicating lower pressure, and the top line represents the C_p distribution on the bottom surface of

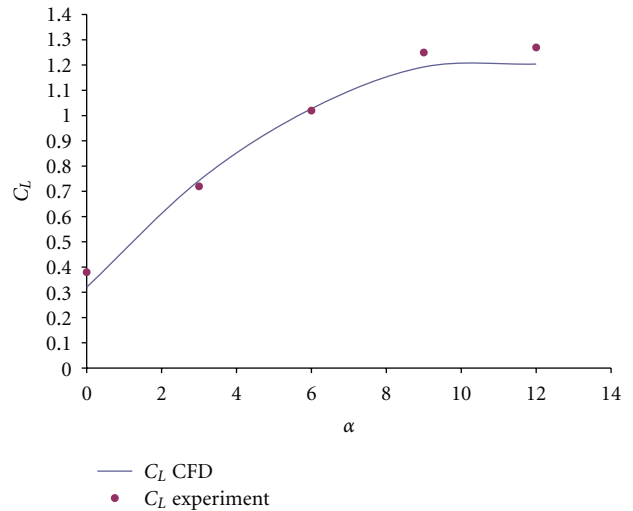


FIGURE 4: Comparison of C_L Versus α of CFD simulation results with NREL experimental data.

the airfoil indicating higher pressure. As the angle of attack increases from 0 to 12 for any Re , the area under the C_p curve increases indicating larger pressure difference between the bottom and the top surfaces. Similar trend is observed for different Re with the same angle of attack. These are expected trends for any airfoil.

3.2.2. Integrated Pressure Coefficient, C_p . Figure 8 represents the overall integrated pressure coefficient (C_p) as a function of angle of attack (α) of NACA 63-421 airfoil at the three different Reynolds numbers. As expected, as we increase the angle of attack, the overall pressure coefficient increases for all six airfoils. However, within the same airfoil, C_p has little change as we move from a lower Reynolds number ($Re = 68,459$) to a higher Reynolds number ($Re = 958,422$). The C_p of NACA 63-218 airfoil increases continuously as we increase the angle of attack which indicates that it has not reached the stall condition yet, while the C_p plot of the other airfoils starts to flatten at around 11° to 12° of angle of attack which indicates that it is close to its stall condition. In addition, NACA 63-218, NACA 63-421, NACA 64-421, and NACA 65-421 airfoils have small integrated C_p (C_p around 1.3 or 1.4) at stall condition which are much smaller than FX 63137 and E 387 airfoils (C_p around 1.6 or 1.8). Thus, we can conclude that the stall conditions could vary significantly between various airfoil profiles.

3.2.3. Coefficient of Lift, C_L . Figure 9 shows the plot of lift coefficient for NACA 63-421 airfoil. C_L is plotted as functions of angles of attack and Reynolds number. The general trends of all the plots are similar as expected; that is, C_L increases with increasing α and Re . Some of the observations from the plots are as follows.

- (i) The variations of C_L between different Re are not significant.
- (ii) The differences are more significant at higher α for NACA 65-421 and E 387 airfoil.

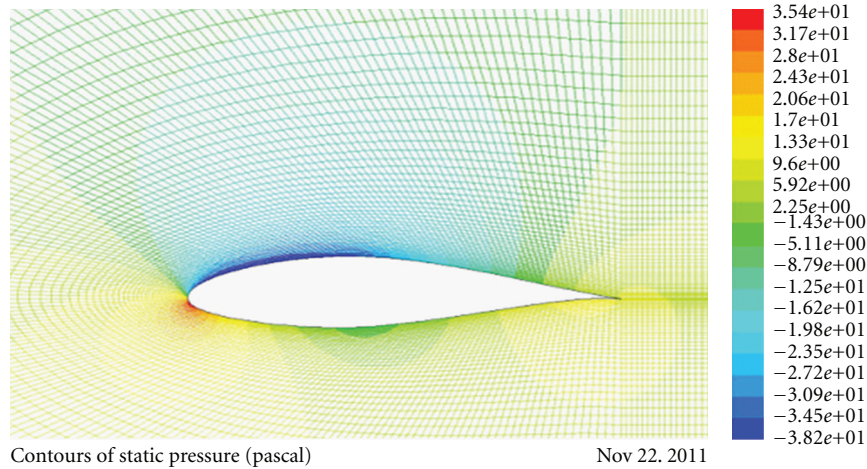


FIGURE 5: Colour contour of static pressure around NACA 64-421 airfoil at $\alpha = 6$ and $Re = 479,210$.

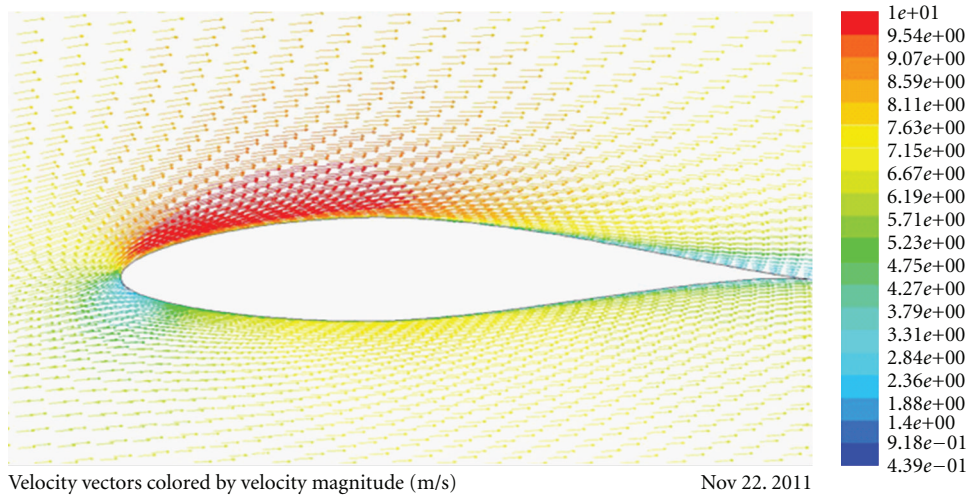


FIGURE 6: Colour velocity vectors by velocity magnitude around NACA 64-421 airfoil at $\alpha = 6$ and $Re = 479,210$.

- (iii) C_L for NACA 63-218 at all Re did not reach the stall conditions; that is, the stall condition will be reached at much higher than $\alpha = 12^\circ$.
- (iv) Both FX 63-137 and E 387 indicate reaching stall condition at around $\alpha = 12^\circ$.
- (v) Both FX 63-137 and E 387 show smaller variation with Re and reach higher values of $C_L =$ around 1.8 and 1.6 at $\alpha = 12^\circ$.

It is obvious from the previous observations that different airfoils behave differently with angle of attack and Reynolds numbers.

3.2.4. Coefficient of Drag, C_D . Drag Coefficient as a function of angle of attack of NACA 63-421 at the three different Reynolds numbers is shown in Figure 10. As the velocity goes down from $v = 7$ m/s ($Re = 479,210$) to $v = 1$ m/s ($Re = 68,459$), the C_D curves increase drastically for all six airfoils, while if we increase the velocity from $v = 7$ m/s to

$v = 14$ m/s ($Re = 958,422$), the C_D curves do not change a lot. As expected, for lower Re and larger α , the higher is the Drag Coefficient. For instance, NACA 64-421 airfoil has the highest C_D ($C_D = 0.5259$) at $Re = 68,459$ and $\alpha = 12^\circ$. Hence there is an optimum combination of α and Re for the maximum ratio of C_L by C_D for each airfoil. These optimum conditions are presented in the next sections.

The CFD simulation results for the 15 cases are shown in Table 1 of NACA 63-421 airfoil where the design variables and objective functions are given in normalized form.

3.3. Response Surface Approximation. The CFD data of 15 cases were used to generate a response surface for each of the two objective functions for each airfoil shape. The response surfaces were fit using standard least-square regression with quadratic polynomial using JMP [15]. The following response surfaces for each of the objective functions were obtained as functions of the two design variables of NACA 63-421 airfoil:

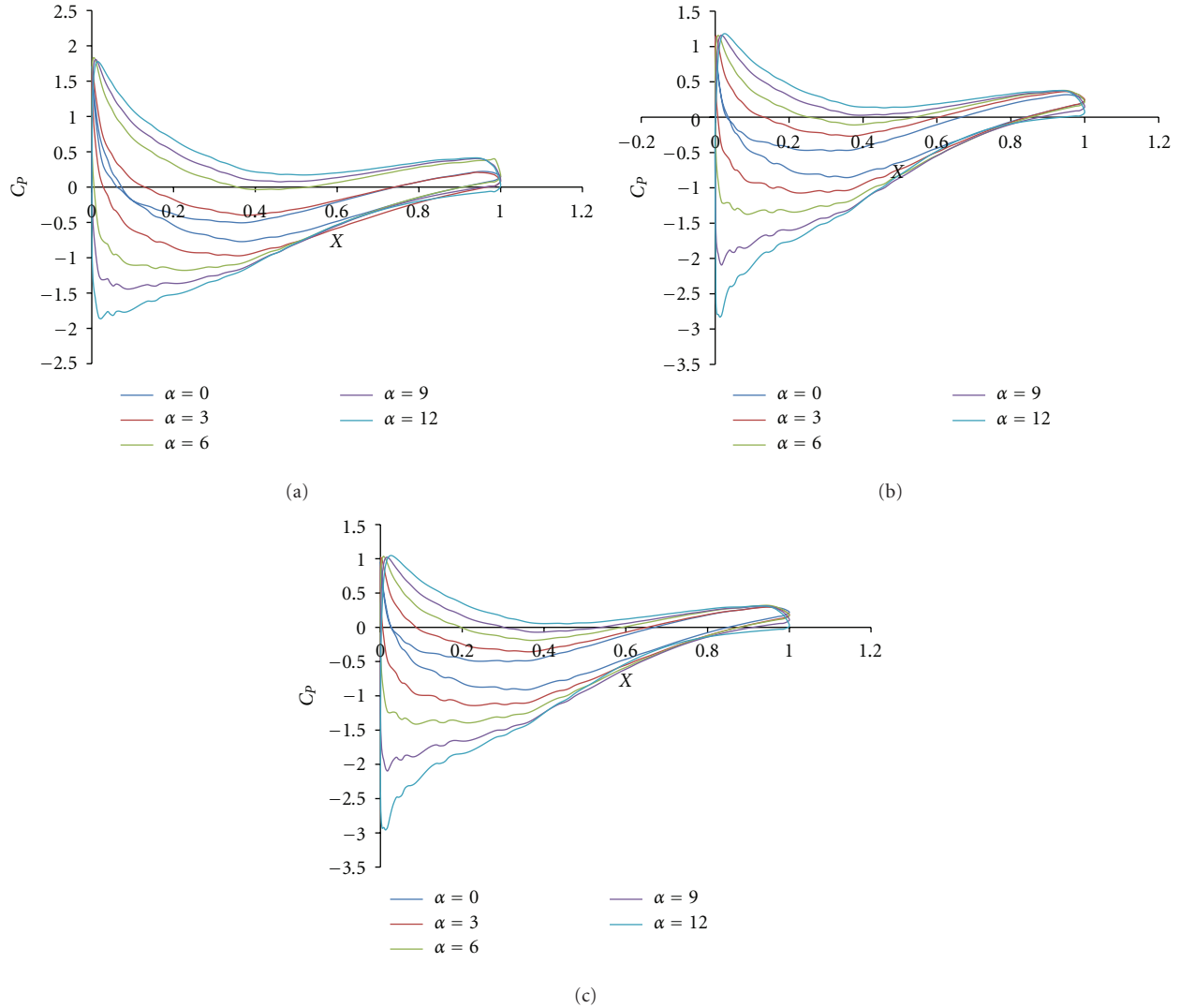


FIGURE 7: (a) C_p distribution of NACA 63-421 airfoil at $Re = 68,459$. (b) C_p distribution of NACA 63-421 airfoil at $Re = 479,210$. (c) C_p distribution of NACA 63-421 airfoil at $Re = 958,422$.

Lift Coefficient

$$(C_L) = 0.1306 + (0.1646 * Re) + (1.2649 * \alpha) - (0.0766 * Re * Re) - (0.1732 * Re * \alpha) - (0.3843 * \alpha * \alpha). \quad (5)$$

Drag Coefficient

$$(C_D) = 0.6795 - (1.6805 * Re) + (0.1358 * \alpha) + (1.1322 * Re * Re) - (0.2220 * Re * \alpha) + (0.2329 * \alpha * \alpha). \quad (6)$$

The quality of the response surface of this airfoil is shown in Table 2. The response surface for the entire objective had very high adjusted coefficient of both C_L and C_D which indicate good capabilities for this airfoil.

3.4. Optimization Results. In order to obtain the Pareto optimal solutions, the two response surface equations were incorporated in the NSGA-II code with the input parameters as mentioned in the previous section. After the simulation, the code generates a file containing 100 non-dominated solutions created during the final iteration. Non-dominated values are the best values according to the desired maximization of the objective functions among the entire population. For better understanding 2D plots of C_L versus C_D and C_L/C_D versus C_L are depicted using only 100 nondominated solutions for NACA 63-421 airfoil in Figures 11 and 12. The C_L versus C_D plot represents 100 best combinations of C_L and C_D corresponding to the best combinations of Re and α . Therefore, the designer can choose any of these combinations and get good results. But, to be able to get one optimum result of these 100 combinations, we can plot C_L/C_D versus C_L . For example, for NACA 63-421 airfoil, the optimum point is at $C_L = 0.717$ for C_L/C_D around 40. This optimum

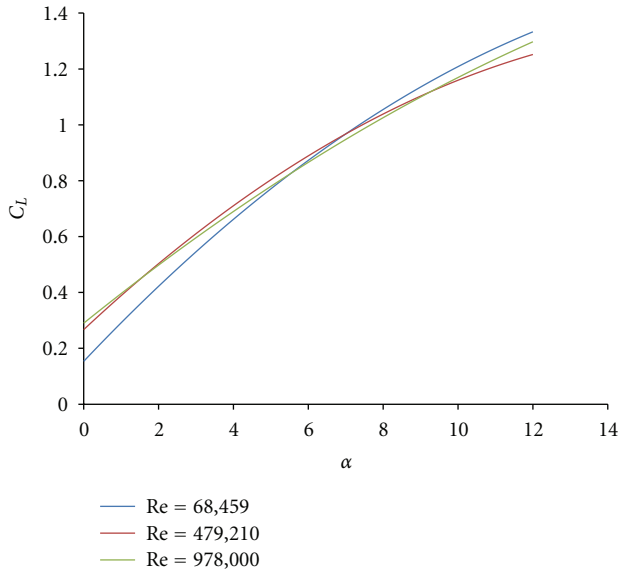


FIGURE 8: Integrated pressure coefficient of NACA 63-421 airfoil at different Re.

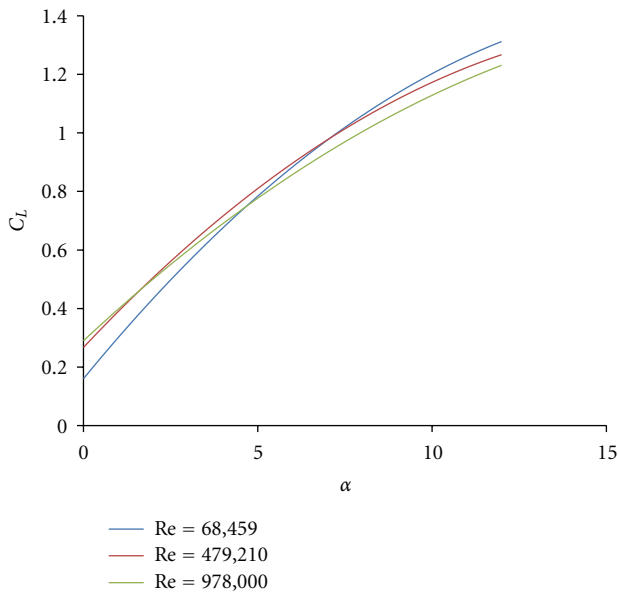


FIGURE 9: CFD simulation results of C_L versus α of NACA 63-421 airfoil.

C_L at the maximum value of C_L/C_D corresponds to an angle of attack of around 4° .

Similar optimizations were performed on all the airfoil shapes. The results obtained are as follows: for NACA 63-218 airfoil, the optimum $C_L = 0.54$ and $C_D = 0.026$ at $\alpha = 4.58$ and $Re = 777,284$; for E387 airfoil, the best combination is at $\alpha = 2.90$ and $Re = 721,398$ which give $C_L = 0.7$ and $C_D = 0.129$; for FX 63137 airfoil, the optimum $C_L = 0.976$ and $C_D = 0.024$ at $\alpha = 2.10$ and $Re = 730,996$; for NACA 63-421 airfoil, $C_L = 0.717$ and $C_D = 0.018$ for $Re = 770,937$

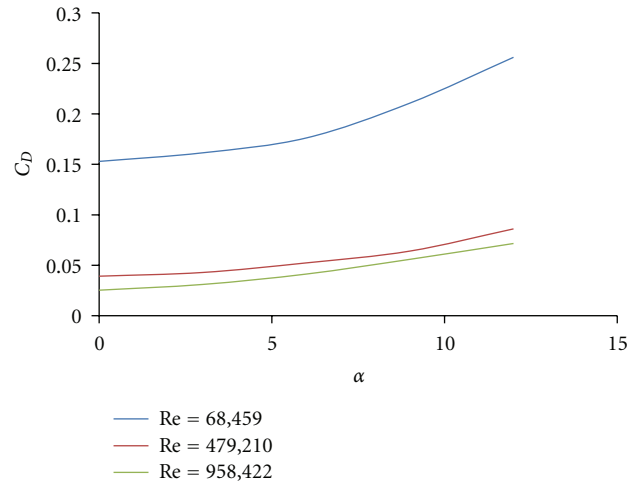


FIGURE 10: CFD simulation results of C_D versus α of NACA 63-421 airfoil.

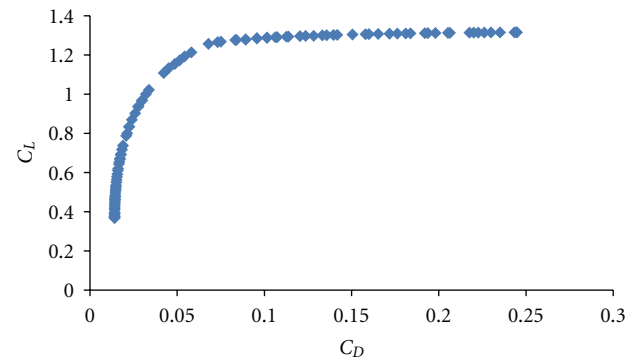


FIGURE 11: 2D presentation of non-dominated solutions of C_L versus C_D .

and $\alpha = 4.06$; for NACA 64-421 airfoil, at $\alpha = 3.12$ and $Re = 725,083$ for $C_L = 0.68$ and $C_D = 0.02$; finally for NACA 65-421 airfoil, the optimum $C_L = 0.775$ and $C_D = 0.023$ corresponding to $\alpha = 3.07$ and $Re = 759,718$. The optimum C_L corresponding to maximum C_L/C_D as a function of angle of attack for all the airfoils was plotted in Figure 13. From this figure, the designer can choose the airfoil shape corresponding to the angle of attack dictated by the twist angle he/she is using. For example, if the twist angle is 4° at any blade section, the designer can use NACA 63-421 airfoil shape for that section of the blade in order to get the optimum C_L .

4. Conclusions

The Pareto optimal front in multiobjective optimization problem is useful to visualize the tradeoffs among different objectives. In addition to identify compromise solutions, this also helps the designer set realistic design goals. The goal of the current research is focused on the determination and optimization of wind turbine airfoil performance. For this

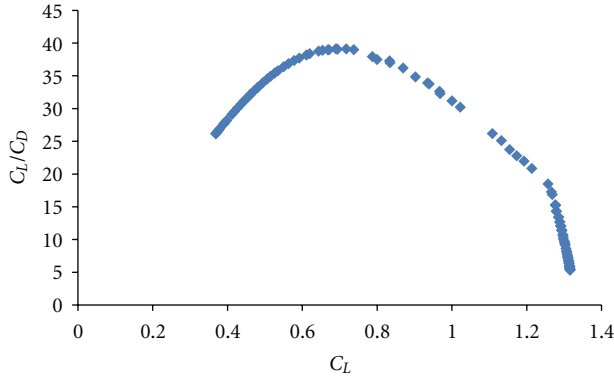


FIGURE 12: 2D presentation of non-dominated solutions of C_L/C_D versus C_L .

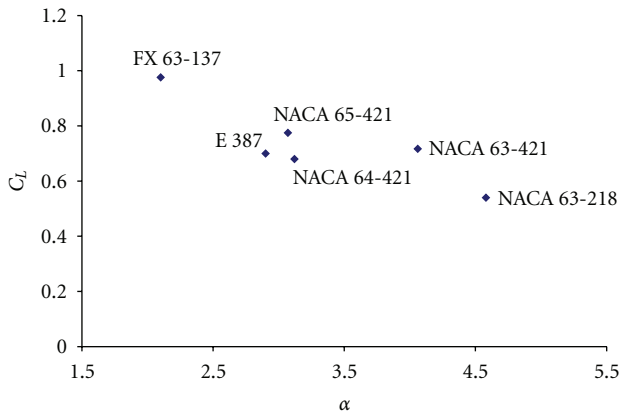


FIGURE 13: Optimum C_L versus α for all airfoils.

TABLE 1: Normalized design variables and objective function values from CFD simulations of NACA 63-421.

CFD normalized results			
Re	A	C_L	C_D
0.499999	0	0.208173299	0.152746
0.499999	0.25	0.467045629	0.167201
0.499999	0.5	0.682900599	0.204313
0.499999	0.75	0.868028883	0.25002
0.499999	1	0.967890613	0.335964
1	0	0.227377477	0.098445
1	0.25	0.450145952	0.120713
1	0.5	0.657935167	0.16095
1	0.75	0.828468275	0.217986
1	1	0.937932094	0.279319
0.071428	0	0.145183592	0.597703
0.071428	0.25	0.372561069	0.630909
0.071428	0.5	0.718397603	0.688374
0.071428	0.75	0.877093255	0.822994
0.071428	1	1	1

TABLE 2: Quality parameters of response surface of NACA 63-421 airfoil.

Observations	C_L	C_D
R^2	0.994164	0.992416
R^2 Adj	0.990921	0.988203
Root Mean Square Error	0.028065	0.031312
Mean of Response	0.627276	0.381842

purpose, six different two-dimensional airfoil profiles were studied over two important design variables. The NSGA-II approach of optimization and response surface methodology has been used to generate Pareto optimal front. The optimum C_L , corresponding to the best combination of α and Re, is different from one airfoil shape to another. In summary, the proposed systematic approach is very useful for optimization of designs with many variables and objectives and can be practically applied in many disciplines.

Acknowledgment

This work is supported by the National Science Foundation (NSF) through the Center for Energy and Environmental Sustainability (CEES), a CREST Center, award no. 1036593.

References

- [1] US Government, Department of Energy, US Department of Energy on Green House Gases, 2009, <http://www.eia.doe.gov/bookshelf/brochures/greenhouse/Chapter1.htm>.
- [2] Department of Energy, US Fossil Energy, 2009, <http://www.fossil.energy.gov/index.html>.
- [3] C. Kong, J. Bang, and Y. Sugiyama, "Structural investigation of composite wind turbine blade considering various load cases and fatigue life," *Energy*, vol. 30, no. 11-12, pp. 2101–2114, 2005.
- [4] H. Glauert, *The Elements of Aerofoil and Airscrew Theory*, Cambridge Science Classic Series, Cambridge University Press, 2nd edition, 1993.
- [5] R. E. Wilson and P. B. S. Lissaman, "Applied aerodynamics of wind power machines, PB238595," Report NSF-RA-N-74-113, NTIS, Springfield, Va, USA, 1974.
- [6] H. Glauert, "Airplane propellers," in *Aerodynamic Theory*, vol. 4, Dover, 1963.
- [7] M. Hand, D. Simms, L. Fingersh et al., "Unsteady aerodynamics experiment phase vi: wind tunnel test configurations and available data campaigns," Tech. Rep. NREL/TP-500-29955, NREL, 2001.
- [8] M. Alberdi, M. Amundarain, A. J. Garrido, I. Garrido, O. Casquero, and M. De La Sen, "Complementary control of oscillating water column-based wave energy conversion plants to improve the instantaneous power output," *IEEE Transactions on Energy Conversion*, vol. 26, no. 4, pp. 1021–1032, 2011.
- [9] A. E. Marzani, F. C. Ruiz, M. A. Rodriguez, and M. T. Parra Santos, "Numerical modelling in wave energy conversion systems," *Energy*, vol. 33, no. 8, pp. 1246–1253, 2008.
- [10] "UIUC Airfoil Coordinates Database," http://www.ae.illinois.edu/m-selig/ads/coord_database.html.
- [11] T. Goel, R. Vaidyanathan, R. T. Haftka, W. Shyy, N. V. Queipo, and K. Tucker, "Response surface approximation of pareto

- optimal front in multi-objective optimization,” in *Proceedings of the 10th AIAA/ISSMO Multidisciplinary Analysis and Optimization Conference*, pp. 2230–2245, Albany, NY, USA, September 2004.
- [12] R. H. Myers and D. C. Montgomery, *Response Surface Methodology-Process and Product Optimization Using Designed Experiment*, Wiley-Interscience, 1995.
- [13] K. Deb, *Multi-Objective Optimization using Evolutionary Algorithms*, John Wiley and Sons, New York, NY, USA, 2004.
- [14] M. S. Selig and B. D. McGranahan, *Wind Tunnel Aerodynamic Tests of Six Airfoils for Use on Small Wind Turbines*, University of Illinois at Urbana Champaign, Urbana, Ill, USA, 2004.
- [15] JMP, “The statistical discovery software,” 1989–2002, Version 5, SAS Institute Inc., Cary, NC, USA.

Research Article

CFD Simulation of Transonic Flow in High-Voltage Circuit Breaker

Xiangyang Ye and Mahesh Dhotre

Interrupter Development, ABB Switzerland Ltd, 5401 Baden, Switzerland

Correspondence should be addressed to Xiangyang Ye, xiangyang.ye@ch.abb.com

Received 25 October 2011; Revised 23 January 2012; Accepted 8 February 2012

Academic Editor: Nandkishor Nere

Copyright © 2012 X. Ye and M. Dhotre. This is an open access article distributed under the Creative Commons Attribution License, which permits unrestricted use, distribution, and reproduction in any medium, provided the original work is properly cited.

A high-voltage circuit breaker is an indispensable piece of equipment in the electric transmission and distribution systems. Transonic flow typically occurs inside breaking chamber during the current interruption, which determines the insulating characteristics of gas. Therefore, accurate compressible flow simulations are required to improve the prediction of the breakdown voltages in various test duties of high-voltage circuit breakers. In this work, investigation of the impact of the solvers on the prediction capability of the breakdown voltages in capacitive switching is presented. For this purpose, a number of compressible nozzle flow validation cases have been presented. The investigation is then further extended for a real high-voltage circuit breaker geometry. The correlation between the flow prediction accuracy and the breakdown voltage prediction capability is identified.

1. Introduction

High-voltage gas circuit breakers are one of the most important and complex components in the electric transmission and distribution systems, with main function of opening the circuit under fault conditions and interrupt currents from very small values up to the maximum rated short-circuit current. The current interruption process in such device is quite complex and involves interaction of electric arc, gas flow, ablation, and radiation.

In typical self-blast high-voltage circuit breaker (schematic is shown in Figure 1), the plasma arc is ignited after arcing contacts (1, 2) separate from each other and breaker uses arc energy to create pressure inside a chamber (3) and to blow the arc, at current zero crossing of the alternating current (ac), inside a PTFE nozzle (4). The clearing of hot gas, after arcing contact (2) leaves the nozzle (4) strongly depends on flow pattern inside the nozzle-diffuser system (4-5) which is complex and contains the formation and location of supersonic flow regions, shock fronts, and flow separation and reattachment regions. Design of such system is important for current interruption and subsequent dielectric recovery (better hot gas clearing), as the flow varies strongly throughout the nozzle diffuser system and its

interaction with the electric field generates critical regions characterized by low density and high electric field. The probability of electrical breakdown is higher in such regions.

In capacitive switching, the current interruption occurs at high voltages but low current (no-arc), represents one of the important tests that the breaker needs to pass. During the diffuser design process referred to capacitive switching, since the electrical field distribution does not change much with different diffuser shapes, the dielectric performance of the gas can be evaluated only from the fluid dynamic characteristics. That is, for given electric field distribution, it is desirable to attain highest possible flow density in the diffuser (while not blocking the gas flow from the nozzle, which would eventually lead to the failure in thermal interruption), for better dielectric capability. Since the local flow property determines the dielectric strength of insulating gas, it is important to understand the dynamics of the transonic gas flow, in the design and development of high-voltage circuit breakers.

Computational Fluid Dynamics (CFD) offers a great advantage for simulating and visualizing the processes in high-voltage circuit breakers. The application of CFD simulation can save a number of expensive tests and significantly

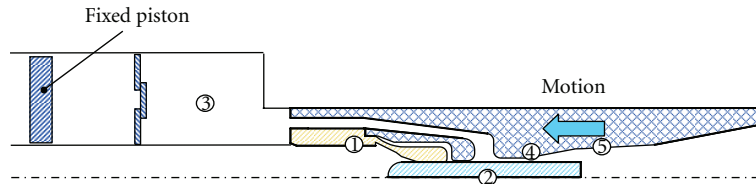


FIGURE 1: Schematic representation of self-blast circuit breaker geometry.

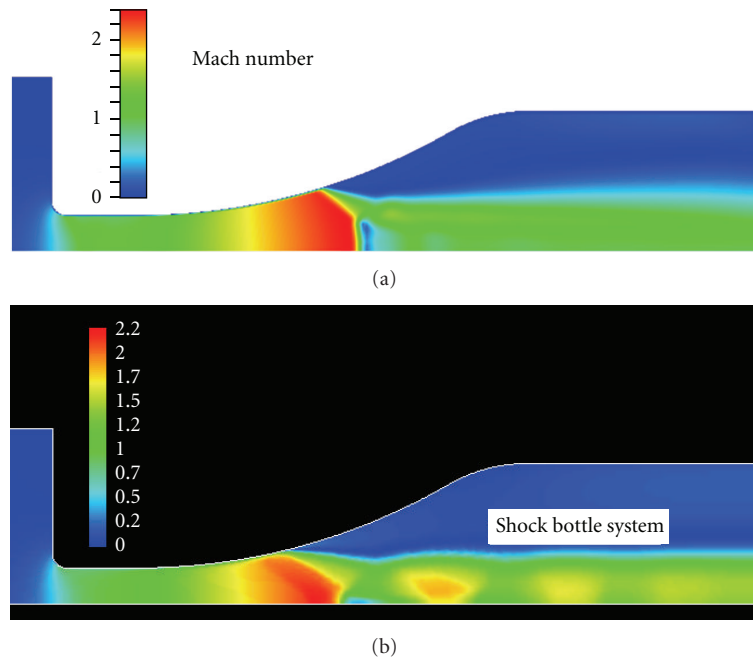


FIGURE 2: Transonic nozzle simulations for typical diffuser geometries for (a) non-conservative method and (b) conservative method.

accelerate the prototyping, which is directly connected to reduction in cost of breaker development. Since flow in breaker is highly complex and nonlinear transonic compressible flow which allows discontinuous shock structure and complicated flow detachments from the diffuser, a high degree of accuracy of flow calculation is required.

In the present work, a benchmark validation study of two solvers for predicting the breakdown voltages in capacitive switching tests in high-voltage circuit breaker geometry is presented. The semi-implicit pressure correction (SIMPLEC) method [1], which is widely adopted in many commercial CFD tools, and the density-based Jameson scheme with explicit Runge-Kutta time marching method [2] are compared. The in-house code has been used for all simulations and two-dimensional axisymmetric simulations are carried out for performance comparison of the two algorithms.

The paper is organized as follows: the main issues in compressible flow simulations are presented in Section 2. Further, the role of the turbulence modeling for transonic nozzle flow simulations, by presenting a validation case based on a 2D nozzle, is demonstrated. In Section 3, CFD validation study for the transient transonic flow in a simple diffuser geometry with different position of electrode (In Figure 1 contact (2)) is presented. In Section 4, validation

study of a compressible flow field with the measured transient flow data from a real high-voltage circuit breaker capacitive switching test duty is performed. In Section 5, influence of the different compressible flow solvers on the prediction of dielectric breakdown voltages in capacitive switching tests is presented. In Section 6, final conclusions are drawn.

2. Main Concerns in Transonic Flow Simulations

There are several features that the ideal CFD simulation tool must possess for the high-voltage circuit breaker application. Since the mechanical or arc-induced pressure build-up in the heating volume generates transonic flow in the diffuser area, the CFD simulation must be able to capture the key physical features of the transonic nozzle flow. These are characterized by the qualities of capturing exact shock location, shock-induced flow separation from the diffuser wall, and the extension of the recirculation zone; see for illustration Figure 2.

The CFD solves the algebraic difference equations which are derived from the partial differential equations, using different space and time discretization methods. One of the widely used methods is to solve a locally elliptic equation for

p and determines other primitive flow variables iteratively. This pressure-correction-based algorithm is widely used in many of the commercial tools. On the other hand, one can make use of the hyperbolic characteristics of the Navier-Stokes equations. Since the flow speed cannot exceed the sonic velocity relative to the background flow velocity, the explicit time marching based on CFL condition [3] can be used. In this case, the solver is based on conserved variables \vec{U} which has an advantage in implementing conservation law constraints on the numerical level.

Conservative and Nonconservative Methodologies. The conservative CFD methods solve the Navier-Stokes equation for conservative variables, the gas density ρ , the flow momentum density $\rho\vec{v}$, and the total energy density E :

$$\frac{\partial}{\partial t} \vec{U} + \nabla \cdot \vec{F}(\vec{U}) = \vec{S}, \quad (1)$$

$$\vec{U} \equiv \begin{pmatrix} \rho \\ \rho\vec{v} \\ E \end{pmatrix}, \quad \vec{F}(\vec{U}) \equiv \begin{pmatrix} \rho\vec{v} \\ \rho\vec{v} \otimes \vec{v} + p\mathbf{I} \\ (E + p)\vec{v} \end{pmatrix}.$$

Here, \vec{v} is the flow velocity vector, p is the static pressure, and the vector \vec{S} represents the viscous stress and heat conduction per unit volume. The system of the equation is closed by equation of state which is given by $p = \rho RT$ for thermally ideal gas, where T is temperature in Kelvin and R is the specific gas constant. For a calorically ideal gas, the internal energy $e \equiv (E/\rho) - (\vec{v}^2/2)$ is given by $e = p/[\rho(\gamma - 1)]$, where γ is the adiabatic exponent. On the contrary, the non-conservative numerical scheme solve the Navier-Stokes equation for nonconservative primitive variables, ρ , \vec{v} , and the enthalpy h .

In order to compare these methods, simulations are presented in Figure 2 for simple diffuser geometry with inlet-to-outlet pressure ratio typically occurring in the high-voltage circuit breaker. Figure 2 illustrates the difference in shock capturing capability of non-conservative and conservative methods. Note that the simulation based on non-conservative method does not capture the shock bottle system after the flow detachment, whereas it is clearly captured by the one based on conservative method.

Turbulence Modeling. The prediction capability of the shock induced flow separation and the trailing recirculation zone is dependent on the detailed modeling of the shock and the boundary layer interaction. In order to investigate the effect of turbulence modeling, simulations are carried out for ‘‘Sajben diffuser,’’ flow experiments [4]. The tested 2D nozzle in these experiments consists of converging and then diverging nozzle (Figure 3, details about experimental set-up is given in [4]). This realizes the supersonic flow which is terminated by a vertical shock located in the downstream area of the throat, for sufficiently high inlet pressures. The vertical shock induces a flow separation with the trailing recirculation zone. The vertical shock position depends on the ratio of the inlet-to-outlet pressures, and the so-called ‘‘strong shock’’ and the ‘‘weak shock’’ cases are examined in

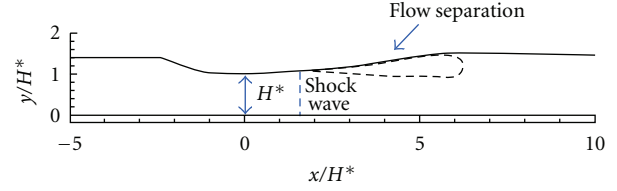


FIGURE 3: The transonic nozzle flow configuration which consists of vertical shock, shock-induced flow separation, and recirculation zone (Sajben Diffuser test case).

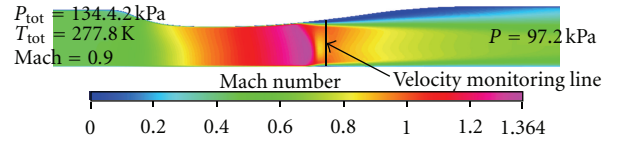


FIGURE 4: The strong shock flow configuration in Sajben nozzle.

the literature. Here, the steady state simulations are only for the strong shock case.

The two turbulence models have been tested, the widely used $k - \epsilon$ and RNG $k - \epsilon$. The size of computation grid used for simulation is in range of 0.1–0.5 mm and has been selected after careful grid sensitivity study. The strong shock case is characterized by the steady inlet-to-outlet pressure ratio given by $p_{\text{exit}}/p_{0,\text{inlet}} = 0.72$, and the compressible flow features are more dominant than the weak shock case. For the strong shock case, measurements show that the shock is located at approximately 2.5 throat heights into the downstream region of the throat (Figure 4). Figure 5(a) shows the simulated and measured pressure distributions along the top wall. It can be observed that there is a difference in predicted shock locations between the two turbulence models. The RNG $k - \epsilon$ model captures the shock better compared to $k - \epsilon$ model. Figure 5(b) shows the simulated and measured velocity profiles along a vertical line located slightly in the downstream region of the shock. Again, the RNG $k - \epsilon$ -based simulation predicts the velocity profile better. As the $k - \epsilon$ -model predicts the shock position further in the downstream region than measurement, the velocity at monitoring line is predicted to be in the upstream region of the shock. This results in the supersonic velocity profile, whereas the RNG $k - \epsilon$ -based simulation predicts subsonic flow along the monitor line. Also, note from Figure 5 that the negative velocities are measured and to a certain extent also better predicted by RNG $k - \epsilon$ -based simulation. This is due to the presence of recirculation region after the flow separation.

3. Flow Simulation in Presence of a Plug

The transient transonic flow in a typical diffuser geometry (Figure 6) is often adopted for high-voltage circuit breakers, in the presence of a plug. The measurements are available at given locations and for different plug positions and can be used for good CFD validation; details of measurements are

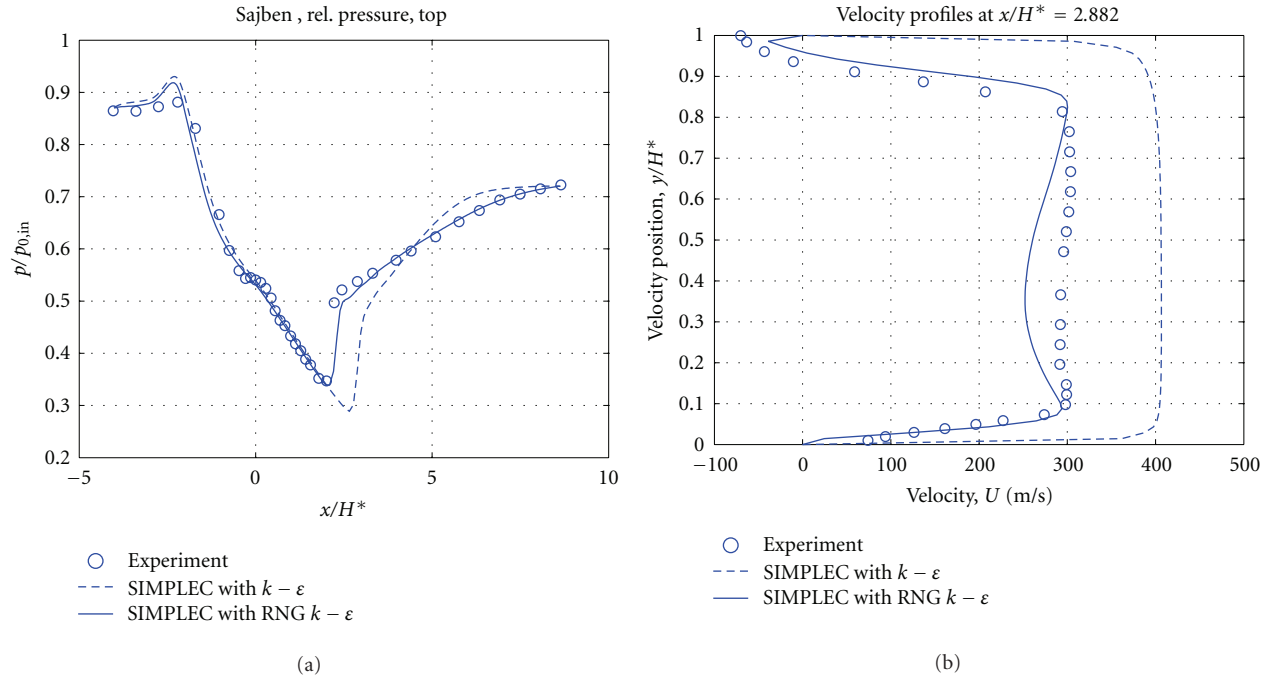


FIGURE 5: Simulated and measured (a) pressure profile along the top wall of Sajben nozzle, (b) velocity profiles along the vertical monitoring line at a slightly downstream of the vertical shock.

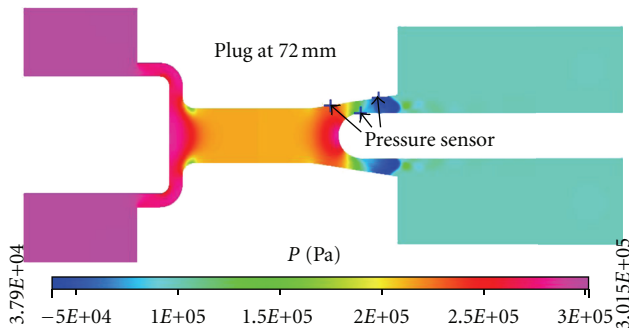


FIGURE 6: Transonic flow configuration at nozzle opening (72 mm case).

given in [5]. For the measurements, three pressure sensors were installed, two along the fixed wall in the diffuser region and the one on the plug. The chosen plug positions in experiment, respectively, represent the plug in the main nozzle area (the 42 mm case), at the nozzle opening (the 72 mm case), and at the fully open position (the 92 mm case) during the high-voltage circuit breaker operation.

The transient CFD simulations for the rising inlet pressure from 1 to 3 bars in 25 ms are performed. The compared benchmark flow simulation algorithms are the SIMPLEC-based solver and the Jameson-method-based solver with $k - \epsilon$ turbulence model. Note that the former is a pressure-correction-based non-conservative solver and the latter is based on conservative method.

Among the three different plug positions, the plug at the nozzle opening (the “72 mm” case) provides the most challenging case for the solver quality evaluations, in terms of capturing the shock. Figure 7 shows the simulated and measured pressure at three different sensor locations. It can be observed that the Jameson-method-based solver with explicit time marching shows better agreement with the measured data. There are two reasons for this. First, because the Jameson method is a conservative scheme, which in principle should have better shock capturing capability, than the non-conservative-method-based SIMPLEC scheme. Second, the Jameson method is based on explicit time marching where the time step size is limited by the sonic speed which transmits local flow information. This explicit scheme should predict better dynamic transient flow phenomena than the SIMPLEC scheme which is based on implicit method.

It can be observed from Figure 7(b) that the SIMPLEC-scheme-based solver overestimates the supersonic flow expansion along the diffuser than real and predict the shock located farther in the downstream region. Of particular interest is the pressure on the plug (Figure 7(c)). The SIMPLEC-scheme-based solver overestimates the compressibility on the plug for lower inlet pressure.

4. Real Circuit Breaker Simulation

In this section, the comparison of two numerical algorithms (the pressure-correction-based semi-implicit SIMPLEC scheme and the density-based explicit Jameson’s method), in predicting transonic flow field configuration inside the high-voltage circuit breaker, is presented. The real

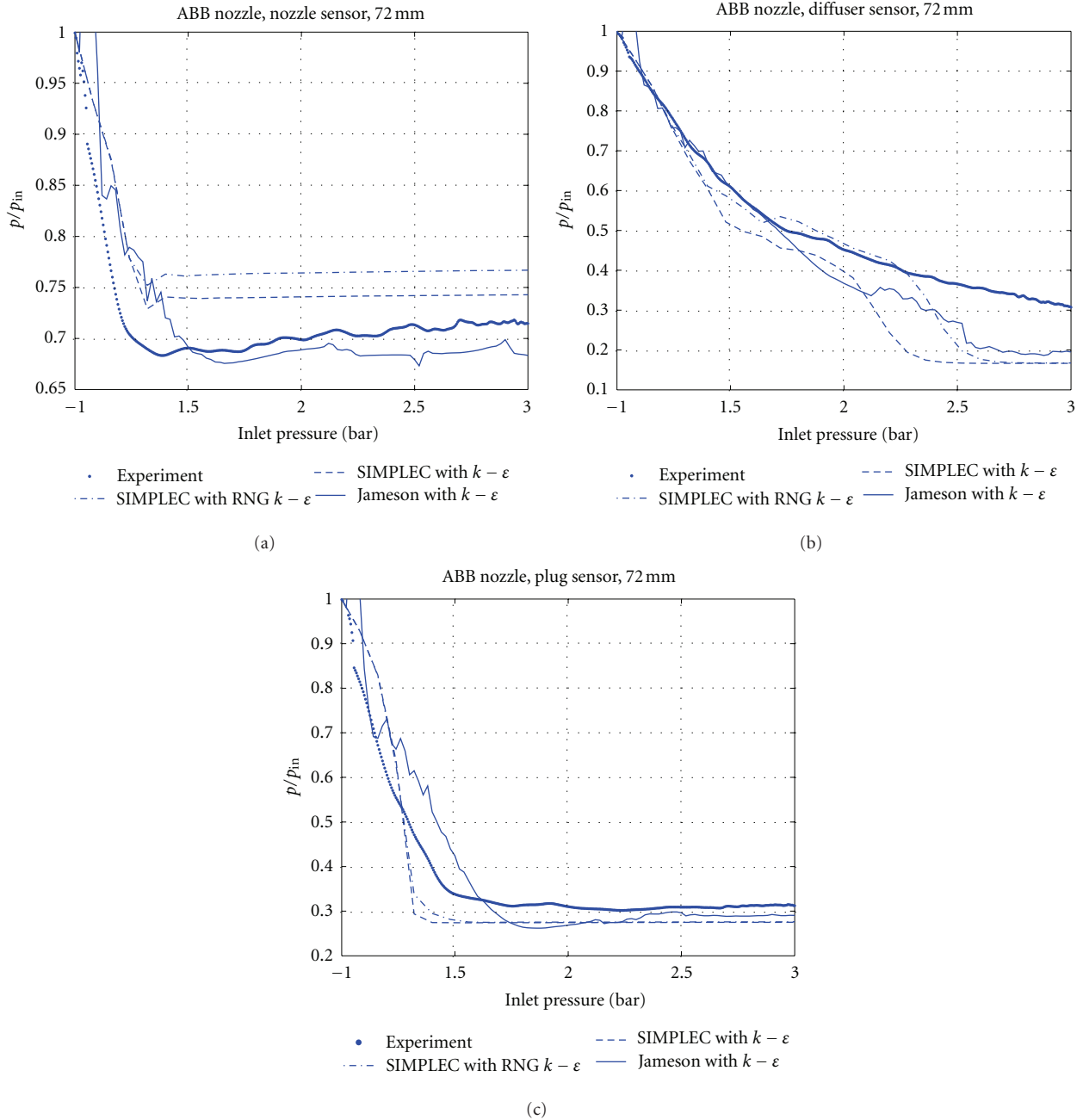


FIGURE 7: Comparison of the predicted pressure ratio and measurement for two different turbulence model.

breaker geometry as shown in Figure 8 is used. For the validation, a no-load switching test has been performed, and the transient pressure data at three different locations in the transonic diffuser area have been monitored.

Figure 8 shows the sketch of the main flow region and locations of pressure sensors of the tested high-voltage circuit breaker. The pressure build-up measurement at the heating chamber has been applied as the inflow boundary of the flow region. The initial filling pressure is set to be 6 bar. As the heating volume compresses, the inlet pressure reaches up to 12 bar, and the big difference between the inflow pressure and the filling pressure generates transonic flow in

the diffuser area where the pressure sensors are implemented. Figure 9 shows the comparison of the simulated and the measured pressure data at different sensor locations. For the simulations, the second-order space accuracy and the first-order time accuracy have been adopted for the SIMPLEC-based solver. The time steps are chosen to be small enough to guarantee that the flow solver shows consistent transient behavior. In order to simulate the moving contacts, a deformable mesh has been used. Note that the simulated pressure curve at time zero does not start with the filling pressure, 6 bar. The reason for this is that the deformable mesh option in the used solver does not allow completely

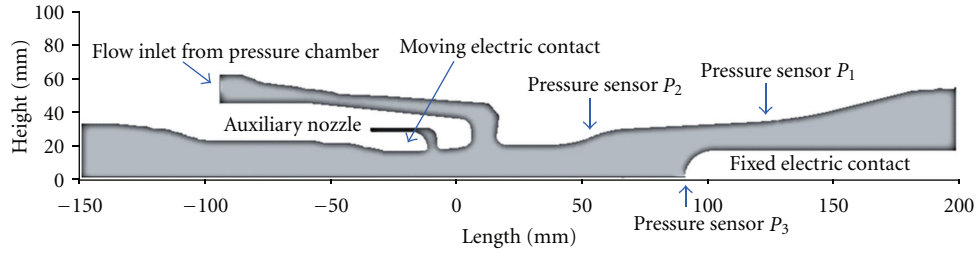


FIGURE 8: The illustrative sketch of the main flow region of the tested high-voltage circuit breaker and the locations of the three pressure sensors.

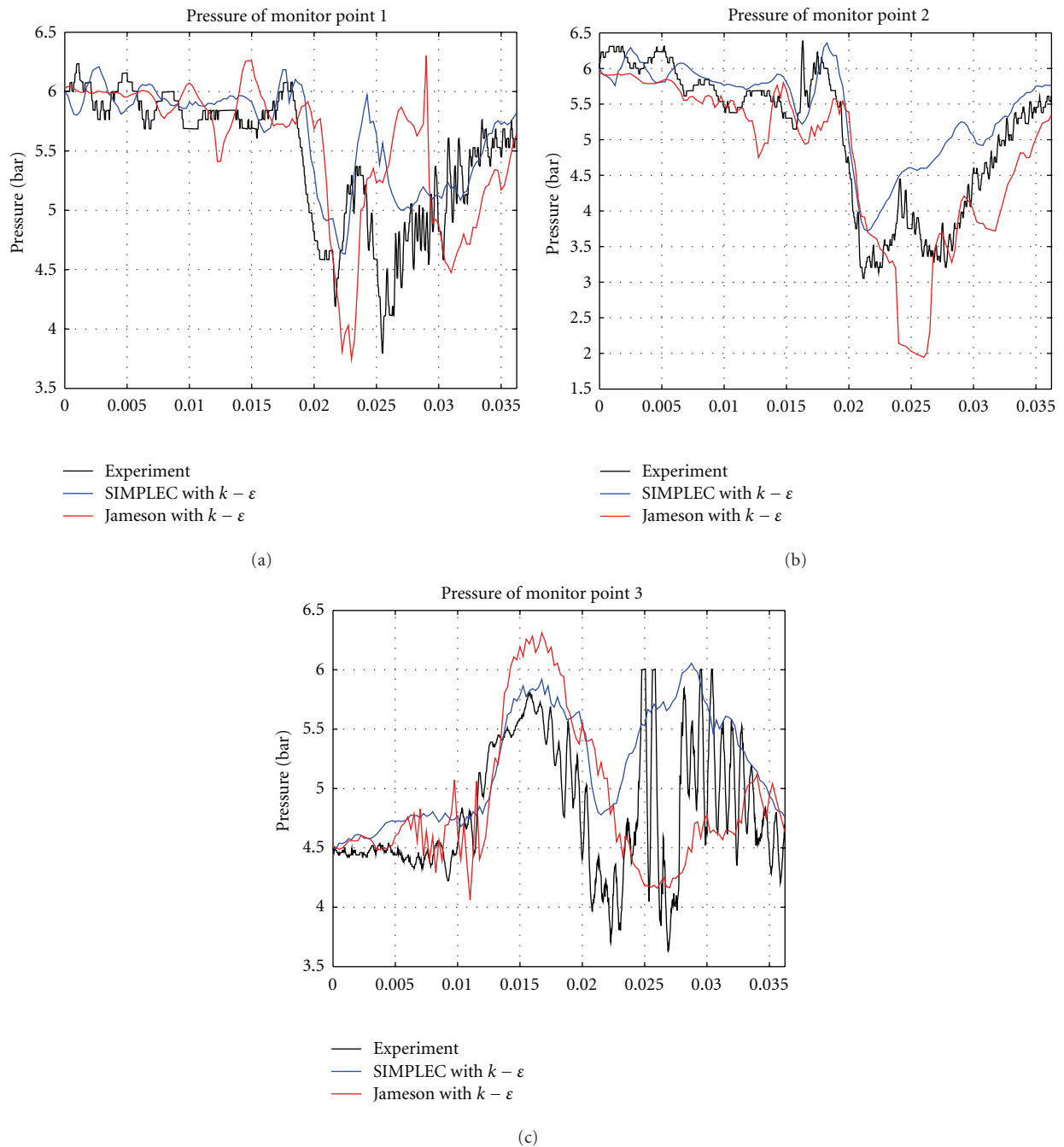


FIGURE 9: Comparison of measurement (black) with simulation with Jameson method (blue) and SIMPLEC (red) for three different monitor points.

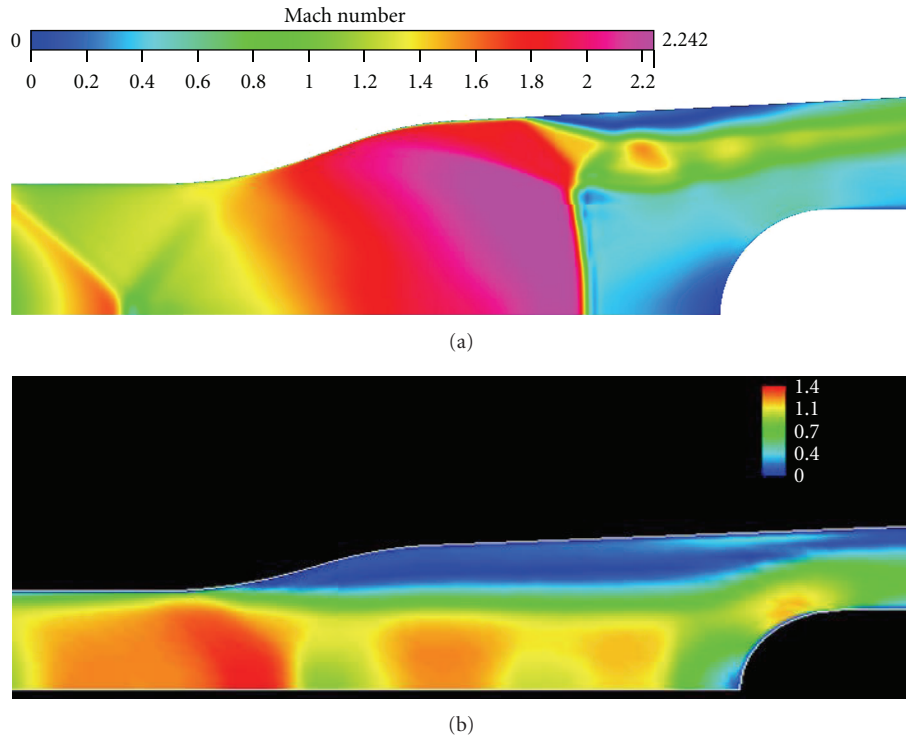


FIGURE 10: Comparison of simulated Mach number configurations at $t = 24$ ms with algorithm of (a) SIMPLEC (b) Jameson.

closed contact position. Therefore, the initial configuration of the transient simulation has been calculated by a steady simulation for a very small contact opening and a very small pressure build-up at the inlet.

For the CFD simulations with the algorithm based on Jameson's method, the explicit Range-Kutta time marching with the second-order accuracy has been used. The space resolution is the standard 2nd-order central difference. In order to stabilize the shock discontinuities, an artificial damping has been applied where necessary. For the moving contacts, CHIMERA mesh is used such that the transient simulation can start from the completely closed contact positions; see [5] for details of the simulation method.

Though not shown in Figure 9, we observed that the SIMPLEC-based simulation well predicts the pressure values in the region beginning from the pressure inlet up to the stagnation point on the symmetry axis, where subsonic flow features dominate. However, as it is shown in Figure 9, it fails to predict the transient pressure values at the monitoring points 1, 2, and 3, both in quantitative and qualitative sense. Note that compressible flow features dominate at these monitoring points. On the other hand, Figure 9 shows that the density-based explicit solver captures the qualitatively correct transient flow behavior, though it shows a deviation from the measured quantitative pressure value at each monitoring point. The reason why it captures the transient dynamics better than the semi-implicit SIMPLEC method is that it resolves the sonic wave which transports the flow information, by restricting time step sizes small enough to obey CFL constraints. The big difference between the two

tested algorithms is manifested at time near $t = 24$ ms. The simulated Mach number configurations at $t = 24$ ms are compared in Figure 10.

There is a qualitative difference in transonic nozzle flow features between the two solvers. The SIMPLEC-method-based solver predicts the supersonic flow attached to the diffuser wall. As the diffuser cross-section area increases, the supersonic flow expands fully before it is terminated by the vertical shock in front of the plug tip. The sensors 1 and 2 are located in the upstream of the shock, where the pressure of the fully expanded supersonic flow is very much low. This is why the SIMPLEC-based solver underestimates the pressure at sensor points 1 and 2. The simulated supersonic flow predicted more expanded supersonic flow with much stronger vertical shock than real. The simulated overexpanded supersonic flow in the diffuser also has an influence on the calculated pressure at the stagnation point just in front of the plug. The SIMPLEC-based simulation underestimates the pressure value at sensor 3, because it suffers from the higher total pressure loss across the strong shock.

On the other hand, the Jameson-method-based solver predicts the supersonic flow which is already detached at the diffuser inlet. The detached jet flow forms a shock bottle system. Sensors 1 and 2 are definitely located at the downstream region after the vertical shock, where the flow is subsonic. The overexpanded subsonic flow then results in higher pressure. This is why the Jameson-method-based solver slightly over-estimates the pressure at sensor points 1 and 2.

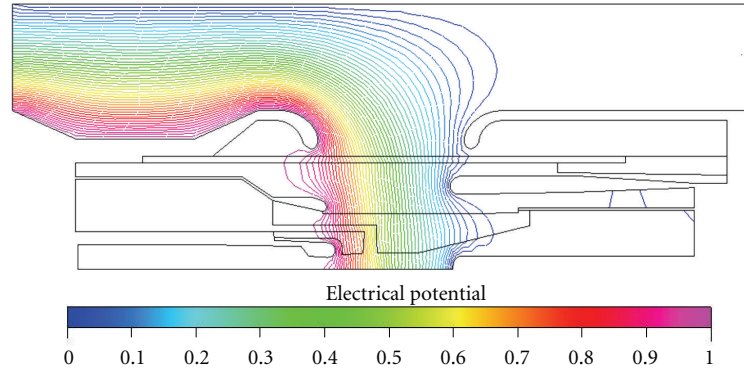


FIGURE 11: Typical electrostatic field distribution for a chosen contact separation.

To summarize, the Jameson-method-based CFD simulation shows better shock capturing capability than the SIMPLEC-method-based solver. The transient shock movement is also better captured by the Jameson-method-based explicit solver, since the semi-implicit SIMPLEC-based solver intrinsically introduces additional numerical viscosity.

5. Influence of Solver Algorithm on Breakdown Voltage Prediction

The prediction of breakdown voltages in capacitive switching tests of high-voltage circuit breaker is a challenging engineering issue. The breakdown voltage is estimated from the known dielectric breakdown criterion in SF₆ gas, which is based on inputs from local flow and electrostatic field configurations. Particularly, the dielectric breakdown voltage U_{bd} is

$$U_{bd} = \left[C \frac{\rho}{\hat{E}} \right]_{\min}. \quad (2)$$

Here, ρ is the local flow density, and \hat{E} is the local electric field strength when a unit voltage is applied to both contacts. The coefficient C contains the information of influences from the surface roughness, area, and voltage frequency on breakdown voltage. The measurements from cold dielectric experiments determine the contents of C . From (2), for the reliable prediction of dielectric breakdown voltage, it is required to know local distribution of flow and electrostatic fields in the breaking chamber for given nozzle and diffuser geometry.

The electrostatic potential can be calculated by solving the following elliptic equation:

$$\nabla \cdot (\epsilon \nabla \phi) = 0. \quad (3)$$

Here, ϵ is the permittivity of the material, and the field strength \vec{E} is calculated by $\vec{E} = -\nabla \phi$. Equation (2) can be solved either by a finite element or finite volume methods, with a high accuracy. Figure 11 shows typical equipotential lines of the electrical field E for a chosen contact separation. While the electric fields can be accurately computed with most of the commercial tools, the prediction of the flow fields poses a more difficult problem.

The breakdown voltages of two capacitive switching test duties of real high-voltage circuit breaker have been estimated. The local flow density is calculated by two different solver algorithms. The electrostatic field is calculated by a third electromagnetic simulation tool. The value of density to electrical field ratio in (2) is estimated by the superposition of the electric field and gas density field distribution as function of time. Figure 12 shows the comparison of the simulated breakdown voltages with the measurements. It can be observed that the CFD calculation with the SIMPLEC method underestimates the breakdown voltage by 10%. This is due to the overestimation of the compressibility of the flow, which expands the supersonic flow at the diffuser area than in reality. This trend is amplified at nozzle opening. Note that the dielectrically most critical point in general is on the plug surface which is located in the diffuser region. On the other hand, the Jameson-method-based CFD tool shows smaller numerical uncertainty. This is mainly due to more precise capturing of the nonlinear flow structure, since the solver controls the conservation law better than the SIMPLEC method.

6. Conclusions

The conservative-density-based explicit flow solver algorithm is superior to SIMPLEC-pressure-correction-method-based CFD solver, in predicting dielectric breakdown voltages in capacitive switching test duties of high-voltage circuit breakers with over-critical pressure ratio.

The SIMPLEC-based simulation shows higher numerical uncertainties than the density-based one, in predicting highly dynamic transonic flow configuration inside the circuit breaker diffuser. The main reason is that while the SIMPLEC scheme is optimal in simulating steady incompressible flow dynamics, it often fails to capture correct nonlinear wave structure of the compressible flow. However, the advantage of SIMPLEC method is that it allows larger computational time step with better numerical stability. But, it diffuses fine time scale transient dynamics away, even if the solution is well converged.

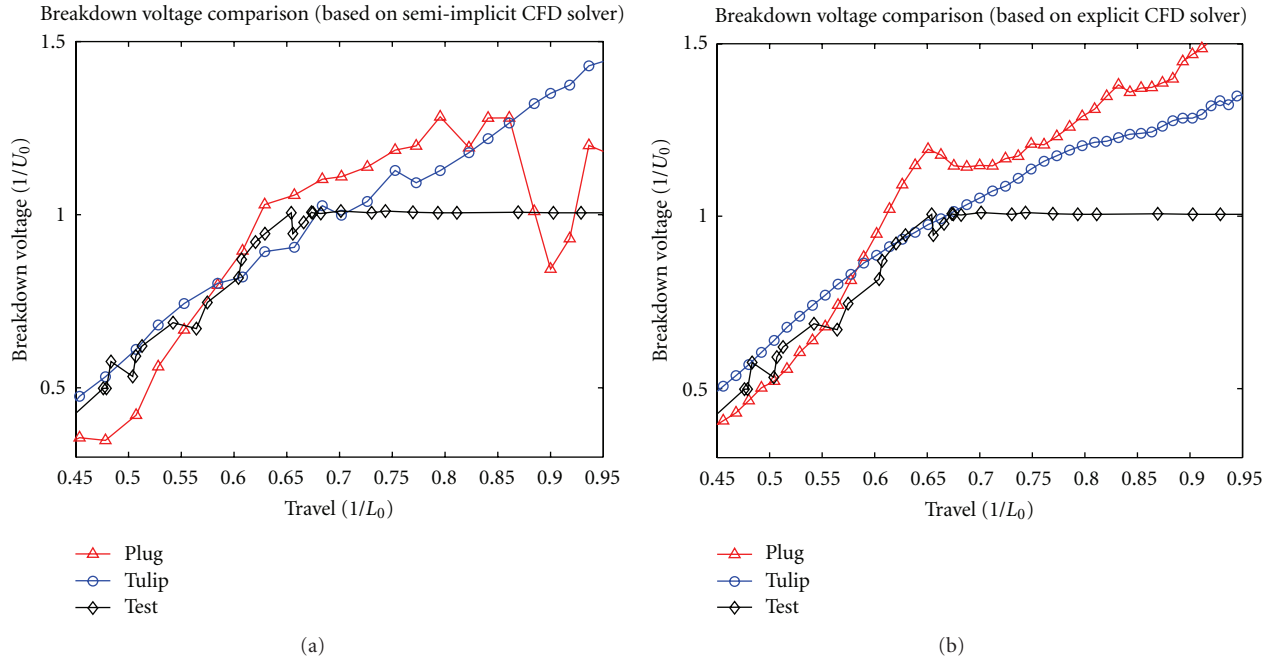


FIGURE 12: Comparison of the measured breakdown voltages with simulation with (a) SIMPLEC (b) Jameson algorithm.

There is significant influence of turbulence model. The shock-induced flow separation has been shown to be governed by the detailed modeling of the shock and the boundary layer interaction. The modeling issues should be further investigated and the optimal modeling concept should be accordingly identified.

The presented study shows that adopting optimal CFD algorithm for dynamic transonic flow simulation inside the breaking chamber of high-voltage circuit breaker can substantially improve the prediction power of dielectric breakdown voltage in capacitive switching of high-voltage circuit breaker. The conservative-density-based solver with advanced turbulence modeling such as RNG $k - \varepsilon$ is recommended.

References

- [1] A. Jameson, W. Schmidt, and E. Turkel, "Numerical solutions of the Euler equations by finite volume methods using Rung-Kutta time—stepping schemes," in *Proceedings of the 14th Fluid and Plasma Dynamic Conference*, Palo Alto, Calif, USA, June 1981.
- [2] J. P. Van Doormaal and G. D. Raithby, "Enhancements of the SIMPLE method for predicting incompressible fluid flows," *Numerical Heat Transfer*, vol. 7, no. 2, pp. 147–163, 1984.
- [3] R. Courant, K. Friedrichs, and H. Lewy, "Über die partiellen Differenzgleichungen der mathematischen Physik," *Mathematische Annalen*, vol. 100, no. 1, pp. 32–74, 1928.
- [4] M. Sajben, T. J. Bogar, and J. C. Kroutil, "Forced oscillation experiments in supercritical diffuser flows," *AIAA Journal*, vol. 22, no. 4, pp. 465–474, 1984.
- [5] X. Ye, K. Muller, and J. Stechbarth, "Progress in the flow simulation of high voltage circuit breakers," *Finite Volumes for Complex Applications II*, 1998.

Research Article

The Flow Pattern in Single and Multiple Submerged Channels with Gas Evolution at the Electrodes

A. Alexiadis,¹ M. P. Dudukovic,² P. Ramachandran,² A. Cornell,¹
J. Wanngård,³ and A. Bokkers⁴

¹Department of Chemical Engineering and Technology, Applied Electrochemistry, Royal Institute of Technology, KTH, 100 44 Stockholm, Sweden

²Department of Energy, Environmental and Chemical Engineering, Washington University in St. Louis, One Brookings Drive, Campus Box 1180, St. Louis, MO 63130, USA

³Process R&D, Technology and Engineering, Eka Chemicals, 445 80 Bohus, Sweden

⁴Research, Development & Innovation, Akzo Nobel Chemicals bv, Zutphenseweg 10, P.O. Box 10, 7400 AA Deventer, The Netherlands

Correspondence should be addressed to A. Alexiadis, alessioa@kth.se

Received 22 November 2011; Accepted 30 January 2012

Academic Editor: Sreepriya Vedantam

Copyright © 2012 A. Alexiadis et al. This is an open access article distributed under the Creative Commons Attribution License, which permits unrestricted use, distribution, and reproduction in any medium, provided the original work is properly cited.

We show that the gas-liquid flow pattern in a single gas-evolving electrochemical channel can be remarkably different from the flow pattern in multiple submerged gas-evolving electrochemical channels. This is due to the fact that in a single channel there is a higher accumulation of small bubbles and these can considerably affect the liquid velocity pattern which in turn may affect the performance of a cell. Since experimental work is often carried out in single channels, while industrial applications almost always involve multiple channels, this study provides insight into the factors that affect the flow pattern in each situation and establishes the basis for relating the behavior of single- and multiple-channel devices.

1. Introduction

Many industrial processes are based on electrochemistry and it is anticipated that, if their efficiency can be improved, they will find increased use in new green technologies. Often, however, high power consumption is associated with these processes and most of the production cost is due to electrical energy. Thus, every advance in optimization and improvement of these processes can lead to significant energy conservation and cost reduction. This provides the motivation for many experimental [1–3] and theoretical [4–6] studies in the field. In many cases (e.g., chlorate production, hypochlorite generation, or perchlorate electrolysis) the industrial scale electrochemical cell consists of a series of channels immersed in a bath of electrolyte. A gas (e.g., hydrogen or oxygen), which is the byproduct of the reaction, is often generated at the electrode surfaces. A generic representation of such industrial scale process is sketched in Figure 1 and contains a series (generally of the order of hundreds) of parallel channels (gaps) between

electrode plates immersed in a large container (reactor) that contains the electrolytes. The electrodes are the walls of the channels in the reactor. Electrochemically evolved gas is produced at the electrodes in the dissolved state; small bubble nucleation starts at the imperfections of the electrode surface and then these bubbles depart into the surrounding, highly supersaturated, electrolyte [7, 8]. The generated bubbles are responsible for the gas-lift effect that promotes global circulation of the liquid in the cell. They also enhance local mixing that helps in continuously refreshing the electrolyte in the vicinity of the electrodes.

In contrast, in the laboratory, experiments are often carried out in a single-channel configuration. The implicit assumption is that, if the single-channel is geometrically similar to the ones in a multiple-channel cell, the observed variables of interest will be approximately the same as in all the channels of the larger system. We find that this assumption, under circumstances frequently encountered in practice, is not necessarily valid and the velocity patterns in the single-channel and in the multichannel configuration

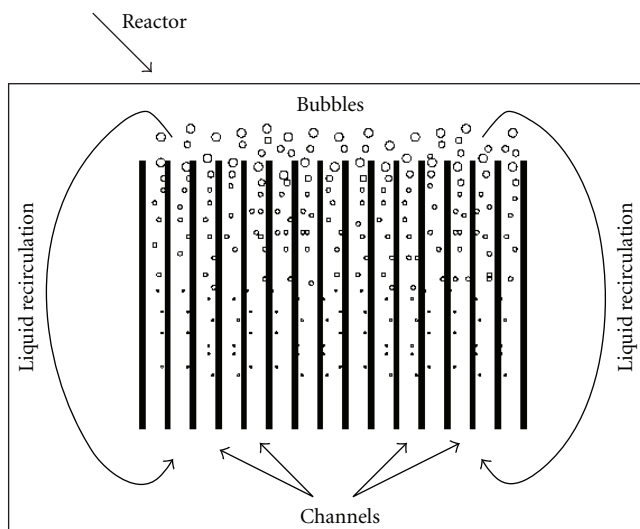


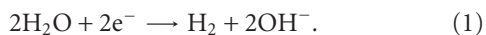
FIGURE 1: Schematic representation of an electrochemical process. A series of plates (the electrodes) are immersed in a larger container (the reactor).

can be significantly different. The extent of the difference depends to a large extent on the current density employed which governs the amount of gas generated and on the coalescence properties of the solution. Above a certain critical current density, in a noncoalescing system, where the bubbles stay small, the flow in the single-channel exhibits a transition from steady laminar to pseudoturbulent regime [9] characterized by vortices and recirculation regions. In the multichannel geometry, on the other hand, the flow does not experience this transition and remains in what we call “quasi-steady” regime. As discussed later on, this difference depends on the fact that the multichannel geometry is usually of the submerged type. The channels, in fact, are completely immersed in the liquid and, therefore, there is a common liquid region above the channels. The calculations performed in this study refer to the specific case of chlorate cells, but similar conclusions can be drawn for different systems [9].

2. The Multichannel and the Single-Channel Systems

We compare the flow pattern, calculated by means of CFD modeling, in the case of the single-channel (Geometry 1 depicted on the left of Figure 2) and the triple-channel (Geometry 2 shown on the right of Figure 2). These channels are sometimes called “gaps” in electrochemical applications.

In both cases, hydrogen is produced at the cathode according to the reaction



Oxygen or any other gas production at the anode is ignored. The volume of O_2 produced in chlorate processes is, in fact, considerably smaller (2–4%) than that of H_2 , while the chlorine produced reacts rapidly with water and is not noticeable as bubbles [3].

2.1. Single-Channel (Geometry 1). In Figure 2 (left), the geometrical configuration of the single-channel is shown. The distance between the two electrodes is $h = 3$ mm, the channel height $L = 90$ mm. The cathode is located on the right wall in the L section at $x = h$, while the anode is located at $x = 0$. An inert section of length $A = 20$ mm is placed between the hydrogen evolving wall and the top. This inert section is often present in laboratory devices but it may not be present in some industrial applications. Our objective is to identify the parameters that determine the flow filed in the active part of the channel, that is, the part in which the wall at $x = h$ is an active cathode. Some additional simulations with other channel lengths (50, 80, and 100 mm) or with a supplementary inert section at the bottom of the channel (10 mm) were carried out in order to verify that the flow pattern in the active part of the single-channel is not affected by these parameters. We consider only a batch electrochemical cell that contains a confined finite volume of liquid. The bottom of the channel is a solid wall and the top corresponds to the liquid-free surface.

2.2. Triple-Channel (Geometry 2). Three channels in parallel joined together by a common bottom and top section (see Figure 2 on the right) are used to represent a simplified version of the multichannel geometry. In this case, the three gaps have the same width $h = 3$ mm and a length L of 90 mm. The width of each wall is 1 mm. The length of the upper and bottom parts are $A = 20$ mm and $B = 10$ mm, respectively. The cathode, where hydrogen is produced according to (1) is located at $x = 7$ mm (two channel widths plus one wall thickness), The whole system is enclosed within an external container, which represents the reactor. The reactor is open at the top. Thus, the lateral and bottom borders are walls, while the top represents the free-liquid surface.

In both cases, the motion of the liquid is exclusively due to the momentum exchange with the rising bubbles. We assume that the physical properties of the gas are those of hydrogen, while the liquid is represented by a highly concentrated aqueous solution (see numerical values for density and viscosity in Section 5). These conditions are chosen having in mind the specific case of chlorate cells, but they can be easily changed to reflect another system. The current density at the electrodes is, in both cases, fixed to $i = 500$ A/m². Additionally, some simulations at lower and higher current densities are also carried out in order to better illustrate the reasons for the differences in the flow patterns observed in Geometry 1 and Geometry 2 as discussed later on. The current density is related to the gas production at the electrode, by Faraday’s law

$$j_{\text{gas}} = \frac{iM}{zF\rho_g}, \quad (2)$$

where i (A/m²) is the current density, M is the hydrogen molecular mass ($2 \cdot 10^{-3}$ kg mol⁻¹), z is the number of electrons involved in the electrochemical reaction ($z = 2$, according to (1)), F is the Faraday constant, ρ_g (kg m⁻³) is the gas density, and j_{gas} (m/s) is the gas superficial velocity at the electrode. The reduction of current density at

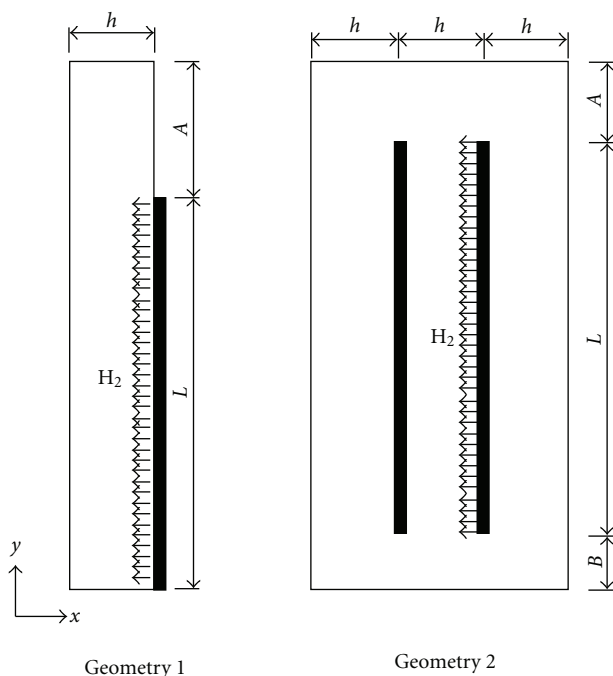


FIGURE 2: Single-channel geometry (Geometry 1) and triple-channel geometry (Geometry 2).

the electrode due to the void fraction, sometimes described by the Bruggemann equation [10], is here ignored.

Some supplementary simulations in Geometry 2 with $L = 50$ mm and an inert section of 20 mm (the same as in Geometry 1) were carried out in order to verify that the flow pattern in the multi-channel is not affected by these parameters. For simplicity, H_2 is generated only from one side of the electrode (Figure 2 on the right). Another simulation was carried out with H_2 produced on both sides. The flow in the third channel and on the top of the reactor is clearly different in this case, but the conclusions concerning the transition between the two flow patterns (Section 5.3) remain the same. We chose to discuss an electrode with only one active side on which hydrogen is produced because, in this way, a more direct comparison with the single-channel is possible. In general, when certain simplifications in the geometry or in the model were possible, we always choose the option that would reduce the difference between the flow patterns in the two geometries. In this way, we have more confidence that the observed differences between the computed flow patterns are real.

3. Modeling

The model for the flow in the gap is based on the following assumptions (details are given in [9]). The fluid is incompressible and Newtonian. The flow field is assumed to be two-dimensional. Temperature and all the physical properties of the channel material and fluid are constant. The bubble diameter is small and the bubbles can be treated as solid spherical particles. (We have already shown that small bubbles are the cause of flow regime transition [9] in a single-channel and in this study we examine their effect

in the multiple channel geometry. The effect of coalescence is the subject of a separate study). In the channel, there is no bubble coalescence or breakup and the bubble size can be considered approximately constant. This last statement deserves additional clarification because it does not always represent reality well. In the region near the cathode, where the void fraction is higher, a variable degree of coalescence is expected. The extent of this coalescence strongly depends on the types of the electrolytes dissolved in water. Ample experimental evidence exists that certain anion/cation couples prevent bubble coalescence in water solutions [11]. Thus, according to the type, distribution, and interaction of the various ions in an electrochemical system, coalescence can be suppressed considerably, partly or not at all. In chlorate cells experiments [2, 3], for instance, it was observed that a certain number of bubbles do not coalesce and maintain their initial small size. In this case, an average bubble diameter of the order of 0.01 mm is a reasonable approximation and some CFD studies [7] adopted this value for their calculations. One can account for the bubble coalescence in the future, but our focus here is to determine whether differences can occur between single- and multichannel flows. Our previous studies [9] indicate that presence of a sufficient number of small bubbles is needed to trigger transition in flow regime in single-channels and we investigate here whether this is the case in multiple-channels also. Thus, the bubble size in our simulations is arbitrarily fixed to 0.01 mm. The gas production at the electrode is determined directly by (2).

The velocity field is computed by solving the continuity and Navier-Stokes equations for a biphasic flow consisting of a dispersed and continuous phase according to the so-called Euler-Euler model. In this approach, both the continuous and dispersed phases are considered to be interpenetrating

continua and the macroscopic description of both phases is derived by averaging the conservation equations for each phase (see, e.g., [12]).

Dispersed phase:

$$\frac{\partial \alpha \rho_g}{\partial t} + \nabla \cdot (\alpha \rho_g \mathbf{v}_g) = 0, \quad (3)$$

$$\begin{aligned} \frac{\partial \alpha \rho_g \mathbf{v}_g}{\partial t} + \mathbf{v}_g \cdot \nabla (\alpha \rho_g \mathbf{v}_g) &= \alpha (\mathbf{g} \rho_g - \nabla p) \\ + \nabla \cdot [\alpha \mu_g (\nabla \mathbf{v}_g + \nabla \mathbf{v}_g^T)] &- \mathbf{M}. \end{aligned} \quad (4)$$

Continuous phase:

$$\frac{\partial (1 - \alpha) \rho_\ell}{\partial t} + \nabla \cdot ((1 - \alpha) \rho_\ell \mathbf{v}_\ell) = 0, \quad (5)$$

$$\begin{aligned} \frac{\partial (1 - \alpha) \rho_\ell \mathbf{v}_\ell}{\partial t} + \mathbf{v}_\ell \cdot \nabla \mathbf{v}_\ell [(1 - \alpha) \rho_\ell] \\ = (1 - \alpha) (\mathbf{g} \rho_\ell - \nabla p) \\ + \nabla \cdot [(1 - \alpha) \mu_\ell (\nabla \mathbf{v}_\ell + \nabla \mathbf{v}_\ell^T)] + \mathbf{M}. \end{aligned} \quad (6)$$

The last term \mathbf{M} in (4) and (6) represents the interfacial momentum transfer, which is usually divided into several different parts each contributing drag, lift, virtual mass forces, interfacial pressure, and so forth (see, e.g., [13]). In our case, only drag is considered (Wen and Yu model [14]). The effect of the lift force was evaluated [9] and resulted in little or no difference in the flow pattern. The possible presence of a slip velocity at the cathode has been discussed in [15]. The effect of bubble collision, which potentially could lead to a more spread layer of gas above the electrode, was here not considered. According to our previous investigations, however, (see [9, 16]) the thickness of this layer should not play a major role on the stability of the flow and, therefore, on the transition between the quasi-steady and the pseudoturbulent regime.

4. Boundary Conditions

Most of the boundaries in both Geometry 1 and Geometry 2 are simply solid walls and at these no slip boundary conditions are assigned for gas and liquid velocities. The only exceptions are the boundary conditions for the gas-phase at the cathode and at the top which represents the free liquid surface. These boundary conditions are hereafter briefly discussed; more details are given in [9, 16].

4.1. Cathode (Gas-Phase). Concerning the liquid phase, the cathode can be viewed as a wall with no-slip conditions. This is a reasonable approximation, although, in this case, not as obvious as it might appear at first sight (more detailed discussion is given in [9]). Concerning the gas, the overall gas mass flux (i.e., the product of the gas velocity and density) at the electrode is known from (2). It is also known that

$$j_{\text{gas}} = \alpha_E u_E, \quad (7)$$

but the values of α_E and u_E are not known separately. The evaluation of both α_E and u_E at the boundary is a recurrent

issue in the Euler-Euler model. In our previous works [9, 15, 16] we showed that the void fraction at the electrode plays a role only in a region very close to the electrode, while the flow and voidage pattern in the rest of the channel are left practically unaffected by the choice of α_E and u_E , provided that their product gives the correct value of j_{gas} . The value of $\alpha_E = 0.5$ was used for numerical efficiency while the value of u_E is calculated from (7). (See [9, 15] for the sensitivity of the results to these parameters.)

4.2. Free-Liquid Surface (Top). At the top free surface, the pressure is always fixed and a portion of the gas, as dictated by the continuity equation, is allowed to escape. Mathematically, this means that the axial gradients of both the gas velocity and the void fraction are set to zero. Concerning the continuous phase, the top is a free-slip surface, as it should be in the case of a gas-liquid interface. In one of our previous works [9], we tested various types of boundary conditions commonly employed in CFD studies at the top of bubble columns or air-lift reactors. We found that, if a long enough section A (see Geometry 1 in Figure 2) is employed the differences in flow pattern in the electrochemically active section L are minimal. For each of the above boundary condition tested at the free surface the ascending liquid “turns around” at the free surface once it reaches the top. This behavior is expected on physical grounds since the liquid cannot escape the system and, thus, it must recirculate at the top. This creates, in the single-channel, a recirculation cell, which, as explained later, is the main reason for the different behavior of the flow in Geometry 1 and Geometry 2.

5. Results and Discussion

A number of simulations at $\mu_\ell = 3 \cdot 10^{-3} \text{ kg m}^{-1} \text{ s}^{-1}$, $\mu_g = 8.76 \cdot 10^{-6} \text{ kg m}^{-1} \text{ s}^{-1}$, $\rho_\ell = 1500 \text{ kg m}^{-3}$, $\rho_g = 0.07 \text{ kg m}^{-3}$, $d = 10^{-5} \text{ m}$, $z = 2$, $M = 2 \cdot 10^{-3} \text{ kg mol}^{-1}$, $i = 500 \text{ A m}^{-2}$, and $h = 3 \cdot 10^{-3} \text{ m}$ were carried out. As already mentioned, the numerical values were chosen having in mind the specific case of a chlorate cell, but the results can be extended to other electrochemical applications. The mesh used is a structured rectangular mesh. It was found [9] that a mesh with a characteristic size of $0.1 \times 0.1 \text{ mm}$, except for the last three cells close to the electrode, which are further divided into 15 smaller cells, is appropriate. Grid independence of the results was checked [9]. The time steps were assumed variable in order to assure a maximum Courant number smaller than 0.5. The overall simulated time was 80s for both configurations. Time averages were computed considering times from 40s to 80s, after verifying that steady state (in statistical sense) is reached. The OpenFOAM (open field operation and manipulation) CFD Toolbox was used to solve (2)–(5) and relevant boundary conditions (see [9] for other numerical details). As already stated, all the physical properties (gas and liquid densities and viscosities, bubble size, etc.), operational variables (current density, wall void fraction, etc.) and numerical parameters (mesh structure and characteristic size, strategy for determining the variable time step, etc.) are the same in the two cases. The only

significant difference is, therefore, the presence of only one gap instead of three and the presence of the external reactor volume in Geometry 2. In the rest of the article, we show that this difference, alone, is responsible for a completely different flow pattern in the system. The interested reader is referred to our previous publications (e.g., [9, 15, 16]) for (i) the consequences of different values of μ_e , ρ_e , d , i , h on the results, (ii) the sensitivity of the flow to the boundary conditions, (iii) the discussion concerning drag and lift coefficients, (iv) a more extensive analysis of the transition between quasi-steady and pseudo-turbulent regimes in a single-channel, (v) grid accuracy, and (vi) the numerical schemes employed.

5.1. The Flow in the Three-Channel Geometry. We begin by describing the flow pattern in the multichannel configuration, because in this configuration the resulting flow is simpler. Figure 3 (dotted line) displays the void fraction profile in the middle of the central channel active height. In the two other channels, the void fraction is considerably smaller. Most of the bubbles, in fact, are either discharged at the top or trapped in the recirculation vortices at the free surface and only a small fraction can reach the two lateral channels. Figure 3 (dotted line) shows that the gas is concentrated in a region near the gas generating electrode, where the void fraction reaches very high values. This is a frequent situation in electrochemical cells and it is known as “gas blanket” formation. The model predicts the existence of this high voidage layer, but a more detailed exploration of this layer would require a submodel at the electrode. The voidage peak should probably be located directly at the electrode and not slightly shifted by 0.03 mm as Figure 3 indicates. This shift seems to be the result of the simplifications discussed in Section 4. We already mentioned, however, that, except for this small region, the void fraction and velocity profiles in the rest of the channel are not affected by these simplifications (see [9] and [15] for details).

In Figure 4, a qualitative description of the flow in Geometry 2 is given, while, in Figure 5, the time-averaged velocity profiles calculated at various locations in the reactor are reported. The locations at which the velocities are displayed in Figure 5 are shown in Figure 4. The three channels are labeled C1, C2, and C3, while the three sections at $x = B + L$ (gap outlet), $x = B + L/2$ (gap center), and $x = B$ (gap inlet) are called S1, S2, and S3, respectively. The notation, used in Figure 4 to identify the location of the reported profiles, specifies the channel first and then the section; C2S1, for instance, means Section 1 of channel 2.

The liquid motion in the channel, schematically represented in Figure 4, is driven by the gas-lift generated at the electrode, which creates a region, close to the electrode, with high upwards velocity. The rest of the liquid in the channel (gap) reacts to this high velocity sheet by moving downwards. In the central gap, therefore, it is possible to distinguish two fluid zones which move in the opposite direction. When the liquid exits from C2, it recirculates into C1 as the negative axial liquid velocities at C1S1, C1S2, and C1S3 in Figure 5 indicate. Besides the internal recirculation in C2, the liquid at the bottom of the reactor goes preferentially into the third

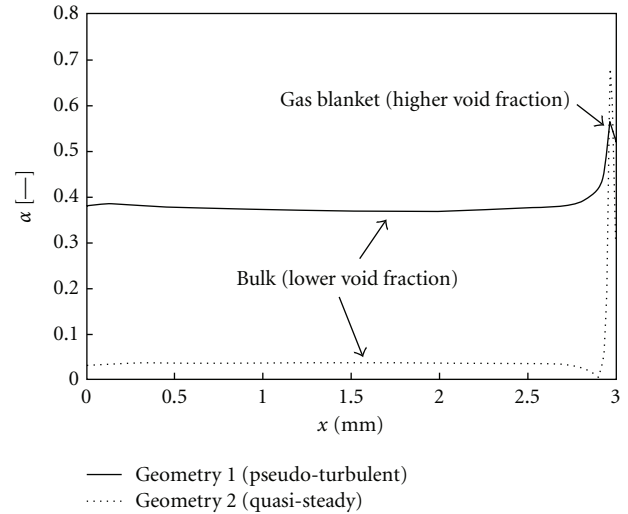


FIGURE 3: Comparison between the time averaged void fraction profile at the center of Geometry 1 (pseudo-turbulent regime, continuous line) and at in the center of the central channel (C2S2) of Geometry 2 (quasi-steady regime, dotted line).

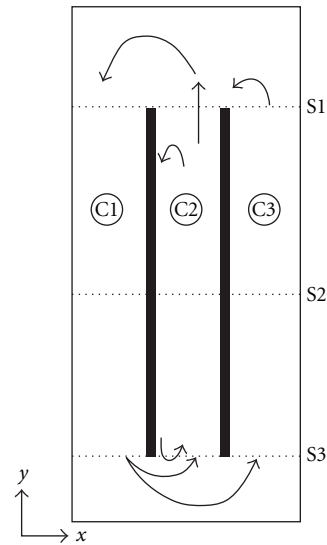


FIGURE 4: Schematic representation of the flow in Geometry 2.

channel rather than the first, as the positive velocities, in Figure 6 (C3S1, C3S2, C3S3), indicate. The fact that the flow in C3 is weakly upwards, rather than downwards as in C1, creates an overall asymmetry in the flow, which has been observed experimentally [2]. This circumstance, however, is probably of little importance for industrial configurations, where the gas is generated at the walls of every channel instead of exclusively in C2 as in this study.

5.2. The Flow in the Single-Channel Geometry. When the simulations are repeated at the same conditions for Geometry 1, the results show a completely different picture. Figure 6 is a snapshot of the instantaneous velocity pattern in Geometry 1. The flow is highly unsteady consisting of

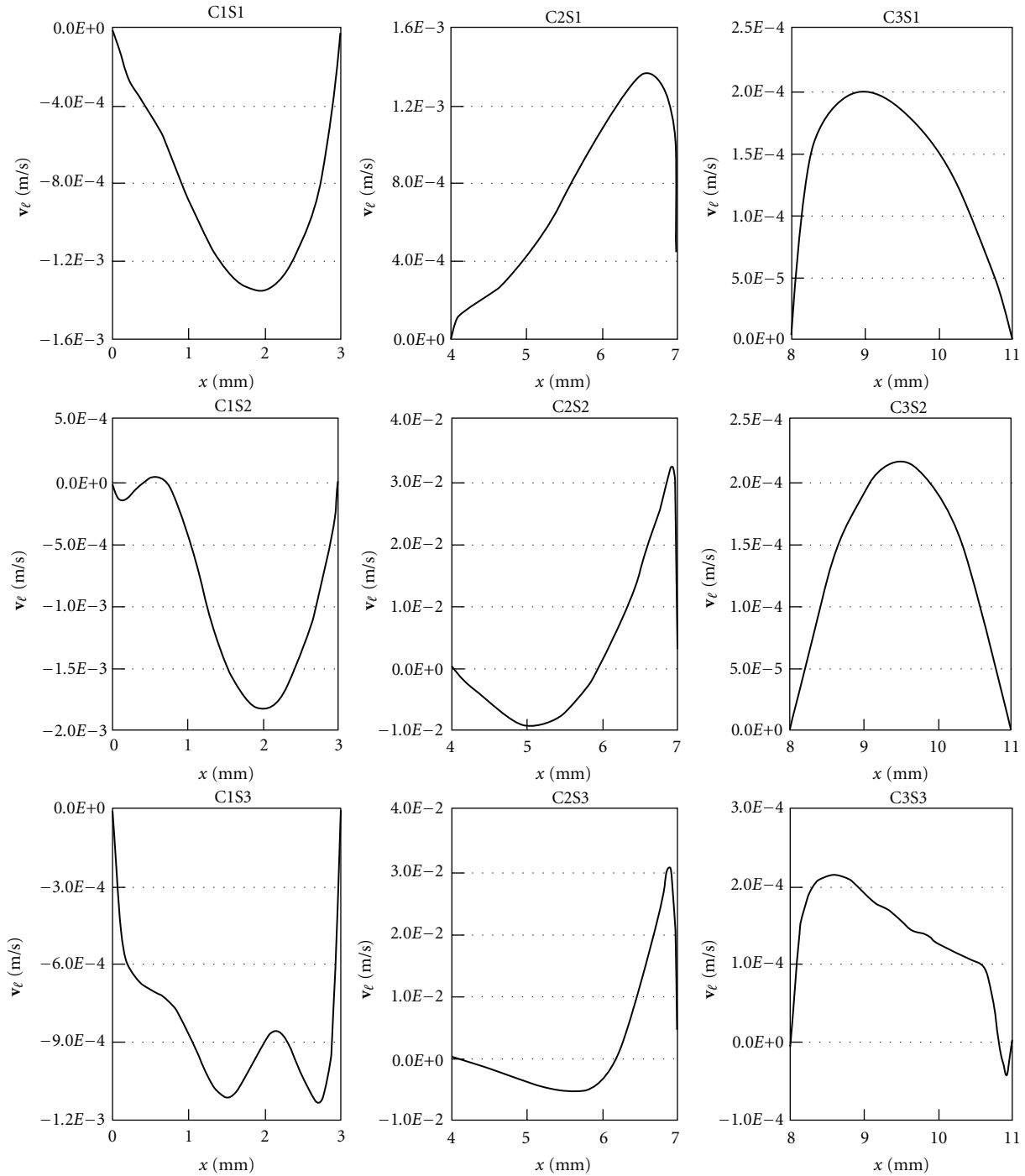


FIGURE 5: Time-averaged profiles of the vertical liquid velocity at various location of Geometry 2.

vortices and recirculation regions. There is a regular flow pattern of vortices with the same characteristic length as the channel width, whose direction of rotation alternates between clockwise and counterclockwise. It is important to note that these structures are not due to the effect of turbulence since the flow is in the laminar regime having, due to the very small bubbles' size and hydrogen density, characteristic particle Reynolds number of the order of 10^{-7} . These fluid structures increase dramatically the liquid

mixing in the gap. Figure 3 (continuous line) shows the time-averaged void fraction profile in the middle of the channel ($y = 25$ mm). If we compare, in Figure 3, the continuous (Geometry 1) and dotted (Geometry 2) curves, it is immediately clear that the more intense mixing in Geometry 1 creates a more uniform void fraction profile. In comparison to the multichannel case, the voidage peak near the electrode wall has a lower value, while the gas volume fraction increases in the bulk of the channel.

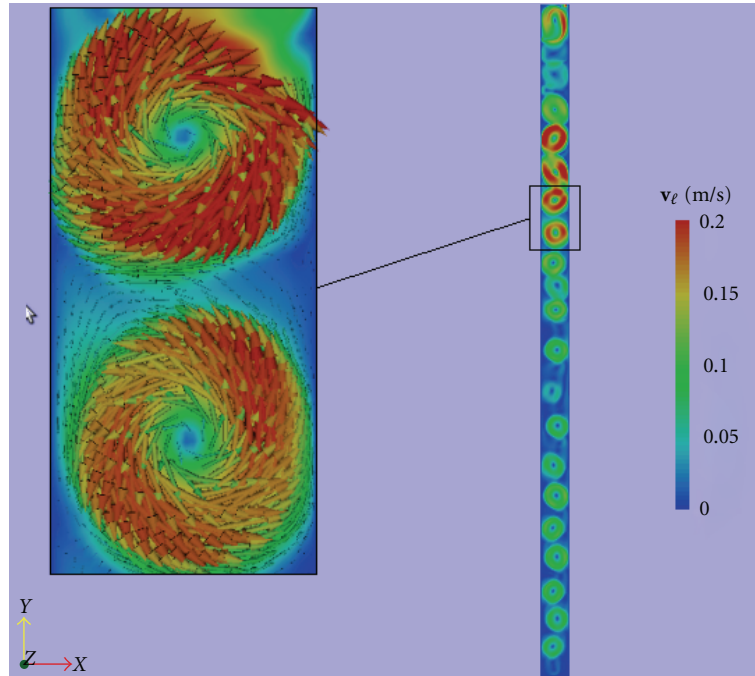


FIGURE 6: Instantaneous liquid velocity magnitude in Geometry 1 (vector representation in detail).

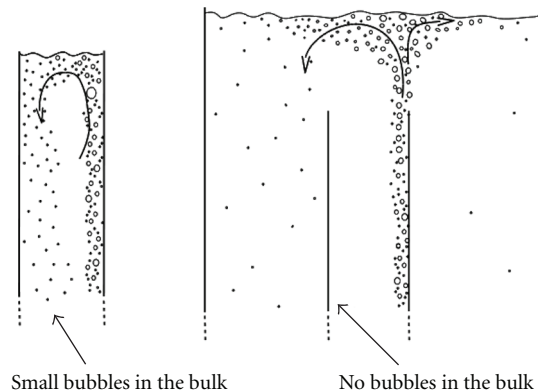


FIGURE 7: Schematic recirculation of small bubbles in single-channel (left) and multichannel (right) systems.

It is important to note that this pseudo-turbulent pattern depends on the gas-generation rate. An additional series of simulations was carried out at various value of current density i . If the value of this parameter is lower than 200 A/m^2 for the case studied here, the regime in the single-channel is similar to the one observed in the multichannel system (quasi-steady regime). Systematic investigation of the transition between pseudo-turbulent and quasi-steady regimes is given in [15].

5.3. The Reasons for the Difference in Single-and Multichannel Flows. At low current densities, the only observed difference in the single-and multiple channel systems concerns the flow at the top of the channel. In the case of a single-channel, the top corresponds to the liquid free surface. In the case of a three-channel system, the free-surface is located above the

channels (see Figure 2), while the section at the end of each single-channel (section S1 in Figure 4) does not represent any real physical boundary. At the free surface, the continuous phase must turn around since the liquid is entirely contained within this boundary and it cannot exit. If the diameter of the bubbles is small, the bubbles tend to follow the liquid flow due to the fact that the relative velocity is very low. In the case of a single-channel, the recirculating flow around the free-surface drags some of the bubbles back in the channel (see Figure 7 on the left). In the multichannel case, we also observe this kind of recirculation at the free-surface, but, in this geometry, the free-surface does not coincide with the top of the channel. As a consequence the bubbles are dragged back into the region above the three channels of Geometry 2 and not into the channel itself (see Figure 7 on the right). We observe the transition to the pseudo-turbulent

regime when the void fraction in the channel bulk reaches a certain critical value. In the single-channel, due to the recirculation at the top, the bubbles tend to accumulate. If we increase the current density above a certain value (around 200 A/m^2), the flow becomes pseudo-turbulent. In the multichannel system, however, the bubbles are never accumulated at the top of a single-channel, but in the region above them; in fact, pseudoturbulence was never observed.

As shown in Figure 4, there is also global recirculation in the system. In order to determine the effect of this global recirculation on the flow pattern, we calculated the flow in Geometry 2 with $B = 0$ (see Figure 2). In this case, section C2S3 is just a wall and no flow can go through it. The flow pattern, however, is not particularly affected by this change and the system remains in the quasi-steady regime. If, on the other hand, we repeat the calculation with $B \neq 0$ and $A = 0$ (with the channels now separated at the top but still connected at the bottom), the transition to pseudo-turbulence occurs as in the single-channel case. We can conclude, therefore, that the main phenomena affecting the flow pattern in the system depend on the conditions at the top of the channel rather than at the bottom. As a final test, we run some single-channel simulations imposing an inlet velocity at the bottom. When this velocity reaches the value of approximately 0.1 m/s , the recirculation pattern responsible for the pseudo-turbulent regime is destroyed. This value, however, is at least one order of magnitude higher than the average inlet velocity at C2S3 (see Figure 5). Thus, the overall recirculation in the reactor does not create at the bottom of the electrochemically active channel an inlet flow large enough to prevent transition to pseudo-turbulence.

A direct experimental comparison of the two systems with the goal of highlighting the difference in the flow patterns is not available in the literature yet. There are, however, some significant clues in the reported studies that seem to confirm our hypotheses concerning the importance of the small bubbles (around $10 \mu\text{m}$) for the aforementioned regime transition. In Boissonneau and Byrne [3], for instance, where, in a single-gap configuration, vortexes and recirculation regions were detected in the flow, the authors also observed that not all the gas was liberated from the solution and that a certain amount of small bubbles, mostly of the diameter less than $10 \mu\text{m}$, was recirculated in the channel.

All these observations are in perfect agreement with a more theoretical approach we employed in one of our previous works [16] in order to investigate the transition from quasi-steady state to pseudo-turbulence in a single-channel. The flow was assumed pseudohomogeneous and piecewise linear, and the effect of velocity and pressure disturbances on the flow stability was investigated by means of the Rayleigh equation (here, we discuss only the results; the lengthy mathematical manipulations are omitted). Our analysis shows that the fundamental parameter for the stability of the flow is the density ratio q between the so-called gas-blanket (the region near the cathode where most of the gas is concentrated, see Figure 3) and the bulk (the rest of the channel where the void fraction is lower, see Figure 3). Above a certain critical q_{cr} , as discussed in [16], the

system becomes unstable and flow disturbances with initial infinitesimal amplitude grow exponentially.

If, as a first approximation, we assume that the gas-blanket is always entirely constituted of gas, the only way to increase the density ratio q between the gas-blanket and the bulk is to decrease the density of the bulk. This happens, for instance, when, due to the flow recirculation at the top of the channel (see the left part of Figure 7), more bubbles are dragged back into the bulk thus reducing the apparent density of this region and increasing the ratio q . When the value of q increases above q_{cr} , the flows become unstable and transition to pseudo-turbulence occurs. In the multichannel case, however, (see the right part of Figure 7) the bubbles, as we already explained, do not recirculate in the bulk. As a consequence q does not increase, the flow remains stable and transition to pseudo-turbulence does not occur.

6. Conclusions

The flow pattern and the void fraction distribution in gas-evolving electrochemical cells can be significantly different in a single-channel than in multichannel configurations as shown in this study. This is mostly due to a recirculation pattern at the top of the single-channel case that contributes to the accumulation of the smallest bubbles. While transition from quasi-steady flow pattern to pseudo-turbulent occurs in single-channel flows at sufficiently high gas production rate (i.e., at high current density) involving sufficiently small bubbles, this transition is averted in multichannel flows. This happens because the gaps in multichannel systems are usually completely immersed in the liquid. Based on the presented results, we conclude that the presence of a region external to the individual channel (gap) plays a significant role in the evolution of the hydrodynamics internal to the gap. If the goal of single-channel laboratory studies is to provide information for large multichannel setups, then appropriate care must be taken to ensure the similarity of flow regime and flow pattern and this issue must be addressed when experiments are planned. For example, if the single-channel (gap) is immersed in a larger experimental apparatus, where global recirculation is allowed, the external flow conditions would probably be similar to the multichannel case and the resulting flow patterns in individual channels comparable.

Notations

α :	The void fraction [–]
α_E :	The void fraction at the electrode [–]
A :	Inert section in Geometry 1 or distance top-electrode in Geometry 2 [m]
B :	Distance top-electrode in Geometry 2 [m]
d :	Bubble diameter [m]
F :	Faraday constant $96487 \text{ A s mol}^{-1}$
g :	Gravity acceleration constant $9.81 \text{ [m s}^{-2}\text{]}$
h :	Distance between the two electrodes [m]
i :	Current density [A m^{-2}]
j_{gas} :	Inlet superficial gas velocity [m s^{-1}]
L :	Active channel height [m]

L_{TOT} : Total height ($L + A$) in Geometry 1 or ($L + A + B$) in Geometry 2 [m]

M : Molecular mass [kg mol^{-1}]

μ_g : Gas viscosity [$\text{kg m}^{-1} \text{s}^{-1}$]

μ_l : Liquid viscosity [$\text{kg m}^{-1} \text{s}^{-1}$]

ρ_g : Gas density [kg m^{-3}]

ρ_l : Liquid density [kg m^{-3}]

t : Time [s]

u_E : Inlet gas velocity at the electrode [m s^{-1}]

v_g : Local and instantaneous gas velocity [m s^{-1}]

v_l : Local and instantaneous liquid velocity [m s^{-1}]

v_{lx} : Component of \mathbf{v}_l in the x -direction [m s^{-1}]

v_{ly} : Component of \mathbf{v}_l in the y -direction [m s^{-1}]

z : Number of electrons involved in the electrode reaction [-].

- [10] L. J. J. Janssen, "Behaviour of and mass transfer at gas-evolving electrodes," *Electrochimica Acta*, vol. 34, no. 2, pp. 161–169, 1989.
- [11] V. S. J. Craig, "Bubble coalescence and specific-ion effects," *Current Opinion in Colloid and Interface Science*, vol. 9, no. 1-2, pp. 178–184, 2004.
- [12] D. A. Drew, "Mathematical-modeling of 2-phase flow," *Annual Review of Fluid Mechanics*, vol. 15, pp. 261–291, 1983.
- [13] D. Z. Zhang and A. Prosperetti, "Momentum and energy equations for disperse two-phase flows and their closure for dilute suspensions," *International Journal of Multiphase Flow*, vol. 23, no. 3, pp. 425–453, 1997.
- [14] C. Y. Wen and Y. H. Yu, "Mechanics of fluidization," *Chemical Engineering Progress Symposium Series*, vol. 62, no. 62, pp. 100–111, 1966.
- [15] A. Alexiadis, M. P. Dudukovic, P. Ramachandran, A. Cornell, J. Wanngard, and A. Bokkers, "On the electrode boundary conditions in the simulation of two phase flow in electrochemical cells," *International Journal of Hydrogen Energy*, vol. 36, no. 14, pp. 8557–8559, 2011.
- [16] A. Alexiadis, M. P. Dudukovic, P. Ramachandran, A. Cornell, J. Wanngard, and A. Bokkers, "Transition to pseudo-turbulence in a narrow gas-evolving channel," *Theoretical and Computational Fluid Dynamics*. In press.

Acknowledgment

This work has been performed under the MELPRIN Project founded by the CEC under the sixth Framework Program.

References

- [1] H. Vogt, "Gas evolving electrodes," in *Comprehensive Treatise of Electrochemistry*, vol. 6, pp. 445–489, Plenum Press, New York, NY, USA, 1983.
- [2] P. Hell and J. Wanngard, *Private Communication*, Eka Chemicals, Mannheim, Germany, 2009.
- [3] P. Boissonneau and P. Byrne, "Experimental investigation of bubble-induced free convection in a small electrochemical cell," *Journal of Applied Electrochemistry*, vol. 30, no. 7, pp. 767–775, 2000.
- [4] M. D. Mat and K. Aldas, "Application of a two-phase flow model for natural convection in an electrochemical cell," *International Journal of Hydrogen Energy*, vol. 30, no. 4, pp. 411–420, 2005.
- [5] M. D. Mat, K. Aldas, and O. J. Ilegbusi, "A two-phase flow model for hydrogen evolution in an electrochemical cell," *International Journal of Hydrogen Energy*, vol. 29, no. 10, pp. 1015–1023, 2004.
- [6] R. Wedin and A. A. Dahlkild, "On the transport of small bubbles under developing channel flow in a buoyant gas-evolving electrochemical cell," *Industrial and Engineering Chemistry Research*, vol. 40, no. 23, pp. 5228–5233, 2001.
- [7] H. Vogt, "The rate of gas evolution at electrodes-II. An estimate of the efficiency of gas evolution on the basis of bubble growth data," *Electrochimica Acta*, vol. 29, no. 2, pp. 175–180, 1984.
- [8] H. Vogt, "The rate of gas evolution of electrodes-I. An estimate of the efficiency of gas evolution from the supersaturation of electrolyte adjacent to a gas-evolving electrode," *Electrochimica Acta*, vol. 29, no. 2, pp. 167–173, 1984.
- [9] A. Alexiadis, M. P. Dudukovic, P. Ramachandran, A. Cornell, J. Wanngard, and A. Bokkers, "Liquid-gas flow patterns in a narrow electro-chemical channel," *Chemical Engineering Science*, vol. 66, pp. 2252–2260, 2011.

Research Article

CFD Modeling of Gas-Liquid Bubbly Flow in Horizontal Pipes: Influence of Bubble Coalescence and Breakup

K. Ekambara, R. Sean Sanders, K. Nandakumar, and J. H. Masliyah

Department of Chemical and Materials Engineering, University of Alberta, Edmonton, AB, Canada T6G 2G6

Correspondence should be addressed to K. Ekambara, ekambara@gmail.com

Received 11 November 2011; Accepted 14 January 2012

Academic Editor: Mahesh T. Dhotre

Copyright © 2012 K. Ekambara et al. This is an open access article distributed under the Creative Commons Attribution License, which permits unrestricted use, distribution, and reproduction in any medium, provided the original work is properly cited.

Modelling of gas-liquid bubbly flows is achieved by coupling a population balance equation with the three-dimensional, two-fluid, hydrodynamic model. For gas-liquid bubbly flows, an average bubble number density transport equation has been incorporated in the CFD code CFX 5.7 to describe the temporal and spatial evolution of the gas bubbles population. The coalescence and breakage effects of the gas bubbles are modeled. The coalescence by the random collision driven by turbulence and wake entrainment is considered, while for bubble breakage, the impact of turbulent eddies is considered. Local spatial variations of the gas volume fraction, interfacial area concentration, Sauter mean bubble diameter, and liquid velocity are compared against experimental data in a horizontal pipe, covering a range of gas (0.25 to 1.34 m/s) and liquid (3.74 to 5.1 m/s) superficial velocities and average volume fractions (4% to 21%). The predicted local variations are in good agreement with the experimental measurements reported in the literature. Furthermore, the development of the flow pattern was examined at three different axial locations of $L/D = 25, 148,$ and 253 . The first location is close to the entrance region where the flow is still developing, while the second and the third represent nearly fully developed bubbly flow patterns.

1. Introduction

Gas-liquid, two-phase flow in horizontal pipes is encountered often in a number of industrial processes. Common applications include chemical plants, evaporators, oil wells and pipelines, fluidized bed combustors, and evaporators. Horizontal bubbly flows have received less attention in the literature than vertical flows, even though this flow orientation is equally important in industrial applications such as hydrotransport, an important technology in bitumen extraction. Experimental observations are also difficult in this case, as the migration of dispersed bubbles towards the top of the pipe, due to buoyancy, causes a highly nonsymmetric volume distribution in the pipe cross-section. This density stratification is not often accompanied by a strong secondary flow. Gas volume fraction, interfacial area concentration, and mean bubble diameter are the three characterizing field variables that characterize the internal flow structure of two-phase, gas-liquid flows in horizontal pipe. In various industrial processes, the gas volume fraction parameter is required for hydrodynamic and thermal design. The interfacial transport of mass, momentum, and energy is proportional to the

interfacial area and the driving forces. This is an important parameter required for a two-fluid model formulation. The mean bubble diameter serves as a link between the gas volume fraction and interfacial area concentration. An accurate knowledge of local distributions of these three parameters is of great importance to the eventual understanding and modelling of the interfacial transfer processes [1].

In the past two decades, significant developments in the modeling of two-phase flow processes have occurred since the introduction of the two-fluid model. In the volume averaged, two-fluid model, the interfacial transfer terms are strongly related to the interfacial area concentration and the local transfer mechanisms such as the degree of turbulence near the interfaces. Fundamentally, the interfacial transport of mass, momentum, and energy are proportional to the interfacial area concentration (a_{ij}) and driving forces. Since the interfacial area concentration a_{ij} represents the key parameter that links the interaction of the phases, significant attention has been paid towards developing a better understanding of the coalescence and breakage effects due to interactions among bubbles and between bubbles and turbulent eddies for gas-liquid bubbly flows [2–5]. The

population balance method is a well-known method for tracking the size distribution of the dispersed phase and accounting for the breakage and coalescence effects in bubbly flows (see, e.g. [6–14]). This approach is concerned with maintaining a record of the number of bubbles initially and tracking their evolution in space over time.

In this work, an attempt has been made to demonstrate the possibility of combining population balance with computational fluid dynamics (CFD) for the case of gas-liquid bubbly flow in the horizontal pipe. The MUSIG model has been implemented in CFX-5.7 to account for the nonuniform bubble size distribution in a gas-liquid flow [7, 15, 16]. The gas volume fraction, interfacial area concentration, Sauter mean diameter, and axial liquid velocity have been predicted for a wide range of gas and liquid flow condition. Further, the development of flow pattern has been studied at three different axial locations. The model predictions are compared with available experimental data from the literature.

2. Mathematical Modelling

2.1. Population Balance Model. Population balance modelling is used in computing the size distribution of the dispersed phase and in accounting for the breakage and coalescence effects in bubbly flows. A general form of the population balance equation is

$$\frac{\partial n_i}{\partial t} + \nabla \cdot (\mathbf{u}_g n_i) = B_B + B_C - D_B - D_C, \quad (1)$$

where \mathbf{u}_g is the gas velocity, n_i represents the number density of size group i , and terms on the right hand side B_B , B_C , D_B , and D_C are, respectively, the “birth” and “death” due to breakup and coalescence of bubbles. The left hand side tracks the spatial and temporal evolution of a class of bubbles, while the right hand side models the exchange between classes due to breakup and coalescence of bubbles. The bubble number density n_i is related to the gas volume fraction α_g by

$$\alpha_g f_i = n_i V_i, \quad (2)$$

where f_i represents the volume fraction of bubbles of group i , and V_i is the corresponding volume of a bubble of group i . It is necessary to provide individual models for each of the breakup and coalescence processes as it depends on the mechanisms and is sensitively dependent on the presence of surfactants, turbulence levels, and so forth. These models are discussed next.

2.1.1. Bubble Breakup Model. The breakup of bubbles in turbulent dispersions employs the model developed by Luo and Svendsen [18]. Binary break-up of the bubbles is assumed, and the model is based on the theories of isotropic turbulence. For binary breakage, a dimensionless variable describing the sizes of daughter drops or bubbles (the breakage volume fraction) can be defined as

$$f_{BV} = \frac{V_i}{V} = \frac{d_i^3}{d^3} = \frac{d_i^3}{d_i^3 + d_j^3}, \quad (3)$$

where d_i and d_j are diameters (corresponding to V_i and V_j) of the daughter bubbles in the binary breakage of a parent bubble with diameter d (corresponding to volume V). The value interval of the breakage volume fraction is between 0 and 1. The break-up rate of bubbles of volume V_j into volume sizes of V_i ($= V_{f_{BV}}$) can be obtained as

$$\begin{aligned} & \frac{\Omega(V_j : V_i)}{(1 - \alpha_g) n_j} \\ &= C \left(\frac{\epsilon}{d_j^2} \right)^{1/3} \int_{\zeta_{\min}}^1 \frac{(1 + \zeta)^2}{\zeta^{11/3}} \exp\left(-\frac{12c_f \sigma}{\beta \rho_l \epsilon^{2/3} d_j^{5/3} \zeta^{11/3}}\right) d\zeta, \end{aligned} \quad (4)$$

where ϵ is the rate of energy dissipation per unit of liquid mass; $\zeta = \lambda/d_j$ is the size ratio between an eddy and a particle in the inertial subrange and consequently $\zeta_{\min} = \lambda_{\min}/d_j$; C and β are determined, respectively, from fundamental consideration of drops or bubbles breakage in turbulent dispersion systems to be 0.923 and 2.0 in Luo and Svendsen [18]; c_f is the increase coefficient of surface area given by

$$c_f = \left[f_{BV}^{2/3} + (1 - f_{BV})^{2/3} - 1 \right]. \quad (5)$$

The birth rate of group i bubbles due to break-up of larger bubbles is

$$B_B = \sum_{j=i+1}^N \Omega(V_j : V_i) n_j. \quad (6)$$

The death rate of group i bubbles due to break-up into smaller bubbles is

$$D_B = \Omega_i n_i \text{ with } \Omega_i = \sum_{k=1}^i \Omega_{ki}. \quad (7)$$

2.1.2. Bubble Coalescence Model. The coalescence of two bubbles is assumed to occur in three steps. The first step where the bubbles collide and trap a layer of liquid between them, a second step where this liquid layer drains until it reaches a critical thickness, and a last step during which this liquid film disappears and the bubbles coalesce. The collisions between bubbles may be caused by turbulence, buoyancy, or laminar shear. Only the first cause of collision (turbulence) is considered in the present model. Indeed collisions caused by buoyancy cannot be taken into account as all the bubbles from each class move at the same speed. The coalescence rate considering turbulent collision taken from Prince and Blanch [19] can be expressed as

$$\chi = \theta_{ij} \exp\left(-\frac{t_{ij}}{\tau_{ij}}\right), \quad (8)$$

where t_{ij} is the contact time for two bubbles given by $(d_{ij}/2)^{2/3} / \epsilon^{1/3}$.

When bubbles collide, a small amount of liquid is entrapped between them, forming a small circular lens or

film of radius R and thickness h . The forces causing the film or lens to grow thinner in pure systems arise from capillary pressure, augmented by compression from a close range Hamaker force which accounts for the mutual attraction of water molecules on opposite sides of the liquid film [19]. For equal size bubbles, Oolman and Blanch [20] derived the thinning formula

$$\frac{-dh}{dt} = \left\{ \frac{8}{R^2 \rho_L} \left[h^2 \left(\frac{2\sigma}{r_b} + \frac{A}{6\pi h^3} \right) \right] \right\}^{1/2}. \quad (9)$$

Prince and Blanch [19] solved the above equation numerically and show that t_{ij} , the time required for two bubbles, having diameters d_i and d_j to coalesce is estimated to be $\{(d_{ij}/2)^3 \rho l / 16\sigma\}^{1/2} \ln(h_0/h_j)$. The equivalent diameter d_{ij} is calculated as suggested by Chesters and Hoffman [21]: $d_{ij} = (2/d_i + 2/d_j)^{-1}$. The parameters h_0 and h_j represent the film thickness when collision begins and critical film thickness at which rupture occurs, respectively. The values of the above parameters depend mainly on the physical properties of the liquid phase and have been experimentally computed for the air-water system. According to Prince and Blanch [19], for air-water systems, experiments have determined h_0 and h_j to be 1×10^{-4} m [22] and 1×10^{-8} m [23], respectively.

The turbulent collision rate θ_{ij} for two bubbles of diameters d_i and d_j is given by

$$\theta_{ij} = \frac{\pi}{4} [d_i + d_j]^2 (\mathbf{u}_{ti}^2 + \mathbf{u}_{tj}^2)^{1/2}, \quad (10)$$

where the turbulent velocity \mathbf{u}_t in the inertial subrange of isotropic turbulence [24] is,

$$\mathbf{u}_t = 1.4 \epsilon^{1/3} d^{1/3}. \quad (11)$$

The birth rate of group i due to coalescence of group k and group l bubbles is:

$$B_C = \frac{1}{2} \sum_{k=1}^N \sum_{l=1}^N \chi_{i,kl} n_i n_j. \quad (12)$$

The death rate of group i due to coalescence with other bubbles is:

$$D_C = \sum_{j=1}^N \chi_{ij} n_i n_j. \quad (13)$$

2.2. Flow Equations. The numerical simulations presented are based on the two-fluid, Eulerian-Eulerian model. The Eulerian modelling framework is based on ensemble-averaged mass and momentum transport equations for each phase. Regarding the liquid phase (α_l) as the continuum and the gaseous phase (bubbles) as the dispersed phase (α_g), these equations without interface mass transfer can be written in standard form as follows.

Continuity equation of the liquid phase

$$\frac{\partial}{\partial t} (\rho_l \alpha_l) + \nabla \cdot (\rho_l \alpha_l \mathbf{u}_l) = 0. \quad (14)$$

Continuity equation of the gas phase

$$\frac{\partial}{\partial t} (\rho_g \alpha_g f_i) + \nabla \cdot (\rho_g \alpha_g \mathbf{u}_g f_i) = S_i. \quad (15)$$

Momentum equation

$$\frac{\partial}{\partial t} (\rho_k \alpha_k \mathbf{u}_k) + \nabla \cdot (\rho_k \alpha_k \mathbf{u}_k \mathbf{u}_k) = -\alpha_k \nabla p + \rho_k \alpha_k g_i + \alpha_k \mu_k \nabla^2 \mathbf{u} + \mathbf{F}_{km} \quad (k, m = l, g). \quad (16)$$

In (15), S_i is a source term that captures the coalescence and break-up processes. The right side of (16) describes the following forces acting on the phase k : the pressure gradient, gravity, and the viscous stress term, and \mathbf{F}_{km} represents the sum of the interfacial forces that include the drag force \mathbf{F}_D , the lift force \mathbf{F}_L , the virtual mass force \mathbf{F}_{VM} , the wall lubrication force \mathbf{F}_{WL} , and the turbulent dispersion force \mathbf{F}_{TD} . Detailed descriptions of each of these forces can be found in Anglart and Nylund [25]; Lahey and Drew [26], and Joshi [27].

The origin of the drag force is due to the resistance experienced by a body moving in the liquid. Viscous stress creates skin drag, and pressure distribution around the moving body creates form drag. The formulation of the drag force is a key issue in multiphase flows. Clift et al. [28] and Joshi et al. [29] have given excellent accounts of this subject. The interphase momentum transfer between gas and liquid due to drag force is given by

$$\mathbf{F}_D = \frac{3}{4} C_D \alpha_g \rho_l \frac{1}{d_s} |\mathbf{u}_l - \mathbf{u}_g| (\mathbf{u}_l - \mathbf{u}_g). \quad (17)$$

The lift force considers the interaction of the bubble with the shear field of the liquid. It acts perpendicular to the main flow direction and is proportional to the gradient of the liquid velocity field. The lift force in terms of the slip velocity and the curl of the liquid phase velocity can be modelled as [30–33]

$$\mathbf{F}_L = C_L \alpha_g \rho_l (\mathbf{u}_g - \mathbf{u}_l) \times \nabla \times \mathbf{u}_l. \quad (18)$$

The wall lubrication force arises because the liquid flow rate between bubble and the wall is lower than between the bubble and the main flow. This results in a hydrodynamics pressure difference driving bubble away from the wall. This force density is approximated as [34]

$$\mathbf{F}_{WL} = -\alpha_g \rho_l \frac{(\mathbf{u}_r - (\mathbf{u}_r \cdot \mathbf{n}_w) \mathbf{n}_w)}{d_s} \max \left[C_1 + C_2 \frac{d_s}{y_w}, 0 \right]. \quad (19)$$

Here, $\mathbf{u}_r = \mathbf{u}_l - \mathbf{u}_g$ is the relative velocity between phases, d_s is the dispersed phase Sauter mean bubble diameter, y_w is the distance to the nearest wall, and \mathbf{n}_w is the unit normal pointing away from the wall.

The turbulent dispersion force, derived by Lopez de Bertodano [35], is based on an analogy with molecular movement. The turbulence-induced dispersion is a function of turbulent kinetic energy and gradient of the volume fraction of the liquid:

$$\mathbf{F}_{TD} = -C_{TD} \rho_l k \nabla \alpha_l. \quad (20)$$

The drag coefficient C_D in (17) has been modelled using Ishii and Zuber [36] drag model. The lift coefficient C_L is theoretically proven to be 0.5 for a spherical bubble in a potential flow [37]. It is also known that (i) C_L becomes smaller than 0.5 for a single small bubble in a viscous flow, as show by Lopez de Bertodano et al. [38] and Lance and Lopez de Bertodano, [39] ($C_L = 0.25$; 0.1, resp.), and (ii) C_L strongly depends on the bubble diameter and decreases with d_s [40]. These facts indicate that C_L is a function of bubble diameter and fluid properties. From this point of view, it is necessary to consider the lift coefficient also to depend on flow conditions. Recently, Tomiyama et al. [41] have developed an empirical correlation for the lift coefficient as a function of Reynolds number and Eotvos number. We have found that this correlation does not perform well for horizontal flows because of the migration of dispersed bubbles towards the top of the pipe. In view of this, we have developed a correlation for lift coefficient in horizontal flows. An interesting finding and a main contribution in this work is that a wide range of flow behavior of two-phase bubbly flows in horizontal pipes is represented by a unique functional relationship between the lift coefficient and the flow Reynolds number. When such closure relations are tested over a wide range of two-phase flows (not only pipe flows, but also bubble columns, etc.) our confidence in using such models to study practical two-phase problems in process equipment will increase over a period of time. Further explanation about C_L is given in the results and discussion. The wall lubrication constants C_1 and C_2 , as suggested by Antal et al., [34], are -0.01 and 0.05 , respectively. The coefficient $C_{TD} = 0.5$ was found to give the good results which is in the recommended range of 0.1 to 1.0 [35]. By definition, the interfacial area concentration a_{ij} for bubbly flows can be determined through the relationship

$$a_{ij} = \frac{6\alpha_g}{d_s}, \quad (21)$$

where d_s is the bubble Sauter mean diameter. The local bubble Sauter mean diameter based on the calculated values of the scalar fraction f_i and discrete bubble sizes d_i can be deduced from

$$d_s = \frac{1}{\sum_i f_i/d_i}. \quad (22)$$

From the drag and nondrag forces above, it is evident that the interfacial area concentration a_{ij} and the bubble Sauter mean diameter in (22) are essential parameters that link the interaction between the liquid and gas (bubbly) phases. In most two-phase flow studies, the common approach of prescribing constant bubble sizes through the mean bubble Sauter diameter is still prevalent. Such an approach does not allow dynamic representation of the changes in the interfacial structure.

2.3. Turbulence Equations. For the continuous liquid phase, a $k-\epsilon$ model is applied with its standard constants: $C_{\epsilon 1} = 1.44$, $C_{\epsilon 2} = 1.92$, $C_\mu = 0.09$, $\sigma_k = 1.0$, and $\sigma_\epsilon = 1.3$. No turbulence model is applied on the dispersed gas phase, but

the influence of the dispersed phase on the turbulence of the continuous phase is taken into account with Sato's additional term [42]. The governing equations for the turbulent kinetic energy k and turbulent dissipation ϵ are

$$\begin{aligned} \frac{\partial}{\partial t}(\rho_l \alpha_l k) + \frac{\partial}{\partial x_i}(\rho_l \alpha_l \mathbf{u}_l k) &= \frac{\partial}{\partial x_i} \left(\alpha_l \left(\mu_l + \frac{\mu_{l,tur}}{\sigma_k} \right) \frac{\partial k}{\partial x_i} \right) \\ &\quad + \alpha_l (G - \alpha_l \rho_l \epsilon), \\ \frac{\partial}{\partial t}(\rho_l \alpha_l \epsilon) + \frac{\partial}{\partial x_i}(\rho_l \alpha_l \mathbf{u}_l \epsilon) &= \frac{\partial}{\partial x_i} \left(\alpha_l \left(\mu_l + \frac{\mu_{l,tur}}{\sigma_\epsilon} \right) \frac{\partial \epsilon}{\partial x_i} \right) \\ &\quad + \alpha_l \frac{\epsilon}{k} (C_{\epsilon 1} G - C_{\epsilon 2} \alpha_l \rho_l \epsilon), \end{aligned} \quad (23)$$

where G is the turbulence production due to viscous and buoyancy forces, which is modeled using

$$\begin{aligned} G &= \mu_t \nabla \mathbf{u} \cdot (\nabla \mathbf{u} + \nabla \mathbf{u}^T) - \frac{2}{3} \nabla \cdot \mathbf{u} (3\mu_t \nabla \cdot \mathbf{u} + \rho_l k) \\ &\quad - \frac{\mu_t}{\rho \sigma_p} \rho_l \beta g \cdot \nabla T. \end{aligned} \quad (24)$$

3. Method of Solution

The multiple size group (MUSIG) model (CFX 5.7 from ANSYS) used in this study combines the population balance method with the break-up [18] and coalescence [19] models in order to predict the bubble size distribution of the dispersed phase, and it uses the Eulerian-Eulerian two-fluid model. A standard two-phase flow calculation, with equation for continuity, momentum, and turbulence for a continuous and a dispersed phase, can be extended to include mass fraction of bubbles within several size ranges using the MUSIG model. The size range of the bubbles is split into several groups with, for example, bands of equal diameter or equal volume. Equations are solved for the mass fraction in each band. The MUSIG model has been implemented in the CFX-5.7 software to account nonuniform bubble size distribution in a gas-liquid mixture. The MUSIG model has been extensively used for different systems [7, 10, 15, 16, 43, 44]. These size fractions provide a more accurate measure of the interfacial area density and therefore allow better calculation of the heat and mass transfer taking place between the continuous and dispersed phases.

In this present study, bubbles ranging from 1 mm to 10 mm diameter are equally divided into 10 classes (see Table 1) as the experimental observation of maximum bubble diameter for highest superficial gas velocity is 6 mm. Even if we have considered the range, model predictions picks up the experimental observation bubble size range. The fate of the discrete bubble sizes so prescribed was tracked using the population balance model. Instead of considering 11 different complete phases, it was assumed that each bubble class travels at the same mean algebraic velocity to reduce the computational time and cost. Therefore, it results in 10 continuity equations for the gas phase coupled with a single continuity equation for the liquid phase. Sensitivity of the number of size groups needed to describe a meaningful

TABLE 1: Diameter of each bubble class tracked in the simulation.

Class index	1	2	3	4	5	6	7	8	9	10
Bubble diameter, d_i (mm)	1.45	2.35	3.25	4.15	5.05	5.95	6.85	7.75	8.65	9.55

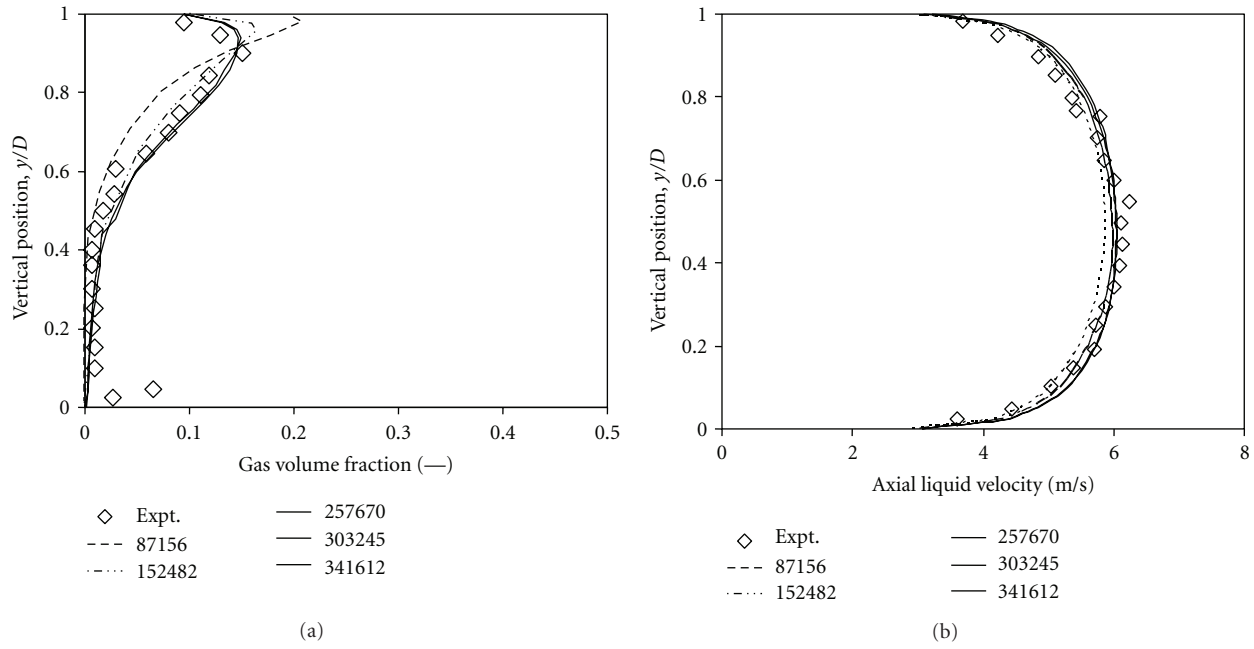


FIGURE 1: Effect of grid size on gas volume fraction and axial liquid velocity.

distribution was examined by dividing the bubble diameters equally into 10, 15, and 20 size groups. The results revealed that no appreciable difference ($\pm 2\%$) was found for the predicted maximum bubble Sauter mean diameter using the 10, 15, or 20 bubble size groups. For the subdivision into 10 size groups, the maximum Sauter bubble diameter was under predicted by a maximum difference of 2%. In view of computational resources and times, it was therefore concluded that the subdivision of the bubbles sizes into 10 size groups was sufficient and all subsequent computational results are based on the discretization of the bubble sizes into 10 groups.

Solution to the coupled sets of governing equations for the balances of mass and momentum of each phase was obtained using CFX 5.7. The conservation equations were discretized using the control volume technique. Computational grid is based on the unstructured set of blocks each containing structured grid. The structured grid within each block is generated using general curvilinear coordinates ensuring accurate representation of the flow boundaries. In order to select an adequate grid resolution, the effect of changing grid size was investigated. Several simulations were carried out using progressively larger number of grid points of 87156, 152482, 257670, 303245, and 341612. Sample grid sensitivity results are shown in Figure 1. It can be seen that there is practically no change in the gas volume

fraction and liquid velocity profiles when the grid size increased beyond 257670. In view of the observed effect of grid size, the simulations have been carried out by using 257670 grid points. Initial simulations were carried out with a coarse mesh to obtain an initially converged solution and to obtain an indication of where a high mesh density was needed. However, a dense mesh required additional computational effort. The velocity-pressure linkage was handled through the SIMPLE procedure. Three-dimensional transient simulations were performed. The time stepping strategy used in the transient simulations to reach a steady state was typically a variable step size strategy according to the following scheme: 100 steps at 1×10^{-4} s, followed by 300 steps at 5×10^{-4} s, 400 steps at 1×10^{-3} s, 1400 steps at 5×10^{-3} s, and 8000 steps at 1×10^{-2} s. Underrelaxation factors between 0.6 and 0.7 were adopted for all flow quantities, and pressure was never underrelaxed. The hybrid-upwind discretization scheme was used for the convective terms. At the inlet, gas, liquid, and the average volume fraction have been specified. At the pipe outlet, a relative average static pressure of zero was specified. For initiating the numerical solution, average volume fraction and parabolic liquid velocity profile are specified as initial conditions. The operating conditions are summarized in Table 2. The liquid and gas superficial velocities were varied between 3.74 to 5.1 m/s and 0.25 to 1.34 m/s, respectively. The fluid data

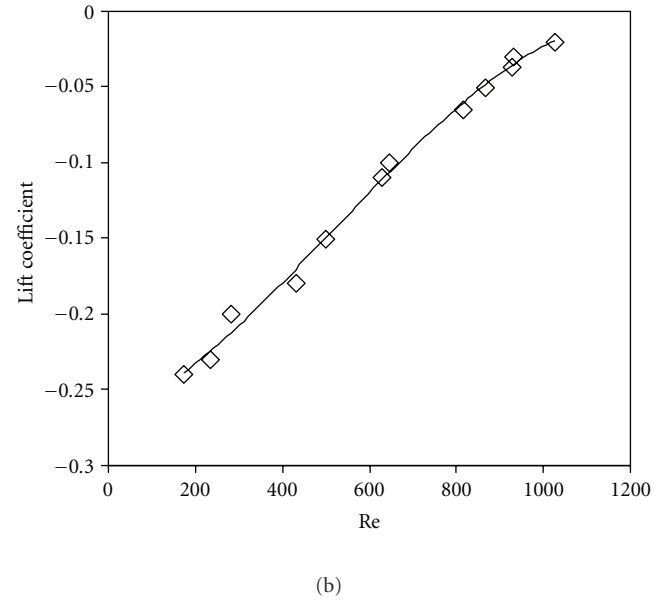
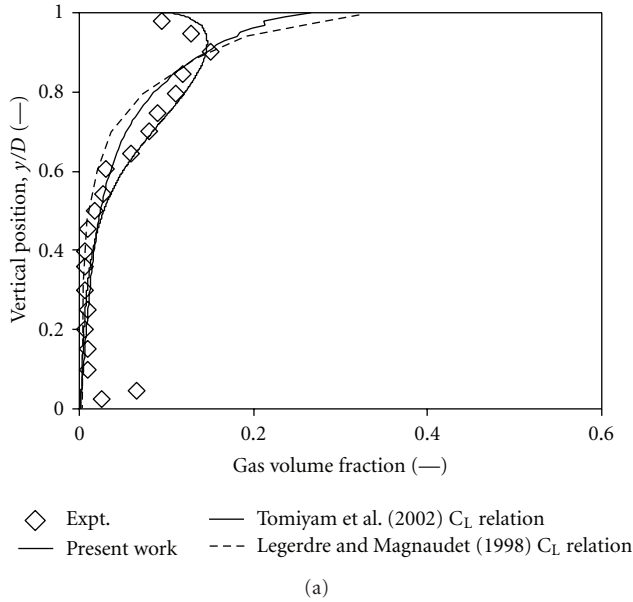
FIGURE 2: Lift coefficient (C_L).

TABLE 2: Operating conditions.

Geometry	50.3 mm ID
Gas phase	Air at 25°C
Liquid phase	Water at 25°C
Gas superficial velocity	0.25–1.34 m/s
Liquid superficial velocity	3.74–5.1 m/s
Average gas volume fraction	0.04–0.205

are taken at room temperature (25°C) and are treated as isothermal and saturated. Therefore, heat and mass transfer effects are neglected in the simulations.

4. Results and Discussion

The CFD simulations are carried out for the experimental conditions reported by Kocamustafaogullari and Wang [17] and Kocamustafaogullari and Huang [1]. The local radial profiles of the gas volume fraction, interfacial area concentration, Sauter mean bubble diameter, and liquid velocities are predicted by solving the coupled two-fluid and population balance models. The predicted results are compared with the experimental data at the axial location of $L/D = 253$ and along a vertical and horizontal line passing through the centre of the pipe axis. Here, y/D and x/R are the normalized vertical and horizontal positions in the pipe.

4.1. Estimation of Lift Coefficient. Accurate prediction of developing bubbly flows in horizontal pipes cannot be carried out without sufficient knowledge of a transverse lift force acting on the bubbles, the force that governs the

transverse migration of a bubble in a shear field. It has been clarified through a number of experiments that the lateral migration strongly depends on bubble size, that is, small bubbles tend to migrate toward the pipe wall which results in a peak in the bubble volume fraction distribution near the wall. Just like the functional form of the drag coefficient for a single particle interaction is extended to multiparticle systems, the functional form of the lift force that captures the lateral migration phenomenon is given by (18) which has C_L as the lift coefficient. Just as the drag coefficient is a function of local Reynolds number based on the slip velocity, one can expect the lift coefficient also to vary with local Reynolds number, and in general, it is an unknown function for such a complex flow field. In the literature, it is used as a fitting parameter, but various values have been reported. Further, the most of the correlations available in the literature were for vertical flows. The correlations of Legendre and Magnaudet [45], Tomiyama et al. [41] have been used in the simulations and the simulation results shown in Figure 2(a). It can be observed that the correlation of Legendre and Magnaudet [45], Tomiyama et al. [41] does not perform well for the horizontal flows because of most the dispersed bubbles migrate towards the top of the pipe, due to buoyancy. The negative lift coefficient needed because this force pushes bubbles to the pipe center. For the given simulation, we need a negative lift coefficient to predict near wall peak for the gas volume fraction profile. We need a correlation which gives negative lift coefficient value. In view of this, we have developed a correlation to be a function of Reynolds number.

The difference between the model predictions and experimental data on the spatial variation of field quantities such as liquid velocity profiles, volume fraction profiles, and interfacial area measurements is minimized by the tuning of this parameter. Bubbly horizontal pipe flow experiments by

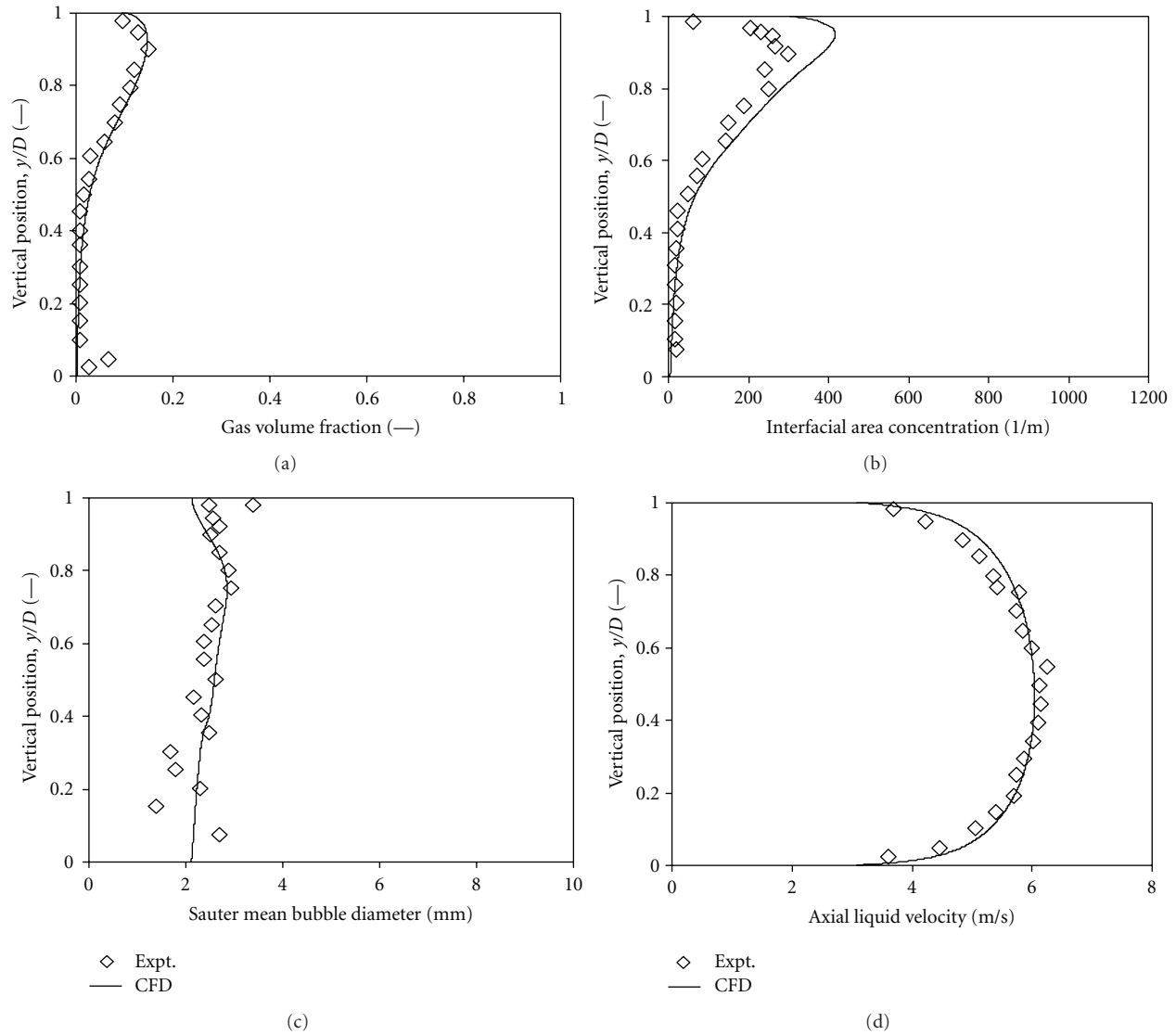


FIGURE 3: Comparison of predicted and experimental data of Kocamustafaogullari and Wang [17] for superficial gas velocity of 0.25 m/s, superficial liquid velocity of 5.1 m/s, and volume fraction 0.043: (a) gas volume fraction, (b) interfacial area concentration, (c) Sauter mean bubble diameter, and (d) axial liquid velocity.

Kocamustafaogullari and Wang [17]; Kocamustafaogullari and Huang [1]; Kocamustafaogullari et al. [46] were chosen for tuning the lift coefficient as they have detailed experimental data on the spatial variation of liquid velocity profiles, volume fraction profiles, and interfacial area measurements. In all the experiments, adiabatic, incompressible, air-water bubbly flows at atmospheric pressure and room temperature were used. The main result of tuning this parameter is shown in Figure 2(b). The estimated values of the lift coefficient at different experimental condition of gas and liquid flow rates were not scattered all over, but exhibited a well-defined correlation with the Reynolds number defined as $Re = d_s V_s \rho_L / \mu_L$, where d_s is the average bubble diameter, and V_s is the slip velocity. We capture this relationship by a polynomial expression of the form, $C_L = a Re^3 + b Re^2 + c Re + d$, where $a = -1 \times 10^{-10}$, $b = 2 \times 10^{-7}$, $c = 2 \times 10^{-4}$, and $d =$

-0.2937 . It is worth noting that the correlation is based on the locally measured properties of turbulence as well as the bubble number density, and hence, one can expect it to be valid irrespective of the dimension of the pipe as well as the liquid system. Such a relationship can then be used back in the simulation for predictive purposes at other flow conditions.

4.2. Gas Volume Fraction. Figures 3(a)–6(a) show the comparison of the predicted gas volume fraction with the experimental data of Kocamustafaogullari and Wang [17] for different superficial gas velocities of 0.25 m/s, 0.50 m/s, 0.80 m/s, and 1.34 m/s at a fixed liquid velocity of 5.1 m/s. Similarly Figures 7(a) and 8(a) show the gas volume fraction for liquid velocities of 3.74 m/s and 4.40 m/s at a fixed gas velocity of 0.51 m/s. The agreement between the predicted

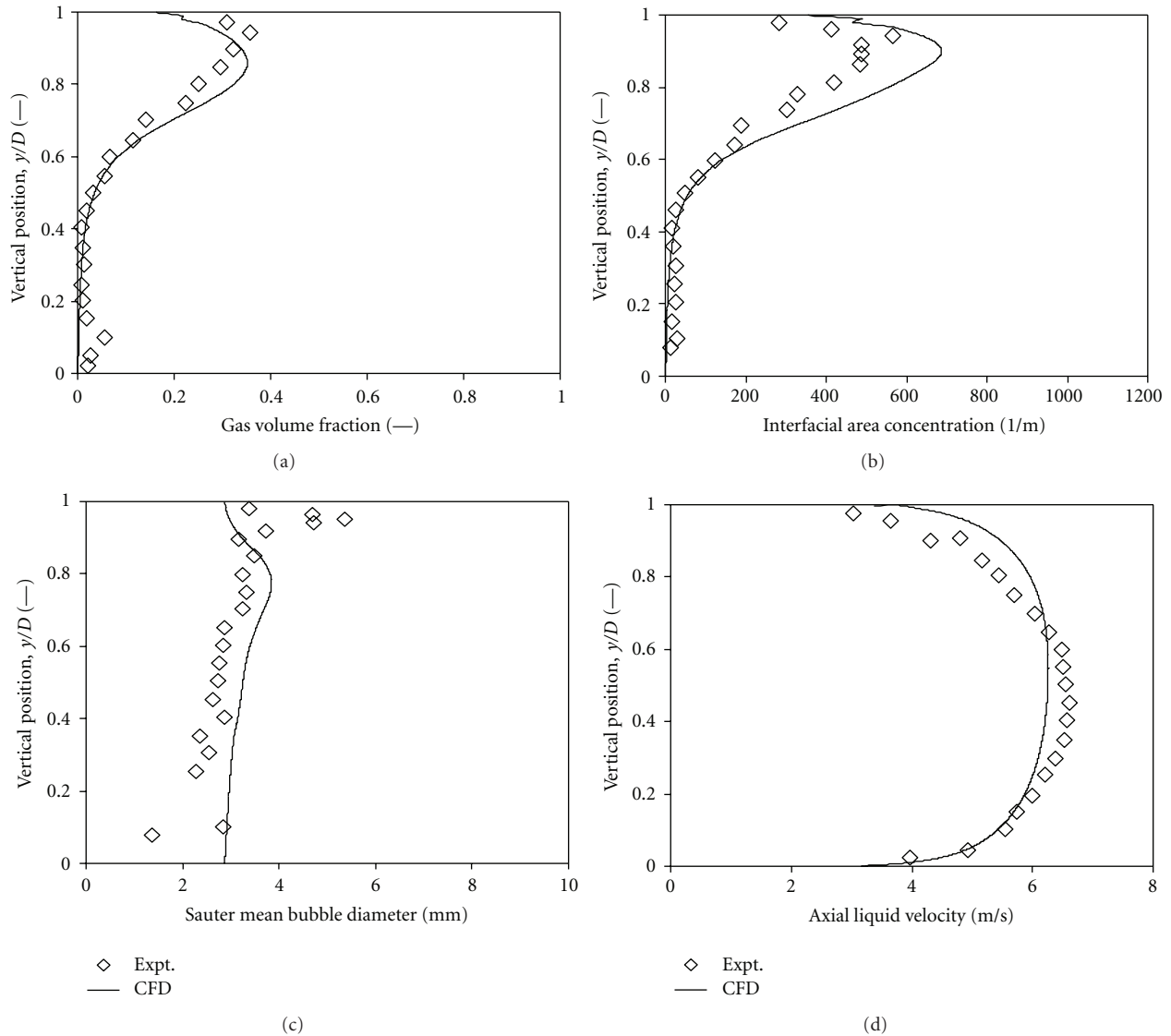


FIGURE 4: Comparison of predicted and experimental data of Kocamustafaogullari and Wang [17] for superficial gas velocity of 0.50 m/s, superficial liquid velocity of 5.1 m/s, and volume fraction of 0.080; (a) gas volume fraction, (b) interfacial area concentration, (c) Sauter mean bubble diameter, and (d) axial liquid velocity.

and the experimental profiles can be seen to be very good. As the superficial gas velocity increases, the average gas volume fraction also increases. It can be observed from these figures that most of the bubbles tend to migrate towards the top of the pipe wall under the dominating influence of buoyancy force. The balance of buoyancy and lift forces causes the profiles of gas volume fraction to show a distinct peak near the top wall at about $y/D = 0.9$ to 0.95 for all the flow conditions. A similar observation was made experimentally by Kocamustafaogullari and Wang [17], Kocamustafaogullari and Huang [1], Kocamustafaogullari et al., [46], and Iskandrani and Kojasoy [47]. At a constant gas superficial velocity of 0.51 m/s in Figures 7 and 8, the average and the peak value of the volume fraction decreases with increasing liquid velocity, as expected. The fact that the spatial variation of the gas volume fraction matches

well with the experimental data over a wide range of flow conditions gives us confidence that the lift coefficient correlation that we have developed is quite appropriate. The real test of this correlation must of course await testing against similar data in a larger diameter pipe. The challenge in developing multiphase flow models using the volume-averaged framework is to develop such closure relationships for each of the individual mechanisms and test their validity under a wide variety of scales and flow conditions. We will be testing this correlation for bubble columns in the near future. The model prediction of gas volume fraction shows relative mean and maximum errors are $\pm 6\%$ and $\pm 19\%$, respectively.

4.3. Interfacial Area Concentration (IAC). The current simulation results and the experimental results of Kocamustafaogullari and Wang [17] on the local interfacial area

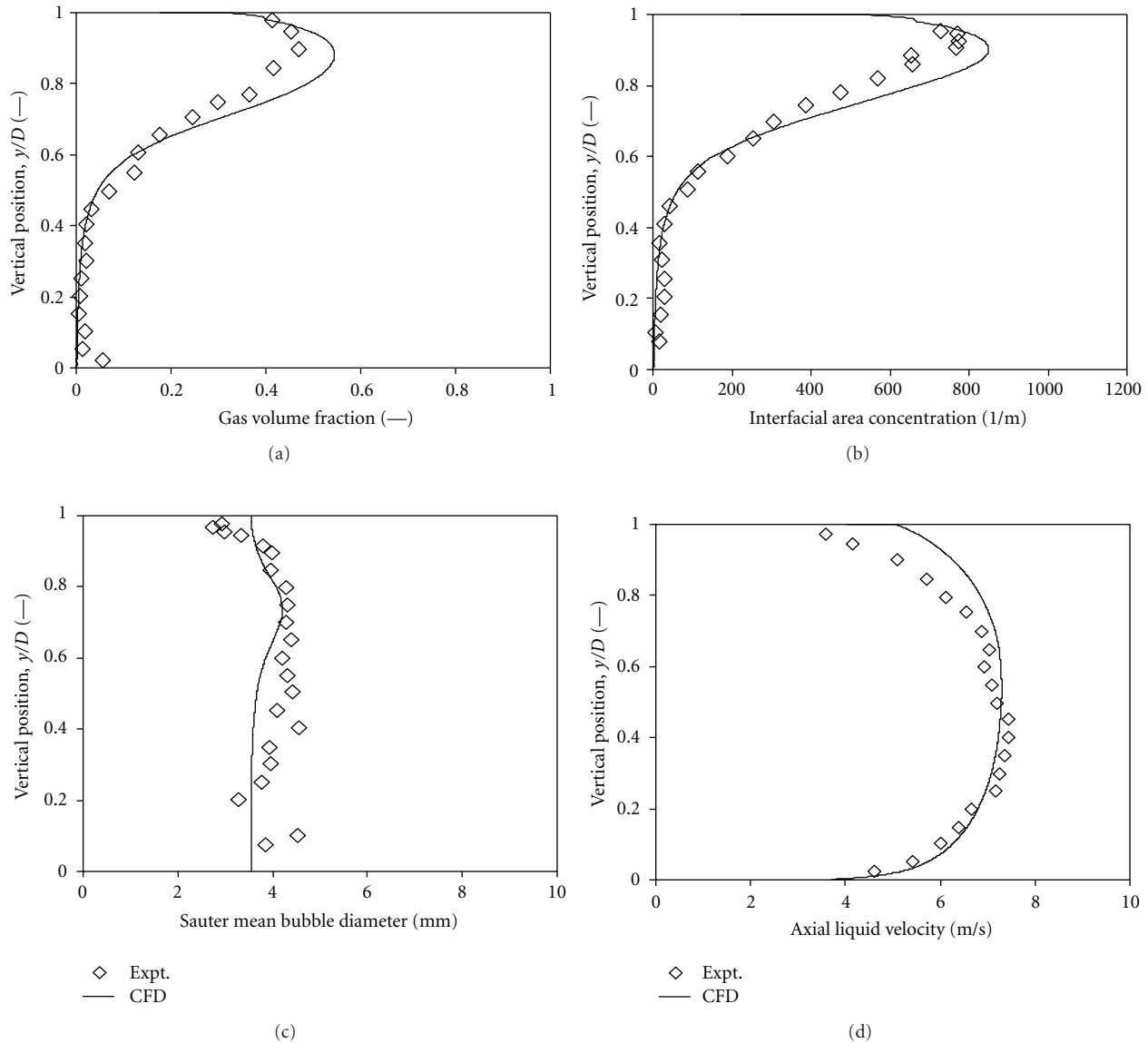


FIGURE 5: Comparison of predicted and experimental data of Kocamustafaogullari and Wang [17] for superficial gas velocity of 0.80 m/s, superficial liquid velocity of 5.1 m/s, and volume fraction of 0.139; (a) gas volume fraction, (b) interfacial area concentration, (c) Sauter mean bubble diameter, and (d) axial liquid velocity.

concentration variation along the vertical direction are compared in Figures 3(b)–8(b). The flow conditions remain the same in the previous section. The CFD prediction shows good agreement with experimental data. From these figures, it can be seen that the interfacial area concentration shows characteristics that are similar to the gas volume fraction distribution. But the interfacial area depends not only on the volume fraction of the phase, but also on the bubble size distribution. Since the volume fraction and the interfacial area are independent measurements, the data on the interfacial area variation along the vertical direction provide a valuable test of the model predictions from the population balance models. Thus, the agreement seen with the gas volume fraction variation in the previous section provides

a level of confidence in the lift coefficient model, while the agreement seen on the interfacial area measurements in the current section provides a level of comfort that the birth and death processes modeled in the population balance model are adequate to describe the bubble dynamics. Further, it can be seen that the local interfacial area concentration can be as high as $1000 \text{ m}^2/\text{m}^3$ towards the top of the pipe in horizontal two-phase flow. These values are quite high compared to vertical bubbly flows. This will result in increasing the intensity of the interfacial transport of mass, momentum, and heat near the top of the pipe. In addition, it can be observed that increasing the superficial gas velocity or decreasing the superficial liquid velocity would increase the local and overall interfacial area concentration and tend to

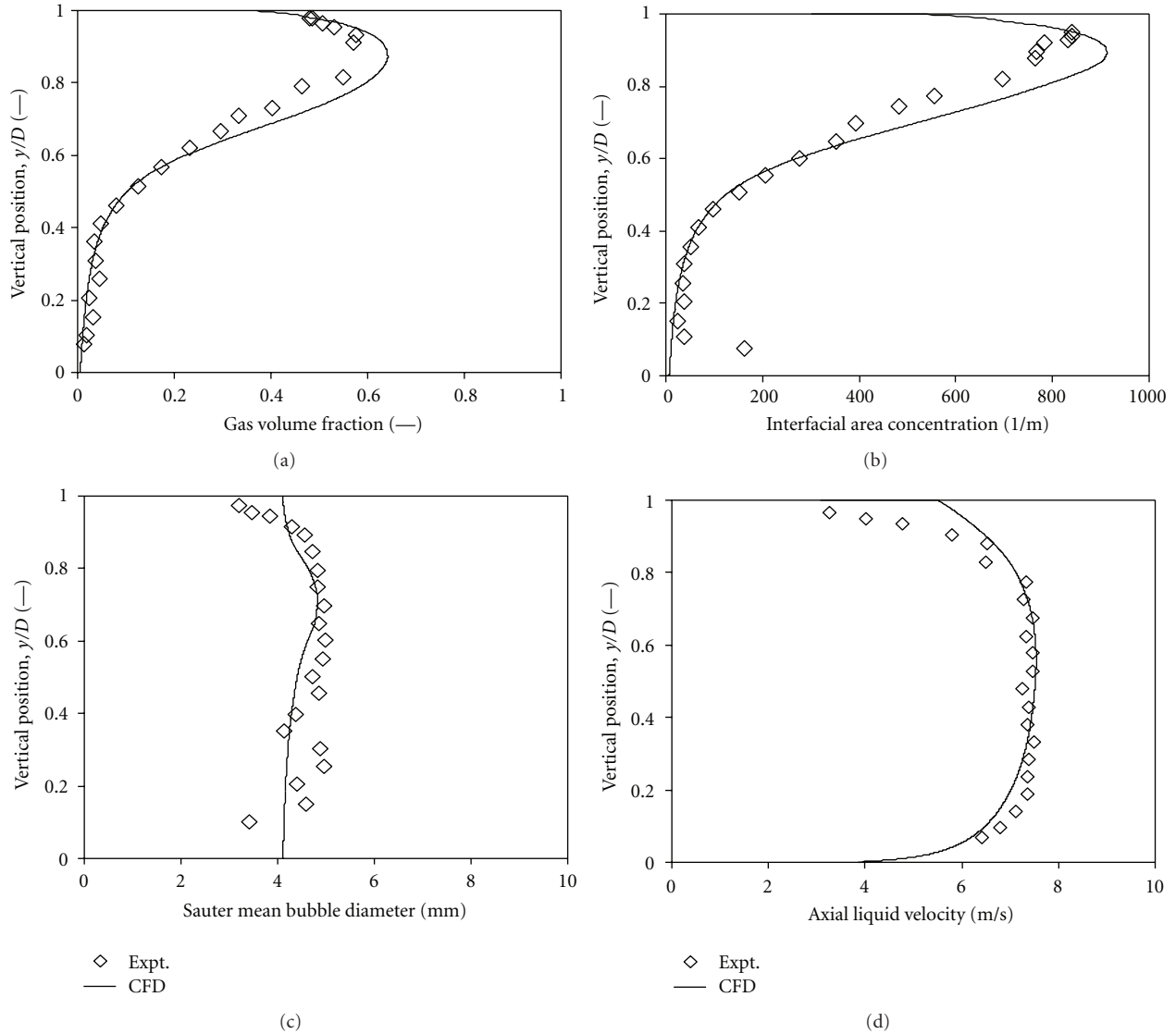


FIGURE 6: Comparison of predicted and experimental data of Kocamustafaogullari and Wang [17] for superficial gas velocity of 1.34 m/s, superficial liquid velocity of 5.1 m/s, and volume fraction of 0.204; (a) gas volume fraction, (b) interfacial area concentration, (c) Sauter mean bubble diameter, and (d) axial liquid velocity.

flatten the interfacial area concentration profile. The model prediction of interfacial area concentration shows relative mean and maximum errors are $\pm 8\%$ and $\pm 22\%$, respectively.

4.4. Sauter Mean Bubble Diameter. The comparison of predicted and experimental data of the local Sauter mean bubble diameter distribution is shown in Figures 3(c)–8(c) for various superficial gas and liquid velocities. The Sauter mean bubble diameters are in the range of 1.5–5 mm, depending on the location and flow conditions. It should be noted that the experimental data on Sauter mean diameter is inferred from other measurements, and it is not a directly measured quantity. The scatter in the experimentally derived data is high, particularly in the lower region where the gas volume fraction is low, indicating that perhaps the signals are weaker in that region. Good agreement was achieved against the mea-

sured bubble size for all the experimental conditions. From these figures, it can be seen that the bubble size distribution is almost uniform in the pipe cross-section except near the wall region. The Sauter mean bubble size tends to reduce close to the top of the pipe wall. This can be attributed to the fact that near the wall a very strong velocity gradient exists, which causes further break-up into smaller bubble sizes. Furthermore, the Sauter mean bubble size is seen to increase with increasing the superficial gas velocity (Figures 3(c)–8(c)) and to decrease with increasing superficial liquid velocity (Figures 7(c)–8(c)). The simulation results capture all of these trends faithfully. The model prediction shows relative mean and maximum errors are $\pm 9\%$ and $\pm 24\%$, respectively.

4.5. Axial Liquid Velocity. Figures 3(d)–8(d) show the comparison of predicted and experimental data of axial liquid

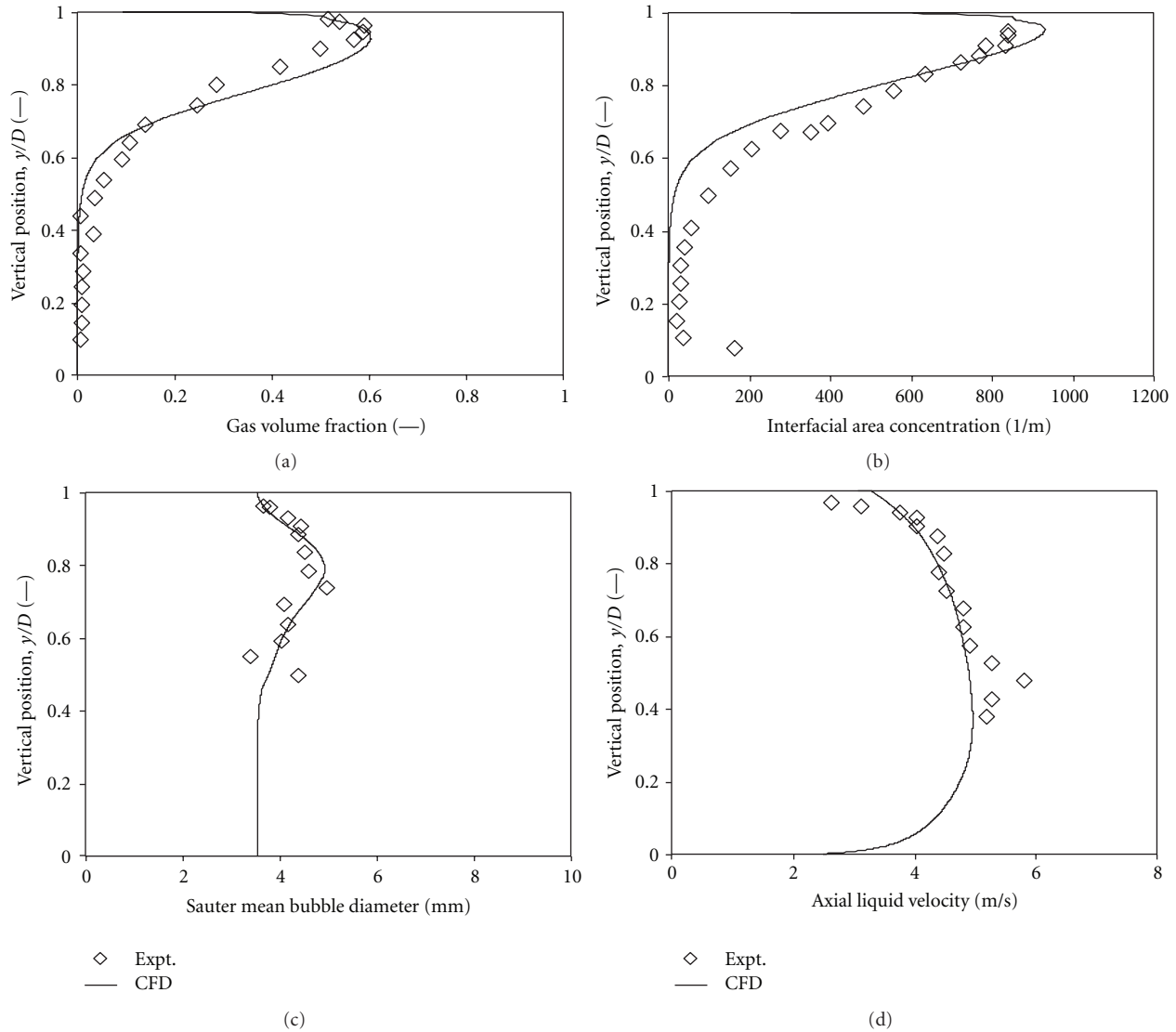


FIGURE 7: Comparison of predicted and experimental data of Kocamustafaogullari and Wang [17] for superficial gas velocity of 0.51 m/s, superficial liquid velocity of 3.74 m/s, and volume fraction of 0.105: (a) gas volume fraction, (b) interfacial area concentration, (c) Sauter mean bubble diameter, and (d) axial liquid velocity.

velocity profiles for different superficial gas and liquid velocities. If only a single liquid phase moves in the pipe, the liquid velocity in the pipe top region will be equal to the velocity in the bottom region, exhibiting a perfect axisymmetry. But these results show that the axial liquid velocity profile has a slight degree of asymmetry due to the presence of gas flow. The degree of asymmetry decreases with increasing liquid flow or decreasing gas flow. For increasingly higher gas velocities (Figures 3(d)–6(d)), the liquid velocity in the upper region of the pipe is slightly lower than in the lower region. This could be attributed to larger volume fraction of gas in the upper region which is the reason for the asymmetric distribution of the liquid velocity. An interesting feature of the velocity profile is that the velocity distribution within the bottom liquid layer resembles closely a fully developed turbulent pipe flow profile irrespective of the liquid and gas superficial velocities. The model prediction of axial liquid

velocity shows relative mean and maximum errors are $\pm 5\%$ and $\pm 14\%$, respectively.

4.6. *Simulation Results.* From the simulation, we can get much more additional information, while some of these quantities are more difficult to measure in an experiment. One such quantity is the slip velocity between the two phases. The variation in the vertical direction of the slip velocity is shown in Figure 9 for various combinations of gas and liquid flow rates. The slip velocity is larger in magnitude near the top region of the pipe, while a smaller slip velocity exists in the bottom part of the pipe. The slip velocity is an important characteristic of two-phase flow, particularly because of the large difference in densities between phases. Relatively smaller bubbles and fewer in number are found in the bottom region, and hence, they tend to move with the liquid resulting in a smaller slip velocity, while relatively larger

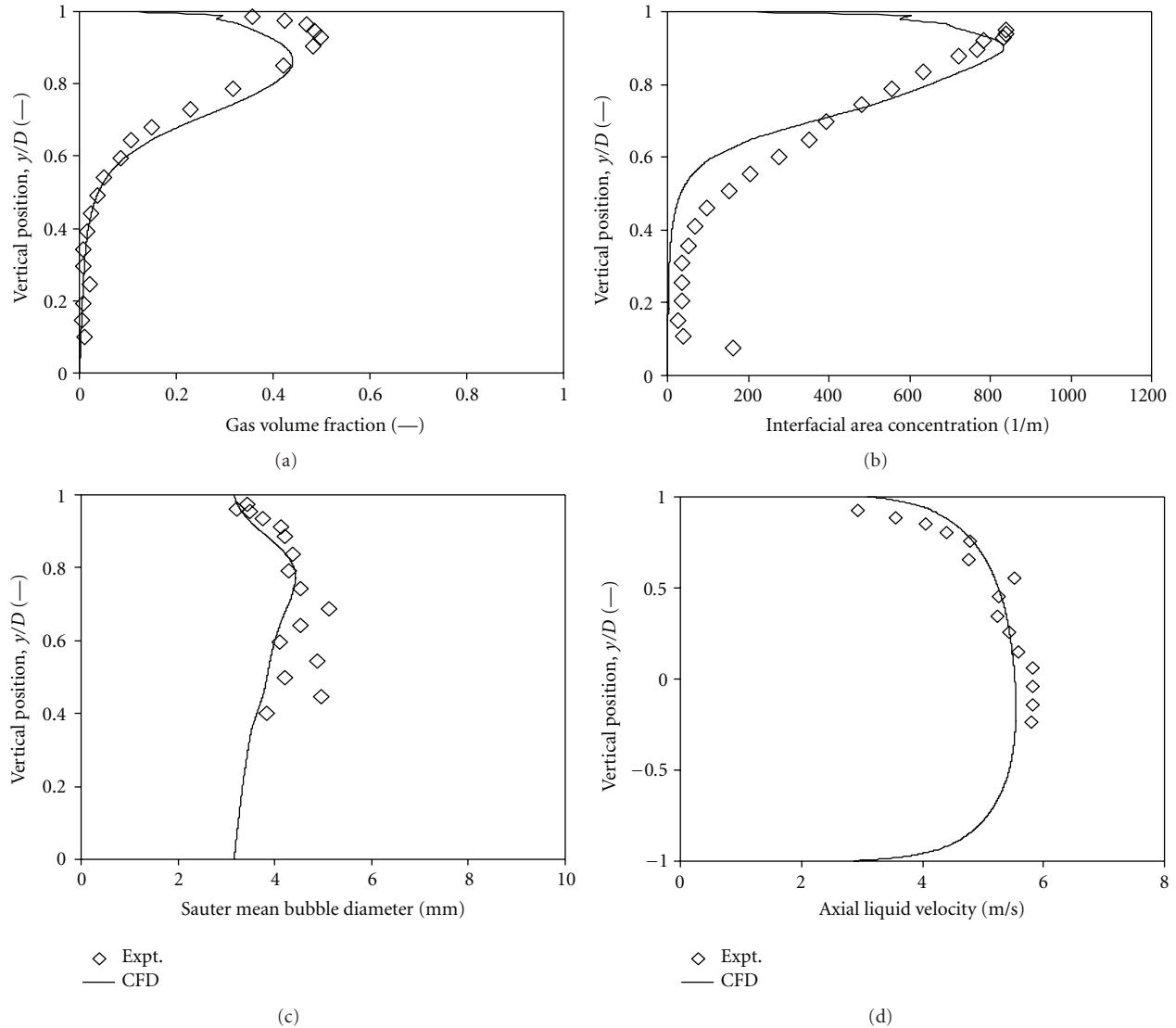


FIGURE 8: Comparison of predicted and experimental data of Kocamustafaogullari and Wang [17] for superficial gas velocity of 0.51 m/s, superficial liquid velocity of 4.4 m/s, and volume fraction of 0.102; (a) gas volume fraction, (b) interfacial area concentration, (c) Sauter mean bubble diameter, and (d) axial liquid velocity.

bubbles and more in number are found near the top of the pipe, resulting in a larger slip velocity.

4.7. Average Interfacial Parameters. While we have used the data on the spatial variation of quantities such as volume fraction and interfacial area to tune the model parameters, from a practical view point one is often interested only in a quantity that is averaged over the pipe cross-section. Hence, area averaged gas volume fraction, interfacial area concentration, and mean bubble diameter at the exit plane are shown in Figure 10 as a function of superficial gas velocity at various liquid velocities of 5.1 m/s, 4.4 m/s, and 3.74 m/s. The average volume fraction and interfacial area increase significantly with increasing superficial gas velocity, as expected. The influence of superficial liquid velocity on the gas volume fraction and interfacial area concentration are less signifi-

cant. Figure 10(c) shows that the average bubble diameter increases slightly with increasing superficial gas velocity, all though the influence is not significant. However, the mean bubble size decreases with increasing superficial liquid velocity. This observation supports the fact that the bubble size is determined primarily by liquid flow turbulence in horizontal flows. Figure 10 compares the measured gas volume fraction, interfacial area, and Sauter bubble mean diameter values with those predicted using CFD-PBM model, and the relative mean and maximum errors are $\pm 4\%$ and $\pm 11\%$, respectively.

4.8. Bubble Size Distribution. The bubble size distribution is determined by bubble coalescence and breakup. In a given system, bubble coalescence and breakup are primarily influenced by the local gas volume fraction and kinetic energy dissipation rate. Because of the nonuniform profiles

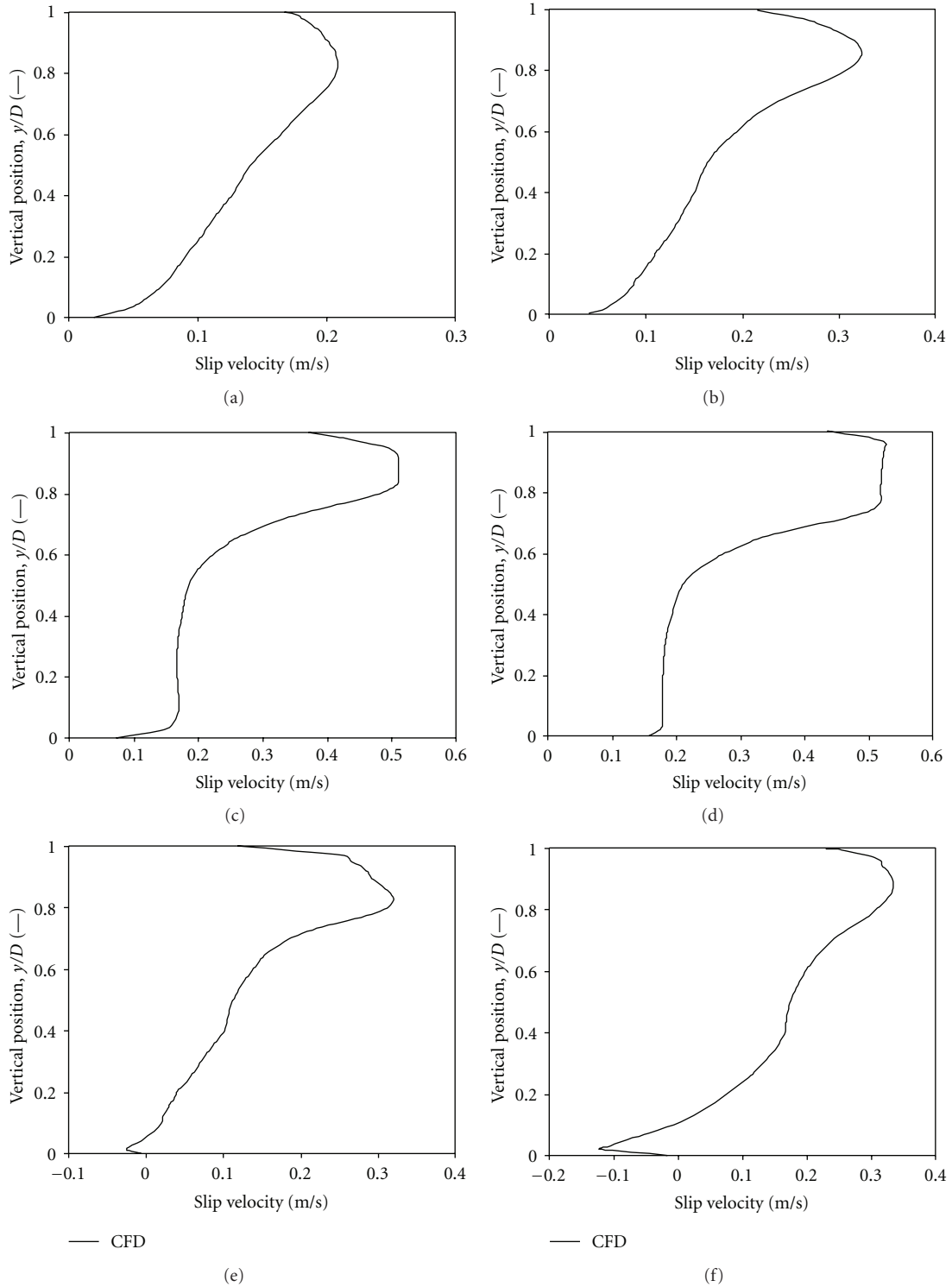


FIGURE 9: Slip velocity at different superficial gas and liquid velocities: (a) $V_G = 0.25$ m/s, $V_L = 5.1$ m/s; (b) $V_G = 0.50$ m/s, $V_L = 5.1$ m/s; (c) $V_G = 0.80$ m/s, $V_L = 5.1$ m/s; (d) $V_G = 1.34$ m/s, $V_L = 5.1$ m/s; (e) $V_G = 0.51$ m/s, $V_L = 3.74$ m/s; (f) $V_G = 0.51$ m/s, $V_L = 4.4$ m/s.

of the gas volume fraction and dissipation rate, the bubble size distribution varies with the position as well. The spatial evolution of bubble size distribution between the inlet and the outlet of the pipe is shown in Figure 11 for a superficial gas velocity of 0.25 m/s and a superficial liquid

velocity of 4.67 m/s. While selecting the bubble size, we have considered a range from 1 to 10 mm, and the experimental observation of bubble size for highest superficial velocity is 6 mm. Figures 11(a), 11(c), and 11(e) show the bubble size distribution that was specified at the pipe inlet.

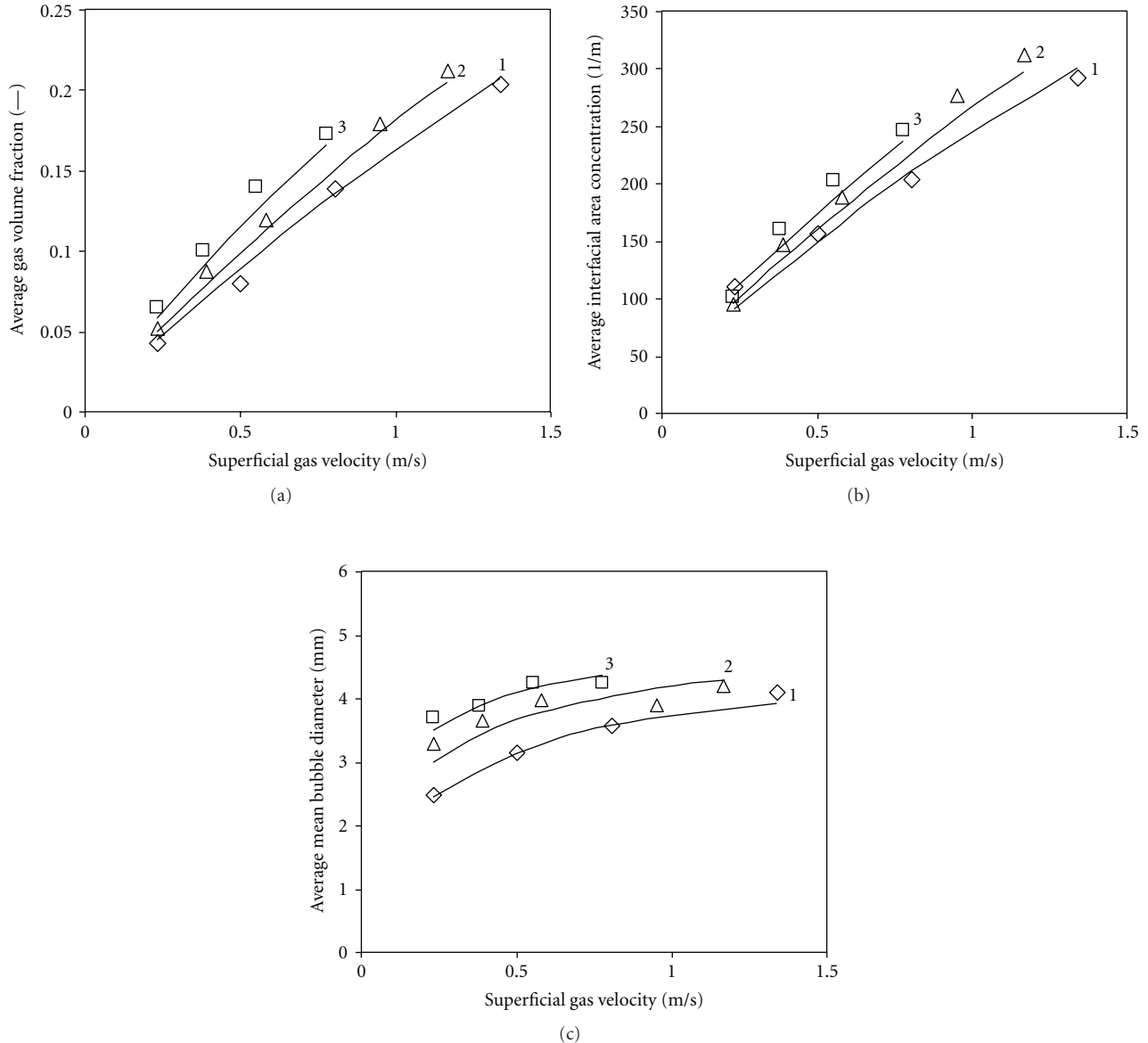


FIGURE 10: Effect of superficial gas and liquid velocity on (a) average gas volume fraction; (b) average interfacial area concentration (c) average mean bubble diameter: (1) $V_L = 5.1$ m/s; (2) $V_L = 4.4$ m/s; (3) $V_L = 3.74$ m/s.

These correspond, respectively, to the monosized bubbles of 1.45 mm (Figure 11(a)), 9.55 mm (Figure 11(c)), and a uniform distribution of bubbles in the range of 1 to 10 mm (Figure 11(e)). The corresponding distribution at the pipe exit is shown on the right hand side in Figures 11(b), 11(d), and 11(f), respectively. It can be seen from these figures that the bubble size distribution function reaches an independent state as determined by the balance between birth and death processes that depend on the local flow conditions, and its original state at the inlet has very little impact. Although this kind of distribution function was not measured in the experiments of Kocamustafaogullari and Wang [17], the spatial variation of the bubble sizes was measured as shown in Figure 3. It is comforting to note that the ranges of bubble sizes measured under similar flow conditions show a range

of 2-3 mm, the same range shown in Figure 11, even though extremely small (1.45 mm) and large (9.55 mm) sizes were used at the pipe inlet.

4.9. Development of Flow Pattern. To see the development of flow pattern in the axial direction, several three-dimensional simulations were carried out using the coupled two-fluid and population balance models. The flow evolution is shown in Figure 12–14 at three different axial locations of $L/D = 25$, 148, and 253. The first location represents close to the entrance of the pipe region where the internal flow develops, and the second and third locations indicate the extent to which the flow has reached a fully developed state, by the lack of further change in flow profiles. Figures 12, 13, and 14 show, respectively, the development of the

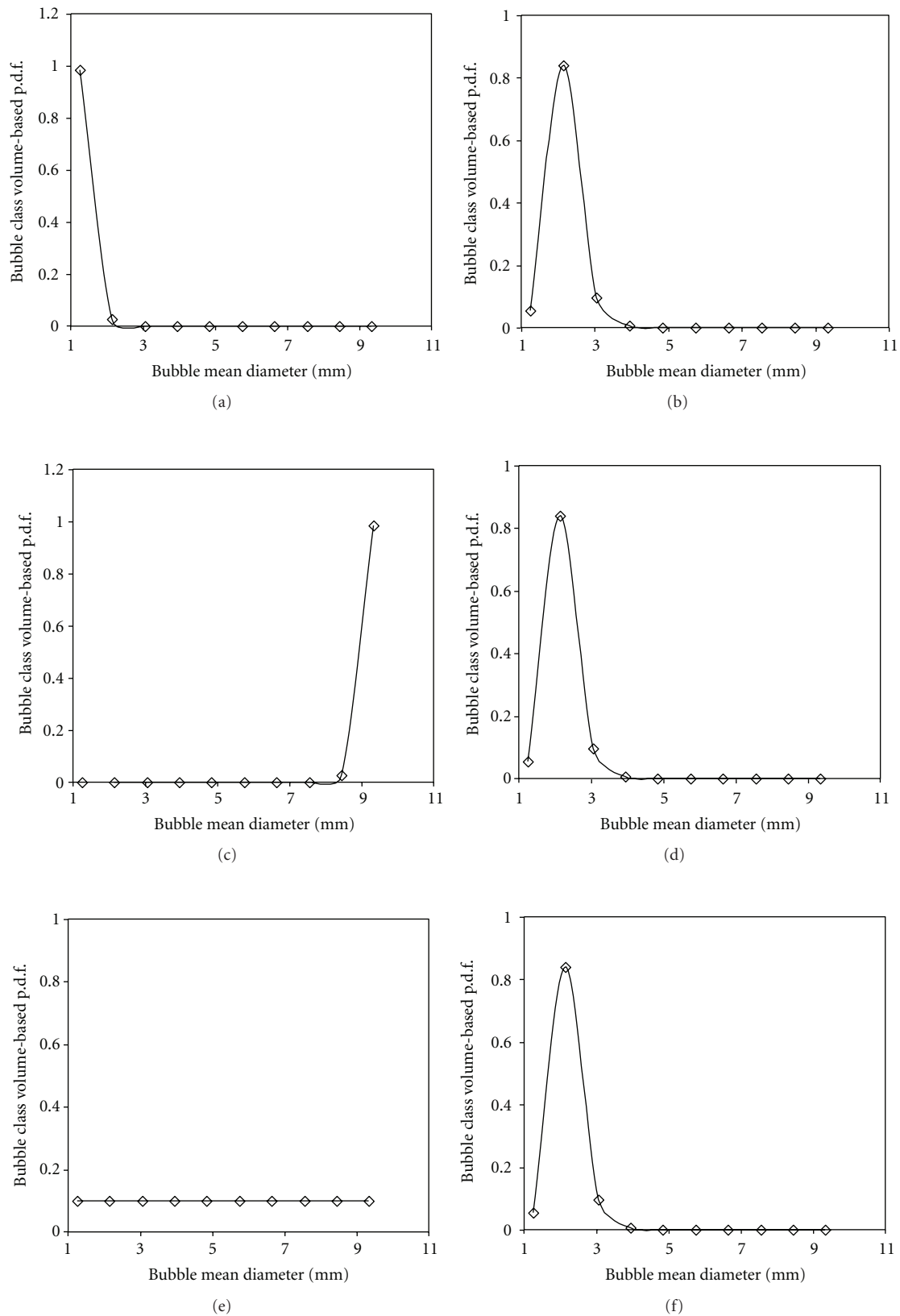


FIGURE 11: The bubble class volume-based p.d.f at inlet and exit of the pipe for superficial gas velocity is 0.25 m/s, superficial liquid velocity is 4.67 m/s, and average volume fraction is 0.043.

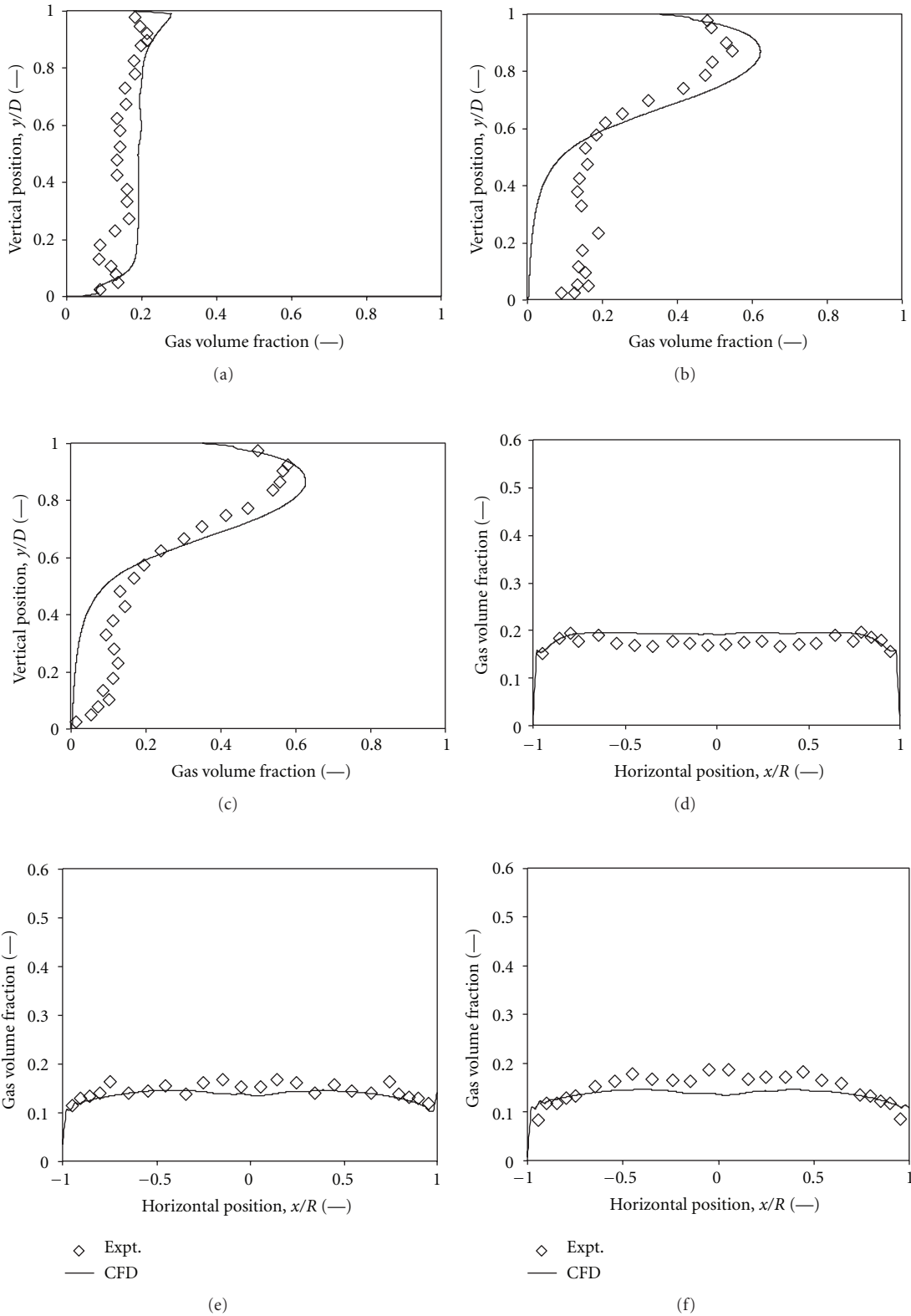


FIGURE 12: Gas volume fraction development in axial direction for superficial gas velocity is 1.21 m/s, superficial liquid velocity is 4.67 m/s, and average volume fraction is 0.205. At vertical position, (a) $L/D = 25$; (b) $L/D = 148$; (c) $L/D = 253$, at horizontal position, (d) $L/D = 25$; (e) $L/D = 148$; (f) $L/D = 253$.

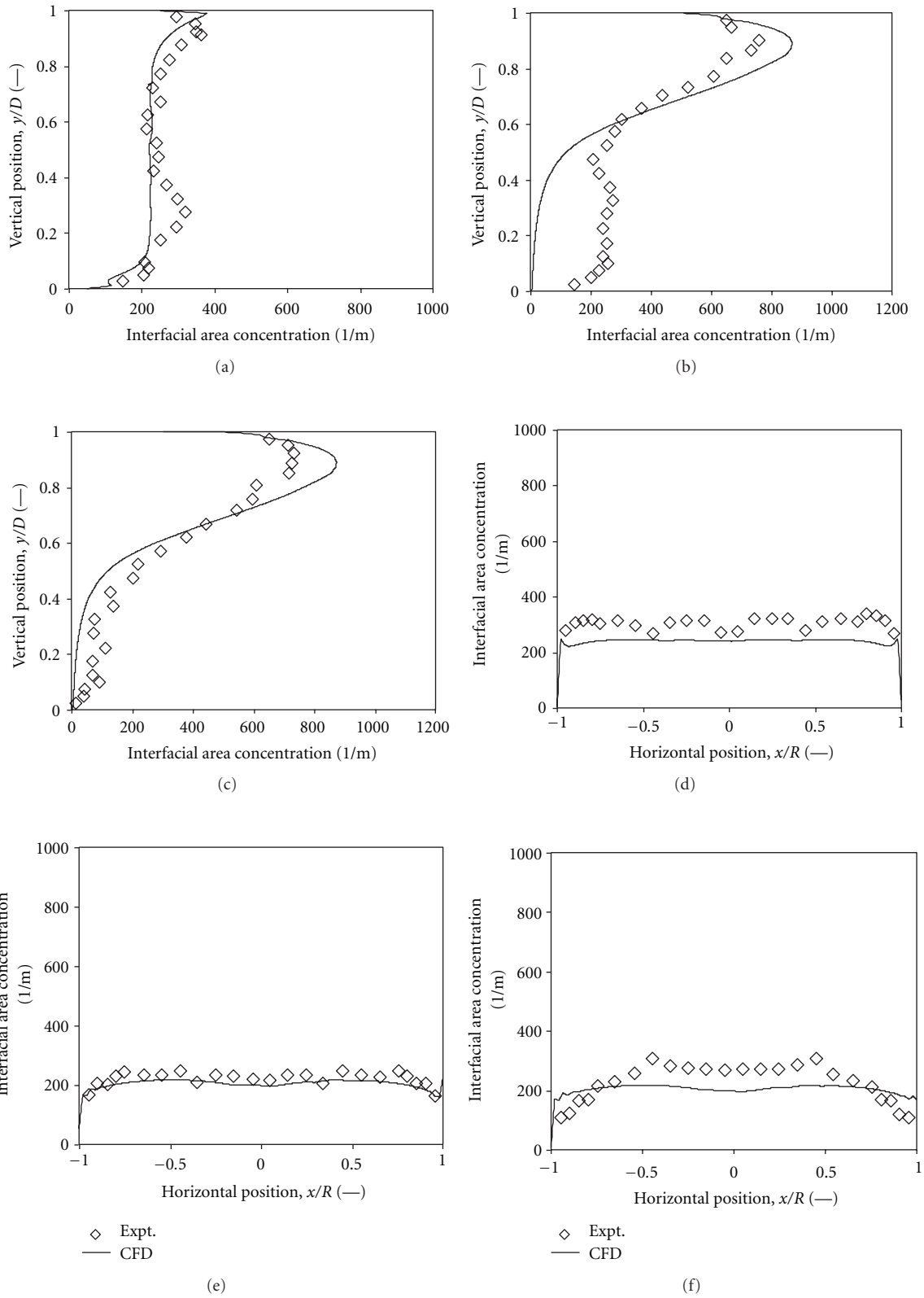


FIGURE 13: Interfacial area concentration (IAC) development in axial direction for superficial gas velocity is 1.21 m/s, superficial liquid velocity is 4.67 m/s, and average volume fraction is 0.205. At vertical position, (a) $L/D = 25$; (b) $L/D = 148$; (c) $L/D = 253$, at horizontal position, (d) $L/D = 25$; (e) $L/D = 148$; (f) $L/D = 253$.

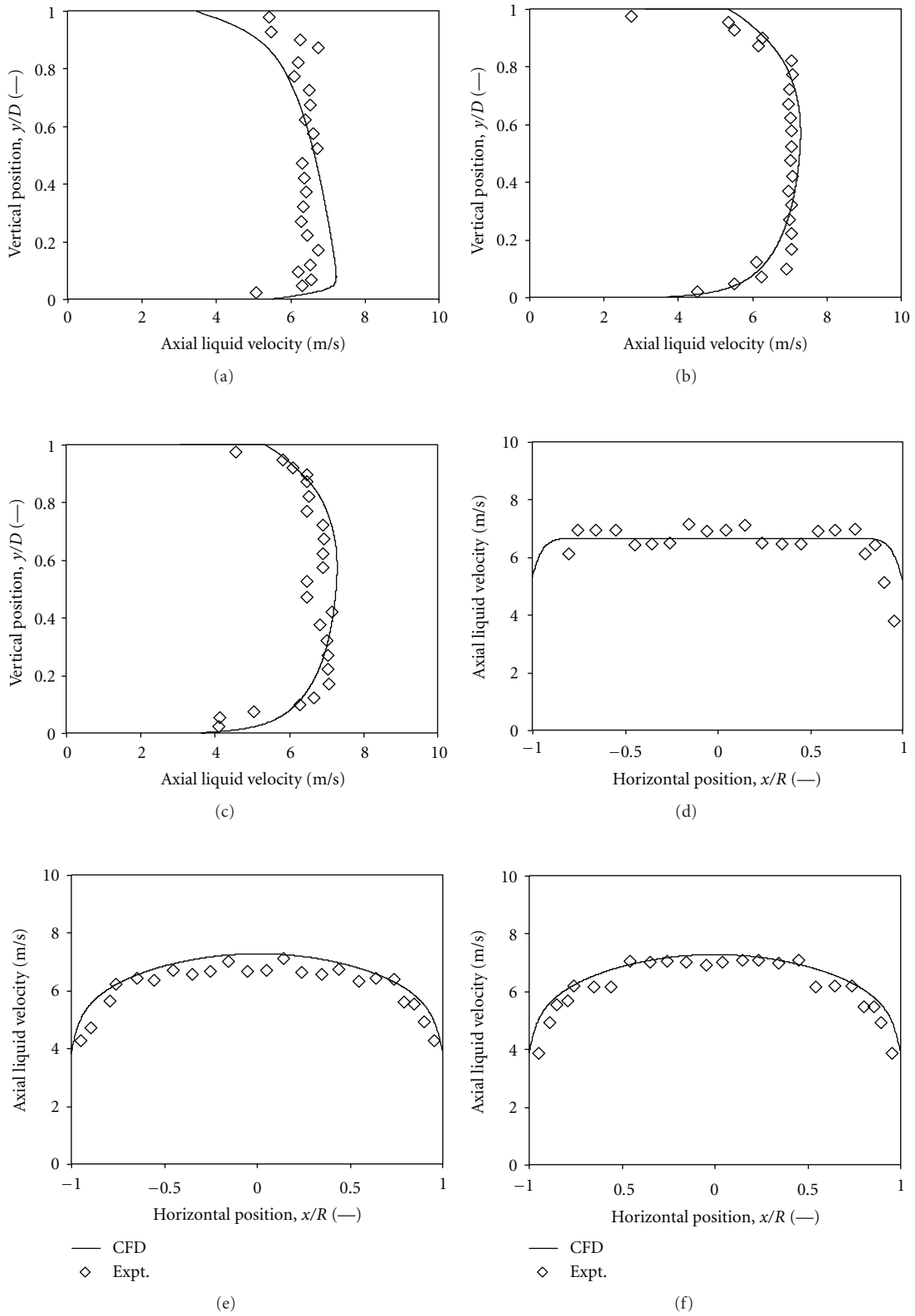


FIGURE 14: Liquid velocity development in axial direction for superficial gas velocity is 1.21 m/s, superficial liquid velocity is 4.67 m/s, and average volume fraction is 0.205. At vertical position, (a) $L/D = 25$; (b) $L/D = 148$; (c) $L/D = 253$, at horizontal position, (d) $L/D = 25$; (e) $L/D = 148$; (f) $L/D = 253$.

local gas volume fraction, interfacial area concentration, and axial liquid velocity in axial direction for the superficial gas velocity of 1.21 m/s and the superficial liquid velocity of 4.67 m/s. Good agreement can be seen between the predicted and experimental data at the axial location of $L/D = 25$. The gas volume fraction and interfacial area concentration do not show a significant variation in the vertical direction, near the entrance of the pipe ($L/D = 25$). This is because the bubble residence time was very small, and the transverse phase segregation due to the gravity has not been established yet. However, from first location ($L/D = 25$) to the second location ($L/D = 148$), the large differences can be observed. From second location ($L/D = 148$) to third location ($L/D = 253$), there is no significant difference was observed, but the fluid segregation due to the buoyancy is still effective. Further, it can be observed from Figure 14 that the axial liquid velocity profile shows nearly the same for all the locations. A slight change in the numerical values of the velocity can be attributed to the expansion of the gas phase associated with the frictional pressure gradient causing a continuous acceleration of the mixture in the axial direction.

5. Conclusions

A two-fluid model coupled with population balance approach is presented in this paper to handle gas-liquid bubbly flows in horizontal pipe. To demonstrate the application of the population balance approach, the average bubble number density transport equation was formulated and implemented for gas-liquid bubbly flows in the CFD code CFX 5.7 to determine the temporal and spatial geometrical changes of the gas bubbles. Population balance combined with coalescence and break-up models were taken into consideration. A detailed comparison has been presented between the CFD simulation and the experimental data reported by Kocamustafaogullari and Wang [17] and Kocamustafaogullari and Huang [1]. Good agreement was seen between the predicted and the experimental data of the volume fraction, interfacial area concentration, Sauter mean bubble diameter, and liquid velocity for a range of superficial gas (0.25 to 1.34 m/s) and liquid (3.74 to 5.1 m/s) velocities and volume fraction (4 to 21%). The experimental and simulated results indicate that the volume fraction and interfacial area concentration have local maxima near the upper pipe wall, and the profiles tend to flatten with increasing liquid flow rate. It was observed that the mean bubble diameter ranged from 1.5 to 5 mm, depending on the location and flow conditions. Further, it was found that increasing the gas flow rate at fixed liquid flow rate would increase the local volume fraction and interfacial area concentration. The simulation results were consistent with experimental observed from the literature. Further, the development of flow pattern was examined at three axial locations $L/D = 25$, 148, and 253. It was found that the prediction shows good agreement with experimental data. The axial liquid mean velocity showed a relatively uniform distribution except near the upper pipe wall. The flow in the bottom part of the pipe exhibits a fully developed turbulent pipe flow profile, whereas in the top of the pipe a different flow exists.

Acknowledgments

The authors gratefully acknowledge the financial support from the Natural Sciences and Engineering Research Council of Canada (NSERC) and Syncrude Canada Ltd. for this project.

References

- [1] G. Kocamustafaogullari and W. D. Huang, "Internal structure and interfacial velocity development for bubbly two-phase flow," *Nuclear Engineering and Design*, vol. 151, no. 1, pp. 79–101, 1994.
- [2] R. Krishna and J. M. van Baten, "Scaling up bubble column reactors with the aid of CFD," *Chemical Engineering Research and Design*, vol. 79, no. 3, pp. 283–309, 2001.
- [3] T. Hibiki and M. Ishii, "Development of one-group interfacial area transport equation in bubbly flow systems," *International Journal of Heat and Mass Transfer*, vol. 45, no. 11, pp. 2351–2372, 2002.
- [4] A. Kitagawa, K. Sugiyama, and Y. Murai, "Experimental detection of bubble-bubble interactions in a wall-sliding bubble swarm," *International Journal of Multiphase Flow*, vol. 30, no. 10, pp. 1213–1234, 2004.
- [5] Z. Xiao and R. B. H. Tan, "A model for bubble-bubble and bubble-wall interaction in bubble formation," *AIChE Journal*, vol. 52, no. 1, pp. 86–98, 2006.
- [6] D. Colella, D. Vinci, R. Bagatin, M. Masi, and E. Abu Bakr, "A study on coalescence and breakage mechanisms in three different bubble columns," *Chemical Engineering Science*, vol. 54, no. 21, pp. 4767–4777, 1999.
- [7] E. Olmos, C. Gentric, Ch. Vial, G. Wild, and N. Midoux, "Numerical simulation of multiphase flow in bubble column reactors. Influence of bubble coalescence and break-up," *Chemical Engineering Science*, vol. 56, no. 21–22, pp. 6359–6365, 2001.
- [8] F. Lehr, M. Millies, and D. Mewes, "Bubble-size distributions and flow fields in bubble columns," *AIChE Journal*, vol. 48, no. 11, pp. 2426–2443, 2002.
- [9] F. B. Campos and P. L. C. Lage, "A numerical method for solving the transient multidimensional population balance equation using an Euler-Lagrange formulation," *Chemical Engineering Science*, vol. 58, no. 12, pp. 2725–2744, 2003.
- [10] P. Chen, J. Sanyal, and M. P. Dudukovic, "CFD modeling of bubble columns flows: implementation of population balance," *Chemical Engineering Science*, vol. 59, no. 22–23, pp. 5201–5207, 2004.
- [11] J. Sanyal, D. L. Marchisio, O. Fox, and K. Dhanasekharan, "On the comparison between population balance models for CFD simulation of bubble columns," *Industrial and Engineering Chemistry Research*, vol. 44, no. 14, pp. 5063–5072, 2005.
- [12] H. A. Jakobsen, H. Lindborg, and C. A. Dorao, "Modeling of bubble column reactors: progress and limitations," *Industrial and Engineering Chemistry Research*, vol. 44, no. 14, pp. 5107–5151, 2005.
- [13] Z. Sha, A. Laari, and I. Turunen, "Multi-phase-multi-size group model for the inclusion of population balances into the CFD simulation of gas-liquid bubbly flows," *Chemical Engineering and Technology*, vol. 29, no. 5, pp. 550–559, 2006.
- [14] T. Wang, J. Wang, and Y. Jin, "A CFD-PBM coupled model for gas-liquid flows," *AIChE Journal*, vol. 52, no. 1, pp. 125–140, 2006.
- [15] S. Lo, "Application of the MUSIG model to bubbly flows," AEAT-1096, AEA Technology, 1996.

- [16] G. H. Yeoh and J. Y. Tu, "Population balance modelling for bubbly flows with heat and mass transfer," *Chemical Engineering Science*, vol. 59, no. 15, pp. 3125–3139, 2004.
- [17] G. Kocamustafaogullari and Z. Wang, "An experimental study on local interfacial parameters in a horizontal bubbly two-phase flow," *International Journal of Multiphase Flow*, vol. 17, no. 5, pp. 553–572, 1991.
- [18] H. Luo and H. F. Svendsen, "Theoretical model for drop and bubble break-up in turbulent dispersions," *AIChE Journal*, vol. 42, no. 5, pp. 1225–1233, 1996.
- [19] M. J. Prince and H. W. Blanch, "Bubble coalescence and break-up in air-sparged bubble columns," *AIChE Journal*, vol. 36, no. 10, pp. 1485–1499, 1990.
- [20] T. O. Oolman and H. W. Blanch, "Bubble coalescence in stagnant liquids," *Chemical Engineering Communications*, vol. 43, no. 4–6, pp. 237–261, 1986.
- [21] A. K. Chesters and G. Hofman, "Bubble coalescence in pure liquids," *Applied Scientific Research*, vol. 38, no. 1, pp. 353–361, 1982.
- [22] R. D. Kirkpatrick and M. J. Lockett, "The influence of approach velocity on bubble coalescence," *Chemical Engineering Science*, vol. 29, no. 12, pp. 2363–2373, 1974.
- [23] J. W. Kim and W. K. Lee, "Coalescence behavior of two bubbles in stagnant liquids," *Journal of Chemical Engineering of Japan*, vol. 20, no. 5, pp. 448–453, 1987.
- [24] J. C. Rotta, *Turbulente Stromungen*, B. G. Teubner, Stuttgart, Germany, 1974.
- [25] H. Anglart and O. Nylund, "CFD application to prediction of void distribution in two-phase bubbly flows in rod bundles," *Nuclear Engineering and Design*, vol. 163, no. 1-2, pp. 81–98, 1996.
- [26] R. T. Lahey Jr. and D. A. Drew, "The analysis of two-phase flow and heat transfer using a multidimensional, four field, two-fluid model," *Nuclear Engineering and Design*, vol. 204, no. 1–3, pp. 29–44, 2001.
- [27] J. B. Joshi, "Computational flow modelling and design of bubble column reactors," *Chemical Engineering Science*, vol. 56, no. 21-22, pp. 5893–5933, 2001.
- [28] R. Clift, J. R. Grace, and M. E. Weber, *Bubbles, Drops, and Particles*, Academic Press, New York, NY, USA, 1978.
- [29] J. B. Joshi, U. V. Parasu, Ch. V. Prasad et al., "Gas holdup structures in bubble column reactors," *Proceedings of the Indian National Science Academy*, vol. 64, pp. 441–567, 1998.
- [30] I. Zun, "The transverse migration of bubbles influenced by walls in vertical bubbly flow," *International Journal of Multiphase Flow*, vol. 6, no. 6, pp. 583–588, 1980.
- [31] N. H. Thomas, T. R. Auton, K. Sene, and J. C. R. Hunt, "Entrapment and transport of bubbles by transient large eddies in turbulent shear flow," in *Proceedings of the BHRA International Conference on the Physical Modelling of Multi-Phase Flow*.
- [32] D. A. Drew and S. L. Passman, *Theory of Multicomponent Fluids*, Springer, New York, NY, USA, 1999.
- [33] A. Tomiyama, "Drag, lift and virtual mass forces acting on a single bubble," in *Proceedings of the 3rd International Symposium on Two-Phase Flow Modelling and Experimentation*, pp. 22–24, Pisa, Italy, September 2004.
- [34] S. P. Antal, R. T. Lahey, and J. E. Flaherty, "Analysis of phase distribution in fully developed laminar bubbly two-phase flow," *International Journal of Multiphase Flow*, vol. 17, no. 5, pp. 635–652, 1991.
- [35] M. A. Lopez de Bertodano, *Turbulent bubbly two-phase flow in a triangular duct*, Ph. D. dissertation, Rensselaer Polytechnic Institute, 1992.
- [36] M. Ishii and N. Zuber, "Drag coefficient and relative velocity in bubbly, droplet or particulate flows," *AIChE Journal*, vol. 25, no. 5, pp. 843–855, 1979.
- [37] T. R. Auton, "The lift force on a spherical body in a rotational flow," *Journal of Fluid Mechanics*, vol. 183, pp. 199–218, 1987.
- [38] M. A. Lopez de Bertodano, R. T. Lahey Jr., and O. C. Jones, "Phase distribution in bubbly two-phase flow in vertical ducts," *International Journal of Multiphase Flow*, vol. 20, no. 5, pp. 805–818, 1994.
- [39] M. Lance and M. A. Lopez de Bertodano, "Phase distribution and wall effects in bubbly two-phase flows," *Multiphase Science and Technology*, vol. 8, no. 1–4, pp. 69–123, 1994.
- [40] A. Tomiyama, A. Sou, I. Zun, N. Kanami, and T. Sakaguchi, "Effects of Eotvos number and dimensionless liquid volumetric flux on lateral motion of a bubble in a laminar duct flow," in *Advances in Multiphase Flow*, pp. 3–15, 1995.
- [41] A. Tomiyama, H. Tamai, I. Zun, and S. Hosokawa, "Transverse migration of single bubbles in simple shear flows," *Chemical Engineering Science*, vol. 57, no. 11, pp. 1849–1858, 2002.
- [42] Y. Sato and K. Sekoguchi, "Liquid velocity distribution in two-phase bubble flow," *International Journal of Multiphase Flow*, vol. 2, no. 1, pp. 79–95, 1975.
- [43] R. D. S. Cavalcanti, S. R. D. Neto, and E. O. Vilar, "A computational fluid dynamics study of hydrogen bubbles in an electrochemical reactor," *Brazilian Archives of Biology and Technology*, vol. 48, pp. 219–229, 2005.
- [44] J. Y. Tu, G. H. Yeoh, G. C. Park, and M. O. Kim, "On population balance approach for subcooled boiling flow prediction," *Journal of Heat Transfer*, vol. 127, no. 3, pp. 253–264, 2005.
- [45] D. Legendre and J. Magnaudet, "The lift force on a spherical bubble in a viscous linear shear flow," *Journal of Fluid Mechanics*, vol. 368, pp. 81–126, 1998.
- [46] G. Kocamustafaogullari, W. D. Huang, and J. Razi, "Measurement and modeling of average void fraction, bubble size and interfacial area," *Nuclear Engineering and Design*, vol. 148, no. 2-3, pp. 437–453, 1994.
- [47] A. Iskandrani and G. Kojasoy, "Local void fraction and velocity field description in horizontal bubbly flow," *Nuclear Engineering and Design*, vol. 204, no. 1–3, pp. 117–128, 2001.